

COMPTES RENDUS DE L'ACADÉMIE DES SCIENCES

1778-7025 (electronic)

Géoscience *Sciences de la Planète*



Volume 353, Special Issue S2, 2021

Special issue / Numéro thématique

Perspectives on alkaline magmas / *Perspectives sur les magmas alcalins*

Guest editor / Rédacteur en chef invité

Bruno Scaillet

Académie des sciences — Paris



INSTITUT DE FRANCE
Académie des sciences



Comptes Rendus

Géoscience

Objective of the journal

Comptes Rendus Géoscience is an internationally peer-reviewed electronic journal covering the full range of earth sciences and sustainable development. It publishes original research articles, review articles, historical perspectives, pedagogical texts, and conference proceedings of unlimited length, in English or French. *Comptes Rendus Géoscience* is published according to a virtuous policy of diamond open access, free of charge for authors (no publication fees) as well as for readers (immediate and permanent open access).

Editorial director: Étienne Ghys

Editors-in-chief: Éric Calais, Michel Campillo, François Chabaux, Ghislain de Marsily

Editorial Board: Jean-Claude André, Pierre Auger, Mustapha Besbes, Sylvie Bourquin, Yves Bréchet, Marie-Lise Chanin, Philippe Davy, Henri Décamps, Sylvie Derenne, Michel Faure, François Forget, Claude Jaupart, Jean Jouzel, Eric Karsenti, Amaëlle Landais, Sandra Lavorel, Yvon Le Maho, Mickaele Le Ravalec, Hervé Le Treut, Benoit Noetinger, Carole Petit, Valérie Plagnes, Pierre Ribstein, Didier Roux, Bruno Scaillet, Marie-Hélène Tusseau-Vuillemin, Élisabeth Vergès

Editorial secretary: Adenise Lopes

About the journal

All journal's information, including the text of published articles, which is fully open access, is available from the journal website at <https://comptes-rendus.academie-sciences.fr/geoscience/>.

Author enquiries

For enquiries relating to the submission of articles, please visit this journal's homepage at <https://comptes-rendus.academie-sciences.fr/geoscience/>.

Contact

Académie des sciences

23, quai de Conti, 75006 Paris, France

Tel: (+33) (0)1 44 41 43 72

CR-Geoscience@academie-sciences.fr



The articles in this journal are published under the license
Creative Commons Attribution 4.0 International (CC-BY 4.0)
<https://creativecommons.org/licenses/by/4.0/deed.en>



Contents / Sommaire

Bruno Scaillet	
Perspectives on alkaline magmas	1-5
Ray Macdonald, John C. White, Harvey E. Belkin	
Peralkaline silicic extrusive rocks: magma genesis, evolution, plumbing systems and eruption	7-59
Violaine Sautter, Valerie Payre	
Alkali magmatism on Mars: an unexpected diversity	61-90
Daniele Maestrelli, Giacomo Corti, Marco Bonini, Domenico Montanari, Federico Sani	
Caldera collapse and tectonics along the Main Ethiopian Rift: reviewing possible relationships	91-109
Silvio G. Rotolo, Stéphane Scaillet, Fabio Speranza, John C. White, Rebecca Williams, Nina J. Jordan	
Volcanological evolution of Pantelleria Island (Strait of Sicily) peralkaline volcano: a review	111-132
Nina J. Jordan, John C. White, Ray Macdonald, Silvio G. Rotolo	
Evolution of the magma system of Pantelleria (Italy) from 190 ka to present	133-149
Paola Stabile, Fabio Arzilli, Michael Robert Carroll	
Crystallization of peralkaline rhyolitic magmas: pre- and syn-eruptive conditions of the Pantelleria system	151-170
Ray Macdonald, Bogusław Bagiński, Marcin Stachowicz, Harvey E. Belkin, Jan Pawłowski, Jakub Kotowski	
Magma mixing and exsolution phenomena in peralkaline rhyolites: insights from the Gold Flat Tuff, Nevada	171-186
Ali Akbar Khezerlou, Michel Grégoire, Nasir Amel, Mohsen Moayyed, Ahmad Jahangiri, Mohammad Kilzi	
Whole rock and mineral chemistry of hornblenditic xenoliths in volcanic alkaline rocks from the northern part of Uromieh Dokhtar magmatic belt (NW Iran)	187-215
Valentin Mollé, Fabrice Gaillard, Zineb Naby, Johann Tuduri, Ida Di Carlo, Saskia Erdmann	
Crystallisation sequence of a REE-rich carbonate melt: an experimental approach ...	217-231
Zineb Naby, Fabrice Gaillard, Johann Tuduri, Ida Di Carlo	
No direct effect of F, Cl and P on REE partitioning between carbonate and alkaline silicate melts	233-272

Lydéric France, Florian Brouillet, Sarah Lang

Early carbonatite magmatism at Oldoinyo Lengai volcano (Tanzania): carbonatite–silicate melt immiscibility in Lengai I melt inclusions 273-288

María Jiménez-Mejías, Joan Andújar, Bruno Scaillet, Ramón Casillas

Experimental determination of H₂O and CO₂ solubilities of mafic alkaline magmas from Canary Islands 289-314

Pierangelo Romano, Ida Di Carlo, Joan Andújar, Silvio G. Rotolo

Water solubility in trachytic and pantelleritic melts: an experimental study 315-331



Perspectives on alkaline magmas / *Perspectives sur les magmas alcalins*

Perspectives on alkaline magmas

Bruno Scaillet^{® a}

^a Institut des Sciences de la Terre d'Orléans, UMR 7327, Université
d'Orléans-CNRS-BRGM, 1a rue de la Férollerie, 45071, Orléans, France
E-mail: bruno.scaillet@cnrs.fr

Although volumetrically minor on Earth [e.g. Marks and Markl, 2017], magmas rich in alkalis are actively studied for several reasons. One is that they represent a significant component in the building of many volcanic islands, notably those related to active hotspot settings [e.g. Jeffery and Gertisser, 2018], hence a threat for those islands which are densely populated. The study of such islands offers also a unique geochemical window into the functioning of deep seated structures (in the lower mantle) that ultimately feed many of these oceanic volcanoes [e.g. Moreira et al., 2012]. Alkali magmas are similarly abundant in the intermediate stage of rift-related settings, and perhaps the best example of such an occurrence is nowadays represented by the East African rift zone [e.g. Macdonald, 2002]. There, besides the volcanic hazards associated with active alkali magmatic centres [e.g. Biggs et al., 2011], interest in their study comes from the geothermal energy they fuel [Varet, 2020]: such a C-free and local source of energy is actively exploited in countries hosting the rift zone, such as Kenya or Ethiopia, to the benefit of their populations.

Another socio-economic reason is that alkali magma series end with fractionated products notoriously rich in many rare metals (Nb, Ta, ...) which are vital for the functioning of modern societies (<https://eos.org/science-updates/geological-surveys-unite-to-improve-critical-mineral-security>).

But why it is so? Peralkaline rhyolites, termed comendites or pantellerites, and possibly many of

their undersaturated counterparts (phonolites sensu lato), are largely believed to be the by-products of extensive (>80%) basalt fractionation [Macdonald et al., 2021a], carrying with them all elements not easily incorporated in the structure of the main rock-forming minerals. The excess of alkalis over alumina (i.e., peralkaline) that typifies oversaturated and most undersaturated alkaline felsic magmas, is a key contributing factor that boosts the potential of the silicate melt to accommodate many elements (ions having high field strength or large radius), which are otherwise excluded from its structure (such as it happens in metaluminous liquids). This chemical effect induces an equally important physical one: the excess of alkalis is indeed known to decrease the viscosity of silicate melts [Dingwell et al., 1998], which facilitates melt segregation processes, hence the potential for the system to isolate sizeable metal-rich bodies. Along the same line of reasoning, the propensity and capacity of alkali magmas to concentrate climate affecting species, such as halogens or sulphur [Scaillet and Macdonald, 2006], is also a major reason to study them so as to quantify the volatile yields into the atmosphere of their eruptions, and their short to long term environmental impact [e.g. Oppenheimer, 2003].

When the parental basalt is rich in alkalis, it typically gives rise to phonolite magmas as common felsic derivatives. In general, the richness of the parental basalt in alkalis reflects the largely incompatible behaviour of alkalis during the incipient stages of

partial melting of a “normal” mantle. But it is worth noting that it can be also due to the metasomatism of the same mantle (leading to its enrichment in alkalis) by a geodynamic process, such as subduction. Possible examples of the latter process include the threatful Vesuvius–Campi Flegrei or Tambora volcanoes [Cioni et al., 1995, Orsi et al., 1996, Self et al., 2004], which, though related to a subduction context, have produced abundant evolved alkali magmas (phonolite–trachyte), in sharp contrast to common convergent zones whose prevailing magmatic output is characterized by the andesite–dacite–rhyolite sub-aluminous association.

In some instances at least, the fractionation towards undersaturated derivatives can go a step further, producing carbonatites, possibly via immiscibility with a silicate melt [Hamilton et al., 1979]: hence, this magmatic series is characterized by a binary end point, so to speak, and not by the phonolite eutectic alone as a cursory look of the petrogeny residua system would suggest: for that reason (extensive fractionation), carbonatites may concentrate a bunch of industrially important elements, in particular the Rare Earth Elements (REE), that make these rocks so interesting. But carbonatites may equally represent the very first moment of mantle partial melting [e.g. Gaillard et al., 2008], being for that reason extremely enriched in some critical elements as well: having the same term to quote either the start or the end of an evolutionary process is a source of ambiguity, to say the least, and clearly of confusion for teaching. It underscores the limits of current terminology to classify rocks, and in any case their limited petrogenetic value, at least to anyone interested in putting numbers on the process (which temperature, which pressure, which water content, which $fO_2 \dots$?). Save the grand categories, that is, a basalt will be almost always hotter than a rhyolite, simplifying rock terminology should be a general objective of future studies. A more fundamental reason to keep working on alkali magmas is their recent discovery as abundant rocks outcropping on the surface of Mars [Stolper et al., 2013], a planet free of plate tectonic motion as we know it on Earth, which therefore calls perhaps for a different mode of alkali magma production on the distant red body relative to what happens on our blue one.

Defining the conditions of alkali magmas production and evolution, that is, their pressure–

temperature–redox path, their volatile and metal endowments, or their lifetime, is therefore essential to take full advantage of the beneficial aspects of this peculiar magmatism for what concerns its usage in our society, but also to understand the evolution of planets and rocky bodies populating the Solar system. In this special issue, some strands of the different aspects listed above are addressed or reviewed.

Macdonald et al. [2021a] report a detailed state of the art of the occurrence and petrogenesis of the quartz-saturated variety of the alkaline clan (comendite, pantellerite), reviewing *inter alia* the geodynamic context, mode of production and evolution till eruption of such magmas, using for that purpose all information available. Sautter and Payre [2021], provide an informative review of our current knowledge about the magmatic alkali rocks which have been revealed by orbiting spacecrafts or those scrutinized so far by the rovers/landers active on the surface of Mars, and the implications of these findings for magma production on Mars, as well as for the petrogenesis of Martian meteorites which were until recently the only accessible rocks of that planet. Maestrelli et al. [2021] take on a terrestrial tectonic perspective and review the relationships between the rift evolution and calderas in an area, the East African Rift, where the peralkaline rhyolites were first used by Norman L. Bowen, the father of modern igneous petrology, to propose a mechanism able to drive a liquid from a metaluminous towards a peralkaline condition [via the so-called plagioclase effect, Bowen, 1937]. More specifically, Maestrelli et al. [2021] look at calderas in the central portion of the Main Ethiopian Rift. These structures are the geomorphologic evidence left over by powerful, and devastating if they were to happen today, ignimbrite-forming eruptions. They are rooted into shallow reservoirs hosting peralkaline rhyolites, and their shape and orientation bear evidence, these authors conclude, of the intimate links existing between volcanism and tectonic in this area, but also of the possible role played by pre-existing tectonic structures on the architecture of plumbing systems feeding volcanoes in rift settings.

Rotolo et al. [2021] present the current state of knowledge of the volcanological evolution of the island of Pantelleria, where the term pantellerite was coined, in large part because more than 80% of rocks outcropping there is made of well pre-



Figure 1. Photograph of the 2021 Cumbre Vieja eruption at La Palma, Canary islands. The picture shows the land around the newly born cone covered by the tephra produced by the explosive fragmentation of the H_2O – CO_2 –S-rich erupting alkali basalt (dark, ash-rich, clouds), and the same but more degassed basalt feeding a glowing lava fountain supplying a descending lava flow (Photograph by B. Scaillet).

served strongly peralkaline rhyolites. Their review of available geochronological data and field constraints on volumes of magma erupted led them to suggest that the volcanic activity at Pantelleria may well be on a waning trend. Jordan et al. [2021] review in turn the petrological and geochemical evidence of magma evolution in the reservoirs active beneath Pantelleria during the last 190 ky, where the pantellerites and associated trachytes were stored, stressing out the extensive fractionation process that such magmas require to be produced, as illustrated by the extreme enrichment (Zr, Nb, Cl...) or depletion (Sr, Ni,...) that some elements achieve. They also suggest that comendite and pantellerite liquids may signal different conditions of magma evolution, comendites reflecting deeper and more oxidized conditions than pantellerites. Stabile et al. [2021] focus on the determination of pre-eruptive conditions of those magmas, but also on what happens during their decompression in the conduit, both aspects being considered in light of available experimental constraints, highlighting the difference with the more viscous metaluminous rhyolites, notably with respect to the conditions leading to magma fragmentation during

eruption.

Macdonald et al. [2021b] illustrate how a detailed mineralogical and crystallographical study can give information on processes of magma evolution, in this particular case mixing, using the example of the Gold Flatt Tuff, an extensive peralkaline ignimbrite sheet outcropping in Nevada, USA. In doing so, they report also the first occurrence of chevkinite-group minerals in a pantellerite: chevkinite is a Ti- and REE-rich mineral that reflects the extreme content in some elements (LREE) reached by these magmas and the authors suggest it may replace aenigmatite, another Ti-bearing silicate diagnostic of the peralkaline condition in evolved magmas. Khezerlou et al. [2021] study shows what can be learnt about the mantle source of some alkali magmas, by looking at mantle xenoliths brought up to the surface by alkali basalts from the Uromieh Dokhtar magmatic belt in NW Iran, which the authors show, may inherit their alkali character from a previous subduction event. Mollé et al. [2021] report new experiments bearing on the stability of bastnaesite, the main REE host mineral in carbonatites, concluding that this phase is most likely hydrothermal in origin, not magmatic. Similarly, Nabyl

et al. [2021] provide experimental constraints on the partitioning of REE between carbonatites and conjugate silicate liquids, exploring in particular the role of F, Cl, or P. The experimental results lead the authors to conclude that these elements play no significant role on REE behaviour in carbonatites. France et al. [2021] use rocks erupted 11 ky ago by the only active carbonatite volcano on Earth, Oldoinyo Lengai in Tanzania [Dawson, 1964]. They document, via the study of melt inclusions hosted by nepheline, the coexistence of silicate and carbonate liquids, concluding that immiscibility is a long lasting process in the Oldoinyo Lengai reservoir, showing in addition that it operates over a significant temperature interval.

The two last papers of the volume bear on the volatiles cargo of alkali magmas. Jiménez Maria et al. [2021] have experimentally defined the solubility laws of water and CO₂ in alkali basalts from Tenerife in the Canary archipelago, which were emitted recently on that island, being similar in composition to those erupted nearby either at El Hierro island in 2011 or to that ejected by La Palma's current eruption (at this time of writing, Figure 1). The new experimental constraints allow the authors to get refined pressure estimates of magma storage regions of Canarian basaltic volcanism, which is an important piece of information in the context of volcanic hazard assessment. Finally, Romano et al. [2021] revisit the solubility of water in peralkaline rhyolite and trachyte melts, providing improved experimental constraints on this topic, in an effort to better define the pressure depth of the magma reservoirs feeding peralkaline felsic eruptions on the still active Pantelleria island and elsewhere.

The papers that constitute this special issue obviously do not cover all aspects of alkali magmas, but illustrate nicely the variety of concerns behind them and the diversity in approaches used to document, characterize, and ultimately understand this fascinating clan.

Conflicts of interest

Author have no conflict of interest to declare.

Acknowledgements

Bruno Scaillet acknowledges support from both LabEx VOLTAIRE (LABX-100-01) and EquipEx

PLANEX (ANR-11-EQPX-0036) projects, which made the laboratory work reported in several papers of this special issue possible. He also warmly thanks François Chabaux for his supervision of this special issue and Adenise Lopes for her efficient help in the editorial processing.

References

- Biggs, J., Bastow, I. D., Keir, D., and Lewi, E. (2011). Pulses of deformation reveal frequently recurring shallow magmatic activity beneath the Main Ethiopian Rift. *Geochem. Geophys. Geosyst.*, 12(9), article no. Q0AB10.
- Bowen, N. L. (1937). Recent high-temperature research on silicates and its significance in igneous geology. *Am. J. Sci.*, 5(193), 1–21.
- Cioni, R., Civetta, L., Marianelli, P., Metrich, N., Santacroce, R., and Sbrana, A. (1995). Compositional layering and syn-eruptive mixing of a periodically refilled shallow magma chamber: the AD 79 Plinian eruption of Vesuvius. *J. Petrol.*, 36(3), 739–776.
- Dawson, J. B. (1964). Carbonatitic volcanic ashes in northern Tanganyika. *Bull. Volcanol.*, 27(1), 81–91.
- Dingwell, D. B., Hess, K. U., and Romano, C. (1998). Extremely fluid behavior of hydrous peralkaline rhyolites. *Earth Planet. Sci. Lett.*, 158(1-2), 31–38.
- France, L., Brouillet, F., and Lang, S. (2021). Early carbonatite magmatism at Oldoinyo Lengai volcano (Tanzania): carbonatite-silicate melt immiscibility in Lengai I melt inclusions. *C. R. Geosci.*, 353(S2), 273–288.
- Gaillard, F., Malki, M., Iacono-Marziano, G., Pichavant, M., and Scaillet, B. (2008). Carbonatite melts and electrical conductivity in the asthenosphere. *Science*, 322(5906), 1363–1365.
- Hamilton, D. L., Freestone, I. C., Dawson, J. B., and Donaldson, C. H. (1979). Origin of carbonatites by liquid immiscibility. *Nature*, 279(5708), 52–54.
- Jeffery, A. J. and Gertisser, R. (2018). Peralkaline felsic magmatism of the Atlantic islands. *Front. Earth Sci.*, 6, article no. 145.
- Jiménez Maria, M., Andújar, J., Scaillet, B., and Casilas, R. (2021). Experimental determination of H₂O and CO₂ solubilities of mafic alkaline magmas from Canary Islands. *C. R. Geosci.*, 353(S2), 289–314.

- Jordan, N., White, J., Macdonald, R., and Rotolo, S. (2021). Evolution of the magma system of Pantelleria (Italy) from 190 ka to present. *C. R. Geosci.*, 353(S2), 133–149.
- Khezerlou, A. A., Grégoire, M., Nasir, A., Mohsen, M., Ahmad, J., and Mohammad, K. (2021). Whole rock and mineral chemistry of hornblenditic xenoliths in volcanic alkaline rocks from the northern part of Uromieh Dokhtar magmatic belt (NW Iran). *C. R. Geosci.*, 353(S2), 187–215.
- Macdonald, R. (2002). Magmatism of the Kenya Rift Valley: a review. *Earth Environ. Sci. Trans. R. Soc. Edinb.*, 93(3), 239–253.
- Macdonald, R., Baginski, B., Stachowicz, M., Belkin, H., Pawłowski, J., and Kotowski, J. (2021a). Magma mixing and exsolution phenomena in peralkaline rhyolites: insights from the Gold Flat Tuff, Nevada. *C. R. Geosci.*, 353(S2), 171–186.
- Macdonald, R., White, J., and Belkin, H. (2021b). Peralkaline silicic extrusive rocks: magmagenesis, evolution, plumbing systems and eruption. *C. R. Geosci.*, 353(S2), 7–59.
- Maestrelli, D., Corti, G., Bonini, M., Montanari, D., and Sani, F. (2021). Caldera collapse and tectonics along the Main Ethiopian rift: reviewing possible relationships. *C. R. Geosci.*, 353(S2), 91–109.
- Marks, M. A. and Markl, G. (2017). A global review on agpaitic rocks. *Earth Sci. Rev.*, 173, 229–258.
- Mollé, V., Gaillard, F., Naby, Z., Tuduri, J., Di Carlo, I., and Erdmann, S. (2021). Crystallisation sequence of a REE-rich carbonate melt: an experimental approach. *C. R. Geosci.*, 353(S2), 217–231.
- Moreira, M., Kanzari, A., and Madureira, P. (2012). Helium and neon isotopes in São Miguel island basalts, Azores Archipelago: New constraints on the “low ^3He ” hotspot origin. *Chem. Geol.*, 322, 91–98.
- Naby, Z., Gaillard, F., Tuduri, J., and Di Carlo, I. (2021). No direct effect of F, Cl and P on REE partitioning between carbonate and alkaline silicate melts. *C. R. Geosci.*, 353(S2), 233–272.
- Oppenheimer, C. (2003). Climatic, environmental and human consequences of the largest known historic eruption: Tambora volcano (Indonesia) 1815. *Prog. Phys. Geogr.*, 27(2), 230–259.
- Orsi, G., De Vita, S., and Di Vito, M. (1996). The restless, resurgent Campi Flegrei nested caldera (Italy): constraints on its evolution and configuration. *J. Volcanol. Geotherm. Res.*, 74(3–4), 179–214.
- Romano, P., Di Carlo, I., Andújar, J., and Rotolo, S. G. (2021). Water solubility in trachytic and pantelleritic melts: an experimental study. *C. R. Geosci.*, 353(S2), 315–331.
- Rotolo, S. G., Scaillet, S., Speranza, F., White, J. C., Williams, R., and Jordan, N. J. (2021). Volcanological evolution of Pantelleria Island (Strait of Sicily) peralkaline volcano: a review. *C. R. Geosci.*, 353(S2), 111–132.
- Sautter, V. and Payre, V. (2021). Alkali magmatism on Mars: an unexpected diversity. *C. R. Geosci.*, 353(S2), 61–90.
- Scaillet, B. and Macdonald, R. (2006). Experimental and thermodynamic constraints on the sulphur yield of peralkaline and metaluminous silicic flood eruptions. *J. Petrol.*, 47(7), 1413–1437.
- Self, S., Gertisser, R., Thordarson, T., Rampino, M. R., and Wolff, J. A. (2004). Magma volume, volatile emissions, and stratospheric aerosols from the 1815 eruption of Tambora. *Geophys. Res. Lett.*, 31(20).
- Stabile, P., Arzilli, F., and Carroll, M. R. (2021). Crystallization of peralkaline rhyolitic magmas: pre- and syn-eruptive conditions of the Pantelleria system. *C. R. Geosci.*, 353(S2), 151–170.
- Stolper, E. M. et al. (2013). The petrochemistry of Jake_M: A Martian mugearite. *Science*, 341(6153), article no. 1239463.
- Varet, J. (2020). Developing geothermal energy at local level in Africa: “Geothermal Village” R&D project. In *First EAGE Workshop on Geothermal Energy and Hydro Power in Africa*, volume 2020, pages 1–5. European Association of Geoscientists & Engineers.



Perspectives on alkaline magmas / *Perspectives sur les magmas alcalins*

Peralkaline silicic extrusive rocks: magma genesis, evolution, plumbing systems and eruption

Ray Macdonald^{a, b}, John C. White^{*, c} and Harvey E. Belkin^{*, d}

^a Department of Geochemistry, Mineralogy and Petrology, University of Warsaw, 02-089 Warszawa, Poland

^b Environment Centre, Lancaster University, Lancaster LA1 4YQ, UK

^c Department of Physics, Geosciences & Astronomy, Eastern Kentucky University, Richmond, KY 40475, USA

^d U.S. Geological Survey, 11142 Forest Edge Drive, Reston, VA 20190-4026, USA

E-mails: raymacdonald186@gmail.com (R. Macdonald), john.white@eku.edu (J. C. White), harveybelkin@gmail.com (H. E. Belkin)

Abstract. Peralkaline silicic extrusive rocks are an important component of the volcanological record. Here we review several aspects of their formation and evolution, including the tectonic settings in which they occur, their main petrological and geochemical features, the magmatic lineages along which they evolve, and the parameters (T , P , fO_2 , melt water contents) that control the lineages. Particular attention is paid to the composition of the extraordinary melts formed at the lowest temperatures. Various lines of evidence are presented to explain the silica gaps in some lineages. The partial melting of continental crust and the role of crustal contamination are considered to be of relatively minor importance in their genesis. High P - T experiments aimed at quantifying the lineages are assessed. Geophysical and petrological evidence for the depth and nature of the plumbing systems are presented. Differentiation mechanisms within reservoirs and the ubiquity of the formation of compositional zonation are discussed, as are the timescales involved. Volcanic hazards and the environmental impact of eruptions are described and a brief assessment of the ore potential of the extrusives is given.

Keywords. Peralkaline silicic rocks, Tectonic settings, Plumbing systems, Hazards, Ore potential.

Available online 8th December 2021

1. Introduction

The focus of the review is on sequences of extrusive rocks that include peralkaline (Peralkaline Index, P.I. = mol. $(Na_2O + K_2O)/Al_2O_3 > 1$) and silica-oversaturated (quartz-normative) members, i.e., quartz trachytes and rhyolites. Peralkaline phonolites

are not included, hence the term silicic is preferred to felsic, which would include silica-undersaturated and silica-oversaturated rocks. Classification of the rocks of the various sequences is by the total alkalis-silica scheme [Le Bas et al., 1986]; the peralkaline types are further classified using the scheme of Macdonald [1974].

Peralkaline silicic extrusive rocks play important roles in many aspects of volcanology, petrology, geochemistry, economic geology and volcanic hazards.

* Corresponding author.

(1) They can form large volumes of eruptive material, resulting in significant additions to crustal growth. For example, Oligocene ignimbrites of the western plateau in Ethiopia had a dense-rock-equivalent volume of at least 60,000 km³ [Ayalew *et al.*, 2002]. Within the Main Ethiopian Rift, peralkaline rhyolites represent 90% of the volcanic products [Trua *et al.*, 1999]. A phase of pantelleritic activity in central Kenya at 6.36–8.13 Ma originally covered an area of 40,000 km² [Claessens *et al.*, 2016]. The Deccan flood basalts, India, have a preserved volume of 1.5×10^6 km³. Peralkaline rhyolites associated with them have a volume between 500 and 1000 km³ [Lightfoot *et al.*, 1987] and could have had a volume of 50,000 km³ [Javoy and Courtillot, 1989].

(2) In the past 20 years, there has been a remarkable surge in our understanding of magmatic systems. Volcanological and petrological studies of peralkaline extrusive rocks are revealing the complexity of the evolution of peralkaline silicic centres, all of which are to some degree unique, in, for example, the interplay of petrogenetic processes, the range of lithologies, the nature of the magma chambers and the detailed P–T–X conditions under which the magmas evolve. Such studies can also help to reveal magmatic phase associations and stability relationships in intrusive equivalents, which are complicated by secondary processes.

(3) Volcanic hazards. Many peralkaline volcanoes have the potential to erupt soon, with the consequent effects on life and property. For example, the Corbetti, Aluto, Bora and Haledebi volcanoes in the Ethiopian Rift have shown recent signs of unrest [Biggs *et al.*, 2011, Hutchison *et al.*, 2016a,b] and in the Kenya Rift the Longonot and Menengai caldera volcanoes [Biggs *et al.*, 2009] and Olkaria volcanic complex [Clarke *et al.*, 1990] could also erupt in the near future. The eruption of Changbaishan-Tianchi volcano, China/North Korea, in AD 946 (the “Millennium Eruption” or “Generalized Millennium Eruption”; Pan *et al.*, 2020) was one of the two largest Holocene eruptions on Earth, the other being the great eruption of Tambora, Indonesia, in 1815 CE (Figure 1).

(4) There is an increasing awareness that peralkaline eruptions may, through, *inter alia*, sulphur emissions, have considerable environmental effects, to the extent of contributing to global cooling [Scaillet and Macdonald, 2006a]. There is a clear need to un-



Figure 1. The Changbaishan-Tianchi volcano, China/North Korea, the site in 946 CE of one of the two largest Holocene eruptions on Earth. The caldera is 5.5 km wide. Source: Global Volcano Program, Smithsonian Institution.

derstand the mechanisms of such emissions and to be able to predict their likely size.

(5) Peralkaline granites can be hosts for rare-metal deposits, such as Strange Lake, Canada [Salvi and Williams-Jones, 2006], the Ambohimirahavavy complex, Madagascar [Estrade *et al.*, 2014], Khan Bogd, Mongolia [Kynicky *et al.*, 2011], the Haldzan Buragtag massif, Mongolian Altai [Kovalenko *et al.*, 2009] and the Siwana peralkaline granite, India [Mondal *et al.*, 2021]. The extrusive equivalents carry important information on the rare-metal enrichment processes during the magmatic stages and provide a basis on which the effects of hydrothermal enrichment processes can be assessed. Furthermore, peralkaline extrusive rocks can show strong enrichment in critical rare metals and may also show large tonnages and grades. If their occurrences as superficial deposits makes them open to pit mining, they are worthy of increased exploration.

These issues require a full understanding of how peralkaline centres are initiated and how they evolve. This review focusses, therefore, on what we see as advances in our knowledge and on attempts to identify some of the gaps in that knowledge. Particular aspects addressed include the nature of the mantle sources of peralkaline silicic suites, the tectonic settings in which they occur, the nature and controls of their liquid lines of descent, the *P–T–fO₂*–melt water conditions under which they evolve, petrogenetic models of their origin, the nature and evolution of

peralkaline silicic magmatic systems, volcanic hazards associated with such systems, certain environmental effects of eruptive magmatism and their potential as hosts for ore deposits. The peralkaline types are further classified using the scheme of Macdonald [1974].

2. Tectonic settings

A major issue in the petrogenesis of peralkaline silicic rocks is whether they are associated with a particular tectonic setting or settings and therefore with specific types of crust and mantle. In fact, they can occur over a very wide range of settings, as follows.

2.1. Continental extension zones

The major occurrences of peralkaline silicic extrusive suites are in continental rift valleys. We noted above, for example, the huge volumes of Oligocene to Recent peralkaline silicic volcanics associated with the Ethiopian (Figure 2a) and Kenyan sections of the East African Rift System (EARS). The majority of occurrences are in extensional zones related to regional doming, perhaps a result of mantle plumes. Pantelleria, the type locality of pantellerite, is located in the NW–SE trending Strait of Sicily Rift Zone. The rift cuts the Pelagian Block, a promontory of the African plate. Felsic rocks of the Marie Byrd Land Province, Antarctica, include comendites, pantellerites, trachytes and phonolites and occur in an area of late Cenozoic doming similar to those in the EARS [LeMasurier *et al.*, 2011, 2018] (Figure 2b).

Flood rhyolite lavas (~37.4 Ma) of the Davis Mountains volcanic field, Trans-Pecos Texas, are composed of mildly peralkaline quartz trachyte to rhyolite [Parker, 2019]. One such flood lava, the comenditic Bracks Rhyolite, had a minimum original extent of 1000 km² and a volume of 75 km³ [Henry *et al.*, 1990]. The field formed on Grenville basement north of the Ouachita fold belt, which formed in the late Palaeozoic as a result of closure of an ocean basin between North America and South America [Parker *et al.*, 2017]. Magmatism may have been related to upwelling of asthenospheric mantle above the foundered Farallon slab. Closely associated with the flood lavas is the pantelleritic Gomez Tuff, which was erupted from, and ponded within, the Buckhorn caldera at 37.33 ± 0.07 Ma, possibly covering

an area as large as 14,000 km² [Parker and White, 2008] (Figure 2c). At ~220 km³, it may be the largest known pantellerite eruption. Alkalic magmatism in the Davis Mountains may be attributed to asthenospheric upwelling over the foundering Farallon slab over a 10 Ma time span, during which silicic magmatism transitioned south-westward [Parker and Henderson, 2021]. Associated in time with the Davis Mountains volcanic field is the Pine Canyon caldera volcano in Big Bend National Park, Texas, which erupted, *inter alia*, peralkaline quartz trachyte and rhyolite. White *et al.* [2006] suggested that the volcano was formed in an early phase of post-collisional continental rifting resulting from lithospheric delamination and sinking of the detached lithosphere.

2.2. Oceanic islands

Peralkaline silicic rocks are known from many ocean islands, occurring in several different settings, as comprehensively reviewed by Jeffery and Gertisser [2018] for the Atlantic Ocean. The Canary Islands in the NE Atlantic may be related to relatively fixed plumes rising from the core–mantle boundary into the African plate from the late Jurassic to Recent [Hornle *et al.*, 1995]. van den Bogaard [2013] has nominated the islands as the oldest hotspot track in the Atlantic Ocean and the longest lived on Earth. On Gran Canaria, a Miocene basaltic shield is overlain by ~20 trachytic to peralkaline rhyolitic ignimbrites erupted from the large (~20 km across), multiply reactivated Tejeda caldera [Schmincke and Sumita, 2010, Troll and Schmincke, 2002]. Iceland lies on the Mid-Atlantic Ridge above the Icelandic plume; peralkaline silicic rocks are known from several centres, including Thorsmörk [Jørgensen, 1980], Torfajökull [McGarvie *et al.*, 2006], Öraefajökull [Prestvik *et al.*, 2001] and Ljósuffjöll [Flude *et al.*, 2008].

Comenditic trachytes and pantellerites are known from São Miguel and Terceira Islands, Azores [Mungall and Martin, 1995, Jeffery *et al.*, 2016, Pimentel *et al.*, 2016, 2021, D’Orsano *et al.*, 2017]. The Azores are located near the triple junction between the Eurasian, African and North American plates and are related to shear motions between the plates [Miranda *et al.*, 1998, Hildenbrand *et al.*, 2014]. Bouvetøya, which has erupted comenditic rhyolites, is located near a triple junction on the South Atlantic Ridge, possibly above a mantle plume [Imsland *et al.*,

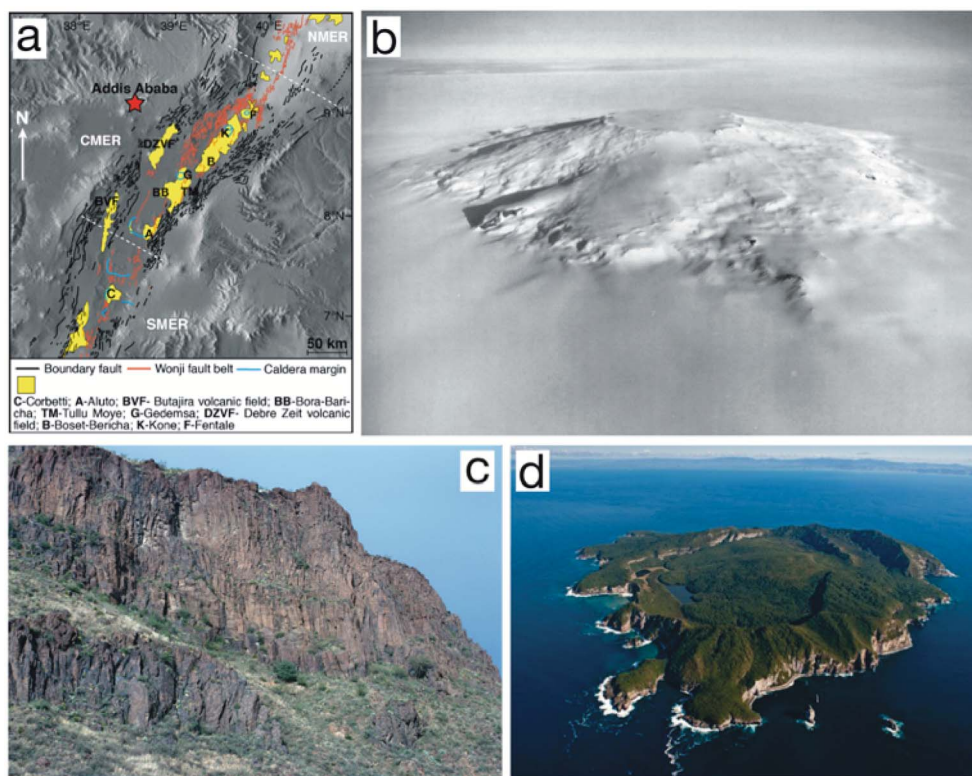


Figure 2. Examples of peralkaline extrusive rocks in various tectonic settings. (a) Volcanoes in part of the Main Ethiopian Rift (MER; N-Northern, C- Central, S-Southern). Redrawn from Iddon and Edmonds [2020]. (b) Mt Takahe, Marie Byrd Land, Antarctica. The summit caldera is ~8 km wide. (US Navy photograph TMA 1718 F33 022). (c) The Gomez Tuff, here ~100 m thick, overlying the darker Star Mountain Rhyolite lava. Little Aguja Canyon, Boy Scout Ranch, Texas. Photo courtesy of Professor Don Parker. (d) Mayor Island, pictured from the northeast, with New Zealand in the background. The caldera is 3 km wide.

1977, Prestvik *et al.*, 1999]. Ascension Island lies close to the Ascension fracture zone, a right-lateral offset of the Mid-Atlantic Ridge; it may overlie a local mantle melting anomaly or “hotspot” [Evangelidis *et al.*, 2004]. The island has erupted comendites [Weaver *et al.*, 1996, Kar *et al.*, 1998, Jicha *et al.*, 2013].

The Rallier-du-Baty Peninsula forms the southwestern part of the Kerguelen Archipelago (Indian Ocean); magmatic activity, which included comenditic trachyte, is related to the long-lived Kerguelen plume [Gagnevin *et al.*, 2003]. Easter Island is located on the Easter hotspot, on the Nazca plate ~350 km east of the East Pacific Rise. Its products include comendites [Haase *et al.*, 1997]. Due to its tectonomagmatic features, including low eruptive rate, scat-

tered rift zones and scarce lateral collapses, Vezzoli and Acocella [2009] considered it to represent an end-member type of hotspot volcano. The island of Socorro, Mexico, lies on the northern Mathematician Ridge which defines the location of a mid-ocean ridge spreading centre, abandoned at 3.5 Ma when activity shifted to the East Pacific Rise [Bohrson and Reid, 1995].

2.3. Subduction-related settings

Peralkaline silicic rocks also occur in various settings in what can broadly be considered collisional zones, formed either during active subduction or post-collision. They usually occupy local extensional

zones in such settings; we are unaware of any formed in a purely contractional setting, perhaps because shallow magma reservoirs tend not to form there. The Mayor Island volcano, which is dominated by pantelleritic eruptives [Barclay *et al.*, 1996], lies offshore from the North Island of New Zealand (Figure 2d). Its location is controlled by localized extension related to a back-arc rift onto the edge of the New Zealand continental crust [Cole, 1990, Houghton *et al.*, 1992]. Like Mayor Island, the volcanic rocks, including comendites, of the D'Entrecasteaux Islands, Papua New Guinea, are broadly related to the subduction of the Pacific Plate under the Australian Plate [Smith, 1976, Smith *et al.*, 1977]. The islands lie west of a spreading centre which has been propagating into the Australian continent and thus represent an early stage of continental breakup.

Miocene peralkaline volcanism in west-central British Columbia, Canada, has been linked to lithospheric fracturing above the northern edge of the subducted Juan de Fuca plate [Bevier *et al.*, 1979]. Further north, in northern British Columbia, the Mount Edziza Volcanic Complex, which includes comenditic eruptives, is thought to have formed in a late Cenozoic extension zone related to transcurrent motion along the adjacent continental margin [Souther and Hicks, 1984, Souther *et al.*, 1984]. There are extensive peralkaline occurrences in the western sector of the Trans-Mexican Volcanic Belt [Mahood, 1980, 1981a,b, Mahood *et al.*, 1985, Nelson and Hegre, 1990, Aguirre-Diaz and Morton-Bermea, 2018, Sosa-Ceballos *et al.*, 2018], perhaps related to extension created by an eastward jump of the East Pacific Rise during opening of the Gulf of California [Luhr *et al.*, 1985]. In the central sector of the Belt, comendites were erupted at 7.3–6.6 Ma from the Amzacala caldera, although the centre is bracketed between subduction-related, calc-alkaline volcanism [Aguirre-Diaz and Morton-Bermea, 2018]. The Aculco Caldera Complex is located in the eastern part of the Belt and shows the unusual, possibly unique, feature of mixing between mildly peralkaline and calc-alkaline magmas in the post-caldera volcanism [Sosa-Ceballos *et al.*, 2018]. At the Nemrut volcano, Lake Van, Turkey, some peralkaline units show evidence that magmas from the neighbouring, subalkaline Süphan volcano have occasionally entered the Nemrut system [Sumita and Schmincke, 2013a,b]. Yan *et al.* [2018] argued that the late Creta-

ceous tectonic setting of SE China, when peralkaline rhyolites were formed in the Yunshan caldera complex, was changed from a collisional to an extensional environment, perhaps related to the rollback of the subducting palaeo-Pacific plate.

Comendites occur on Palmarola Island (Tyrrhenian Sea, Italy) which is located along the boundary between the Italian continental shelf and the opening Tyrrhenian Sea. Geochemically, the volcanic rocks have a collisional imprint but also have features consistent with having been erupted in a within-plate setting [Cadoux *et al.*, 2005]. The formation of Early Miocene peralkaline rhyolites on Sardinia, the type locality of comendite, was related to the subduction of an oceanic plate beneath the European continental plate, although details of the subduction process remain unresolved [Morra *et al.*, 1994, Lustrino *et al.*, 2013].

It appears, therefore, that the formation of peralkaline silicic rocks is not critically dependent on tectonic environment or crustal thickness; the main requirement is that the setting is extensional, with the proviso that there are periods of tectonic quiescence and low magma flux so that strongly evolved magmas can be generated in the upper parts of the magma reservoirs [Bohrson and Reid, 1997, Hutchison *et al.*, 2018, Siegburg *et al.*, 2018].

3. Nature of mantle sources

There is a consensus that peralkaline magmas evolve from melts generated in the mantle, but less agreement on the nature of the source mantle. The source that produces alkali basalts parental to silicic peralkaline rocks has been variably attributed to metasomatically enriched mantle [Di Bella *et al.*, 2008, Markl *et al.*, 2010], asthenospheric mantle enriched by “primitive” material from a deep mantle plume [Civetta *et al.*, 1998, Rogers *et al.*, 2000, Halldórsson *et al.*, 2014], or mantle enriched by recycled Mid-Ocean Ridge Basalt (MORB) [Esperança and Crisci, 1995, Avanzinelli *et al.*, 2014, White *et al.*, 2020]. This section examines whether the nature of the source mantle is an important factor in promoting peralkalinity. Information on the mineralogy and composition of the mantle sources and on melting processes within the mantle can be inferred from the composition of the primary basalts at each centre, where a primary magma is the melt which was in equilib-

rium with the residual crystalline assemblage in the upper mantle region where melting took place. There are, however, remarkably few records of rocks potentially representing primary magmas in peralkaline-oversaturated suites. A picritic basalt from the Emurungogolak volcano, Kenya Rift Valley, with a magnesium number ($\text{Mg-number} = 100 \times \text{Mg}/(\text{Mg} + \text{Fe})$, with all Fe as Fe^{2+}) of 69 and a Ni content of 259 ppm, was shown by Weaver [1977] to be olivine-cumulitic. A “picritic basalt” from the Erta’Ale Range, Ethiopia, has Mg-number 61 and Ni 75 [Barberi *et al.*, 1974] and is a magnesian basalt. The primary magmas of peralkaline suites have clearly experienced high-pressure fractionation histories and have reached final equilibration at crustal pressures.

Information on the composition of primary magmas has to come, therefore, *via* geochemical modelling. Few studies have attempted to estimate the nature of the primary melt and degree of melting of the mantle source required to generate the primary magmas. Using rare earth element (REE) inversion, Neave *et al.* [2012] calculated that for Pantelleria melt generation was by $\sim 1.7\%$ melting of a light REE (La-Gd; LREE)-enriched peridotitic source at depths of 60–100 km, to produce a primary magma with Mg-number 69. The parental Pantelleria alkali basalts were then formed by 35% fractional crystallization of the primary melts. White *et al.* [2020] argued that the Pantescan magmas formed from a higher degree of partial melting ($\sim 6\%$) of a Depleted MORB Mantle (DMM)-dominated mantle enriched with a component of recycled MORB. For Gedemsa volcano, Giordano *et al.* [2014] argued that the primary magmas were formed by 7% partial melting of a complex mantle source with mantle-derived and crust-derived components.

Trace element modelling, mainly using REE and based on the compositions of parental basalts, generally indicates that the partial melting takes place either in the garnet facies [Lowenstern *et al.*, 2006, Mahood and Baker, 1986] or over the spinel/garnet facies transition [e.g., Kenya Rift Valley—Latin *et al.*, 1993, Macdonald, 1994, Macdonald *et al.*, 2001] and Pantelleria [White *et al.*, 2009, 2020, Neave *et al.*, 2012]. Depending on the geothermal gradient, the depth range for the transition is 60–100 km, although LeMasurier *et al.* [2011] estimated a rather deeper source, 110–140 km, for primary magmas of Marie Byrd Land, Antarctica. White *et al.* [2020] suggested

that partial melting beneath Pantelleria may have been initiated at depth of 120–130 km, which they attributed to the presence of abundant fusible eclogitic material in the mantle.

Various mantle components have been invoked, even for the same suite. Esperança and Crisci [1995] suggested that the primary magmas of the Pantescan basalts were formed in lithosphere made fertile by long-term reworking of continental lithosphere by asthenosphere-derived melts and mixed with present-day MORB-type melts. Civetta *et al.* [1998] argued that the mantle sources under Pantelleria are heterogeneous and involve at least two geochemical components, a relatively depleted (MORB-like) component and an enriched High- μ (HIMU)-like component, with the possible involvement of a third, Enriched Mantle 1-type component. On the basis of Sr–Nd–Pb and U-series isotopic data, Avanzinelli *et al.* [2014] argued that mafic magmas on Pantelleria originated in the asthenospheric mantle with little or no interaction with either the subcontinental lithospheric mantle (SCLM) or continental crust. Certain hawaiites, however, had a different origin: they were either related to interaction with partial melts of the SCLM or were formed in a mantle source enriched by recycled crustal material. White *et al.* [2013] suggested that the high Ti–P and low Ti–P series on the island originated from asthenospheric spinel lherzolite and that the high Ti–P primary magmas formed at greater depths (92.2 ± 4.4 km) than those of the low Ti–P series (76.1 ± 7.8 km). White *et al.* [2020] argued that both suites were derived from a DMM-dominated mantle enriched with a component of recycled MORB and possibly other components. The Pantescan case is a rather good example of the non-uniqueness of isotopic data in identifying precisely the nature of the mantle sources.

Using geochemical and Sr–Nd–Pb isotope data, Giordano *et al.* [2014] suggested that mafic eruptions of the Gedemsa and Fanta’Ale (Fantale; Fentale) volcanoes, Main Ethiopian Rift, were formed by 7% modal batch melting of mantle comprising 12% subcontinental lithospheric mantle and 88% depleted mantle. In contrast, the high $^3\text{He}/^4\text{He}$ values of several centres, including Gedemsa, support the presence of the “C” mantle component, common to ocean islands. Yan *et al.* [2018] suggested that the source for peralkaline rhyolites of the Yunshan caldera complex, SE China, was a subduction zone-

enriched mantle wedge which had interacted with depleted asthenospheric melts. Generally speaking, although isotope and trace element data strongly indicate that peralkaline magmas are ultimately derived from enriched mantle sources, they are equivocal on the nature of the enrichment even at the same volcanic centre. However, the simple but critical point in terms of the future attainment of peralkalinity in a suite is that the mantle source must be fertile and capable of generating alkali basalt on partial melting.

4. Petrographic and geochemical features

4.1. Petrography

The most commonly occurring phenocryst phases in peralkaline trachytes and rhyolites are alkali feldspar, quartz, olivine, clinopyroxene, ilmenite, magnetite, aenigmatite, amphibole and less commonly biotite. Accessory microphenocrysts include zircon, fluorapatite, fluorite, pyrrhotite and chevkinite-(Ce). Dozens of combinations of these phases have been recorded in the literature but generally the dominant assemblage in trachytes and comendites is alkali feldspar + fayalitic olivine + hedenbergite + ilmenite + fluorapatite, and that in pantellerites is alkali feldspar + hedenbergite + aenigmatite \pm quartz \pm amphibole. White *et al.* [2005] proposed a generalized “reaction series” for pantelleritic rocks with increasing peralkalinity, decreasing temperature (~ 950 to 700 °C), and increasing oxygen fugacity relative to the fayalite-magnetite-quartz (FMQ) buffer: (1) augite + fayalite + ilmenite + magnetite (P.I. $< \sim 1.4$) (2) augite + fayalite + ilmenite ($\sim 1.4 < \text{P.I.} < \sim 1.5$); (3) sodian augite or hedenbergite + fayalite + ilmenite + aenigmatite ($\sim 1.5 < \text{P.I.} < \sim 1.7$); (4) sodian hedenbergite or aegirine-augite + ilmenite + aenigmatite \pm amphibole ($\sim 1.7 < \text{P.I.} < \sim 1.9$); and (5) aegirine-augite + aenigmatite \pm amphibole (P.I. $> \sim 1.9$).

Macdonald *et al.* [2011] have reviewed the distribution of the phenocrysts over the compositional range of peralkaline trachytes and rhyolites and have also considered the stability relationships between them. Aspects of these relationships are discussed in various sections below. Here, we enter a plea that all published chemical analyses of peralkaline extrusive rocks be accompanied by a list of phenocryst assemblages for *each* analysis. Such assemblages record important, often subtle, information on the conditions

under which the host rock formed. Generalized assemblages may hide important relationships. For example, do aenigmatite and ilmenite phenocrysts co-exist and at what specific bulk-rock composition did quartz join the crystallizing assemblage? These features can reveal evidence of, *inter alia*, the $f\text{O}_2$ and $p\text{H}_2\text{O}$ under which the host magmas evolved.

4.2. Geochemistry

Peralkaline rocks are defined by their unusual major element geochemistry, with a greater abundance of alkalis (Na + K) than Al. Although this often implies a high concentration of Na_2O (up to ~ 8 wt%), it often also occurs because of very low concentrations of Al_2O_3 (down to ~ 6 wt%) that may also be accompanied by very high concentrations of FeO^* (up to ~ 9 wt%) despite $\text{SiO}_2 > 69$ wt%. This peculiar major element geochemistry is also reflected in the unusually high abundances of halogens and incompatible trace elements. Peralkaline silicic rocks generally contain high levels of F, Cl, high-field-strength elements (HFSE), REE and certain large ion lithophile elements (LILE), with relative abundances that typically demonstrate an Ocean Island Basalt (OIB) type pattern. The maximum abundances of these elements can certainly be very high: Cl > 1 wt% [Green Tuff, Pantelleria; Liszewska *et al.*, 2018], F > 2 wt%, Zr > 6000 ppm and LREE (La–Sm) > 1500 ppm (Gold Flat Tuff, Nevada; Macdonald *et al.*, 2019, and Rb > 1000 ppm [Olkaria complex, Kenya; Marshall *et al.*, 2009]. However, the ranges are very large, e.g. Zr 10^2 – 10^3 ppm. Comparing the compilations of analytical data for peralkaline and metaluminous rhyolitic obsidians by Macdonald and Bailey [1973] and Macdonald *et al.* [1992], respectively, shows that the peralkaline types have concentrations of such elements as the LREE, Nb and Zr ten to 25 times greater than those in the metaluminous varieties. On the other hand, concentrations of Cl are only 5 to 10 times greater [Lowenstern, 1994]. While peralkaline silicic rocks can also show strong depletion in such incompatible elements as Ba and Sr, with levels commonly < 10 ppm, these features are also found in subalkaline rhyolites and cannot be used as a distinguishing feature of peralkalinity.

Among the more important consequences of peralkaline compositions are (i) the effects of high halogen contents and high alkalinity on melt viscosity,

and (ii) the potential for the high abundances of certain rare metals to be concentrated into potential ore deposits.

4.3. Viscosity

Melt viscosity can strongly influence processes such as crystallization, crystal-melt separation, degassing and the dynamics of eruption, the main controls on viscosity being temperature and melt composition. It has long been inferred from geological evidence that peralkaline silicic magmas have lower viscosities than their metaluminous counterparts [Schmincke, 1974, Mahood, 1984], resulting from the higher volatile contents and lower degrees of melt polymerization. While there is a general correlation between P.I. and melt viscosity, the relationship is not linear; Stabile *et al.* [2016] showed that the Fe oxidation state has an effect on viscosity, decreasing $\text{Fe}^{2+}/\text{Fe}^*$ resulting in increasing viscosity.

The viscosities of peralkaline silicic melts have been determined experimentally [Stevenson and Wilson, 1997, Stevenson *et al.*, 1998, Di Genova *et al.*, 2013, Stabile *et al.*, 2016] and the results have been incorporated into various models of melt viscosity [Dingwell *et al.*, 1998, Giordano *et al.*, 2008]. The results have confirmed that peralkaline silicic melts have lower viscosities than their metaluminous equivalents, by as much as 2–3 orders of magnitude, e.g., 10^{10} – 10^{11} Pa·s, Stevenson and Wilson, 1997; $10^{9.6}$ – $10^{13.6}$ Pa·s, Stabile *et al.*, 2016, 2021]. On Pantelleria, for example, the volcanological consequences of the low viscosities include the ubiquity of welded and rheomorphic pumice falls and high-grade to extremely high-grade ignimbrites [Rotolo *et al.*, 2021]. Eruption columns are inferred to have been low [Mahood and Hildreth, 1986], which minimizes cooling of particles during fountaining and facilitates extensive welding. In later sections, we discuss the role of melt viscosity in such topics as magma chamber dynamics, the speed of development of zoned magma reservoirs, and the efficiency of magma mixing.

5. Geothermometry and geobarometry

In the following sections, we shall often refer to estimates of the crystallization conditions of peralkaline silicic magmas. First, we describe here the various methods used in the geothermometric and geobarometric estimates.

5.1. Geothermometry

Several techniques have been used to estimate the temperatures at which the phenocryst assemblages formed. In principle, the geothermometers could, when carefully tied to petrographic features, track the changes in temperature during the crystallization of individual magma batches from liquidus to near-solidus conditions.

As noted earlier, the use of two-oxide geothermometry in peralkaline silicic rocks is commonly hampered by the absence of coexisting oxides. A further constraint may be analytical imprecision due to very low Mg contents of the oxides, leading to relatively large errors in calculating Mg/Mn ratios and thus to failure in passing the Bacon and Hirschmann [1988] Mn–Mg partitioning test for equilibrium. Also, the uncertainties associated with the method [± 30 °C; cf. Blundy and Cashman, 2008] may limit the identification of temperature variations in zoned deposits. Different calculation schemes are used, including Andersen *et al.* [1993], Ghiorso and Evans [2008] and Sauerzapf *et al.* [2008], but where tested on the same rocks appear to give similar results [Jeffery *et al.*, 2017, Macdonald *et al.*, 2019]. The oxides re-equilibrate over short timescales and most probably reflect the final pre-eruptive temperatures.

In the Quartz-Ulvospinel-Ilmenite-Fayalite (QUILF) thermobarometer [Andersen *et al.*, 1993] temperature is calculated from Fe–Mg–Ca exchange between olivine and clinopyroxene; it cannot, therefore, be used in the most evolved pantellerites where olivine is typically absent. Several studies have presented QUILF temperatures, with the following ranges: peralkaline trachytes 709–865 °C; [Ren *et al.*, 2006, D’Orsano *et al.*, 2017]; comendites 680–740 °C [White *et al.*, 2006, Marshall *et al.*, 2009]; pantellerites 668–748 °C [Ren *et al.*, 2006, Parker and White, 2008, Macdonald *et al.*, 2019]. Trachytes parental to comendite and pantellerite typically have temperatures >790 °C [Romano *et al.*, 2020]; lower temperatures are recorded in trachytes with high P.I. (>1.3) that are thought to have evolved via fractional crystallization of assemblage of alkali feldspar + quartz from peralkaline rhyolite [Ren *et al.*, 2006].

Temperature estimates based on equilibrium pyroxene–glass pairs have been proposed by Putirka [2008] and Masotta *et al.* [2013]. For these models, the pressure of equilibration and the melt water con-

tent must be known or assumed. Also, the pyroxenes must have a jadeite component. The models were applied to the peralkaline rhyolites of the Nemrut volcano, Turkey, by Macdonald *et al.* [2015] giving the range $808\text{--}862\text{ }^{\circ}\text{C} \pm 45\text{ }^{\circ}\text{C}$ (Putirka model) and $721\text{--}881\text{ }^{\circ}\text{C} \pm 18.2\text{ }^{\circ}\text{C}$ (Masotta *et al.*, model).

The alkali feldspar-melt geothermometer of Putirka [2008] was used by Zou *et al.* [2010] to calculate the magmatic temperatures at the comenditic Changbaishan-Tianchi volcano. Rocks from two localities gave $741\text{ }^{\circ}\text{C}$ and $752\text{ }^{\circ}\text{C} (\pm 30\text{ }^{\circ}\text{C})$. Neave *et al.* [2012] used the geothermometer to estimate the temperature for the Cuddia di Mida pantellerite on Pantelleria as $802 \pm 23\text{ }^{\circ}\text{C}$, assuming a depth of 1.5 kbar and an H_2O content of 4 wt% based on SIMS data. The same methodology was applied by D'Orlando *et al.* [2017] to the comenditic trachyte component of the Lajes Ignimbrite, Terceira Island, and gave $850\text{--}900\text{ }^{\circ}\text{C} \pm 23\text{ }^{\circ}\text{C}$. Shortly before eruption, pantelleritic magmas at Aluto were in the narrow temperature range $718\text{--}765\text{ }^{\circ}\text{C}$ [Gleeson *et al.*, 2017]. Jeffery *et al.* [2017] found alkali feldspar-melt temperatures for various peralkaline trachyte ignimbrites of Terceira lying between 912 and $857\text{ }^{\circ}\text{C}$. These temperatures are higher than those from two-oxide thermometry, perhaps reflecting the earlier crystallization of the feldspars.

As far as we know, the only study to apply the Ti-in-zircon method [Watson *et al.*, 2006] to a peralkaline extrusive rock is that by Zou *et al.* [2010] to the Changbaishan-Tianchi comendites. A TiO_2 activity was assumed (0.5) and the resulting average temperatures for two rocks were $702 \pm 28\text{ }^{\circ}\text{C}$ and $702 \pm 43\text{ }^{\circ}\text{C}$, within the uncertainties of those estimated by the alkali feldspar-melt technique.

Appreciating that Petrogeny's Residua System (Q–Or–Ab) does not accurately represent the compositions of peralkaline silicic rocks, Thompson and MacKenzie [1967] determined phase relationships in the system Q–Or–Ab– H_2O with added acmite (4.5%) and Na-metasilicate (4.5%), designed to simulate pantelleritic melts. They proposed the existence of a low-temperature zone towards, and along, which peralkaline melts evolve, broadly analogous to the zone in the non-peralkaline system. Parker and White [2008] and Liszewska *et al.* [2018] estimated the equilibration temperatures of the Gomez Tuff, Texas, and Green Tuff, Pantelleria, respectively, by plotting them into projections of the experimental

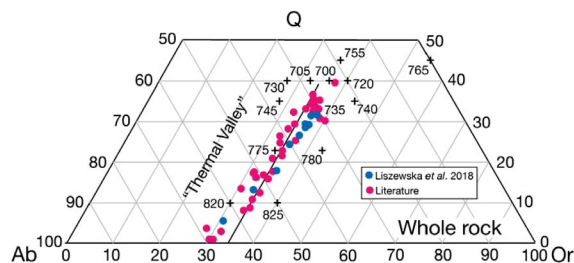


Figure 3. Whole-rock analyses of Green Tuff (Pantelleria) projected into the Q–Or–Ab plane in the Q–Or–Ab–Ac–Ns system at $P_{\text{H}_2\text{O}} = 1000$ bar [modified from Liszewska *et al.*, 2018]. The crosses mark temperatures on the alkali feldspar liquidus surface [Carmichael and MacKenzie, 1963].

system Q–Or–Ab– H_2O –Ac–Ns. For the Gomez Tuff, the temperature was $\sim 750\text{ }^{\circ}\text{C}$; for the Green Tuff, the lowest temperatures were $\sim 700\text{ }^{\circ}\text{C}$ (Figure 3).

Significant information on temperatures of equilibration has come from high temperature–pressure experiments [Mahood and Baker, 1986, Scaillet and Macdonald, 2001, 2003, 2006b, Di Carlo *et al.*, 2010, Romano *et al.*, 2018, 2020, 2021]. The main results are discussed below (Section 11) but one of the most important is that peralkaline rhyolites can achieve (near)liquidus temperatures lower than $700\text{ }^{\circ}\text{C}$. Experimental information on solidus temperatures is hampered by the difficulty of crystallizing minerals at near-solidus conditions. In experiments on pantellerites, Scaillet and Macdonald [2001] and Di Carlo *et al.* [2010] estimated solidus temperatures of $\sim 660\text{ }^{\circ}\text{C}$.

The combination of thermodynamic estimates and experimental results has meant that the temperature ranges over which peralkaline trachytes and rhyolites equilibrate are rather well established, even for individual eruptive units. For example, Martel *et al.* [2013] estimated that the metaluminous to peralkaline trachytes of the Chaîne des Puys evolved in a reservoir (or reservoirs) where the temperatures increased from 700 to $825\text{ }^{\circ}\text{C}$ downwards. The range within the reservoir that erupted the Green Tuff, Pantelleria, was $\sim 900\text{--}700\text{ }^{\circ}\text{C}$ [Liszewska *et al.*, 2018].

5.2. Geobarometry

Low pressures of formation of peralkaline silicic rocks are commonly inferred from geological

evidence, such as the close association of caldera volcanoes and high-level intrusions [Mahood, 1984, Lowenstern *et al.*, 2006, Wei *et al.*, 2013]. More quantitative approaches use water solubility models, thermodynamic modelling and constraints imposed by experiments.

(a) The depth of a magma storage system can be estimated using water solubility models, such as those of Di Matteo *et al.* [2004] and Papale *et al.* [2006]. If the magma water content can be estimated, from, for example, melt inclusions, and water saturation is assumed, then the minimum pressure of the system can be calculated. Lanzo *et al.* [2013] used the Papale *et al.* [2006] model and a measured water content of 4.2 wt% to show that the Green Tuff, Pantelleria, had a saturation pressure of 65 MPa, equivalent to ~2.5 km depth. According to Romano *et al.* [2021] and Stabile *et al.* [2021], the Papale *et al.* model tends to slightly overestimate water solubility in such melt compositions. On the basis of new experimental determinations of water solubility in trachytic and pantelleritic rocks from Pantelleria, Romano *et al.* [2021] estimated the depth of the felsic reservoirs on the island to deepen from 2.4 to 3.5 km. Using the Di Matteo *et al.* formulation and a water content of 4.2 wt%, Jeffery *et al.* [2017] found that the minimum equilibration pressure of the magma system on Terceira which generated a suite of peralkaline ignimbrites was ~80 MPa (~3 km depth).

(b) Thermodynamic modelling involves the use of thermodynamic data from the literature, e.g., for the activity of the silica and ilmenite components and attempts to determine the stability of possible mineral phases over ranges of P – T – fO_2 . Magmatic differentiation in peralkaline systems has been modelled using the MELTS algorithm [Ghiorso and Sack, 1995] and the updated version rhyolite-MELTS [Gualda *et al.*, 2012]. For isobaric systems, MELTS minimizes Gibbs free energy to determine phase equilibrium relationships, given the P – T – fO_2 conditions. It then removes the equilibrium assemblage from the melt to produce a new melt; the model then proceeds stepwise.

White *et al.* [2009] used MELTS to model the origin of Pantescan pantellerites from an alkali basalt parent. They found that at low pressure (0.1 GPa) fractional crystallization of basalt with 1.0–1.5 wt% H_2O at $fO_2 < FMQ$ produced a metaluminous trachyte with P.I. 0.89–0.97 and water contents 3.34–4.06 wt%.

No MELTS model, however, successfully resulted in a pantelleritic melt.

The various approaches have almost all shown that the transition from trachyte to rhyolite normally occurs at high crustal levels, in the range 2–5 km. However, the majority of petrogenetic models link these high-level reservoirs to deeper reservoirs, often down to the crust–mantle boundary; aspects of these broader magmatic systems are discussed below (Sections 13–15).

5.3. Oxygen fugacity

Estimates of the fO_2 under which peralkaline rhyolites crystallize have been made using coexisting oxides [Nicholls and Carmichael, 1969, White *et al.*, 2005, Beier *et al.*, 2006, Jeffery *et al.*, 2017], QUILF equilibria, and by imposing the redox conditions during high- P – T experiments [Mahood and Baker, 1986, Scaillet and Macdonald, 2001, 2003, 2006b, Di Carlo *et al.*, 2010, Jeffery *et al.*, 2017, Romano *et al.*, 2018, 2019, 2020, 2021]. Using the 750 °C temperature estimated by projection into the Q–Or–Ab–Ac–Ns– H_2O system and QUILF equilibria and assuming a pressure of 2 kbar, Parker and White [2008] found log fO_2 values in the range –17.24 to –17.78 for the Gomez Tuff. Liszewska *et al.* [2018] used thermodynamic modelling to show that the temperature range in the Green Tuff, Pantelleria, ranged from 900 °C (comenditic trachytes) to 700 °C (pantellerites), with fO_2 FMQ –1.5 to FMQ –0.5, and $aSiO_2$ relative to quartz saturation of 0.74–1.00.

Most studies have shown that the magmas evolve under conditions close to the FMQ buffer (FMQ \pm 1), i.e., they are relatively reduced (Figure 4). Exceptions include lavas of Ascension Island where the range is FMQ –1.8 to FMQ –2.4 [Chamberlain *et al.*, 2016]. Beier *et al.* [2006] found that certain trachytes of the Sete Cidades volcano, São Miguel, Azores, are more oxidized, with fO_2 values approaching the HM buffer. They related this to high volatile contents of the magmas, perhaps a result of the assimilation of crustal rocks.

6. Magmatic lineages

This section outlines the various liquid lines of descent along which peralkaline suites evolve, pointing out differences between them and relating the

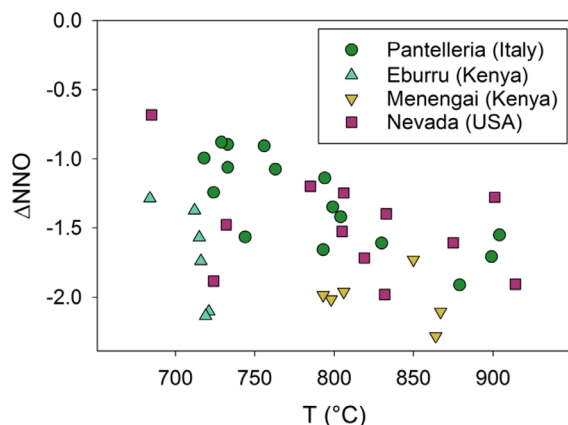


Figure 4. Plot of temperature (T) versus oxygen fugacity (fO_2) relative to the nickel–nickel oxide buffer at 100 MPa [ΔNNO ; O’Neil and Pownceby, 1993, Pownceby and O’Neil, 1994] for representative samples from Pantelleria [Mahood and Stimac, 1990, White *et al.*, 2005, 2009, Liszewska *et al.*, 2018, Romano *et al.*, 2018, 2019, 2020], Eburru [Ren *et al.*, 2006], Menengai [Macdonald *et al.*, 2011], and the Black Mountain volcanic centre, Nevada [Macdonald *et al.*, 2019].

differences to the crystallizing assemblages and the external parameters which controlled them. Our approach is that the majority of peralkaline suites are essentially basalt-driven systems, in the sense that basalt has been the parental magma from which more evolved rocks have been derived or has provided the heat source for partial melting of various crustal rocks [Mahood and Baker, 1986, Bohrsen and Reid, 1997, Macdonald, 2012]. The review acknowledges, therefore, the primary role of basalt and attempts to evaluate the various factors which lead to peralkaline silicic end points, particularly their polybaric fractionation histories.

The following section is divided into (i) the recognition of parental basalts; and (ii) one-stage models, where basaltic magma fractionates more or less continuously to trachytic or rhyolitic endmembers. We mainly use ten selected suites which we consider to be representative of the main types of basalt–peralkaline rhyolite sequences (Table 1), although other suites are introduced where particularly relevant. Suites come from continental and oceanic settings, have different assemblages of rock types, may

or may not show composition gaps, range from sodic to mildly potassic, and followed different evolutionary paths.

6.1. Parental basalts

The most primitive (generally most magnesian) basalts at peralkaline centres are taken to be potential parental magmas, with the caveat that for any system there is no unique primary, and thus parental, magma. The coexisting basalt in coeval eruptions and mixed magmas may *represent* the parental magma but cannot *be* it. Significant variation in the composition of putative parental basalts is found in individual centres, ranging from four derivative (?) suites on Ascension Island [Weaver *et al.*, 1996] through three on Terceira, Azores [Self and Gunn, 1976, Mungall and Martin, 1995] and Socorro Island [Bohrson and Reid, 1995], to at least two on Pantelleria [Civetta *et al.*, 1998, White *et al.*, 2009, 2020, Avanzinelli *et al.*, 2014]. Thus, treating each of our chosen units as one magmatic lineage is a simplification.

Table 2 lists analyses of rocks inferred by the original authors to represent, or be close to, the parental magmas to basalt–trachyte/rhyolite suites. The basalts range from mildly nepheline-normative to mildly hypersthene-normative and may be described as alkali to transitional basalts. Mg-numbers vary from 50 to 65. The ranges represent the degree of fractionation encountered between mantle source and the point of initial equilibration of each suite within the crust. There is significant variation in most major elements; for example, at 6 wt% MgO, K_2O , TiO_2 and P_2O_5 show ranges of more than $\times 2$ Table 3. Na_2O contents are in the relatively narrow range 3–4 wt%. K_2O values in 9 of the representative suites are between 0.8 and 1.2 wt%; those from Easter Island and Nandewar are 0.4 and 1.9 wt%, respectively. Na_2O/K_2O ratios reflect mainly the variation in K_2O contents and range from 2 to ~ 7 . The next section explores whether the diversity of peralkaline silicic extrusive rocks is derived from differing parental basalts, is a result of different fractionation histories, or is a combination of both factors.

6.2. One-stage models: magmatic lineages

Numerous studies have concluded that the peralkaline trachytes and rhyolites are ultimately formed by

Table 1. Representative basalt–peralkaline rhyolite suites

Suite	Nature	Rock types	Composition gap (SiO ₂ range, wt%)	References
Boina	EARS	B, M, Be, T, P	X	1, 2
Erta’Ale	EARS	B, H, M, Be, Pt, C	X	3
Gedemsa	EARS	B, M, Be, Mt, Ct, Pt, P	X	4, 5
Olkaria	EARS	B, H, M, Be, Mt, Ct, C	X	6, 7
Pantelleria	Rifted margin	B, M, Mt, Ct, Pt, P	50–62	8, 9, 10
Ascension	Atlantic ocean	B, H, M, Be, Mt, Ct, C	X	11
Easter hotspot	Pacific ocean	B, M, Be, T, C	62–66	12
Socorro	Pacific ocean	B, H, M, Ct, Pt, P	54–61	13, 14
Terceira	Atlantic ocean	B, H, M, Be, Ct, C, P	60–65	15
Nandewar	Cont. intraplate	H, Ta, Tr, Mt, Ct, C	51–58	16

B, basalt; Be, benmoreite; C, comendite; Ct, comenditic trachyte; H, hawaiite; M, mugearite; Mt, metaluminous trachyte; P, pantellerite; Pt, pantelleritic trachyte; Ta, trachyandesite; Tr, trachyte. EARS, East African Rift System. References: 1, Barberi *et al.*, 1975; 2, Field *et al.*, 2012; 3, Barberi *et al.*, 1974; 4, Peccerillo *et al.*, 2003; 5, Giordano *et al.*, 2014; 6, Macdonald *et al.*, 2008; 7, Marshall *et al.*, 2009; 8, Civetta *et al.*, 1998; 9, White *et al.*, 2009; 10, Neave *et al.*, 2012; 11, Weaver *et al.*, 1996; 12, Haase *et al.*, 1997; 13, Bohrsen and Reid, 1995; 14, Bohrsen and Reid, 1997; 15, Mungall and Martin, 1995; 16, Stolz, 1985.

Table 2. Rocks identified as parental basalts in representative suites

Suite	Boina	Erta’Ale	Gedemsa	Olkaria	Pantelleria	Ascension	Easter Is.	Socorro	Terceira	Nandewar
wt%										
SiO ₂	46.75	48.10	48.19	47.04	46.00	47.53	47.77	48.52	47.92	46.63
TiO ₂	2.30	1.45	2.01	1.83	3.50	2.67	2.45	2.97	3.03	2.21
Al ₂ O ₃	13.93	13.20	16.90	15.73	14.90	15.8	15.32	15.94	13.75	13.84
FeO*	10.96	10.31	9.91	11.07	11.30	11.50	10.65	10.82	11.27	10.78
MnO	0.19	0.17	0.20	0.18	0.18	0.17	0.17	0.17	0.20	0.15
MgO	9.75	10.13	8.47	7.77	7.01	6.65	8.58	6.78	7.71	9.66
CaO	10.08	12.06	9.19	11.85	11.00	10.35	9.82	9.67	10.66	8.37
Na ₂ O	2.70	2.45	2.75	2.41	3.50	2.81	2.98	3.43	3.20	3.12
K ₂ O	0.80	0.35	0.89	0.44	1.44	0.65	0.61	1.07	0.98	1.05
P ₂ O ₅	0.35	0.24	0.39	0.24	0.99	0.59	0.31	0.58	0.62	0.60
LOI/H ₂ O ⁺	0.78	1.04	0.79	−0.13	—	−0.44	—	—	0.0	2.60
Total	98.59	99.50	99.69	98.43	99.82	98.28	98.66	99.95	99.34	99.01
Norm ne	—	—	6.0	—	5.7	—	—	0.12	0.80	—
Norm hy	2.7	3.8	—	3.0	—	10.5	5.3	—	—	0.48
Mg-no.	61.3	63.6	60.4	55.6	52.5	50.7	62.8	52.8	54.9	65.2
Cr (ppm)	—	—	227	71	—	156	269	146	268	277
Ni (ppm)	70	210	127	37	—	97	155	92	93	169

FeO*, all Fe as Fe²⁺. Dash, no data. LOI, loss on ignition. Pantelleria data for high-Ti basalt suite. Terceira for rift-related suite.

Table 3. Selected geochemical features of peralkaline suites

	Maximum value (at MgO in brackets)				Concentration at 6 wt% MgO				P.I.*
	FeO*	TiO ₂	Al ₂ O ₃	P ₂ O ₅	Al ₂ O ₃	Na ₂ O	K ₂ O	FeO*	
	(MgO value in brackets)								
Boina	16 (5.0)	3.4 (5.0)	16 (6.0)	0.7 (3.5)	16.0	3.1	1.1	15.0	≈0.1
Erta'Ale	17 (4.8)	3.1 (5.0)	16 (11)	1.2 (3.2)	15.5	3.1	0.8	14.0	1.2
Gedemsa	10 (8.0)	2.1 (5.1)	19 (4.2)	0.6 (5.0)	17.5	3.1	1.2	11.0	0.8
Olkaria	13 (5.0)	3.2 (3.5)	16 (8.0)	1.1 (3.5)	15.0	3.0	1.0	12.5	0.4
Pantelleria	14 (5.0)	4.0 (5.3)	16 (6.2)	1.3 (6.8)	16.0	3.5	1.0	11.5	0.3
Ascension	14 (7.0)	3.2 (4.5)	18 (3.5)	1.3 (3.5)	15.5	3.2	0.9	13.0	0.1
Easter hotspot	14 (6.0)	3.5 (5.5)	17 (8.0)	0.5 (7.5)	16.0	3.1	0.4	14.0	≈0.1
Socorro	14 (3.5)	4.2 (4.7)	16 (6.5)	1.8 (4.0)	16.0	3.8	1.0	11.5	0.2
Terceira-1	14 (4.0)	3.5 (4.0)	18 (3.5)	0.9 (2.8)	16.0	3.5	0.9	12.0	0.3
Terceira-2	13 (5.0)	4.0 (6.0)	17 (2.0)	1.5 (4.0)	14.0	3.7	1.0	12.5	0.3
Nandewar	13 (6.7)	3.0 (6.0)	17 (1.3)	1.6 (5.8)	15.0	3.5	1.9	12.0	0.5

PI.*, peralkalinity index (mol. (Na₂O + K₂O)/Al₂O₃) achieved at given MgO value. Terceira-1 is comendite trend; Terceira-2 is pantellerite trend.

protracted fractional crystallization of alkali basalt magmas, along liquid lines of descent which include ferrobasalt, mugearite, benmoreite and metaluminous trachyte [Barberi *et al.*, 1975, Weaver, 1977, Novak and Mahood, 1986, Mungall and Martin, 1995, Civetta *et al.*, 1998, Peccerillo *et al.*, 2003, Lowenstern *et al.*, 2006, Macdonald *et al.*, 2008, Parker and White, 2008, White *et al.*, 2009, Ronga *et al.*, 2010, Rooney *et al.*, 2012, Hutchison *et al.*, 2016a, Gleeson *et al.*, 2017, Jeffery *et al.*, 2017]. Although all these sequences generated peralkaline silicic end-members, the evolutionary paths were all to some extent unique. As noted above, ten extrusive suites are used here to illustrate the range of magmatic lineages (Table 1). The lineages are presented in Figure 5, using MgO as a differentiation index. To avoid overcrowded plots, we use four *illustrative* suites for each oxide. Important geochemical markers for all suites are given in Table 3.

The suites all show a rather similar pattern of a gentle increase in SiO₂ abundances until ~3 wt% MgO, when SiO₂ is ~50 wt%, and then a sharper rise to values >70 wt%. For Al₂O₃, differentiation normally results in peaked trends, with maximum abundances being reached over a considerable range of MgO values, 0.5–8 wt%, and at variable maximum Al₂O₃ abundances, 16–19 wt% (Table 3). At So-

corro, however, Al₂O₃ levels decrease continuously [Bohrson and Reid, 1995]. In the “flat”/decreasing trends, plagioclase is reported to be the modally dominant phenocryst in the basalts [Weaver, 1977, Nelson and Hegre, 1990, Bohrson and Reid, 1995, Gioncada and Landi, 2010]. Interestingly, however, Al shows peaked behaviour even in suites where plagioclase is a phenocryst phase in the basalts (Tables 2, 3), implying that it has not been a significant fractionating phase in the basaltic magmas. Perhaps the crystals were not dense enough to separate from melt efficiently. Plagioclase formation is dependent on the Al/(Mg + Fe) ratio of the melt and on the *p*H₂O in the melt: low *p*H₂O tends to promote early crystallization [Gaetani *et al.*, 1993].

As far as we are aware, only two extrusive peralkaline suites have passed through a two-feldspar stage, where plagioclase and alkali feldspar phenocrysts coexisted in equilibrium; where plagioclase is reported, it invariably forms cores in alkali feldspar and is residual from a higher-temperature stage [Barberi *et al.*, 1974, White *et al.*, 2009, Romengo *et al.*, 2012]. The two exceptions are the Chopine trachyte from the Massif Central in France [Martel *et al.*, 2013] and the Katenmening trachytes, Silali volcano, Kenya [Macdonald *et al.*, 1995]. In a later section (Section 11), we examine the experimental information

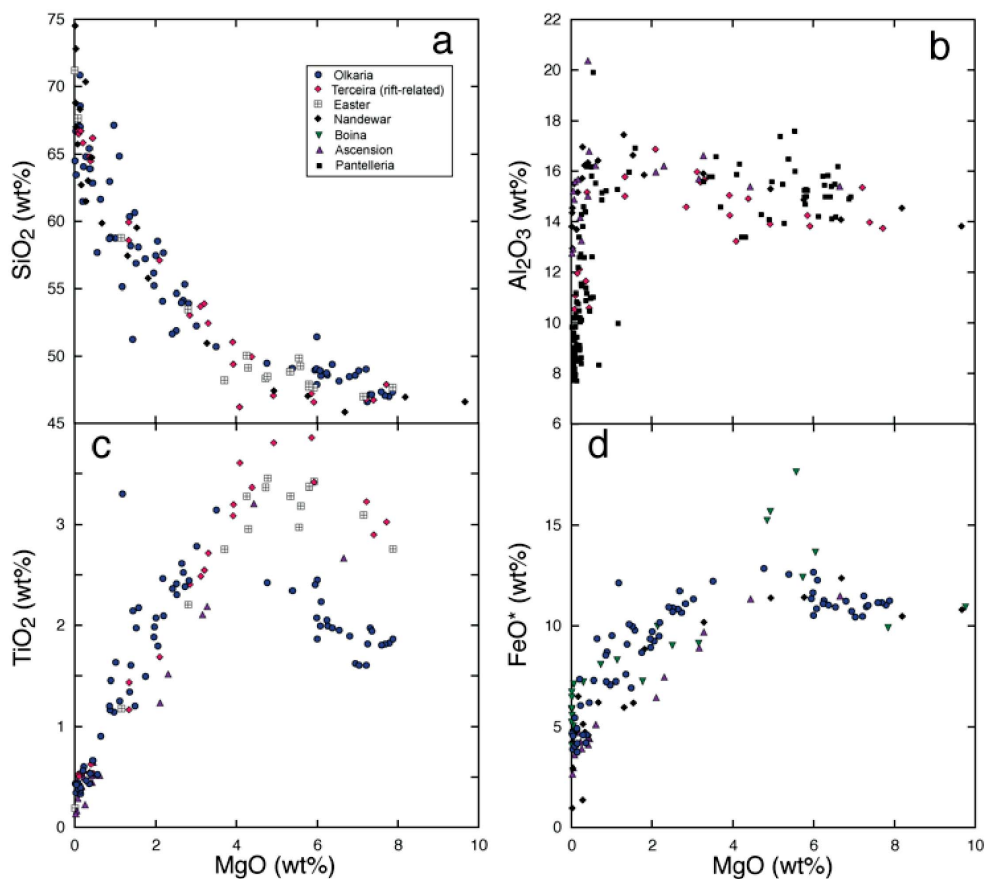


Figure 5. Plots of SiO_2 against MgO for selected oxides for basalt–peralkaline rhyolite suites. Each box contains data for four suites, chosen to represent different behaviours. In the Terceira case only data for the rift-related basalt–pantellerite sequence is used; for Ascension, analyses are from the intermediate Zr/Nb sequence. Data sources: Ascension—Weaver *et al.* [1996]; Boina—Barberi *et al.* [1975]; Easter Island—Haase *et al.* [1997]; Nandewar—Stolz [1985]; Olkaria—Macdonald *et al.* [2008], Marshall *et al.* [2009]; Pantelleria—Mahood and Baker [1986], Civetta *et al.* [1998], Avanzinelli *et al.* [2004], Ferla and Meli [2006], White *et al.* [2009]; Socorro—Bohrson and Reid [1995, 1997]; Terceira—Mungall and Martin [1995].

for the stability relationships of the Chopine trachyte and its significance for the development of peralkalinity. At Silali, the two-feldspar trachytes fit compositionally between mugearites and trachytes and have been modelled as part of the liquid line of descent.

Early plagioclase crystallization usually results in CaO increasing in residual melts until clinopyroxene joins the assemblage when abundances fall (e.g., at 6 wt% MgO ; Nandewar and Easter). The order of appearance of plagioclase and clinopyroxene is dependent on melt $\text{Ca}/(\text{Mg} + \text{Fe})$ ratio and on $p\text{H}_2\text{O}$. As noted above, high water activities reduce plagioclase

stability, resulting in melts with higher Al_2O_3 contents [Gaetani *et al.*, 1993], e.g., as suggested for Aluto magmas by Gleeson *et al.* [2017]. Crystallization of clinopyroxene can affect the composition of residual melts in several ways. It depletes the melt in CaO and increases the FeO^*/MgO ratio. If the pyroxene is nepheline-normative, it may exacerbate the trend towards silica saturation. More importantly, significant entry of Al into pyroxene will promote the peralkalinity of the residual melts; Bryan [1976] and Weaver [1977] invoked aluminous titanite as effective in promoting peralkalinity in the Socorro

and Emuruangogolak suites, respectively. Mahood and Baker [1986] crystallized Al- and Ti-rich clinopyroxenes in their experimental study of Pantescan basalts, affecting both the degree of silica saturation and the peralkalinity. In contrast, in their crystallization experiments of comendites from the Olkaria complex, Scaillet and Macdonald [2003] found that the crystallization of calcic clinopyroxene in slightly peralkaline rhyolites inhibited the increase in melt peralkalinity by counteracting the effects of feldspar.

In most suites, FeO* and TiO₂ show a peaked behaviour, with maximum values in the range 5–7 wt% MgO. In contrast, at Gedemsa, both show continuous decreases with decreasing MgO content. Many authors have ascribed the peaked trends to build-up of Fe and Ti in the melt until FeTi-oxides join the fractionating assemblage, when they are then removed from the melt. The point at which they appear as phenocrysts is dependent, *inter alia*, on fO_2 ; more reduced magmas will delay oxide crystallization. The trends are normally consistent with phenocryst assemblages, which show oxides appearing in the intermediate (hawaiitic–mugearitic) magmas. The Fe–Ti depletion trends at Gedemsa [Peccerillo *et al.*, 2003] and Nemrut [Macdonald *et al.*, 2015] have been explained, on the basis of geochemical modelling, by FeTi-oxides joining the fractionating assemblage in the basaltic magmas, yet in neither case was oxide reported as a phenocryst phase in the basalts. Another problem can be the high proportions of oxides required by geochemical modelling which are greater than the observed proportions [e.g., on Pantelleria: White *et al.*, 2009, Neave *et al.*, 2012]. Neave *et al.* [2012], whose models required 12% magnetite to reproduce the liquids, appealed to preferential settling of oxides prior to eruption but this is not consistent with the common occurrence in these rocks of oxide–clinopyroxene clusters.

Na₂O levels increase to the trachyte stage, but then either increase or decrease towards rhyolitic compositions as feldspars become sodic. In the Olkaria suite, considerable scatter in the rhyolites is related to Na loss on devitrification or secondary hydration. All suites show general increases in K₂O abundances, although at variable rates. In some suites, e.g., the rate increases at 3–4 wt% MgO (Olkaria); in others (Boina) the rate is rather constant. In both the Ascension and Nandewar suites K₂O levels

fall in the most evolved rocks (MgO < 1 wt%). Gleeson *et al.* [2017] found that at the Aluto volcano crystallization of sanidine resulted in K depletion in residual melts, as predicted by rhyolite-MELTS modelling.

The series showing peaked Fe–Ti trends almost invariably show a similar behaviour of P. Maximum P₂O₅ concentrations are, however, usually achieved at lower MgO levels (Table 3). The peak concentrations for P reflect the appearance of apatite in the fractionating assemblage although this is not always noted petrographically. For example, apatite is not listed as a phenocryst phase in the mafic Gedemsa rocks [Peccerillo *et al.*, 2003]. It is not clear what stabilizes apatite crystallization; the peak concentrations range from 0.6 to 1.8 wt% P₂O₅ (Table 3), so it cannot simply be P activity.

A notable feature of apatite compositions in the suites is the variable degrees of britholite (REE + Si) enrichment. Macdonald *et al.* [2012] suggested that the controlling factor might be the F/Cl ratio of the host rocks, britholite enrichment being stronger in magmas with F > Cl (e.g. Menengai and Olkaria) than in those with Cl > F (Pantelleria). The suggestion needs to be tested with data from more suites.

6.3. Status of minor mafic phases

It is important to establish whether minor sodic phases can fractionate from peralkaline rhyolites because their appearance would slow down the increase in peralkalinity of residual melts. Mbowou *et al.* [2012] and Renna *et al.* [2013] have invoked arfvedsonite fractionation in comendites from Lake Chad and Corsica, respectively, but the process was not satisfactorily modelled. Indeed, we know of no natural extrusive suite where a strong case for fractionation of either aegirine or sodic amphibole has been made.

The case for aenigmatite is more equivocal. White *et al.* [2009], for example, referred to aenigmatite as being part of the fractionating assemblage from metaluminous trachyte to pantellerite on Pantelleria but none of the models presented contained aenigmatite. In their modelling of the rhyolite array at the Main Ethiopian Rift volcanoes, Iddon and Edmonds [2020] proposed a fractionating assemblage including 19% aenigmatite, yet aenigmatite occurs only in minor modal amounts in pantellerites, usually < 3%. Gleeson *et al.* [2017] argued that aenigmatite is not

accurately modelled because of a lack of experimental data to constrain its thermodynamic properties. Liszewska *et al.* [2018] have argued that a subgroup of melts in the Green Tuff on Pantelleria evolved along a quartz–alkali feldspar–aenigmatite cotectic. Such a trend would be open to experimental testing. Of course, aenigmatite usually appears very late during magma evolution when crystal separation may be hampered by melt viscosity, and thus has little real effect on the liquid trend [Mungall and Martin, 1995, Gleeson *et al.*, 2017].

Perhaps the most fully documented occurrence of biotite phenocrysts in comendites is from the Olkaria complex, Kenya Rift Valley [Macdonald *et al.*, 1987, Marshall *et al.*, 2009], where it occurs as subhedral to euhedral crystals 0.5–1.5 mm long. Geochemical modelling by Macdonald *et al.* [1987] did not find a role for biotite in the differentiation of the comendites and it must be assumed that it was, at least in this case, a non-fractionating phase. Jeffery *et al.* [2016] found minor amounts of biotite phenocrysts in comenditic trachytes of the Furnas volcano, São Miguel, Azores, and using rhyolite-MELTS calculated that there was ~1% biotite fractionation in the latest evolutionary stages. In contrast, Jeffery *et al.* [2017] reported biotite phenocrysts in the comenditic trachytes of the Grotta de Vale Ignimbrite Formation on Terceira but found no evidence from geochemical modelling that it was a fractionating phase. Gleeson *et al.* [2017] reported biotite forming <2% of the phenocryst assemblage in peralkaline rhyolites of the Aluto volcano but did not identify it in their modelled fractionating assemblages. In contrast, using major element mass balance calculations White *et al.* [2006] found that biotite was part of the fractionating assemblage in the comenditic Emory Peak Rhyolitic Member in the Pine Canyon caldera, Trans-Pecos Texas, accompanying alkali feldspar, quartz, magnetite, zircon and monazite. Further study of biotite–phyric suites can continue to test the efficacy of biotite fractionation but on current evidence its role seems normally to be minor.

6.4. *Status of kaersutite and orthopyroxene fractionation*

This section discusses the potential role of “unseen”, usually higher pressure, phases in magma evolution. Two recent studies have focused attention on

the possible role of kaersutite in the differentiation of alkali basalt to trachyte. Nekvasil *et al.* [2004] experimentally simulated incremental crystal fractionation of a *hy*-normative hawaiite towards sodic rhyolite. The experimental conditions were pressure 9.3 kbar, temperatures 1250–860 °C, bulk water content of the hawaiite > ~0.5 wt% and fO_2 ~1.5 log units below FMQ. The most evolved residual melts generated were trachytic, with SiO₂ ~64 wt%, relatively low Na₂O/K₂O ratios (~1), and compositions on the peraluminous/metaluminous boundary (mol. Al₂O₃/(CaO + Na₂O + K₂O) ≈ 1). The earliest stages were dominated by olivine–clinopyroxene crystallization but at 1060 °C kaersutite joined the assemblage and was the dominant phase down to 900 °C. An important result was an acceleration of silica enrichment and production of trachytic residual melts, the “mafic rhyolites” of Nekvasil *et al.* [2004]. The experiments outlined, therefore, a possible role for kaersutite fractionation at deep crustal pressures, although they did not proceed as far as producing peralkaline melts.

In the unusual, perhaps unique, case of the Marie Byrd Land province, West Antarctica, LeMasurier *et al.* [2011] proposed that pantellerites were derived by fractional crystallization of basanite magma. Their model suggested that basanite was generated within the asthenosphere at depths >50 km and then fractionated within the lithosphere (~30–35 km) to form metaluminous trachyte. The critical mechanism for crossing the thermal divide from silica-undersaturated to silica-saturated melts was fractionation of kaersutite, which LeMasurier *et al.* [2011] were able to model geochemically. Note the consistency between the inferred depth of kaersutite crystallization and the experimental results (9.3 kbar) of Nekvasil *et al.* [2004]. The trachytic melts then rose to high crustal levels (≤5 km), where fractionation under low fO_2 and low P_{H_2O} favoured a high plagioclase/clinopyroxene ratio and generation of pantelleritic magmas. Kaersutite phenocrysts were not recognized in the suite, which LeMasurier *et al.* [2011] ascribed to complete resorption during ascent from mantle depths. Geochemical modelling also showed the possibility that the pantellerites could have been derived by crystallization of an *ol-hy*-normative basalt but such rocks are not known in association with the pantellerites. The interesting dilemma, then, was to invoke a major fractionating

phase which is not seen, or a hypothetical parent magma which is not seen, in the actual rocks.

Other studies have invoked, on the basis of geochemical modelling, amphibole crystallization from the intermediate members of peralkaline suites. Mungall and Martin [1995] found that including amphibole in the fractionating assemblage was necessary in order to model the transition from mugearite to felsic magma in the peralkaline suites of Terceira, Azores. In contrast, Jeffery *et al.* [2017] found, from least-squares mass balance models, that inclusion of amphibole resulted in model failure. During modelling of the basalt–comenditic trachyte suite from the Rallier-du-Baty Peninsula, Kerguelen, Gagnevin *et al.* [2003] suggested that certain aspects of the HFSE distribution could be explained by crystallization of amphibole at an intermediate stage. Field *et al.* [2012] referred to disequilibrium amphibole occurring in a Dabbahu (Boina) pantellerite, which may be relict from an earlier fractionation stage. The potential role of amphibole in the evolution of peralkaline silicic suites seems to be a real possibility if, for the moment, not robustly documented.

Orthopyroxene phenocrysts have been reported in the comenditic Shungura Tuff, Kenya [Martz and Brown, 1981], comenditic ignimbrites of the Black Mountain volcanic centre, Nevada [Vogel *et al.*, 1987], the comenditic Wild Horse Mesa Tuff, California [McCurry, 1988], and comendites of the Nemrut volcano, Turkey [Macdonald *et al.*, 2015]. Sumner and Wolff [2003] recorded hypersthene phenocrysts in trachytes and comendites of the “TL” ignimbrite, Gran Canaria, the hypersthene reacting to clinopyroxene and magnetite in the comendite. Using MELTS modelling, Rooney *et al.* [2012] showed that comendites of the Chefe Donsa suite, Ethiopia, could have been formed by 70% fractionation from trachyte magma of an assemblage including orthopyroxene; however, no orthopyroxene phenocrysts were recorded in the rocks.

As far as we are aware, no experimental study of a peralkaline silicic rock has yet generated orthopyroxene and its stability range in peralkaline magmas is far from clear. It cannot, however, be precluded that some peralkaline suites pass through the orthopyroxene stability field at high pressure, the mineral normally being resorbed at lower pressure. Orthopyroxene was described in the trachyandesite to sodic trachyte portion of the composite P1 ig-

nimbrite at Gran Canaria, Canary Islands [Freundt and Schmincke, 1995], where it occurs in equilibrium with clinopyroxene, plagioclase, ilmenite, and magnetite that suggest higher temperatures (900–815 °C), more oxidizing conditions ($fO_2 > FMQ$), and potentially higher pressures (340 ± 150 MPa) that are described for most peralkaline systems. Orthopyroxene was also reported in alkalic (but metaluminous) rhyolite from the Kane Wash Tuff [Kane Springs Wash Caldera, Nevada; Novak and Mahood, 1986], where the equilibrium mineral assemblage also provides evidence of higher temperatures (>820 °C) and pressures (~ 480 MPa) with oxygen fugacities at or slightly above the FMQ buffer.

7. The peralkaline silicic endpoint(s)

Silicic suites reach peralkalinity, in the sense of having a molecular excess of ($Na_2O + K_2O$) over Al_2O_3 , when SiO_2 contents are in the range 62–70 wt% (MgO ~ 1 wt%), i.e., in the trachyte–rhyolite range. They enter “peralkaline space” at different points and then follow different trends (Figure 6). In detail, in many centres the magmas follow more than one trend. On Pantelleria, for example, almost all the eruptive episodes followed slightly different trends [Jordan *et al.*, 2021]. On Terceira two trends are discernible from mafic to silicic: one follows a slightly lower Al, higher Fe trend and ends up as pantellerites; the other follows a slightly higher Al, lower Fe trend and produces comenditic trachytes and comendites [Mungall and Martin, 1995]. The two trends were a result of different primary basalts and the timing and extent of FeTi-oxide fractionation. The different trends must be a result of different fractionating assemblages and therefore of initial compositional differences and/or variable conditions of crystallization. LeMasurier [2019] used mass balance modelling to show that comendites and pantellerites of Marie Byrd Land followed separate pathways *via* fractional crystallization. The pathway to comendites involved fractionating a relatively large proportion of FeTi-oxides and a low plagioclase/pyroxene ratio; that to pantellerites involved lower proportions of FeTi-oxides and higher plagioclase/pyroxene ratios.

All trends, including those of glasses produced experimentally from pantellerites, tend to converge on a small range of compositions, the endpoints of

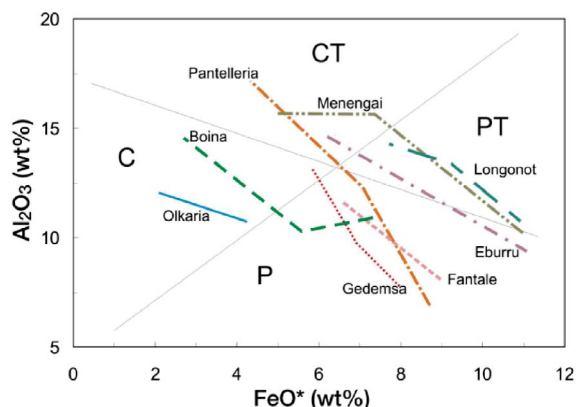


Figure 6. Trends of selected peralkaline suites on an FeO^* – Al_2O_3 plot [after Macdonald *et al.*, 2011]. Rock types: C, Comendite; CT, Comenditic Trachyte; P, Pantellerite; PT, Pantelleritic Trachyte.

which have $\text{FeO}^* \sim 13$ wt% and $\text{Al}_2\text{O}_3 \sim 5$ wt% (Figure 7a). Macdonald *et al.* [2012] referred to these endpoints as the effective minima compositions (EMC) for peralkaline silicic magmas. The use of the term *effective* alluded to the fact that melts more evolved than this are highly unlikely to separate from their crystal mush hosts. The relatively high density due to the high Fe contents and their normal occurrence as low melt fractions are also likely to inhibit crustal ascent and they remain trapped at depth. Possible extruded exceptions are a pantellerite obsidian (lava?) from Fantale, Ethiopia [Lacroix, 1930] and a lava from the Mt Takahe volcano, Marie Byrd Land [LeMasurier *et al.*, 2018]. It is important to note that, at least at Boseti, the highly evolved compositions were reached by the fractionation of alkali feldspar + fayalite + hedenbergite + oxide \pm quartz assemblages, the dominant assemblage in the associated pantellerites.

Increasing fractionation, as measured by P.I., is accompanied by Si enrichment until P.I. reaches about 2.00, when the trend reverses to Si decrease (Figure 7b). It is as yet unclear what mineral assemblage has generated the Si-depletion trend, although quartz fractionation may have been involved. In two extraordinary cases, the melt evolved significantly beyond the EMC. A matrix glass from the Boseti volcano, Ethiopia, has 2.2 wt% Al_2O_3 and 16.99 wt% FeO^* [Macdonald *et al.*, 2012], and interstitial glass from the Mt Takahe pantellerite has 1.70 wt% Al_2O_3 ,

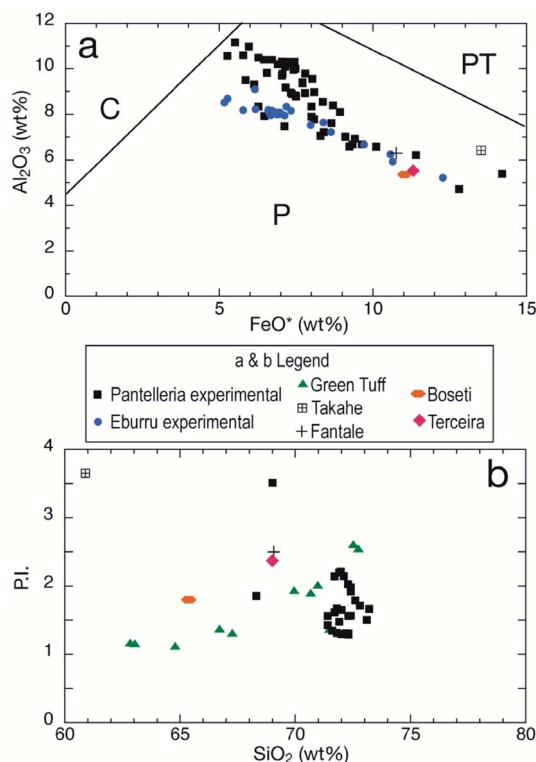


Figure 7. (a) FeO^* – Al_2O_3 plot of highly evolved pantelleritic compositions. Data for Eburru and Pantelleria are for glasses produced experimentally from Eburru and Pantescan pantellerites by Scaillet and Macdonald [2006b] and Di Carlo *et al.* [2010], respectively. Fantale: obsidian from the Fantale volcano, Ethiopia [Lacroix, 1930]. Boseti: average lighter matrix glass in sample B375, Boseti volcano, Ethiopia [Macdonald *et al.*, 2012]. Melt inclusion in fayalite, Terceira Island, Azores [Mungall and Martin, 1995]. Mt Takahe, lava from Mt Takahe volcano, Marie Byrd Land [LeMasurier *et al.*, 2018]. (b) SiO_2 –Peralkalinity Index (P.I.) plot for selected suites and rocks. Data sources: Green Tuff, Pantelleria—Liszewska *et al.* [2018]; Boseti, Fantale, Takahe and Terceira—as for Figure 7. Experimental glasses determined on Pantescan pantellerite at $P = 25$ – 150 MPa, $T = 680$ – 800 °C, $f\text{O}_2 \leq \text{NNO}$, and $\text{H}_2\text{O}_{\text{melt}}$ up to 6 wt% [Di Carlo *et al.*, 2010]. Experimental glasses from Eburru—Scaillet and Macdonald [2006b]. Rock types: C, Comendite; P, Pantellerite; PT, Pantelleritic Trachyte.

16.25 wt% FeO* and a P.I. of 13.6 [LeMasurier *et al.*, 2018]. It plots in the trachyte field in the TAS classification. Presumably these compositions were a result of massive feldspar crystallization; this would be consistent with the observation that alkali feldspar is the only phenocryst in the Takahe host rock.

An unresolved question is whether there is, in fact, more than the small range of EMC in the natural systems shown in Figures 7a and b. We noted earlier (Section 5) the presence in the Q-Ab-Or-Ac-Ns system of a low-temperature zone, equivalent to the low-temperature valley in the granite system, towards which peralkaline silicic melts migrate during fractional crystallization. This would seem to be consistent with the convergence of natural and experimental melts towards the EMC on Figures 7a and b. However, on the basis of alkali feldspar–liquid relationships in Menengai trachytes, Macdonald *et al.* [2011] argued that there might in fact be more than one such low-temperature zone, with, in particular, certain pantelleritic trachytes following different trend(s) to comendites and pantellerites. For the Menengai melts to reach the EMC a sharp decrease in FeO*/Al₂O₃ ratios would be required (Figure 6). A set of experiments comparable to those by Scaillet and Macdonald [2006b] and Di Carlo *et al.* [2010] would help to resolve this issue.

Whether a given suite reaches the minimum composition(s) is simply a function of the degree of fractionation achieved. All peralkaline silicic suites have the *potential* to generate pantellerites given suitable tectonic and thermal conditions and assuming that the lowest-temperature melts can be satisfactorily separated from crystals.

8. Geochemical modelling

A major approach to using the analytical data base of peralkaline silicic rocks is geochemical modelling, where various mathematical and thermodynamic models are used to test the viability of petrogenetic processes, such as fractional crystallization, partial melting and magma mixing. This section outlines the most commonly employed models, commenting on their strengths and weaknesses.

The MELTS and rhyolite-MELTS models [Gualda *et al.*, 2012] have been increasingly widely used to investigate the role of fractional crystallization under variable P – T – fO_2 conditions, and with variable

starting water contents [Peccerillo *et al.*, 2003, Ronga *et al.*, 2010, White *et al.*, 2009, Çubukçu *et al.*, 2012, Rooney *et al.*, 2012, Macdonald *et al.*, 2015, Jeffery *et al.*, 2017, Hutchison *et al.*, 2018]. Generally, the models have been successful at predicting the liquid lines of descent and the mineral assemblages and compositions. Rhyolite-MELTS does not, however, model accurately the formation of hydrous phases such as amphibole, biotite, and apatite [Gualda *et al.*, 2012]. Rooney *et al.* [2012] found that rhyolite-MELTS tends to overestimate melt P₂O₅ concentrations, as a result of deficiencies in the apatite solubility model. In their modelling of fractional crystallization in peralkaline ignimbrites of Terceira, Jeffery *et al.* [2017] noted that rhyolite-MELTS failed to model conditions at temperatures <850 °C, especially the feldspar compositions.

One result of the geochemical modelling is the information it has provided on the existence, or otherwise, of the so-called Daly Gap. In the next section, the modelling results are incorporated with other lines of evidence to explore the significance of the gap in peralkaline silicic systems.

9. Significance of the Daly Gap

In some peralkaline-oversaturated suites, marked by crosses in Table 1, there is an essentially complete series of *melt* compositions between basalt and trachyte, although intermediate members, roughly corresponding to mugearites and benmoreites, are usually volumetrically minor, especially in continental volcanoes. Other suites, however, show composition gaps, albeit over different SiO₂ ranges (Table 1). The absence or scarcity of intermediate magmas is the basis of the Daly Gap, the significance of which has exercised the minds of petrologists since the days of Bunsen [1851] without a completely satisfactory resolution. The majority of recent studies on peralkaline silicic suites have ascribed the formation of the trachyte and rhyolite members to protracted fractional crystallization of basaltic magma and several mechanisms to explain the Daly Gap have been proposed.

9.1. Physical controls

The apparent absence of intermediate eruptives has been related to various physical controls. Weaver [1977], for example, suggested that high density

and/or crystal content prevented their eruption at Emuruangogolak volcano, Kenya, and Mungall and Martin [1995] and Jeffery *et al.* [2017] attributed their absence from Pico Alto, Terceira, at least partly to similar controls. Rooney *et al.* [2012] have proposed that, at Ethiopian Rift volcanoes, intermediate melts are not extracted from crystal–liquid mushes because there has been insufficient crystallization to form a rigid framework, generally at about 50–60% crystallinity. Sieburg *et al.* [2018] also argued that mafic magmas cannot dynamically ascend through low-density felsic reservoirs.

9.2. Rapid differentiation through a short crystallization interval

In some suites evolving from basalt to peralkaline rhyolite, geochemical modelling has shown that SiO_2 values do not change linearly. There are stages, especially in intermediate compositions, where the values can change rapidly over a short temperature interval [Mushkin *et al.*, 2002]. White *et al.* [2009] and Gleeson *et al.* [2017] have proposed this mechanism to explain the Daly Gaps at Pantelleria and Aluto volcanoes, respectively. Figure 8 shows the rate of change of SiO_2 during fractional crystallization at Aluto volcano modelled by Gleeson *et al.* [2017] for assumed wall-rock temperatures of 500 and 300 °C. The gap, or a relative scarcity of intermediate magmas, occurs at broadly similar SiO_2 values, e.g., 50–62 wt% at Pantelleria and 50–64 wt% at Aluto, reflecting the broadly similar fractionating assemblages in these peralkaline systems.

9.3. Plutonic xenoliths

Some studies have suggested that the missing intermediate rocks are represented by plutonic xenoliths. Comagmatic hypabyssal xenoliths of intermediate composition fill the compositional gap in the lavas of the Santa Barbara and Pico Alto volcanoes, Terceira [Mungall and Martin, 1995]. Freundt-Malecha *et al.* [2001] considered monzonitic and syenitic xenoliths in the rhyolite–trachyte–basalt composite ignimbrite P1 on Gran Canaria to be the “missing links” in the bimodal suite. Boulders of amphibole-bearing monzonites and monzogabbros in the Rallier-du-Batty Peninsula, Kerguelen are thought by Gagnevin *et al.*

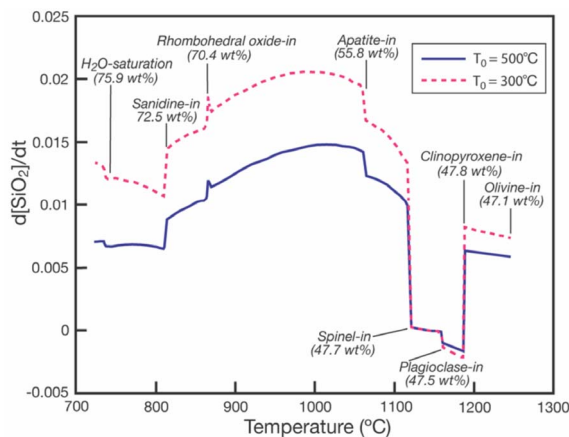


Figure 8. SiO_2 variation as a function of time ($d[\text{SiO}_2]/dt$) in silicate melt during fractional crystallization, plotted against magmatic temperature. Two wall-rock temperatures (T_0) were assumed in the modelling (500 and 300 °C). Order of phenocryst appearance inferred for Aluto volcano, Ethiopia. Note the sharp increases in $d[\text{SiO}_2]/dt$ when FeTi-oxides, and to a lesser extent apatite, crystallize. Modified from Gleeson *et al.* [2017].

[2003] to represent intermediate magmas formed at depth but not erupted. Syenitic xenoliths are common in the Green Tuff, Pantelleria (Figure 9a). Ferla and Meli [2006] reported syenogabbroic and syenodioritic xenoliths in trachytic lavas of Pantelleria which compositionally fill the gap between basalts and trachytes on the island. However, they concluded from mineralogical and geochemical evidence that they had formed by the mixing of hawaiitic and trachytic magmas. Detailed petrographical study is clearly required to determine the origin of plutonic xenoliths.

9.4. Magmatic enclaves

Many studies have recorded the presence in the salic members of enclaves representing chilled melts of intermediate composition, e.g. trachybasaltic inclusions on Mayor Island [Ewart *et al.*, 1968, Rutherford, 1978], leucoandesites in Caenozoic comendites of SW Sardinia [Morra *et al.*, 1994]; mafic enclaves at Pantelleria [Ferla and Meli, 2006], trachyandesitic inclusions in the Gold Flat pantellerite, Nevada [Mac-

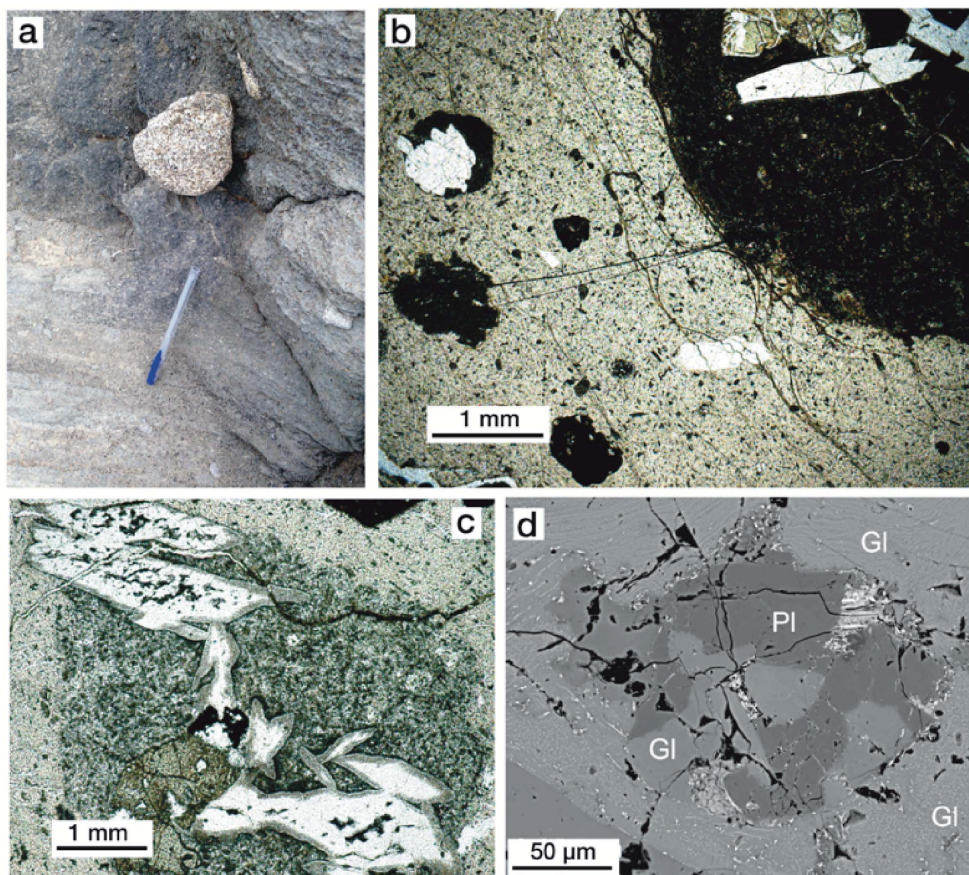


Figure 9. (a) Syenite nodule in pantelleritic Green Tuff, Pantelleria. (b) Mafic inclusions (dark) in comendite (light brown). Largest inclusion contains a disaggregated gabbroic xenolith; inclusion at top right contains a partially resorbed alkali feldspar xenocryst. (c) Disaggregating syenite xenolith in magmatic inclusion of intermediate composition in comendite host. (b) and (c), from Greater Olkaria Volcanic Complex, Kenya [based on Macdonald *et al.*, 2008]. (d) Highly resorbed plagioclase (Pl) antecryst (An_{26-23}) with glass (Gl) in pantellerite, Gold Flat Tuff, Nevada [Macdonald *et al.*, 2019].

donald *et al.*, 2019] and mafic enclaves in comendites of the Olkaria Complex [Figure 9b; Macdonald *et al.*, 2008]. While apparently providing strong evidence for the presence of intermediate magmas in the system, some studies have interpreted them as the products of mixing between basalt and trachyte magmas [Ferla and Meli, 2006, Romengo *et al.*, 2012]. As noted for the plutonic xenoliths, petrographic and mineral chemical studies are needed to determine the mode of origin. The sample shown in Figure 9c shows a complex assemblage of a disaggregating syenite xenolith in a magmatic inclusion of intermediate composition in a comendite host from the Olkaria Complex [Macdonald *et al.*, 2008].

9.5. *Phenocryst assemblages*

Megacryst assemblages in peralkaline trachytes and rhyolites often provide evidence for the crystallization of magmas of intermediate composition, for example plagioclase cores to alkali feldspar phenocrysts and forsteritic cores to olivine phenocrysts in rhyolites [White *et al.*, 2009, Macdonald *et al.*, 2012, 2019, Jeffery *et al.*, 2017, Liszewska *et al.*, 2018, Iddon *et al.*, 2019, Parker, 2019, Neave, 2020]. The crystals are not in equilibrium with their host melts and are taken to be residual from an earlier stage of crystallization and from less evolved magmas (Figure 9d).

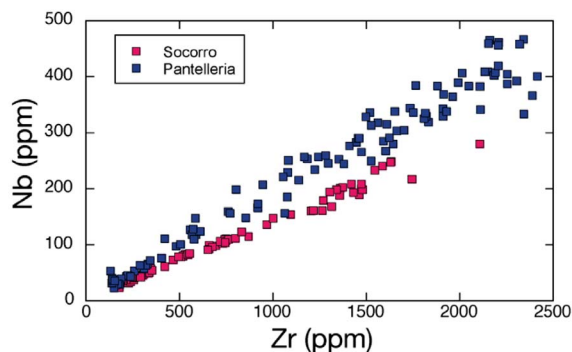


Figure 10. Zr–Nb plot for eruptive suites of Pantelleria and Socorro. Data sources: Pantelleria, Avanzinelli *et al.* [2004], Civetta *et al.* [1998], White *et al.* [2009]; Socorro, Bohrsen and Reid [1997].

9.6. *Geophysical evidence for intermediate magmas at depth*

Based on a positive gravity anomaly beneath Pantelleria, Mattia *et al.* [2007] suggested that it may be a result of high-density intermediate magmas trapped deep in the system. Similarly, a positive gravity anomaly in the shallow crust beneath Aluto caldera may provide evidence for the density filtering of intermediate magmas forming a Daly Gap [Iddon *et al.*, 2019]. The anomalies do not, however, provide unequivocal evidence for the nature of the source rocks; they could, for example, be hawaiitic or mixed magma rocks.

9.7. *The need for a full petrographic basis*

We discuss here one aspect of composition gaps which highlights the need for detailed petrographic information to accompany the geochemical data. The basalt–peralkaline rhyolite suites of Socorro Island and Pantelleria are in many ways closely similar (Figure 10). The range of lithologies is from alkali basalt through hawaiite to trachyte to comenditic trachyte (\pm pantelleritic trachyte) to pantellerite. The major and trace element compositions of the main components are broadly similar. A Zr–Nb plot (Figure 11) shows strongly positive relationships in both suites, with slightly different Zr/Nb ratios. The continuous nature of the trends could be taken to point

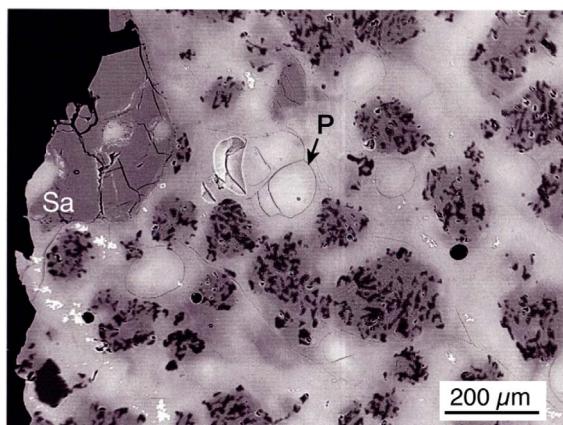


Figure 11. Partial melting of syenite xenolith (residual sanidine crystal (Sa) at top left) to form a pale glass with perlitic cracks (P) and a darker glass with feldspar microlites and vermicular quartz. Olkaria complex, Kenya, BSE image. After Macdonald *et al.* [2008].

to crystal fractionation as the dominant differentiation mechanism. However, the Zr–Nb plot disguises the fact that there is, as noted above, a major composition gap in both series, SiO_2 ~54–61 wt% on Socorro and 50–62 wt% on Pantelleria. In both suites, trachytic rocks have certain trace element contents overlapping those in mafic rocks, the overlap being partly used to propose two different petrogenetic histories.

For Pantelleria, White *et al.* [2009] showed that the gap is at least partly filled by feldspar-accumulitic trachytes, with, *inter alia*, lower incompatible trace elements (ITE) and higher Ba contents than the non-accumulitic equivalents, thus confirming the existence of the Daly Gap in *magmatic* compositions. They were, however, able to model compositional variation in the suite as dominated by fractional crystallization, suggesting that the compositional gap was a result of rapid crystallization. Such a model cannot be applied to Socorro, where the rocks are aphyric or sparsely phyrlic. Bohrsen and Reid [1995, 1997] used the overlapping trace element evidence to suggest that the mafic and silicic rocks on Socorro had independent origins, the silicic rocks having been formed by partial melting of alkali basalts or gabbros. Thus, the essentially continuous nature of the Zr–Nb relationships masks, for Pantelleria, the existence

of a composition gap, and, for Socorro, may relate to independently evolving magmas. The point to be stressed from this example is that the significance of composition gaps can be properly assessed only on the basis of full petrographic information.

In summary, we take the view that in the majority of peralkaline silicic suites the bulk of petrological and geochemical evidence points to fractional crystallization having produced an essentially continuous range of melts, some of which were prevented from being erupted through physical or thermodynamic discrimination.

10. Role of crust

In this section, three processes involving crustal rocks are considered: (i) two-stage models, where mafic rocks are partially melted to form peralkaline melts or their parental melts; (ii) partial melting of continental crust; and (iii) crustal contamination.

10.1. Two-stage models

Two-stage models for the origin of peralkaline silicic rocks usually involve partial melting of mafic rocks (underplated?) to form trachyte, followed by fractional crystallization of the trachyte to form peralkaline rhyolites [Pantelleria: Lowenstern and Mahood, 1991; Avanzinelli *et al.*, 2004; Socorro: Bohrson and Reid, 1997; Ethiopia; Trua *et al.*, 1999]. The models have been developed partly to explain the volumetric excess in many peralkaline provinces of felsic rocks over mafic rocks, and the absence or scarcity of intermediate compositions as explanations for the Daly Gap. Other factors invoked include trace element features inconsistent with a fractional crystallization hypothesis but compatible with partial melting [Bohrson and Reid, 1997; Trua *et al.*, 1999], the relatively low water contents of pantellerites [Lowenstern and Mahood, 1991] and evidence from clinopyroxene chemistry, where compositional trends in pyroxenes in mafic and silicic rocks indicate different parental magmas [Avanzinelli *et al.*, 2004]. The [Lowenstern and Mahood, 1991] model fails, however, to take account of polybaric degassing episodes at Pantelleria [White *et al.*, 2009], whilst White *et al.* [2009] showed that clinopyroxene chemistry at Pantelleria is actually more compatible with fractional crystallization than partial melting.

Major element geochemical modelling has been used to confirm the potential viability of the partial melting of the alkali basalt/gabbro model. Bohrson and Reid [1997] calculated that moderate degrees (5–10%) of modal equilibrium melting of Socorro alkali basalts could generate magmas compositionally similar to the Socorro felsic rocks. Using equilibrium melting models, Peccerillo *et al.* [2003] found that about 10–30% melting of a basalt/gabbro could generate the Gedemsa felsic rocks. However, as White *et al.* [2009] have stressed, major element mass balance models cannot effectively discriminate between (Rayleigh) fractional crystallization and equilibrium batch melting, a point acknowledged by Peccerillo *et al.* [2003] and Bohrson and Reid [1997].

Syenogabbroic and syenodioritic xenoliths in trachytic lavas from Pantelleria contain glass which varies in composition from metaluminous trachyte to peralkaline quartz trachyte to pantellerite. The glasses are thought to have formed by partial melting of the hosts [Ferla and Meli, 2006]. However, in detail they are not similar to other Pantescan pantellerites. Comendites of the Olkaria complex, Kenya Rift Valley, contain syenitic xenoliths in basalts which also experienced partial melting [Macdonald *et al.*, 2008]. The glasses range from \pm c-normative to ac-normative. In one example (Figure 11), partial melting produced a pale, peralkaline glass and a darker glass containing vermicular quartz and feldspar microlites. It is poorer in SiO_2 , TiO_2 , FeO^* , MnO and CaO , and richer in Al_2O_3 , Na_2O and K_2O than the peralkaline variety. This is consistent with an increasing ratio of alkali feldspar to mafic components in the residual solid as melting proceeded. The peralkaline glasses are comenditic but compositionally distinct from the host comendites, as in the Pantescan case above. It appears, then, that although peralkaline melts may be generated locally by the partial melting of xenoliths, they do not generally follow the main liquid line of descent.

As noted by Scaillet and Macdonald [2003] and Caricchi *et al.* [2006], no experimental study has yet produced peralkaline melts by partial melting of crustal rocks, ranging from underplated basalts and gabbros to higher-level, more salic lithologies. Such a process would need volatile fluxing, as suggested by Bailey [1980], Bailey and Macdonald [1987] and Scaillet and Macdonald [2003], but that has not been demonstrated experimentally either.

10.2. *Partial melting of continental crust*

Here we discuss models of the formation of peralkaline silicic rocks by the partial melting of continental crust; basalt may be the heat source promoting the melting. Recourse to crustal melting models has commonly been made to explain the large volumes of silicic rocks in some provinces compared to the associated basalts. However, models of crust–basalt interactions have shown that the amount of basalt needed to generate a given amount of silicic magma by melting via enthalpy transport is broadly similar to that needed for crystal fractionation [Barboza and Bergantz, 2000, Dufek and Bergantz, 2005].

Through comparison of the major element compositions of the comendites of the Olkaria (Naivasha) complex with phase equilibria in the system $\text{Na}_2\text{O}–\text{K}_2\text{O}–\text{Al}_2\text{O}_3–\text{SiO}_2$, Bailey and Macdonald [1970] suggested that the comendites represent a path of increasing partial melting of crustal rocks in the presence of an alkali-bearing vapour. Macdonald *et al.* [1987] also invoked a model for the Olkaria rocks of partial melting of heterogeneous crustal source rocks, followed by variable amounts of fractional crystallization, calling on an important role for volatiles in promoting peralkalinity and in controlling trace element distribution patterns. Davies and Macdonald [1987] showed that whereas Sr–Nd isotope relationships are consistent with formation of the Olkaria rhyolites by fractionation of the associated basalts by AFC, Pb isotopic systematics showed that the basalts and rhyolites are not cogenetic. They proposed that the rhyolites represent crustal melts formed at ~6 km depth. U-series disequilibria and Th-isotopes were used by Black *et al.* [1997] to confirm the crustal origin of the rhyolites. More recently, Macdonald *et al.* [2008] presented evidence from matrix glasses in the trachytes that the rhyolites are in fact the products of crystal fractionation of basalt, but they did not offer an explanation for the differences in Pb isotope compositions.

The Pine Canyon caldera, Trans-Pecos Magmatic Province, Texas, erupted peralkaline quartz trachyte, rhyolite and high-silica rhyolite lavas and ash-flow tuffs about 32–33 Ma [White *et al.*, 2006]. The trachytes and rhyolites can be related to associated basalts and mugearites by fractional crystallization, but the peralkaline high-silica rhyolite is thought to have formed by ~5% partial melting of mafic gran-

ulite at <25 km depth, melting having been promoted by heat from basaltic intrusions coupled with metasomatism by a F-rich volatile phase. High-silica comendite associated with the Pine Canyon system are strongly depleted in incompatible trace elements compared to the trachyte-low silica rhyolite series and have much lower Zr/Hf, Nb/Ta, and Ce/Yb ratios consistent with a crustal origin [Joachim *et al.*, 1986, Green, 1995, White and Urbanczyk, 2001]. This conclusion was supported by a major element mass balance model with good results ($\Sigma r^2 = 0.370$) and a geologically reasonable residual assemblage that requires a similar amount of high-silica comenditic melt (~4%) as trace element models (~5%).

10.3. *Role of crustal contamination*

Many studies have invoked a role for crustal contamination, and specifically Assimilation–Fractional Crystallization (AFC), in the evolution of peralkaline rhyolitic suites. The evidence always comes from trace element and isotopic data which are shown to be incompatible with closed-system evolutionary models. Few (if any) papers have dealt with the mechanism of contamination, e.g. by incorporation of partially melted host rock, or by some sort of selective diffusive process.

Transitional basalts of the Olkaria (Naivasha) complex, Kenya, are thought to have assimilated variable amounts of Proterozoic amphibolite facies crust Davies and Macdonald [1987]. Bohrsen and Reid [1995] argued that the alkali basalts of the Socorro suite assimilated small amounts of Fe-oxyhydroxides, an important constituent of metalliferous sediments, in small magma chambers located in the shallow oceanic crust or within the volcanic edifice. Contamination of peralkaline trachytes on São Miguel, Azores, by syenites altered by seawater was proposed by Snyder *et al.* [2004]. Alkali basalt at the Pine Canyon caldera, Trans-Pecos Texas, evolved by ~60–70% fractional crystallization coupled with significant assimilation of shale wall rock (M_d/M_c (mass assimilated/mass crystallized) = 0.3–0.4) to produce peralkaline quartz trachyte [White *et al.*, 2006].

Mafic magmas in various suites of the Main Ethiopian Rift experienced variable degrees of contamination at various depths in the heterogeneous Pan-African crust [Rooney *et al.*, 2012, Trua *et al.*,

1999]. Fractional crystallization of the Gedemsa magmas was accompanied by small amounts of assimilation of crustal material ($M_a/M_c < 0.1$) [Peccerillo *et al.*, 2003]. Small degrees of contamination have also been invoked for the Marie Byrd Land suite (<3%; LeMasurier *et al.* [2011]). In contrast, Hutchison *et al.* [2016a, 2018] and Gleeson *et al.* [2017] argued that several volcanoes of the Main Ethiopian Rift which have erupted basalts and peralkaline rhyolites show evidence of no, or minimal, crustal assimilation. Hutchison *et al.* [2018] suggested that this might, at least partly, be because the crust becomes less fusible as rifts mature. White *et al.* [2020] also found that the basalts of Pantelleria experienced no significant crustal component. The Millennium eruption of the Changbaishan-Tianchi volcano apparently involved magmas showing no evidence of contamination [Wei *et al.*, 2013].

An important question is whether the assimilation can significantly change the direction of the liquid line of descent of residual melts, in particular the transition from silica-undersaturation to silica-oversaturation. One possible example is from the Leyva Canyon volcano, Trans-Pecos Magmatic Province, Texas, where White and Urbanczyk [2001] found that mixing of ne-normative basaltic magma with a high- Al_2O_3 crustal component resulted, *inter alia*, with silica-oversaturated mildly peralkaline felsic rocks.

11. Experimental evidence for the origin of peralkaline silicic rocks

11.1. Experiments on mafic compositions

Mahood and Baker [1986] studied experimentally the least-evolved basalt from Pantelleria under anhydrous conditions at 1 atm along the FMQ buffer and at 8 kbar to determine the liquid line of descent. The 1 atm experiments reproduced more closely the natural trend. However, after even ~70% crystallization, the SiO_2 content of the melt was still 50 wt%, far removed from the trachytic members of the suite. Nekvasil *et al.* [2004] attempted to generate peralkaline silicic melts by experimental simulation of incremental crystal fractionation of a hawaiitic magma. They suggested that the spectrum from hawaiiite to rhyolite could be produced by fractionation at 9.3 kbar with bulk water contents (in the starting material)

of >~0.5 wt% at $f\text{O}_2$ ~1.5 log units below FMQ. The most evolved melt synthesized had 63.99 wt% SiO_2 and a P.I. of 0.89, i.e., it was a metaluminous trachyte. Caricchi *et al.* [2006] conducted an experimental study of a hydrous, transitional alkaline basalt at 0.5 to 1 GPa and 950 to 1100 °C. They found that melts in fractional crystallization experiments approached the natural rock trend leading to the transition from subaluminous to peralkaline residual melts. However, the most evolved melt had 61.94 wt% and a P.I. of 0.71, considerably removed from peralkalinity. Similar results were found by White *et al.* [2009] during geochemical modelling of the transition from basalt to trachyte; in this case, equilibrium crystallization models produced melts with low P.I. (0.62–0.78); fractional crystallization was required to generate peralkalinity.

The failure of the experiments to produce peralkaline silicic compositions probably reflects the fact that in nature the most peralkaline products represent only a very small fraction of the starting basalt, in the case of pantellerites <5%. Such small melt fractions would not normally be discernible in the experiments. Attempting to quantify conditions in intermediate compositions, Rondet *et al.* [2019] conducted high P – T experiments on a trachyandesite from the Pavin Massif Central, France. The phenocryst assemblage was plagioclase, amphibole, clinopyroxene and Fe–Ti oxides. Matrix glass and melt inclusions had trachytic compositions, some being mildly peralkaline. The experiments constrained the pre-eruptive conditions as 970–975 °C, 150–200 MPa, NNO + 1.5, and 4.5–5.5 wt% melt H_2O . The experimental glasses, however, were trachytic but peraluminous.

11.2. Metaluminous to peralkaline transition

Evidence on the transition from metaluminous to peralkaline trachytes was provided by the experiments of Martel *et al.* [2013] on rocks from the Chaîne des Puys, French Massif Central. Rocks from seven intrusive bodies were studied at pressures between 200 and 400 MPa, temperatures between 700 and 900 °C, at water saturation and $f\text{O}_2$ of NNO + 1. Two of the intrusions can be used to exemplify the results, Chopine (P.I. 1.08) and Clierzou (P.I. 0.89). Chopine contains phenocrysts of plagioclase, alkali feldspar, FeTi-oxides, biotite and clinopyroxene; Clierzou has

plagioclase, FeTi-oxides and amphibole. The phenocryst assemblages were reproduced fairly well by the experiments. Given the nature of the mineral assemblage, particularly the plagioclase and biotite in the Chopine rock, it might be expected that residual melts would, with decreasing temperature, show increasing SiO₂ contents and increasing peralkalinity. However, in both cases increasingly evolved melts were *less* peralkaline. The authors had to make corrections to their Na₂O analyses, to allow for possible Na volatilization during the experiment, and it is possible that the values presented are lower than the true values, lowering the P.I. of the glasses. In their experimental study of a pantelleritic pumice from the Green Tuff, Romano *et al.* [2020] found that initially the P.I. became lower than in the starting material and then increased to 2.1, an effect not seen in the natural rocks [Liszewska *et al.*, 2018].

Romano *et al.* [2018] used metaluminous trachytes from Pantelleria to examine the transition towards peralkalinity. Experimental conditions were 750–950 °C, 0.5–1.5 kbar, $fO_2 < NNO$ and at fluid saturation (with X_{H_2O} between 0 and 1). The residual glasses after 80 wt% crystallization had comenditic trachyte composition, produced by a massive crystallization of alkali feldspar. The experiments thus provided sound evidence for the metaluminous to peralkaline transition.

11.3. *Experiments on peralkaline rhyolites*

High P – T experiments on comendites have been conducted by Scaillet and Macdonald [2001, 2003] and on pantellerites by Scaillet and Macdonald [2006b], Di Carlo *et al.* [2010] and Romano *et al.* [2020]. In most cases, the experiments reproduced the natural phase assemblages and liquid lines of descent fairly well [Romano *et al.*, 2020]. Important general results were that (i) peralkaline silicic magmas can exist at temperatures below 700 °C; (ii) equilibration pressures are <5 kbar; (iii) most suites evolve at or just below FMQ; (iv) peralkaline silicic melts are normally water-rich (>4 wt%).

Despite considerable progress, certain problems remain. For example, the stability fields and compositions of amphibole are not well constrained. Romano *et al.* [2020] synthesized amphibole in the Green Tuff but it is absent in the natural rocks. The crystallization conditions of biotite have not been

fully documented, the factors controlling the crystallization of quartz are poorly known, and the relationships between ilmenite and aenigmatite have still not been fully resolved. It appears that the stability ranges of the phases are highly sensitive to melt composition, and to even small variations in intensive parameters, as reviewed by Romano *et al.* [2020]. However, the experimental data can be used as a useful complement to thermodynamic modelling which, as noted above, is not always successful in peralkaline compositions.

12. Fluids and degassing

The presence of dissolved volatiles in silicate melts is fundamentally important. (i) Volatiles affect the abundances and compositions of phases crystallizing in magma and their subsequent stability. (ii) They affect the physical properties of the magma, such as density and viscosity, and thus magma chamber dynamics, including the role of convection. (iii) They also affect fractionation rates and thus the nature and extent of the liquid line of descent. (iv) On reaching saturation, volatiles exsolve as bubbles, potentially driving volcanic eruptions and influencing the volcanic eruptive style. In this section, we discuss aspects of the volatile concentrations in peralkaline magmas and certain of the effects of degassing on magma evolution.

12.1. *Volatile concentrations in peralkaline silicic magmas*

Various methods have been used to estimate the volatile contents of peralkaline magmas. Abundances in obsidians and matrix glasses can provide such estimates but they are almost always minimum values due to the degassing of the host magmas before, during and after eruption. Melt inclusions in phenocryst phases can contain true magmatic values but care must be taken to ensure that the inclusions have not leaked or undergone some post-entrapment crystallization. For example, restored pre-eruptive melt H₂O contents of Olkaria comendites using δD and matrix H₂O values yielded values of up to 5.7 wt%, about twice the maximum found in the melt inclusions [Wilding *et al.*, 1993]. Water values in the literature are in the range 3.5–5.8 wt%,

except for a value of 7.9 ± 0.5 wt% for a comenditic trachyte pumice from Puy Chopine, Massif Central, France [Martel *et al.*, 2013]. In their review of studies of peralkaline magmatism in the Atlantic Ocean, Jeffery and Gertisser [2018] found that estimated melt water values ranged from 1.5 to 9.1 wt%. Although the situation varies from island to island, they noted that the highest values occur in the most peralkaline (evolved) rocks, suggesting that the H₂O concentrations are controlled largely by fractional crystallization.

Levels of CO₂ are usually low, <150 ppm [Lowenstern and Mahood, 1991, Gioncada and Landi, 2010, Field *et al.*, 2012, Neave *et al.*, 2012, Lanzo *et al.*, 2013]. Such low values strongly suggest that most of the CO₂ is lost from the magmatic system during the pre-pantellerite evolutionary stages. Lowenstern [1994] suggested that the low CO₂ contents of Pantescan pantellerites (<100 ppm) are consistent with saturation with a mixed H₂O–CO₂ vapour at 50–100 MPa. Neave *et al.* [2012] used the H₂O and CO₂ contents to estimate a maximum equilibration pressure of 1.5 kbar (150 MPa). Iddon and Edmonds [2020] argued that basalts stored beneath the Main European Rift are saturated in CO₂ at up to 18 km in the upper crust, much of the CO₂ being lost by diffusive degassing.

Fluorine abundances in peralkaline rhyolites can be very high, e.g., ≤ 2.2 wt% in the pantelleritic Gold Flat ignimbrite in Nevada [Macdonald *et al.*, 2019], or very low, e.g., ≤ 0.13 wt% in the Green Tuff, Pantelleria [Liszewska *et al.*, 2018]. The high values are in part made possible by the tendency of F to partition into the melt during magma evolution [Webster *et al.*, 1993, Barclay *et al.*, 1996]. Fluorine can influence phase relationships in magmas, e.g., by affecting the point at which quartz joins the crystallizing assemblage, and by determining the stability and composition of amphibole. By forming complexes with various elements, e.g., Zr and REE, it may increase their solubility.

In peralkaline silicic magmas, Cl partitions between melt, vapour, and saline liquids. How it partitions determines, *inter alia*, when it is degassed from the melt. For example, high and constant levels of Cl (up to 1 wt%) in pantellerites are because they are saturated with H₂O–NaCl fluids at low pressures [Metrich and Rutherford, 1992, Lowenstern, 1994]. As an example of degassing, White *et al.* [2009] showed

that a Cl-rich aqueous phase exsolved in the transition pantelleritic trachyte to pantellerite on Pantelleria. Neave *et al.* [2012] noted that Cl abundances in melt inclusions in the pantellerites are consistent with partitioning of Cl into a subcritical hypersaline fluid at low pressures, while Lanzo *et al.* [2013] used combined H₂O and Cl data to estimate a confining pressure of ~50 MPa for Pantescan pantellerites.

An important source of information on volatile contents and behaviour has been through high *P–T* experiments where the imposed volatile contents can be assessed by their success in matching the observed mineral assemblages and compositions. The high-water values are consistent with experimental studies on peralkaline rhyolites \pm trachytes [Scaillet and Macdonald, 2001, 2003, 2006b, Di Carlo *et al.*, 2010, Romano *et al.*, 2018]. The hydrous nature, along with the reduced nature indicated by the *f*O₂ values and low temperatures of equilibration (see above), prompted Macdonald [2012] to refer to peralkaline silicic magmatism as being of “cold-wet-reduced” type. This view was opposed to that of Bachmann and Bergantz [2008] who proposed that in hotspot systems high-silica rhyolites are of hot-dry-reduced type.

Hydrocarbon-bearing fluid inclusions have been reported in alkaline rocks of both silica-oversaturated [Strange Lake Pluton: Salvi and Williams-Jones, 2006] and silica-undersaturated [Khibiny and Lovozero massifs: Nivin *et al.*, 2005; Ilímaussaq complex: Krumrei and Markl, 2005] affinity. There is an active debate about the origin of the hydrocarbons: Salvi and Williams-Jones [2006], for example, ascribed their formation to wall rock alteration reactions, while Krumrei and Markl [2005] favoured a high-temperature magmatic origin for the hydrocarbons. As far as we know, nobody has reported hydrocarbons in a peralkaline silicic extrusive rock. If the absence is real, it is telling us something about the oxidation conditions during mantle melting or during magma transport.

12.2. Degassing

Simple mass balance calculations (and realistic amounts of fractional crystallization) indicate that if a primary basalt is generated with 1.5 wt% water and subsequently fractionates through to trachyte (where

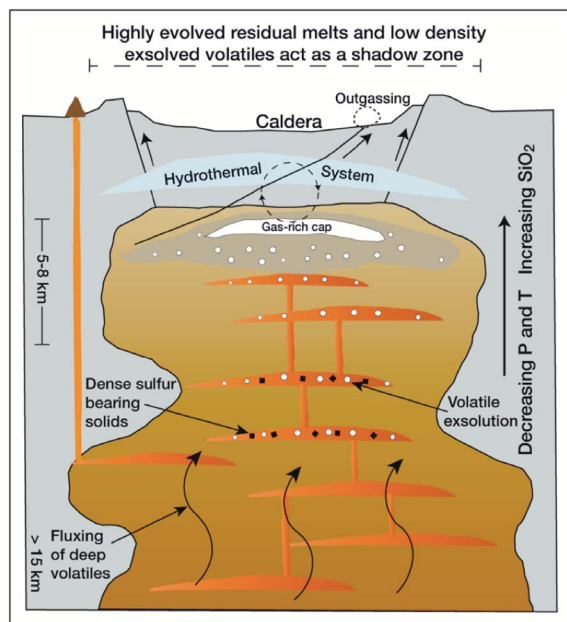


Figure 12. Cartoon of a magma system beneath the axial part of the Main Ethiopian Rift, stressing the behaviour of volatiles at various levels. Redrawn from Iddon and Edmonds [2020].

$F = 0.1$) in an essentially closed system with continuous partitioning of water into the melt, the trachyte magma will contain 15 wt% water. This is considerably higher than the maximum water solubility, ~8 wt%, determined experimentally in such magmas [Di Matteo *et al.*, 2004, Martel *et al.*, 2013]. Loss by degassing must occur. The question then arises: “At what level(s) did the various melts in the basalt–trachyte sequence degas?” Based on MELTS modelling of the basalt–pantellerite sequence on Pantelleria, White *et al.* [2009] inferred that exsolution of a halogen-rich aqueous fluid occurred when the melts had reached 59 wt% SiO_2 and then at 64 wt% SiO_2 . In their study of peralkaline volcanoes of the Main Ethiopian Rift, Iddon and Edmonds [2020] suggested that at the Daly Gap the magma become saturated in sulphide and an exsolved volatile phase. There was then further degassing in shallow reservoirs (6–8 km), with a substantial exsolved volatile phase. Their model of the magma systems includes details of volatile behaviour down to at least 15 km (Figure 12).

The compositions of the degassed phases are dependent, *inter alia*, on the nature of the dissolved

volatiles and on magma dynamics, particularly the rate of ascent. CO_2 is less soluble than H_2O , SO_2 , F and Cl and will normally enter a volatile phase at higher pressures and be degassed. An absence or scarcity of CO_2 in the salic members of the sequence, as in the Pantescan pantellerites, is no guarantee that it did not play an important role in magma genesis. However, we are unaware of any direct occurrence of a peralkaline silicic suite with carbonatites; it may well be that significant amounts of CO_2 are not required for the formation of their primary mafic magmas.

13. The early evolutionary stages

13.1. Initiation of magmatic activity

The first stage involves the rise of mafic magmas from the mantle, first into lower crustal storage zones and then into holding zones at various crustal levels. In some centres, mafic magmas erupt onto the surface, e.g., the volcanoes of Marie Byrd Land, Antarctica [LeMasurier *et al.*, 2011], and the Guilherme Moniz and Cinco Picos volcanoes on Terceira [Self and Gunn, 1976, Jeffery *et al.*, 2017]. In other cases, the magmas ascend into the upper crust, generally to 1–5 km depth, and stall, allowing the development of the plumbing systems in which the peralkaline members form. Ongoing work on peralkaline systems has shown that they are all to some degree unique, as a perusal of cartoon models of their plumbing systems reveals, e.g., Dunkley *et al.* [1993], Macdonald *et al.* [1994, 2008], Troll and Schmincke [2002], Sumner and Wolff [2003], Marshall *et al.* [2009], Neave *et al.* [2012], Jeffery *et al.* [2016, 2017], Gleeson *et al.* [2017], Aguirre-Diaz and Morton-Bermea [2018], Andreeva *et al.* [2018], Hutchison *et al.* [2018], Liszewska *et al.* [2018], Sosa-Ceballos *et al.* [2018], Gottsmann *et al.* [2020], Neave [2020]. The magmatic systems vary in shape, size, depth, longevity and internal structure. Models involving single reservoirs range from balloon- or mushroom-shaped (Figures 13a and b), a series of stacked sills (Figure 13c), and the transcrustal model of Hammond *et al.* [2020; Figure 13d]. More complex models include that for Silali volcano, Kenya, where Macdonald *et al.* [1995] proposed a series of sill-like reservoirs, some of which had collapsed after eruption, allowing basaltic magmas to

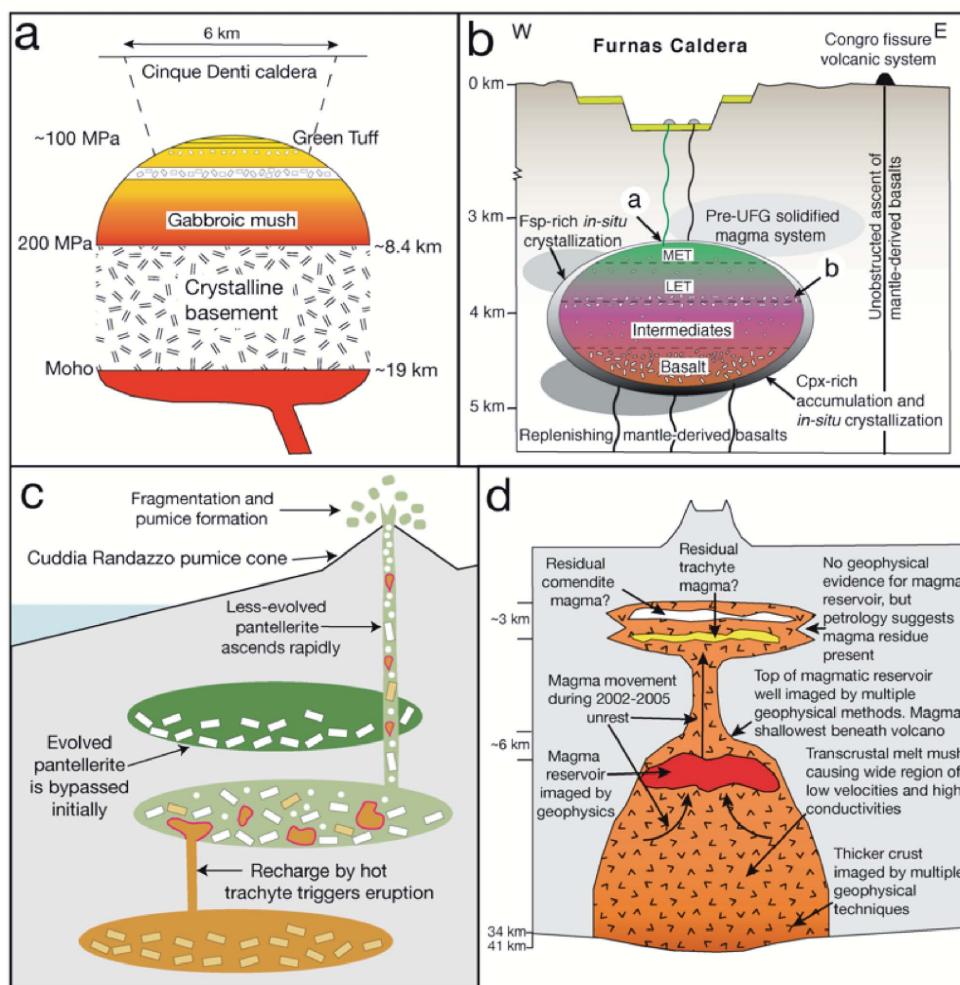


Figure 13. To show the diversity of peralkaline silicic magma systems. (a) The mushroom-shaped model inferred for the Pantescan system prior to eruption of the Green Tuff. Redrawn after Liszewska *et al.* [2018]. (b) Model of the shallow plumbing system of Furnas volcano shows a density-stratified reservoir with a cap of evolved trachytes (MET) overlying less evolved trachytes (LET). After Jeffery *et al.* [2016]. (c) Inferred reservoir structure of the Cuddia Randazzo–Khaggiar system, Pantelleria, when the pumice cone formed. Note the interconnections between the stacked bodies. Redrawn from Neave [2020]. (d) Cartoon model of the magma plumbing system beneath Changbaishan–Tianchi volcano, constructed from geophysical and petrological evidence. Note the thickened crust. Redrawn from Hammond *et al.* [2020].

pass through them. At the Olkaria centre, following a period of caldera collapse subsequent eruptions were from many small, partially interconnected reservoirs. Based on Interferometric Synthetic Aperture Radar (InSAR) data for Dabbahu volcano, Field *et al.* [2012] modelled the presence of a series of

stacked sills (reservoirs) over a 1–5 km depth range. Clearly there is no “standard” model for the plumbing systems—their nature will depend on such factors as local tectonics, mechanism and rate of magma input from depth, and volatile contents and their effect on viscosity. In the following sections, we present

some of the evidence used in elucidating the nature of, and processes within, peralkaline magma systems.

13.2. *Geological information on depth of reservoirs*

Noting that peralkaline caldera volcanoes commonly contain lithic clasts from the volcanic edifice, including cognate syenites, but lack subjacent crustal lithologies, Mahood [1984] proposed that their magma reservoirs are shallow. The Alid volcanic centre in Eritrea is an elliptical structural dome, 5×7 km, formed during uplift caused by shallow intrusion of rhyolitic magma. Given that the intrusion formed at $<2\text{--}3$ km depth and had a diameter of 3 to 5 km, Lowenstern *et al.* [2006] calculated that the intrusion has a volume of between 7 and 65 km^3 . Based on the distribution of mafic cones at the Changbaishan-Tianchi volcano, inferred as indicating the presence of a shadow zone, Wei *et al.* [2013] estimated that the subsurface comendite body could be ~ 20 km in diameter. Assuming a 10:1 diameter/thickness proportion [Jellinek and DePaolo, 2003], the resulting volume would be $\sim 600\text{ km}^3$.

Attempting to illustrate the relationship between the erupted deposits and the related reservoir, Macdonald *et al.* [2014] pictured the young trachytic Longonot volcano, Kenya, and the Mesoproterozoic syenitic complex Kûngnât, Greenland, as complementary magmatic systems and developed a model of a single trachytic centre throughout its life cycle. Many petrogenetic and volcanological features were shown to be shared by the two complexes, pointing to their similar development despite the great age difference.

13.3. *Petrological information*

From determination of volatiles, mainly H_2O and CO_2 , in melt inclusions in phenocrysts, saturation pressures can be calculated using solubility models, such as those of Di Matteo *et al.* [2004] and Papale *et al.* [2006]. The pressure estimates are then converted to depth. The method relies on the magmas having been volatile-saturated prior to eruption and suitable crustal density models being available. Using the technique, Field *et al.* [2012] estimated that volatile saturation pressures for historic pantellerites of the Dabbahu volcano are in the range 43–207 MPa

and inferred that magma storage depths for these eruptions are $\sim 1\text{--}5$ km below sea level. Neave *et al.* [2012] also used H_2O and CO_2 data to estimate equilibration pressure for Pantescan pantellerites of up to 1.5 kbar. For the Green Tuff ignimbrite, Pantelleria, which is virtually CO_2 -free, Lanzo *et al.* [2013] found a pressure interval of 45–65 MPa. Considering the possibility that some water may have been lost by degassing of the melt inclusions, they preferred a storage depth of 2.5 km. Jeffery *et al.* [2017] postulated that ignimbrites of Terceira were stored at pressures up to ~ 135 MPa, equivalent to 3.7 km depth.

A useful summary of magma storage conditions in various peralkaline systems, based on geochemical modelling and experimental evidence, has been presented by Gleeson *et al.* [2017; their Table 3].

14. *Geophysical information on nature of reservoirs*

The ways in which peralkaline reservoirs develop and evolve are dependent on many factors: the regional and local tectonics, their size and shape, magma compositions, volatile behaviour, and how open the system is. Geophysical techniques are increasingly being used to provide information on such aspects of magma plumbing systems as their shape and size, the distribution of zones of melt accumulation, and the paths of melt migration. A comprehensive review of the main techniques is provided by Magee *et al.* [2018]. Here we describe some results as applied to peralkaline silicic systems.

14.1. *Ground deformation*

One method of looking inside an active volcano is to measure surface deformation, resulting from subsurface magmatic or hydrothermal processes. The deformation can provide information on the levels of magma accumulation and migration and, sometimes, on conditions within the magma reservoir, such as cooling and contraction. Traditionally based on the placement of multiple sensors around the volcano, measurements can now be made globally using satellites and it is now known that over 220 volcanoes around the world were actively deforming in 2016 [Biggs and Pritchard, 2017].

Interferometric Synthetic Aperture Radar (InSAR) is a remote sensing technique using microwave

electromagnetic radiation to detect, *inter alia*, displacements of the Earth's surface. Mattia *et al.* [2007] used InSAR, and Electronic Distance Measurement (EDM) and levelling data, to identify the point source of ground deformation beneath the Pantelleria caldera. Their preferred model was of a simple spherical source at ~ 4 km beneath the island. Using InSAR, Biggs *et al.* [2009] detected episodic geodetic activity at four central volcanoes in the central Kenya Rift (Paka, Menengai, Longonot and Suswa) over the period 1997–2007. Inflation of Paka is shown in Figure 14a). InSAR data were used by Biggs *et al.* [2011] to quantify the amount of uplift and subsidence beneath four volcanoes in the Main Ethiopian Rift. They modelled the sources as penny-shaped cracks at depths of between <2.5 and ~ 5 km. In contrast, Field *et al.* [2012] modelled InSAR and seismic evidence from the Dabbahu volcano to show that a system of thin stacked sills in the depth range ~ 1 to 5 km best fits the ground deformation data. A period of inflation at Aluto in 2008 was explained by Hutchison *et al.* [2016a,b] as reflecting fluid injection into a magma reservoir at *ca.* 5.1 ± 0.5 km depth. Wei *et al.* [2013] interpreted the increased levels of seismicity and ground deformation (especially uplift) in mid-2002 at the Changbaishan-Tianchi volcano as reflecting an episode of magma recharge and/or volatile exsolution at depths of ~ 5 km, although the unrest did not culminate in an eruption. Iddon and Edmonds [2020] have noted that a high fraction of dissolved volatiles in the evolved melts can also have an effect on ground displacements.

14.2. Gravimetry

Gravimetric studies of volcanoes measure changes in the gravitational field caused by the subsurface distribution of magma. Several circular-shaped positive gravity anomalies have been identified along the northern Main Ethiopian Rift and some are associated with rhyolitic volcanoes, such as Gedemsa. In most, there is a density decrease from the bottom (~ 20 km) to the top (<4 km) of the anomaly. Peccerillo *et al.* [2003] interpreted the data as supporting the hypothesis that the silicic centres developed above large intrusions of mafic magma, crystallization of which as ultramafic to mafic rocks explains the gravimetric data. Mahatsente *et al.* [1999] located a positive gravity anomaly in the shallow crust beneath Aluto which Iddon *et al.* [2019] suggested may

provide evidence of crystallized intermediate magmas. A $2850 \text{ kg}\cdot\text{m}^{-3}$ body determined in the gravity survey of the Boset (Boseti) volcano by Cornwell *et al.* [2006] may represent the same chamber identified by Whaler and Hautot [2006] using magnetotellurics as a small, shallow, high conductivity low at <1 km depth beneath the volcano.

Based on the results of geodetic and gravimetric surveys, data modelling and other geophysical observations, Gottsmann *et al.* [2020] presented the model of the upper crustal plumbing system beneath the Corbetti caldera shown in Figure 14b. SBDTZ is the seismic brittle–ductile transition zone. The current magma intrusion lies within a crystal mush zone. A peralkaline rhyolitic system is thought to lie at the top of the intrusion and feeds the explosive magmatism at the centre. There is a hydrothermal system at 0.2–1.0 km depth (not shown).

14.3. Seismic imaging

Many studies of active volcanoes and volcanic regions have determined variations in seismic velocity. High velocity anomalies observed in shallow crustal regions beneath active volcanoes have commonly been interpreted as cooled magma bodies whereas low velocity anomalies have almost invariably been interpreted as areas of melt accumulation, often in the depth range 8–15 km [Lees, 2007, Masturyono *et al.*, 2001]. The seismic imaging is consistent with the presence of no more than a few tens of percent of melt in a crystal mush model [Lees, 2007, Huang *et al.*, 2015]. Sometimes, however, the various geophysical methods provide contrasting results. Iddon *et al.* [2019], for example, have noted that seismic and deformation data for the Aluto volcano point to the existence of a shallow magma reservoir, whereas magnetotelluric methods have failed to identify a volume of enhanced electrical conductivity in the crust which would be consistent with the presence of partial melt.

In their study of the seismic velocity structure of Aluto caldera, Wilks *et al.* [2020] concluded that volatiles exsolved from a deep melt-rich body (>10 km depth) migrated into a shallow volume of rock containing over-pressurized gas which is shown by abundant seismicity and low V_p/V_s (Figure 14c). This exchange of fluids causes the restless behaviour of Aluto. Using seismic records, Hammond *et al.*

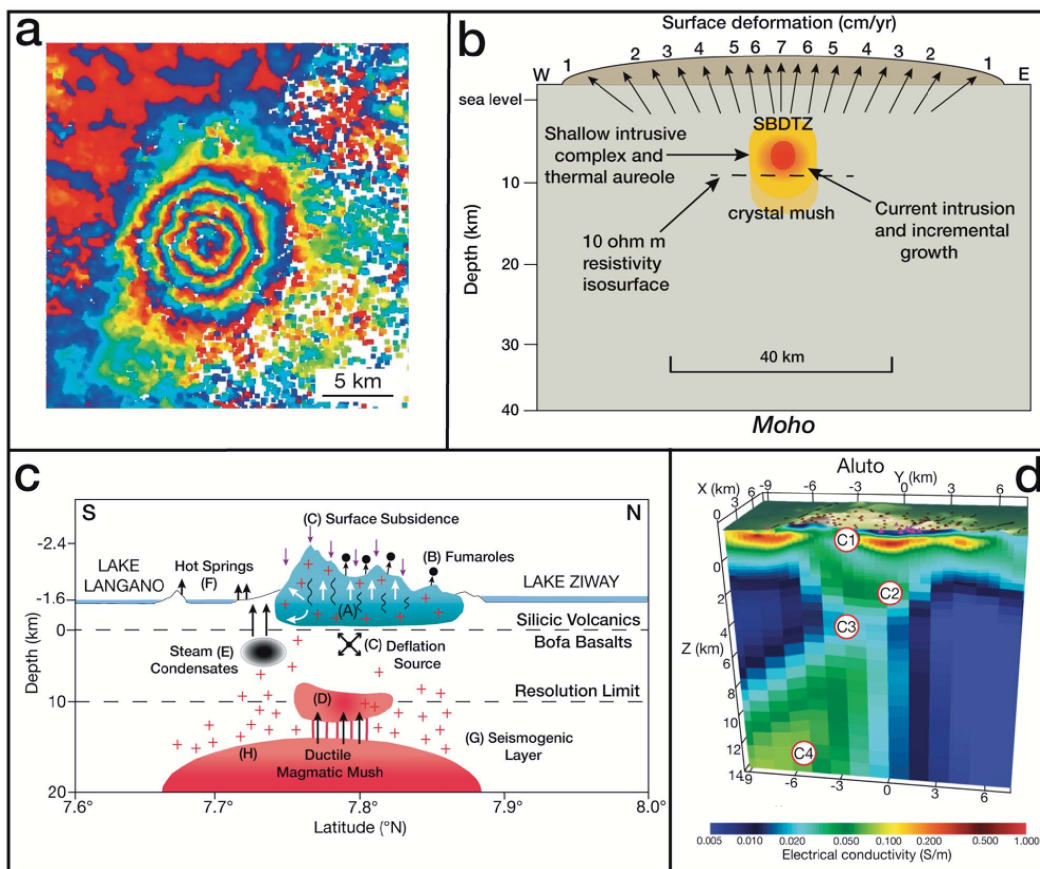


Figure 14. (a) Inflation episodes at Paka volcano, Kenya Rift Valley, 2006–2007. Each colour cycle represents 2.8 cm of displacement in the satellite line of sight. From Biggs *et al.* [2009]. (b) Upper crustal plumbing system beneath Corbetti caldera, modelled from geodetic and gravimetric data by Gottsmann *et al.* [2020]. (c) Subsurface structure of Aluto volcano, modelled by Wilks *et al.* [2020] from seismic data. Zone A exhibits high seismicity within a region of over-pressurized gas; B is a zone of fumarolic activity; Zone C exhibits surface deflation; D has a significant melt component derived from greater depth; Zone H is a reservoir of magmatic mush. (d) Electrical conductivity model of Aluto volcano [Samrock *et al.*, 2021]. Conductors C1 to C4 are explained in the text.

[2020] found a significant velocity reduction at 4–8 km depth which they interpreted as a zone of partial melt. Interestingly, they also presented evidence that melt is present over a wide region of low velocities and high conductivities and extends through the crust as a “transcrustal mush zone” (Figure 14d). Although models of transcrustal magmatic systems are gaining in popularity [Annen *et al.*, 2015, Cashman *et al.*, 2017, Sparks and Cashman, 2017], this may be the first application to a peralkaline silicic system.

The total volumes and melt fractions of seismically inferred reservoirs are potentially important in

providing information on the possibility of future eruptions. For example, Hammond *et al.* [2020] suggested that recharge of their seismically identified partial melt zone beneath Changbaishan-Tianchi volcano was responsible for the episode of unrest from 2002–2005.

14.4. Magnetotelluric surveying

Magnetotelluric (MT) surveying uses variations in the Earth’s electromagnetic field to determine the distribution of electrical conductivity in the sub-

face. In volcanic systems, the electrical conductivity is controlled by, *inter alia*, the presence of melt, magmatic or meteoric brine or hydrothermal zones [Samrock *et al.*, 2021]. Applying the technique to the Aluto volcano in the Main Ethiopian Rift, Samrock *et al.* [2021] proposed the model shown in Figure 14d. The conductor C1 is a clay cap. Conductor C2, at depths of ~1–4 km, is interpreted as a magmatic heat source for a hydrothermal zone which lies between C1 and C2. The conducting zone C4 at depths >8 km is the lower crustal zone of melt accumulation and thus the parental magma reservoir. C3 represents magmatic pathways connecting C2 and C4. In their MT study of the Changbaishan-Tianchi volcano, Yang *et al.* [2021] identified three high conductivity zones at depths of 3–5, 10–16 and 40–60 km. They suggested that the deepest might be related to melting of the asthenospheric mantle, the middle crustal zone is a magma chamber, and the upper crustal anomaly is a porous saline zone.

The various geophysical techniques, especially when tied to petrological studies, are revealing in increasing detail the scale, structure, and dynamics of magmatic systems. Considerable insights are being made into how the plumbing systems work and the potential for future eruptions.

15. Establishment of zoned magma chambers

A majority of recent studies have shown that the upper crustal magma reservoirs are compositionally zoned. One of the strongest lines of evidence is the eruption of ignimbrites with variations in bulk-rock and phenocryst compositions and in estimated P – T – P_{volatile} conditions. The scale of the zonation is very variable and seems to be independent of eruptive volume. For example, the Green Tuff, Pantelleria, has a Dense Rock Equivalent (DRE) volume of ~10 km³ and is zoned from comenditic trachyte to pantellerite. The comenditic Bracks Rhyolite, Trans-Pecos Texas, with a volume of 75 km³, is compositionally homogeneous [Henry *et al.*, 1990], and the pantelleritic Gomez Tuff, also in Trans-Pecos Texas, shows only minimal variation despite having a volume of ~220 km³ [Parker and White, 2008].

A simplified model of zonation would show a rhyolitic cap overlying trachytic magmas which become progressively more feldspar-rich with depth in the reservoir, into a so-called mush zone, as proposed

for peralkaline silicic systems by Macdonald *et al.* [1994, 1995, 2019], Sumner and Wolff [2003], Marshall *et al.* [2009], White *et al.* [2009], Wolff *et al.* [2015], D’Orsano *et al.* [2017], Jeffery and Gertisser [2018], Iddon *et al.* [2019] and Gottsmann *et al.* [2020]. A further variation may be the presence of mixed magma layers, or layers with different phenocryst abundances. Boundaries between layers may be sharp or show evidence of crystal transport across them.

How quickly is compositional zonation established? After eruption of the Green Tuff ignimbrite, Pantelleria, the magmatic system had evolved from metaluminous trachytic to pantelleritic compositions in a few thousand years Mahood and Hildreth [1986]. Leat *et al.* [1984] argued for the Menengai caldera volcano that extensive compositional zonation developed through thicknesses exceeding 10² m in times of 10²–10³ years. At some centres in the Olkaria complex, compositional zonation developed rapidly, in a few thousand years at most [Marshall *et al.*, 2009]. The rapidity of the processes in these systems was at least partly due to the very low melt viscosities.

16. Differentiation mechanisms

16.1. Fractional crystallization

In the majority of recent studies of peralkaline systems, geochemical modelling has established fractional crystallization as the dominant mechanism driving the transition basalt to trachyte/rhyolite [e.g., Novak and Mahood, 1986, Mungall and Martin, 1995, Peccerillo *et al.*, 2003, Lowenstern *et al.*, 2006, Flude *et al.*, 2008, Jeffery and Gertisser, 2018, Macdonald *et al.*, 2008, Parker and White, 2008, Marshall *et al.*, 2009, Ronga *et al.*, 2010, Neave *et al.*, 2012, Giordano *et al.*, 2014, Hutchison *et al.*, 2016a,b, Jeffery *et al.*, 2016, 2017, Gleeson *et al.*, 2017, Aguirre-Diaz and Morton-Bermea, 2018, Iddon *et al.*, 2019, Iddon and Edmonds, 2020]. The main magmatic lineages were discussed earlier (Section 6); in detail, they reflect the ambient P – T – fO_2 – P_{volatile} conditions in each system, especially during the earlier stages of evolution. As Macdonald [2012], Gleeson *et al.* [2017], Jeffery and Gertisser [2018] and Romano *et al.* [2020] have shown, the crystallization conditions for peralkaline trachyte–rhyolite systems tend to be broadly similar. Ultimately this is reflected in

the observation, discussed above (Section 7), that all peralkaline silicic suites have the potential to evolve towards the effective minimum composition(s).

The efficiency of crystal fractionation in the crustal reservoirs is partly dependent on the rate at which crystals grow. Rogers *et al.* [2004] estimated that the fractionation rate (calculated by dividing the magma fraction crystallized by the time period of differentiation) for evolution of the hawaiite-trachyte sequence at the Longonot volcano, Kenya, was $\sim 0.2 \times 10^{-4}$ /year, whereas fractionation in the trachytes was more rapid, up to 3×10^{-4} /year. Lowenstern *et al.* [2006] found rather similar rates for the basalt-comendite suite at the Alid volcanic centre ($2\text{--}3 \times 10^{-5}$ /year). They further estimated that the production rate of comendite was 2×10^{-4} to 1.0×10^{-3} km³/year, broadly similar to the value of 2.5×10^{-3} km³/year proposed for the Olkaria comendites by Heumann and Davies [2002], which, they claim, are comparable to much larger metaluminous silicic systems.

16.2. Magma mingling and mixing

Magma mingling and mixing have been recognized in the majority of, if not all, peralkaline silicic systems. Macdonald [2012], for example, has listed several examples from the Kenya Rift Valley and Jeffery and Gertisser [2018] refer to occurrences in Atlantic Islands. The evidence takes several forms, including compositionally banded pumice fiamme and pumice clasts; quenched enclaves; and disequilibrium phenocryst assemblages (Figure 15). Various lithological combinations are found. Macdonald *et al.* [2008] recorded two-, three- and four-component mixes of basalt, mugearite, benmoreite, trachyte and rhyolite in comendites of the Olkaria complex, Kenya. An important feature of these rocks is that they can reveal the presence in the plumbing system of magmas that were never erupted as discrete units.

One of the most remarkable examples of mixing is the Miocene P1 ignimbrite (14.1 Ma) on Gran Canaria [Freundt and Schmincke, 1995, Schmincke and Sumita, 2010]. The body has a volume of ~ 43 km³ and comprises four components: crystal-poor to highly phyric rhyolite, sodic trachyandesites through mafic to evolved trachytes, Na-poor trachyandesites, and two varieties of basalt. The rocks record two

contemporaneous fractionation series and some rocks were modified by selective contamination of alkali feldspar. The components were then intensely mixed during eruption.

Younger ignimbrites on Gran Canaria also point to complex processes in the reservoir. Troll and Schmincke [2002] recorded in Ignimbrite “A” (13.63 ± 0.3 Ma) a complex history of magma mixing, feldspar resorption and inter-magma batch transport. Ignimbrite “TL” (13.4 Ma) contained three magma compositions, comendite, trachyte and benmoreite, which were involved in mixing before during withdrawal [Sumner and Wolff, 2003]. An interesting conclusion was that intrusion of benmoreite magma into the chamber occurred over several months to years.

In some suites, intermediate composition magmas were formed only by mingling of mafic and felsic magmas [Novak and Mahood, 1986, Ferla and Meli, 2006, Lowenstern *et al.*, 2006, Flude *et al.*, 2008, Romengo *et al.*, 2012]. At Silali, Kenya [Macdonald *et al.*, 1995], Gedemsa, Ethiopia [Peccerillo *et al.*, 2003], Olkaria, Kenya [Macdonald *et al.*, 2008] and Nemrut volcano, Turkey [Çubukçu *et al.*, 2012], mixed magma intermediates occur in addition to non-mixed rocks.

16.3. Resorption/remobilization of cumulates

The recognition that the magmatic reservoirs can contain feldspar-rich layers, and thus the possibility of feldspar-cumulitic layers, led to suggestions that the compositions of magmas may be affected by crystal resorption [Sumner and Wolff, 2003, Macdonald *et al.*, 2008, White *et al.*, 2009, Wolff *et al.*, 2015, Jeffery *et al.*, 2017, Iddon *et al.*, 2019]. Most recently, Wolff *et al.* [2020] used Ba and Eu enrichments to suggest that many compositionally zoned felsic tuffs, including the Green Tuff, Pantelleria, show crystal-scale evidence for formation of magma by thermal rejuvenation of high-crystallinity (>50%) mush (Figure 16). One consequence is to blur the distinction between the compositions of evolved melts and crystal mushes. Cumulate remelting is clearly a viable process in peralkaline magmatic systems and must be considered in petrogenetic models. This is particularly pertinent in the light of the suggestion of Hutchison *et al.* [2018, p. 215] that 16–30% of the volume generated by crustal extension beneath a silicic complex would be filled by magmatic cumulates.

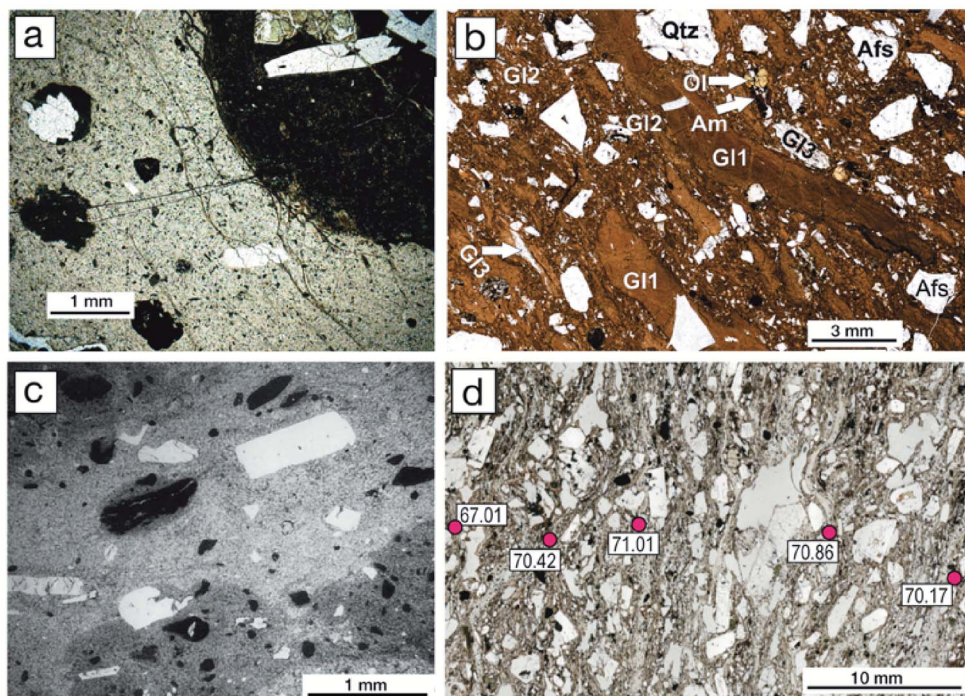


Figure 15. (a) Mingling of basalt (dark) and comendite (light brown), Greater Olkaria Volcanic Complex. The grey material to left may be a third component. From Macdonald *et al.* [2008, Figure 3d]. (b) Mingling of two pantelleritic melts (GI1 and GI2) and comenditic melt (GI3), also marked are alkali feldspar (Afs), amphibole (Am), olivine (Ol), and quartz (Qtz), Gold Flat Tuff, Nevada [Macdonald *et al.*, 2019]. (c) Mingling of trachyte (darker) and comendite (lighter) in ignimbrite “TL”, Gran Canaria. The trachyte encloses dense, angular benmoreite globules. Based on Sumner and Wolff [2003]. (d) Streaky mingling of trachytic and pantelleritic magmas at the micron scale, values are wt% SiO₂ Green Tuff, Pantelleria [Liszewska *et al.*, 2018].

17. Evacuating the reservoir

Various mechanisms have been proposed to initiate eruption. Differentiation of an initially water-poor silicic magma can yield highly fractionated, low-density magmas with high water contents. The uppermost parts of the reservoir can become oversaturated in water, causing an excess pressure which can lead to eruption [Blake, 1984, Gioncada and Landi, 2010, Landi and Rotolo, 2015, Gleeson *et al.*, 2017]. Alternatively, the trigger may be mafic magma recharge, for which there is strong evidence in the presence of mixed magma rocks [Sumner and Wolff, 2003, Flude *et al.*, 2008, Pan *et al.*, 2017, Macdonald *et al.*, 2019, Neave, 2020]. In an interesting variant, Pimentel *et al.* [2016] showed that the eruption of comenditic trachytes in 1761 CE on Terceira Island

was triggered by stresses related to contemporaneous trachybasalt eruption but with no mixing of the magmas.

The modes of eruption from compositionally zoned high-level reservoirs are very variable. Draw-down may be simple, with progressively deeper layers being incorporated [Blake and Ivey, 1986]. In Figure 17a, the eruption of an ash-flow tuff from the Menengai volcano, Kenya, tapped through several compositional layers in the reservoir [Macdonald *et al.*, 1994]. During the eruption of ignimbrite “TL” on Gran Canaria, mingling of comenditic and trachytic magmas with benmoreitic globules and a feldspar-rich trachytic layer occurred (before and) during eruption [Figure 17b; Sumner and Wolff, 2003]. Mahood *et al.* [1985] described, in the Guadalajara Ignimbrite, Mexico, the simultaneous

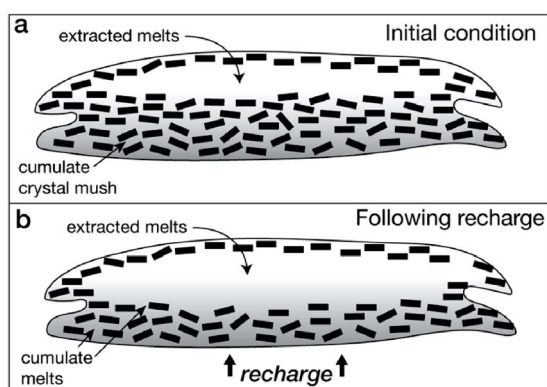


Figure 16. (a) Initial condition of a hypothetical system containing a cumulate mush. (b) After recharge by less evolved magma, the cumulates are partially melted. Based on Wolff *et al.* [2020].

eruption of two comenditic magmas of slightly different composition. The basal member of the Gold Flat Tuff, Nevada, contained pantelleritic and comenditic melts derived from separate reservoirs, which were mixed during eruption [Macdonald *et al.*, 2019].

18. Timescales of growth and eruptive periodicity

Peralkaline silicic volcanoes can grow and evolve rapidly. For example, Menengai and Longonot in the Kenya Rift, and Mayor Island, New Zealand, developed shield volcanoes, followed by two periods of caldera collapse, over periods in the range 130–400 ka. Based on the Kenyan examples, Hutchison *et al.* [2016a] inferred that the edifice-building phase at Aluto lasted for 150–400 ka, followed by major ignimbrite eruptions at 310 ka, a period of repose lasting 250 ka and then episodic post-caldera activity after 60 ka. Activity at Aluto was, therefore, episodic on a variety of scales. On Pantelleria perhaps as many as five caldera collapses have occurred in the past 190 ka [Jordan *et al.*, 2018]. The trachytic–rhyolitic cone of Changbaishan–Tianchi has been growing for 1.12 Ma [Andreeva *et al.*, 2018]. On the basis of evidence from the Alid volcanic centre, Eritrea, Lowenstern *et al.* [2006] estimated that extraction of basalt from the mantle source through to the

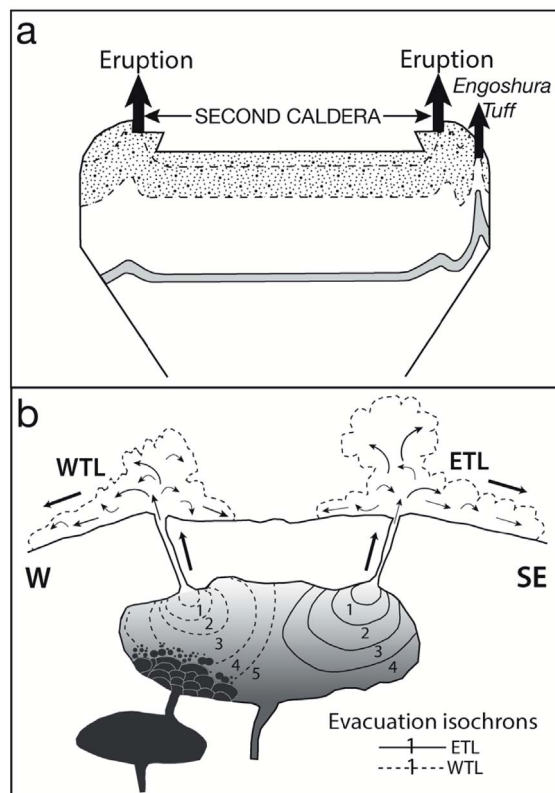


Figure 17. Reservoir evacuation processes. (a) Eruption of the second caldera-forming ash-flow tuff, Menengai volcano, Kenya. Dashed lines represent isochemical surfaces. The Engoshura Tuff (Eng. Tuff) was perhaps erupted from a vent tapping a zone of strong compositional gradient, tapping into a Ba-rich layer. Redrawn from Macdonald *et al.* [1994]. (b) Ignimbrite “TL”, Gran Canaria. Eruptions from the western lobe (WTL) tapped into a layer of intrusive benmoreite which was absent beneath the eastern lobe (ETL). Redrawn from Sumner and Wolff [2003].

formation of comenditic rhyolites took some 30,000–50,000 years.

Information is accumulating on the eruption periodicities of peralkaline systems, allowing some insights into magmatic processes. For example, Iddon *et al.* [2019] presented a model to show that eruption intervals for post-caldera pantellerites at Aluto were greater than the upper limits calculated for melt segregation from their crystal mush, providing

no obstacle to a fractional crystallization origin. On Mayor Island, the mean eruption interval is around 4000 years [35 events in ~130 ka: Houghton *et al.*, 1992]. At the Nemrut volcano, Turkey, major eruptions of silicic magmas for the past ~190 ka appear to have occurred at intervals spaced some 20,000–40,000 years apart, which Sumita and Schmincke [2013a] interpreted as being the incubation times for the silicic magmas to build into large eruptible volumes. Based on the style and volume of recent eruptions, Hutchison *et al.* [2016a] suggested that silicic eruptions at Aluto volcano, Main Ethiopian Rift, occur at an average rate of 1 per 1000 years. McNamara *et al.* [2018] suggested that the volcano has erupted at least 24 times in the Holocene, most eruptions occurring in three bursts at 11 ka, 6.1 ka and ~3.5 ka. The three main felsic episodes over the last 230 ka at the Boset-Bericha Volcanic Complex, also in the Main Ethiopian Rift, occurred at ~230 ka, ~119 ka, and since ~16 ka, may indicate an overall frequency of around 100 ka [Siegburg *et al.*, 2018]. The mean eruption intervals for post-caldera pantellerites at Aluto have been estimated at 300–400 years by Iddon *et al.* [2019]. The magma system of Terceira has erupted at least seven ignimbrites and several smaller-scale eruptions over the past ~60 ka, typical eruption volumes (DRE) being ~1–2 km³ [Jeffery *et al.*, 2017].

The increasing recognition that magmatic systems contain significant volumes of mush zones that are transitional into solid rock has made it difficult to distinguish the so-called volcanic and plutonic stages in their evolution. What information is available on the age of the last eruption of a peralkaline system (i.e., the end of the volcanic stage) and its entering a phase where its future will be dominated by cooling-induced crystallization (the plutonic stage)? Certain aspects of Pantelleria may suggest that it will not erupt again. (i) In the last ~190 ka, there have been two, and possibly five, episodes of caldera collapse [Jordan *et al.*, 2018]. (ii) After formation of the last caldera at 46 ± 1 ka, a resurgent dome formed on the caldera floor. (iii) The most peralkaline products were erupted at the time of the formation of the second caldera. (iv) On the basis of new ⁴⁰Ar/³⁹Ar dating and geodetic evidence of deflation and subsidence of the most recent caldera floor, Scaillet *et al.* [2011] proposed that the intracaldera system, in stasis since 7 ka, is on the wane and that there is no evidence of a

forthcoming eruption in the next 2 ka. (v) This is perhaps consistent with the results of a seismic survey in 2006–2007 and of signals recorded during 2010–2014 that Pantelleria has a very low rate of seismicity [Spampinato *et al.*, 2017]. Nevertheless, renewed input of mafic magma into the system could result in its rejuvenation.

19. Volcanic hazards

Several peralkaline silicic volcanoes have the potential to erupt in the near future. One of the most spectacular is the Changbaishan-Tianchi volcano, China/North Korea. When it erupted around 946 CE, it deposited ~100 km³ of comendite-trachyte ejecta which spread as far as northern Japan, a distance of some 1000 km, where some 4–5 cm of ash were deposited [Horn and Schmincke, 2000, Wei *et al.*, 2013, Pan *et al.*, 2017]. With a Volcanic Explosivity Index (VEI) of 7, the eruption is one of the two largest Holocene eruptions on Earth. From 2002–2005, there were marked increases in seismicity, deformation and the hydrogen and helium contents of spring waters, causing regional concern. The unrest did not result in an eruption, but it stressed the need for complete and continuous monitoring, especially since millions of people live close to the volcano [Wei *et al.*, 2013]. The magmas of the Millennium Eruption may have been stored in the crust for 10,000–20,000 years before eruption [Zou *et al.*, 2010, Wei *et al.*, 2013]; future eruptions may not be imminent.

Throughout the East African Rift System, it appears that shallow magmatic processes are currently operating on a decadal timescale [Biggs *et al.*, 2011]. In the Kenya sector, three centres (Paka, Menengai and Longonot) showed signs of inflation or deflation over the period 1997–2008, as determined by InSAR [Biggs *et al.*, 2009]. The Olkaria volcano complex, associated with the caldera centres, is a multi-centred comenditic dome field which last erupted at 180 ± 50 yBP [Clarke *et al.*, 1990]. Menengai, Olkaria and Longonot are located in densely populated areas and present important hazards to life and property. Further north, in the Main Ethiopian Rift, four volcanic centres (Aluto, Corbetti, Bora and Haledebi) experienced deformation from 1993 to 2010 [Biggs *et al.*, 2011, Gleeson *et al.*, 2017; see also Fontijn *et al.*, 2018]. As in Kenya, the hazard implications are significant; for example,

6.8 million people live within 100 km of Aluto. On the basis of a newly developed probabilistic volcanic hazard assessment methodology, Clarke *et al.* [2020] argued that numerous settlements, amenities and economically valuable geothermal infrastructure lie within the most hazardous regions of the Aluto caldera. More than 250,000 people could be endangered by an even modest-scale eruption (0.5 km^3 of magma) from the Corbetti Volcanic system [Rapprich *et al.*, 2016].

In an earlier phase of magmatic activity, layers of tephra 15–20 cm thick and compositionally similar to the Oligocene Ethiopian plateau ignimbrites have been found in the central Indian Ocean ~2600 km away from the ignimbrites. Ayalew *et al.* [2002] speculated that the tephra layers represent distal fallout from the Ethiopian ignimbrite-forming eruptions.

On Pantelleria, ash from the eruption of the Green Tuff ignimbrite [$45.7 \pm 1.0 \text{ Ma}$; Scaillet *et al.*, 2013] reached as far as the Dodecanese, 1300 km away [Margari *et al.*, 2007]. As noted above, there is much uncertainty about the volcano's future eruptive potential, but careful monitoring is necessary. Mayor Island is the emergent portion of a compound lava shield built predominantly of peralkaline rhyolites. A caldera formed during two or three collapse periods some 6300 years ago. The most recent eruption is thought to have occurred 500–1000 years ago [Houghton *et al.*, 1992]. Ash from the caldera-forming event produced tephra deposits up to 70 cm thick on mainland North Island, New Zealand.

Nemrut volcano, adjacent to Lake Van in Turkey, is the country's most active volcano. Magmatism for ~570,000 years has been dominated by peralkaline trachytes and rhyolites [Macdonald *et al.*, 2015], the most recent eruption, ~500 years ago, being of comenditic lava flows in a rift valley on the northern flank of the volcano [Peretyazhko *et al.*, 2015]. The active Furnas central volcano on São Miguel, Azores, is considered to be one of the most hazardous in the archipelago. There have been ten young (<5 ka) sub-Plinian eruptions of comenditic trachyte [Jeffery *et al.*, 2016], the latest occurring in 1761 CE [Pimentel *et al.*, 2016]. Pimentel *et al.* [2021] describe the potentially devastating effects on the 55,000 inhabitants of a future ignimbrite-forming eruption of Pico Alto volcano, Terceira.

A further, and perhaps underestimated, hazard is the emission of CO_2 and radon from active sys-

tems. For example, D'Alessandro *et al.* [2018] have estimated that the total CO_2 output of the volcanic/geothermal system of Pantelleria is 24.2 tons per day and have pointed to areas on the island which are at high risk to human health from indoor concentrations exceeding European Union threshold values. It is perhaps inevitable that such high concentrations also characterize other systems and detailed monitoring is required.

20. Environmental impact

On the basis of experimental data, Scaillet and Macdonald [2006a] showed that the fluid/melt partitioning of S in peralkaline rhyolites is lower than in metaluminous rhyolites, i.e., less S enters the fluid phase, especially under CO_2 -rich conditions. Sulphur, ultimately derived from basaltic parents, can concentrate in the melt, eventually to be lost to the atmosphere during eruption. The estimated volume of the peralkaline rhyolites associated with the Ethiopian Trap flood sequences is $60,000 \text{ km}^3$ DRE [Ayalew *et al.*, 2002]. Assuming that the rhyolites were derived from alkali basalt with 1 wt% melt water and 1000 ppm S, and that the derivative melts had 5–6 wt% dissolved water coexisting with 4–6 wt% fluid with up to 1 wt% S, then eruption of the rhyolites could have released 10^{17} g of S into the atmosphere. These are amounts comparable to estimated releases from the basaltic members of the flood activity. The flood sequences coincided with a worldwide cooling event and Ayalew *et al.* [2002] and Scaillet and Macdonald [2006a] speculated that the S released from the rhyolites was an important contributor to the cooling.

Using a broadly similar technique, Neave *et al.* [2012] estimated that the total S yield from the explosive eruption of the Green Tuff, Pantelleria ($45.7 \pm 1 \text{ ka}$; $\sim 7 \text{ km}^3$ DRE) was 80–160 Mt which almost certainly had at least local environmental effects. Claessens *et al.* [2016] recorded a 1.8 Ma period of Late Miocene pantelleritic magmatism in central Kenya. They noted that their eruption coincided with a period of aridity in East Africa, with vegetation being pushed towards a more grass-dominated type. Using the Scaillet and Macdonald [2006a] and Neave *et al.* [2012] results as a model, Claessens *et al.* [2016] speculated that very significant amounts of S entered the atmosphere, producing such environmental effects as a surface temperature decrease, the direct

effect of acid rain on the fauna and flora, and acidification of lakes. Iddon and Edmonds [2020] estimated that an explosive, caldera-forming eruption ($VEI > 5$) in the Main Ethiopian Rift could outgas, in addition to 6 Mt of CO_2 , 390 Mt of S into the lower troposphere or stratosphere. Ayalew *et al.* [2002] noted that eruption of the Ethiopian plateau ignimbrites coincided with a long-term Oligocene global cooling and may have accelerated the shift towards glacial conditions. The coincidence at least draws attention to the potential for Ethiopian Oligocene volcanism, and indeed any major peralkaline eruption, to have caused environmental stress.

However, the magnitude of an eruption may not by itself have global impact. Xu *et al.* [2013] found no stratospherically loaded sulphate spike associated with the Millennium eruption of Changbaishan-Tianchi in the volcanism record from the GISP ice core. They reasoned that the sulphate aerosols were not transported to the Arctic region, probably due to its relatively low stratospheric sulphur emission. The eruption probably had limited regional climatic effects.

21. Ore deposit potential

Critical elements and/or materials are defined as those elements for which a marked increase in usage has emerged, relative to past consumption. These elements or materials are usually listed as strategic based on assessed risks to their supply and/or impact to potential supply restrictions. Although the particular element list varies as a function of assessor, country, or economic union, they have many things in common. The critical elements include two general groups: (1) traditional commodities that have either very limited occurrences or supply such as Co and Sn and/or are involved in new technologies such as Mn and Sb, (2) and elements such as REE, Y, Nb, Ta that are used in new technologies such as electric vehicles, smartphones, wind power generation, and superalloys for jet engines and turbine blades.

The magmatic processes that yield peralkaline magmas enrich the final products in incompatible elements such as REE, HFSE, etc. [e.g., Mahood and Stimac, 1990]. The concentration of these elements can be further enhanced by late-stage magmatic and hydrothermal fluids, and supergene processes. Peralkaline intrusives have been explored and mined for

these elements for many decades (e.g., Bokan Mountain, Alaska, USA, Strange Lake, Canada, Lovozero, Russia, Siwana Complex, India, and Norra Kärr, Sweden). As of this writing, we know of only one active mine in peralkaline extrusives, although there is and has been much exploration. We will restrict our discussion to REE and U as examples of the ore deposit potential of peralkaline extrusives.

In the last 100 years, the world's REE production went through three stages, placer mining of mainly monazite, the bastnäsite-rich Mountain Pass carbonatite, California, USA, and from the early 1990s, in China from the Bayan Obo deposit and ion-adsorption clay deposits. Currently, China accounts for >85% of the world's REE production [Schulz *et al.*, 2017]. With the rapidly increasing use of REE in modern technology, current REE deposit exploration considers all potential sources. Mungall and Martin [1996] described a peralkaline rhyolite, Terceira, Azores, with extreme enrichment of HFSE in the glass and suggest that this occurrence is analogous to the Strange Lake, CA intrusive; however, mining in the Azores is improbable. Chandler and Spandler [2020] report active exploration in a peralkaline rhyolite complex in the Peak Range volcanics in central Queensland, Australia that is extremely enriched in REE and HFSE. The secondary ore mineral assemblage and REE redistribution observed is interpreted to be due to a combination of hydrothermal alteration by fluids derived from subadjacent devolatilizing magma bodies, and late-stage supergene processes. They speculate that hydrothermal alteration is pervasive in the region and that deposits with high grades are likely.

Uranium is included in some critical element lists due to military, medical isotope and energy production, and satellite-energy uses. The Streltsova caldera hosts the largest U mine and reserves in Russia. The ore developed through an extensive hydrothermal system that mobilized U from both the Late Jurassic peralkaline volcanics as well as from the Hercynian subalkaline granitic basement [Chabiron *et al.*, 2003]. Castor and Henry [2000] describe exploration of large U deposits in Tertiary volcanics in Nevada and Oregon, USA. The peralkaline McDermitt and Virgin Valley calderas host rhyolites with U contents up to 15 ppm; much of the ore is hydrothermal with high Zr contents. Also of considerable importance, the largest Li deposit in the USA (~2 Mt)

occurs in basins adjacent to the McDermitt caldera. The Li has been leached from peralkaline rhyolite lavas and ash by hydrothermal and meteoric fluids [Benson *et al.*, 2017] and is bound in clay in ash-rich sediments. The Cumberland Hill (New Brunswick, CA) peralkaline rhyolite is highly enriched in incompatible elements including U (up to ~20 ppm). Gray *et al.* [2010] suggest that the combination of a high U content and the probable supergene remobilization into the host sedimentary basin would create an area with high U ore potential.

The interplay of various factors makes a mineral deposit economic, such as tonnage and grade, amenability to mining and processing, acceptable low values of deleterious components, the impact on the environment, and market demand and price. Peralkaline extrusives with the requisite tonnage and grade, would be good candidates for mining mainly due to their surficial position conducive to open pit mining and their relative ease of beneficiation. Exploration targets should also observe the potential for hydrothermal and/or meteoric fluid element mobilization to nearby sedimentary hosts.

22. Final remarks

What exciting developments do we foresee for studies of peralkaline silicic extrusives? Some examples are: (i) Combined petrological/geophysical approaches to understanding reservoir processes will guide us to identifying the important signals of impending eruptions and to assessing the environmental hazards related to S and CO₂ emissions. (ii) Many large peralkaline provinces remain understudied, such as the Black Mountain Volcanic Centre, SW Nevada [Sawyer *et al.*, 1994], the Marie Byrd Land Province, Antarctica [LeMasurier *et al.*, 2018], and the Davis Mountains volcanic field, Trans-Pecos Texas [Parker, 2019]. (iii) The increasing demand for rare metals and the diversifying of sources means that peralkaline extrusive will become legitimate exploration targets, assuming all social and environmental issues can be resolved satisfactorily. (iv) Studies of the most highly evolved peralkaline melts are providing new insights into the extremes of magmatic processes. (v) On a personal note, we look forward to a further understanding of the dimensions and genesis of the reservoirs that fed the huge Ethiopian ignimbrite fields.

Conflicts of interest

Authors have no conflict of interest to declare.

Acknowledgement

We warmly thank Bruno Scaillet for encouraging us to prepare this review.

References

- Aguirre-Diaz, G. d. J. and Morton-Bermea, O. (2018). Geochemistry of the Amazcala Caldera, Querétaro, Mexico: An unusual peralkaline center in the central Mexican Volcanic Belt. *Bol. Soc. Geol. Mex.*, 70, 731–760.
- Andersen, D. J., Lindsley, D. H., and Davidson, P. M. (1993). A Pascal program to assess equilibria among Fe–Mg–Mn–Ti oxides, pyroxene, olivine, and quartz. *Comput. Geosci.*, 19, 1333–1350.
- Andreeva, O. A., Yarmolyuk, V. V., Andreeva, I. A., and Borisovskiy, S. E. (2018). Magmatic evolution of Changbaishan Tianchi volcano, China–North Korea: evidence from mineral-hosted melt and fluid inclusions. *Petrology*, 26, 515–545.
- Annen, C., Blundy, J. D., Leuthold, J., and Sparks, R. S. J. (2015). Construction and evolution of igneous bodies: Towards an integrated perspective of crustal magmatism. *Lithos*, 230, 206–221.
- Avanzinelli, R., Bindi, L., Menchetti, S., and Conticelli, S. (2004). Crystallization and genesis of peralkaline magmas from Pantelleria Volcano, Italy: an integrated petrological and crystal-chemical study. *Lithos*, 73, 41–69.
- Avanzinelli, R., Braschi, E., Marchioni, S., and Bindi, L. (2014). Mantle melting in within-plate continental settings: Sr–Nd–Pb and U-series isotope constraints in alkali basalts from the Sicily Channel (Pantelleria and Linosa Islands, Southern Italy). *Lithos*, 188, 113–129.
- Ayalew, D., Barbey, P., Marty, B., Reisberg, L., Yirgo, G., and Pik, R. (2002). Source, genesis and timing of giant ignimbrite deposits associated with Ethiopian continental flood basalts. *Geochim. Cosmochim. Acta*, 66, 1429–1448.
- Bachmann, O. and Bergantz, G. W. (2008). Rhyolites and their source mushes across tectonic settings. *J. Petrol.*, 40, 2277–2285.

- Bacon, C. R. and Hirschmann, M. M. (1988). Mg/Mn partitioning as a test for equilibrium between co-existing Fe-Ti oxides. *Am. Mineral.*, 73, 57–61.
- Bailey, D. K. (1980). Volcanism, Earth degassing and replenished lithosphere mantle. *Philos. Trans. R. Soc. Lond. A*, 297, 309–322.
- Bailey, D. K. and Macdonald, R. (1970). Petrochemical variations among mildly peralkaline (comendite) obsidians from the oceans and continents. *Contrib. Mineral. Petrol.*, 28, 340–351.
- Bailey, D. K. and Macdonald, R. (1987). Dry peralkaline felsic liquids and carbon dioxide flux through the Kenya Rift dome. In Mysen, B. O., editor, *Magmatic Processes: Physiochemical Principles*, pages 91–105. Geological Society, London, Special Publications.
- Barberi, F., Ferrara, G., Santacrose, R., Treuil, M., and Varet, J. (1975). A transitional basalt-pantellerite sequence of fractional crystallization, the Boina Centre (Afar, Ethiopia). *J. Petrol.*, 16, 22–56.
- Barberi, F., Santacrose, R., and Varet, J. (1974). Silicic peralkaline volcanic rocks of the Afar Depression (Ethiopia). *Bull. Volcanol.*, 38, 755–790.
- Barboza, S. A. and Bergantz, G. W. (2000). Metamorphism and anatexis in the mafic complex contact aureole, Ivrea Zone, northern Italy. *J. Petrol.*, 41, 1307–1327.
- Barclay, J., Carroll, M. R., Houghton, B. F., and Wilson, C. J. N. (1996). Pre-eruptive volatile content and degassing history of an evolving peralkaline volcano. *J. Volcanol. Geotherm. Res.*, 74, 75–87.
- Beier, C., Haase, K. M., and Hansteen, T. H. (2006). Magma evolution of the Sete Cidades volcano, São Miguel, Azores. *J. Petrol.*, 47, 1375–1411.
- Benson, T. R., Coble, M. A., Rytuba, J. J., and Mahood, G. A. (2017). Lithium enrichment in intracontinental rhyolite magmas leads to Li deposits in caldera basins. *Nat. Commun.*, 8, 1–9.
- Bevier, M. L., Armstrong, R. L., and Souther, J. G. (1979). Miocene peralkaline volcanism in west-central British Columbia—its temporal and plate-tectonics setting. *Geology*, 7, 389–392.
- Biggs, J., Anthony, E. Y., and Ebinger, C. J. (2009). Multiple inflation and deflation events at Kenya volcanoes, East African Rift. *Geology*, 37, 979–982.
- Biggs, J., Bastow, I. D., Keir, D., and Lewt, E. (2011). Pulses of deformation reveal frequently recurring shallow magmatic activity beneath the Main Ethiopian Rift. *Geochem. Geophys. Geosyst.*, 12, 1–11.
- Biggs, J. and Pritchard, M. E. (2017). Global volcano monitoring: what does it mean when volcanoes deform? *Elements*, 13, 17–22.
- Black, S., Macdonald, R., and Kelly, M. R. (1997). Crustal origin for peralkaline rhyolites from Kenya: evidence from U-series disequilibria and Th-isotopes. *J. Petrol.*, 38, 277–297.
- Blake, S. (1984). Volatile oversaturation during the evolution of silicic magma chambers as an eruption trigger. *J. Geophys. Res.*, 89, 8237–8244.
- Blake, S. and Ivey, G. N. (1986). Density and viscosity gradients in zoned magma chambers, and their influence on withdrawal dynamics. *J. Volcanol. Geotherm. Res.*, 27, 153–178.
- Blundy, J. and Cashman, K. (2008). Petrologic reconstruction of magmatic system variables and processes. *Rev. Mineral. Geochem.*, 69, 179–239.
- Bohrson, W. A. and Reid, M. R. (1995). Petrogenesis of alkaline basalts from Socorro Island, Mexico: Trace element evidence for contamination of ocean island basalt in the shallow ocean crust. *J. Geophys. Res.*, 100, 24555–24576.
- Bohrson, W. A. and Reid, M. R. (1997). Genesis of silicic peralkaline volcanic rocks in an ocean island setting by crustal melting and open-system processes: Socorro Island, Mexico. *J. Petrol.*, 38, 1137–1166.
- Bryan, W. B. (1976). A basalt-pantellerite association from Isla Socorro, Islas Revillagigedo, Mexico. In Aoki, H. and Iizuka, S., editors, *Volcanoes and Tectonosphere*, pages 78–91. Tokai University Press, Tokyo, Japan.
- Bunsen, R. (1851). Über die Prozesse der vulkanischen Gesteinsbildungen Islands. *Ann. Phys. Chem.*, 83, 197–272.
- Cadoux, A., Pinti, D. L., Aznar, C., Chieso, S., and Gillot, P.-Y. (2005). New chronological and geochemical constraints on the genesis and geological evolution of Ponza and Palmarola Volcanic Islands (Tyrrhenian Sea, Italy). *Lithos*, 81, 121–151.
- Caricchi, L., Ulmer, P., and Peccerillo, A. (2006). A high-pressure experimental study on the evolution of the silicic magmatism of the Main Ethiopian Rift. *Lithos*, 91, 46–58.
- Carmichael, I. S. E. and MacKenzie, W. S. (1963). Feldspar-liquid equilibria in pantellerites: an experimental study. *Am. J. Sci.*, 261, 382–396.

- Cashman, K. V., Sparks, R. S. J., and Blundy, J. D. (2017). Vertically extensive and unstable magmatic systems: A unified view of igneous processes. *Science*, 355, article no. eaag3055.
- Castor, S. B. and Henry, C. D. (2000). Geology, geochemistry, and origin of volcanic rock-hosted uranium deposits in northwestern Nevada and southeastern Oregon, USA. *Ore Geol. Rev.*, 16(1–2), 1–40.
- Chabiron, A., Cuney, M., and Poty, B. (2003). Possible uranium sources for the largest uranium district associated with volcanism: the Streltsovka caldera (Transbaikalia, Russia). *Miner. Depos.*, 38(2), 127–140.
- Chamberlain, K. J., Barclay, J., Preece, K., Brown, R. J., and Davidson, J. P. (2016). Origin and evolution of silicic magmas at ocean islands: perspectives from a zoned fall deposit on Ascension Island, South Atlantic. *J. Volcanol. Geotherm. Res.*, 327, 349–360.
- Chandler, R. and Spandler, C. (2020). The Igneous Petrogenesis and Rare Metal Potential of the Peralkaline Volcanic Complex of the Southern Peak Range, Central Queensland, Australia. *Lithos*, 358, article no. 105386.
- Civetta, L., D'Antonio, M., Orsi, G., and Tilton, G. R. (1998). The geochemistry of volcanic rocks from Pantelleria Island, Sicily Channel: petrogenesis and characteristics of the mantle source region. *J. Petrol.*, 39, 1453–1491.
- Claessens, L., Veldkamp, A., Schoorl, J. M., Wijbrans, J. R., van Gorp, W., and Macdonald, R. (2016). Large scale pantelleritic ash flow eruptions during the Late Miocene in central Kenya and evidence for significant environmental impact. *Glob. Planet Change*, 145, 30–41.
- Clarke, B., Tierz, P., Calderm, E., and Yirgu, G. (2020). Probabilistic volcanic hazard assessment for pyroclastic density currents from pumice cone eruptions at Aluto volcano, Ethiopia. *Front. Earth Sci.*, 8, article no. 348.
- Clarke, M. C. G., Woodhall, D. G., Allen, D., and Darling, G. (1990). *Geological, Volcanological and Hydrogeological Controls on the Occurrence of Geothermal Activity in the Area Surrounding Lake Naivasha, Kenya*. Ministry of Energy, Nairobi, Kenya.
- Cole, J. W. (1990). Structural control and origin of volcanism in the Taupo Volcanic Zone, New Zealand. *Bull. Volcanol.*, 52, 445–459.
- Cornwell, D. G., MacKenzie, G. D., England, R. W., Maguire, P. K. H., Asfaw, L. M., and Oluma, B. (2006). Northern main Ethiopian rift crustal structure from new high-precision gravity data. In Yirgu, G., Ebinger, C. J., and Maguire, P. K. H., editors, *The Afar Volcanic Province Within the East African Rift System*, volume 259, pages 307–321. Geological Society, London, Special Publications, London, UK.
- Çubukçu, H. E., Ulusoy, I., Aydar, E., Ersoy, O., Şen, E., Gourgaud, A., and Guillou, H. (2012). Mt. Nemrut volcano (Eastern Turkey): Temporal petrological evolution. *J. Volcanol. Geotherm. Res.*, 209–210, 33–60.
- D'Alessandro, W., Brusca, L., Cinti, D., Gagliano, A. I., Longo, M., Pecoraino, G., Pfanz, H., Pizzino, L., Raschi, A., and Voltattorni, N. (2018). Carbon dioxide and radon emissions from the soils of Pantelleria island (southern Italy). *J. Volcanol. Geotherm. Res.*, 362, 49–63.
- Davies, G. R. and Macdonald, R. (1987). Crustal influences in the petrogenesis of the Naivasha basalt-comendite complex: combined trace element and Sr–Nd–Pb isotope constraints. *J. Petrol.*, 28, 1009–1031.
- Di Bella, M., Russo, S., Petrelli, M., and Peccerillo, A. (2008). Origin and evolution of the Pleistocene magmatism of Linosa Island (Sicily Channel, Italy). *Eur. J. Mineral.*, 20, 587–601.
- Di Carlo, I., Rotolo, S. G., Scaillet, B., Buccheri, V., and Pichavant, M. (2010). Phase equilibrium constraints on pre-eruptive conditions of recent felsic explosive volcanism at Pantelleria Island, Italy. *J. Petrol.*, 51, 2245–2276.
- Di Genova, D., Romano, C., Hess, K. U., Vona, A., Giodano, D., Dingwell, D. B., and Behrens, H. (2013). The rheology of peralkaline rhyolites from Pantelleria island. *J. Volcanol. Geotherm. Res.*, 249, 201–216.
- Di Matteo, V., Carroll, M. R., Behrens, H., Vetere, F., and Brooker, R. A. (2004). Water solubility in trachytic melts. *Chem. Geol.*, 212, 187–196.
- Dingwell, D. B., Hess, K.-U., and Romano, C. (1998). Extremely fluid behavior of hydrous peralkaline rhyolites. *Earth Planet. Sci. Lett.*, 158, 31–38.
- D'Oriano, C., Landi, P., Pimentel, A., and Zanon, V. (2017). Magmatic processes revealed by anorthoclase textures and trace element modelling: The case of the Lajes Ignimbrite eruption (Terceira Island, Azores). *J. Volcanol. Geotherm. Res.*, 347, 44–

- 63.
- Dufek, J. D. and Bergantz, G. W. (2005). Lower crustal magma genesis and preservation: A stochastic framework for the evaluation of basalt-crust interaction. *J. Petrol.*, 46, 2167–2195.
- Dunkley, P. N., Smith, M., Allen, D. G., and Darling, W. G. (1993). *The geothermal activity and geology of the northern sector of the Kenya Rift Valley*, volume SC93/1 of *British Geological Survey research report*.
- Esperança, S. and Crisci, G. M. (1995). The island of Pantelleria: A case for the development of DMM-HIMU isotopic compositions in a long-lived extensional setting. *Earth Planet. Sci. Lett.*, 136, 167–182.
- Estrade, G., Salvi, S., Béziat, D., Rakotovo, S., and Rakotonirafy, R. (2014). REE and HFSE mineralization in peralkaline granites of the Ambohimirahavy alkaline complex, Ampasindava peninsula, Madagascar. *J. Afr. Earth Sci.*, 94, 141–155.
- Evangelidis, C. P., Minshull, T. A., and Henstock, T. J. (2004). Three-dimensional crustal structure of Ascension Island from active source seismic tomography. *Geophys. J. Int.*, 159, 311–325.
- Ewart, A., Taylor, S. R., and Cappel, A. C. (1968). Geochemistry of the pantellerites of Mayor Island, New Zealand. *Contrib. Mineral. Petrol.*, 17, 116–140.
- Ferla, P. and Meli, C. (2006). Evidence of magma mixing in the Daly Gap of alkaline suites: a case study from the enclaves of Pantelleria (Italy). *J. Petrol.*, 47, 1467–1507.
- Field, L., Blundy, J., Brooker, R. A., and Wright, T. (2012). Magma storage conditions beneath Dabbahu Volcano (Ethiopia) constrained by petrology, seismicity and satellite geodesy. *Bull. Volcanol.*, 74, 981–1004.
- Flude, S., Burgess, R., and McGarvie, D. W. (2008). Silicic volcanism at Ljósufjöll, Iceland: Insights into evolution and eruptive history from Ar–Ar dating. *J. Volcanol. Geotherm. Res.*, 169, 154–175.
- Fontijn, K., McNamara, K., Tadesse, A. Z., Pyle, D. M., Dessalegn, F., Hutchison, W., Mather, T. A., and Yirgu, G. (2018). Contrasting styles of post-caldera volcanism along the Main Ethiopian Rift: implications for contemporary volcanic hazards. *J. Volcanol. Geotherm. Res.*, 356, 90–113.
- Freundt, A. and Schmincke, H.-U. (1995). Petrogenesis of rhyolite-trachyte-basalt composite ignimbrite P1, Gran Canaria, Canary Islands. *J. Geophys. Res.*, 100, 455–474.
- Freundt-Malecha, B., Schmincke, H.-U., and Freundt, A. (2001). Plutonic rocks of intermediate composition on Gran Canaria: The missing link of the bimodal volcanic suite. *Contrib. Mineral. Petrol.*, 141, 430–445.
- Gaetani, G. A., Grove, T. L., and Bryan, W. B. (1993). The influence of water on the petrogenesis of subduction-related igneous rocks. *Nature*, 365, 332–334.
- Gagnevin, D., Ethien, R., Bonin, B., Moine, B., Féraud, G., Gerbe, M. C., Cottin, J. Y., Michon, G., Tourpin, S., Mamias, G., Perrache, C., and Giret, A. (2003). Open-system processes in the genesis of silica-oversaturated alkaline rocks of the Rallier-du-Batty Peninsula, Kerguelen Archipelago (Indian Ocean). *J. Volcanol. Geotherm. Res.*, 123, 267–300.
- Ghiorso, M. S. and Evans, B. W. (2008). Thermodynamics of rhombohedral oxide solid solutions and a revision of the Fe–Ti two-oxide geothermometer and oxygen-barometer. *Am. J. Sci.*, 308, 957–1039.
- Ghiorso, M. S. and Sack, R. O. (1995). Chemical mass transfer in magmatic processes: IV. A revised and internally consistent thermodynamic model for the interpolation and extrapolation of liquid–solid equilibria in magmatic systems at elevated temperature and pressure. *Contrib. Mineral. Petrol.*, 119, 197–212.
- Gioncada, A. and Landi, P. (2010). The pre-eruptive volatile contents of recent basaltic and pantelleritic magmas at Pantelleria (Italy). *J. Volcanol. Geotherm. Res.*, 180, 191–201.
- Giordano, A., Russell, D. K., and Dingwell, D. B. (2008). Viscosity of magmatic liquids: a model. *Earth Planet. Sci. Lett.*, 271, 123–134.
- Giordano, F., D'Antonio, M., Civetta, L., Tonarini, S., Orsi, G., Ayalew, D., Yirgu, G., Dell'Erba, F., Di Vito, M. A., and Isaia, R. (2014). Genesis and evolution of mafic and felsic magmas at Quaternary volcanoes within the Main Ethiopian Rift: Insights from Gedemsa and Fanta'Ale complexes. *Lithos*, 188, 130–144.
- Gleeson, M. L. M., Stock, M. J., Pyle, D. M., Mather, T. A., Hutchison, W., Yirgu, G., and Wade, J. (2017). Constraining magma storage conditions at a restless volcano in the Main Ethiopian Rift using phase equilibria models. *J. Volcanol. Geotherm. Res.*, 337, 44–61.
- Gottsmann, J., Biggs, J., Lloyd, R., Biranho, Y., and Lewi, E. (2020). Ductility and compressibility accommodate high magma flux beneath a silicic con-

- tinental rift caldera: insights from Corbetti caldera (Ethiopia). *Geochem. Geophys. Geosyst.*, 21, article no. e2020GC008952.
- Gray, T., Dostal, J., McLeod, M., Keppie, D., and Zhang, Y. (2010). Geochemistry of Carboniferous peralkaline felsic volcanic rocks, central New Brunswick, Canada: examination of uranium potential. *Atl. Geol.*, 46, 173–184.
- Green, T. H. (1995). Significance of Nb/Ta as an indicator of geochemical processes in the crust-mantle system. *Chem. Geol.*, 120, 347–359.
- Gualda, G. A., Ghiorsio, M. S., Lemons, R. V., and Carley, T. L. (2012). Rhyolite-MELTS: a modified calibration of MELTS optimized for silica-rich, fluid-bearing magmatic systems. *J. Petrol.*, 53, 875–890.
- Haase, K. M., Stoffers, P., and Garbe-Schönberg, C. D. (1997). The petrogenetic evolution of lavas from Easter Island and neighbouring seamounts, near-ridge hotspot volcanoes in the SE Pacific. *J. Petrol.*, 38, 785–813.
- Halldórsson, S. A., Hilton, D. R., Scarsi, P., Abebe, T., and Hopp, J. (2014). A common mantle plume source beneath the entire East African Rift System revealed by coupled helium-neon systematics. *Geophys. Res. Lett.*, 41, 2304–2311.
- Hammond, J. O. S., Wu, J.-P., Ri, K.-S., Wei, W., Yu, J.-N., and Oppenheimer, C. (2020). Distribution of partial melt beneath Changbaishan/Paektu volcano, China/Democratic People's Republic of Korea. *Geochem. Geophys. Geosyst.*, 21, article no. e2019GC008461.
- Henry, C. D., Price, J. G., Rubin, J. N., and Laubach, S. E. (1990). Case study of an extensive silicic lava: the Bracks Rhyolite, Trans-Pecos Texas. *J. Volcanol. Geotherm. Res.*, 43, 113–132.
- Heumann, A. and Davies, G. R. (2002). U–Th disequilibrium and Rb–Sr age constraints on the magmatic evolution of peralkaline rhyolites from Kenya. *J. Petrol.*, 43, 557–577.
- Hildenbrand, A., Weis, D., Madureira, P., and Marques, F. O. (2014). Recent plate re-organization at the Azores Triple Junction: evidence from combined geochemical and geochronological data on Faial, S. Jorge and Terceira volcanic islands. *Lithos*, 210, 27–39.
- Hoernle, K. A., Zhang, Y. S., and Graham, D. (1995). Seismic and geochemical evidence for large-scale mantle upwelling beneath the eastern Atlantic and western and central Europe. *Nature*, 374, 34–39.
- Horn, S. and Schmincke, H.-U. (2000). Volatile emission during the eruption of Baitoushan Volcano (China/North Korea) ca. 969 AD. *Bull. Volcanol.*, 61, 537–555.
- Houghton, B. F., Weaver, S. D., Wilson, C. J. N., and Lanphere, M. A. (1992). Evolution of a Quaternary peralkaline volcano: Mayor Island, New Zealand. *J. Volcanol. Geotherm. Res.*, 51, 217–236.
- Huang, H.-H., Lin, F.-C., Schmandt, B., Farrell, J., Smith, R. B., and Tsai, V. C. (2015). The Yellowstone magmatic system from the mantle plume to the upper crust. *Science*, 348(6236), 773–776.
- Hutchison, W., Biggs, J., Mather, T. A., Pyle, D. M., Lewi, F., Yirgu, G., Caliro, S., Chiodini, G., Clor, I. F., and Fischer, T. P. (2016b). Causes of unrest at silicic calderas in the East African Rift: New constraints from InSAR and soil-gas chemistry at Aluto volcano, Ethiopia. *Geochem. Geophys. Geosyst.*, 17, 3008–3030.
- Hutchison, W., Mather, T. A., Pyle, D. M., Boyce, A. J., Gleeson, M. L. M., Yirgu, G., Blundy, J. D., Ferguson, D. J., Vye-Brown, C., Millar, I. L., Sims, K. W. W., and Finch, A. A. (2018). The evolution of magma during continental rifting: New constraints from the isotopic and trace element signatures of silicic magmas from Ethiopian volcanoes. *Earth Planet. Sci. Lett.*, 489, 203–218.
- Hutchison, W., Pyle, D. M., Mather, T. A., Yirgu, G., Biggs, J., Cohen, B. E., Barfod, D. N., and Lewi, F. (2016a). The eruptive history and magmatic evolution of Aluto volcano: new insights into silicic peralkaline volcanism in the Ethiopian rift. *J. Volcanol. Geotherm. Res.*, 328, 9–33.
- Iddon, F. and Edmonds, M. (2020). Volatile-rich magmas distributed through the upper crust in the Main Ethiopian Rift. *Geochem. Geophys. Geosyst.*, 21, article no. e2019GC08904.
- Iddon, F., Jackson, C., Hutchison, W., Fontijn, K., Pyle, D. M., Mather, T. A., Yirgu, G., and Edmonds, M. (2019). Mixing and crystal scavenging in the Main Ethiopian Rift revealed by trace element systematics in feldspars and glasses. *Geochem. Geophys. Geosyst.*, 20, 230–259.
- Imsland, P., Larsen, J. G., Prestvik, T., and Sigmond, E. M. (1977). The geology and petrology of Bouvetøya, south Atlantic Ocean. *Lithos*, 10, 213–234.
- Javoy, M. and Courtillot, V. (1989). Intense acidic volcanism at the Cretaceous-Tertiary boundary. *Earth Planet. Sci. Lett.*, 94, 409–416.

- Jeffery, A. J. and Gertisser, R. (2018). Peralkaline felsic magmatism of the Atlantic islands. *Front. Earth Sci.*, 6, article no. 145.
- Jeffery, A. J., Gertisser, R., O'Driscoll, B., Pacheco, J. M., Whitley, S., Pimentel, A., and Self, S. (2016). Temporal evolution of a post-caldera, mildly peralkaline magmatic system: Furnas volcano, São Miguel, Azores. *Contrib. Mineral. Petrol.*, 171, article no. 42.
- Jeffery, A. J., Gertisser, R., Self, S., Pimentel, A., O'Driscoll, B., and Pacheco, J. M. (2017). Petrogenesis of the peralkaline ignimbrites of Terceira, Azores. *J. Petrol.*, 58, 2365–2402.
- Jellinek, A. M. and DePaolo, D. J. (2003). A model for the origin of large silicic magma chambers: precursors of caldera-forming eruptions. *Bull. Volcanol.*, 65, 363–381.
- Jicha, B. R., Singer, B. S., and Valentine, M. J. (2013). $^{40}\text{Ar}/^{39}\text{Ar}$ geochronology of subaerial Ascension Island and a re-evaluation of the temporal progression of basaltic to rhyolitic volcanism. *J. Petrol.*, 54, 2581–2596.
- Joachim, K. P., Seufert, H. M., Spettel, B., and Palme, H. (1986). The solar-system abundances of Nb, Ta, and Y, and the relative abundances of refractory lithophile elements in differentiated planetary bodies. *Geochem. Cosmochem. Acta*, 50, 1173–1183.
- Jordan, N. J., Rotolo, S. G., Williams, R., Speranza, E., McIntosh, W. C., Branney, M. J., and Scaillet, S. (2018). Explosive eruptive history of Pantelleria, Italy: repeated caldera collapse and ignimbrite formation at a peralkaline volcano. *J. Volcanol. Geotherm. Res.*, 349, 42–73.
- Jordan, N. J., White, J. C., Macdonald, R., and Rotolo, S. G. (2021). Evolution of the magma system of Pantelleria (Italy) from 190 ka to present. *C. R. Géosci.*, 353(S2), 133–149.
- Jørgensen, K. A. (1980). The Thorsmörk ignimbrite: an unusual comenditic pyroclastic flow in southern Iceland. *J. Volcanol. Geotherm. Res.*, 8, 7–22.
- Kar, A., Weaver, B., Davidson, J., and Colucci, M. (1998). Origin of differentiated volcanic and plutonic rocks from Ascension Island, South Atlantic Ocean. *J. Petrol.*, 39, 1009–1024.
- Kovalenko, V. I., Yarmolynk, V. V., Kovatch, D. V., Kovalenko, D. V., Kozlovskiy, A. M., Andreeva, I. A., Kotov, A. B., and Sal'nikova, E. B. (2009). Variations in isotope composition and of critical ratios of incompatible trace elements as reflections of source mixing for alkaline granitoids and basites from the Khaldzan Buregtey massif and of the rare-metal deposit there. *Petrology*, 17, 249–275.
- Krumrei, T. V. and Markl, G. (2005). Fluid inclusions in sodalite from the peralkaline Ilimaussaq complex, South Greenland: an indicator of fluid composition changes. In *Peralkaline Rocks: Sources, Economic Potential and Evolution from Alkaline Melts*, pages 59–60. PERALK Workshop on Peralkaline Rocks, Tuebingen, Germany. Abstract.
- Kynicky, J., Chakmouradian, A. R., Xu, C., Krmicek, J., and Galiova, M. (2011). Distribution and evolution of zirconium mineralization in peralkaline granites and associated pegmatites of the Khan Bogd complex, southern Mongolia. *Can. Mineral.*, 49, 947–965.
- Lacroix, A. (1930). Les roches hyperalkalines du Massif du Fantale et du col de Balla. *Mém. Soc. Géol. Fr.*, 14, 89–102.
- Landi, P. and Rotolo, S. G. (2015). Cooling and crystallization recorded in trachytic enclaves hosted in pantelleritic magmas (Pantelleria, Italy): Implications for pantellerite petrogenesis. *J. Volcanol. Geotherm. Res.*, 301, 169–179.
- Lanzo, G., Landi, P., and Rotolo, S. G. (2013). Volatiles in pantellerite magmas: A case study of the Green Tuff Plinian eruption (Island of Pantelleria, Italy). *J. Volcanol. Geotherm. Res.*, 262, 153–163.
- Latin, D., Norry, M. J., and Tarzey, R. J. E. (1993). Magmatism in the Gregory Rift, East Africa: evidence for melt generation in a plume. *J. Petrol.*, 34, 1007–1027.
- Le Bas, M. J., Le Maitre, R. W., Streickeisen, A., and Zanettin, B. (1986). A chemical classification of volcanic rocks based on the total alkali–silica diagram. *J. Petrol.*, 27, 745–750.
- Leat, P. T., Macdonald, R., and Smith, R. L. (1984). Geochemical evolution of the trachytic caldera volcano Menengai, Kenya. *J. Geophys. Res.*, 89, 8571–8592.
- Lees, J. M. (2007). Seismic tomography of magmatic systems. *J. Volcanol. Geotherm. Res.*, 167, 37–56.
- LeMasurier, W. E. (2019). Rhyolites from the mantle, Marie Byrd Land, west Antarctica. In *American Geophysical Union Fall Meeting*. Abstract No. 548106.
- LeMasurier, W. E., Choi, S. H., Kawachi, Y., Mukasa, S. B., and Rogers, N. W. (2011). Evolution of

- pantellerite-trachyte-phonolite volcanoes by fractional crystallization of basanite magma in a continental rift setting, Marie Byrd Land, Antarctica. *Contrib. Mineral. Petrol.*, 162, 1175–1199.
- LeMasurier, W. E., Choi, S. H., Kawachi, Y., Mukasa, S. B., and Rogers, N. W. (2018). Dual origins for pantellerites, and other puzzles, at Mount Takahe volcano, Marie Byrd Land, West Antarctica. *Lithos*, 296–299, 142–162.
- Lightfoot, P. C., Hawkesworth, C. J., and Sethna, S. F. (1987). Petrogenesis of rhyolites and trachytes from the Deccan trap: Sr, Nd and Pb isotope and trace element evidence. *Contrib. Mineral. Petrol.*, 85, 44–54.
- Lisewska, K. M., White, J. C., Macdonald, R., and Bagiński, B. (2018). Compositional and thermodynamic variability in a stratified magma chamber: Evidence from the Green Tuff Ignimbrite (Pantelleria, Italy). *J. Petrol.*, 59, 2245–2272.
- Lowenstern, J. B. (1994). Chlorine, fluid immiscibility, and degassing in peralkaline magmas from Pantelleria, Italy. *Am. Mineral.*, 79, 353–369.
- Lowenstern, J. B., Charlier, B. L. A., Clynne, M. A., and Wooden, J. L. (2006). Extreme U–Th disequilibrium in rift-related basalts, rhyolites and granophyric granite and the timescale of rhyolite generation, intrusion and crystallization at Alid volcanic center, Eritrea. *J. Petrol.*, 47, 2105–2122.
- Lowenstern, J. B. and Mahood, G. A. (1991). New data on magmatic H₂O contents with implications for petrogenesis and eruptive dynamics at Pantelleria. *Bull. Volcanol.*, 54, 78–83.
- Luhr, J. F., Nelson, S. A., Allan, J. F., and Carmichael, I. S. E. (1985). Active rifting in southwestern Mexico: Manifestations of an incipient eastward spreading ridge jump. *Geology*, 13, 54–57.
- Lustrino, M., Fedeale, L., Melluso, L., Morra, V., Ronga, F., Geldmacher, J., Duggen, S., Agostini, S., Cuciniello, C., Franciosi, L., and Meisel, T. (2013). Origin and evolution of Cenozoic magmatism of Sardinia (Italy). A combined isotopic (Sr–Nd–Pb–O–Hf–Os) and petrological view. *Lithos*, 180–181, 138–158.
- Macdonald, R. (1974). Nomenclature and petrochemistry of the peralkaline oversaturated extrusive rocks. *Bull. Volcanol.*, 38, 498–516.
- Macdonald, R. (1994). Petrological evidence regarding the evolution of the Kenya Rift Valley. *Tectonophysics*, 236, 373–390.
- Macdonald, R. (2012). Evolution of peralkaline silicic complexes: Lessons from the extrusive rocks. *Lithos*, 152, 11–22.
- Macdonald, R., Bagiński, B., Belkin, H. E., White, J. C., and Noble, D. C. (2019). The Gold Flat Tuff, Nevada: insights into the evolution of peralkaline silicic magmas. *Lithos*, 328–329, 1–13.
- Macdonald, R., Bagiński, B., Leat, P. T., White, J. C., and Dzierżanowski, P. (2011). Mineral stability in peralkaline silicic rocks: Information from trachytes of the Menengai volcano, Kenya. *Lithos*, 125, 553–568.
- Macdonald, R., Bagiński, B., Ronga, F., Dzierżanowski, P., Lustrino, M., Marzoli, A., and Melluso, L. (2012). Evidence for extreme fractionation of peralkaline silicic magmas, the Boseti volcanic complex, Main Ethiopian Rift. *Mineral. Petrol.*, 104, 163–175.
- Macdonald, R., Bagiński, B., and Upton, B. G. J. (2014). The volcano-pluton interface: The Longonot (Kenya) and Kûngnât (Greenland) peralkaline complexes. *Lithos*, 196–197, 232–241.
- Macdonald, R. and Bailey, D. K. (1973). *The Chemistry of the Peralkaline Oversaturated Obsidians*. US Geol. Surv. Prof. Paper 440-N-1.
- Macdonald, R., Belkin, H. E., Fitton, J. G., Rogers, N. W., Nejbert, K., Tindle, A. G., and Marshall, A. S. (2008). The roles of fractional crystallization, magma mixing, crystal mush remobilization and volatile-melt interactions in the genesis of a young basalt-peralkaline rhyolite suite, the Greater Olkaria Volcanic Complex, Kenya Rift Valley. *J. Petrol.*, 49, 1515–1547.
- Macdonald, R., Davies, G. R., Bliss, C. M., Leat, P. T., Bailey, D. K., and Smith, R. L. (1987). Geochemistry of high-silica peralkaline rhyolites, Naivasha, Kenya Rift Valley. *J. Petrol.*, 28, 979–1008.
- Macdonald, R., Davies, G. R., Upton, B. G. J., Dunkley, P. N., Smith, M., and Leat, P. T. (1995). Petrogenesis of Silali volcano, Gregory Rift, Kenya. *J. Geol. Soc., Lond.*, 152, 703–720.
- Macdonald, R., Navarro, J. M., Upton, B. G. J., and Davies, G. R. (1994). Strong compositional zonation in peralkaline magma, Menengai, Kenya Rift Valley. *J. Volcanol. Geotherm. Res.*, 60, 301–325.
- Macdonald, R., Rogers, N. W., Fitton, J. G., Black, S., and Smith, M. (2001). Plume-lithosphere interactions in the generation of the basalts of the Kenya Rift, East Africa. *J. Petrol.*, 42, 877–900.

- Macdonald, R., Smith, R. L., and Thomas, J. E. (1992). *Chemistry of the Subalkalic Silicic Obsidians*. US Geol. Surv. Prof. Paper 1523.
- Macdonald, R., Sumita, M., Schmincke, H.-U., Bagiński, B., White, J. C., and Ilnicki, S. (2015). Peralkaline felsic magmatism at the Nemrut volcano, Turkey: impact of volcanism on the evolution of Lake Van (Anatolia) IV. *Contrib. Mineral. Petrol.*, 169, article no. 34.
- Magee, C., Stevenson, C. T. E., Ebmeier, S. K., Keir, D., Hammond, J. O. S., Gottsman, J. H., Whaler, K. A., Schofield, N., Jackson, C. A.-L., Petronis, M. S., O'Driscoll, B. O., Morgan, J., Cruden, A., Vollgger, S. A., Dering, G., Micklethwaite, S., and Jackson, M. D. (2018). Magma plumbing systems: a geophysical perspective. *J. Petrol.*, 59, 1217–1251.
- Mahatsente, R., Jentzsch, G., and Jahr, T. (1999). Crustal structure of the Main Ethiopian Rift from gravity data: 3-dimensional modeling. *Tectonophysics*, 31, 363–382.
- Mahood, G. and Hildreth, W. (1986). Geology of the peralkaline volcano at Pantelleria, Strait of Sicily. *Bull. Volcanol.*, 48, 143–172.
- Mahood, G. A. (1980). Geological evolution of a Pleistocene rhyolitic center—Sierra La Primavera, Jalisco, Mexico. *J. Volcanol. Geotherm. Res.*, 8, 199–230.
- Mahood, G. A. (1981a). A summary of the geology and petrology of the Sierra La Primavera, Jalisco, Mexico. *J. Geophys. Res.*, 86, 10137–10152.
- Mahood, G. A. (1981b). Chemical evolution of a Pleistocene rhyolitic center—Sierra La Primavera, Jalisco, Mexico. *Contrib. Mineral. Petrol.*, 77, 129–149.
- Mahood, G. A. (1984). Pyroclastic rocks and calderas associated with strongly peralkaline magmatism. *J. Geophys. Res.*, 89, 8540–8552.
- Mahood, G. A. and Baker, D. R. (1986). Experimental constraints on depths of fractionation of mildly alkali basalts and associated felsic rocks: Pantelleria, Strait of Sicily. *Contrib. Mineral. Petrol.*, 93, 251–264.
- Mahood, G. A., Gilbert, C. M., and Carmichael, I. S. E. (1985). Peralkaline and metaluminous mixed-liquid ignimbrites of the Guadalajara region, Mexico. *J. Volcanol. Geotherm. Res.*, 25, 259–271.
- Mahood, G. A. and Stimac, J. A. (1990). Trace-element partitioning in pantellerites and trachytes. *Geochim. Cosmochim. Acta*, 54(8), 2257–2276.
- Margari, V., Pyle, D. M., Bryant, C., and Gibbard, P. L. (2007). Mediterranean tephra stratigraphy revisited: results from a long terrestrial sequence on Lesbos Island, Greece. *J. Volcanol. Geotherm. Res.*, 163, 34–54.
- Markl, G., Marks, M. A. W., and Frost, B. R. (2010). On the controls of oxygen fugacity in the generation and crystallization of peralkaline melts. *J. Petrol.*, 51, 1831–1847.
- Marshall, A. S., Macdonald, R., Rogers, N. W., Fitton, J. G., Tindle, A. G., Nejbert, K., and Hinton, R. W. (2009). Fractionation of peralkaline silicic magmas: the Greater Olkaria Volcanic Complex, Kenya Rift Valley. *J. Petrol.*, 50, 323–359.
- Martel, C., Champallier, R., Prouteau, G., Pichavant, M., Arbaret, L., Balcone-Boissard, H., Boudon, G., Boivin, P., Bourdier, J.-L., and Scaillet, B. (2013). Trachyte phase relations and implication for magma storage conditions in the Chaîne des Puys (French Massif Central). *J. Petrol.*, 54, 1071–1107.
- Martz, A. M. and Brown, F. H. (1981). Chemistry and mineralogy of some Plio-Pleistocene tuffs from the Shungura Formation, southwest Ethiopia. *Quat. Res.*, 16, 240–257.
- Masotta, M., Mollo, S., Freda, C., Gaeta, M., and Moore, G. (2013). Clinopyroxene-liquid thermometer and barometers specific to alkaline differentiated magmas. *Contrib. Mineral. Petrol.*, 166, 1545–1561.
- Masturyono, M. R., Wark, D. A., Roecker, S. W., Fauzi, I., and Sukhyar, G. (2001). Distribution of magma beneath the Toba caldera complex, north Sumatra, Indonesia, constrained by three-dimensional P wave velocities, seismicity, and gravity data. *Geochem. Geophys. Geosyst.*, 2, article no. 2000GC00096.
- Mattia, M., Bonaccorso, A., and Guglielmino, F. (2007). Ground deformations in the Island of Pantelleria (Italy): Insights into the dynamic of the current intereruptive period. *J. Geophys. Res.*, 112, article no. B11406.
- Mbowou, G. I. B., Lagmet, C., Nomade, S., Ngounouno, I., Déruelle, B., and Ohnenstetter, D. (2012). Petrology of the Late Cretaceous peralkaline rhyolites (pantellerite and comendite) from Lake Chad, Central Africa. *J. Geosci.*, 57, 127–141.
- McCurry, M. (1988). Geology and petrology of the Woods Mountain Volcanic Center, southeastern

- California: implications for the genesis of peralkaline rhyolite ash flow tuffs. *J. Geophys. Res.*, 93, 14835–14855.
- McGarvie, D. W., Burgess, R., Tindle, A. G., Tuffen, H., and Stevenson, J. A. (2006). Pleistocene rhyolitic volcanism at the Torfajökull central volcano, Iceland: eruption ages, glaciovolcanism, and geochemical evolution. *Jokull*, 56, 57–75.
- McNamara, K., Cashman, K. V., Rust, A. C., Fontijn, K., Chalié, F., Tomlinson, E. L., and Yirgu, G. (2018). Using lake sediment cores to improve records of volcanism at Aluto volcano in the Main Ethiopian Rift. *Geochem. Geophys. Geosyst.*, 19, 3164–3188.
- Metrich, N. and Rutherford, M. J. (1992). Experimental study of chlorine in hydrous silicic melts. *Geochim. Cosmochim. Acta*, 56, 607–616.
- Miranda, J. M., MendesVictor, L. A., Simões, J. Z., Luis, J. F., Matias, L., Shimamura, H., Shiobara, H., Nemoto, H., Mochizuki, H., Hirn, A., and Lépine, J. C. (1998). Tectonic setting of the Azores Plateau deduced from a OBS survey. *Mar. Geophys. Res.*, 20, 171–182.
- Mondal, S., Upadhyay, D., and Banerjee, A. (2021). REE mineralization in Siwana peralkaline granite, western India—role of fractional crystallization, hydrothermal remobilization, and feldspar–fluid interaction. *Lithos*, 396–397, article no. 106240.
- Morra, V., Secchi, F. A., and Assorgia, A. (1994). Petrogenetic significance of peralkaline rocks from Cenozoic calc-alkaline volcanism from SW Sardinia, Italy. *Chem. Geol.*, 118, 109–142.
- Mungall, J. E. and Martin, R. F. (1995). Petrogenesis of basalt-comendite and basalt-pantellerite suites, Terceira, Azores, and implications for the origin of ocean-island rhyolites. *Contrib. Mineral. Petrol.*, 119, 43–55.
- Mungall, J. E. and Martin, R. F. (1996). Extreme differentiation of peralkaline rhyolite, Terceira, Azores: a modern analogue of Strange Lake, Labrador? *Can. Mineral.*, 34, 769–777.
- Mushkin, A., Stein, M., Halicz, I., and Navon, O. (2002). The Daly gap: low-pressure fractionation and heat-loss from a cooling magma chamber. *Geochim. Cosmochim. Acta*, 66(Supplement 1), article no. A539.
- Neave, D. A. (2020). Chemical variability in peralkaline magmas and magma reservoirs: insights from the Khaggjar lava flow, Pantelleria, Italy. *Contrib. Mineral. Petrol.*, 175, article no. 39.
- Neave, D. A., Fabbro, G., Herd, R. A., Petrone, C. M., and Edmonds, M. (2012). Melting, differentiation and degassing at the Pantelleria volcano, Italy. *J. Petrol.*, 53, 637–663.
- Nekvasil, H., Dondolini, A., Horn, J., Filiberto, J., Long, H., and Lindsley, D. H. (2004). The origin and evolution of silica-saturated alkalic suites: an experimental study. *J. Petrol.*, 45, 693–721.
- Nelson, S. A. and Hegre, J. (1990). Volcán Las Navajas, a Pliocene-Pleistocene trachyte/peralkaline rhyolite volcano in the northwestern Mexican volcanic belt. *Bull. Volcanol.*, 52, 186–204.
- Nicholls, J. and Carmichael, I. S. E. (1969). Peralkaline acid liquids: a petrological study. *Contrib. Mineral. Petrol.*, 20, 268–294.
- Nivin, V. A., Treloar, P. J., Konopleva, N. G., and Ikonovsky, S. V. (2005). A review of the occurrence, form and origin of C-bearing species in the Khibiny Alkaline Igneous Complex, Kola Peninsula. *Lithos*, 85, 93–112.
- Novak, S. W. and Mahood, G. A. (1986). Rise and fall of a basalt-trachyte-rhyolite magma system at the Kane Springs Wash Caldera, Nevada. *Contrib. Mineral. Petrol.*, 94, 352–373.
- O'Neil, H. S. C. and Pownceby, M. I. (1993). Thermodynamic data from redox reactions at high temperatures. I. an experimental and theoretical assessment of the electrochemical method using stabilized zirconia electrolytes, with revised values for the Fe–FeO, Co–CoO, Ni–NiO, and Cu–Cu₂O oxygen buffers, and new data for the W–WO₂ buffer. *Contrib. Mineral. Petrol.*, 114, 296–314.
- Pan, B., de Silva, S. I., Xu, J., Chen, Z., Miggins, D. P., and Wei, W. (2017). The VEI-7 Millennium eruption, Changbaishan-Tianchi volcano, China/DPRK: New field, petrological, and chemical constraints on stratigraphy, volcanology, and magma dynamics. *J. Volcanol. Geotherm. Res.*, 343, 45–59.
- Pan, B., de Silva, S. I., Xu, J., Liu, S., and Xu, D. (2020). Late Pleistocene to present day eruptive history of the Changbaishan-Tianchi volcano, China/DPRK: New field, geochronological and chemical constraints. *J. Volcanol. Geotherm. Res.*, 399, article no. 106870.
- Papale, P., Moretti, R., and Barbaro, D. (2006). The compositional dependence of the saturation surface of H₂O + CO₂ fluids in silicate melts. *Chem. Geol.*, 229, 78–95.

- Parker, D. F. (2019). Generation of alkali flood rhyolite: Insights from evolution of the Paisano volcano, Davis mountains, Trans-Pecos Texas, USA. *J. Volcanol. Geotherm. Res.*, 374, 120–130.
- Parker, D. F. and Henderson, G. D. (2021). Geochemical evolution of the Paradise Mountain caldera complex, Davis Mountains: Implications for the tectonic and magmatic evolution of Trans-Pecos Texas and adjacent Mexico. *Lithos*, 404–405, article no. 106453.
- Parker, D. F. and White, J. C. (2008). Large-scale silicic alkali magmatism associated with the Buckhorn Caldera, Trans-Pecos Texas, USA: comparison with Pantelleria, Italy. *Bull. Volcanol.*, 70, 403–415.
- Parker, D. F., White, J. C., Ren, M., and Barnes, M. (2017). Basement control of alkalic flood rhyolite magmatism of the Davis Mountains volcanic field, Trans-Pecos Texas, USA. *Lithos*, 292–293, 234–249.
- Peccerillo, A., Barberio, M. R., Yirgu, G., Ayalew, D., Barbieri, M., and Wu, T. W. (2003). Relationships between mafic and peralkaline silicic magmatism in continental rift settings: a petrological, geochemical, and isotopic study of the Gedemsa volcano, central Ethiopian rift. *J. Petrol.*, 44, 2002–2032.
- Peretyazhko, I. S., Savina, E. A., and Karmanov, N. S. (2015). Comendites and pantellerites of Nemrut Volcano, Easter Turkey: genesis and relations between the trachyte-comenditic, comenditic and pantelleritic melts. *Petrology*, 23, 576–622.
- Pimentel, A., Self, S., Pacheco, J. M., Jeffery, A. J., and Gertisser, R. (2021). Eruption style, emplacement dynamics and geometry of peralkaline ignimbrites: Insights from the Lajes-Angra ignimbrite formation, Terceira Island, Azores. *Front. Earth Sci.*, 9, article no. 673686.
- Pimentel, A., Zanon, V., de Groot, L. V., Hipólito, A., Di Chiara, A., and Self, S. (2016). Stress-induced comenditic trachyte effusion triggered by trachybasalt intrusion: multidisciplinary study of the AD 1761 eruption at Terceira Island (Azores). *Bull. Volcanol.*, 78, article no. 22.
- Pownceby, M. I. and O’Neil, H. S. C. (1994). Thermodynamic data from redox reactions at high temperatures III. Activity-composition relations in Ni–Pd alloys from EMF measurements at 850–1250 K, and calibration of the NiO + Ni–Pd assemblage as a redox sensor. *Contrib. Mineral. Petrol.*, 116, 327–339.
- Prestvik, T., Goldberg, S., and Goles, G. (1999). Petrogenesis of the volcanic suite of Bouvetøya (Bouvet Island), South Atlantic. *Norsk Geol. Tidsskr.*, 79, 205–218.
- Prestvik, T., Goldberg, S., Karlsson, H., and Grönvold, K. (2001). Anomalous strontium and lead isotope signatures in the off-rift Örfajökull central volcano in south-east Iceland. Evidence for enriched endmember(s) of the Iceland mantle plume? *Earth Planet. Sci. Lett.*, 190, 211–220.
- Putirka, K. (2008). Thermobarometers and barometers for volcanic systems. In Putirka, K. and Tephley, E., editors, *Minerals, Inclusions and Volcanic Processes*, volume 69, pages 61–120. PERALK Workshop on Peralkaline Rocks, Tuebingen, Germany.
- Rappich, V., Žáček, V., Verner, K., Erban, V., Goslar, T., Bekele, Y., Legesa, E., Hroch, T., and Hejtmánková, P. (2016). Wendo Koshe Pumice: The latest Holocene silicic explosive eruption product of the Corbetti Volcanic System (Southern Ethiopia). *J. Volcanol. Geotherm. Res.*, 310, 159–171.
- Ren, M., Omenda, P. A., Anthony, E. Y., White, J. C., Macdonald, R., and Bailey, D. K. (2006). Application of the QUILF thermobarometer to the peralkaline trachytes and rhyolites of the Eburru volcanic complex, East African Rift, Kenya. *Lithos*, 91, 109–124.
- Renna, M. R., Tribuzio, R., and Braga, R. (2013). Petrogenetic relationships between peralkaline rhyolite dykes and mafic rocks in the post-Variscan gabbroic complex from Bocca di Tenda (northern Corsica, France). *Contrib. Mineral. Petrol.*, 165, 1073–1085.
- Rogers, N. W., Evans, P. J., Blake, S., Scott, S. C., and Hawkesworth, C. J. (2004). Rates and time-scales of fractional crystallization from ^{238}U – ^{230}Th – ^{226}Ra disequilibrium in trachyte lavas from Longonot volcano, Kenya. *J. Petrol.*, 45, 1747–1776.
- Rogers, N. W., Macdonald, R., Fitton, J. G., George, R., Smith, M., and Barreiro, B. (2000). Two mantle plumes beneath the East African rift system: Sr, Nd and Pb isotope evidence from Kenya Rift basalts. *Earth Planet. Sci. Lett.*, 176, 387–400.
- Romano, P., Andújar, J., Scaillet, B., Romengo, N., di Carlo, I., and Rotolo, S. G. (2018). Phase equilibria of Pantelleria trachytes (Italy): constraints on pre-eruptive conditions and on the metaluminous to peralkaline transition in silicic magmas. *J. Petrol.*, 59, 559–588.
- Romano, P., Di Carlo, I., Andújar, J., and Rotolo, S. G.

- (2021). Water solubility in trachytic and pantelleritic melts: an experimental study. *C. R. Géosci.*, 353(S2), 315–331.
- Romano, P., Scaillet, B., White, J. C., Andújar, J., Di Carlo, I., and Rotolo, S. G. (2020). Experimental and thermodynamic constraints on mineral equilibrium in pantelleritic magmas. *Lithos*, 376–377, article no. 105793.
- Romano, P., White, J. C., Ciulla, A., Di Carlo, I., D’Orlando, C., Landi, P., and Rotolo, S. G. (2019). Volatiles and trace element contents in melt inclusions from the zoned Green Tuff ignimbrite (Pantelleria, Sicily): petrological inferences. *Ann. Geo-phys.*, 61, article no. VO09.
- Romengo, N., Landi, P., and Rotolo, S. G. (2012). Evidence of basaltic magma intrusions in a trachytic magma chamber at Pantelleria (Italy). *Period. Mineral.*, 81, 163–178.
- Rondet, M., Martel, C., and Bourdier, J.-L. (2019). The intermediate step in fractionation trends of mildly alkaline volcanic suites: An experimental insight from the Pavin trachyandesite (Massif Central, France). *C. R. Géosci.*, 351, 525–539.
- Ronga, F., Lustrino, M., Marzoli, A., and Melluso, L. (2010). Petrogenesis of a basalt-comendite-pantellerite rock suite: the Boseti volcanic complex (Main Ethiopian Rift). *Mineral. Petrol.*, 98, 227–243.
- Rooney, T. O., Hart, W. K., Hall, C. M., Ayalew, D., Ghiorso, M. S., Hidalgo, P., and Yirgu, G. (2012). Peralkaline magma evolution and the tephra record in the Ethiopian Rift. *Contrib. Mineral. Petrol.*, 164, 407–426.
- Rotolo, S. G., Scaillet, S., Speranza, F., White, J. C., Williams, R., and Jordan, N. J. (2021). Volcanological evolution of Pantelleria Island (Strait of Sicily) peralkaline volcano: a review. *C. R. Géosci.*, 353(S2), 111–132.
- Rutherford, N. F. (1978). A comment on the source of Mayor Island pantellerite magma. *N. Z. J. Geol. Geophys.*, 21, 449–453.
- Salvi, S. and Williams-Jones, A. E. (2006). Alteration, HFSE mineralisation and hydrocarbon formation in peralkaline igneous systems: Insights from the Strange Lake Pluton, Canada. *Lithos*, 91, 19–34.
- Samrock, F., Grayver, A. V., Bachmann, O., Karakas, O., and Saar, M. O. (2021). Integrated magnetotelluric and petrological analysis of felsic magma reservoirs: Insights from Ethiopian rift volcanoes. *Earth Planet. Sci. Lett.*, 559, article no. 116765.
- Sauerzapf, U., Lattard, D., Burchard, M., and Engelmann, R. (2008). The titanomagnetite-ilmenite equilibrium: new experimental data and thermobarometric application to the crystallization of basic to intermediate rocks. *J. Petrol.*, 49, 1161–1185.
- Sawyer, D. A., Fleck, R. J., Lanphere, M. A., Warren, R. G., Broxton, D. E., and Hudson, M. R. (1994). Episodic caldera volcanism in the Miocene southwestern Nevada volcanic field: Revised stratigraphic framework, $^{40}\text{Ar}/^{39}\text{Ar}$ geochronology, and implications for magmatism and extension. *Geol. Soc. Am. Bull.*, 106, 1304–1318.
- Scaillet, B. and Macdonald, R. (2001). Phase relations of peralkaline silicic magmas and petrogenetic implications. *J. Petrol.*, 42, 825–845.
- Scaillet, B. and Macdonald, R. (2003). Experimental constraints on the relationships between peralkaline rhyolites of the Kenya Rift Valley. *J. Petrol.*, 44, 1867–1894.
- Scaillet, B. and Macdonald, R. (2006a). Experimental and thermodynamic constraints on the sulphur yield of peralkaline and metaluminous silicic flood eruptions. *J. Petrol.*, 47, 1413–1437.
- Scaillet, B. and Macdonald, R. (2006b). Experimental constraints on pre-eruption conditions of conditions of pantelleritic magmas: evidence from the Eburru complex, Kenya Rift. *Lithos*, 91, 95–108.
- Scaillet, S., Rotolo, S. G., La Felice, S., and Vita-Scaillet, G. (2011). High-resolution $^{40}\text{Ar}/^{39}\text{Ar}$ chronostratigraphy of the post-caldera (<20 ka) volcanic activity at Pantelleria, Sicily Strait. *Earth Planet. Sci. Lett.*, 309, 280–290.
- Scaillet, S., Vita-Scaillet, G., and Rotolo, S. G. (2013). Millennial-scale phase relationships between ice-core and Mediterranean marine records: insights from high-precision $^{40}\text{Ar}/^{39}\text{Ar}$ dating of the Green Tuff of Pantelleria, Sicily Strait. *Quat. Sci. Rev.*, 78, 141–154.
- Schmincke, H.-U. (1974). Volcanological aspects of peralkaline silicic welded ash flow tuffs. *Bull. Volcanol.*, 39, 594–636.
- Schmincke, H.-U. and Sumita, M. (2010). *Geological Evolution of the Canary Islands*. Gorres-Verlag, GMBH, Koblenz.
- Schulz, K. J., DeYoung Jr., J. H., Seal II, R. R., and Bradley, D. C. (2017). *Critical mineral resources of the United States—an introduction (No. 1802-A)*. U.S. Geological Survey.

- Self, S. and Gunn, B. M. (1976). Petrology, volume and age relations of alkaline and saturated peralkaline volcanics from Terceira, Azores. *Contrib. Mineral. Petrol.*, 54, 293–313.
- Siegburg, M., Gernon, T. M., Bull, J. M., Keir, D., Barfod, D. N., Taylor, R. N., Abebe, B., and Ayele, A. (2018). Geological evolution of the Boset-Bericha Volcanic Complex, Main Ethiopian Rift: $^{40}\text{Ar}/^{39}\text{Ar}$ evidence for episodic Pleistocene to Holocene volcanism. *J. Volcanol. Geotherm. Res.*, 351, 115–133.
- Smith, I. E. M. (1976). Peralkaline rhyolites from the D'Entrecasteaux Islands, Papua New Guinea. In Johnson, R. W., editor, *Volcanism in Australasia*, pages 275–285. Elsevier, Amsterdam.
- Smith, I. E. M., Chappell, B. W., Ward, G. K., and Freeman, R. S. (1977). Peralkaline rhyolites associated with andesitic arcs of the southwest Pacific. *Earth Planet. Sci. Lett.*, 37, 230–236.
- Snyder, D. C., Widom, E., Pietruszka, A. G., and Carlson, R. W. (2004). The role of open-system processes in the development of silicic magma chambers: a chemical and isotopic investigation of the Fogo A trachyte deposit, São Miguel, Azores. *J. Petrol.*, 45, 723–738.
- Sosa-Ceballos, G., Macías, J. L., Avellán, D. R., Salazar-Hermenegildo, N., Boijseauneau-López, M. E., and Pérez-Orozco, J. D. (2018). The Acoculco Caldera Complex magmas: Genesis, evolution and relation with the Acoculco geothermal system. *J. Volcanol. Geotherm. Res.*, 358, 288–306.
- Souther, J. G., Armstrong, R. L., and Harakal, J. (1984). Chronology of the peralkaline, late Cenozoic Mount Edziza Volcanic Complex, northern British Columbia, Canada. *Geol. Soc. Am. Bull.*, 95, 337–349.
- Souther, J. G. and Hicks, C. S. (1984). Crystal fractionation of the basalt—comendite series of the Mt. Edziza Complex, British Columbia: major and trace elements. *J. Volcanol. Geotherm. Res.*, 21, 79–106.
- Spampinato, S., Ursino, A., Barbano, M. S., Pirrotta, C., Rapisarda, S., Larocca, G., and Platania, P. R. (2017). A reappraisal of seismicity and eruptions of Pantelleria Island and the Sicily Channel (Italy). *Pure Appl. Geophys.*, 174, 2475–2493.
- Sparks, R. S. J. and Cashman, K. V. (2017). Dynamic magma systems: implications for forecasting volcanic activity. *Elements*, 13, 35–40.
- Stabile, P., Arzilli, F., and Carroll, M. R. (2021). Crystalization of peralkaline rhyolitic magmas: pre- and syn-eruptive conditions of the Pantelleria system. *C. R. Géosci.*, 353(S2), 151–170.
- Stabile, P., Webb, S., Knipping, J. L., Behrens, H., Paris, E., and Giuli, G. (2016). Viscosity of pantelleritic and alkali-silicate melts: Effect of Fe redox state and Na/(Na+K) ratio. *Chem. Geol.*, 442, 73–82.
- Stevenson, R. J., Bagdassarov, N. S., Dingwell, D. B., and Romano, C. (1998). The influence of trace amounts of water on the viscosity of rhyolites. *Bull. Volcanol.*, 60, 89–97.
- Stevenson, R. J. and Wilson, L. (1997). Physical volcanology and eruption dynamics of peralkaline agglutinates from Pantelleria. *J. Volcanol. Geotherm. Res.*, 79, 97–122.
- Stolz, A. J. (1985). The role of fractional crystallization in the evolution of the Nandewar volcano, north-eastern New South Wales, Australia. *J. Petrol.*, 26, 1002–1026.
- Sumita, M. and Schmincke, H.-U. (2013a). Impact of volcanism on the evolution of Lake Van (Turkey). II. Temporal evolution of Nemrut Volcano (eastern Anatolia) during the past ca. 0.4 Ma. *J. Volcanol. Geotherm. Res.*, 253, 15–34.
- Sumita, M. and Schmincke, H.-U. (2013b). Impact of volcanism on the evolution of Lake Van. I: evolution of explosive volcanism of Nemrut Volcano (eastern Anatolia) during the past >400,000 years. *Bull. Volcanol.*, 75, 1–32.
- Sumner, J. M. and Wolff, J. (2003). Petrogenesis of mixed-magma, high-grade, peralkaline ignimbrite “TL” (Gran Canaria): diverse styles of mixing in a replenished, zoned magma chamber. *J. Volcanol. Geotherm. Res.*, 126, 109–126.
- Thompson, R. N. and MacKenzie, W. S. (1967). Feldspar-liquid equilibria in peralkaline acid liquids: an experimental study. *Am. J. Sci.*, 265, 714–734.
- Troll, V. R. and Schmincke, H.-U. (2002). Magma mixing and crustal recycling recorded in ternary feldspar from compositionally zoned peralkaline ignimbrite A, Gran Canaria, Canary Islands. *J. Petrol.*, 43, 243–270.
- Trua, T., Deniel, C., and Mazzuoli, R. (1999). Crustal control in the genesis of Plio-Quaternary bimodal magmatism of the Main Ethiopian Rift (MER): geochemical and isotopic (Sr, Nd, Pb) evidence. *Chem. Geol.*, 155, 201–231.
- van den Bogaard, P. (2013). The origin of the Canary Island Seamount Province—New ages of old

- seamounts. *Nat. Sci. Rep.*, 3, article no. 2107.
- Vezzoli, L. and Acocella, V. (2009). Easter Island, SE Pacific: An end-member type of hotspot volcanism. *Geol. Soc. Am. Bull.*, 121, 869–886.
- Vogel, T. A., Ryerson, F. J., Noble, D. C., and Younker, L. W. (1987). Limits to magma mixing based on chemistry and mineralogy of pumice fragments erupted from a chemically zoned magma body. *J. Geol.*, 95, 659–670.
- Watson, E. B., Wark, D. A., and Thomas, J. B. (2006). Crystallization thermometers for zircon and rutile. *Contrib. Mineral. Petrol.*, 151, 413–433.
- Weaver, B., Kar, A., Davidson, J., and Colucci, M. (1996). Geochemical characteristics of volcanic rocks from Ascension Island, South Atlantic Ocean. *Geothermics*, 25, 449–470.
- Weaver, S. D. (1977). The Quaternary caldera volcano Emuruangogolak, Kenya Rift, and the petrology of a bimodal ferrobasalt-pantelleritic trachyte association. *Bull. Volcanol.*, 40, 209–230.
- Webster, J. D., Taylor, R. P., and Bean, C. (1993). Pre-eruptive melt composition and constraints on degassing of a water-rich pantellerite magma, Fantale volcano, Ethiopia. *Contrib. Mineral. Petrol.*, 114, 53–62.
- Wei, H., Liu, G., and Gill, J. (2013). Review of eruptive activity at Tianchi volcano, Changbaishan, north-east China: Implications for possible future eruptions. *Bull. Volcanol.*, 75, article no. 708.
- Whaler, K. A. and Hautot, S. (2006). The electrical resistivity of the crust beneath the northern Main Ethiopian Rift. In Yirgu, G., Ebinger, C. J., and Maguire, P. K. H., editors, *The Afar Volcanic Province Within the East African Rift System*, volume 259, pages 293–305. Geological Society, Special Publications, London.
- White, J. C., Benker, S. C., Ren, M., Urbanczyk, K. M., and Corrick, D. W. (2006). Petrogenesis and tectonic setting of the peralkaline Pine Canyon caldera, Trans-Pecos Texas, USA. *Lithos*, 91, 74–94.
- White, J. C., Neave, D. A., Rotolo, S. G., and Parker, D. F. (2020). Geochemical constraints on basalt petrogenesis in the Strait of Sicily Rift Zone (Italy): Insights into the importance of short lengthscale mantle heterogeneity. *Chem. Geol.*, 545, article no. 119650.
- White, J. C., Parker, D. F., and Ren, M. (2009). The origin of trachyte and pantellerite from Pantelleria, Italy: Insights from major element, trace element, and thermodynamic modelling. *J. Volcanol. Geotherm. Res.*, 179, 33–55.
- White, J. C., Ren, M., and Parker, D. F. (2005). Variation in mineralogy, temperature, and oxygen fugacity in a suite of strongly peralkaline lavas and tuffs, Pantelleria, Italy. *Can. Mineral.*, 43, 1331–1347.
- White, J. C., Rotolo, S. G., and Parker, D. (2013). *Petrologic Constraints on Melting Conditions in the Strait of Sicily Rift Zone. Basalt 2013: Cenozoic Magmatism in Central Europe. April 2013, Görlitz, Germany.* 19–20.
- White, J. C. and Urbanczyk, K. M. (2001). Origin of a silica-oversaturated quartz trachyte \pm rhyolite suite through combined crustal melting, magma mixing, and fractional crystallization: the Leyva Canyon volcano, Trans-Pecos Magmatic Province, Texas. *J. Volcanol. Geotherm. Res.*, 111, 155–182.
- Wilding, M. C., Macdonald, R., Davies, J. R., and Fallick, A. E. (1993). Volatile characteristics of peralkaline rhyolites from Kenya: an ion microprobe, infrared spectroscopic and hydrogen isotope study. *Contrib. Mineral. Petrol.*, 44, 681–690.
- Wilks, M., Rawlinson, N., Kendall, J.-M., Nowacki, A., Biggs, J., Ayele, A., and Wookey, J. (2020). The coupled magmatic and hydrothermal systems of the restless Aluto caldera, Ethiopia. *Front. Earth Sci.*, 8, article no. 579699.
- Wolff, J. A., Ellis, B. S., Ramos, F. C., Starkel, W. A., Boroughs, S., Oiln, P. H., and Bachmann, O. (2015). Remelting of cumulates as a process for producing chemical zoning in silicic tuffs: A comparison of cool, wet and hot, dry rhyolitic magma systems. *Lithos*, 336–337, 275–286.
- Wolff, J. A., Forni, F., Ellis, B. S., and Szymanowski, D. (2020). Europium and barium enrichments in compositionally zoned felsic tuffs: A smoking gun for the origin of chemical and physical gradients by cumulate melting. *Earth Planet. Sci. Lett.*, 340, article no. 116251.
- Xu, J., Pan, B., Liu, T., Hajdas, I., Zhao, B., Yu, H., Liu, R., and Zhao, P. (2013). Climatic impact of the Millenium eruption of Changbaishan volcano in China: New insights from high-precision radio-carbon wiggle-match dating. *Geophys. Res. Lett.*, 40, 54–59.
- Yan, L., He, Z., Beier, C., and Klemd, R. (2018). Geochemical constraints on the link between volcanism and plutonism at the Yunshan caldera complex, SE China. *Contrib. Mineral. Petrol.*, 173, ar-

ticle no. 4.

- Yang, B., Lin, W., Hu, X., Fang, H., Qiu, G., and Wang, G. (2021). The magma system beneath Changbaishan-Tianchi volcano, China/North Korea: constraints from three-dimensional magnetotelluric imaging. *J. Volcanol. Geotherm. Res.*, 419, article no. 107385.
- Zou, H., Fan, Q., and Zhang, H. (2010). Rapid development of the great Millennium eruption of Changbaishan (Tianchi) Volcano, China/North Korea: Evidence from U–Th zircon dating. *Lithos*, 119, 289–296.



Perspectives on alkaline magmas / *Perspectives sur les magmas alcalins*

Alkali magmatism on Mars: an unexpected diversity

Violaine Sautter[✉] *, ^a and Valerie Payre[✉] ^{b, c}

^a IMPMC-UMR, CNRS7590-Sorbonne Université, 61 rue Buffon, 75231 Paris, France

^b Rice University, Houston, TX77005-1892, USA

^c Department of Physics and Astronomy, Northern Arizona University, Flagstaff, AZ 86011, USA

E-mails: violaine.sautter@mnhn.fr (V. Sautter), valerie.payre@nau.edu (V. Payre)

Abstract. Despite an apparent north/south topographic dichotomy that formed >4.0 Ga, the young Martian meteorites (<2.4 Ga) and first-order remote sensing observations revealed a surface of Mars that is uniformly basaltic. This simplistic vision has been challenged by the discovery of a brecciated meteorite and additional spacecraft data that all point to the presence of alkaline igneous rocks, thereby demonstrating an unexpected igneous diversity on Mars. In the present paper, we review a variety of effusive alkaline rocks (basalts to trachytes) recognized so far in the southern hemisphere of Mars as observed from a unique 4.47 Ga Martian meteorite, as well as ground, and orbital data. The complementarity of effusive alkaline rocks and plutonic orthopyroxene-rich rocks in early Mars is discussed. We propose that mantle-derived magmas at high extent of melting at rather low pressure either erupted forming orthopyroxene-rich lavas, or crystallized at shallow crustal depths, fractionating orthopyroxene which sank to the bottom of the chamber and residual alkaline magmas which erupted at the surface of Mars. Widespread low pressure fractionation processes could also be related to heavy bombardment on the early Martian crust generating melt sheets that ultimately differentiated. The Noachian crust is more diverse than being merely basaltic.

Keywords. Mars, Martian meteorite, Orbital spacecraft, In situ rover, Noachian crust, Alkaline igneous trend.

Available online 8th September 2021

1. Introduction

The chemistry and mineralogy of the Martian surface have increasingly been better constrained these past 40 years thanks to Martian meteorites and remote analyses obtained by rovers, landers, and orbiting spacecraft. All the data sets available from Mars until 2012 were in agreement with a homogeneous basaltic Martian crust with a Fe-rich tholeiitic composition [McSween et al., 2003, 2009, McSween, 2015, Udry

et al., 2020], consistent with liquids produced by partial melting of the mantle and transport of those magmatic liquids toward the surface [Baratoux et al., 2011, 2013]. The simple view of Mars being a basalt-covered world had been challenged these past ten years by recent observations of differentiated rocks that combine new Martian meteorite finds [Agee et al., 2013, Humayun et al., 2013, Santos et al., 2015, Hewins et al., 2017], remote analyses from the Mars Science Laboratory (MSL) *Curiosity* rover [Cousin et al., 2017, Payré et al., 2020, Sautter et al., 2016, 2015, 2014, Stolper et al., 2013], and spectroscopic

* Corresponding author.

signatures observed from orbit by visible and very near infrared [Carter and Poulet, 2013, Wray et al., 2013]. Most orbital and ground observations of evolved felsic igneous rocks are located in the southern hemisphere that concentrates the most ancient terrains (3.5–4.5 Ga). The geoid to topographic ratios calculated from orbital data also question the basaltic nature of the crust, suggesting buried felsic crustal components beneath the mafic surface in the southern hemisphere, [Baratoux et al., 2014, Sautter et al., 2016, Wieczorek and Zuber, 2004]. As a whole, the large variations in silica and alkali contents within igneous rocks throughout the ancient southern hemisphere expand the diversity of the magmatic history on Mars and highlight its complexity, especially in ancient times.

In this chapter, we will review the occurrence of alkali-rich igneous rocks recognized so far on Mars. We will then discuss potential scenarios including the nature of crystallization processes producing alkaline rocks on Mars. Finally, such differentiated magmatism in a terrestrial planet such as Mars without plate tectonics (i.e. in a stagnant lid system) will be discussed.

2. Martian geology at planetary scale as seen from orbit

Martian geology has been studied in the last decades through an increasing number of orbital spacecraft. Orbital observations of the Martian crust have been performed at a number of different spatial scales using a variety of remote sensing techniques, each of which provides different but complementary information such as the topography, mineralogy, and chemistry of surface materials.

The Mars Orbiter Laser Altimeter (MOLA) onboard the Mars Global Surveyor spacecraft revealed one of the first evident features when looking at a global map of Mars, which is the topographic dichotomy between the northern hemispheric lowlands and the southern hemispheric highlands (Figure 1a). Examining the map closer, highly craterized highlands stand out from smooth lowlands (Figure 1a). Counting craters and inferring the density of craters following lunar crater density regressions enable geologists to date the surface of Mars (Figure 1b [Carr and Head, 2010, Hartmann and Neukum,

2001]. Martian time is divided into four main periods, pre-Noachian >4.1 Ga, Noachian 4.1–3.7 Ga, Hesperian 3.7–3.2 Ga, and Amazonian 3.2 Ga—today (Figure 1b). The topographic dichotomy is associated with an age dichotomy, with the highly craterized highlands in the southern hemisphere concentrating ancient terrains >3.5 Ga, older than most terrestrial surfaces where Archean terrains are less than 6%, and the smooth lowlands in the northern hemisphere presenting younger surfaces <3.7 Ga [Wyatt et al., 2004]. Overall, the vast majority of the southern highlands are dominated by brecciated terrains that are mid-Noachian in age (3.95–3.8 Ga) and a few scattered patchy areas of early Noachian age (4.1–3.95 Ga) such as the Cimmeria–Sirenum massif.

The Gamma-Ray Spectrometer (GRS) onboard the Mars Odyssey spacecraft measures the surface geochemistry. GRS measurements and global distribution maps have been published for potassium, thorium, iron, silicon, chlorine, and hydrogen [Boynton et al., 2007], and more recently aluminum [Karunatillake et al., 2009] and sulfur [Karunatillake et al., 2014; Table 1]. The GRS instrument typically samples the first tens of centimeter below the surface avoiding the analyses of dust and surface coating, which is convenient for a dusty world such as Mars. GRS elemental maps are convenient when evaluating the nature of Mars surface, but the spatial resolution is low, being approximately equal to the spacecraft altitude (~300 km/pixel; Table 1). With such a resolution, where large 150–200 km diameter craters are represented by one-half pixel only, the crustal composition of both hemispheres appears to be homogeneous, by definitely missing compositional anomalies that are less than tens of kilometers in scale. Measurements indicate that the first tens of centimeters below the surface of Mars has a SiO₂ composition ranging from 39 to 50 wt%, suggesting that mafic rocks are volumetrically dominant. All volcanic provinces identified by GRS are at first order uniformly basaltic [Taylor et al., 2010, Baratoux et al., 2011]. Although basaltic in composition, some terrains are more concentrated in Si, K and Th (Si > 19.9 wt%, K > 0.38 wt%, Th > 0.57 ppm) and more depleted in Fe (Fe < 15.4 wt%) than elsewhere. Combining the Si, Fe, K, and Th abundance maps [Figure 2; Boynton et al., 2007] with a geological age map [Tanaka et al., 2014] highlights six distinct regions enriched in incompatible elements (Th and K “hotspots”) located in the

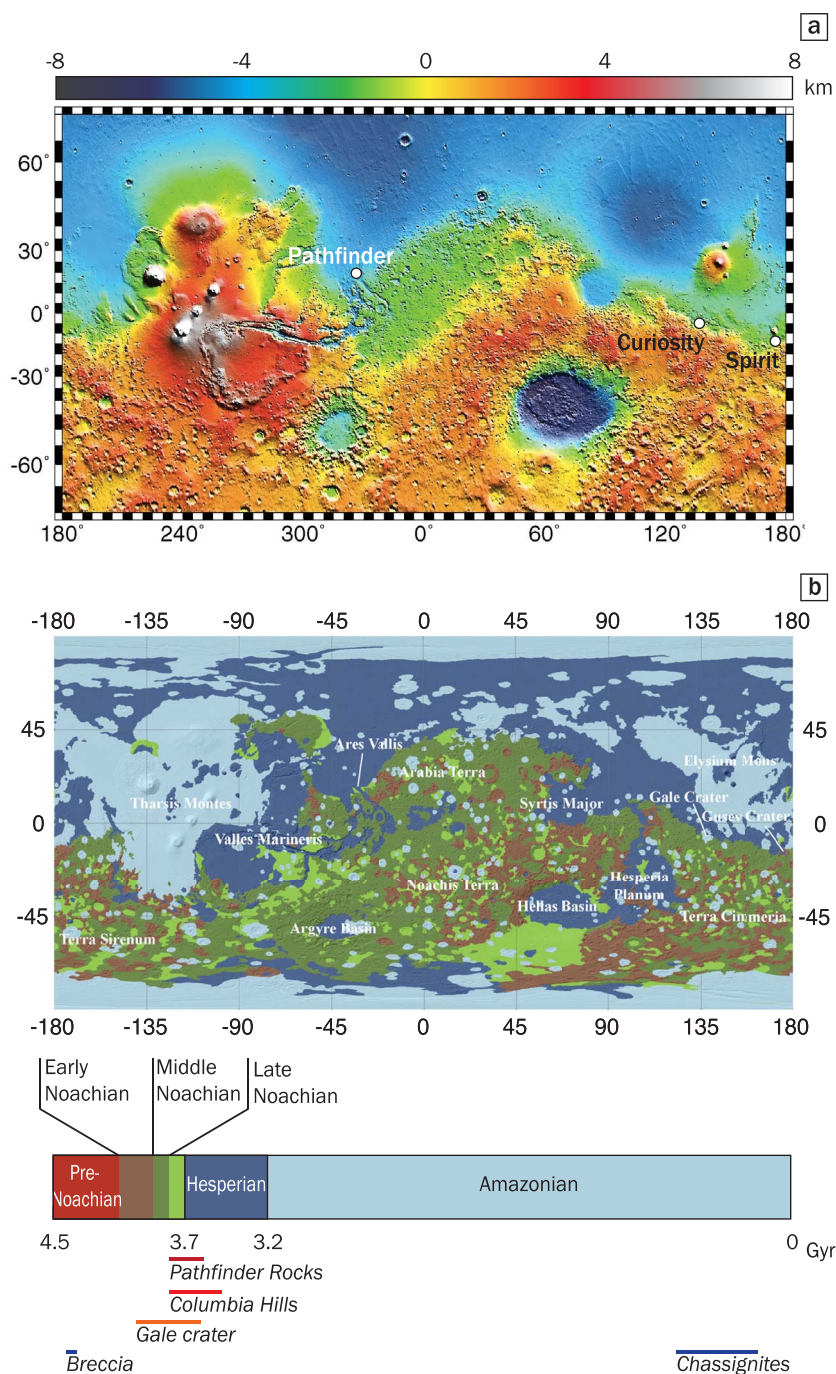


Figure 1. (a) MOLA (Mars Orbital Laser Altimeter) relief topographic global map of Mars. (b) Simplified chronostratigraphic map from Tanaka et al. [2014], with the age of crystallization of alkaline materials observed at the surface of Mars and in the Martian meteorites. Note that the early Noachian units are sparse and that the middle Noachian unit is the most common unit of Noachian terrains.

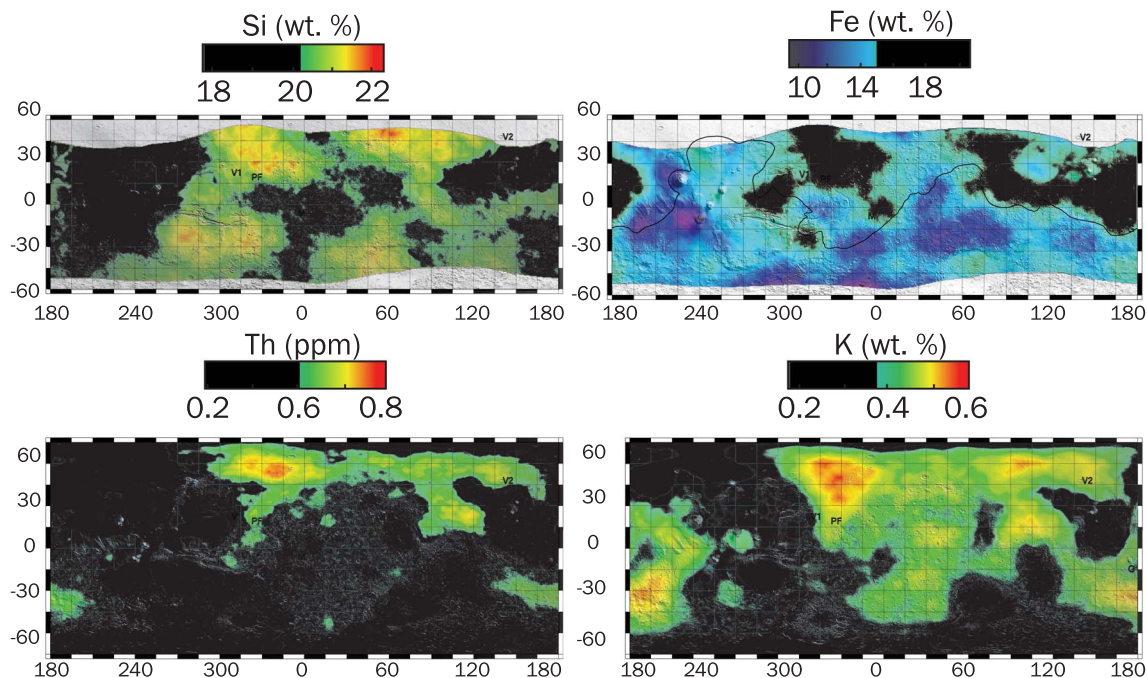


Figure 2. Mars Odyssey Gamma-Ray Spectrometer (GRS) data for the abundance of Si, Fe, Th and K displayed over a shaded relief of Mars. Colored areas underline terrains containing SiO₂ > 42.6 wt%, K₂O > 0.45 wt%, Th > 0.57 ppm, and FeO < 19.8 wt%—i.e., upper and lower half of the measured compositions, making them relatively Si–K–Th rich and Fe poor in comparison with surrounding terrains. Landing sites are indicated in white: V1—Viking 1; V2—Viking 2; PF—Pathfinder; M—Opportunity in Meridiani Planum; G—Spirit in Gusev Crater; C—Curiosity in Gale.

Table 1. Summary of orbital instruments for measuring the composition and mineralogy of the surface of Mars

	Spatial resolution	Penetration depth	Observation data
GRS	300 km/pixel	Tens of cm	Si, Al, Fe, K, Th, S, Cl, and H
OMEGA	300 m/pixel	0.4–5 μm ^a	Mineralogy
CRISM	18 m/pixel	0.4–4 μm ^a	Mineralogy
TES	3 km/pixel	6–50 μm ^a	Mineralogy and thermal inertia
THEMIS	100 m/pixel	7–15 μm ^a	Thermal inertia and qualitative composition/mineralogy

^aFrom Ehlmann and Edwards [2014].

southern hemisphere and dated at early–mid-Noachian (yellow areas in Figure 3): (1) **Terra Tyrrhena** on the north of Hellas Planitia at 60–70° W/15° S ; (2) **Xanthe Terra 1** located more in the north at 50–45° W/–5°–5° S; (3) **Xanthe Terra 2** slightly on the north of Valles Marineris 50° W/10° S; (4) **Noachis Terra** located between Argyre Planitia and Hellas Planitia impact basins 15° E/50° S; (5)

Terra Sirenum 170°–165° W/30°–50° S near the landing site of the Soviet Mars 3 mission; (6) **Terra Cimmeria** located on the south of the renowned volcanic region Elysium Planitia between 135° E/15° S and 165° E/40° S. The low spatial resolution raise questions about whether such “hot spots” are related to regional exposures of igneous bedrock, to spatial averaging of sedimentary rocks, or both.

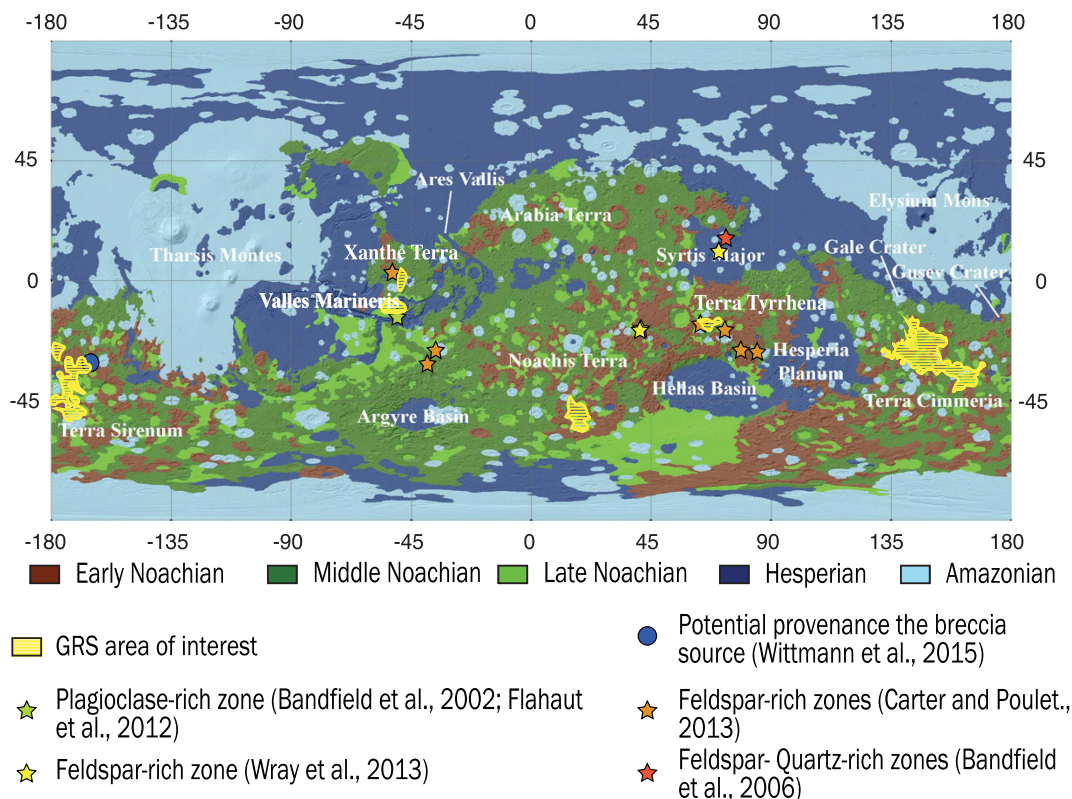


Figure 3. Simplified geological map from Tanaka et al. [2014] where yellow-hatched areas correspond to early Noachian terrains relatively Si–K–Th rich as presented in Figure 5. Colored stars indicate Noachian terrains where feldspar-rich rocks have been detected with orbital instruments (CRISM and TES).

The diagnosis of basaltic dominance at the sub-surface is supported as well by mineral mapping provided by optical and infrared spectroscopy (visible and near infrared (VNIR): OMEGA and CRISM [Bibring, 2005, Murchie et al., 2007]; thermal infrared (TIR): TES and THEMIS [Christensen et al., 2001, 2004; Table 1]. They provide measurements of Martian surface at high spatial resolution compared to GRS (Table 1): TES 3 km/pixel; OMEGA 300 m/pixel; THEMIS 100 m/pixel; and CRISM 18 m/pixel. At first glance, the mineralogy of the southern hemisphere is dominated by mafic mineral associations including olivine [Koeppen and Hamilton, 2008], low-Ca pyroxene (LCP corresponding to orthopyroxene and pigeonite) and high-Ca pyroxene (HCP corresponding to augite, diopside, and hedenbergite) making Mars appear to be covered by basaltic lava flows [Christensen et al., 2005, Hamilton et al., 2005, Poulet et al., 2009, Ody et al., 2013, Riu et al.,

2019]. Note that the distinction between the different kinds of pyroxene referred to as LCP and HCP using near infrared and thermal infrared spectroscopy is difficult to assess. Observations of pyroxene repartition throughout the planet indicate the pronounced contribution of LCP in ancient terrains at a similar or higher level than that of HCP. This contrasts with younger locations where LCP is virtually absent [Mustard et al., 2005, Poulet et al., 2009]. Such mineral mapping provides a biased petrographic perception of the crust. First of all, the principal pit-fall of infrared spectroscopic techniques is a small penetration depth (typically a few microns for VNIR and several μm for TIR; Table 1). The dust cover and/or secondary coatings thus obscure the signature of primary rocks when present. Then, the main felsic igneous minerals like feldspar and quartz are spectrally neutral (transparent) in the visible and VNIR and cannot be detected using this technique

unless the rock contains a limited amount of Fe-rich minerals like olivine and pyroxene [5–40 vol.%; Carter and Poulet, 2013, Rogers and Nekvasil, 2015]. The detection of feldspar is slightly better with thermal infrared spectroscopy as plagioclase shows absorption features in the available spectral range [Hanna et al., 2012], but the spatial resolution of the thermal infrared TES instrument is poor compared to the visible and VNIR CRISM instrument. Orbital spectrometers most likely missed most of the felsic terrains potentially outcropping throughout the southern hemisphere. The detection of feldspar-rich terrains at the surface is therefore overlooked.

Somewhat surprisingly, highly feldspar-rich whitish rocks were identified by visible-VNIR spectroscopy in various scattered Noachian locations in the southern highlands. Some of them are located within the K–Th–Si “hot spots” mentioned above (Figure 3). In **Terra Tyrrhena**, dated from early to mid-Noachian, the CRISM instrument and orbital imaging revealed the occurrence of bright rocks containing 60–95 vol.% of feldspar in a crater rim associated with Al-rich clay, which likely formed from alteration of a felsic outcrop. These have been interpreted as anorthosites [Carter and Poulet, 2013]. Similarly, in a crater rim in **Xanthe Terra** and **Noachis Terra 1**, CRISM data revealed the same kind of formation but these were interpreted as granitoids [Rogers and Nazarian, 2013, Wray et al., 2013].

Close to **Xanthe Terra 2** where CRISM data also revealed light-toned feldspar-rich materials [Wray et al., 2011], the Valles Marineris canyon provides a unique vertical section through time, dated between the early Hesperian at the top and the early Noachian at the bottom. Orbital images revealed light-toned massive bedrock at the bottom of the canyon [Flahaut et al., 2012], which is dominated by LCP according to CRISM data, and large amounts of plagioclases according to TES measurements [~26%; Bandfield, 2002]. [Flahaut et al., 2012] suggest that the LCP-rich light-toned massive rocks are an exposure of a Noachian pristine crust. Large amounts of plagioclases have been revealed by TES analyses, but the spatial resolution of the TES instrument does not allow the precise identification of the nature of the plagioclase-bearing unit [Bandfield, 2002]. Finally, two large areas in **Terra Sirenum** and **Terra Cimmeria**, from early to late Noachian (Figure 3), have been interpreted as a thick 4.2 Ga crustal

component that presents the strongest remnant crustal magnetism [Bouley et al., 2020, Connerney et al., 2005]. A geomorphological study revealed early Noachian volcanic edifices likely being shield-like volcanoes with 50–100 km diameter and 2–3 km height [Xiao et al., 2012]. According to these authors, the ancient volcanoes could be the remnants of a larger population that occurred in early Noachian.

Orbital data revealed several Noachian areas scattered throughout the southern hemisphere with both lithophile-rich concentrations and feldspar-rich signatures associated sometimes with kaolin and/or LCP, demonstrating potential early evolved magmatic processes. Although orbital observations are essential to map out some representative minerals at the surface of the planet, imaging and instrumental resolution are insufficient to identify unambiguously the petrography of any Martian outcrop. If LCP are abundant in Noachian terrains, the nature of the host rocks is not established, potentially being basalts, norites, gabbros, or orthopyroxene cumulates. Similarly, it is impossible to distinguish anorthosite rocks from granites or alkaline lava flows, from orbit.

To summarize, all orbital data combined indicate at first order that the magmatic surface of Mars is overall basaltic with LCP/HCP ratio increasing in terrains older than 3.7 Ga. Scattered Noachian outcrops present felsic rocks, while Hesperian and Amazonian domains seem exclusively basaltic and LCP poor.

3. Martian meteorites

To date, Martian meteorites are the only available petrographic samples which enable constraining the composition of Martian surface and interior, and this will continue so till the Mars Sample Return Mission from Jezero crater scheduled for 2028–2030 [Haltigin et al., 2018].

At the time of writing, a set of 252 Martian meteorites has been found and includes igneous rocks (including pairs) and one breccia (<http://www.imca.cc/mars/martian-meteorites.htm>, Udryetal2020). Oxygen isotope measurements revealed that Martian meteorites share a common mass fractionation trend [Clayton and Mayeda, 1996, 1983], indicating an origin from the same planetary body. The definitive link with Mars was made from the isotopic composition of trapped atmospheric gases extracted from shock melt pockets within meteorites that were

identical to the Martian atmospheric composition measured by Viking landers [Bogard and Johnson, 1983]. Martian meteorites offer a unique opportunity to study a large number of surface or subsurface localities compared to the three landing sites analyzed by rover missions (see Figure 1a). Cosmic ray exposures indicating the ejection age of rocks [Eugster et al., 2002] nevertheless revealed that the 252 meteorites sampled just a few locations on Mars, up to ~11 only [Udry et al., 2020]. Martian samples are thus representatively limited but are nevertheless extremely valuable, offering a unique opportunity to thoroughly study a number of surface and subsurface localities, in Earth-based state-of-the-art laboratories that provide high precision—petrological, mineralogical, and geochemical data, unobtainable by landed and orbital spacecraft instruments [McSween et al., 2009]). Martian meteorites are divided into several groups that are described in the following paragraphs.

3.1. *Shergottite–Nakhlite–Chassignite*

Most Martian meteorites, the so-called SNC, are divided into three main groups shergottite, nakhlite, and chassignite representing respectively 82%, 14%, and 3% of all Martian meteorites (<https://www.imca.cc/mars/martian-meteorites.htm>). Such an apparent diversity actually hides first order common features. A vast majority of SNC contain abundant, often coarse-grained, pyroxene and olivine grains compared to the low amounts of maskelynite (shocked amorphous feldspar crystals), which represent less than 25% of the rock. In other words, Martian meteorites essentially come from mafic and ultramafic cumulates that crystallized at depth. SNC composition thus corresponds to depleted-alkali basalts in the Total Alkali Silica (TAS) diagram (Figure 5).

Shergottites, which are the dominant group, are further subdivided into basaltic, picritic, and lherzolitic shergottites. Among the basaltic subgroup, most meteorites are coarse-textured with high pyroxene/maskelynite ratio (i.e. superchondritic CaO/Al₂O₃ ratio) and are merely represented by mafic to ultramafic cumulates resulting from the fractionation of basaltic liquid at depth. Note that only few basaltic shergottites have a true basaltic cotectic composition (QUE 94201, EET790001, NWA,

Los Angeles, NWA 8159). Picritic shergottite subgroup containing up to 7–29% olivine phenocrysts tends to be less affected by crystal accumulation processes and thus is closer in texture to olivine basalt [Gross et al., 2011]. Lherzolitic shergottites are olivine–pyroxene ultramafic cumulates. Collectively, the whole set of shergottites is young, dated at 0.16 to 2.4 Gyr i.e. late Amazonian [Lapen et al., 2017, Nyquist et al., 2001, and reference therein].

Nakhlites and chassignites are clinopyroxene–olivine-rich cumulates sharing common features, such as a ~1.3 Ga Amazonian crystallization age and an ejection age of 11.8 Ma, suggesting that they were part of the same hypabyssal intrusions or thick lava flows or sills [Nyquist et al., 2001, Udry et al., 2020]. Melt inclusions within cumulus olivine of chassignites are sometimes evolved with alkaline compositions [Nekvasil et al., 2007].

Although shergottites provide isotope anomalies of importance for the pre-Noachian global scale differentiation timing, i.e., core–mantle differentiation and primary crust formation [Dauphas and Pourmand, 2011, Debaille et al., 2009, Elkins-Tanton et al., 2005], these young volcanic SNC meteorites do not provide any direct insights into the petrography of the early Noachian crust. Only two specimens out of 252 Martian meteorites, of early Noachian age, might tell us more about the nature of the early Martian crust: an orthopyroxenite and a regolithic breccia.

3.2. *The orthopyroxenite Allan Hills 84001*

The Allan Hills (ALH 84001) meteorite found in Antarctica, is a coarse-grained cataclastic orthopyroxenite cumulate of its own group that was added to the SNC classification [Mittlefehldt, 1994, Thomas-Keprta et al., 2009]. ALH84001 has been dated to be from Noachian, revised from 4.5 Gyr to 4.091 ± 0.03 Ga according to Lu–Hf isotope data [Lapen et al., 2010]. This age is consistent with 4.074 Ga obtained by Pb isotopes [Bouvier et al., 2009, Lapen et al., 2010]. The meteorite contains 97% orthopyroxene crystals (En₇₀Fs₂₇Wo₃), 2% chromite, 1% maskelynite (An₃₅Ab₆₂Or₃), and 0.15% phosphate with minor augite, olivine, and secondary Fe–Mg–Ca carbonates [Mittlefehldt, 1994]. Its cumulate nature and its mineralogy homogenized by sub-solidus diffusion processes make the bulk rock composition to shift

from that of the parental melt because of crystal accumulation. This meteorite is thus of complex use for the reconstruction of magmatic process on early Mars although the parental melt of ALH 84001 might share some affinities with that of shergottites [Barrat and Bollinger, 2010].

3.3. *The regolithic Martian breccia*

The Martian breccia NWA 7034 and its paired stones (7533/7475/7906/7907/8114/8171/8674/10922/Rabt Sbayta 003) are of exceptional interest to study the early Martian crust [Agee et al., 2013, Humayun et al., 2013, Wittmann et al., 2015]. To cite Agee et al. [2013], “NWA 7034 is not just one rock, but it is like a geological field area conveniently aggregated in one rock”. The NWA 7034 and paired meteorites are the first indurated polymict breccia from Mars that could be representative of the craterized ancient surface of the southern hemisphere [Wittmann et al., 2015]. Zircon grains found within some lithic clasts have been dated to be ~4.47 Ga old, making them one of the oldest fragments currently described from Mars [Humayun et al., 2013, Nyquist et al., 2016]. The breccia provides unique insights into the nature of the primitive crust and early magmatism on Mars. It is formed by a mixing of effusive and extrusive igneous polymineralic coarse-grained clasts, including felsic and mafic clasts, monomineralic fragments up to 2 mm size (mainly pyroxenes and feldspars), volcanic deposits, and clast-laden impact melts embedded in a fine-grained crystalline matrix [Agee et al., 2013, Hewins et al., 2017, Humayun et al., 2013, McCubbin et al., 2016a, Nyquist et al., 2016, Santos et al., 2015, Wittmann et al., 2015]. Each of those components is described below.

3.3.1. *The breccia components*

The most striking feature of the breccia observed for the first time in a Martian meteorite is the presence of 4.47 Ga leucocratic felsic igneous clasts embedded in a dark recrystallized clastic groundmass, contrasting with all the young SNC (Figure 4a hand specimen, 4b, c polished section). Described as trachy-andesites, trachytes, and monzonites, felsic clasts are alkaline and represent between 0.14 and 0.28% of the breccia sections [Agee et al., 2013, Hewins et al., 2017, Humayun et al., 2013, Santos et al., 2015, Wittmann et al., 2015].

They are mainly formed by feldspars including andesine and alkali feldspar such as perthitic orthoclase (Or₈₈ and antiperthite) and Na-rich plagioclase (Ab_{70–90}), pyroxenes like pigeonite, enstatite, augite (En₃₃Wo₄₇Fs₂₀), and sometimes diopside. Euhedral chlorapatite is abundant. Zircon and Ti-bearing spinel grains are accessory phases. If most clasts contain anhedral augite partly molden around feldspar grains, there are also stringy augite grains with subophitic to alkali feldspar laths. Felsic clast composition is elevated in lithophile incompatible elements in comparison with all other Martian meteorites, which typically contain less than 0.3 wt% K₂O and ~0.6 ppm Th (Table 2, K₂O > 5.6 wt%, Rb > 326 ppm, Ba > 345 ppm, and Th up to 28 ppm [Humayun et al., 2013, Taylor and McLennan, 2009, <http://www.imca.CC/mars/martian-meteorites.htm>].

This is also true when compared to the Martian crustal average (K₂O = 0.45 wt%, Rb = 12.5 ppm, Ba = 55 ppm, and Th = 0.7 ppm): see Table 2; Figure 5; [Taylor and McLennan, 2009], suggesting that they were formed by crystallization of an evolved melt.

Mafic clasts are norites, microbasalts, and basaltic andesites. Noritic clasts contain orthopyroxene including inverted pigeonite, augite, plagioclase (An ~ 50–30), rare alkali feldspar, Cr-bearing spinel and small amounts of chlorapatite and zircon [Agee et al., 2013, Hewins et al., 2017, Humayun et al., 2013, Santos et al., 2015, Wittmann et al., 2015]. Orthopyroxene crystals are mostly En_{74–44}Fs_{24–54}Wo_{2–3}, similar to the cumulate crystal analyzed within the orthopyroxenite ALH84001 [Hewins et al., 2017]. Augite grains coexisting with orthopyroxene equilibrated at temperature of 800–900 °C. Although basaltic clast compositions are characteristic of mafic rocks (SiO₂ < 49.5 wt%, Table 2), Na₂O contents are higher than the average crustal composition, and MgO concentrations are mostly lower (Table 2; Figure 5). On the whole, a vast majority of the lithic clasts found in the meteoritic breccia covers the alkali field in the TAS diagram from basaltic to trachytic end-members (Figure 5).

Monomineralic fragments (up to 2 mm) embedded within the matrix of the breccia are essentially plagioclase (An_{50–30}), with small domains of exsolved K-feldspar, and magnesian orthopyroxene (En_{80–73}), as well as magnetite–chromite and chlorapatite. All of these clasts and fragments are embedded in a

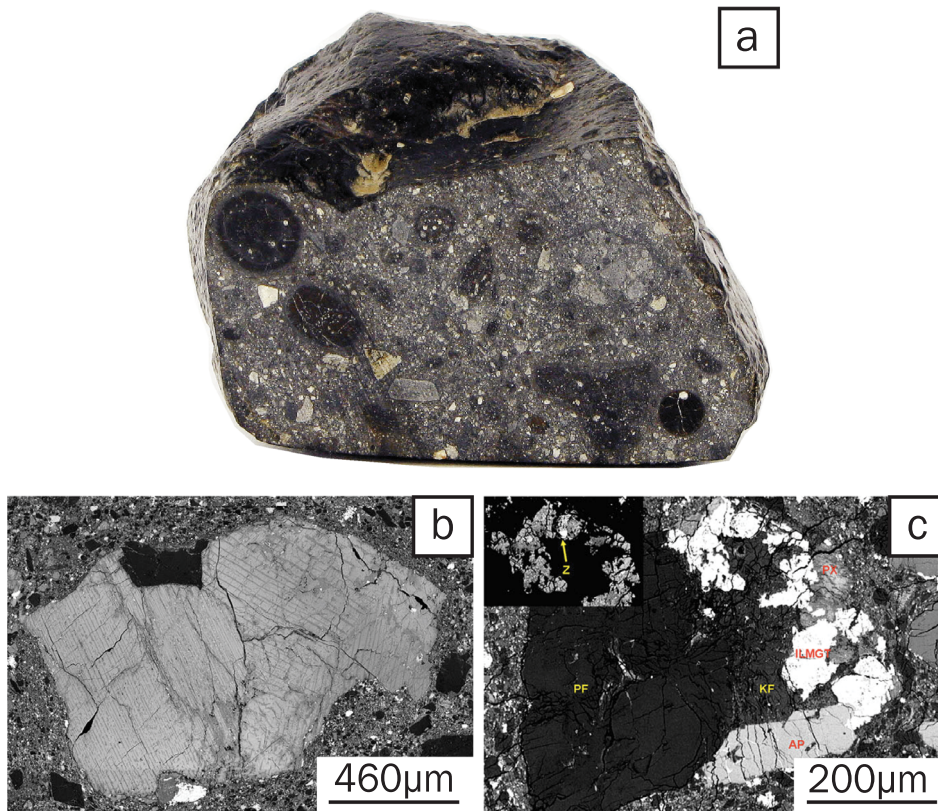


Figure 4. Images of the Martian breccia. (a) Picture of the 4.6× enlarged interior hand specimen of NWA 7475 (image courtesy of Luc Labenne). Numerous light colored felspathic lithic fragments and dark melt spherules are visible in this section. (b) Backscattered electron (BSE) image of noritic clast 7533-5B from NWA 7533 breccia with large piegonite clasts (light gray) and exsolution lamellae associated with andesine crystals (black rectangular shape) within the fine-grained matrix (from Hewins et al. [2017]). (c) BSE image of a large monzonitic clast 7533-4Z from NWA 7533 breccia (from Hewins et al. [2017]).

crystalline and annealed inter-clast matrix, mainly composed of micron-sized plagioclase feldspar grains, with micro- and nano- granular pyroxene crystals. It is of importance to note that except for one olivine, no others have been found within the breccia, as opposed to a majority of SNC meteorites where olivine is ubiquitous. Although most of monomineralic compositions are similar to those of minerals contained within noritic–monzonitic clasts, composition of orthopyroxene extends to more magnesian compositions. Because they are never associated with plagioclase, monomineralic orthopyroxene has been assumed to originate from an orthopyroxenite rock. Interestingly, the orthopyroxene compositions are similar to those of ALH 84001 cumu-

late crystals [Mittlefehldt, 1994] and are isotopically enriched as well [Lapen et al., 2010].

3.3.2. Formation mechanisms of the lithic clasts

High nickel content and high PGE concentrations measured in the breccia suggest the contribution of at least 5–15% of a chondritic impactor [Deng et al., 2020, Humayun et al., 2013]. The large development of exsolution features in coarse crystals in noritic and monzonitic fragments or in mineral clasts, point to slow cooling potentially with a deep-seated plutonic origin, compared to the microbasaltic clasts that likely formed shortly afterward. Therefore, the Martian breccia is thought to be representative of a reworked Noachian regolith, possibly excavated by

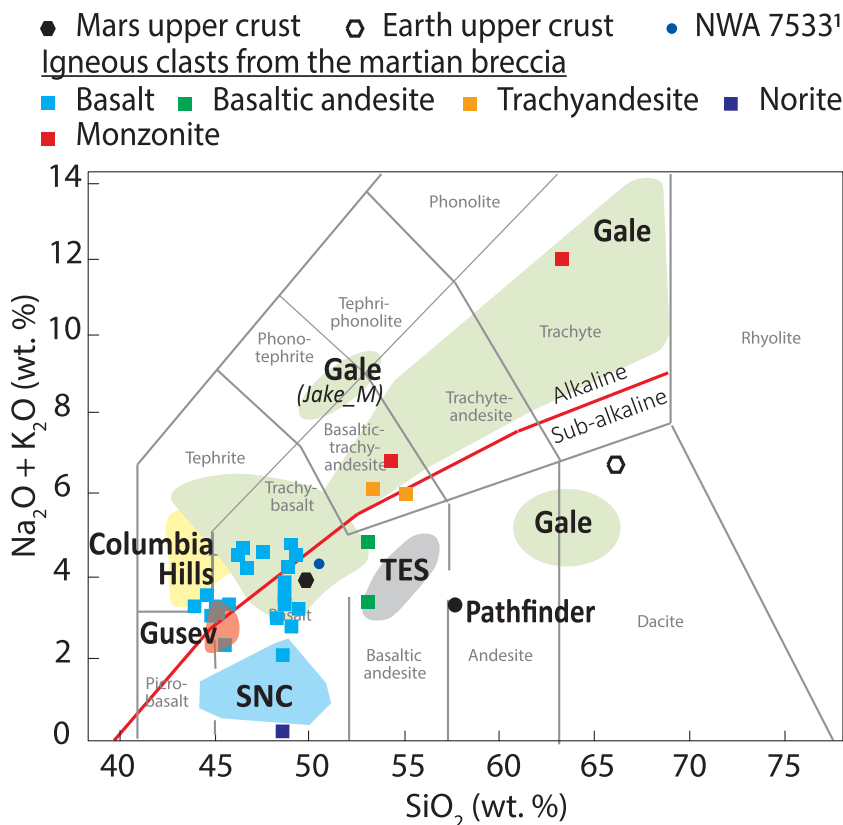


Figure 5. Total alkali content versus silica content adapted from Sautter et al. [2016] allowing geochemical classification of Martian meteorites and rocks analyzed *in situ* in Ares Vallis (Pathfinder), Gusev plain, Columbia Hills, and Gale crater. ¹Refers to the bulk composition of NWA 7533 from Humayun et al. [2013].

several deep impact melt sheets generated by chondritic impactor(s) [Hewins et al., 2017]. The age of 4.43 Ga of five out of ten zircons found within the noritic–monzonitic fragments indicate a common origin by differentiation of a re-melted primary Martian crust within a large impact melt sheet 100 Myr after the Solar System formation [Hewins et al., 2017]. The age of these zircon grains is strikingly similar to the age of the earliest terrestrial [Valley et al., 2001, Wilde et al., 2001] and lunar zircons [Nemchin et al., 2009], suggesting a coeval crust formation on Earth, Moon, and Mars. Zircon grains analyzed in some of the 4.35 Ga trachy-andesitic clasts [Tartèse et al., 2014] crystallized under oxidizing conditions similarly to magmas that formed the terrestrial crust during the Hadean epoch, pointing to a complex Noachian crust and another similarity with the Hadean terrestrial crust.

To summarize, the early Noachian Martian breccia supports the existence of several ancient melts that formed in the southern highlands by impacts on a primordial crust somewhat differentiated and more or less weathered, 100 Myr after solar system formation [Hewins et al., 2017]. These impacts generated deep alkali-rich melts where fractional crystallization produced noritic rocks at the bottom and alkali-rich monzonitic rocks in the upper part (Figure 6). These new data from the polymict breccia support an early formation of the Martian crust as well as its somewhat alkali-rich nature.

4. Ground data from rover observations

Rovers and landers allow *in situ* measurements of the Martian surface at much higher spatial resolution compared to orbital data. The chemical composition

Table 2. Major and trace element composition of the most representative igneous clasts in the Martian breccia compared to that of the averaged Martian crust

	NWA7533				NWA7034			NWA 7475	NWA 7034	Average
	Monzonite		Norite	Microbasalt	Basalt-andesite	Trachy-andesite		Bulk	Bulk	Mars crust
	Clast II	Clast II	Clast IX	Clast VI	Clast 1	Clast 77	Clast 56			
Major elements										
SiO ₂	53.0	63.0	48.2	47.6	53.6	53.5	54.50	48.3	47.6	49.3
TiO ₂	0.40	0.20	0.53	1.11	0.70	1.90	1.20	1.02	0.98	0.98
Al ₂ O ₃	13.6	17.5	0.86	13.7	12.8	16.5	12.30	10.7	11.2	10.5
FeO _T	8.05	3.60	28.7	13.9	13.2	10.9	12.10	16.6	13	18.2
MgO	3.60	0.80	15.0	6.59	9.70	2.20	7.41	10.9	7.81	9.06
CaO	11.4	2.20	5.48	10.6	6.30	10.1	4.27	7.04	8.93	6.92
Na ₂ O	1.81	5.00	0.13	4.36	3.20	4.60	3.27	2.8	3.74	2.97
K ₂ O	5.58	7.20	0.21	0.32	0.2	0.40	2.79	0.47	0.34	0.45
Total	97.4	99.5	99.10	98.20	99.7	100.1	97.90	97.8	93.6	98.4
Trace elements										
Rb	327	387	12.3	4.60	—	—	—	—	17.1	12.5
Sr	142	105	6.00	181	—	—	—	—	115	—
Th	28.5	1.19	0.18	0.92	—	—	—	—	2.64	0.70
Ba	644	345	47.0	89.0	—	—	—	—	—	55.0

Major element composition are in wt% and trace elements are in ppm.

“—” corresponds to the absence of any data.

Compositions of clasts within NWA 7533 are from Humayun et al. [2013], and those in NWA 7034 are from Santos et al. [2015].

Bulk composition of NWA 7475 and NWA 7034 are from Wittmann et al. [2015] and Agee et al. [2013], respectively.

The average Martian crust composition is from Taylor and McLennan [2009].

and mineralogy of the Martian surface obtained from ground analyses provide ground truth for orbital experiments and allow a certain group of meteorites found on Earth to be linked to Mars. Each landing site is unique and contributes to our understanding of the diversity of Martian rocks and the wide range of geological processes that generated them. Over time, rover and lander payloads have become increasingly sophisticated, improving their ability to characterize rock texture, mineralogy, and geochemistry at hand specimen scale. The Alpha Particle X-ray spectrometer (APXS), which had been onboard all the rovers since the earliest mission in 1997, measures the elemental whole-rock composition of ~1.7 cm diameter spots on rock surface [Gellert et al., 2013, and references therein]. As an example of sophisticated instruments onboard the most recent rover (Mars Science Laboratory *Curiosity* rover, 2012), the Chem-

Cam laser-induced breakdown spectrometer (LIBS) is the first laser sent to Mars, which allows to measure the composition of rocks located at distance from the rover, without the necessity of rock contact [Maurice et al., 2012, Wiens et al., 2012]. The CheMin instrument analyzes the mineralogy of drilled rocks using X-ray diffraction [XRD; Blake et al., 2012]. The Mars Hand Lens Imager (MAHLI) is the most resolved imager ever made for a Martian mission.

Since 1997, four missions have landed thousands of kilometers away from each other in equatorial regions of Mars (Figure 1): Mars *Pathfinder* in 1997, the Mars exploration rovers (MER) *Spirit* and *Opportunity* in 2004, and *Curiosity* since 2012 (Figure 1). Three of them allow the analysis of Noachian/early Hesperian terrains on Mars, providing new insights into the early Martian crust that is coeval with Archean cratons on Earth: *Pathfinder* rover, which

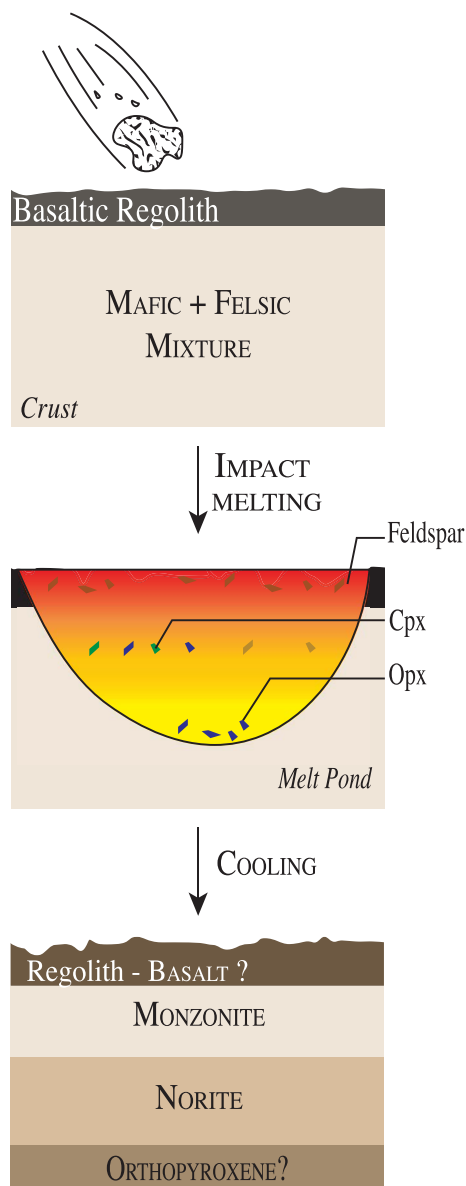


Figure 6. Sketch of the formation of igneous clasts within the Martian breccia (adapted from Hewins et al. [2017]).

landed in *Ares Vallis*; the *Spirit* rover in *Gusev crater*; and *Curiosity* in *Gale crater* (Figure 1).

In *Ares Vallis* (Figure 1a,b), *Pathfinder* traveled within the mouth of a large outflow channel located on the south of *Chryse Planitia*, where debris washed down from the southern hemisphere was concentrated [McSween et al., 1999, and references therein], thus sampling a variety of rocks originating from a

small area including fragments of the Noachian crust. The APXS instrument onboard the lander analyzed five Si-rich and alkali-poor ($\text{SiO}_2 \sim 57.7 \pm 1.7 \text{ wt\%}$; $\text{Na}_2\text{O} + \text{K}_2\text{O} \sim 5.3 \pm 0.7 \text{ wt\%}$) igneous rocks identified as andesites, which likely formed between late Noachian and early Hesperian [Foley et al., 2003, McSween et al., 1999]. The andesitic interpretation is still questioned because of the absence of sophisticated imager and tools that could identify minerals within rocks. The compositions of the five rocks can be either explained by crystallization of an evolved primary melt or by alteration processes in acidic conditions [Foley et al., 2003, McSween et al., 1999]. No consensus has been reached.

Gusev crater, where the *Spirit* rover landed in 2004, is located in the *Aeolis region* along the dichotomy boundary at the northern edge of the highly cratered Noachian southern highlands and south of the Medusae fosse formation (Figure 1a,b). The crater floor is covered by a Hesperian basaltic flow [$\sim 3.65 \text{ Gyr}$; Greeley et al., 2005] containing prominent olivine phenocrysts (Adirondack class) with $\text{Mg\#} > 0.5$ comparable to olivine-phyric shergottites (see Section 3.1). The volcanic flow embays terrains of the *Columbia Hills*, a series of elevated outcrops distinctive from the rocks of the crater floor. The field relationship between the base of the Columbia Hills stratigraphic sequence and the crater floor itself is still unclear. Columbia Hills could either represent a central uplift of older Noachian crater floor [McCoy et al., 2008] or post-date the crater formation and its filling by Hesperian olivine basalt lava flow [Arvidson et al., 2006]. The volcanic flows at Columbia Hills were identified as the first alkali-basalt lithologies described on Mars (e.g. Wishstone, Backstay, and Irvine Figure 5). These alkali-rich rocks range from aphanitic basalts (Irvine-class dyke) and trachy-basalts (Backstay float) to blocks of tuff, i.e. plagioclase-bearing pyroclastic rocks or impact ejecta that have experienced moderate alteration (Wishstone class, [Ruff et al., 2006]). Irvine, Backstay, and Wishstone are likely weakly affected by secondary processes and are usually referred to as alkaline volcanic rocks or alkali-basalts [McSween et al., 2006a]. They are aphanitic rocks that likely contain olivine and pyroxene and have $\text{Na}_2\text{O} + \text{K}_2\text{O}$ ranging from 3 wt% to 5.5 wt% and SiO_2 contents $< 52 \text{ wt\%}$ [Arvidson et al., 2008, Ming et al., 2008]. They still present a significant chemical diver-

sity. Irvine is a sub-alkaline basalt that is similar to Adirondack-class basalts with much higher K_2O concentrations, slightly higher Na_2O , and lower CaO and Al_2O_3 . In contrast to Irvine, Backstay contains more elevated Al_2O_3 contents and has a higher $Mg\#$ (53.3) than Adirondack-class basalts (50.1), Irvine (46.2), and Humboldt Peak basalt (49.7). The Wishstone class basalts are part of the Watchtower stratified outcrop and present tephritic composition, with $Na_2O + K_2O$ ranging from 1.5 to 5.5 wt% and SiO_2 contents <52 wt% [Arvidson et al., 2008, Ming et al., 2008]. These mafic rocks extended the compositional range of igneous rocks encountered on Mars to the alkaline domain. Although not visually identified [McSween et al., 2006a, Squyres et al., 2007, 2006], normative andesine–oligoclase values in Columbia Hills rocks range up to $\sim 55\%$ and several rocks such as Backstay contain up to 7% of normative K-feldspar [Ming et al., 2006], which is consistent with the strong plagioclase signature in Mini-TES spectra observed in Wishstone [Squyres et al., 2006].

Gale crater, where the *Curiosity* rover landed in 2012, is located as well in the **Aeolis region** along the dichotomy boundary (Figure 1a,b). The crater, 155 km in diameter, was formed by an impact in early Hesperian time within a 4.21 Gyr old basement [Le Deit et al., 2013, Farley et al., 2014]. The Mars Science Laboratory (MSL) mission is the first mission to probe such ancient terrains (\sim early Noachian). The analyses of 180 igneous rocks along *Curiosity's* 20 km traverse makes *Gale crater* the most thoroughly documented Noachian igneous terrains on Mars [Cousin et al., 2017]. Broadly speaking, magmatic materials were found either as float rocks (loose boulders) scattered on a sedimentary unit characterized by discontinuous sandstones at the foot of an alluvial fan, or as large rounded clasts within conglomerates. Floats, which could result from the disaggregation of conglomerates, are interpreted to have originated from a subsurface magmatic sequence exposed in the northern crater wall. Transportation through stream water would have deposited the floats on the crater floor, at the end of an alluvial fan. No magmatic outcrop has been detected from orbit within the crater wall or outside the crater, suggesting that it now is buried beneath a basaltic regolith [Sautter et al., 2015]. Onboard the rover, the Chemistry Camera instrument (ChemCam) identified a large diversity of float igneous rocky blocks using a highly resolved

remote micro imager (RMI) enabling textural characterization, and a laser-induced breakdown spectroscopy (LIBS), which allows chemical analyses at a micrometric scale (laser spot diameter: 350–550 μm). The floats and clasts range from darkish and grayish mafic rocks to unexpected light-toned felsic igneous rocks [Sautter et al., 2014, 2015, 2016, Cousin et al., 2017]. Overall, volcanic rocks discovered in Gale crater highlight an extensive compositional diversity. Two magmatic suites including five groups of rocks [Cousin et al., 2017] have been identified: an alkaline trend with basalts and basanites, gabbros and norites, trachy-andesites, mugearites, and trachytes, and a sub-alkaline trend including plutonic rocks such as diorites and quartzo-diorites (Figures 5–7). Interestingly, the coarse-grained component of the soils analyzed in the vicinity of the igneous materials is also felsic in composition [Méslin et al., 2013] providing supporting evidence for local felsic bedrock. For the purpose of the present paper, we will focus on alkaline effusive rocks, i.e., the basalt, trachy-basalt, trachy-andesite, and trachyte sequence (Figure 7). Numerous rocks within this sequence show extreme contents of alkali elements, especially for potassium. Representative compositions of one igneous rock from each described group are summarized in Table 3 and shown in the TAS diagram in Figure 5.

Basalts correspond to dark-toned rocks with aphanitic textures showing local conchoidal fractures (Figure 7a). Most individual crystals are indistinguishable, and most basalts contain feldspar microliths, which are smaller than the ChemCam laser beam ($\ll 350$ μm). The dark groundmass is dominated by Mg-pigeonite (the so-called LCP). In contrast to the olivine phenocrysts described in Adirondack-class basalts from Gusev crater, olivine crystals have never been observed in the Gale dark rocks. The lack of olivine is explained by the whole-rock composition showing that basalts and basanites are Fe rich with a large range of low Mg number ($Mg\#, 0.15 < Mg\# < 0.5$) in comparison with previous rover and lander missions ($Mg\# > 0.5$) [Cousin et al., 2017, McSween et al., 2006b, Squyres et al., 2006].

Jake Matejevic (Jake_M), analyzed by both the APXS and the ChemCam instruments, was described as the first Martian mugearite [Stolper et al., 2013]. Dark gray in color, it has a basaltic composition that is highly alkali-rich (up to 7 wt% Na_2O and

Table 3. Composition of representative rocks for each igneous group identified in Gale crater compared to the Martian average crust for reference

	Basalt Gunflint	Trachy-basalt HarrisonCl	Trachyte Meeting_House	Gabbro La_Reine	Diorite Noriss2	<i>Average Mars Crust</i>
<i>Major elements</i>						
SiO ₂	48.4	57.0	65.0	50.30	57.8	49.3
TiO ₂	1.41	0.62	0.90	0.92	1.08	0.98
Al ₂ O ₃	7.92	19.4	15.4	11.2	18.2	10.5
FeO _T	22.6	6.59	5.34	16.8	8.48	18.2
MgO	10.8	1.90	1.71	11.9	1.92	9.06
CaO	5.17	1.96	2.76	5.73	5.46	6.92
Na ₂ O	2.53	6.08	5.26	2.80	6.18	2.97
K ₂ O	1.17	2.78	3.61	0.30	0.91	0.45
Total	100.0	100.0	100.0	100.0	100.0	98.4
<i>Trace elements</i>						
Rb	44	93	92	21	81	12.5
Sr	48	115	60	34	232	
Ba	49	114	964	87	205	55
<i>CIPW norm</i>						
Quartz	—	—	11.9	—	—	
Plagioclase	34.5	58.3	53.1	47.8	68.5	
Orthoclase	8.70	16.0	21.6	2.17	5.20	
Nepheline	—	4.58	—	—	—	
Diopside	15.1	8.88	1.34	8.77	6.50	
Hypersthene	11.4	—	10.8	21.2	11.5	
Olivine	28.6	8.24	—	19.0	2.21	
Ilmenite	1.80	1.14	1.71	1.15	1.98	
Rutile	—	—	—	—	—	
Density	2.84	2.79	2.74	3.14	2.84	
Mg #	45.9	36.6	36.0	55.8	28.7	

The composition of these rocks are normed to 100% and are from Cousin et al. [2017]. Major element concentrations are expressed in wt% and trace element contents are in ppm.

CIPW norm in % illustrates the potential mineralogy according to the composition. The occurrence of quartz, feldspars, pyroxenes and oxides are in agreement with single point analyses and imaging observations (see Cousin et al. [2017] for more details).

“—” corresponds to 0%.

2 wt% K₂O, Figure 5), and 16% to 17% normative nepheline. This alkaline rock is fractionated like most of the basaltic rocks encountered in Gale crater, as illustrated by its low MgO contents (MgO = 4.5 wt%). Based on comparison with terrestrial mugearites, [Stolper et al., 2013] interpreted Jake_M

as the product of extensive fractional crystallization of an alkali-basaltic liquid. Note that the igneous nature of Jake_M is debated due to its ambiguous texture and composition [e.g., Mangold et al., 2017].

Trachy-basalts/andesites are porphyritic rocks with large feldspar euhedral crystals (up to a few

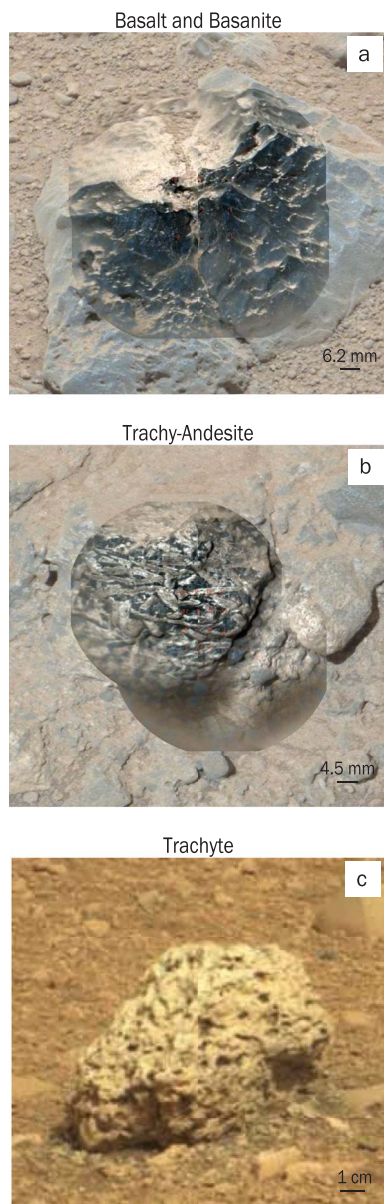


Figure 7. (a–c) RMI images merged with Mastcam images of igneous rocks encountered at Gale crater adapted from Cousin et al. [2017]. From (a) to (c), those rocks are named Pisolet, Harrison, and Becraft.

centimeters) embedded in a dark-gray fine-grained mesostasis with a ferro-augite composition [Figure 7b; Sautter et al., 2015, Cousin et al., 2017]. Feldspar proportion range from 47% to 57% of the

rocks, except for one rock named Bindi presenting 80% of coarse feldspar with a typical cumulate texture. Feldspar compositions range from andesine to oligoclase [Cousin et al., 2017, Payré et al., 2020].

Trachytes are leucocratic rocks with almost no visible grains, presenting conchoidal fractures, and having sometimes a vesiculated or pumiceous appearance (Figure 7c). The ground mass is dominated by alkali feldspar compositions, mainly anorthoclase-like and sometimes sanidine-like. Trachyte composition is alkali-rich ($\text{Na}_2\text{O} \sim 5 \text{ wt\%}$ and $\text{K}_2\text{O} \sim 3.5 \text{ wt\%}$; Figure 5) with a low Mg number (0.3). Felsic rocks, which include trachy-andesites and trachytes, are enhanced in incompatible major and trace elements in comparison with the Martian crustal average (e.g., $0.4 < \text{K}_2\text{O} < 3.8 \text{ wt\%}$, $\text{Rb} \gg 50 \text{ ppm}$, $\text{Ba} \gg 60 \text{ ppm}$ [Payré et al., 2017; Table 3]).

To summarize, rover exploration allows deciphering two igneous series, a sub-alkaline suite that includes the potential andesites from *Ares Vallis* and the quartz-diorites from *Gale crater* (Figure 5), and an alkaline suite that comprises the alkaline rocks found in *Colombia Hills* and *Gale crater*. The alkaline olivine-free (Mg-poor) characteristic of effusive rocks at Gale crater is similar to the early Noachian alkaline clasts from the regolithic meteorite and the Wishstone rocks (possibly of Noachian age) analyzed by the *Spirit* rover. All together, the orbital and rover data and the Martian brecciated meteorite analyses, especially of the Noachian effusive rocks in Gale crater and the 4.47 Ga felsic clasts in the Martian breccia, point to diversified, evolved and alkaline rocks produced early in Martian history.

5. Discussion: origin of alkaline magmatism on Mars

Except for the andesitic and dioritic rocks detected by the *Mars Pathfinder* and the *Curiosity* missions, Noachian igneous materials from Mars are grouped into two lithologies: alkaline rocks and orthopyroxene (LCP)-bearing rocks. The following subsections discuss how such rocks could have been formed.

5.1. How did alkaline rocks form on Mars?

Alkaline melts found on Mars can be generated through various mechanisms including (1) low degree of partial melting of a primitive Martian mantle or a metasomatised mantle source, (2) fractional

crystallization of a basaltic liquid in the presence of water or under high pressure conditions that delay the crystallization of plagioclase toward high fractionation degrees, and (3) crustal assimilation of crustal rocks.

(1) Magmas formed by partial melting of the mantle are primary, i.e., largely unaffected by fractional crystallization. In this case, alkali-rich liquids are formed by low degree of partial melting of either a primitive mantle or a regionally K-metasomatized mantle source [Schmidt and McCoy, 2010, Schmidt et al., 2014]. Low degree of partial melting of a primitive fertile mantle (containing <1% garnet) has been suggested from the Martian breccia bulk composition [Humayun et al., 2013, Sautter et al., 2015]. Broadly speaking, Mars is able to generate magmas that are on average richer in alkali content than the Earth because geochemical models predict that bulk silicate Mars contains 30% more elevated Na concentrations and 15% higher K concentrations than bulk silicate Earth [Palme and O'Neill, 2014, Wanke and Dreibus, 1988]. As a result, alkaline magmas should be more common on Mars than they are on Earth, where alkaline lavas represent less than 1 vol.% of terrestrial igneous rocks [Winter et al., 2010]. Based on elevated K/Ti ratio [Filiberto, 2017], mantle metasomatism has been suggested for the generation of some alkali rocks from Gale crater, including Jake_M [Rice et al., 2017, Schmidt and McCoy, 2010, Schmidt et al., 2016, Treiman and Medard, 2016], although the Martian interior is thought to be dry according to low H₂O estimations within the parental melt of Martian meteorites [150–850 ppm; Filiberto et al., 2016, McCubbin et al., 2016b]. Note that water estimates of the mantle are obtained from SNC, which again are young volcanic rocks resulting from melting of a dehydrated mantle that is likely distinct in composition and water content from the primitive mantle [McCubbin et al., 2012].

(2) Fractional crystallization has been suggested to explain the diversity of alkaline igneous materials in Columbia Hills, Gale crater, within the Martian breccia, and chassignites [Roger H Hewins et al., 2017, Nekvasil et al., 2007]. The Columbia Hills alkaline rocks have been interpreted to be formed by fractional crystallization of either a primitive oxidized basaltic magma with Adirondack-like compositions at various pressures [0.1–1 GPa or 10–80 km; McSween et al., 2006a] or primary basaltic

liquids produced by various partial melting degrees of the mantle [Schmidt and McCoy, 2010]. If true, alkaline rocks from Columbia Hills would post-date the Adirondack-class basalts located within the Gusev crater floor plains whereas the chronology between Columbia Hills and the Gusev crater floor has not been firmly established [Arvidson et al., 2006, Squyres et al., 2006].

Using pMELTS thermodynamical models Ghiorso et al. [2002], Sautter et al. [2015] showed that basaltic end-members of Gale crater rocks may have first originated by low degree of partial melting (6%) of primitive mantle at pressure 1 GPa (~80 km depth) before undergoing fractional crystallization at a pressure of 1 bar. Running additional thermodynamical models, Udry et al. [2014, 2018] propose that felsic alkaline rocks from Gale crater were produced by fractional crystallization at crustal depths (up to 0.4 GPa or ~35 km) of basaltic liquids containing 0.5 wt% of H₂O. Note that the large andesine and oligoclase phenocrysts within a trachy-andesite (Figure 7b) in Gale crater can also be explained by fractional crystallization at crustal depth (up to 0.4 GPa) of a basaltic liquid with 0.5 wt% of H₂O, which formed by relatively low extent of melting of a primitive mantle composition [Payré et al., 2020]. If igneous, Jake_M in Gale crater likely derived as well from melts that have undergone fractional crystallization at depth (≤ 0.4 GPa) with or without the presence of water [Stolper et al., 2013, Collinet et al., 2015]. Although fractionation models seem to match the composition and mineralogy of Gale crater alkaline rocks, trachytic liquids would be produced at >60% of fractionation degree, reaching the critical crystallinity that rheologically prevents eruption [Brophy, 1991].

Felsic and alkaline clasts from the breccia have been interpreted to come from fractionation at the top of an evolved impact melt sheet [Figure 6; Hewins et al., 2017, Humayun et al., 2013]. Comparison between experimental works and terrestrial intra-plate rocks suggest that melts trapped into cumulus olivine of several chassignites were similar to alkaline more or less silica-saturated hawaiite, likely produced by hydrous fractional crystallization of a basaltic melt at pressures >0.4 GPa [Nekvasil et al., 2007].

(3) Crustal assimilation is a common process on Earth that can enrich melts in incompatible elements contained within the crust and that can sometimes increase the alkalinity of the liquids [Beard and Lof-

gren, 1991]. According to thermodynamical models, Ostwald et al. [2020] propose that felsic alkaline rocks from Gale crater could be formed by crustal assimilation followed by fractional crystallization of a basaltic liquid at crustal pressures (up to 0.6 GPa or ~50 km) with $\text{H}_2\text{O} = 0\text{--}0.5\text{ wt\%}$.

In summary, the Hesperian or Noachian alkaline rocks from Columbia Hills and the Amazonian evolved melts included within olivine cumulus of chassignites were likely produced by fractional crystallization at crustal depths, the Noachian alkaline clasts within the Martian breccia potentially formed by fractionation at the top of an alkaline-rich impact melt sheet of a preexisting alkaline crust that was produced 4.43 Ga ago by low degree of partial melt of a fertile mantle, and the formation of Noachian alkaline rocks from Gale crater remain debated (mantle metasomatism, or fractional crystallization certainly accompanied by crustal assimilation; Figure 1). Note that according to partial melting experiments [Collinet et al., 2015], low extent of melting of a primitive mantle composition cannot reproduce trachy-andesitic and trachytic compositions observed in Gale crater. In any case, alkaline igneous materials from Mars were produced by crustal magmatic processes common on Earth [Basaltic Volcanism Study Project, 1981].

5.2. *How did low calcium pyroxene-rich magmatic rocks form?*

While Hesperian and Amazonian lavas are olivine- and HCP-rich basaltic flows, LCP-rich outcrops are a striking feature of the Noachian magmatism [Baratoux et al., 2013, Mustard et al., 2005, Poulet et al., 2009]. As a reminder, HCP corresponds to augite, diopside, and hedenbergite, while LCP corresponds to pigeonite and orthopyroxene. Noachian LCP-rich rocks can be either effusive (basalts) or plutonic rocks (norites or LCP-rich cumulates). Orbital spectroscopy is unable to distinguish between lithologies due to the lack of close imaging and the identification of a potentially incomplete mineral assemblage. Within the Noachian meteorites, LCP-rich rocks are plutonic: LCP cumulates (ALH 84001 and LCP mineral clasts within the breccia) and noritic clasts within the breccia. In contrast to Noachian LCP-rich rocks, Amazonian SNC meteorites are olivine-rich basalts (olivine-phyric shergottites) and olivine-rich or HCP-rich cumulates (lherzolitic shergottites,

nakhrites and chassignites). On the ground, Hesperian lavas at Gusev are olivine-rich basalts, while Gale crater basalts formed in Noachian time are olivine-free and have generally a low non-chondritic Ca/Al ratio. All together, Noachian basaltic rocks are LCP-rich and olivine-free whilst Hesperian to Amazonian cumulate rocks are generally LCP-poor and olivine-rich with the exception of sparse evolved melts observed within Amazonian meteorites (Figure 1).

Assuming that primary unfractionated magmas produced by partial melting of a primitive mantle are the main building blocks of the Martian crust, Baratoux et al. [2013] modeled the transition in pyroxene composition particularly prominent at the Noachian/Hesperian period boundary with LCP/(HCP+LCP) ratio decreasing from 0.4 to 0.2 [Poulet et al., 2009]; and reference therein). Under batch melting conditions, liquids are in thermodynamic equilibrium with the base of the lithosphere and directly ascending to the surface without fractionation. The composition of the primary melts and the crystallization sequence at the surface were calculated for partial melting at different depths (i.e. thickness of the lithosphere which increases from Noachian to more recent time) and different temperatures accounting for cooling of the mantle with time. High degrees of melting lead to a significant contribution of orthopyroxene at shallow depths while melting of olivine is inhibited, favoring the formation of Si-rich liquids in Noachian time compared to Hesperian/Amazonian periods. Overall, high degrees of melting at low pressures favor the crystallization of LCP-rich olivine-poor assemblages within Noachian melts, explaining the lack of olivine in basaltic clasts of the regolithic breccia and in igneous rocks from Gale crater that all formed at lower crustal pressures. Such high degrees of partial melting can be explained as follows. Early in Mars history, the mantle was warmer, thus producing high melting point melts as suggested by Baratoux et al. [2013, 2011]. Mantle plumes, which are thought to have existed in Noachian time [e.g., Citron et al., 2018, Harder and Christensen, 1996], could also contribute to high degree liquids. The lithosphere in Noachian was thinner than later in time. High degrees of partial melting at shallow depths would thus be common in Noachian time.

The orbital observations of large LCP-rich terrains can be explained by (1) the rapid ascent of LCP-rich

liquids produced by high degrees of melting, leading to the formation of vast LCP-rich effusive lavas at the surface of Mars. No fractionation would occur. Another possibility is that (2) LCP-rich liquids are stuck at depths because of a low rate of ascending. In that case, magmas would crystallize, fractionating LCP crystals at the bottom, forming orthopyroxene cumulates, i.e., intrusive rocks, and leaving behind a differentiated alkaline liquid that could erupt and produce feldspar-rich basaltic rocks as observed at Gale crater. Another hypothesis that can be envisioned is (3) heavy bombardment on a LCP-rich crust which was formed by LCP-rich primary magmas formed by high degree of partial melting. The melt sheets induced by wide impacts could fractionate LCP sinking at the bottom leaving behind residual alkaline melts, as suggested by the lithic clasts of the regolithic breccia NWA 7533 and its paired meteorites. The two latter scenarios can explain both LCP cumulates observed within Noachian meteorites, and alkaline olivine-free rocks observed in Gale and Gusev crater. The thickening of the Martian crust and the global cooling of the planet interior likely led in recent times to crystallization events at depth as suggested by the occurrence of evolved melts trapped within some Amazonian chassignites.

Recent results obtained for the past ten years both from spacecraft and meteorite analyses offer exceptional new insights into magmatic processes on early Mars. This extensive data set points to an early magmatic history of Mars considerably more complex than previously acknowledged. The coexistence of alkali rocks and LCP-bearing rocks in the Noachian epoch leaves diverse questions unanswered. Is alkali magmatism coeval with LCP fractionation at depth at a global scale within early Noachian terrains? If so, Noachian LCP-rich areas detected from orbit would likely correspond to cumulate outcrops. Alternatively, LCP-detections from orbit could correspond to LCP-rich lava flows (unfractionated liquid migrating to the surface).

5.3. *Alkaline magmatism in a stagnant lid system*

Mars is considered as a stagnant lid system as no apparent plate tectonics has been observed. Volcanism on Mars can thus be considered as analogous to terrestrial intra-plate magmatism and oceanic

hotspot volcanism. In such settings, alkaline volcanism is common on Earth, although representing <1 vol.% of terrestrial rocks [Winter et al., 2010]. High pressure of melting (>1 GPa), metasomatism, low degree of partial melting, and fractional crystallization of mantle-derived magmas lead to the formation of alkaline rocks on Earth as observed for example in the Terceira island in Azores [Nekvasil et al., 2000] and the Ngatutura basalts in New Zealand [Briggs et al., 1990]. Such formation contexts are consistent with the generation of alkaline rocks on Mars, as discussed in Section 5.1. According to geochemical models, the terrestrial bulk silicate contains 30% less Na concentrations and 15% lower K concentrations than the Martian bulk silicate [Palme and O'Neill, 2014, Wanke and Dreibus, 1988]. Hence, Martian magmas derived from the mantle should be on average richer in alkali contents than the Earth. This is consistent with the average crust being formed by relatively low extent of melting (10%), which favors the accumulation of alkali as suggested by [Kiefer, 2003], and the high amount of radioactive elements like K in the southern hemisphere [Thiriet et al., 2018]. Yet, only a few locations on Mars present alkaline igneous rocks, suggesting that they might be hidden under subsequent late Noachian to Hesperian and Amazonian basaltic materials observed at the surface of Mars from orbit. Interestingly, most alkaline rocks discovered from Mars are felsic, meaning that felsic alkaline rocks are likely buried under a few meters of basaltic flows. The topographic-geoid ratio derived from geophysical data obtained from orbit supports the existence of light differentiated crustal components underneath heavy basaltic rocks [Baratoux et al., 2014]. The occurrence of a large amount of buried alkaline differentiated rocks can explain such observation, implying that the vast majority of the Martian data set might be biased: young SNC sampling localized regions and rover and orbital data mainly measuring young surface basaltic components (>>3.7 Ga). If true, the Martian crust would be extremely complex, with potential orthopyroxene cumulates at the bottom, alkaline felsic components at the upper part, and a homogeneous basaltic cover on the top. Note that isotopic analyses of zircons from the meteorite breccia reveal an enriched basaltic or andesitic crust extracted as soon as 20 Myr after the solar system formation [Bouvier et al., 2018], i.e., coeval to the terrestrial primordial crust forma-

tion [Elkins-Tanton, 2008, Valley et al., 2014]. Fractional crystallization and assimilation of such a crust would lead to alkaline felsic components, especially with a supply of alkali elements within the crust from mantle-derived melts.

Alkaline felsic magmatism discovered on Mars is mostly ancient, >3.7 Ga, and zircon grains found in felsic clasts of NWA 7034 are as old as the most ancient zircons ever dated on Earth [>4.4 Ga; Valley et al., 2014]. Terrestrial zircons are the oldest fragments of our planet, and no rock witnessing the magmatic history of Hadean time exists, mainly because of an efficient plate tectonic system that started early in the terrestrial history [e.g., Kamber et al., 2005, Marchi et al., 2014]. With its stagnant lid, Mars preserved such ancient rocks, and the contemporaneous age of Martian and terrestrial zircons and crust formation suggest a similar magmatism on early Earth and Mars.

6. Conclusion

While terrestrial plate tectonics and significant volcanism have erased the first continental crust on Earth, numerous impact bombardments and extensive basaltic volcanism have likely buried a differentiated crust on Mars. Scattered portions of the early Noachian to Noachian crust can still be observed in several excavations and crater walls in the southern hemisphere, as analyzed in Gale crater and other locations as inferred from orbital data. This is precisely the intensity of bombardment on early Mars that might have generalized melt sheets on surfaces initially covered by LCP-rich lava flows formed by melting of hot mantle beneath a thin primordial crust. Fractionation of those melt sheets would favor the fractionation of LCP cumulates at the bottom and alkali residual melts close to the surface, as suggested by the lithic clasts of the regolithic Martian meteorites. Fractionation at crustal depths of LCP-rich primary liquids produced by high extent of melting of the mantle would also lead to the formation of LCP at depths, later forming LCP cumulates similar to the orthopyroxenite ALH 84001, leaving alkaline residual melts that would erupt at the surface of Mars forming alkaline rocks as those observed in Gale crater. The *Insight* mission that landed on Mars in November 2019 has the first successful onboard seismometer (SEIS) ever sent to Mars [Lognonné et al., 2019].

Probing for the Martian interior, especially the deep crust, seismic data should be able to identify putative deep vertical crustal stratification inferred from surfaces analyses. At Jezero crater, the Mars 2020 *Perseverance* mission probes terrains even older than those of previous ground missions. With a caching system onboard, the *Perseverance* rover is the first of its kind to prepare future Mars sample missions that will likely bring back critical data in terms of Mars' ancient evolved magmatism and its age, providing powerful key information regarding the volcanic history on primitive Earth.

References

- Agee, C. B., Wilson, N. V., McCubbin, F. M., Ziegler, K., Polyak, V. J., Sharp, Z. D., Asmerom, Y., Nunn, M. H., Shaheen, R., Thiemens, M. H., Steele, A., Fogel, M. L., Bowden, R., Glamoclija, M., Zhang, Z., and Elardo, S. M. (2013). Unique meteorite from early Amazonian Mars: Water-Rich basaltic breccia Northwest Africa 7034. *Science*, 339, 780–785.
- Arvidson, R. E., Ruff, S. W., Morris, R. V., Ming, D. W., Crumpler, L. S., Yen, A. S., Squyres, S. W., Sullivan, R. J., Bell, J. F., Cabrol, N. A., Clark, B. C., Farrand, W. H., Gellert, R., Greenberger, R., Grant, J. A., Guinness, E. A., Herkenhoff, K. E., Hurowitz, J. A., Johnson, J. R., Klingelhöfer, G., Lewis, K. W., Li, R., McCoy, T. J., Moersch, J., McSween, H. Y., Murchie, S. L., Schmidt, M., Schröder, C., Wang, A., Wiseman, S., Madsen, M. B., Goetz, W., and McLennan, S. (2008). Spirit Mars rover mission to the Columbia Hills, gusev crater: mission overview and selected results from the Cumberland Ridge to home plate. *J. Geophys. Res.*, 113, article no. E12833.
- Arvidson, R. E., Squyres, S. W., Anderson, R. C., Bell, J. F., Blaney, D., Brückner, J., Cabrol, N. A., Calvin, W. M., Carr, M. H., Christensen, P. R., Clark, B. C., Crumpler, L., Des Marais, D. J., de Souza, P. A., d'Uston, C., Economou, T., Farmer, J., Farrand, W. H., Folkner, W., Golombek, M., Gorevan, S., Grant, J. A., Greeley, R., Grotzinger, J., Guinness, E., Hahn, B. C., Haskin, L., Herkenhoff, K. E., Hurowitz, J. A., Hviid, S., Johnson, J. R., Klingelhöfer, G., Knoll, A. H., Landis, G., Leff, C., Lemmon, M., Li, R., Madsen, M. B., Malin, M. C., McLennan, S. M., McSween, H. Y., Ming, D. W., Moersch, J., Morris, R. V., Parker, T., Rice, J. W., Richter, L., Rieder, R., Rodionov, D. S., Schröder, C., Sims, M.,

- Smith, M., Smith, P., Soderblom, L. A., Sullivan, R., Thompson, S. D., Tosca, N. J., Wang, A., Wänke, H., Ward, J., Wdowiak, T., Wolff, M., and Yen, A. (2006). Overview of the spirit Mars exploration rover mission to gusev crater: landing site to backstay rock in the Columbia Hills. *J. Geophys. Res.*, 111, article no. E02S01.
- Bandfield, J. L. (2002). Global mineral distributions on Mars. *J. Geophys. Res.*, 107, article no. 5042.
- Baratoux, D., Samuel, H., Michaut, C., Toplis, M. J., Monnereau, M., Wiczorek, M., Garcia, R., and Kurita, K. (2014). Petrological constraints on the density of the Martian crust. *J. Geophys. Res.*, 119, 1707–1727.
- Baratoux, D., Toplis, M. J., Monnereau, M., and Gasnault, O. (2011). Thermal history of Mars inferred from orbital geochemistry of volcanic provinces. *Nature*, 472, 338–341.
- Baratoux, D., Toplis, M. J., Monnereau, M., and Sautter, V. (2013). The petrological expression of early Mars volcanism. *J. Geophys. Res.*, 118, 59–64.
- Barrat, J.-A. and Bollinger, C. (2010). Geochemistry of the Martian meteorite ALH 84001, revisited. *Meteorit. Planet. Sci.*, 45, 495–512.
- Basaltic Volcanism Study Project (1981). *Basaltic Volcanism on the Terrestrial Planets*. Pergamon Press, New York.
- Beard, J. S. and Lofgren, G. E. (1991). Dehydration melting and water-saturated melting of basaltic and andesitic greenstones and amphibolites at 1, 3, and 6.9 kb. *J. Petrol.*, 32, 365–401.
- Bibring, J.-P. (2005). Mars surface diversity as revealed by the OMEGA/Mars express observations. *Science*, 307, 1576–1581.
- Blake, D., Vaniman, D., Achilles, C., Anderson, R., Bish, D., Bristow, T., Chen, C., Chipera, S., Crisp, J., Des Marais, D., Downs, R. T., Farmer, J., Feldman, S., Fonda, M., Gailhanou, M., Ma, H., Ming, D. W., Morris, R. V., Sarrazin, P., Stolper, E., Treiman, A., and Yen, A. (2012). Characterization and calibration of the chemin mineralogical instrument on Mars science laboratory. *Space Sci. Rev.*, 170, 341–399.
- Bogard, D. D. and Johnson, P. (1983). Martian gases in an antarctic meteorite? *Science*, 221, 651–654.
- Bouley, S., Keane, J. T., Baratoux, D., Langlais, B., Matsuyama, I., Costard, F., Hewins, R., Payré, V., Sautter, V., Séjourné, A., Vanderhaeghe, O., and Zanda, B. (2020). A thick crustal block revealed by reconstructions of early Mars highlands. *Nat. Geosci.*, 13, 1–5.
- Bouvier, A., Blichert-Toft, J., and Albarède, F. (2009). Martian meteorite chronology and the evolution of the interior of Mars. *Earth Planet. Sci. Lett.*, 280, 285–295.
- Bouvier, L. C., Costa, M. M., Connelly, J. N., Jensen, N. K., Wielandt, D., Storey, M., Nemchin, A. A., Whitehouse, M. J., Snape, J. E., Bellucci, J. J., Moynier, F., Agranier, A., Gueguen, B., Schönbächler, M., and Bizzarro, M. (2018). Evidence for extremely rapid magma ocean crystallization and crust formation on Mars. *Nature*, 558, 586–589.
- Boynton, W. V., Taylor, G. J., Evans, L. G., Reedy, R. C., Starr, R., Janes, D. M., Kerry, K. E., Drake, D. M., Kim, K. J., Williams, R. M. S., Crombie, M. K., Dohm, J. M., Baker, V., Metzger, A. E., Karunatilake, S., Keller, J. M., Newsom, H. E., Arnold, J. R., Brückner, J., Englert, P. A. J., Gasnault, O., Sprague, A. L., Mitrofanov, I., Squyres, S. W., Trombka, J. I., d'Uston, L., Wänke, H., and Hamara, D. K. (2007). Concentration of H, Si, Cl, K, Fe, and Th in the low- and mid-latitude regions of Mars. *J. Geophys. Res.*, 112, article no. E12S99.
- Briggs, R. M., Utting, A. J., and Gibson, I. L. (1990). The origin of alkaline magmas in an intraplate setting near a subduction zone: the Ngatutura Basalts, North Island, New Zealand. *J. Volcanol. Geotherm. Res.*, 40, 55–70.
- Brophy, J. G. (1991). Composition gaps, critical crystallinity, and fractional crystallization in orogenic (calc-alkaline) magmatic systems. *Contrib. Mineral. Petrol.*, 109, 173–182.
- Carr, M. H. and Head, J. W. (2010). Geologic history of Mars. *Earth Planet. Sci. Lett.*, 294, 185–203.
- Carter, J. and Poulet, F. (2013). Ancient plutonic processes on Mars inferred from the detection of possible anorthositic terrains. *Nat. Geosci.*, 6, 1008–1012.
- Christensen, P. R., Bandfield, J. L., Hamilton, V. E., Ruff, S. W., Kieffer, H. H., Titus, T. N., Malin, M. C., Morris, R. V., Lane, M. D., Clark, R. L., Jakosky, B. M., Mellon, M. T., Pearl, J. C., Conrath, B. J., Smith, M. D., Clancy, R. T., Kuzmin, R. O., Roush, T., Mehall, G. L., Gorelick, N., Bender, K., Murray, K., Dason, S., Greene, E., Silverman, S., and Greenfield, M. (2001). Mars global surveyor thermal emission spectrometer experiment: investigation description and surface science results. *J. Geophys.*

- Res.*, 106, 23823–23871.
- Christensen, P. R., Jakosky, B. M., Kieffer, H. H., Malin, M. C., McSween Jr, H., Nealsen, K., Mehall, G., Silverman, S., Ferry, S., Caplinger, M., and Ravine, M. (2004). The thermal emission imaging system (THEMIS) for the Mars 2001 odyssey mission. *Space Sci. Rev.*, 110, 85–130.
- Christensen, P. R., McSween, H. Y., Bandfield, J. L., Ruff, S. W., Rogers, A. D., Hamilton, V. E., Gorelick, N., Wyatt, M. B., Jakosky, B. M., Kieffer, H. H., Malin, M. C., and Moersch, J. E. (2005). Evidence for magmatic evolution and diversity on Mars from infrared observations. *Nature*, 436, 504–509.
- Citron, R. I., Manga, M., and Tan, E. (2018). A hybrid origin of the Martian crustal dichotomy: Degree-1 convection antipodal to a giant impact. *Earth Planet. Sci. Lett.*, 491, 58–66.
- Clayton, R. N. and Mayeda, T. K. (1983). Oxygen isotopes in eucrites, shergottites, nakhlites, and chassignites. *Earth Planet. Sci. Lett.*, 62, 1–6.
- Clayton, R. N. and Mayeda, T. K. (1996). Oxygen isotope studies of achondrites. *Geochim. Cosmochim. Acta*, 60, 1999–2017.
- Collinet, M., Médard, E., Charlier, B., Vander Auwera, J., and Grove, T. L. (2015). Melting of the primitive martian mantle at 0.5–22 GPa and the origin of basalts and alkaline rocks on Mars. *Earth Planet. Sci. Lett.*, 427, 83–94.
- Connerney, J. E. P., Acuña, M. H., Ness, N. F., Kletetschka, G., Mitchell, D. L., Lin, R. P., and Reme, H. (2005). Tectonic implications of Mars crustal magnetism. *Proc. Natl. Acad. Sci. USA*, 102, 14970–14975.
- Cousin, A., Sautter, V., Payré, V., Forni, O., Mangold, N., Gasnault, O., Le Deit, L., Johnson, J., Maurice, S., Salvatore, M., Wiens, R. C., Gasda, P., and Rapin, W. (2017). Classification of igneous rocks analyzed by ChemCam at Gale crater, Mars. *Icarus*, 288, 265–283.
- Dauphas, N. and Pourmand, A. (2011). Hf–W–Th evidence for rapid growth of Mars and its status as a planetary embryo. *Nature*, 473, 489–492.
- Debaille, V., Brandon, A. D., O'Neill, C., Yin, Q.-Z., and Jacobsen, B. (2009). Early martian mantle overturn inferred from isotopic composition of nakhlite meteorites. *Nat. Geosci.*, 2, 548–552.
- Deng, Z., Moynier, F., Villeneuve, J., Jensen, N. K., Liu, D., Cartigny, P., Mikouchi, T., Siebert, J., Agranier, A., Chaussidon, M., and Bizzarro, M. (2020). Early oxidation of the martian crust triggered by impacts. *Sci. Adv.*, 6, article no. eabc4941.
- Ehlmann, B. L. and Edwards, C. S. (2014). Mineralogy of the Martian surface. *Annu. Rev. Earth Planet. Sci.*, 42, 291–315.
- Elkins-Tanton, L. T. (2008). Linked magma ocean solidification and atmospheric growth for Earth and Mars. *Earth Planet. Sci. Lett.*, 271, 181–191.
- Elkins-Tanton, L. T., Zaranek, S. E., Parmentier, E. M., and Hess, P. C. (2005). Early magnetic field and magmatic activity on Mars from magma ocean cumulate overturn. *Earth Planet. Sci. Lett.*, 236, 1–12.
- Eugster, O., Busemann, H., Lorenzetti, S., and Terribilini, D. (2002). Ejection ages from krypton-81-krypton-83 dating and pre-atmospheric sizes of martian meteorites. *Meteorit. Planet. Sci.*, 37, 1345–1360.
- Farley, K. A., Malespin, C., Mahaffy, P., Grotzinger, J. P., Vasconcelos, P. M., Milliken, R. E., Malin, M., Edgett, K. S., Pavlov, A. A., Hurowitz, J. A., Grant, J. A., Miller, H. B., Arvidson, R., Beegle, L., Calef, F., Conrad, P. G., Dietrich, W. E., Eigenbrode, J., Gellert, R., Gupta, S., Hamilton, V., Hassler, D. M., Lewis, K. W., McLennan, S. M., Ming, D., Navarro-Gonzalez, R., Schwenzer, S. P., Steele, A., Stolper, E. M., Sumner, D. Y., Vaniman, D., Vasavada, A., Williford, K., Wimmer-Schweingruber, R. F., Team, the M.S.L.S., Blake, D. F., Bristow, T., DesMarais, D., Edwards, L., Haberle, R., Hoehler, T., Hollingsworth, J., Kahre, M., Keely, L., McKay, C., Wilhelm, M. B., Bleacher, L., Brinckerhoff, W., Choi, D., Dworkin, J. P., Floyd, M., Freissinet, C., Garvin, J., Glavin, D., Harpold, D., Martin, D. K., McAdam, A., Raaen, E., Smith, M. D., Stern, J., Tan, F., Trainer, M., Meyer, M., Posner, A., Voytek, M., Anderson, R. C., Aubrey, A., Behar, A., Blaney, D., Brinza, D., Christensen, L., Crisp, J. A., DeFlores, L., Feldman, J., Feldman, S., Flesch, G., Hurowitz, J., Jun, I., Keymeulen, D., Maki, J., Mischna, M., Morookian, J. M., Parker, T., Pavri, B., Schoppers, M., Sengstacken, A., Simmonds, J. J., Spanovich, N., Juarez, M. d. I. T., Webster, C. R., Yen, A., Archer, P. D., Cucinotta, F., Jones, J. H., Morris, R. V., Niles, P., Rampe, E., Nolan, T., Fisk, M., Radziemski, L., Barraclough, B., Bender, S., Berman, D., Dobrea, E. N., Tokar, R., Williams, R. M. E., Yingst, A., Leshin, L., Cleghorn, T., Huntress, W., Manhes, G., Hudgins, J., Olson, T., Stewart, N., Sarrazin, P., Vicenzi, E., Wilson, S. A.,

- Bullock, M., Ehresmann, B., Peterson, J., Raffin, S., Zeitlin, C., Fedosov, F., Golovin, D., Karpushkina, N., Kozyrev, A., Litvak, M., Malakhov, A., Mitrofanov, I., Mokrousov, M., Nikiforov, S., Prokhorov, V., Sanin, A., Tretyakov, V., Varenikov, A., Vostrukhin, A., Kuzmin, R., Clark, B., Wolff, M., Botta, O., Drake, D., Bean, K., Lemmon, M., Anderson, R. B., Herkenhoff, K., Lee, E. M., Sucharski, R., Hernandez, M. A. d. P., Avalos, J. J. B., Ramos, M., Kim, M.-H., Plante, I., Muller, J.-P., Ewing, R., Boynton, W., Downs, R., Fitzgibbon, M., Harshman, K., Morrison, S., Kortmann, O., Palucis, M., Williams, A., Lugmair, G., Wilson, M. A., Rubin, D., Jakosky, B., Balic-Zunic, T., Frydenvang, J., Jensen, J. K., Kinch, K., Koefoed, A., Madsen, M. B., Stipp, S. L. S., Boyd, N., Campbell, J. L., Perrett, G., Pradler, I., VanBommel, S., Jacob, S., Owen, T., Rowland, S., Savijarvi, H., Boehm, E., Bottcher, S., Burmeister, S., Guo, J., Kohler, J., Garcia, C. M., Mueller-Mellin, R., Bridges, J. C., McConnochie, T., Benna, M., Franz, H., Bower, H., Brunner, A., Blau, H., Boucher, T., Carmosino, M., Atreya, S., Elliott, H., Halleaux, D., Renno, N., Wong, M., Pepin, R., Elliott, B., Spray, J., Thompson, L., Gordon, S., Newsom, H., Ollila, A., Williams, J., Bentz, J., Nealson, K., Popa, R., Kah, L. C., Moersch, J., Tate, C., Day, M., Kocurek, G., Hallet, B., Sletten, R., Francis, R., McCullough, E., Cloutis, E., ten Kate, I. L., Kuzmin, R., Fraeman, A., Scholes, D., Slavney, S., Stein, T., Ward, J., Berger, J., and Moores, J. E. (2014). In situ radiometric and exposure age dating of the Martian surface. *Science*, 343, article no. 1247166.
- Filiberto, J. (2017). Geochemistry of Martian basalts with constraints on magma genesis. *Chem. Geol.*, 466, 1–14.
- Filiberto, J., Gross, J., and McCubbin, F. M. (2016). Constraints on the water, chlorine, and fluorine content of the Martian mantle. *Meteorit. Planet. Sci.*, 51, 2023–2035.
- Flahaut, J., Quantin, C., Clenet, H., Allemand, P., Mustard, J. F., and Thomas, P. (2012). Pristine Noachian crust and key geologic transitions in the lower walls of Valles Marineris: Insights into early igneous processes on Mars. *Icarus*, 221, 420–435.
- Foley, C. N., Economou, T., Clayton, R. N., and Dietrich, W. (2003). Calibration of the Mars Pathfinder alpha proton X-ray spectrometer. *J. Geophys. Res.*, 108(E12), article no. 8095.
- Gellert, R., Berger, J. A., Boyd, N., Brunet, C., Campbell, J. L., Curry, M., Elliott, B., Fulford, P., Grotzinger, J., Hipkin, V., Hurowitz, J. A., King, P. L., Leshin, L. A., Limonadi, D., Pavri, B., Marchand, G., Perrett, G. M., Scodary, A., Simmonds, J. J., Spray, J., Squyres, S. W., Thompson, L., VanBommel, S., Pradler, I., Yen, A. S., and MSL Science Team (2013). Initial MSL APXS Activities and Observations at Gale Crater, Mars. In *The 44th Lunar and Planetary Science Conference Abs. Proceeding, Contribution*, page 1432.
- Ghiorso, M. S., Hirschmann, M. M., Reiners, P. W., and Kress, V. C. (2002). The pMELTS: A revision of MELTS for improved calculation of phase relations and major element partitioning related to partial melting of the mantle to 3 GPa. *Geochem. Geophys. Geosystems*, 3, 1–35.
- Greeley, R., Foing, B. H., McSween, H. Y., Neukum, G., Pinet, P., van Kan, M., Werner, S. C., Williams, D. A., and Zegers, T. E. (2005). Fluid lava flows in Gusev crater, Mars. *J. Geophys. Res. E*, 110, article no. E05008.
- Gross, J., Treiman, A. H., Filiberto, J., and Herd, C. D. K. (2011). Primitive olivine-phyric shergottite NWA 5789: Petrology, mineral chemistry and cooling history imply a magma similar to Yamato 980459. *Meteorit. Planet. Sci.*, 46(1), 116–133.
- Haltigin, T., Lange, C., Mugnuolo, R., Smith, C., Haltigin, T., Lange, C., Mugnolo, R., Smith, C., Amundsen, H., Bousquet, P., Conley, C., Debus, A., Dias, J., Falkner, P., Gass, V., Harri, A.-M., Hauber, E., Ivanov, A., Ivanov, A., Kminek, G., Korablev, O., Koschny, D., Larranaga, J., Marty, B., McLennan, S., Meyer, M., Nilsen, E., Orleanski, P., Orosei, R., Rebuffat, D., Safa, F., Schmitz, N., Siljeström, S., Thomas, N., Vago, J., Vandaele, A.-C., Voirin, T., and Whetsel, C. (2018). iMARS Phase 2. *Astrobiology*, 18, S1–S131.
- Hamilton, V. E., McSween, H. Y., and Hapke, B. (2005). Mineralogy of Martian atmospheric dust inferred from thermal infrared spectra of aerosols. *J. Geophys. Res.*, 110, article no. E12006.
- Hanna, K. L. D., Thomas, I. R., Bowles, N. E., Greenhagen, B. T., Pieters, C. M., Mustard, J. F., Jackson, C. R. M., and Wyatt, M. B. (2012). Laboratory emissivity measurements of the plagioclase solid solution series under varying environmental conditions. *J. Geophys. Res.*, 117. <https://doi.org/10.1029/2012JE004184>.
- Harder, H. and Christensen, U. R. (1996). A one-plume model of martian mantle convection. *Na-*

- ture, 380, 507–509.
- Hartmann, W. K. and Neukum, G. (2001). Cratering chronology and the evolution of Mars. *Space Sci. Rev.*, 96, 165–194.
- Hewins, R. H., Zanda, B., Humayun, M., Nemchin, A., Lorand, J.-P., Pont, S., Deldicque, D., Bellucci, J. J., Beck, P., Leroux, H., Marinova, M., Remusat, L., Göpel, C., Lewin, E., Grange, M., Kennedy, A., and Whitehouse, M. J. (2017). Regolith breccia Northwest Africa 7533: Mineralogy and petrology with implications for early Mars. *Meteorit. Planet. Sci.*, 52, 89–124.
- Humayun, M., Nemchin, A., Zanda, B., Hewins, R. H., Grange, M., Kennedy, A., Lorand, J.-P., Göpel, C., Fieni, C., Pont, S., and Deldicque, D. (2013). Origin and age of the earliest Martian crust from meteorite NWA 7533. *Nature*, 503, 513–516.
- Kamber, B. S., Whitehouse, M. J., Bolhar, R., and Moorbath, S. (2005). Volcanic resurfacing and the early terrestrial crust: Zircon U-Pb and REE constraints from the Isua Greenstone Belt, southern West Greenland. *Earth Planet. Sci. Lett.*, 240, 276–290.
- Karunatillake, S., Wray, J. J., Gasnault, O., McLennan, S. M., Rogers, A. D., Squyres, S. W., Boynton, W. V., Skok, J. R., Ojha, L., and Olsen, N. (2014). Sulfates hydrating bulk soil in the Martian low and middle latitudes. *Geophys. Res. Lett.*, 41, 7987–7996.
- Karunatillake, S., Wray, J. J., Squyres, S. W., Taylor, G. J., Gasnault, O., McLennan, S. M., Boynton, W., El Maarry, M. R., and Dohm, J. M. (2009). Chemically striking regions on Mars and Stealth revisited. *J. Geophys. Res.*, 114, article no. E12001.
- Kiefer, W. S. (2003). Melting in the martian mantle: Shergottite formation and implications for present-day mantle convection on Mars. *Meteorit. Planet. Sci.*, 38, 1815–1832.
- Koeppen, W. C. and Hamilton, V. E. (2008). Global distribution, composition, and abundance of olivine on the surface of Mars from thermal infrared data. *J. Geophys. Res.*, 113, article no. E05001.
- Lapen, T. J., Richter, M., Andreasen, R., Irving, A. J., Satkoski, A. M., Beard, B. L., Nishiizumi, K., Jull, A. J. T., and Caffee, M. W. (2017). Two billion years of magmatism recorded from a single Mars meteorite ejection site. *Sci. Adv.*, 3, article no. e1600922.
- Lapen, T. J., Richter, M., Brandon, A. D., Debaille, V., Beard, B. L., Shafer, J. T., and Peslier, A. H. (2010). A younger age for ALH84001 and its geochemical link to Shergottite sources in Mars. *Science*, 328, 347–351.
- Le Deit, L., Hauber, E., Fueten, F., Pondrelli, M., Rossi, A. P., and Jaumann, R. (2013). Sequence of infilling events in gale crater, Mars: Results from morphology, stratigraphy, and mineralogy. *J. Geophys. Res.*, 118, 2439–2473.
- Lognonné, P., Banerdt, W. B., Giardini, D., Pike, W. T., Christensen, U., Laudet, P., de Raucourt, S., Zweifel, P., Calcutt, S., Bierwirth, M., Hurst, K. J., Ijpelaan, F., Umland, J. W., Llorca-Cejudo, R., Larson, S. A., Garcia, R. E., Kedar, S., Knapmeyer-Endrun, B., Mimoun, D., Mocquet, A., Panning, M. P., Weber, R. C., Sylvestre-Baron, A., Pont, G., Verdier, N., Kerjean, L., Facto, L. J., Gharakanian, V., Feldman, J. E., Hoffman, T. L., Klein, D. B., Klein, K., Onufer, N. P., Paredes-Garcia, J., Petkov, M. P., Willis, J. R., Smrekar, S. E., Drilleau, M., Gabsi, T., Nebut, T., Robert, O., Tillier, S., Moreau, C., Parise, M., Aveni, G., Ben Charef, S., Bennour, Y., Camus, T., Dandonneau, P. A., Desfoux, C., Lecomte, B., Pot, O., Revuz, P., Mance, D., tenPierick, J., Bowles, N. E., Charalambous, C., Delahunty, A. K., Hurley, J., Irshad, R., Liu, H., Mukherjee, A. G., Standley, I. M., Stott, A. E., Temple, J., Warren, T., Eberhardt, M., Kramer, A., Kühne, W., Miettinen, E.-P., Monecke, M., Aicardi, C., André, M., Baroukh, J., Borrien, A., Bouisset, A., Boutte, P., Brethomé, K., Brysbaert, C., Carlier, T., Deleuze, M., DesMarres, J. M., Dilhan, D., Doucet, C., Faye, D., Faye-Refalo, N., Gonzalez, R., Imbert, C., Larigauderie, C., Locatelli, E., Luno, L., Meyer, J.-R., Mialhe, F., Mouret, J. M., Nonon, M., Pahn, Y., Paillet, A., Pasquier, P., Perez, G., Perez, R., Perrin, L., Pouilloux, B., Rosak, A., Savin de Larclause, I., Sicre, J., Sodki, M., Toulemont, N., Vella, B., Yana, C., Alibay, F., Avalos, O. M., Balzer, M. A., Bhandari, P., Blanco, E., Bone, B. D., Bousman, J. C., Bruneau, P., Calef, F. J., Calvet, R. J., D'Agostino, S. A., de los Santos, G., Deen, R. G., Denise, R. W., Ervin, J., Ferraro, N. W., Gengl, H. E., Grinblat, F., Hernandez, D., Hetzel, M., Johnson, M. E., Khachikyan, L., Lin, J. Y., Madzunkov, S. M., Marshall, S. L., Mikkilides, I. G., Miller, E. A., Raff, W., Singer, J. E., Sunday, C. M., Villalvazo, J. E., Wallace, M. C., Banfield, D., Rodriguez-Manfredi, J. A., Russell, C. T., Trebi-Ollennu, A., Maki, J. N., Beucier, E., Böse, M., Bonjour, C., Berenguer, J. L., Ceylan, S., Clinton, J., Conejero, V., Daubar, I., Dehant, V., Delage, P., Euchner, F., Estève, I., Fayon, L., Ferraioli, L., Johnson,

- C. L., Gagnepain-Beyneix, J., Golombek, M., Khan, A., Kawamura, T., Kenda, B., Labrot, P., Murdoch, N., Pardo, C., Perrin, C., Pou, L., Sauron, A., Savoie, D., Stähler, S., Stutzmann, E., Teanby, N. A., Tromp, J., van Driel, M., Wieczorek, M., Widmer-Schmidrig, R., and Wookey, J. (2019). SEIS: insight's seismic experiment for internal structure of Mars. *Space Sci. Rev.*, 215, article no. 12.
- Mangold, N., Schmidt, M. E., Fisk, M. R., Forni, O., McLennan, S. M., Ming, D. W., Sautter, V., Sumner, D., Williams, A. J., Clegg, S. M., Cousin, A., Gasnault, O., Gellert, R., Grotzinger, J. P., and Wiens, R. C. (2017). Classification scheme for sedimentary and igneous rocks in Gale crater, Mars. *Icarus*, 284, 1–17.
- Marchi, S., Bottke, W. F., Elkins-Tanton, L. T., Bierhaus, M., Wuenemann, K., Morbidelli, A., and Kring, D. A. (2014). Widespread mixing and burial of Earth's Hadean crust by asteroid impacts. *Nature*, 511, 578–582.
- Maurice, S., Wiens, R. C., Saccoccio, M., Barraclough, B., Gasnault, O., Forni, O., Mangold, N., Baratoux, D., Bender, S., Berger, G., Bernardin, J., Berthé, M., Bridges, N., Blaney, D., Bouyé, M., Caïs, P., Clark, B., Clegg, S., Cousin, A., Cremers, D., Cros, A., DeFlores, L., Derycke, C., Dingler, B., Dromart, G., Dubois, B., Dupieux, M., Durand, E., d'Uston, L., Fabre, C., Faure, B., Gaboriaud, A., Gharsa, T., Herkenhoff, K., Kan, E., Kirkland, L., Kouach, D., Lacour, J.-L., Langevin, Y., Lasue, J., Le Mouélic, S., Lescure, M., Lewin, E., Limonadi, D., Manhès, G., Mauchien, P., McKay, C., Meslin, P.-Y., Michel, Y., Miller, E., Newsom, H. E., Orttner, G., Paillet, A., Parès, L., Parot, Y., Pérez, R., Pinet, P., Poitrasson, F., Quertier, B., Sallé, B., Sotin, C., Sautter, V., Séran, H., Simmonds, J. J., Sirven, J.-B., Stiglich, R., Striebig, N., Thocaven, J.-J., Toplis, M. J., and Vaniman, D. (2012). The ChemCam instrument suite on the Mars science laboratory (MSL) rover: Science objectives and mast unit description. *Space Sci. Rev.*, 170, 95–166.
- McCoy, T. J., Sims, M., Schmidt, M. E., Edwards, L., Tornabene, L. L., Crumpler, L. S., Cohen, B. A., Soderblom, L. A., Blaney, D. L., Squyres, S. W., Arvidson, R. E., Rice, J. W., Tréguier, E., d'Uston, C., Grant, J. A., McSween, H. Y., Golombek, M. P., Haldemann, A. F. C., and de Souza, P. A. (2008). Structure, stratigraphy, and origin of Husband Hill, Columbia Hills, Gusev Crater, Mars. *J. Geophys. Res.*, 113, article no. E06S03.
- McCubbin, F. M., Boyce, J. W., Novak-Szabo, T., Santos, A., Tartese, R., Muttik, N., Domokos, G., Vazquez, J. A., Keller, L. P., Moser, D. E., Jerolmack, D. J., Shearer, C. K., Steele, A., Elardo, S. M., Rahman, Z., Anand, M., Delhaye, T., and Agee, C. B. (2016a). Geologic history of Martian regolith breccia Northwest Africa 7034: Evidence for hydrothermal activity and lithologic diversity in the Martian crust. *J. Geophys. Res. E*, 121, 2120–2149.
- McCubbin, F. M., Boyce, J. W., Srinivasan, P., Santos, A. R., Elardo, S. M., Filiberto, J., Steele, A., and Shearer, C. K. (2016b). Heterogeneous distribution of H₂O in the Martian interior: Implications for the abundance of H₂O in depleted and enriched mantle sources. *Meteorit. Planet. Sci.*, 51, 2036–2060.
- McCubbin, F. M., Hauri, E. H., Elardo, S. M., Kaaden, K. E. V., Wang, J., and Shearer, C. K. (2012). Hydrous melting of the martian mantle produced both depleted and enriched shergottites. *Geology*, 40, 683–686.
- McSween, H. Y. (2015). Petrology on Mars. *Am. Mineral.*, 100, 2380–2395.
- McSween, H. Y., Grove, T. L., and Wyatt, M. B. (2003). Constraints on the composition and petrogenesis of the Martian crust. *J. Geophys. Res.*, 108(E12), article no. 5135.
- McSween, H. Y., Murchie, S. L., Crisp, J. A., Bridges, N. T., Anderson, R. C., Bell, J. F., Britt, D. T., Brückner, J., Dreibus, G., Economou, T., Ghosh, A., Golombek, M. P., Greenwood, J. P., Johnson, J. R., Moore, H. J., Morris, R. V., Parker, T. J., Rieder, R., Singer, R., and Wänke, H. (1999). Chemical, multispectral, and textural constraints on the composition and origin of rocks at the Mars Pathfinder landing site. *J. Geophys. Res.*, 104, 8679–8715.
- McSween, H. Y., Ruff, S. W., Morris, R. V., Bell, J. F., Herkenhoff, K., Gellert, R., Stockstill, K. R., Tornabene, L. L., Squyres, S. W., Crisp, J. A., Christensen, P. R., McCoy, T. J., Mittlefehldt, D. W., and Schmidt, M. (2006a). Alkaline volcanic rocks from the Columbia Hills, Gusev crater, Mars. *J. Geophys. Res.*, 111, article no. E09S91.
- McSween, H. Y., Taylor, G. J., and Wyatt, M. B. (2009). Elemental composition of the Martian crust. *Science*, 324, 736–739.
- McSween, H. Y., Wyatt, M. B., Gellert, R., Bell, J. F., Morris, R. V., Herkenhoff, K. E., Crumpler, L. S., Milam, K. A., Stockstill, K. R., Tornabene, L. L.,

- Arvidson, R. E., Bartlett, P., Blaney, D., Cabrol, N. A., Christensen, P. R., Clark, B. C., Crisp, J. A., Des Marais, D. J., Economou, T., Farmer, J. D., Far-
rand, W., Ghosh, A., Golombek, M., Gorevan, S., Greeley, R., Hamilton, V. E., Johnson, J. R., Joliff, B. L., Klingelhöfer, G., Knudson, A. T., McLennan, S., Ming, D., Moersch, J. E., Rieder, R., Ruff, S. W., Schröder, C., de Souza, P. A., Squyres, S. W., Wänke, H., Wang, A., Yen, A., and Zipfel, J. (2006b). Characterization and petrologic interpretation of olivine-rich basalts at Gusev Crater, Mars. *J. Geophys. Res.*, 111, article no. E02S10.
- Meslin, P.-Y., Gasnault, O., Forni, O., Schroder, S., Cousin, A., Berger, G., Clegg, S. M., Lasue, J., Maurice, S., Sautter, V., Le Mouelic, S., Wiens, R. C., Fabre, C., Goetz, W., Bish, D., Mangold, N., Ehlmann, B., Lanza, N., Harri, A.-M., Anderson, R., Rampe, E., McConnochie, T. H., Pinet, P., Blaney, D., Leveille, R., Archer, D., Barraclough, B., Bender, S., Blake, D., Blank, J. G., Bridges, N., Clark, B. C., DeFlores, L., DeLapp, D., Dromart, G., Dyar, M. D., Fisk, M., Gondet, B., Grotzinger, J., Herkenhoff, K., Johnson, J., Lacour, J.-L., Langevin, Y., Leshin, L., Lewin, E., Madsen, M. B., Melikechi, N., Mezzacappa, A., Mischna, M. A., Moores, J. E., Newsom, H., Ollila, A., Perez, R., Renno, N., Sirven, J.-B., Tokar, R., de la Torre, M., d'Uston, L., Vaniman, D., Yingst, A., MSL Science Team, Kempainen, O., Minitti, M., Cremers, D., Bell, J. F., Edgar, L., Farmer, J., Godber, A., Wadhwa, M., Wellington, D., McEwan, I., Newman, C., Richardson, M., Charpentier, A., Peret, L., King, P., Weigle, G., Schmidt, M., Li, S., Milliken, R., Robertson, K., Sun, V., Baker, M., Edwards, C., Farley, K., Griffes, J., Miller, H., Newcombe, M., Pilorget, C., Rice, M., Siebach, K., Stack, K., Stolper, E., Brunet, C., Hipkin, V., Marchand, G., Sanchez, P. S., Favot, L., Cody, G., Steele, A., Fluckiger, L., Lees, D., Nefian, A., Martin, M., Gailhanou, M., Westall, F., Israel, G., Agard, C., Baroukh, J., Donny, C., Gaboriaud, A., Guillemot, P., Lafaille, V., Lorigny, E., Paillet, A., Perez, R., Saccoccio, M., Yana, C., Armiens-Aparicio, C., Rodriguez, J. C., Blazquez, I. C., Gomez, F. G., Gomez-Elvira, J., Hettrich, S., Malvitte, A. L., Jimenez, M. M., Martinez-Frias, J., Martin-Soler, J., Martin-Torres, F. J., Jurado, A. M., Mora-Sotomayor, L., Caro, G. M., Lopez, S. N., Peinado-Gonzalez, V., Pla-Garcia, J., Manfredi, J. A. R., Romeral-Planello, J. J., Fuentes, S. A. S., Martinez, E. S., Redondo, J. T., Urqui-O'Callaghan, R., Mier, M.-P. Z., Chipera, S., Mauchien, P., Manning, H., Fairen, A., Hayes, A., Joseph, J., Squyres, S., Sullivan, R., Thomas, P., Dupont, A., Lundberg, A., DeMarines, J., Grinspoon, D., Reitz, G., Prats, B., Atlaskin, E., Genzer, M., Haukka, H., Kahanpaa, H., Kauhanen, J., Kempainen, O., Paton, M., Polkko, J., Schmidt, W., Sili, T., Wray, J., Wilhelm, M. B., Poitrasson, F., Patel, K., Gorevan, S., Indyk, S., Paulsen, G., Gupta, S., Schieber, J., Geffroy, C., Baratoux, D., Cros, A., Lee, Q.-M., Pallier, E., Parot, Y., Toplis, M., Brunner, W., Heydari, E., Achilles, C., Oehler, D., Sutter, B., Cabane, M., Coscia, D., Israel, G., Szopa, C., Robert, F., Nachon, M., Buch, A., Stalport, F., Coll, P., Francois, P., Raulin, F., Teinturier, S., Cameron, J., Dingler, R., Jackson, R. S., Johnstone, S., Little, C., Nelson, T., Williams, R. B., Jones, A., Kirkland, L., Treiman, A., Baker, B., Cantor, B., Caplinger, M., Davis, S., Duston, B., Edgett, K., Fay, D., Hardgrove, C., Harker, D., Herrera, P., Jensen, E., Kennedy, M. R., Krezoski, G., Krysak, D., Lipkaman, L., Malin, M., McCartney, E., McNair, S., Nixon, B., Posiolova, L., Ravine, M., Salamon, A., Saper, L., Stoiber, K., Supulver, K., Van Beek, J., Van Beek, T., Zimdar, R., French, K. L., Iagnemma, K., Miller, K., Summons, R., Goesmann, F., Hviid, S., Johnson, M., Lefavor, M., Lyness, E., Breves, E., Fassett, C., Bristow, T., DesMarais, D., Edwards, L., Haberle, R., Hoehler, T., Hollingsworth, J., Kahre, M., Keely, L., McKay, C., Wilhelm, M. B., Bleacher, L., Brinckerhoff, W., Choi, D., Conrad, P., Dworkin, J. P., Eigenbrode, J., Floyd, M., Freissinet, C., Garvin, J., Glavin, D., Harpold, D., Jones, A., Mahaffy, P., Martin, D. K., McAdam, A., Pavlov, A., Raaen, E., Smith, M. D., Stern, J., Tan, F., Trainer, M., Meyer, M., Posner, A., Voytek, M., Anderson, R. C., Aubrey, A., Beege, L. W., Behar, A., Brinza, D., Calef, F., Christensen, L., Crisp, J. A., Feldman, J., Feldman, S., Flesch, G., Hurowitz, J., Jun, I., Keymeulen, D., Maki, J., Morookian, J. M., Parker, T., Pavri, B., Schoppers, M., Sengstacken, A., Simmonds, J. J., Spanovich, N., Vasavada, A. R., Webster, C. R., Yen, A., Cucinotta, F., Jones, J. H., Ming, D., Morris, R. V., Niles, P., Nolan, T., Radziemski, L., Berman, D., Dobra, E. N., Williams, R. M. E., Lewis, K., Cleghorn, T., Huntress, W., Manhes, G., Hudgins, J., Olson, T., Stewart, N., Sarrazin, P., Grant, J., Vicenzi, E., Wilson, S. A., Bullock, M., Ehresmann, B., Hamilton, V., Hassler, D., Peterson, J., Rafkin,

- S., Zeitlin, C., Fedosov, F., Golovin, D., Karpushkina, N., Kozyrev, A., Litvak, M., Malakhov, A., Mitrofanov, I., Mokrousov, M., Nikiforov, S., Prokhorov, V., Sanin, A., Tret'yakov, V., Varenikov, A., Vostrukhin, A., Kuzmin, R., Wolff, M., McLennan, S., Botta, O., Drake, D., Bean, K., Lemmon, M., Schwenzer, S. P., Lee, E. M., Sucharski, R., Hernandez, M. A. d. P., Avalos, J. J. B., Ramos, M., Kim, M.-H., Malespin, C., Plante, I., Muller, J.-P., Navarro-Gonzalez, R., Ewing, R., Boynton, W., Downs, R., Fitzgibbon, M., Harshman, K., Morrison, S., Dietrich, W., Kortmann, O., Palucis, M., Sumner, D. Y., Williams, A., Lugmair, G., Wilson, M. A., Rubin, D., Jakosky, B., Balic-Zunic, T., Frydenvang, J., Jensen, J. K., Kinch, K., Koefoed, A., Stipp, S. L. S., Boyd, N., Campbell, J. L., Gellert, R., Perrett, G., Pradler, I., VanBommel, S., Jacob, S., Owen, T., Rowland, S., Atlaskin, E., Savijarvi, H., Boehm, E., Bottcher, S., Burmeister, S., Guo, J., Kohler, J., Garcia, C. M., Mueller-Mellin, R., Wimmer-Schweingruber, R., Bridges, J. C., Benna, M., Franz, H., Bower, H., Brunner, A., Blau, H., Boucher, T., Carmosino, M., Atreya, S., Elliott, H., Halleaux, D., Renno, N., Wong, M., Pepin, R., Elliott, B., Spray, J., Thompson, L., Gordon, S., Williams, J., Vasconcelos, P., Bentz, J., Nealson, K., Popa, R., Kah, L. C., Moersch, J., Tate, C., Day, M., Kocurek, G., Hallet, B., Sletten, R., Francis, R., McCullough, E., Cloutis, E., ten Kate, I. L., Kuzmin, R., Arvidson, R., Fraeman, A., Scholes, D., Slavney, S., Stein, T., Ward, J., and Berger, J. (2013). Soil diversity and hydration as observed by ChemCam at Gale crater, Mars. *Science*, 341, article no. 1238670.
- Ming, D. W., Gellert, R., Morris, R. V., Arvidson, R. E., Brückner, J., Clark, B. C., Cohen, B. A., d'Uston, C., Economou, T., Fleischer, I., Klingelhöfer, G., McCoy, T. J., Mittlefehldt, D. W., Schmidt, M. E., Schröder, C., Squyres, S. W., Tréguier, E., Yen, A. S., and Zipfel, J. (2008). Geochemical properties of rocks and soils in Gusev crater, Mars: Results of the alpha particle X-ray spectrometer from Cumberland Ridge to home plate. *J. Geophys. Res.*, 113(E12), article no. E12S39.
- Ming, D. W., Mittlefehldt, D. W., Morris, R. V., Golden, D. C., Gellert, R., Yen, A., Clark, B. C., Squyres, S. W., Farrand, W. H., Ruff, S. W., Arvidson, R. E., Klingelhöfer, G., McSween, H. Y., Rodionov, D. S., Schroder, C., de Souza Jr., P. A., and Wang, A. (2006). Geochemical and mineralogical indicators of aqueous processes in the Columbia Hills of Gusev crater, Mars. *J. Geophys. Res.*, 111, article no. E072S12.
- Mittlefehldt, D. W. (1994). ALH84001, a cumulate orthopyroxenite member of the martian meteorite clan. *Meteoritics*, 29, 214–221.
- Murchie, S., Arvidson, R., Bedini, P., Beisser, K., Bibring, J.-P., Bishop, J., Boldt, J., Cavender, P., Choo, T., Clancy, R. T., Darlington, E. H., Des Marais, D., Espiritu, R., Fort, D., Green, R., Guinness, E., Hayes, J., Hash, C., Heffernan, K., Hemmler, J., Heyler, G., Humm, D., Hutcheson, J., Izenberg, N., Lee, R., Lees, J., Lohr, D., Malaret, E., Martin, T., McGovern, J. A., McGuire, P., Morris, R., Mustard, J., Pelkey, S., Rhodes, E., Robinson, M., Roush, T., Schaefer, E., Seagrave, G., Seelos, F., Silverglate, P., Slavney, S., Smith, M., Shyong, W.-J., Strohhahn, K., Taylor, H., Thompson, P., Tossman, B., Wirzbürger, M., and Wolff, M. (2007). Compact reconnaissance imaging spectrometer for Mars (CRISM) on Mars reconnaissance orbiter (MRO). *J. Geophys. Res.*, 112, article no. E05S03.
- Mustard, J. F., Poulet, E., Gendrin, A., Bibring, J.-P., Langevin, Y., Gondet, B., Mangold, N., Bellucci, G., and Altieri, F. (2005). Olivine and pyroxene diversity in the crust of Mars. *Science*, 307, 1594–1597.
- Nekvasil, H., Filiberto, J., McCubbin, F. M., and Lindsley, D. H. (2007). Alkalic parental magmas for chassignites? *Meteorit. Planet. Sci.*, 42, 979–992.
- Nekvasil, H., Simon, A., and Lindsley, D. H. (2000). Crystal fractionation and the evolution of intraplate hy-normative igneous suites: Insights from their Feldspars. *J. Petrol.*, 41, 1743–1757.
- Nemchin, A., Timms, N., Pidgeon, R., Geisler, T., Reddy, S., and Meyer, C. (2009). Timing of crystallization of the lunar magma ocean constrained by the oldest zircon. *Nat. Geosci.*, 2, 133–136.
- Nyquist, L. E., Bogard, D. D., Shih, C.-Y., Greshake, A., Stöffler, D., and Eugster, O. (2001). Ages and Geologic Histories of Martian Meteorites. In *Chronology and Evolution of Mars, Space Sciences Series of ISSI*, pages 105–164. Springer, Dordrecht.
- Nyquist, L. E., Shih, C.-Y., McCubbin, F. M., Santos, A. R., Shearer, C. K., Peng, Z. X., Burger, P. V., and Agee, C. B. (2016). Rb–Sr and Sm–Nd isotopic and REE studies of igneous components in the bulk matrix domain of Martian breccia Northwest Africa 7034. *Meteorit. Planet. Sci.*, 51, 483–498.
- Ody, A., Poulet, E., Bibring, J.-P., Loizeau, D., Carter, J., Gondet, B., and Langevin, Y. (2013). Global investigation of olivine on Mars: Insights into crust and

- mantle composition. *J. Geophys. Res.: Planets*, 118, 234–262.
- Ostwald, A. M., Udry, A., Gazel, E., and Payre, V. (2020). Assimilation-fractional crystallization on Mars as a formation process for Felsic rocks. In *51st Lunar and Planetary Science Conference*.
- Palme, H. and O'Neill, H. S. C. (2014). Cosmochemical estimates of mantle composition. In Holland, H. D. and Turekian, K. K., editors, *Treatise on Geochemistry*, pages 1–39. Elsevier, Oxford, 2nd edition.
- Payré, V., Fabre, C., Cousin, A., Sautter, V., Wiens, R. C., Forni, O., Gasnault, O., Mangold, N., Meslin, P.-Y., Lasue, J., Ollila, A., Rapin, W., Maurice, S., Nachon, M., Le Deit, L., Lanza, N., and Clegg, S. (2017). Alkali trace elements in Gale crater, Mars, with ChemCam: Calibration update and geological implications. *J. Geophys. Res.*, 122, 650–679.
- Payré, V., Siebach, K. L., Dasgupta, R., Udry, A., Rampe, E. B., and Morrison, S. M. (2020). Constraining ancient magmatic evolution on Mars using crystal chemistry of detrital igneous minerals in the sedimentary Bradbury Group, Gale crater, Mars. *J. Geophys. Res.*, 125, article no. e2020JE006467.
- Poulet, F., Mangold, N., Platevoet, B., Bardintzeff, J.-M., Sautter, V., Mustard, J. F., Bibring, J.-P., Pinet, P., Langevin, Y., Gondet, B., and Aléon-Toppani, A. (2009). Quantitative compositional analysis of martian mafic regions using the MEx/OMEGA reflectance data: 2 Petrological implications. *Icarus*, 201, 84–101.
- Rice, M. S., Gupta, S., Treiman, A. H., Stack, K. M., Calef, F., Edgar, L. A., Grotzinger, J., Lanza, N., Le Deit, L., Lasue, J., Siebach, K. L., Vasavada, A., Wiens, R. C., and Williams, J. (2017). Geologic overview of the Mars science laboratory Rover mission at the Kimberley, Gale crater, Mars: Overview of MSL at the Kimberley. *J. Geophys. Res.*, 122, 2–20.
- Riu, L., Poulet, F., Bibring, J.-P., and Gondet, B. (2019). The M3 project: 2 — Global distributions of mafic mineral abundances on Mars. *Icarus*, 322, 31–53.
- Rogers, A. D. and Nazarian, A. H. (2013). Evidence for Noachian flood volcanism in Noachis Terra, Mars, and the possible role of Hellas impact basin tectonics. *J. Geophys. Res.: Planets*, 118(5), 1094–1113.
- Rogers, A. D. and Nekvasil, H. (2015). Feldspathic rocks on Mars: Compositional constraints from infrared spectroscopy and possible formation mechanisms: Feldspathic rocks on Mars: constraints. *Geophys. Res. Lett.*, 42, 2619–2626.
- Ruff, S. W., Christensen, P. R., Blaney, D. L., Farrand, W. H., Johnson, J. R., Michalski, J. R., Moersch, J. E., Wright, S. P., and Squyres, S. W. (2006). The rocks of Gusev crater as viewed by the Mini-TES instrument. *J. Geophys. Res.*, 111. <https://doi.org/10.1029/2006JE002747>.
- Santos, A. R., Agee, C. B., McCubbin, F. M., Shearer, C. K., Burger, P. V., Tartèse, R., and Anand, M. (2015). Petrology of igneous clasts in Northwest Africa 7034: Implications for the petrologic diversity of the martian crust. *Geochim. Cosmochim. Acta*, 157, 56–85.
- Sautter, V., Fabre, C., Forni, O., Toplis, M. J., Cousin, A., Ollila, A. M., Meslin, P. Y., Maurice, S., Wiens, R. C., Baratoux, D., Mangold, N., Le Mouélic, S., Gasnault, O., Berger, G., Lasue, J., Anderson, R. A., Lewin, E., Schmidt, M., Dyar, D., Ehlmann, B. L., Bridges, J., Clark, B., and Pinet, P. (2014). Igneous mineralogy at Bradbury rise: The first ChemCam campaign at Gale crater. *J. Geophys. Res.*, 119, 30–46.
- Sautter, V., Toplis, M. J., Beck, P., Mangold, N., Wiens, R., Pinet, P., Cousin, A., Maurice, S., LeDeit, L., Hewins, R., Gasnault, O., Quantin, C., Forni, O., Newsom, H., Meslin, P.-Y., Wray, J., Bridges, N., Payré, V., Rapin, W., and Le Mouélic, S. (2016). Magmatic complexity on early Mars as seen through a combination of orbital, in-situ and meteorite data. *Lithos*, 254–255, 36–52.
- Sautter, V., Toplis, M. J., Wiens, R. C., Cousin, A., Fabre, C., Gasnault, O., Maurice, S., Forni, O., Lasue, J., Ollila, A., Bridges, J. C., Mangold, N., Le Mouélic, S., Fisk, M., Meslin, P.-Y., Beck, P., Pinet, P., Le Deit, L., Rapin, W., Stolper, E. M., Newsom, H., Dyar, D., Lanza, N., Vaniman, D., Clegg, S., and Wray, J. J. (2015). In situ evidence for continental crust on early Mars. *Nat. Geosci.*, 8, 605–609.
- Schmidt, M. E., Campbell, J. L., Gellert, R., Perret, G. M., Treimann, A. H., Blaney, D. L., Ollila, A., Calef, F. J., Edgar, L., Elliot, B. E., Grotzinger, J., Hurowitz, J., King, P. L., Minetti, M. E., Sautter, V., Stack, K., Berger, J. A., Bridges, J. C., Ehlman, B. L., Forni, O., Leshin, L. A., Lewis, K. W., McLennan, S. M., Ming, D. W., Newsom, H., Squyres, S. W., Stolper, E. M., Thopson, L., VanBommel, S., Wiens, R., and MSL Science Team (2014). Geochemical diversity in the first rocks examined by Curiosity

- rover in Gale Crater: evidence for and significance of an alkali and volatile-rich igneous source. *J. Geophys. Res.: Planets*, 119, 64–81.
- Schmidt, M. E., Izawa, M. R. M., Thomas, A. P., Thompson, L., and Gellert, R. (2016). Diverse Igneous Protolith Contributions to Sediments in Gale Crater: Variable Metasomatism of the Mars Mantle. *Meteorit. Planet. Sci.*, 51(A555), article no. 6074.
- Schmidt, M. E. and McCoy, T. J. (2010). The evolution of a heterogeneous Martian mantle: Clues from K, P, Ti, Cr, and Ni variations in Gusev basalts and shergottite meteorites. *Earth Planet. Sci. Lett.*, 296, 67–77.
- Squyres, S. W., Aharonson, O., Clark, B. C., Cohen, B. A., Crumpler, L., de Souza, P. A., Farrand, W. H., Gellert, R., Grant, J., Grotzinger, J. P., Haldemann, A. F. C., Johnson, J. R., Klingelhofer, G., Lewis, K. W., Li, R., McCoy, T., McEwen, A. S., McSween, H. Y., Ming, D. W., Moore, J. M., Morris, R. V., Parker, T. J., Rice, J. W., Ruff, S., Schmidt, M., Schroder, C., Soderblom, L., and Yen, A. (2007). Pyroclastic activity at home plate in Gusev crater, Mars. *Science*, 316, 738–742.
- Squyres, S. W., Arvidson, R. E., Blaney, D. L., Clark, B. C., Crumpler, L., Farrand, W. H., Gorevan, S., Herkenhoff, K. E., Hurowitz, J., Kusack, A., McSween, H. Y., Ming, D. W., Morris, R. V., Ruff, S. W., Wang, A., and Yen, A. (2006). Rocks of the Columbia Hills: Rocks of the Columbia Hills. *J. Geophys. Res.*, 111, article no. E02S11.
- Stolper, E. M., Baker, M. B., Newcombe, M. E., Schmidt, M. E., Treiman, A. H., Cousin, A., Dyar, M. D., Fisk, M. R., Gellert, R., King, P. L., Leshin, L., Maurice, S., McLennan, S. M., Minitti, M. E., Perrett, G., Rowland, S., Sautter, V., Wiens, R. C., MSL Science Team, Kempainen, O., Bridges, N., Johnson, J. R., Cremers, D., Bell, J. F., Edgar, L., Farmer, J., Godber, A., Wadhwa, M., Wellington, D., McEwan, I., Newman, C., Richardson, M., Charpentier, A., Peret, L., Blank, J., Weigle, G., Li, S., Milliken, R., Robertson, K., Sun, V., Edwards, C., Ehlmann, B., Farley, K., Griffes, J., Grotzinger, J., Miller, H., Pilorget, C., Rice, M., Siebach, K., Stack, K., Brunet, C., Hipkin, V., Leveille, R., Marchand, G., Sanchez, P. S., Favot, L., Cody, G., Steele, A., Fluckiger, L., Lees, D., Nefian, A., Martin, M., Gailhanou, M., Westall, F., Israel, G., Agard, C., Baroukh, J., Donny, C., Gaboriaud, A., Guillemot, P., Lafaille, V., Lorigny, E., Paillet, A., Perez, R., Saccoccio, M., Yana, C., Armiens-Aparicio, C., Rodriguez, J. C., Blazquez, I. C., Gomez, F. G., Gomez-Elvira, J., Hettrich, S., Malvitte, A. L., Jimenez, M. M., Martinez-Frias, J., Martin-Soler, J., Martin-Torres, F. J., Jurado, A. M., Mora-Sotomayor, L., Caro, G. M., Lopez, S. N., Peinado-Gonzalez, V., Pla-Garcia, J., Manfredi, J. A. R., Romeral-Planello, J. J., Fuentes, S. A. S., Martinez, E. S., Redondo, J. T., Urqui-O'Callaghan, R., Mier, M.-P. Z., Chipera, S., Lacour, J.-L., Mauchien, P., Sirven, J.-B., Manning, H., Fairen, A., Hayes, A., Joseph, J., Squyres, S., Sullivan, R., Thomas, P., Dupont, A., Lundberg, A., Melikechi, N., Mez-zacappa, A., DeMarines, J., Grinspoon, D., Reitz, G., Prats, B., Atlaskin, E., Genzer, M., Harri, A.-M., Haukka, H., Kahanpaa, H., Kauhanen, J., Kempainen, O., Paton, M., Polkko, J., Schmidt, W., Siili, T., Fabre, C., Wray, J., Wilhelm, M. B., Poitrasson, F., Patel, K., Gorevan, S., Indyk, S., Paulsen, G., Gupta, S., Bish, D., Schieber, J., Gondet, B., Langevin, Y., Gef-froy, C., Baratoux, D., Berger, G., Cros, A., d'Uston, C., Forni, O., Gasnault, O., Lasue, J., Lee, Q.-M., Meslin, P.-Y., Pallier, E., Parot, Y., Pinet, P., Schroder, S., Toplis, M., Lewin, E., Brunner, W., Heydari, E., Achilles, C., Oehler, D., Sutter, B., Cabane, M., Coscia, D., Israel, G., Szopa, C., Teinturier, S., Dromart, G., Robert, F., Le Mouelic, S., Mangold, N., Nachon, M., Buch, A., Stalport, F., Coll, P., Francois, P., Raulin, F., Cameron, J., Clegg, S., DeLapp, D., Dingler, R., Jackson, R. S., Johnstone, S., Lanza, N., Little, C., Nelson, T., Williams, R. B., Kirkland, L., Baker, B., Cantor, B., Caplinger, M., Davis, S., Duston, B., Edgett, K., Fay, D., Hardgrove, C., Harker, D., Herrera, P., Jensen, E., Kennedy, M. R., Krezoski, G., Krysak, D., Lipkaman, L., Malin, M., McCartney, E., McNair, S., Nixon, B., Posiolova, L., Ravine, M., Salamon, A., Saper, L., Stoiber, K., Supulver, K., Van Beek, J., Van Beek, T., Zimdar, R., French, K. L., Iagnemma, K., Miller, K., Summons, R., Goesmann, F., Goetz, W., Hviid, S., Johnson, M., Lefavor, M., Lyness, E., Breves, E., Fassett, C., Blake, D. F., Bristow, T., DesMarais, D., Edwards, L., Haberle, R., Hoehler, T., Hollingsworth, J., Kahre, M., Keely, L., McKay, C., Wilhelm, M. B., Bleacher, L., Brinckerhoff, W., Choi, D., Conrad, P., Dworkin, J. P., Eigenbrode, J., Floyd, M., Freissinet, C., Garvin, J., Glavin, D., Harpold, D., Mahaffy, P., Martin, D. K., McAdam, A., Pavlov, A., Raaen, E., Smith, M. D., Stern, J., Tan, F., Trainer, M., Meyer, M., Posner, A., Voytek, M., Anderson, R. C., Aubrey, A., Beegle, L. W., Behar, A., Blaney,

- D., Brinza, D., Calef, F., Christensen, L., Crisp, J., DeFlores, L., Ehlmann, B., Feldman, J., Feldman, S., Flesch, G., Hurowitz, J., Jun, I., Keymeulen, D., Maki, J., Mischna, M., Morookian, J. M., Parker, T., Pavri, B., Schoppers, M., Sengstacken, A., Simmonds, J. J., Spanovich, N., Juarez, M. d. I. T., Vasavada, A., Webster, C. R., Yen, A., Archer, P. D., Cucinotta, F., Jones, J. H., Ming, D., Morris, R. V., Niles, P., Rampe, E., Nolan, T., Radziemski, L., Barraclough, B., Bender, S., Berman, D., Dobrea, E. N., Tokar, R., Vaniman, D., Williams, R. M. E., Yingst, A., Lewis, K., Cleghorn, T., Huntress, W., Manhes, G., Hudgins, J., Olson, T., Stewart, N., Sarrazin, P., Grant, J., Vicenzi, E., Wilson, S. A., Bullock, M., Ehresmann, B., Hamilton, V., Hassler, D., Peterson, J., Rafkin, S., Zeitlin, C., Fedosov, F., Golovin, D., Karpushkina, N., Kozyrev, A., Litvak, M., Malakhov, A., Mitrofanov, I., Mokrousov, M., Nikiforov, S., Prokhorov, V., Sanin, A., Tretyakov, V., Varenikov, A., Vostrukhin, A., Kuzmin, R., Clark, B., Wolff, M., Botta, O., Drake, D., Bean, K., Lemmon, M., Schwenzer, S. P., Anderson, R. B., Herkenhoff, K., Lee, E. M., Sucharski, R., Hernandez, M. A. d. P., Avalos, J. J. B., Ramos, M., Jones, A., Kim, M.-H., Malespin, C., Plante, I., Muller, J.-P., Navarro-Gonzalez, R., Ewing, R., Boynton, W., Downs, R., Fitzgibbon, M., Harshman, K., Morrison, S., Dietrich, W., Kortmann, O., Palucis, M., Sumner, D. Y., Williams, A., Lugmair, G., Wilson, M. A., Rubin, D., Jakosky, B., Balic-Zunic, T., Frydenvang, J., Jensen, J. K., Kinch, K., Koefoed, A., Madsen, M. B., Stipp, S. L. S., Boyd, N., Campbell, J. L., Pradler, I., VanBommel, S., Jacob, S., Owen, T., Atlaskin, E., Savijarvi, H., Boehm, E., Bottcher, S., Burmeister, S., Guo, J., Kohler, J., Garcia, C. M., Mueller-Mellin, R., Wimmer-Schweingruber, R., Bridges, J. C., McConnochie, T., Benna, M., Franz, H., Bower, H., Brunner, A., Blau, H., Boucher, T., Carmosino, M., Atreya, S., Elliott, H., Halleaux, D., Renno, N., Wong, M., Pepin, R., Elliott, B., Spray, J., Thompson, L., Gordon, S., Newsom, H., Ollila, A., Williams, J., Vasconcelos, P., Bentz, J., Nealson, K., Popa, R., Kah, L. C., Moersch, J., Tate, C., Day, M., Kocurek, G., Hallet, B., Sletten, R., Francis, R., McCullough, E., Cloutis, E., ten Kate, I. L., Kuzmin, R., Arvidson, R., Fraeman, A., Scholes, D., Slavney, S., Stein, T., Ward, J., Berger, J., and Moores, J. E. (2013). The Petrochemistry of Jake_M: A Martian Mugearite. *Science*, 341, article no. 1239463.
- Tanaka, K. L., Robbins, S. J., Fortezzo, C. M., Skinner, J. A., and Hare, T. M. (2014). The digital global geologic map of Mars: Chronostratigraphic ages, topographic and crater morphologic characteristics, and updated resurfacing history. *Planet. Space Sci.*, 95, 11–24.
- Tartèse, R., Anand, M., McCubbin, F. M., Santos, A. R., and Delhaye, T. (2014). Zircons in Northwest Africa 7034: Records of crustal evolution on Mars. In *The 45th Lunar and Planetary Science Conference Abstracts Proceedings, Contribution*, page 2020.
- Taylor, G. J., Martel, L. M. V., Karunatillake, S., Gasnault, O., and Boyton, W. V. (2010). Mapping Mars geochemically. *Geology*, 38, 183–186.
- Taylor, S. R. and McLennan, S. (2009). *Planetary Crusts: Their Composition, Origin and Evolution*. Cambridge University Press, Cambridge.
- Thiriet, M., Michaut, C., Breuer, D., and Plesa, A.-C. (2018). Hemispheric dichotomy in Lithosphere thickness on Mars caused by differences in crustal structure and composition. *J. Geophys. Res.*, 123, 823–848.
- Thomas-Keprta, K. L., Clemett, S. J., McKay, D. S., Gibson, E. K., and Wentworth, S. J. (2009). Origins of magnetite nanocrystals in Martian meteorite ALH 84001. *Geochim. Cosmochim. Acta*, 73, 6631–6677.
- Treiman, A. H. and Medard, E. (2016). Mantle metasomatism in Mars: Potassic basaltic sandstone in gale crater derived from partial melt of phlogopite-peridotite. In *GSA Annual Meeting in Denver, Colorado, USA, 2016*. article no. 285851.
- Udry, A., Balta, J. B., and McSween, H. Y. (2014). Exploring fractionation models for Martian magmas: Fractionation of Martian primary magmas. *J. Geophys. Res.*, 119, 1–18.
- Udry, A., Gazel, E., and McSween, H. Y. (2018). Formation of evolved rocks at Gale crater by crystal fractionation and implications for Mars crustal composition. *J. Geophys. Res.*, 123, 1525–1540.
- Udry, A., Howarth, G. H., Herd, C. D. K., Day, J. M. D., Lapen, T. J., and Filiberto, J. (2020). What martian meteorites reveal about the interior and surface of Mars. *J. Geophys. Res.*, 125, article no. e2020JE006523.
- Valley, J. W., Cavosie, A. J., Ushikubo, T., Reinhard, D. A., Lawrence, D. F., Larson, D. J., Clifton, P. H., Kelly, T. F., Wilde, S. A., Moser, D. E., and Spicuzza, M. J. (2014). Hadean age for a post-magma-ocean

- zircon confirmed by atom-probe tomography. *Nat. Geosci.*, 7, 219–223.
- Valley, J. W., King, E. M., Peck, W. H., Graham, C. M., and Wilde, S. A. (2001). The Cool Early Earth: Oxygen Isotope Evidence for Continental Crust and Oceans on Earth at 4.4 Ga. In *AGU Spring Meet. Abstr. V51A-01*.
- Wanke, H. and Dreibus, G. (1988). Chemical composition and accretion history of terrestrial planets. *Philos. Trans. Royal Soc. A*, 325, 545–557.
- Wieczorek, M. A. and Zuber, M. T. (2004). Thickness of the Martian crust: Improved constraints from geoid-to-topography ratios. *J. Geophys. Res.*, 109, article no. E01009.
- Wiens, R. C., Maurice, S., Barraclough, B., Saccoccio, M., Barkley, W. C., Bell, J. F., Bender, S., Bernardin, J., Blaney, D., Blank, J., Bouyé, M., Bridges, N., Bultman, N., Caïs, P., Clanton, R. C., Clark, B., Clegg, S., Cousin, A., Cremers, D., Cros, A., DeFlores, L., DeLapp, D., Dingler, R., D'Uston, C., Darby Dyar, M., Elliott, T., Enemark, D., Fabre, C., Flores, M., Forni, O., Gasnault, O., Hale, T., Hays, C., Herkenhoff, K., Kan, E., Kirkland, L., Kouach, D., Landis, D., Langevin, Y., Lanza, N., LaRocca, F., Lasue, J., Latino, J., Limonadi, D., Lindensmith, C., Little, C., Mangold, N., Manhes, G., Mauchien, P., McKay, C., Miller, E., Mooney, J., Morris, R. V., Morrison, L., Nelson, T., Newsom, H., Ollila, A., Ott, M., Pares, L., Perez, R., Poitrasson, F., Provost, C., Reiter, J. W., Roberts, T., Romero, F., Sautter, V., Salazar, S., Simmonds, J. J., Stiglich, R., Storms, S., Striebig, N., Thocaven, J.-J., Trujillo, T., Ulibarri, M., Vaniman, D., Warner, N., Waterbury, R., Whitaker, R., Witt, J., and Wong-Swanson, B. (2012). The Chem-Cam instrument suite on the Mars science laboratory (MSL) Rover: Body unit and combined system tests. *Space Sci. Rev.*, 170, 167–227.
- Wilde, S. A., Valley, J. W., Peck, W. H., and Graham, C. M. (2001). Evidence from detrital zircons for the existence of continental crust and oceans on the Earth 4.4 Gyr ago. *Nature*, 409, 175–178.
- Winter, L. S., Tosdal, R. M., Mortensen, J. K., and Franklin, J. M. (2010). Volcanic stratigraphy and geochronology of the cretaceous lancones basin, Northwestern Peru: Position and timing of giant VMS deposits. *Econ. Geol.*, 105, 713–742.
- Wittmann, A., Korotev, R. L., Jolliff, B. L., Irving, A. J., Moser, D. E., Barker, I., and Rumble, D. (2015). Petrography and composition of Martian regolith breccia meteorite Northwest Africa 7475. *Meteorit. Planet. Sci.*, 50, 326–352.
- Wray, J. J., Hansen, S. T., Dufek, J., Swayze, G. A., Murchie, S. L., Seelos, F. P., Skok, J. R., Irwin, R. P., and Ghiorso, M. S. (2013). Prolonged magmatic activity on Mars inferred from the detection of felsic rocks. *Nat. Geosci.*, 6, 1013–1017.
- Wray, J. J., Milliken, R. E., Dundas, C. M., Swayze, G. A., Andrews-Hanna, J. C., Baldridge, A. M., Chojnacki, M., Bishop, J. L., Ehlmann, B. L., Murchie, S. L., Clark, R. N., Seelos, F. P., Tornabene, L. L., and Squyres, S. W. (2011). Columbus crater and other possible groundwater-fed paleolakes of Terra Sirenum, Mars. *J. Geophys. Res.*, 116, article no. E01001.
- Wyatt, M. B., McSween, H. Y., Tanaka, K. L., and Head, J. W. (2004). Global geologic context for rock types and surface alteration on Mars. *Geology*, 32, 645–648.
- Xiao, L., Huang, J., Christensen, P. R., Greeley, R., Williams, D. A., Zhao, J., and He, Q. (2012). Ancient volcanism and its implication for thermal evolution of Mars. *Earth Planet. Sci. Lett.*, 323–324, 9–18.



Perspectives on alkaline magmas / *Perspectives sur les magmas alcalins*

Caldera collapse and tectonics along the Main Ethiopian Rift: reviewing possible relationships

Daniele Maestrelli^{*, a}, Giacomo Corti^a, Marco Bonini^a, Domenico Montanari^a
and Federico Sani^{b, a}

^a CNR-IGG, Consiglio Nazionale delle Ricerche, Istituto di Geoscienze e Georisorse,
Via G. La Pira, 4, Firenze, Italy

^b Dipartimento di Scienze della Terra, Università di Firenze, Via G. La Pira, 4, Firenze,
Italy

E-mails: daniele.maestrelli@gmail.com, daniele.maestrelli@igg.cnr.it (D. Maestrelli),
Giacomo.Corti@igg.cnr.it (G. Corti), marco.bonini27@gmail.com (M. Bonini),
domenico.montanari@igg.cnr.it (D. Montanari), federico.sani@unifi.it (F. Sani)

Abstract. The Main Ethiopian Rift (MER) represents an area where volcanism and tectonics interact to create closely linked volcano-tectonic features. This linkage is paramount in the axial portion of the rift, where magmatic segments localize several large peralkaline eruptive centres. Many of them evolved into caldera collapse (the best preserved of which are younger than <1 Ma) generating large ignimbrites and registering the interaction between magmatism and tectonics along the MER. In this work we review the structure of the main collapsed calderas along the axial portion of the MER, to summarize the relationships between volcanism and tectonics proposed in the literature explaining their structural evolution. By doing this, we infer that tectonics had a strong influence in controlling the elongation of the majority of examined calderas. This control was induced by reactivation of inherited crustal fabrics or by stretching of the magma reservoirs under the MER regional stress field.

Keywords. Caldera collapse, Peralkaline calderas, Inherited faults, Regional tectonics, Caldera elongation, Tectonic controls, Main Ethiopian Rift.

Available online 5th July 2021

1. Introduction

The collapse of calderas is a volcano-tectonic process associated with the eruption/depletion or the lateral migration of magma from a magmatic chamber [e.g., Williams, 1941, Roche and Druitt, 2001, Druitt and Sparks, 1984, Lipman, 1997, Gudmundsson et al., 2016, Neal et al., 2019, Sigmundsson, 2019], causing

the volume of rock overlaying the latter to subside and form circular to elliptical depressions that may span from hundreds of meters to tens of kilometres in diameter. This process implies the eruption up to thousands of km³ of magma, leading to a subsidence of the topographic caldera floor up to few kilometres [e.g., Druitt and Sparks, 1984, Lipman, 1984, 1997]. Caldera collapse is widely distributed in all the tectonic contexts [e.g., Geyer and Marti, 2008] and is a paramount process in continental rift settings, where extension and thinning of the lithosphere is associ-

* Corresponding author.

ated with the inlet and emplacement of magma bodies at crustal levels. The Main Ethiopian Rift (MER), in the East African Rift System, does not make exception, showing hundreds of major volcanic centres along its whole length (and surrounding areas). Some of these volcanic systems eventually evolved into caldera collapse, leading to the emplacement of large ignimbritic sheets and plinian pumice fallout deposits with a peralkaline composition that cover the rift floor and a large part of the surrounding areas [Peccerillo *et al.*, 2003 and reference therein]. Indeed, magmatism and tectonics in the MER are crucially linked and their mutual relationships have been investigated since long time [e.g., Corti, 2009 and references therein]. Nonetheless, the active and passive role of magma ascent on tectonic processes is still widely debated [e.g., Bonini *et al.*, 1997, 2001, Boccaletti *et al.*, 1999, Ebinger and Casey, 2001, Kendall *et al.*, 2005, Casey *et al.*, 2006, Corti, 2008, Bastow *et al.*, 2010, Wadge *et al.*, 2016], and similarly is the role of pre-existing and rift-related tectonic structures during caldera collapse [e.g., Acocella *et al.*, 2002, Rampey *et al.*, 2010]. Calderas in the MER have focused the interest of researchers since the early stages of geological exploration of the rift, and many studies contributed to document their volcanic, petrological and structural evolution [e.g., Di Paola, 1971, 1972, Mohr and Wood, 1976, Mohr *et al.*, 1980, Spera and Crisp, 1981, WoldeGabriel *et al.*, 1992, Le Turdu *et al.*, 1999, Acocella *et al.*, 2002, Peccerillo *et al.*, 2003, Casey *et al.*, 2006, Rampey *et al.*, 2010, Giordano *et al.*, 2014, Hutchison *et al.*, 2016a,b, Corti *et al.*, 2018, Lloyd *et al.*, 2018]. Despite caldera collapse is generally accommodated by a system of outward-dipping reverse faults and inward-dipping normal ring faults [e.g., Acocella, 2007], existing tectonic structures may interact with caldera-related structures, and influence the eccentricity of the caldera system. Several researches claimed, in fact, an important role of tectonic structures on the evolution of such systems, indicating that both inherited (older) and rift-related structures are key factors controlling the collapse [e.g., Acocella *et al.*, 2002, 2004, Holohan *et al.*, 2005, 2008, Maestrelli *et al.*, 2020, 2021a,b, Bonini *et al.*, 2021].

In this work, we aim to review the structural characteristics of the main collapsed calderas occurring along the magmatic segments of the MER, to discuss their setting in the frame of the tectonic evolution of

the area. We finally aim to summarise in which cases tectonic structures may have influenced the development of the examined caldera collapse systems.

2. MER tectono-magmatic evolution

The MER represents the northernmost, ~1000 km-long, sector of the East African Rift System (EARS), and results from relative motion between the Nubia and Somalia plates, which is occurring in a roughly E–W direction at rates of ~4–6 mm/yr [e.g., Billham *et al.*, 1999, Saria *et al.*, 2014]. The MER is classically subdivided in three main sectors reflecting different stages of evolution [e.g., Hayward and Ebinger, 1996, Agostini *et al.*, 2011a]. The Northern MER (N-MER; Figure 1), extending from the Afar Depression to the Lake Koka area, is the most evolved sector, and is marked by magma-dominated processes. The Southern MER (S-MER) has its northern boundary in the Lake Awasa area, and is nowadays experiencing fault-dominated extensional processes, with limited volcanism, reflecting the youngest stage of evolution. The Central MER (C-MER), located halfway through the MER, shows intermediate features. Such different maturity stages, varying from N to S along the MER, may suggest that this rift is propagating southward toward the Turkana Depression, where it links with the Kenya Rift [e.g., Corti *et al.*, 2019], although the timing of rift initiation and propagation is complex and still not fully understood [Balestrieri *et al.*, 2016].

The MER is marked by large boundary faults, formed asynchronously along the rift and characterized by a vertical offset >1 km [e.g., Boccaletti *et al.*, 1998]; these fault systems show different orientation in the N-MER, C-MER, and S-MER sectors, ranging from ~N40° E in N-MER to N30° E in the C-MER and varying between N0° E to N20° E in S-MER (Figure 1). Geological and geophysical data indicate that the large boundary faults have been active between 11 and 2 Ma in the N-MER, whereas they are still active in the C-MER and S-MER. The floor of the present-day rift valley is characterized by a pervasive pattern of short, right-stepping en-echelon faults with throws <100 m and trending obliquely to the rift boundaries. Similarly to the boundary faults, these axial structures, classically named Wonji Fault Belt [WFB; Mohr, 1962b, 1967; Meyer *et al.*, 1975], show different characteristics in the three MER sectors: they are oriented ~N20° E in the N-MER, ~N12° E in

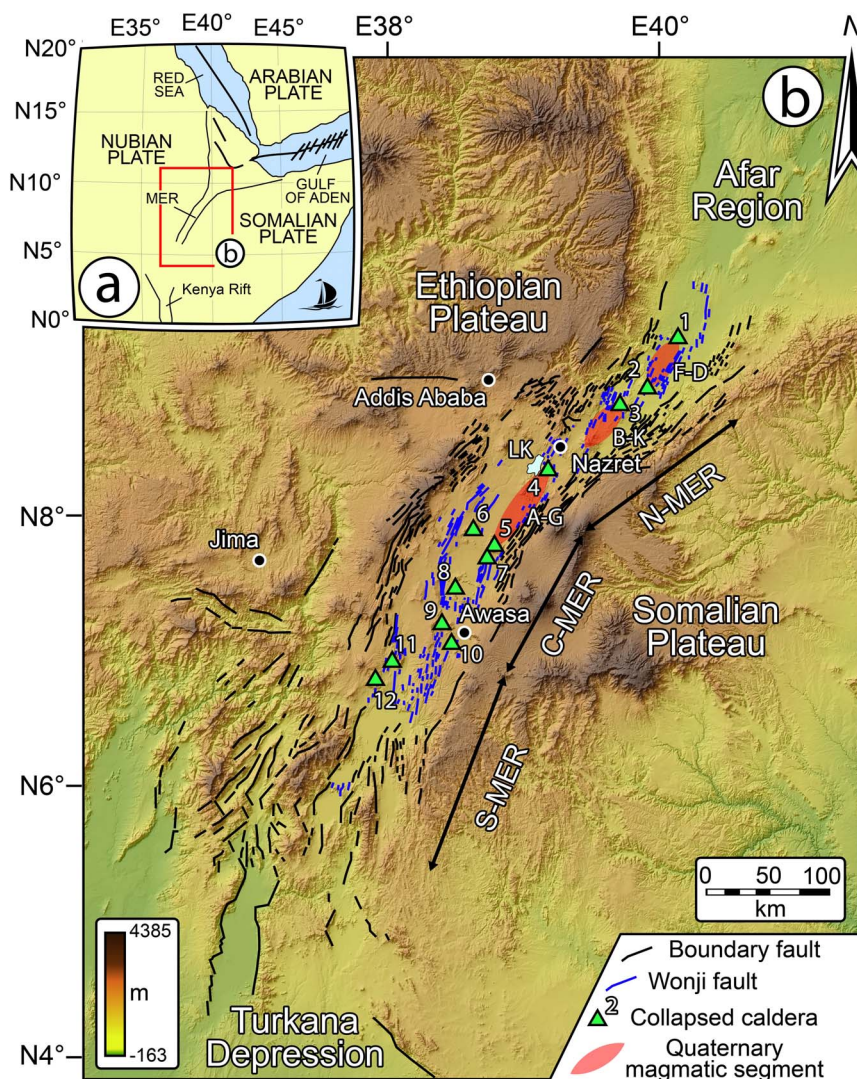


Figure 1. The Main Ethiopian Rift. Black lines mark the major boundary faults, while blue lines show the Wonji faults. Green triangles indicate the calderas described in this study. LK: Lake Koka. (1) Dofen Volcanic Complex (DVC); (2) Fantale; (3) Kone Volcanic Complex (KVC); (4) Gedemsa; (5) Aluto; (6) Gademotta; (7) Munesa; (8) Shala; (9) Corbetti; (10) Awasa; (11) Duguna; (12) Hobitcha. F-D: Fantale–Dofen magmatic segment; Boset–Kone magmatic segment; Aluto–Gedemsa magmatic segment.

the C-MER and roughly N–S in the S-MER; in the N-MER the WFB started forming at around 2 Ma, when the deformation shifted from the boundary faults to the axial portion of the rift, whereas they are in an incipient stage in the C-MER and almost absent in the S-MER [e.g., Agostini *et al.*, 2011a]. Kinematics of WFB faults typically varies between pure dip-slip to slight oblique-slip displacement (dextral or sinis-

tral), consistent with a roughly E–W trending Late Quaternary extension direction (N90°–95°; Agostini *et al.*, 2011b). In the N-MER, the WFB are closely associated with the Quaternary volcanic activity, with alignment of eruptive centres and volcano-tectonic features defining the so-called axial magmatic segments [e.g., Ebinger and Casey, 2001, Casey *et al.*, 2006; Figure 1]. Active faults at the WFB cross-cut

several calderas and facilitate post-caldera basaltic and silicic eruptions forming scoria cones and lava flows [Fontijn *et al.*, 2018]. The axial segmentation of the volcano-tectonic activity is mimicked in a similar segmentation at depth. Tomographic analysis revealed indeed segmented low velocities zones, interpreted as the loci of enhanced melt production from the mantle, suggesting that magma generation and faulting at surface are intimately linked [Keranen *et al.*, 2004, Bastow *et al.*, 2005]. The development of the WFB in the N-MER has been interpreted as reflecting a change in the deformation style from ~2 Ma [e.g., Meyer *et al.*, 1975], with the deactivation of the large-throw boundary faults and migration of strain and volcanic activity to the centre of the rift depression [Morton *et al.*, 1979]. As outlined above, transition from axial tectono-magmatic activity and magma-dominated deformation in the N-MER to marginal faulting with limited volcanism in the S-MER has been interpreted to reflect a North to South transition from more advanced to less advanced rifting stages.

Extension in the Ethiopian region was predated by a complex pre-Tertiary tectonic history responsible of several heterogeneities that influenced rift localization and evolution at both regional scale and local scale [e.g., Mohr, 1962b, Keranen and Klemperer, 2008, Bastow *et al.*, 2008, Keranen *et al.*, 2009]. This phase was followed by an intense basaltic volcanic activity (since ~45 Ma) emplacing the so-called Trap series, characterised by tholeiitic to alkaline lava flows [e.g., Kieffer *et al.*, 2004, Rooney, 2017] intercalated with silicic volcanics to form an up to 3000 m volcanic pile [e.g., Mohr and Zanettin, 1988]. This activity continued during the Miocene with the building of large volcanic edifices on the plateaus surrounding the rift [e.g., Kieffer *et al.*, 2004], and with a second phase of widespread basaltic activity between 12 and 8 Ma [e.g., Bonini *et al.*, 2005]. Later on, at ~6–8 Ma, a major pulse in volcanic activity was confined within the developing rift valley; this activity was characterized by the alternate eruption of large ignimbrite deposits and basaltic magmatism [Boccaletti *et al.*, 1999, Trua *et al.*, 1999]. During the Quaternary, this typical bimodal magmatic activity, mainly occurring as pulsed phases, localized in the axial magmatic segments of the N-MER [e.g., Casey *et al.*, 2006, Hutchison *et al.*, 2016a] synchronously to WFB development, generating tra-

chyte and rhyolite pyroclastites from central emission points (strato-cones and caldera complexes) and subordinated basalts from fissural eruptions [e.g., Chernet and Hart, 1999, Boccaletti *et al.*, 1999, WoldeGabriel *et al.*, 1999, Casey *et al.*, 2006].

The history of the MER, since pre-Tertiary times, therefore shows how tectonics and volcanism are interrelated, indicating that inherited structures at places influenced volcanic activity by localizing eruptions, aligning volcanic centres and guiding dyke orientation [e.g., Wadge *et al.*, 2016]. It was proposed that large silicic centres were emplaced at the tip of magmatic segments, where reduced stress favoured long residence time and consequent magma evolution [e.g., Le Turdu *et al.*, 1999, Peccerillo *et al.*, 2003; Figure 1]. Alternatively, other works suggest that deformation at the centre of the segments is mainly controlled by magmatism, while it is predominantly brittle at the segment tips [e.g., Kurz *et al.*, 2007]. Several volcanoes along the MER evolved as caldera collapse structures, and many authors suggested a role of inherited faults on the development of certain caldera features [e.g., Acocella *et al.*, 2002]. Besides, other studies suggest that tectonic activity was subordinated to magmatism, and that collapsed calderas were not controlled by inherited fabrics [e.g., Casey *et al.*, 2006]. In the following paragraphs, we review the main (twelve) caldera collapses (Figure 1), highlighting their structural setting and aiming to disclose whether tectonic processes played a role during their evolution.

3. Collapsed calderas along the MER

We describe collapsed calderas and their structural setting from N to S, grouping them according to the three main rift sectors (N-MER, Figure 2; C-MER, Figure 3; S-MER, Figure 4). This choice reflects the difference in the evolutionary stage of the three sectors, consequently influencing the setting in which caldera collapse occurred. Characteristics of Ethiopian calderas have been reported in Table 1, which has been compiled from the literature and new data deriving from this study.

Table 1. Summary of caldera features described in this work and compiled from literature

Name	MER sector	Lat.	Long.	Age oldest	Age youngest	Axial ratio (L_A/S_A) ⁽³⁾	Long axis trend	Rocks	Caldera features	Area	Strain $\ln(L_A/S_A)$ ⁽³⁾	
Dofen	N	9.35°	40.13°	1.7 Ma ⁽¹⁾	Historic	2.56 ⁽³⁾	ed	N113° E	Trachy-basaltic lava flows, rhyolite flows and domes ⁽¹⁾	Summit caldera on a strained magmatic edifice	1 × 1 km, considering the summit collapse	0.940 ⁽³⁾
Fantale	N	8.98°	39.90°	168 ± 38 Ka ⁽²⁾	1820 a.d. ⁽³⁾	1.58 ⁽²⁾ 1.67 ⁽³⁾ 1.77 ⁽³⁾ 1.61 ⁽³⁾ 1.64 ⁽³⁾	N112° E ⁽²⁾ N111–114° E ⁽³⁾ N107 ± 4° E ⁽⁴⁾	Ignimbrite, pumices, ash fallout, obsidian, rhyolites, basaltic lavas ⁽³⁾	Nested inside major caldera; Fault-controlled margins	2.9 × 4.4 km ⁽²⁾ 2.5 × 4.5 km ⁽⁴⁾	0.457 0.513 ⁽³⁾ 0.571 ⁽³⁾ 0.476 ⁽³⁾	
Kone (3 main cald.: Kone or Gariboldi, Korke, Birenti)	N	8.84°	39.69°	<0.32 Ma ⁽⁵⁾	1810 a.d. ⁽⁵⁾	1.49 ⁽³⁾	N94 ± 17E ⁽⁴⁾	Pumices and ash fallout, ignimbrites and rhyolitic lavas, trachytes, basalt flows ⁽³⁾	Nested; Fault-controlled margins	5.0 × 7.5 km ⁽⁴⁾ 95 km ²⁽⁵⁾	0.399	
Gedemsa	N	8.36°	39.17°	0.88 Ma ⁽³⁾ 0.8 Ma ⁽⁴⁾	0.29–0.2 Ma ⁽³⁾ 0.32–0.26 Ma ⁽⁶⁾ 0.1 Ma ⁽⁴⁾	1.315 ⁽²⁾ 1.23 ⁽³⁾	N75° E ⁽²⁾ N86° E ⁽⁴⁾	Trachytic, rhyolitic and obsidian lavas, Ignimbrite, surges and fallout ^(4,7)	Fault-controlled margins	7.3 × 9.6 ⁽²⁾ 7 × 9 km ⁽⁴⁾	0.274 0.207 ⁽³⁾	
Aluto	C	7.74°	38.78°	0.27–0.15 Ma ⁽⁸⁾ 316–306 Ka ⁽⁹⁾	21–9.4–2 Ka ⁽⁸⁾ >60 Ka ⁽⁹⁾	1.72 ⁽²⁾	N90° E ⁽⁸⁾	Trachytic, Ignimbrites, pumices, obsidian ⁽⁹⁾		8.6 × 5.0 km ⁽⁹⁾	0.542	
Shala (O'a)	C	7.47°	38.50°	0.24 Ma ⁽⁸⁾	0.18 Ma ⁽⁸⁾	1,143 (O'a)	N105–110° E	Ignimbrite, pumices, rhyolites, basalts ^(4,8)	Nested?	16 × 14 km (O'a)	0.133	
Corbetti	C/S	7.20°	38.36°	0.24 Ma ⁽⁸⁾	0.18–0.1 Ma ^(8,11)	1.43 ⁽²⁾	N104° E ⁽²⁾ N135° E ^(7,10)	Ignimbrite, pumices ⁽⁹⁾	Nested? Fault-controlled margins	12 × 10 km ^(7,10)	0.357	
Awasa	C/S	7.04°	38.43°	1.0 Ma ⁽¹²⁾ 1.85–1.1 Ma ⁽¹¹⁾	~1900 a.d. ⁽¹²⁾	1.75 1.333	≈E–W*	Ignimbrite	Nested?; Strongly eroded	35 × 20 30 × 40 km ⁽¹²⁾	0.560 0.288	
Duguna	S	6.91°	38.01°	0.46–0.43 Ma ⁽¹⁴⁾	?	1,333	N35° E	Pumices, ash fall ⁽¹³⁾		8 × 6 km	0.288	
Hobitcha	S	6.79°	37.88°	?	?	?	N110° E	Rhyolites	Strongly eroded	~10 km diam.	?	

Reference legend: (1) Chernet, 2005; (2) Hunt et al., 2019 and reference therein; (3) Casey et al., 2006; (4) Acocella et al., 2002 and reference therein; (5) Rampey et al., 2010 and reference therein; (6) Peccerillo et al., 2003; (7) Di Paola, 1971; (8) Le Turdu et al., 1999; (9) Hutchison et al., 2016b and reference therein; (10) Di Paola, 1972; (11) Hutchison et al., 2016a; (12) Newhall and Dzurisin, 1988; (13) Corti et al., 2013 and reference therein; (14) Bigazzi et al., 1993. Where not specified the data here reported belong to this study. ed.: edifice. The strain (or natural strain) is calculated, following Casey et al. [2006], as the natural logarithm of the caldera long axis (L_A) and short axis (S_A) ratio.

* The elongation of Awasa is roughly E–W, but the presence of erosional embayments does not allow for a clear definition of the caldera major axis.

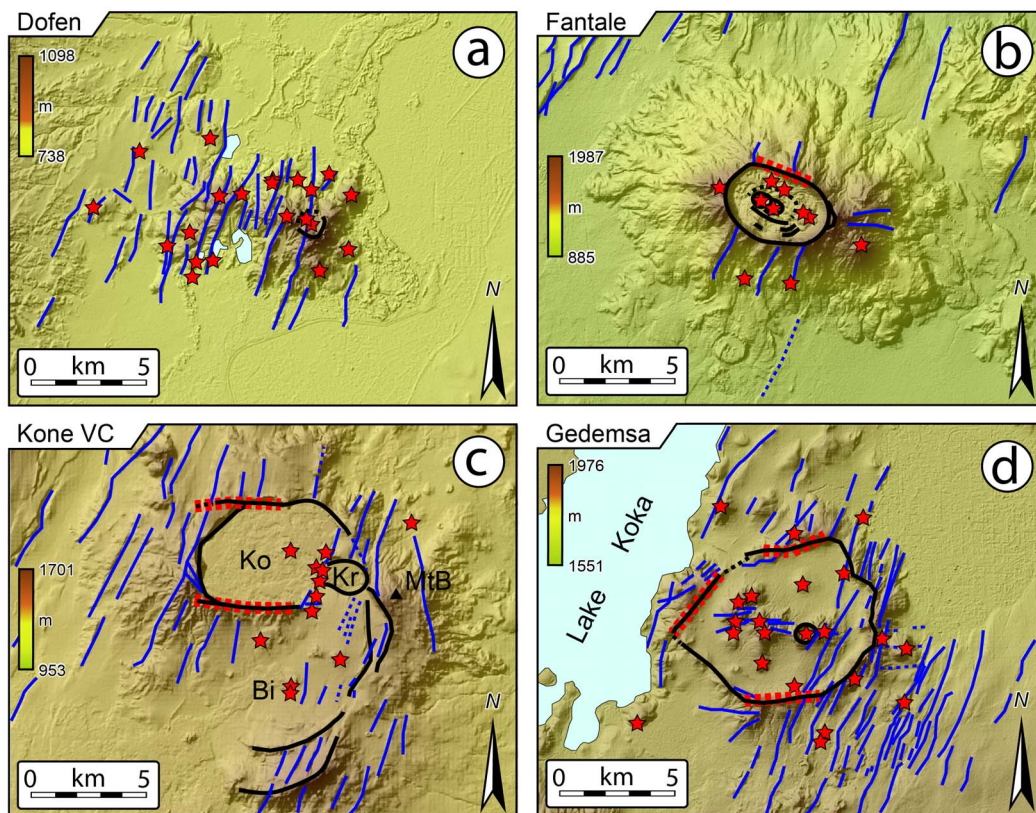


Figure 2. (a) Dofen Volcanic Complex. This volcanic complex, defining the northern tip of the Dofen Fantale magmatic segments, shows a small collapsed caldera. Structures and emission points are mapped after Casey *et al.* [2006]. (b) Fantale Caldera showing NW–SE elongation. Caldera and tectonic structures are mapped after Acocella *et al.* [2002]. (c) Kone Volcanic Complex (KVC), which is composed of the remnants of the Birenti Caldera (Bi), Kone Caldera (Ko) and the Korke Embayment (Kr). MtB: Mount Birenti (black triangle). Caldera location is indicated in Figure 1. Caldera and tectonic structures are mapped after Acocella *et al.* [2002] and Rampey *et al.* [2010]. (d) Gedemsa Caldera showing two major rectilinear caldera walls. Caldera and tectonic structures are mapped after Korme *et al.* [1997], Acocella *et al.* [2002] and Hutchison *et al.* [2016a]. Newly mapped tectonic structures are interpreted on 30 m resolution ALOS DEMs. Black thick lines indicate caldera structures (dashed black lines for uncertain caldera structures), while blue lines indicate tectonic structures. Red stars indicate volcanic emission points. Thick red dashed lines indicate fault-controlled caldera margin, as inferred by Acocella *et al.* [2002] and Hunt *et al.* [2019].

3.1. *N-MER calderas*

3.1.1. *Dofen volcanic complex (DVC)*

The felsic Dofen volcanic complex (DVC; Figures 1b and 2a) is located at the northern tip of the Dofen–Fantale magmatic segment and is represented by a NW–SE elongated relief (Figure 5). This relief has been interpreted to be a strained volcanic

edifice in a $\sim N110^\circ E$ direction [Casey *et al.*, 2006], nowadays dissected by several NNE–SSW trending faults and fractures (Figures 2a and 5). The volcanic system lays, together with the Fantale Caldera more to the south, within an east-dipping half-graben bounded by a 60–80 m-high fault scarp [Casey *et al.*, 2006]. K/Ar dating ascribes the Dofen complex to 1.7 Ma but historical lava flows testify ongoing activ-

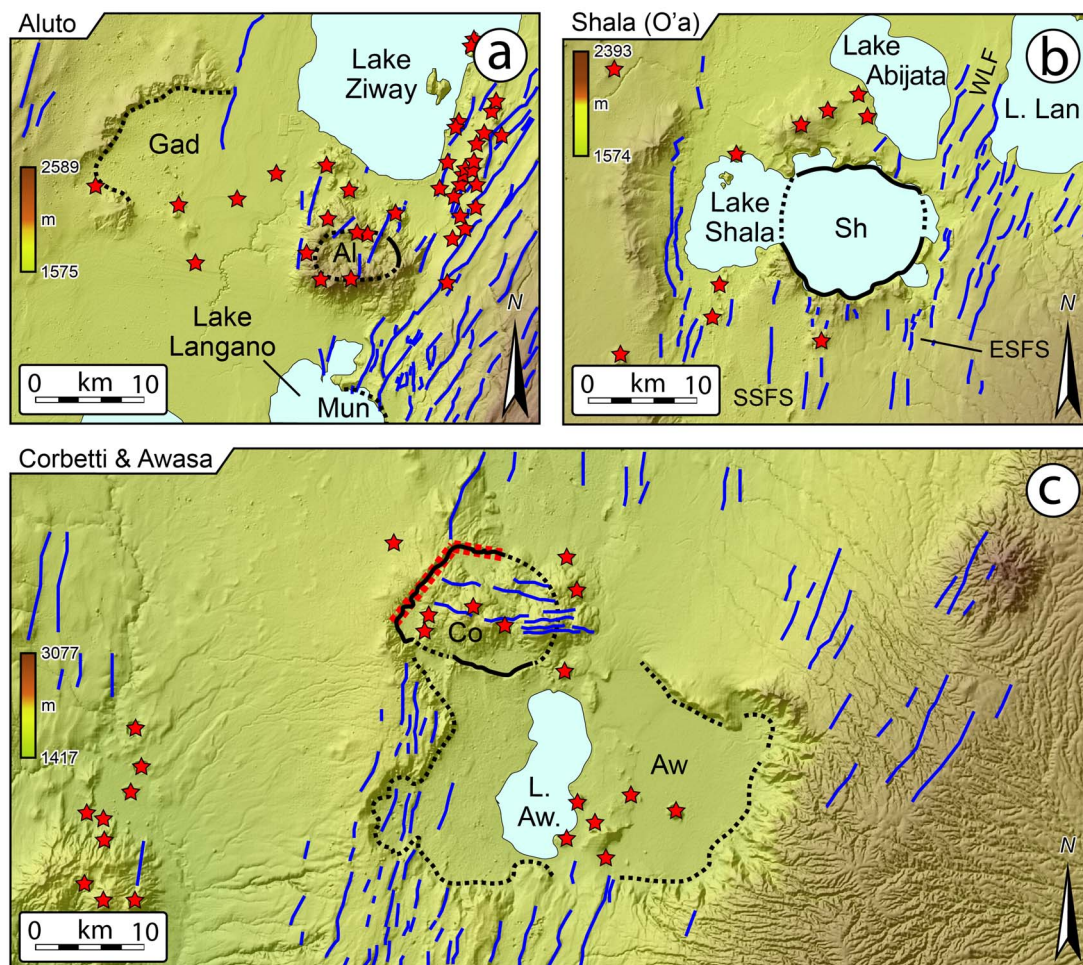


Figure 3. (a) Aluto Caldera (Al) and the remnants of the Gademotta (Gad) and Munesa (Mun) calderas. Structures are redrawn after Hutchison *et al.* [2016a,b]. L. Lan.: Lake Langano. (b) Shala Caldera. Structures are redrawn after Hutchison *et al.* [2016a,b]; Mohr *et al.* [1980] and Le Turdu *et al.* [1999]. L. Lan.: Lake Langano; SSFS: Southern Shala Fault System; ESFS: Eastern Shala Fault System; WLF: West Langano Fault. (c) Corbetti (Co) and Awasa (Aw) calderas. L. Aw.: Lake Awasa. Structures are redrawn and modified after Di Paola [1971], Korme *et al.* [1997], Hutchison *et al.* [2016a], Lloyd *et al.* [2018] and Hunt *et al.* [2019]. Caldera location is indicated in Figure 1. Symbol and legend are as in Figure 2.

ity [Chernet, 2005; Table 1]. In its central portion, normal faults with throw >100 m dismantled what Casey *et al.* [2006] refer to a “caldera complex”. Nonetheless, no clear evidence of large caldera structures can be interpreted from DEMs, except for the small depression (~1 km in diameter) occurring in the eastern portion of the volcanic complex. Several emission points align with NE–SW trending structures, interpreted by Casey *et al.* [2006] as the surface expression of dyke segments.

3.1.2. *Fantale caldera*

Fantale is one of the most active volcanoes in the MER and is located at the southern tip of the Dofen–Fantale magmatic segment [Figure 1; Casey *et al.*, 2006]. Its volcanic history was dominated by eruption of intermediate and silicic volcanics, ranging from ignimbrite pumices and ash falls in the early stages to lava flows (obsidian and rhyolites) in later stages [Hunt *et al.*, 2019]. Obsidian flows and basaltic

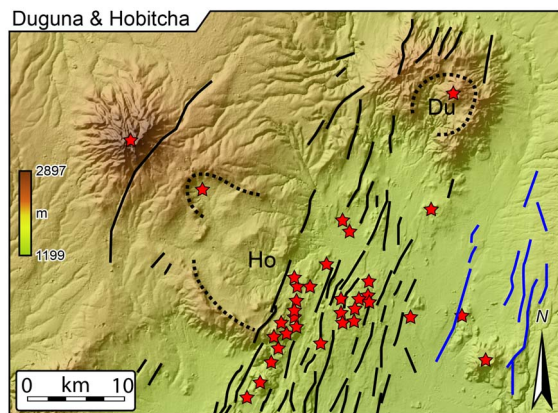


Figure 4. Duguna volcanic complex with summit caldera collapse and the remnants of the Hobitcha Caldera. Structures are redrawn after Corti *et al.* [2013], Chernet [2011] and Minissale *et al.* [2017]. Black lines indicate rift boundary faults, while blue lines indicate the axial Wonji Faults. All other symbols are as those in Figure 2. Caldera location is indicated in Figure 1.

lavas were erupted in 1820 [Gibson, 1969]. Acocella *et al.* [2002] identified in the area NNE–SSW trending WFB faults (mean trend $N23^\circ E \pm 5^\circ$), with a maximum displacement of 100 m, and described the elliptical caldera ($\sim 2.5 \times 4.5$ km, or 2.9×4.4 km, following Hunt *et al.*, 2019; Table 1) as characterized by a topographic subsidence of 100 m (Figures 2b and 5; Table 1). Inside Fantale, a smaller nested caldera (40 m deep) is visible. WNW–ESE trending vertical faults crosscut the caldera rim and several monogenic vents are reported by Acocella *et al.* [2002] in the caldera depression as well as along the rim, organized in trails sub-parallel to caldera elongation. Outside the caldera, Acocella *et al.* [2002] report vent distribution as mainly controlled by NNE–SSW trending Wonji structures, with no evidence of WNW–ESE trending structures. Casey *et al.* [2006] reported that the $\sim N$ trending faults ($N10^\circ E$) displace historical fissure lava flows erupted from the southern flank of the Fantale volcano in 1810 and 1820 [e.g., Williams *et al.*, 2004]. Hunt *et al.* [2019] suggest that the rectilinear, northern caldera margin may be controlled by a fault (Figure 2b). Finally, Temtime *et al.* [2020] investigated and modelled rhyolitic dyke intrusion accompanied by ground fractures that occurred in 2015 NW of Fantale Caldera. The trend of the ground fractures ranges

between $\sim 35^\circ$ and 5° and the modelling suggested that the dyke strike $\sim 29^\circ \pm 2^\circ$ [Temtime *et al.*, 2020].

3.1.3. Kone volcanic complex (KVC)

The Kone volcanic complex (KVC, Rampey *et al.*, 2010; Figures 1 and 2c; Table 1), also referred as Gariboldi, is a major Quaternary composite caldera system where at least seven Pleistocene to Recent caldera collapses (with eruption in historic period) were recognised [Mohr, 1962a, Cole, 1969, Rampey *et al.*, 2010]. Located ~ 30 km SW of Fantale, it represents the northern tip of the so-called Boset–Kone Magmatic segment (Figure 1) and is composed of three superimposed major caldera depressions, respectively named Birenti, which is nowadays visible as several isolated segments of caldera wall, Kone and Korke [Cole, 1969, Rampey *et al.*, 2010]. The nature of the remnants of the caldera walls suggest that the Birenti Caldera is composed of at least two nested calderas (Figure 2c), with an inferred diameter of ~ 11 km and an area of ~ 95 km² for this composite caldera collapse that is the oldest of the KVC [Rampey *et al.*, 2010]. Other data about the KVC can be found in Table 1.

The Kone Caldera rim is described by Rampey *et al.* [2010] as a horseshoe structure opening to E with the northern portion of the rim extending SW (~ 350 m), where ~ 200 m of caldera wall material are exposed together with ~ 150 m of pyroclastic caldera forming deposits (Figure 2c). Rampey *et al.* [2010] reported that the Kone Caldera wall is moderately incised by post collapse erosion and that the southern part of the western margin is cut by a E–W trending fault. In the surrounding areas, Acocella *et al.* [2002] mapped NNE–SSW trending WFB faults ($N20^\circ \pm 3^\circ$) (Figure 5), and described alignments of monogenic vents in the eastern portion of the caldera, trending approximately $N17^\circ$, therefore subparallel to regional NNE–SSW faults.

3.1.4. Gedemsa caldera

The Gedemsa Caldera is located east of Lake Koka, ~ 80 km south of the KVC (Figure 1), along the axial part of the MER [Acocella *et al.*, 2002] and in the proximity of the northern tip of the Aluto–Gedemsa magmatic segment [Casey *et al.*, 2006 and reference therein; Figure 1]. Its activity, clustered in three distinguishable phases (pre-caldera, caldera and post caldera activity), as detailed by Hutchison *et al.*

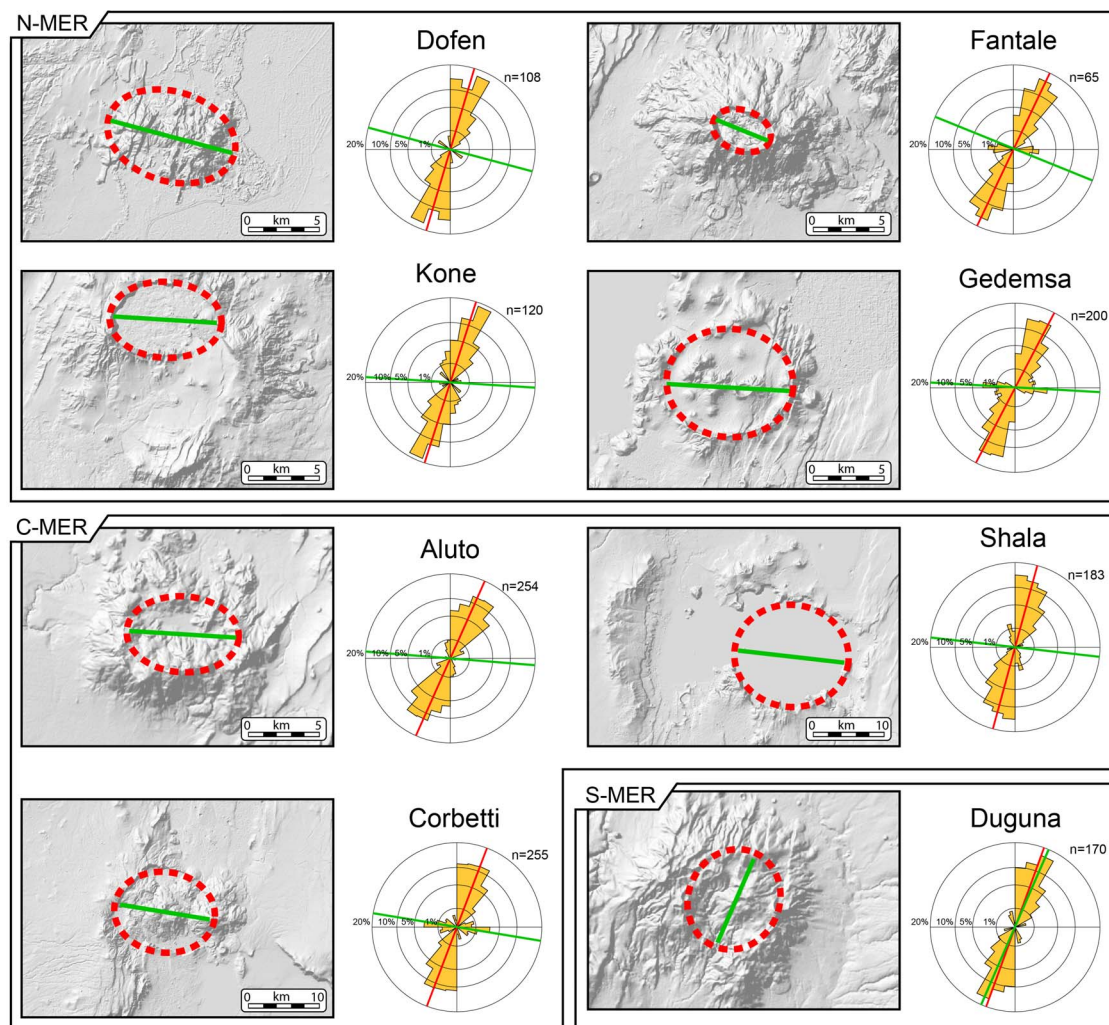


Figure 5. Caldera elongation and regional structures orientation for the examined volcanic and caldera complexes in along the MER. Rose diagram (length weighted) shows mapped tectonic structures reported in Figures 2, 3 and 4. Red line indicate the average trend of tectonic structures while green lined shows the trend of caldera elongation corresponding to the caldera major axis (see also Table 1). Red thick dashed lines indicate the inferred geometry of the calderas.

[2016a] and Hunt et al. [2019], mainly produced silicic with few subordinated mafic and intermediate products [e.g., Di Paola, 1972]. Lavas (trachytes, rhyolites and obsidians) and pyroclastics (ignimbrites, surges and fallout) were mainly erupted, compositionally ranging from hawaite to rhyolite, with mafic components erupted only during post-caldera activity [Peccerillo et al., 1995]. Di Paola [1972] indicated that the NNE–SSW regional faults affect the col-

lapsed caldera, especially in its eastern portion. Hunt et al. [2019] suggest that some of the caldera margins, expressed as rectilinear faults may be controlled by inherited structures (Figure 2d). Acocella et al. [2002] identified the same NNE–SSW trending faults and characterized them as extensional WFB fractures and faults (average trend $N22^\circ \pm 3^\circ$) with maximum vertical displacement of ~ 100 m (Figures 2d and 5; Table 1). The northern and southern rims have an

E–W strike, while to the west and to the east NNE–SSW rectilinear faults mark the caldera rim, defining an overall rhomboidal shape.

3.2. *C-MER calderas*

3.2.1. *Aluto caldera*

Aluto is a major silicic eruptive centre situated in the tectonically controlled lacustrine Ziway-Shala basin [e.g., Di Paola, 1972, Le Turdu *et al.*, 1999, Benvenuti *et al.*, 2002], which experienced caldera collapse with large explosions and associated extensive ignimbrite deposits [Hutchison *et al.*, 2015, 2016b]. This volcano lays between the Gademotta Caldera remnants (20 km to the NE) and the Munesa Caldera remnants to the South, the latter being masked by Lake Langano (Figure 3). These two large silicic calderas, nowadays exposed only in scattered and highly eroded portions, ceased their activity before 1 Ma and are considered two of the largest calderas developed along the MER [Hutchison *et al.*, 2016b, and reference therein; Table 1]. A detailed description of the Aluto eruptive history is provided by Hutchison *et al.* [2016a,b], which defined a three-stage evolution, depicting pre-caldera, caldera and post-caldera activity. Nowadays, the Aluto Caldera shows a marked E–W trending elongation (Figure 5), despite no major faults with a similar trend are observed inside the depression, or outside, in the proximity of the caldera (Figure 3a). At places, the caldera rims are dissected by N–NE-trending Wonji faults (Figure 5), which are absent in the area between Aluto and Gademotta remnants. Higher density of such faults is observed east of the Aluto Caldera, near the remnants of the Munesa Caldera, where several faults structures are visible in correspondence of the Lake Langano banks (Figure 3a) and that extends also below the lake surface, as highlighted by geophysical data [Le Turdu *et al.*, 1999].

3.2.2. *Shala (O'a) caldera*

Shala, or O'a, Caldera lays ≈ 40 km south of the Aluto Caldera, in an area that is completely obscured by Lake Shala. The most evident remnants of this large collapse (that occurred around 0.24 Ma, Mohr *et al.*, 1980, Le Turdu *et al.*, 1999, Table 1) are the northern and southern scarps, which mostly cut ignimbrites and pumices and subordinately rhyolitic lavas [Di Paola, 1972]. Toward east and west, the

caldera margins were eroded and the entire caldera edifice including the caldera ring faults were masked by the lake [Mohr *et al.*, 1980]. Connection of rim remnants suggests a limited E–W elongation of the caldera collapse area (Figure 5, Table 1), but no direct data can be obtained about internal caldera structure and morphology. Several faults belonging to the WFB are visible around the Lake Shala with an overall NNE–SSW trend, some of which were named by Le Turdu *et al.* [1999] as Southern Shala Fault System and Eastern Shala Fault System (Figure 3b). The WFB was active during the Shala volcanic complex evolution and appears to have been active up to the Holocene [Mohr *et al.*, 1980, Le Turdu *et al.*, 1999]. No E–W trending faults are observed in the caldera proximity (Figure 3b), but Mohr *et al.* [1980] report sparse ESE-trending transverse faults on the caldera eastern side.

3.2.3. *Corbetti caldera and Awasa caldera remnants*

The Corbetti Caldera is located ≈ 30 km southwest of the Shala Caldera, close to the Awasa (or Hawassa) Caldera remnants in the Lake Awasa Basin [Hutchison *et al.*, 2016a; Figure 3c]. The Corbetti Caldera has been the object of many studies in the past and in recent times, which have detailed its major features [Di Paola, 1971, 1972, Hunt *et al.*, 2019; Table 1]. Besides, pre-caldera activity was followed at Corbetti by large ignimbrite eruption and caldera formation around 182 ± 28 ka BP [Hutchison *et al.*, 2016a]. Based on geodetic and magnetotelluric data, Lloyd *et al.* [2018] hypothesize the presence of a \approx E–W trending regional structures extending down to ~ 30 km in the crust and associated magma emplacement and caldera collapse elongation (Figure 5). Intra-caldera structures show a similar trend (Figures 3a and 5) and crosscut the inferred caldera rim on its eastern side, and align with post-caldera volcanic emission points. Nonetheless, outside the caldera no E–W trending structures are observed, and faults in the Corbetti–Awasa area show an NNE–SSW trend consistent with the WFB (Figure 5). Hunt *et al.* [2019] report that some of the caldera margins characterised by a rectilinear trend may be controlled by faults (Figure 3c). The Awasa remnants, covering an area of $\approx 35 \times 20$ km (Table 1), testify a much larger collapse (one of the three largest occurred along the C-MER, with Munesa and Gademotta collapses; Hutchison *et al.*, 2016b, and references therein). This

caldera experienced its major caldera-forming eruption around 1.85–1.1 Ma [WoldeGabriel *et al.*, 1990] and is nowadays strongly eroded, with the caldera floor partly obscured by Lake Awasa.

3.3. *S-MER calderas*

3.3.1. *Duguna and Hobitcha*

The Duguna Caldera [Newhall and Dzurisin, 1988] is a large volcanic centre located at the northernmost tip of the S-MER, ≈ 20 km southwest of the Awasa Caldera. This volcanic complex shows a summit caldera collapse, which produced pumices and ashfall deposits [Chernet, 2011], roughly elongated along a NE–SW trend (Figures 4 and 5), and covers an approximate area of $\approx 8 \times 6$ km (Table 1). Ages of 430–460 ka have been reported for the eastern flank of the Duguna volcano [Bigazzi *et al.*, 1993; Table 1]. The pre-caldera volcanic edifice is crosscut by NE–SW trending rift boundary faults (Figures 4 and 5), and Wonji faults with a similar trend surface southeast of Duguna, along the axial sector of the MER [Corti *et al.*, 2013]. The boundary faults also seem to align with several minor volcanic emission points and crosscut the remnant of the larger Hobitcha Caldera remnants, a horseshoe-shaped rhyolitic centre, with a diameter of ~ 10 km [Chernet, 2011, Corti *et al.*, 2013; Table 1].

4. Discussion: interaction between calderas and regional tectonics in the MER

The direction of extension along the MER was reconstructed by several authors based on structural data and GPS vectors, suggesting a direction of horizontal stretching ranging between N135° E and N105° E [e.g., Chorowicz *et al.*, 1994, Bilham *et al.*, 1999, Chu and Gordon, 1999, Acocella *et al.*, 2002, Keir *et al.*, 2006]. Nonetheless, other studies suggested a partly different extension direction trending around N90°–100° [e.g., Bonini *et al.*, 1997, Boccaletti *et al.*, 1998, Fernandes *et al.*, 2004, Pizzi *et al.*, 2006, Agostini *et al.*, 2011b, Saria *et al.*, 2014, Stamps *et al.*, 2021]. It is well known that elongated calderas may reflect the regional stress field [e.g., Bosworth *et al.*, 2000, 2003] and thus extension along the MER may have controlled caldera elongation [Casey *et al.*, 2006]. Notably, the elongation of the examined calderas

(except for the summit Duguna Caldera) is mostly parallel to the proposed N90°–100° trending extension direction acting on the MER (Figure 5).

Nonetheless, several mechanisms were proposed in literature to justify caldera elongation and the trend of associated volcano-tectonic features (e.g., vent alignments). Robertson *et al.* [2015] summarized the main mechanism to explain caldera elongation along the Kenya Rift. These authors report that caldera elongated shape may be induced by (i) the pre-collapse elongation of the underlying magma chamber (Figure 6a, b, c), which may be in turn driven by other processes, as explained below, (ii) poly-phased collapse resulting into nested calderas (Figure 6d), assuming an overall elongated geometry, (iii) fault-controlled caldera rim (Figure 6e) and (iv) post-collapse events or continued stretching (Figure 6f, g). More specifically, the elongation of the magma chamber can depend upon magma migration and emplacement along pre-existing structures [e.g., Montanari *et al.*, 2020; Figure 6c] or by the orientation of the stress field (Figure 6a, b), such that the long caldera axis may be parallel to the minimum horizontal stress (Figure 6a), assuming a mechanism analogue to borehole breakout [e.g., Bosworth *et al.*, 2000, 2003], or the maximum horizontal stress [Figure 6b; e.g., Wadge *et al.*, 2016]. In this frame, the analysis of associated volcanic features may help to discern between the two latter cases [e.g., Bonini, 2012]. Poly-phased collapse is likely the simplest mechanism to explain caldera elongation: subsequent collapse and nested caldera formation may in fact induce an apparent composite caldera elongation, which may, or may not, reflect an underlying elongated magma chamber (Figure 6d). Collapse may induce caldera elongation when in presence of inherited linear crustal structures, reactivated during the collapse or when distorted by local structures [e.g., Acocella *et al.*, 2002, 2004, Holohan *et al.*, 2005, 2008, Maestrelli *et al.*, 2020, 2021a,b] (i.e., fault-controlled caldera rim, Figure 6e). Post-collapse events can finally at least in part contribute to create elongated caldera depressions (e.g., post collapse erosion or continued strain due to regional stretching after caldera collapse, Figure 6f, g). These mechanisms, summarized by Robertson *et al.* [2015], can be considered valid worldwide and therefore, their applicability can be also tested for calderas occurring along the MER.

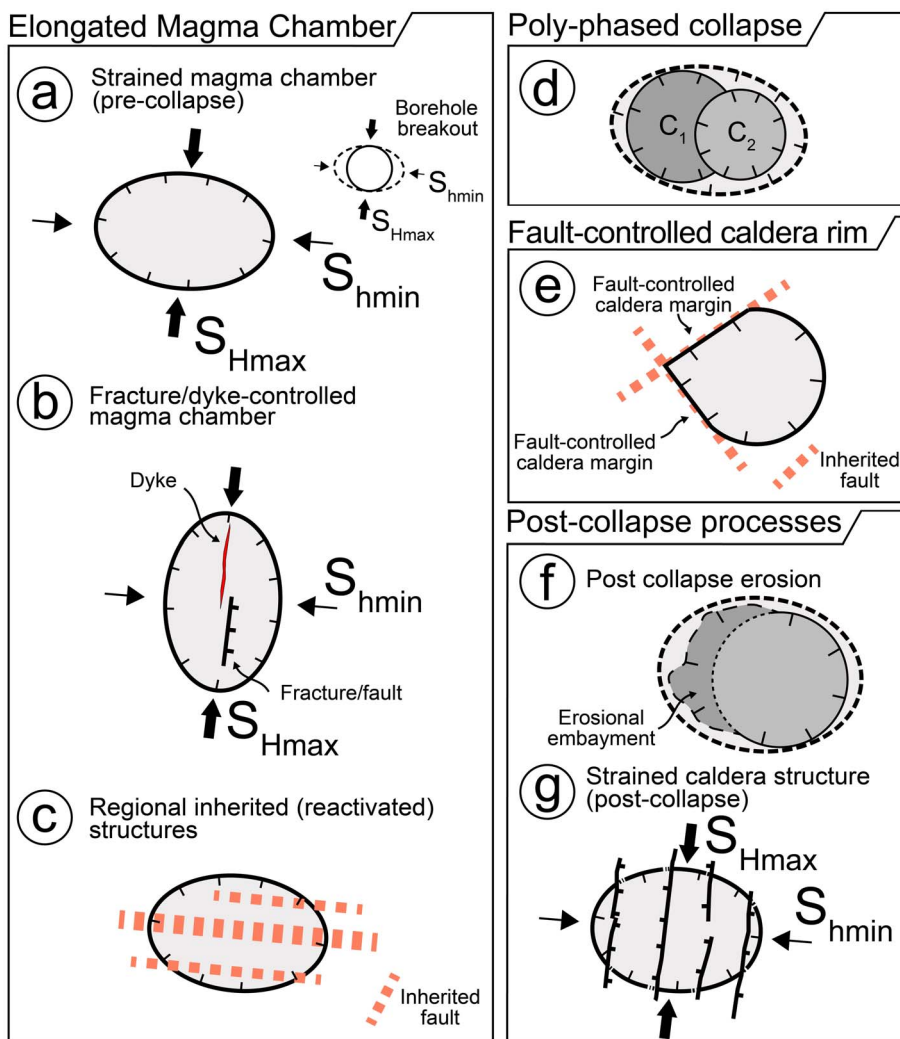


Figure 6. Sketch inspired and modified from Robertson *et al.* [2015, and reference therein] summarizing the possible mechanisms contributing to caldera elongation. (a–c) Caldera elongation controlled by an elongated magma chamber. This may occur as a result of (a) tectonic strain (in analogy to the borehole breakout mechanism; e.g., Mazzarini *et al.*, 2010), (b) elongation along induced fractures/dykes or (c) magma emplacement along regional reactivated structures. (d) Nested collapse may control the overall composite caldera elongation. (e) The presence of existing discontinuities can produce elongated caldera depressions. Other shallow crustal processes (not shown in the figure; e.g., asymmetrical subsidence, pre-collapse topography) can produce similar elongation [Robertson *et al.*, 2015]. (f–g) Post-collapse processes, such as erosion or strain of the caldera structure due to regional stretching (i.e., parallel to the direction of extension and orthogonal to regional faults that therefore dissect the caldera structure), may finally contribute to the caldera elongation. See the text for details. S_{Hmax} : maximum horizontal stress; S_{hmin} : minimum horizontal stress; C_1 and C_2 : primary and subsequent collapses.

In this regard, Acocella *et al.* [2002] suggested a forcing of structural inheritance in controlling the elongation of the Fantale, Kone and Gedemsa calderas (Figures 2, 5). Nevertheless, no major ESE–WNW inherited structures (i.e., parallel to caldera elongation) are exposed in the surrounding areas of the caldera (Figures 2, 5), but they occur on the plateaus as large-throw sub-vertical faults, suggesting that they may be present as buried structures beneath the rift floor (Figure 6c). These sub-vertical regional structures may have been reactivated as left-lateral strike slip structures during E–W rifting, creating preferential local areas of unclamping favourable for magma ascent and emplacement, consequently forcing caldera elongation and generating vent alignments (Figure 6c). In this model, the Wonji faults do not control the caldera structural setting and simply influence post-caldera activity by localizing points of emission outside the caldera [Acocella *et al.*, 2002, Fontijn *et al.*, 2018]. At the Corbetti Caldera (Figures 3, 5), Lloyd *et al.* [2018] hypothesize the presence of an E–W trending regional structure extending downward into the crust for at least 30 km. They propose that these structures may be related to the Goba-Bonga lineament, as also supported by detailed geological-structural analysis [Corti *et al.*, 2018] and geophysical data [Lavayssière *et al.*, 2019], and suggest a similar model to Acocella *et al.* [2002] for magma emplacement and caldera elongation. Conversely, Casey *et al.* [2006] suggested an active role of regional stretching on the elongation of the calderas along the MER, as the mechanism sketched in Figure 6g. Besides, the regional stress field may induce magma chamber elongation, as sketched in Figure 6a. In our interpretation, these two mechanism can explain the average E–W to ESE–WNW trend of caldera elongation along the MER, which is coherent with the \approx E–W direction of regional extension (cf. with Figure 5). Out of the examined calderas, only Duguna shows a moderate NNE–SSW elongation (Figure 5), and we speculate that it may follow the trend of regional structures (Figure 6b), which is there represented by the boundary faults (Figure 4).

Poly-phased collapse, producing nested calderas, was suggested by Rampey *et al.* [2010] for the Kone Caldera, in contrast with the hypothesis of a tectonic control exerted by E–W regional structures proposed by Acocella *et al.* [2002], as well as with the stretching of the magma chamber under regional

stress. Likely, poly-phased collapse also occurred at other calderas along the MER (e.g., Shala Caldera). Nonetheless, for several calderas showing marked elongation, it unlikely represents the main mechanism leading to an elliptical shape, since no other major nested calderas are observed (e.g. Fantale, Aluto and Corbetti calderas).

Inherited local structures may have played a role during the collapse of specific calderas along the MER (e.g., reactivated as caldera faults). For example, some margins of the Fantale, Kone, Gedemsa and Corbetti calderas (Figures 2 and 3) are indicated by Acocella *et al.* [2002] and Hunt *et al.* [2019] as fault-controlled, and likely resulted from the reactivation of inherited structures during the collapse (Figure 6e).

Although post-caldera erosion (Figure 6f) represents an active mechanism occurring at several calderas, as testified by many embayments visible along caldera margins [Hunt *et al.*, 2019; e.g., Awasa and Shala calderas, Figure 3b, c], this process seems to act at a different (smaller) scale to justify the marked elongation of some of the examined calderas (e.g., Fantale, Corbetti), where caldera margins are still well traceable. Therefore, in our interpretation it cannot be considered as a main mechanism shaping elongated calderas in the MER.

Overall, based on the above considerations, we infer that elongation of the magmatic chamber and the regional stretching are the most effective mechanism controlling the elliptical caldera geometry of the considered MER calderas (Figure 5). As noted earlier, the first process may reflect the influence of the regional stress (Figure 6a) or possibly the effect exerted by inherited crustal structures along which magma is preferentially emplaced as an oblate magma body, resulting afterward in an elongated collapse (Figure 6c). Beside, regional stretching may at least in part contribute to elongate calderas after collapse [Casey *et al.*, 2006; Figure 6g], as several calderas are dissected by regional faults trending to an high angle to the caldera major axis (i.e., the caldera elongation; Figure 5). Nonetheless, this mechanism cannot represent the exclusive mechanism, as normal faults observed in the area are not sufficient to justify caldera elongation. We therefore suggest that these processes (i.e., magmatic chamber elongation, inherited crustal structures reactivation and regional stretching) are the main concurring mechanisms driving the forma-

tion of elongated calderas along the MER, although other processes may contribute to caldera elongation globally (Figure 6d, e, f).

5. Concluding remarks

In this study, we have reviewed the structural characteristics of the main collapsed calderas that occur along the axis of the Northern, Central and Southern sectors of the Main Ethiopian Rift. These peralkaline calderas bear a strong linkage with the tectonics of this continental rift, showing several features suggesting a tectonic control on their development. Specifically, most of the examined calderas have a moderate to marked elongation and some of them (e.g., Fantale, Kone, Gedemsa and Corbetti calderas) have experienced a tectonic control exerted by pre-existing faults reactivated during the collapse (i.e., fault-controlled caldera rim; Figure 6e). Although poly-phased collapse leading to nested calderas (Figure 6d) may explain the elongation of some of the examined calderas (e.g., Shala and Kone volcanic complexes), it is not observed at other calderas, for which different mechanisms should be taken into account. Finally, post-collapse processes (e.g., caldera erosion; Figure 6f) likely act at a different (local) scale to justify markedly elongated calderas. We therefore propose that the main mechanisms responsible for caldera elongation along the MER are likely related to the elongation of the subsurface magma body and to regional stretching. Magma chamber elongation may depend on the regional stress field (Figure 6a, b) or the presence of regional existing structures reactivated during the emplacement of magma (Figure 6c). Regional stretching may at least partly contribute to elongate circular collapsed calderas (Figure 6g). Nonetheless, future studies are required to better define the main controls on caldera development and elongation in the MER, as well as to further investigate the relationships with tectonic processes.

Acknowledgements

We would like to thank Bruno Scaillet for inviting us to contribute to this special Volume. We are grateful to Hugues Raimbourg and to an anonymous Reviewer for their helpful comments that greatly improved the quality of our manuscript. This work has been funded by the Italian Ministero

dell'Università e della Ricerca (MiUR) through PRIN Grant 2017P9AT72.

References

- Acocella, V. (2007). Understanding caldera structure and development: An overview of analogue models compared to natural calderas. *Earth Sci. Rev.*, 85(3–4), 125–160.
- Acocella, V., Funiciello, R., Marotta, E., Orsi, G., and De Vita, S. (2004). The role of extensional structures on experimental calderas and resurgence. *J. Volcanol. Geotherm. Res.*, 129(1–3), 199–217.
- Acocella, V., Korme, T., Salvini, F., and Funiciello, R. (2002). Elliptic calderas in the Ethiopian Rift: control of pre-existing structures. *J. Volcanol. Geotherm. Res.*, 119(1–4), 189–203.
- Agostini, A., Bonini, M., Corti, G., Sani, F., and Manetti, P. (2011b). Distribution of Quaternary deformation in the central main Ethiopian rift, East Africa. *Tectonics*, 30, article no. TC4010.
- Agostini, A., Bonini, M., Corti, G., Sani, F., and Mazzarini, F. (2011a). Fault architecture in the Main Ethiopian Rift and comparison with experimental models: implications for rift evolution and Nubia–Somalia kinematics. *Earth Planet. Sci. Lett.*, 301(3–4), 479–492.
- Balestrieri, M. L., Bonini, M., Corti, G., Sani, F., and Philippson, M. (2016). A refinement of the chronology of rift-related faulting in the Broadly Rifted Zone, southern Ethiopia, through apatite fission-track analysis. *Tectonophysics*, 671, 42–55.
- Bastow, I. D., Nyblade, A. A., Stuart, G. W., Rooney, T. O., and Benoit, M. H. (2008). Upper mantle seismic structure beneath the Ethiopian hot spot: rifting at the edge of the African low-velocity anomaly. *Geochemistry, Geophys. Geosystems*, 9, article no. Q12022.
- Bastow, I. D., Pilidou, S., Kendall, J. M., and Stuart, G. W. (2010). Melt-induced seismic anisotropy and magma assisted rifting in Ethiopia: evidence from surface waves. *Geochemistry, Geophys. Geosystems*, 11(6). <https://doi.org/10.1029/2010GC003036>.
- Bastow, I. D., Stuart, G. W., Kendall, J. M., and Ebinger, C. J. (2005). Upper-mantle seismic structure in a region of incipient continental breakup: northern Ethiopian rift. *Geophys. J. Int.*, 162(2), 479–493.
- Benvenuti, M., Carnicelli, S., Belluomini, G., Dainelli, N., Di Grazia, S., Ferrari, G. A., Iasio, C., Sagri,

- M., Ventra, D., Atnafu, B., and Kebede, S. (2002). The Ziway–Shala lake basin (main Ethiopian rift, Ethiopia): a revision of basin evolution with special reference to the Late Quaternary. *J. Afr. Earth Sci.*, 35(2), 247–269.
- Bigazzi, G., Bonadonna, F. P., Di Paola, G. M., and Giuliani, A. (1993). K–Ar and fission track ages of the last volcano-tectonic phase in the Ethiopian Rift Valley (Tullu Moye area). In Abbate, E., Sagri, M., and Sassi, F. P., editors, *Geology and Mineral Resources of Somalia and Surrounding Regions*, volume 113 of *Relazi Monogr. Agrarie Subtrop. Trop.*, pages 311–322. Ist. Agron. per l'Oltremare, Florence, Italy.
- Bilham, R., Bendick, R., Larson, K., Mohr, P., Braun, J., Tesfaye, S., and Asfaw, L. (1999). Secular and tidal strain across the Main Ethiopian Rift. *Geophys. Res. Lett.*, 26(18), 2789–2792.
- Boccaletti, M., Bonini, M., Mazzuoli, R., Abebe, B., Piccardi, L., and Tortorici, L. (1998). Quaternary oblique extensional tectonics in the Ethiopian Rift (Horn of Africa). *Tectonophysics*, 287(1–4), 97–116.
- Boccaletti, M., Mazzuoli, R., Bonini, M., Trua, T., and Abebe, B. (1999). Plio-Quaternary volcanotectonic activity in the northern sector of the Main Ethiopian Rift: relationships with oblique rifting. *J. Afr. Earth Sci.*, 29(4), 679–698.
- Bonini, M. (2012). Mud volcanoes: indicators of stress orientation and tectonic controls. *Earth Sci. Rev.*, 115(3), 121–152.
- Bonini, M., Corti, G., Innocenti, F., Manetti, P., Mazzarini, F., Abebe, T., and Pecskey, Z. (2005). Evolution of the Main Ethiopian Rift in the frame of Afar and Kenya rifts propagation. *Tectonics*, 24(1), article no. TC1007.
- Bonini, M., Maestrelli, D., Corti, G., Del Ventisette, C., Moratti, G., Carrasco-Núñez, G., Giordano, G., Lucci, F., Norini, G., Piccardi, L., Urbani, S., and Montanari, D. (2021). Modeling intra-caldera resurgence settings: laboratory experiments with application to the Los Humeros Volcanic Complex (Mexico). *J. Geophys. Res. Solid Earth*, 126(3), article no. e2020JB020438.
- Bonini, M., Sokoutis, D., Mulugeta, G., Boccaletti, M., Corti, G., Innocenti, F., Manetti, P., and Mazzarini, F. (2001). Dynamics of magma emplacement in centrifuge models of continental extension with implications for flank volcanism. *Tectonics*, 20, 1053–1065.
- Bonini, M., Souriot, T., Boccaletti, M., and Brun, J. P. (1997). Successive orthogonal and oblique extension episodes in a rift zone: laboratory experiments with application to the Ethiopian Rift. *Tectonics*, 16(2), 347–362.
- Bosworth, W., Burke, K., and Strecker, M. (2000). Magma chamber elongation as an indicator of intraplate stress field orientation: “borehole breakout mechanism” and examples from the Late Pleistocene to Recent Kenya Rift Valley. In: (Ed.) Mark Jessell, and Janos Urai, Stress strain and structure, a volume in honour of Win D. Means. *J. Virtual Explor.*, 2, article no. 5. Electronic Edition, ISSN 1441-8142.
- Bosworth, W., Burke, K., and Strecker, M. (2003). Effect of stress fields on magma chamber stability and the formation of collapse calderas. *Tectonics*, 22(4). <https://doi.org/10.1029/2002TC001369>.
- Casey, M., Ebinger, C., Keir, D., Gloaguen, R., and Mohamed, F. (2006). Strain accommodation in transitional rifts: extension by magma intrusion and faulting in Ethiopian rift magmatic segments. *Geol. Soc. Lond. Spec. Publ.*, 259(1), 143–163.
- Chernet, T. (2005). Geological and hydrothermal alteration mapping of the Dofen geothermal prospect and adjacent western escarpment (Ethiopia). In *Proceedings of the World Geothermal Congress, Antalya, Turkey*, pages 24–29.
- Chernet, T. (2011). Geology and hydrothermal resources in the northern Lake Abaya area (Ethiopia). *J. Afr. Earth Sci.*, 61(2), 129–141.
- Chernet, T. and Hart, W. K. (1999). Petrology and geochemistry of volcanism in the northern Main Ethiopian Rift-southern Afar transition region. *Acta Vulcanol.*, 11, 21–42.
- Chorowicz, J., Collet, B., Bonavia, F. F., and Korme, T. (1994). Northwest to north-northwest extension direction in the Ethiopian rift deduced from the orientation of extension structures and fault-slip analysis. *Geol. Soc. Am. Bull.*, 106(12), 1560–1570.
- Chu, D. and Gordon, R. G. (1999). Evidence for motion between Nubia and Somalia along the Southwest Indian Ridge. *Nature*, 398(6722), 64–67.
- Cole, J. W. (1969). Gariboldi volcanic complex, Ethiopia. *Bull. Volcanol.*, 33(2), 566–578.
- Corti, G. (2008). Control of rift obliquity on the evolution and segmentation of the main Ethiopian rift. *Nat. Geosci.*, 1, 258–262.
- Corti, G. (2009). Continental rift evolution: from

- rift initiation to incipient break-up in the Main Ethiopian Rift, East Africa. *Earth Sci. Rev.*, 96(1–2), 1–53.
- Corti, G., Cioni, R., Franceschini, Z., Sani, F., Scaillet, S., Molin, P., Isola, I., Mazzarini, F., Brune, S., Keir, D., Erbello, A., Muluneh, A., Illsley-Kemp, F., and Glerum, A. (2019). Aborted propagation of the Ethiopian rift caused by linkage with the Kenyan rift. *Nat. Commun.*, 10(1), 1–11.
- Corti, G., Sani, F., Agostini, S., Philippon, M., Sokoutis, D., and Willingshofer, E. (2018). Off-axis volcano-tectonic activity during continental rifting: Insights from the transversal Goba-Bonga lineament, Main Ethiopian Rift (East Africa). *Tectonophysics*, 728, 75–91.
- Corti, G., Sani, F., Philippon, M., Sokoutis, D., Willingshofer, E., and Molin, P. (2013). Quaternary volcano-tectonic activity in the Soddo region, western margin of the Southern Main Ethiopian Rift. *Tectonics*, 32(4), 861–879.
- Di Paola, G. M. (1971). Geology of the Corbetti Caldera area (Main Ethiopian Rift Valley). *Bull. Volcanol.*, 35(2), 497–506.
- Di Paola, G. M. (1972). The Ethiopian Rift Valley (between 7°00' and 8°40' lat. north). *Bull. Volcanol.*, 36(4), 517–560.
- Druitt, T. H. and Sparks, R. S. J. (1984). On the formation of calderas during ignimbrite eruptions. *Nature*, 310(5979), 679–681.
- Ebinger, C. J. and Casey, M. (2001). Continental breakup in magmatic provinces: an Ethiopian example. *Geology*, 29(6), 527–530.
- Fernandes, R. M. S., Ambrosius, B. A. C., Noomen, R., Bastos, L., Combrinck, L., Miranda, J. M., and Spakman, W. (2004). Angular velocities of Nubia and Somalia from continuous GPS data: implications on present-day relative kinematics. *Earth Planet. Sci. Lett.*, 222(1), 197–208.
- Fontijn, K., McNamara, K., Tadesse, A. Z., Pyle, D. M., Dessalegn, F., Hutchison, W., Mather, T. A., and Yirgu, G. (2018). Contrasting styles of post-caldera volcanism along the Main Ethiopian Rift: implications for contemporary volcanic hazards. *J. Volcanol. Geotherm. Res.*, 356, 90–113.
- Geyer, A. and Marti, J. (2008). The new worldwide collapse caldera database (CCDB): a tool for studying and understanding caldera processes. *J. Volcanol. Geotherm. Res.*, 175(3), 334–354.
- Gibson, I. L. (1969). The structure and volcanic geology of an axial portion of the Main Ethiopian Rift. *Tectonophysics*, 8(4–6), 561–565.
- Giordano, F., D'Antonio, M., Civetta, L., Tonarini, S., Orsi, G., Ayalew, D., Yirgu, G., Dell'Erba, F., Di Vito, M. A., and Isaia, R. (2014). Genesis and evolution of mafic and felsic magmas at Quaternary volcanoes within the Main Ethiopian Rift: insights from Gedemsa and Fanta 'Ale complexes. *Lithos*, 188, 130–144.
- Gudmundsson, M. T., Jónsdóttir, K., Hooper, A., et al. (2016). Gradual caldera collapse at Bárðarbunga volcano, Iceland, regulated by lateral magma outflow. *Science*, 353(6296). <https://doi.org/10.1126/science.aaf8988>.
- Hayward, N. J. and Ebinger, C. J. (1996). Variations in the along-axis segmentation of the Afar Rift system. *Tectonics*, 15(2), 244–257.
- Holohan, E. P., de Vries, B. V. W., and Troll, V. R. (2008). Analogue models of caldera collapse in strike-slip tectonic regimes. *Bull. Volcanol.*, 70(7), 773–796.
- Holohan, E. P., Troll, V. R., Walter, T. R., Münn, S., McDonnell, S., and Shipton, Z. K. (2005). Elliptical calderas in active tectonic settings: an experimental approach. *J. Volcanol. Geotherm. Res.*, 144(1–4), 119–136.
- Hunt, J. A., Pyle, D. M., and Mather, T. A. (2019). The geomorphology, structure, and lava flow dynamics of peralkaline rift volcanoes from high-resolution digital elevation models. *Geochemistry, Geophys. Geosystems*, 20, 1508–1538.
- Hutchison, W., Fusillo, R., Pyle, D. M., Mather, T. A., Blundy, J. D., Biggs, J., Yirgu, G., Cohen, B. E., Brooker, R. A., Barfod, D. N., and Calvert, A. T. (2016a). A pulse of mid-Pleistocene rift volcanism in Ethiopia at the dawn of modern humans. *Nat. Commun.*, 7(1), 1–12.
- Hutchison, W., Mather, T. A., Pyle, D. M., Biggs, J., and Yirgu, G. (2015). Structural controls on fluid pathways in an active rift system: A case study of the Aluto volcanic complex. *Geosphere*, 11(3), 542–562.
- Hutchison, W., Pyle, D. M., Mather, T. A., Yirgu, G., Biggs, J., Cohen, B. E., Barfod, D. N., and Lewi, E. (2016b). The eruptive history and magmatic evolution of Aluto volcano: new insights into silicic peralkaline volcanism in the Ethiopian rift. *J. Volcanol. Geotherm. Res.*, 328, 9–33.
- Keir, D., Ebinger, C. J., Stuart, G. W., Daly, E., and

- Ayele, A. (2006). Strain accommodation by magmatism and faulting as rifting proceeds to breakup: seismicity of the northern Ethiopian rift. *J. Geophys. Res. Solid Earth*, 111(B5), article no. B05314.
- Kendall, J. M., Stuart, G. W., Ebinger, C. J., Bastow, I. D., and Keir, D. (2005). Magma-assisted rifting in Ethiopia. *Nature*, 433(7022), 146–148.
- Keranen, K. and Klemperer, S. L. (2008). Discontinuous and diachronous evolution of the Main Ethiopian Rift: implications for the development of continental rifts. *Earth Planet. Sci. Lett.*, 265, 96–111.
- Keranen, K., Klemperer, S. L., Gloaguen, R., and Group, E. W. (2004). Three-dimensional seismic imaging of a protoridge axis in the Main Ethiopian rift. *Geology*, 32(11), 949–952.
- Keranen, K., Klemperer, S. L., Julia, J., Lawrence, J. L., and Nyblade, A. (2009). Low lower-crustal velocity across Ethiopia: is the Main Ethiopian Rift a narrow rift in a hot craton? *Geochemistry, Geophys. Geosystems*, 10, article no. Q0AB01.
- Kieffer, B., Arndt, N., Lapierre, H., Bastien, F., Bosch, D., Pecher, A., Yirgu, G., Ayalew, D., Weis, D., Jerram, D. A., Keller, F., and Meugniot, C. (2004). Flood and shield basalts from Ethiopia: magmas from the African superswell. *J. Petrol.*, 45(4), 793–834.
- Korme, T., Chorowicz, J., Collet, B., and Bonavia, F. F. (1997). Volcanic vents rooted on extension fractures and their geodynamic implications in the Ethiopian Rift. *J. Volcanol. Geotherm. Res.*, 79(3–4), 205–222.
- Kurz, T., Gloaguen, R., Ebinger, C., Casey, M., and Abebe, B. (2007). Deformation distribution and type in the Main Ethiopian Rift (MER): a remote sensing study. *J. Afr. Earth Sci.*, 48(2–3), 100–114.
- Lavayssière, A., Greenfield, T., Keir, D., Ayele, A., and Kendall, J. M. (2019). Local seismicity near the actively deforming Corbetti volcano in the Main Ethiopian Rift. *J. Volcanol. Geotherm. Res.*, 381, 227–237.
- Le Turdu, C., Tiercelin, J.-J., Gibert, E., Travi, Y., Lezar, K.-E., Richert, J.-P., Massault, M., Gasse, F., Bonnefille, R., Decobert, M., Gensous, B., Jeudy, V., Tamrat, E., Mohammed, M. U., Martens, K., Atanafu, B., Chernet, T., Williamson, D., and Taieb, M. (1999). The Ziway–Shala lake basin system, Main Ethiopian Rift: influence of volcanism, tectonics, and climatic forcing on basin formation and sedimentation. *Palaeogeogr. Palaeoclimatol. Palaeoecol.*, 150(3–4), 135–177.
- Lipman, P. W. (1984). The roots of ash flow calderas in western North America: windows into the tops of granitic batholiths. *J. Geophys. Res. Solid Earth*, 89(B10), 8801–8841.
- Lipman, P. W. (1997). Subsidence of ash-flow calderas: relation to caldera size and magma-chamber geometry. *Bull. Volcanol.*, 59(3), 198–218.
- Lloyd, R., Biggs, J., Wilks, M., Nowacki, A., Kendall, J.-M., Ayele, A., Lewi, E., and Eysteinnsson, H. (2018). Evidence for cross rift structural controls on deformation and seismicity at a continental rift caldera. *Earth Planet. Sci. Lett.*, 487, 190–200.
- Maestrelli, D., Bonini, M., Corti, G., Del Ventisette, C., Moratti, G., and Montanari, D. (2021a). Exploring fault propagation and the role of inherited structures during caldera collapse through laboratory experiments. *J. Volcanol. Geotherm. Res.*, 414, article no. 107232.
- Maestrelli, D., Bonini, M., Corti, G., Del Ventisette, C., Moratti, G., and Montanari, D. (2021b). A database of laboratory analogue models of caldera collapse testing the role of inherited structures. *Front. Earth Sci.*, 9, article no. 618258.
- Maestrelli, D., Montanari, D., Corti, G., Del Ventisette, C., Moratti, G., and Bonini, M. (2020). Exploring the interactions between rift propagation and inherited crustal fabrics through experimental modeling. *Tectonics*, 39(12), article no. e2020TC006211.
- Mazzarini, F., Musumeci, G., Montanari, D., and Corti, G. (2010). Relations between deformation and upper crustal magma emplacement in laboratory physical models. *Tectonophysics*, 484, 139–146.
- Meyer, W., Pilger, A., Rosler, A., and Stets, J. (1975). Tectonic evolution of the northern part of the Main Ethiopian Rift in Southern Ethiopia. In Pilger, A. and Rosler, A., editors, *Afar Depression of Ethiopia*, pages 352–362. Schweizerbart, Stuttgart.
- Minissale, A., Corti, G., Tassi, F., Darrah, T. H., Vaselli, O., Montanari, D., Montegrossi, G., Yirgu, G., Selmo, E., and Teclu, A. (2017). Geothermal potential and origin of natural thermal fluids in the northern Lake Abaya area, Main Ethiopian Rift, East Africa. *J. Volcanol. Geotherm. Res.*, 336, 1–18.
- Mohr, P., Mitchell, J. G., and Reynolds, R. G. H. (1980). Quaternary volcanism and faulting at O'a Caldera, Central Ethiopian Rift. *Bull. Volcanol.*, 43(1), 173.
- Mohr, P. and Zanettin, B. (1988). The Ethiopian flood basalt province. In *Continental Flood Basalts*,

- pages 63–110. Springer, Dordrecht.
- Mohr, P. A. (1962a). Surface cauldron subsidence with associated faulting and fissure basalt eruptions at Gariboldi Pass, Shoa, Ethiopia. *Bull. Volcanol.*, 24(1), 421–428.
- Mohr, P. A. (1962b). The Ethiopian Rift system. *Bull. Geophys. Observ. Addis Ababa*, 5, 33–62.
- Mohr, P. A. (1967). The Ethiopian Rift system. *Bull. Geophys. Observ. Addis Ababa*, 11, 1–65.
- Mohr, P. A. and Wood, C. A. (1976). Volcano spacings and lithospheric attenuation in the Eastern Rift of Africa. *Earth Planet. Sci. Lett.*, 33(1), 126–144.
- Montanari, D., Del Ventisette, C., and Bonini, M. (2020). Lateral magma migration through interconnected sills: Evidence from analogue modeling. *Earth Planet. Sci. Lett.*, 551, article no. 116568.
- Morton, W. H., Rex, D. C., Mitchell, J. G., and Mohr, P. (1979). Riftward younging of volcanic units in the Addis Ababa region, Ethiopian rift valley. *Nature*, 280(5720), 284–288.
- Neal, C. A., Brantley, S. R., Antolik, L., et al. (2019). The 2018 rift eruption and summit collapse of Kīlauea Volcano. *Science*, 363(6425), 367–374.
- Newhall, C. G. and Dzurisin, D. (1988). *Historical Unrest at the Large Calderas of the World. Vol. 2*, volume 1855 of *US Geological Survey*. Department of the Interior.
- Peccerillo, A., Barberio, M. R., Yirgu, G., Ayalew, D., Barbieri, M., and Wu, T. W. (2003). Relationships between mafic and peralkaline silicic magmatism in continental rift settings: a petrological, geochemical and isotopic study of the Gedemsa volcano, central Ethiopian rift. *J. Petrol.*, 44(11), 2003–2032.
- Peccerillo, A., Gezahegn, Y., and Dereje, A. (1995). Genesis of acid volcanics along the Main Ethiopian Rift: a case history of the Gedemsa volcano. *Sinet*, 18(1), 23–50.
- Pizzi, A., Coltorti, M., Abebe, B., Disperati, L., Sacchi, G., and Salvini, R. (2006). The Wonji fault belt (Main Ethiopian Rift): structural and geomorphological constraints and GPS monitoring. *Geol. Soc. Lond. Spec. Publ.*, 259(1), 191–207.
- Rampey, M. L., Oppenheimer, C., Pyle, D. M., and Yirgu, G. (2010). Caldera-forming eruptions of the Quaternary Kone volcanic complex, Ethiopia. *J. Afr. Earth Sci.*, 58(1), 51–66.
- Robertson, E. A. M., Biggs, J., Cashman, K. V., Floyd, M. A., and Vye-Brown, C. (2015). Influence of regional tectonics and pre-existing structures on the formation of elliptical calderas in the Kenyan Rift. *Geol. Soc. Lond. Spec. Publ.*, 420(1), 43–67.
- Roche, O. and Druitt, T. H. (2001). Onset of caldera collapse during ignimbrite eruptions. *Earth Planet. Sci. Lett.*, 191(3–4), 191–202.
- Rooney, T. O. (2017). The Cenozoic magmatism of East-Africa: Part I—Flood basalts and pulsed magmatism. *Lithos*, 286, 264–301.
- Saria, E., Calais, E., Stamps, D. S., Delvaux, D., and Hartnady, C. J. H. (2014). Present-day kinematics of the East African Rift. *J. Geophys. Res. Solid Earth*, 119(4), 3584–3600.
- Sigmundsson, F. (2019). Calderas collapse as magma flows into rifts. *Science*, 366(6470), 1200–1201.
- Spera, F. J. and Crisp, J. A. (1981). Eruption volume, periodicity, and caldera area: relationships and inferences on development of compositional zonation in silicic magma chambers. *J. Volcanol. Geotherm. Res.*, 11(2–4), 169–187.
- Stamps, D. S., Kreemer, C., Fernandes, R., Rajaonarison, T. A., and Rambolamanana, G. (2021). Redefining East African Rift System kinematics. *Geology*, 49(2), 150–155.
- Temtime, T., Biggs, J., Lewi, E., and Ayele, A. (2020). Evidence for active rhyolitic dike intrusion in the Northern Main Ethiopian Rift from the 2015 Fentale Seismic Swarm. *Geochemistry, Geophys. Geosystems*, 21(6), article no. e2019GC008550.
- Trua, T., Deniel, C., and Mazzuoli, R. (1999). Crustal control in the genesis of Plio-Quaternary bimodal magmatism of the Main Ethiopian Rift (MER): geochemical and isotopic (Sr, Nd, Pb) evidence. *Chem. Geol.*, 155, 201–231.
- Wadge, G., Biggs, J., Lloyd, R., and Kendall, J. M. (2016). Historical volcanism and the state of stress in the East African Rift System. *Front. Earth Sci.*, 4, article no. 86.
- Williams, F. M., Williams, M. A. J., and Aumento, F. (2004). Tensional fissures and crustal extension rates in the northern part of the Main Ethiopian Rift. *J. Afr. Earth Sci.*, 38(2), 183–197.
- Williams, H. (1941). Calderas and their origin. *Univ. Calif. Publ. Geol. Sci.*, 21, 239–346.
- WoldeGabriel, G., Aronson, J. L., and Walter, R. C. (1990). Geology, geochronology, and rift basin development in the central sector of the Main Ethiopia Rift. *Geol. Soc. Am. Bull.*, 102, 439–458.
- WoldeGabriel, G., Walter, R. C., Aronson, J. L., and

Hart, W. K. (1992). Geochronology and distribution of silicic volcanic rocks of Plio-Pleistocene age from the central sector of the Main Ethiopian Rift. *Quat. Int.*, 13, 69–76.

WoldeGabriel, G., Walter, R. C., Hart, W. K., Mertzman, S. A., and Aronson, J. L. (1999). Temporal relations and geochemical features of felsic volcanism in the central sector of the Main Ethiopian Rift. *Acta Vulcanol.*, 11, 53–68.



Perspectives on alkaline magmas / *Perspectives sur les magmas alcalins*

Volcanological evolution of Pantelleria Island (Strait of Sicily) peralkaline volcano: a review

Silvio G. Rotolo^{*, a, b}, Stéphane Scaillet^c, Fabio Speranza^d, John C. White^e,
Rebecca Williams^f and Nina J. Jordan^g

^a Dipartimento di Scienze della Terra e del Mare, Università di Palermo, Via Archirafi 22, 90123 Palermo, Italy

^b Istituto Nazionale di Geofisica e Vulcanologia, Sezione Palermo, Via U. La Malfa 153, 90146, Palermo, Italy

^c CNRS, Institut des Sciences de la Terre d'Orléans (ISTO), 1A rue de la Ferrollerie, 45071, Orléans, France

^d Istituto Nazionale di Geofisica e Vulcanologia, Sezione Roma 2, Via di Vigna Murata 605, 00143 Rome, Italy

^e Department of Geosciences, Eastern Kentucky University, 521 Lancaster Avenue, Richmond KY 40475, USA

^f Department of Geog., Geol. and Envir. University of Hull, Cottingham Road, Hull, HU6 7RX, UK

^g School of Geog., Geol. and Envir., University of Leicester, University Road, Leicester LE1 7RH, UK

E-mails: silvio.rotolo@unipa.it (S. G. Rotolo), stephane.scaillet@cnrs-orleans.fr (S. Scaillet), fabio.speranza@ingv.it (F. Speranza), john.white@eku.edu (J. C. White), Rebecca.Williams@hull.ac.uk (R. Williams), njj5@leicester.ac.uk (N. J. Jordan)

Abstract. Pantelleria volcano has a particularly intriguing evolutionary history intimately related to the peralkaline composition of its explosively erupted magmas. Due to the stratigraphic complexity, studies over the last two decades have explored either only the pre-Green Tuff ignimbrite volcanism or the post-Green Tuff activity. We here focus on the whole evolutionary history, detailing the achievements since the first pioneering studies, in order to illustrate how the adoption and integration of progressively more accurate methods ($^{40}\text{Ar}/^{39}\text{Ar}$, paleomagnetism, petrography, and detailed field study) have provided many important independent answers to unresolved questions. We also discuss rheomorphism, a distinct feature at Pantelleria, at various scales and possible evidence for multiple, now hidden, caldera collapses. Although the evolutionary history of Pantelleria has shown that each ignimbrite event was followed by a period of less intense explosivity (as could be the present-day case), new geochronological and geochemical data may indicate a long-term waning of volcanic activity.

Keywords. Peralkaline volcanism, Ignimbrites, Paleomagnetism, $^{40}\text{Ar}/^{39}\text{Ar}$, Rheomorphism.

Available online 31st March 2021

* Corresponding author.

1. Introduction

Throughout its geologic history, the island of Pantelleria (Figure 1), the type locality of peralkaline rhy-

olitic (pantelleritic) magmatism, has been the setting for dominantly explosive volcanism. The relatively low viscosity of these magmas make the pyroclastic deposits particularly prone to rheomorphism and welding, which obscures primary textural and architectural features. This peculiarity, coupled with discontinuous field exposures and a remarkably complex evolutionary history (*viz.*, overlapping explosive events), has contributed to the difficulty in the advancement of our volcano-stratigraphic knowledge of the island. For these reasons, Pantelleria has been paradigmatic in the establishment of integrated field and geochemical techniques in unraveling the volcanic evolution of such active centers.

In order to appreciate fully the evolution of the volcanic stratigraphy at Pantelleria, we briefly review the history of geologic studies on this island that began with Gemmellaro [1829], who reported the results from his field surveys that he integrated with reports from contemporary naturalists. More than fifty years elapsed before Förstner [1881] published the next study of the island, which included a generalized geologic map (1:100.000) and, most significantly, a few chemical analyses of minerals and of a very peculiar and previously undescribed alkali- and silica-rich effusive rock, for which he proposed the name *pantellerite*. In October 1891, a submarine basaltic eruption 5 km west-northwest offshore of Pantelleria town attracted the attention of naturalist and astronomer Riccò [1892], who precisely described the evolution of the eruption, including exploding scoria at sea now known as *lava balloons*. Significantly, he paid great attention to pre- and syn-eruptive phenomena, such as earthquake swarms, bradyseisms, and other macroseismic effects. These early studies [including Bergeat, 1907] sparked the interest of the American petrographer H. S. Washington, who conducted a field campaign in 1905 and subsequently published three papers [Washington, 1913a,b, 1914] that are now considered the foundation for all later studies, not only for the detailed geological descriptions, but especially for the in-depth discussion of the petrography of pantellerite rocks that much improved the early analytical efforts of Förstner.

There was renewed interest in the geology of Pantelleria during the 1960s, with most studies focused on the volcanology of the island. Borsi *et al.* [1963] published a general overview, and Rittmann

[1967] provided the first detailed study of the volcanic stratigraphy in which he distinguished several ignimbrite and pumice fallout deposits, recognized the central caldera structure, and produced a detailed geological map (1:25.000) of the island. His conclusions were confirmed and further developed in several publications by his collaborator Villari [1969, 1970, 1974], who proposed a basic stratigraphy that recognized several ignimbrite units. In particular, Villari focused on the “*Green ignimbrite*”, the youngest and most widespread pyroclastic unit on the island, whose ignimbritic nature was confirmed by Schmincke [1974]. Wright [1980] was the first to attempt to unravel the complex stratigraphy and lateral correlations of the older pyroclastic units, some of which he interpreted as welded air fall deposits instead of ignimbrites. Geochronological (K–Ar) data were first presented by Barberi *et al.* [1969] and Bigazzi *et al.* [1971] and these were later followed by Cornette *et al.* [1983] and Civetta *et al.* [1984, 1988]. Cornette *et al.* [1983] recognized two partially overlapping caldera structures that they termed the *Lago Caldera* and *Monastero Caldera* (50 ka), the latter of which they associated with the eruption of the Green Tuff (GT). Contemporaneously, Mahood and Hildreth [1983] also described two “nested” calderas on the island, which they termed the *La Vecchia Caldera* (93 ka) and *Cinque Denti Caldera* (55 ka), which differed from those proposed by Cornette *et al.* [1983] in terms of location, size, and significance. The remarkably thorough and insightful paper of Mahood and Hildreth [1986] was ahead of its time and provided the first (and, until now, only) comprehensive and integrated description of the structure and volcanological history of the island. Mahood and Hildreth also put a major focus on the stratigraphy of the pre-GT welded and rheomorphic ignimbrites, supported by a large number of K–Ar ages.

Most of what was published over the next two decades focused on specific petrological and volcanological aspects of the geology of Pantelleria [Avanzinelli *et al.*, 2004, Behncke *et al.*, 2006, Bonaccorso and Mattia, 2000, Civetta *et al.*, 1998, De Guidi and Monaco, 2009, Esperança and Crisci, 1995, Ferla and Meli, 2006, Fulignati *et al.*, 1997, Kovalenko *et al.*, 1994, Lowenstern, 1994, Lowenstern and Mahood, 1991, Mattia *et al.*, 2007, Perugini *et al.*, 2002, Prosperini *et al.*, 2000, Stevenson and Wilson, 1997, Wall-

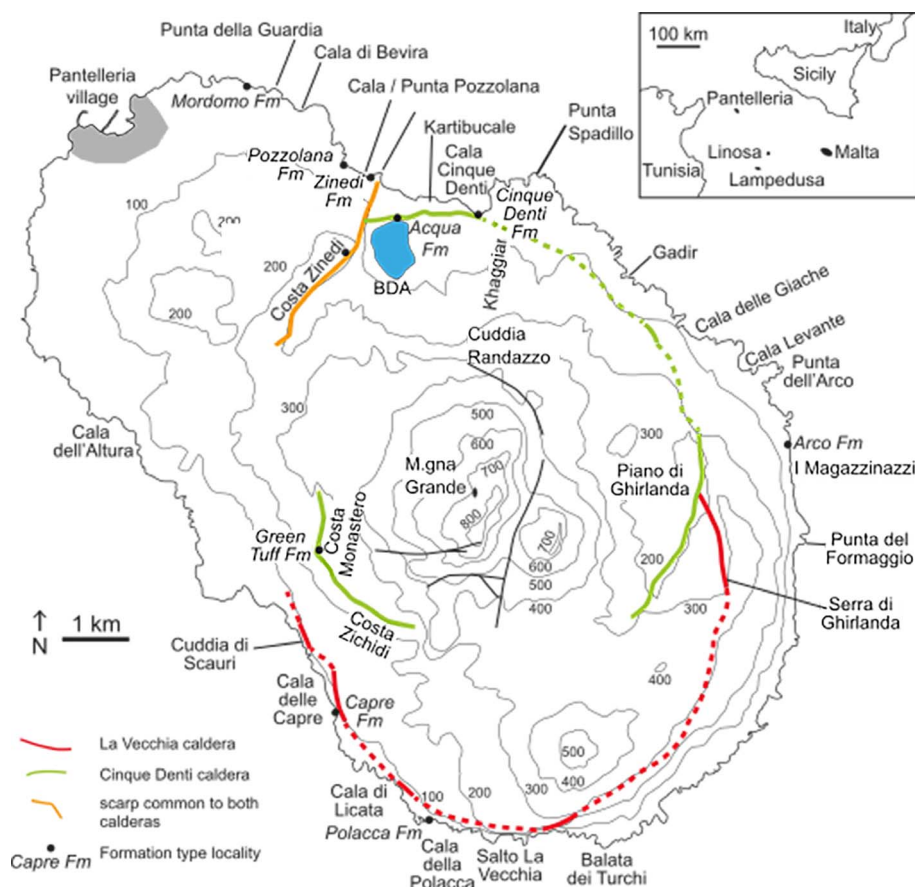


Figure 1. Map of Pantelleria with principal location names and type localities for ignimbrite formations. BDA = Bagno dell'Acqua lake.

mann *et al.*, 1988, White *et al.*, 2005, 2009], with a sharp increase in studies produced over the past ten years [Arzilli *et al.*, 2020, Avanzinelli *et al.*, 2014, Baginski *et al.*, 2018, Campagnola *et al.*, 2016, Conte *et al.*, 2014, Di Carlo *et al.*, 2010, Di Genova *et al.*, 2013, Fouré *et al.*, 2012, Gioncada and Landi, 2010, Giuffrida *et al.*, 2020, Jordan *et al.*, 2021, Hughes *et al.*, 2017, Kelly *et al.*, 2014, Lanzo *et al.*, 2013, Liszewska *et al.*, 2018, Neave, 2020, Neave *et al.*, 2012, Richard, 2015, Romano *et al.*, 2018, 2019, 2020, Romengo *et al.*, 2012, Rotolo *et al.*, 2013, 2017, Scaillet *et al.*, 2011, 2013, Speranza *et al.*, 2010, 2012, White *et al.*, 2020]. Notably missing until 2007 were stratigraphic and geochronological studies, implicitly suggesting to some extent that the great effort made during the 1980s was still considered valid and that methodological improvements in geochronological methods

had yet to come. The first $^{40}\text{Ar}/^{39}\text{Ar}$ study of a pantelleritic enclave in an ignimbrite produced the oldest age reported on Pantelleria [517 ± 19 ka, Rotolo and Villa, 2001], which defined a lower limit for the onset of pantellerite magma production and sparked new interest in the geochronology and volcanic stratigraphy of the island [Jordan *et al.*, 2018, Rotolo *et al.*, 2007, 2013, Scaillet *et al.*, 2011, 2013, Speranza *et al.*, 2010, 2012].

The principal aim of this paper is to review and summarize the existing volcano-stratigraphic knowledge of Pantelleria, which is otherwise scattered between pre- and post-GT papers. In doing so, we try to highlight how methodological improvements have had a decisive impact on developing a fully integrated stratigraphy and time-integrated evolutionary history of the system, portraying a vol-

Table 1. Comparative nomenclature of Pantelleria ignimbrites and their ages

Jordan et al. [2018]	$^{40}\text{Ar}/^{39}\text{Ar}$ age	Rotolo et al. [2013]	$^{40}\text{Ar}/^{39}\text{Ar}$ age (ka)	Speranza et al. [2012]	Mahood and Hildreth [1986]	K/Ar age (ka)	Wright [1980]
Formations		Units		Units (correlations)	Units		Units
Green Tuff	46 ^(*)				Green Tuff	45–50 47–51 ^(**)	B
Mordomo		D = Z	85	D = Z	Z	78–84	C, D, E
					D	88–97	
Acqua		F = Q	107	F	F	101–110	F, G
					Q	104–116	
Cinque Denti	128	P	123	P	P	124–133	G, g, U
				(locally = Q)			
Capre	138	Welded breccia (Br 1)	140–146	Welded breccia	Breccia	104–127	
Arco	179	S	171	S	S	162–209	
Polacca	187	M	181	M	M	169–178	G
Pozzolana	/				H	/	H
Zinedi	/				I	189	I

(*) Age from Scaillet et al. [2013]; (**) age from Civetta et al. [1988].

canological scenario that has far-reaching implications for, but not strictly limited to, other peralkaline volcanoes.

2. The pre-GT volcanological evolution

Rittmann [1967] published the first pre-GT stratigraphy based on eight measured sections and distinguished several ignimbrite and fall units, which he labeled A (younger) to G (older). Villari [1974], on the basis of field evidence and petrographic analyses, recognized several ignimbrite sheets (uncorrelated between different sections), identified a single caldera and distinguished the units as either pre- or post-caldera ignimbrites. The field-based stratigraphic study of Wright [1980], correlated seven welded tuffs across the island (without defining their type localities), plus eight other uncorrelated (minor) members. These were named using non-sequential capital letters, a rather confusing and non-intuitive nomenclature that would continue to be used until 2018. From older to younger these were: I, H, G, F, E, D, C, and B, with the youngest one corresponding to

the GT. On the basis of 37 K/Ar ages coupled with extensive field work, Mahood and Hildreth [1986] described the first detailed stratigraphy of the pre-GT eruptive cycles and units, and recognized nine informal units of welded tuffs/ignimbrites, most of which blanket the entire island. Although their stratigraphy was substantially different in many critical ways from Wright's [1980] (Table 1), they maintained and adapted his convention for naming the units (from older to younger: I, H, M, S, P, Q, F, D, Z and GT), but also did not define any type sections. They did, however, attribute a lithic-rich welded pyroclastic unit visible in the vertical scarp at Cala delle Capre as the caldera-forming unit of the La Vecchia caldera (Figure 1).

Many years later, Speranza et al. [2012] applied paleomagnetic methods to the pre-GT ignimbrites and simplified Mahood and Hildreth's [1986] stratigraphy by merging some ignimbrite units (D and Z) previously considered distinct. They also correlated two pyroclastic breccia units on the opposite sides of the island (NE: Cala Cinque Denti, SW: Cala delle Capre, Figure 1) to the La Vecchia caldera collapse

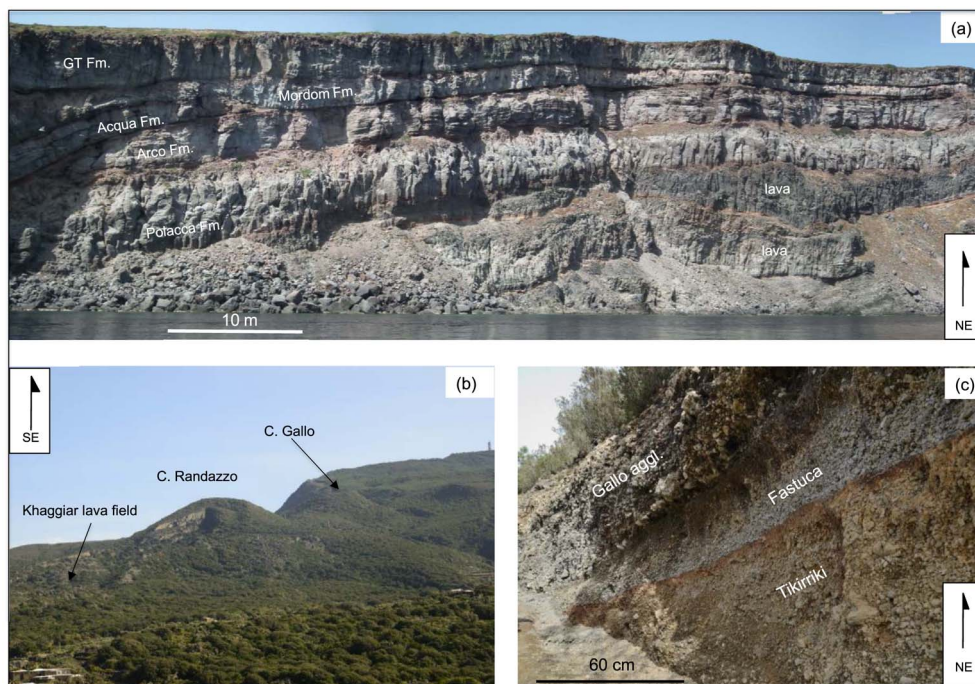


Figure 2. Pre-GT volcanism: field section at Cala della Polacca (SW). (b) Post-GT volcanism: Cuddia Randazzo pumice cone encircling a pantellerite lava dome whose break-up originated in the 2.5 km long Khaggiar lava field. (c) Post-GT volcanism: pumice deposits belonging to young eruptions (Table 2) in the road cut just south of C. Gallo.

and constrained it to 160–130 ka. These new interpretations were integrated with a new geochronological ($^{40}\text{Ar}/^{39}\text{Ar}$ laser-ablation) study of these units [Rotolo *et al.*, 2013] with the following results: (i) the age of the La Vecchia caldera collapse was more tightly constrained to 146–140 ka by dating the juvenile material in the same pyroclastic breccias studied by Speranza *et al.* [2012]; (ii) the age of eruption of other five ignimbrites was substantially refined as follows [following Mahood and Hildreth, 1986]: M = 181 ± 1.2 ka, S = 171 ± 1.7 ka, P = 123 ± 1.6 ka, F = 107 ± 1.4 ka, Z = 85 ± 1.5 ka; and (iii) the conclusion by Speranza *et al.* [2012] on the correlation of the D and Z units was confirmed and dated at 85 ka and units P and Q were also found to be correlative.

It was only after a combined field, $^{40}\text{Ar}/^{39}\text{Ar}$, and petrographic study [Jordan, 2014], later integrated later with paleomagnetic and additional $^{40}\text{Ar}/^{39}\text{Ar}$ data [Jordan *et al.*, 2018], that each of these ignimbrite units (and related pumice fallout, when present) were finally tied to a clearly defined type

locality and renamed accordingly (Table 1). This was a major step forward over the poorly defined and counter-intuitive letter-based scheme. The resulting stratigraphic reconstruction clarified the structural and volcanic dynamics of the Pantelleria edifice by better delineating paroxysmal events and their recurrence through time; they also emphasized the occurrence of an indefinite number of active local centers producing lower explosivity eruptions between each ignimbrite [inter-ignimbrite activity, Jordan, 2014, Jordan *et al.*, 2018]. The erupted (onshore) volumes of these ignimbrites, although limited by the impossibility of knowing the amount of tephra deposited at sea, varied between 0.15 to 0.64 km^3 (D.R.E.), the largest of these belonging to the Polacca Fm. (187 ± 2 ka, Figure 2a) [Jordan *et al.*, 2018]. An important observation of Jordan [2014] and Jordan *et al.* [2018] is the occurrence of lithic breccias in five different ignimbrites, strongly suggesting that at least five caldera collapses occurred, although their morpho-structural

Table 2. Comparison of ages determined with different methods for four key post-GT eruptions

	$^{40}\text{Ar}/^{39}\text{Ar}^{(1)}$	P-mag ⁽²⁾	K/Ar ⁽³⁾	$^{14}\text{C}^{(1)}$	$^{14}\text{C}^{(4)}$	$^{14}\text{C}^{(5)}$
Gallo	7.09 ± 0.8	5.9–6.2			3.03 ± 0.3	5.7 ± 0.1
Randazzo fall			8.2 ± 1.7		5.42 ± 0.22	
					5.75 ± 0.08	
Khaggiar lava flow	8.0 ± 0.8	5.9–6.2	5.5 ± 5.0			
			8.5 ± 4.5			
			11.0 ± 3.0			
Fastuca	9.70 ± 0.6	6.2–6.8		$6.0\text{--}5.8 \pm 0.03$		6.1 ± 0.1

⁽¹⁾Scaillet et al. [2011]; ⁽²⁾Speranza et al. [2010]; ⁽³⁾Civetta et al. [1988]; ⁽⁴⁾Mahood and Hildreth [1986]; ⁽⁵⁾Civetta et al. [1998]. Error in ages is reported as 2-sigma values.

remnants are now totally buried with the exception of the two clearly visible, though discontinuous, La Vecchia and Cinque Denti caldera scarps.

3. The Green Tuff

The GT, the ninth and the youngest of the known and exposed Pantelleria ignimbrites, is undoubtedly the most studied eruptive unit at Pantelleria. Although the age of the GT has long been correlated with the peralkaline distal ash Y-6 [Keller et al., 1978, Anastasakis and Pe-Piper, 2006, Margari et al., 2007], its age was only loosely constrained by a few low-resolution K/Ar dates varying between 46.9 ± 2.0 ka and 50.8 ± 3.6 ka [Cornette et al., 1983, Civetta et al., 1988] and 45 ± 4 ka to 50 ± 4 ka [Mahood and Hildreth, 1986]. It was only recently that this age was refined to a higher resolution estimate at 45.7 ± 1.0 ka by $^{40}\text{Ar}/^{39}\text{Ar}$ laser-ablation dating [Scaillet et al., 2013].

The emplacement dynamics of the GT have been variably interpreted through time. Once viewed as (i) a lava flow [Washington, 1914] or (ii) a welded fall [Mahood, 1984, Wolff and Wright, 1981a,b, Wright, 1980], it later became clear that it involved more high-energy dynamics, consisting of either (iii) a compound ignimbrite [Mahood and Hildreth, 1983, 1986, Orsi and Sheridan, 1984, Villari, 1970], (iv) a diluted ash-flow [Schmincke, 1974], and/or (v) a welded low aspect-ratio ignimbrite [Williams, 2010, Williams et al., 2014]. The frequent and variable-scale rheomorphic folding was interpreted either as post-depositional [Mahood and Hildreth, 1986, Villari, 1970, Wolff and Wright, 1981a,b] or syn-depositional

(with a diachronous emplacement of the pyroclastic currents during essentially three eruptive phases, Catalano et al., 2007, 2014). The GT was correlated to the younger caldera collapse, whose remnants are recognized in the Monastero scarp [*“Monastero caldera”* of Cornette et al., 1983] and the scarp at Cala Cinque Denti [*“Cinque Denti caldera”*, of Mahood and Hildreth, 1986].

The innovative study by Williams [2010] focused on high-resolution chemostratigraphy of multiple sections of the GT. The whole ignimbrite deposit, preceded by a basal unwelded pumice fallout member that crops out in only a few places, was divided into eight time slices [*“entrachrons”* of Branney and Kokeelaar, 2002], each representative of an eruptive timing of a few minutes. Time slices were chemically correlated across the island, providing diachronous snapshots of the areas progressively inundated by the pyroclastic density current (PDC), each with different runout distances influenced by the pre-existing topography: some pulses by-passed topographic barriers whereas others were instead partially or totally halted by the terrain, during the brief time interval (≤ 1.5 h) during which the current was emplaced [Williams et al., 2014]. Williams [2010] questioned whether the GT was the actual eruption that created the Cinque Denti caldera, citing a lack of clear evidence for large-scale caldera collapse during the GT eruption and suggesting that the Cinque Denti scarp could, in many places, be older. The only evidence found for syn-eruptive collapse is a small-volume pyroclastic breccia within the GT section at Monastero, which is proposed as the type locality for the GT ignimbrite (except for its basal fall-

out member, which was defined at the Khattibucale scarp; Williams, 2010).

The (onland) volume of the GT has been recently re-evaluated at 0.28 km^3 (D.R.E.) [Jordan *et al.*, 2018], much lower than previous estimates of 0.49 km^3 and 0.60 km^3 D.R.E. [Mahood and Hildreth, 1986, Wolff and Wright, 1981b, respectively].

4. The post-Green Tuff volcanological evolution

Volcanism following the GT was distributed throughout a large number (>40) of different centers closely spaced in time and space and characterized by mildly explosive and/or effusive activity. Mafic local centers are largely confined to the northwest of the island and are not found within the caldera, felsic centers are commonly found on or near caldera faults [Jordan, 2014].

The first post-caldera event was the eruption of Monte Gibeles–Montagna Grande trachyte lava (ca. 3 km^3 according to Mahood and Hildreth, 1986) in the center of the young caldera. Cornette *et al.* [1983] and Mahood and Hildreth [1983] both supported Washington's view regarding the uplift of the M.gna Grande trachyte lava block [first proposed by Förstner, 1881], with these latter authors providing detailed descriptions of the bordering faults, the hinge, and the offset (“trapdoor uplift”) that caused the displacement of the M. Gibeles source vent. Cornette *et al.* [1983] and Civetta *et al.* [1984], provided the first K/Ar ages (nine in total) for the reconstruction of the recent eruptive history. These were followed by twelve more K/Ar and six ^{14}C ages by Mahood and Hildreth [1986], who proposed a general stratigraphic scheme framed as a “morpho-structural” subdivision of eruptive centers based on their position between or along the caldera rim and radial intra-/extra-caldera faults. Civetta *et al.* [1988] added 39 new K/Ar ages on lavas and tephra, and based on field evidence (e.g., paleosols) proposed a more precise interpretation involving six eruptive cycles, the first being the eruption of the GT and the second the eruption of trachyte from the M. Gibeles vent. Several vents were active during the most recent (sixth) cycle, such as the composite Cuddia Randazzo center (K/Ar age, $8.2 \pm 1.7 \text{ ka}$), which consists of a pumice ring surrounding a coeval pantellerite lava dome (Figure 2b), whose rupture

produced the Khaggiar lava field, which reaches the sea at Punta Spadillo, 2.5 km away from the source vent. The most energetic (strombolian/sub-Plinian) event was the Fastuca eruption, whose source vent is located on the northern slope of M. Grande [Orsi *et al.*, 1991, Rotolo *et al.*, 2007].

The poor age resolution of the K/Ar method (with $\pm 2\text{--}6 \text{ ka}$ 2σ errors) was not precise enough to allow discrimination between young eruptive units in order to place tighter constraints on the youngest eruptions. To distinguish these, Speranza *et al.* [2010] performed the first application of paleomagnetic methods to three key eruptions. Their youngest documented deposit is the Cuddia Gallo agglutinate (Figure 2c), which they bracketed between 5.9 and 6.2 ka, contemporaneous with the Khaggiar lava flow. For comparison, previous K/Ar ages yielded $8.2 \pm 1.7 \text{ ka}$ (Civetta *et al.* [1988], Cuddia Randazzo pumice, co-genetic with Khaggiar lava), whereas ^{14}C gave $5.4 \pm 0.2 \text{ ka}$, on an early Khaggiar lava flow [Mahood and Hildreth, 1986] (Figure 2b, Table 2).

Scaillet *et al.* [2011] conducted the first $^{40}\text{Ar}/^{39}\text{Ar}$ high-resolution laser-ablation dating on anorthoclase phenocrysts from lavas and pumices erupted during the last 20 ka. Due to the very young ages (7–15 ka) and rather K-poor feldspar composition resulting in low $^{40}\text{Ar}^*$ yield, this proved a more efficient approach at resolving the occurrence of $^{40}\text{Ar}_{\text{xs}}$ and/or contamination with feldspar xenocrysts that plagued earlier K/Ar attempts (conducted on large-size aliquots). Scaillet *et al.* [2011] were successful in obtaining new and more precise ages for the recent intra-caldera activity. In particular, the Fastuca eruption was dated at $9.7 \pm 0.6 \text{ ka}$. Scaillet *et al.* [2011] concluded that the eruptive pace is on a long-term wane and coupled this to an overall (though minor) tendency in decreasing differentiation of pantellerite magmas. Further, these new and better-resolved $^{40}\text{Ar}/^{39}\text{Ar}$ data and field observations [see discussion in Scaillet *et al.*, 2011] do not support the five cycles subdivision of post-GT activity proposed by Civetta *et al.* [1988].

Table 2 summarizes the ages of the three youngest eruptions at Pantelleria obtained by different methods: the $^{40}\text{Ar}/^{39}\text{Ar}$ ages are seen to be systematically older than paleomagnetically derived paleosecular variation-tied estimates, which are in turn comparable or slightly older than ^{14}C ages. K/Ar ages appear rather dispersed with relatively high uncertain-

ties. The bias between $^{40}\text{Ar}/^{39}\text{Ar}$ and ^{14}C estimates is well known [Civetta *et al.*, 1998, Mahood and Hildreth, 1986] and was interpreted by Scaillet *et al.* [2011] as intrinsic to the ^{14}C method, possibly due to inefficient insulation of the tephra/soil horizon hosting the charcoal and consequent contamination with modern carbon.

5. Discussion

5.1. *Methodological improvements: application of paleomagnetism to assess correlation of rheomorphic ignimbrite scattered outcrops*

Paleomagnetism addresses the direction and intensity of magnetization measured in volcanic rocks that in turn may reflect the local characteristics of the geomagnetic field (direction and intensity) at the time of eruption and cooling [e.g., Butler, 1992]. A volcanic rock acquires its magnetization when it cools below the Curie temperature (T_c) of its dominant ferromagnetic mineral (typically magnetite, with a T_c of 575 °C) to the ambient temperature. After the volcanic rock has cooled, its magnetization is “frozen” and does not change even when the characteristics of the geomagnetic field change. Direct observations during the last five centuries have shown that both direction and intensity of the geomagnetic field change quite rapidly (up to 6° direction change per century in Europe, e.g., Lanza *et al.*, 2005), a phenomenon known as secular variation (SV) of the geomagnetic field.

The fast temporal change of paleosecular variation (PSV) of the geomagnetic field along with routinely achieved accuracy of paleomagnetic direction determination in volcanics (directions defined with confidence cones of 2°–4° of radius) imply that two volcanics emplaced only 100–200 years apart can be paleomagnetically discriminated. Such high resolution of paleomagnetic age correlation can fully complement radiometric dating: the latter yields absolute ages, while the former—with a dating resolution of about a century—may definitely establish whether two scattered volcanic outcrops belong to the same eruption or not. The best resolution of K/Ar dating is on the order of few millennia, while for laser-based $^{40}\text{Ar}/^{39}\text{Ar}$ techniques can resolve down to 1 ka or better (up to a century for sanidine, Renne *et al.*, 1997). For lower-K anorthoclase crystals it is close

to 0.5 ka [Scaillet *et al.*, 2011] and PSV-based paleomagnetic dating can provide valuable temporal and cross-correlative constraints to complement existing $^{40}\text{Ar}/^{39}\text{Ar}$ ages.

Paleomagnetism had been previously used to assess whether individual lava flows belonged to the same lava field [Bogue and Coe, 1981, Coe *et al.*, 2005, Hagstrum and Champion, 1994, Speranza *et al.*, 2008], whether different welded scoriae were produced by the same eruption [Zanella *et al.*, 2001], and—concerning ignimbrite correlation only in the pioneer works by Grommé *et al.* [1972] and Ort *et al.* [1999] on the mid-Tertiary ignimbrites from the western US and the Campanian ignimbrite from the Phlegraean Fields, respectively. Pantelleria seemed to be an ideal target to use the paleomagnetic correlation method, as the pre-GT ignimbrites were exposed only at isolated sea coves, with many difficulties in their correlation, given also the rheomorphism and the frequent in-depth lateral lithofacies variations. K/Ar dating by Mahood and Hildreth [1986] had not solved the question, as age error bars of ignimbrite units Z, D, F, and Q overlapped. Speranza *et al.* [2012] collected 23 paleomagnetic sites from the aforementioned ignimbrites plus ignimbrite P and the so-called “welded lithic breccia” considered by Mahood and Hildreth [1986] to relate to the La Vecchia caldera collapse.

The paleomagnetic analysis of Pantelleria ignimbrites was successful due to their highly welded character allowing easy coring of compact yet relatively soft ignimbrite matrix. Also, scatter in paleomagnetic direction (Figure 3) proved to be smaller than in lavas, probably due to: (1) the lack of post-emplacement tilt in ignimbrites, compared to lava field sectors with continuous lava supply over weeks or months that can push and tilt already solidified lava blocks; (2) much smaller magnetization intensity of ignimbrites with respect to lavas, implying much smaller magnetic anomalies generated by buried deposits or the volcanic unit itself; local magnetic anomalies in fact represent one of the most significant scatter source of paleomagnetic directions from volcanics [Baag *et al.*, 1995, Speranza *et al.*, 2006].

The main results reached by the paleomagnetic study of the pre-GT ignimbrites by Speranza *et al.* [2012] are as follows:

- Ignimbrites D and Z (now called “Mordomo”

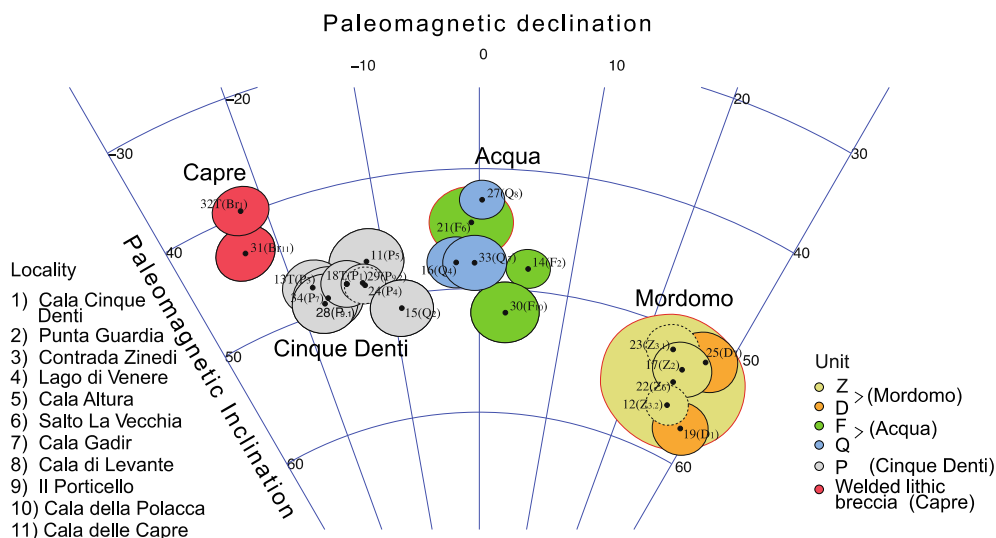


Figure 3. Equal-area projection (lower hemisphere) of mean paleomagnetic directions from ignimbrites of Pantelleria (the “COS” suffix of each site is omitted) by Speranza *et al.* [2012]. Ellipses about the paleomagnetic directions are the projections of alfa-95 confidence cones. Sampling localities initials (detailed in the left) are within each ellipsis in subscript in brackets, at the right of old unit denomination after Mahood and Hildreth [1986]. Updated formational names are after Jordan *et al.* [2018]. The scattered paleomagnetic direction from site Cos20 (Lago di Venere) is omitted. Clustered paleomagnetic directions demonstrate that ignimbrites D/Z (updated name: Mordomo Fm.) and F/Q (Acqua Fm.) coincide, and that the two sites from welded lithic breccia belong to the same ignimbrite (Capre). See Speranza *et al.* [2012] for details.

after Jordan *et al.*, 2018) are both characterized by high 20°–30° declination and 50°–60° inclination values suggesting a common emplacement. This result turned out to be fully consistent with the new $^{40}\text{Ar}/^{39}\text{Ar}$ determinations by Rotolo *et al.* [2013]. Considered together these data indicate a pooled age of 84.7 ± 0.5 ka (2σ , MSWD = 1.15) for this depositional unit.

- A lithic-rich ignimbrite exposed below ignimbrite P (now called “Cinque Denti”) at Cala Cinque Denti (NE Pantelleria coast) paleomagnetically correlates with the “welded lithic breccia” of Cala delle Capre [SW Pantelleria, Mahood and Hildreth, 1986], demonstrating that the La Vecchia caldera-forming eruption occurred at 130–160 ka, based on available K/Ar ages by Mahood and Hildreth [1986]. Such age window was later fully confirmed, and substantially refined at

140.0 ± 1.5 ka by $^{40}\text{Ar}/^{39}\text{Ar}$ dating in Rotolo *et al.* [2013] for the now called “Capre” ignimbrite, later $^{40}\text{Ar}/^{39}\text{Ar}$ dated at a similar age of 137.9 ± 0.8 ka by Jordan *et al.* [2018].

- The paleomagnetic directions of F and Q ignimbrites share similar directional data (within $<10^\circ$), but Speranza *et al.* [2012] did not realize that they could represent the same event. Relying on $^{40}\text{Ar}/^{39}\text{Ar}$ dating, the F/Q ignimbrite correspondence was first proposed by Rotolo *et al.* [2013] and integrated as such in the latest volcanic stratigraphy by Jordan *et al.* [2018], who called it “Acqua” ignimbrite.

To sum up, the integration of paleomagnetism, $^{40}\text{Ar}/^{39}\text{Ar}$ radiometric dating and stratigraphic analysis allowed solving the timing of pre-GT ignimbrite emplacement with a resolution that would have never been attainable using only one or two of those methods. Paleomagnetism of welded ign-

ignimbrites proved to yield very reliable results, more accurate than those obtained by lavas.

The work by Speranza *et al.* [2012], along with pioneer papers by Grommé *et al.* [1972] and Ort *et al.* [1999], and more recent contributions by Ort *et al.* [2013], Finn *et al.* [2016] and Kirscher *et al.* [2020] on the Bolivia, Idaho, and Armenia ignimbrites, respectively, prove that paleomagnetism represents probably the best tool to assess the correlation of ignimbrite outcrops and proximal versus distal volcanic deposits. We expect that in future, paleomagnetism will be highly used on worldwide welded ignimbrites to solve similar volcanological problems, in combination with high-resolution $^{40}\text{Ar}/^{39}\text{Ar}$.

5.2. Methodological improvements: $^{39}\text{Ar}/^{40}\text{Ar}$ dating of young and K-poor feldspar

Although PSV-tied directional data can provide an efficient high-resolution correlation tool in a tightly Earth-referenced coordinate frame, $^{40}\text{Ar}/^{39}\text{Ar}$ remains essential in terms of absolute temporal control. This is especially so for progressively older units both because a master PSV curve has not been established worldwide, and none locally extends very far back in time. $^{40}\text{Ar}/^{39}\text{Ar}$ ages are also insensitive to tectonic unrest and post-cooling tilting characterizing explosive volcanoes (sector collapse, caldera resurgence/foundering, bradyseism, etc.). Methodological progress in the past two decades has considerably improved the resolution of the $^{40}\text{Ar}/^{39}\text{Ar}$ technique in terms of either target (lava flows, fall units, ignimbrite flows) and material processing (single vs. bulk crystal dating, single vs. multiple ion collection). As stated earlier, laser-based $^{40}\text{Ar}/^{39}\text{Ar}$ techniques have reached a resolution narrowing to a century for sanidine [Renne *et al.*, 1997]. Such a performance came about as the result of greatly improved blank levels permitted by laser-based extraction systems compared to older furnace setups. In such systems, the effective $^{40}\text{Ar}/^{39}\text{Ar}$ resolution scales linearly with the K content of the sample such that a fivefold reduction in K results in a fivefold reduction in absolute precision [Scaillet, 2000], practically affording a limiting precision five times bigger (± 0.5 ka, 2σ) for lower-K anorthoclase crystals typical of peralkaline rhyolites [Scaillet *et al.*, 2011].

Detailed $^{40}\text{Ar}/^{39}\text{Ar}$ work at Pantelleria have shown that, beyond precision the major obstacle to building a tightly resolved chronostratigraphy is the occurrence of mixed $^{40}\text{Ar}/^{39}\text{Ar}$ systematics characterized by internally discordant ages scattering beyond individual analytical errors. Except for the GT [Scaillet *et al.*, 2013] and several lava flows and small-sized Strombolian eruptions [Scaillet *et al.*, 2011, 2013, Rotolo *et al.*, 2013], about a half of all units dated so far have proved to be affected by such systematics. Scaillet *et al.* [2011] devised a dedicated two-step protocol combining multi-grain fusion (about 10–15 crystal at a time) with pre-degassing in vacuo to improve both the radiogenic yield and the removal of surface-bound volatiles potentially carrying excess ^{40}Ar . By screening out low-T steps featuring anomalously old ages, this proved essential in producing the first high-resolution $^{40}\text{Ar}/^{39}\text{Ar}$ ages ever produced on such youthful mildly K-enriched material. Systematic application of this approach to selected post-GT units showed this excess component to be dominantly derived from late-stage interaction with atmospheric or hydrothermal agent (i.e., secondary, non-magmatic, component).

A different picture emerged for the older, more explosive, ignimbrite deposits constituting the bulk of the volcano infrastructure prior to the deposition of the GT. Unlike the GT, which displayed well-behaved $^{40}\text{Ar}/^{39}\text{Ar}$ data permitting an age of 45.7 ± 1.0 ka to be confidently resolved [Scaillet *et al.*, 2013], 7 out of 13 pre-GT ignimbrite samples showed discordant $^{40}\text{Ar}/^{39}\text{Ar}$ patterns with internal age variations as great as 400 ka (but more commonly < 40 ka). Notably, such internal variations arise despite the application of the two-step protocol, pointing to the primary (syn-magmatic or syn-depositional) origin of the anomalous ages [Rotolo *et al.*, 2013]. An age in excess of the depositional time may arise due to excess ^{40}Ar contamination in the magma reservoir proper (i.e., via Ar dissolved in the melt, cf. Esser *et al.* [1997]), or as a result of syn-eruptive incorporation of xenocrysts from older deposits, or entrained by the magma en route to the surface.

A characteristic feature of within-unit $^{40}\text{Ar}/^{39}\text{Ar}$ variations is that they cover a relatively reproducible time span, from about zero to ~ 50 kyr. When plotted as a probability density of the age in excess of the depositional age (Figure 4), such systematics reveal striking differences between pre-GT and post-

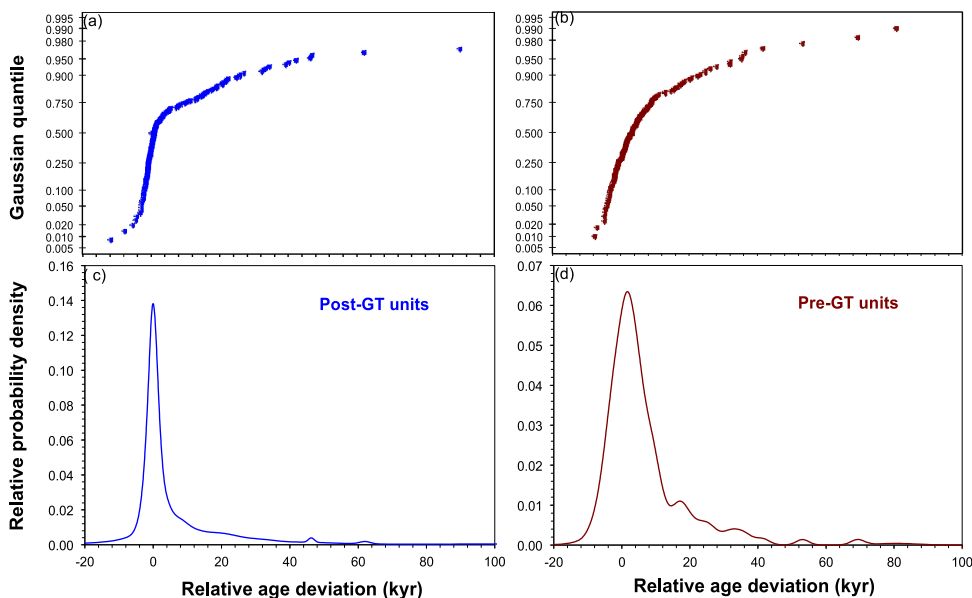


Figure 4. Age deviation probability distribution of anorthoclase $^{40}\text{Ar}/^{39}\text{Ar}$ data from Pantelleria eruptive units predating or post-dating the GT eruption. (a, b) age deviation calculated relative to the depositional age of the parent unit [data from Scaillet *et al.*, 2011, and Rotolo *et al.*, 2013]. (c, d) relative probability density distributions showing the presence of pre-eruptive xenocrysts with a tail extending beyond the dominant near-zero peak. Upper plots: quantile plots scaled assuming a Gaussian distribution. A linear array indicates a Gaussian distribution, which occurs only for the data populating the peak of the post-GT data.

GT units. While both distributions peak near the origin (i.e., no excess ^{40}Ar), post-GT $^{40}\text{Ar}/^{39}\text{Ar}$ ages are more sharply peaked and quite rapidly fade away past 5 kyr of the depositional age (Figure 4c). In contrast, Pre-GT units display a broader distribution with a tail extending well beyond the depositional age, up to 50 kyr and older (Figure 4d). A characteristic break in slope also occurs in the quantile distribution of the sorted post-GT data (Figure 4a) that is not apparent in the pre-GT data distribution which is more rounded and never achieves a linear trend across the data populating the peak (Figure 4b). This statistical difference hints at an intrinsically different mechanism of xenocrystic incorporation. While incorporation of reworked epiclastic/subvolcanic products is clearly accidental in both cases, it is more extensive in the pre-GT ignimbrites units than in the lower-energy post-GT fall deposits. In the latter case, syn-eruptive re-incorporation of older material can be understood to occur at shallower levels than in the higher-energy, highly disruptive, caldera-forming

eruptions.

In this connection, it is remarkable that half of the pre-GT ignimbrites affected by xenocrysts locally display homogeneous (xenocryst-free) systematics [Rotolo *et al.*, 2013, Jordan *et al.*, 2018]. The coexistence in a single depositional unit of lateral variations in xenocryst contamination, with the local absence thereof, indicates that epiclastic mixing dynamics or within-reservoir melt/rock interactions were locally controlled. Should the latter apply, the local control on xenocrystic incorporation would imply sector zoning in the reservoir and, possibly, piecemeal caldera collapse to preserve such a zoning during deposition. With continuous progress in single-grain $^{40}\text{Ar}/^{39}\text{Ar}$ resolution [Jordan *et al.*, 2018] and data productivity, Pantelleria clearly will provide excellent opportunities to refine such time-spatial eruptive dynamics based on systematic $^{40}\text{Ar}/^{39}\text{Ar}$ dating of anorthoclase.

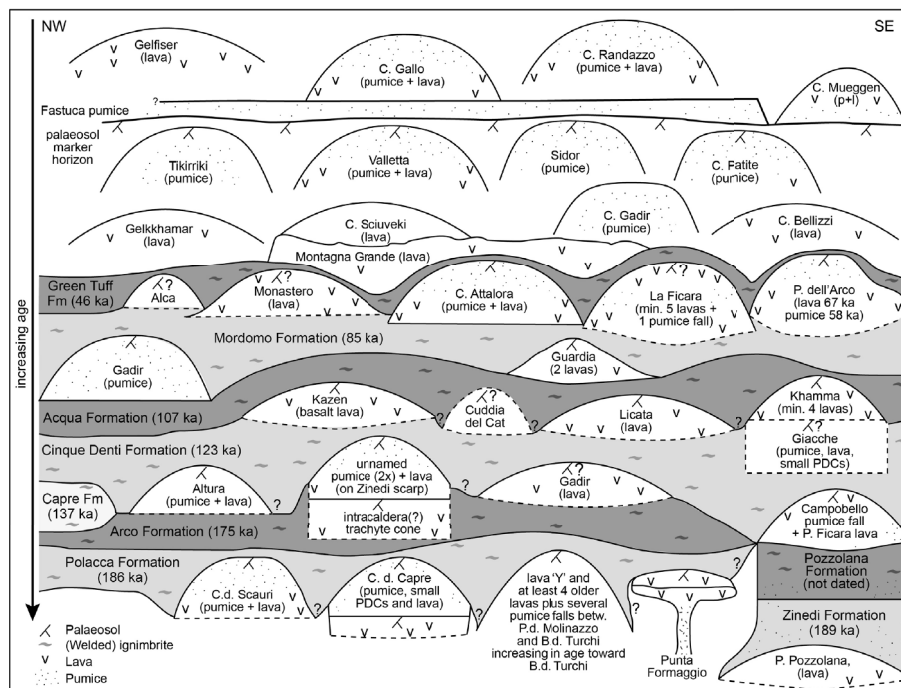


Figure 5. Schematic chronological representation of Pantelleria volcanological evolution based on most recent geochronological ($^{40}\text{Ar}/^{39}\text{Ar}$), paleomagnetic and field data [Jordan *et al.*, 2018, Rotolo *et al.*, 2007, 2013, Scaillet *et al.*, 2011, 2013, Speranza *et al.*, 2010, 2012]. Dashed lines (pre-GT section) or open bases (post-GT section) indicate that the basal contact is not seen in the field. Post-GT basaltic centers have been omitted for clarity.

6. Physical volcanology of a peralkaline volcano

6.1. Local eruption centers versus ignimbrite-forming eruptions

As a defining locality for peralkaline volcanism, it is worth considering the general eruptive styles of Pantelleria eruptions. Broadly, there are ignimbrite eruptions and local (monogenetic) centers, as portrayed in Figure 5 in a scheme that integrates the most recent geochronological, paleomagnetic, and field data for pre- and post-GT eruptive units [Jordan *et al.*, 2018, Rotolo *et al.*, 2007, 2013, Scaillet *et al.*, 2011, 2013, Speranza *et al.*, 2010, 2012]. Ignimbrite eruptions are large eruptions from the caldera. Local centers can be effusive or explosive and have occurred throughout the entire ≥ 324 ka subaerial volcanic history [Jordan *et al.*, 2018, Scaillet *et al.*, 2011

and references therein]. They can produce small ignimbrites, pumice falls and lavas (sometimes spatter fed) and typically show transitions between explosive and effusive activity [Stevenson and Wilson, 1997]. They may be cone- or shield-shaped with a limited dispersal, which in most cases does not exceed several hundred meters (≥ 3 km for the Fastuca eruption, Rotolo *et al.*, 2007) so they are best termed strombolian. Eruption style, magnitude, and periodicity are similar whether pre-GT or post-GT [Jordan *et al.*, 2018].

Whilst the GT is an important marker horizon in that it is widespread and easily recognizable, it should not be used to mark any particular change in eruptive style in Pantelleria's eruptive history. Pumice falls associated with the ignimbrite-forming eruptions are rare; only the GT, Cinque Denti, and Arco Formations have associated pumice falls and these are relatively thin and not widespread. Eruption

columns were sub-Plinian at most [Williams, 2010, Jordan, 2014]. Other peralkaline volcanoes do not produce widespread Plinian precursor pumice falls either [e.g., Terceira: Self, 1976; Kenya: Leat, 1991; Gran Canaria: Schmincke and Sumita, 1998]. This may be because of low magma viscosity and the fact that peralkaline eruptions do not form tall stable eruption columns [Mahood, 1984]. This is a key difference between peralkaline and metaluminous eruptions.

6.2. *Caldera-forming eruptions*

Of eight ignimbrites pre-GT, five comprise of variably widespread significant lithic breccias (GT, Mordomo, Acqua, Arco, and Polacca Formations). Of these, the Acqua breccia is the thickest at ~5 m. Lithic breccias are interpreted to represent an energetic phase of the eruption coupled with vent erosion or widening and are therefore commonly thought to indicate caldera collapse phases of an ignimbrite eruption [Walker, 1985, Druitt and Bacon, 1986]. Only the lithic breccias in the Mordomo Formation and in the Acqua Formation contain plutonic clasts, evidencing excavation from the vent or magma reservoir wall rocks and therefore are the two most likely candidates for caldera-forming eruptions.

There is no compelling evidence for single climactic collapse phases during the GT, Arco or Polacca eruptions. However, as they contain at least local breccias, it is likely that progressive and incremental collapse occurred along reactivated scarps [Walker, 1984].

6.3. *Welding and rheomorphism*

Pantelleria is famed for its welded and rheomorphic pumice falls [e.g., Cala di Tramontana center, Stevenson and Wilson, 1997] and ignimbrites [e.g., The Green Tuff, Orsi and Sheridan, 1984]. The styles and features of Pantelleria rheomorphic ignimbrites are similar to those of other high-grade to extremely high-grade ignimbrites [e.g., the Greys Landing ignimbrite, Idaho, Andrews et al., 2008] including stretching of pumice blocks and lapilli, lineations and foliations, folds on the micro- to meter scale), ramp structures, pull apart structures and tension gashes, gas blisters, upper and basal autobreccias, and rotated clasts (Figure 6a–e). Features more particular to peralkaline rheomorphism

include welding throughout the deposit despite thin deposit thicknesses (even <0.5 m) and on steep slopes, large gas cavities, small glass shards or “globules” showing spherical shapes, and round bubbles in previously deformed pumice particles [Schmincke and Swanson, 1967, Gibson, 1970, Korrington, 1971, Schmincke, 1974, Williams, 2010, Jordan et al., 2018].

Rheomorphism in the ignimbrites is predominantly syn-depositional [Branney et al., 2004, Williams, 2010, Jordan et al., 2018]; hot, sticky particles agglutinated as an aggrading deposit from a PDC. The low viscosities meant that the overriding current was able to cause shearing in the underlying deposit where analysis of kinematic indicators show a change of shear direction with height through the deposit, from which it is possible to infer flow direction of the overriding PDC [Williams, 2010, following Andrews and Branney, 2005, Sumner and Branney, 2002]. In places, there is evidence for post-depositional flow, dominantly down slope [Wolff and Wright, 1981b, Williams, 2010]. The presence of spherical vesicles in strongly flattened fiamme records late-stage exsolution of a gas phase and revesiculation.

Low viscosities [Baker and Vaillancourt, 1994, Di Genova et al., 2013, Mahood, 1984] due to elevated water [Barclay et al., 1996, Lanzo et al., 2013, Lowenstern and Mahood, 1991] and halogen contents [Aines et al., 1990, Carroll, 2005, Gioncada and Landi, 2010, Lanzo et al., 2013, Lowenstern, 1994], despite the rather low pre-eruptive temperatures [Di Carlo et al., 2010, Romano et al., 2018, 2020] and low glass transition temperatures [418–552 °C, Di Genova et al., 2013] of peralkaline melts, are all thought to favor the welding of peralkaline eruptive materials [Dingwell et al., 1998, Quane and Russell, 2005]. Eruption columns are inferred to be low, which minimizes cooling of pyroclastic particles during fountaining [Mahood and Hildreth, 1986]. Early pre-eruptive temperature estimates for the GT assumed high temperatures (~950 °C) based on low viscosities [Mahood, 1984] and the scant data available from Fe–Ti oxide geothermometry, 933–960 °C [Carmichael, 1967, Wolff and Wright, 1981a,b]. But more recent work with silicate mineral equilibrium [White et al., 2005] and experimental petrology [Di Carlo et al., 2010, Romano et al., 2020] have shown these earlier values to be overestimated by >200 °C. The GT, the most rheomorphic of all the ignimbrites, is strongly

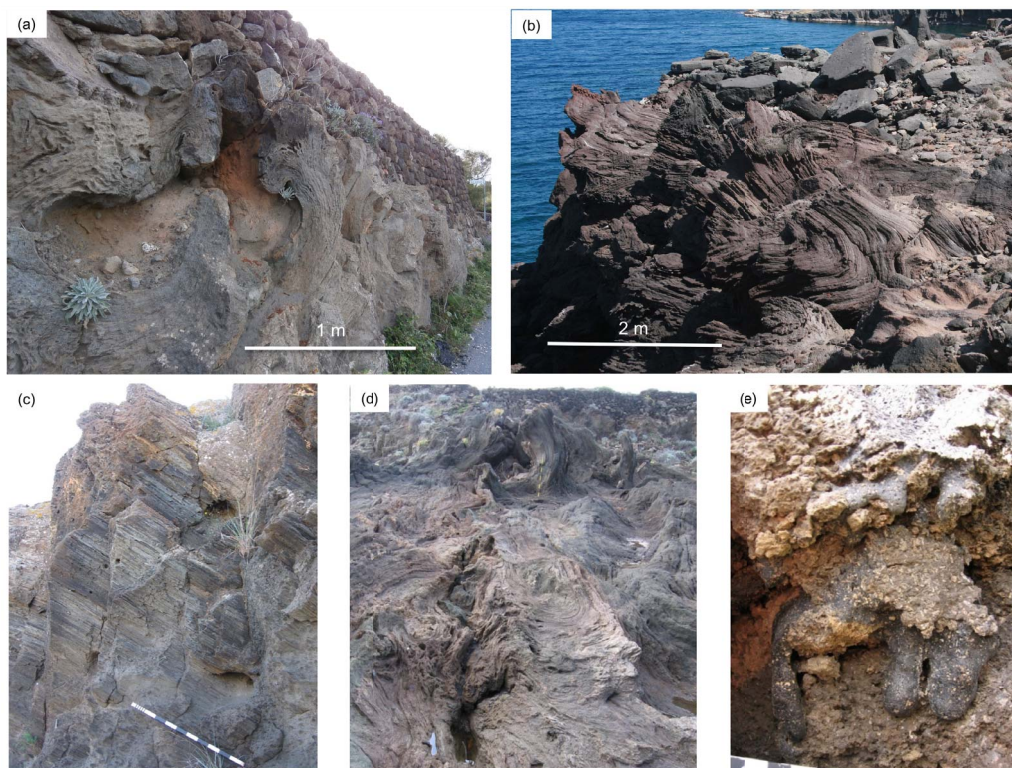


Figure 6. Rheomorphism at various scales. (a) Rheomorphic folding in the GT ignimbrite and (b) in Cinque Denti ignimbrite. (c) Rodded lineations observed in the GT ignimbrite (current direction is from right to left). (d) Rare, localized example of extreme rheomorphism of the GT ignimbrite: large U-shape fold in upper surface, folding foliation. (e) Vitrophyric droplets in the upper trachytic autobreccia of the GT ignimbrite (small scale divisions in 1 cm). This ooze-out feature indicates there were lenses of very low viscosity melt (such as fiamme) compared to the surrounding matrix during cooling.

peralkaline with very high chlorine concentrations (up to 1.1 wt%, Williams, 2010, Lanzo *et al.*, 2013; up to 0.7 wt% for groundmass glass of Mordomo Fm., Jordan, 2014). It should be noted that pre-eruptive H_2O_{melt} contents from melt inclusions in the GT [$H_2O \leq 4.2$ wt%, Lanzo *et al.*, 2013] are comparable with contents from much lower explosivity pantellerite eruptions ($H_2O_{\text{max}} = 4.4$ wt%, Gioncada and Landi [2010]) and with H_2O_{melt} inferred from phase equilibria experiments [Di Carlo *et al.*, 2010, Romano *et al.*, 2020]. This evidence may suggest that other than the pre-eruptive H_2O_{melt} eruptive triggers must be considered; one might be related to an abrupt syn-eruptive viscosity increase due to nanolites growth [Càceres *et al.*, 2020, Di Genova *et al.*, 2020].

7. Did the eruptive pace and the erupted magma volume condition melt evolution and melt productivity?

The depth and the pre-eruptive conditions of pantellerite magma have been constrained at $P = 0.5\text{--}1.2$ kbar, $T = 730$ °C, $H_2O_{\text{melt}} = 4\%$ [Di Carlo *et al.*, 2010, Gioncada and Landi, 2010, Lanzo *et al.*, 2013, Romano *et al.*, 2020], and at $P = 1\text{--}1.5$ kbar, $T = 925$ °C, $H_2O_{\text{melt}} = 2\%$ for trachyte magma (top member of the GT sequence; Romano *et al.* [2018, 2019]). The presence of a long-lived magma reservoir at mid-crustal levels (~ 8 km) that has efficiently homogenized basaltic melts and served as the source of parental magmas to the erupted trachytes and rhyolites was proposed by White *et al.* [2020] and

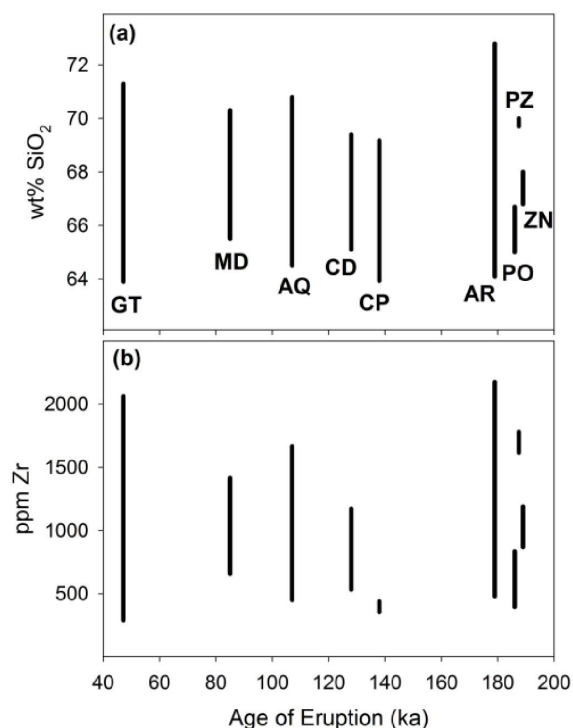


Figure 7. Ages of ignimbrites [Jordan et al., 2018, Rotolo et al., 2013, Scaillet et al., 2013] plotted versus the range of whole rock compositions for SiO₂ (a) and Zr (b) presented in Jordan et al. [2021]. Ignimbrite units displayed include: GT, GT Fm.; MD, Mordomo Fm.; AQ, Acqua Fm.; CD, Cinque Denti Fm.; CP, Capre Fm.; AR, Arco Fm.; PO, Polacca Fm.; PZ, Pozzolana Fm.; ZN, Zinedi Fm. Capre Fm. analyses are from Rotolo et al. [2013] and Jordan [2014].

is supported by the nearly identical incompatible trace-element ratios and patterns on multi-element diagrams recorded in the ignimbrites [Jordan et al., 2021]. These ignimbrites have several common compositional characteristics in addition to similar trace-element ratios, including range of SiO₂ (~64–71 wt%; Figure 7a) and Zr (~500–2000 ppm; Figure 7b) but differ in terms of peralkalinity, iron enrichment, and degree of silica oversaturation [Jordan et al., 2021]. Most of the felsic eruptive products at Pantelleria have been comenditic trachytes and comendites, with only the earliest (Zinedi Fm.) and latest (GT Fm.) ignimbrites having a pantelleritic affinity. Whether these differences are due to pressure,

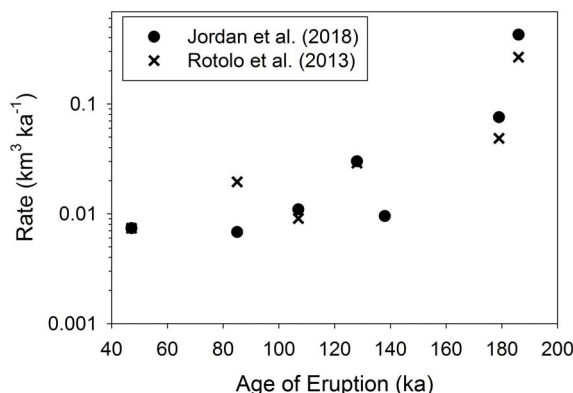


Figure 8. Ages of ignimbrites plotted versus the calculate rate of magma generation. Estimates for the volume of each eruption from Rotolo et al. [2013] and Jordan et al. [2018].

water content, oxygen fugacity, or something else is beyond the scope of this paper and will be the focus of future studies. However, similar range in both SiO₂ and Zr strongly suggest similar degrees and rates of differentiation from trachyte to rhyolite. Considering both effusive and explosive products, Mahood and Hildreth [1986] suggested a frequent rate (13 ± 6 ka) for felsic eruptions on Pantelleria over the past 190 ka. However, when one considers only the seven major ignimbrites to erupt over the past 186 ka, there has been a steady increase in time between eruptions accompanied by a decrease in eruptive volumes which seems to suggest an overall decline in magmatic activity at Pantelleria (Figure 8) with rates declining from 0.076 to 0.007 km³·ka⁻¹. These calculated rates based on the data of Jordan et al. [2021] are consistent with the estimates of 0.008–0.055 km³·ka⁻¹ calculated by Mahood and Hildreth [1986]. Calculated rates using the volume estimates of Rotolo et al. [2013] also show a similar, secular decline from 0.049 to 0.007 km³·ka⁻¹. This waning tendency was also observed by Scaillet et al. [2011] in post-GT mildly explosive activity.

8. Conclusions

The history of the Pantelleria peralkaline volcano is usually divided into an early history dominated by nine ignimbrite eruptions and at least two, but up to five, caldera collapses, followed by a later (post-GT)

history, characterized by numerous (>40) low explosivity to effusive eruptions produced from several closely spaced (spatially and temporally) eruptive vents.

The ignimbrites have a remarkably complex stratigraphy due to discontinuous exposures, rapid lateral facies variations, and ubiquitous but highly variable welding and rheomorphism. Inter-ignimbrite activity was characterized by small to moderate explosive or effusive eruptions from scattered vents, whose remnants are now only in few places poorly visible along some coastal scarps. The periodicity of ignimbrite-forming eruptions alternated with lower magnitude events (in a geological scenario that could be similar to the present day one following the eruption of the GT), which raises many still-unanswered questions about triggering mechanisms.

For the above reasons, Pantelleria represents an emblematic case history about the approaches adopted to untangle the volcanostratigraphy and portray its evolutionary history. Early approaches, based on field studies supported by K/Ar ages, defined a basis for future studies, but suffered heavily from the obfuscation caused by the rheological peculiarities of peralkaline magmas and tephra that added to the intrinsic uncertainty of the K/Ar dating. Only in the past ten years has the pre- and post-GT stratigraphy been investigated with multiple absolute/correlative chronological methods ($^{40}\text{Ar}/^{39}\text{Ar}$ geochronology, paleomagnetism) coupled to accurate field and petrographic characterization of pyroclastic products. Despite the possible drawbacks about the application of paleomagnetic methods on peralkaline rheomorphic ignimbrites (in principle still plastic below the closure temperature of principal ferromagnetic minerals) and the ability to date K-poor feldspars in young rocks by $^{40}\text{Ar}/^{39}\text{Ar}$, the congruence of these two methods, within a well-defined field and petrographic context, provided answers to the majority of the open problems with a resolution otherwise unattainable.

Combining $^{40}\text{Ar}/^{39}\text{Ar}$ ages with petrochemical data of seven major ignimbrites erupted during the last 186 ka reveal a slight stretching of ignimbrite recurrence time, coupled to a decrease in erupted magma volumes. This tendency apparently holds also for the post-GT eruptive activity (violent strombolian at most).

Recommendations for future research include additional $^{40}\text{Ar}/^{39}\text{Ar}$ dating of the post-GT trachyte lavas and some still undated minor ignimbrites and local centers, and additional paleomagnetic studies of the emplacement temperatures of some key ignimbrites. Also, the variations in degrees of rheomorphism, and a structural study with detailed analysis of the viscosity, pre- and syn-eruptive halogen content and emplacement temperature, could be a valuable avenue for future study.

Acknowledgments

We wish to thank two anonymous reviewers for their thorough and helpful comments. The Ar/Ar facility at ISTO is supported by the LABEX project VOLTAIRE (ANR-10-LABX-100-01), the Région Centre project ARGON, and the project EQUIPES PLANEX (ANR-11-EQPX-0036). RW acknowledges Natural Environment Research Council studentship grant NER/S/A/2006/14156. NJJ gratefully acknowledges funding from the German Academic Exchange Service, Geological Society of London, Mineralogical Society of Great Britain and Ireland, Geologists Association, Quaternary Research Association, Volcanic and Magmatic Studies Group and the Department of Geology at the University of Leicester.

References

- Aines, R. D., Lowenstern, J. B., and Mahood, G. (1990). Evidence for CO_2 rich vapor in pantellerite magma chambers. *EOS Trans. Am. Geophys. Union*, 43, 1700.
- Anastasakis, G. and Pe-Piper, G. (2006). An 18 m thick volcanoclastic interval in Pantelleria Trough, Sicily Channel, deposited from a large gravitative flow during the Green Tuff eruption. *Mar. Geol.*, 231, 201–219.
- Andrews, G. D. M. and Branney, M. J. (2005). Folds, fabrics, and kinematic criteria in rheomorphic ignimbrites of the Snake River Plain, Idaho: Insights into emplacement and flow. *Geol. Soc. Amer. Field Guide*, 6, 311–327.
- Andrews, G. D. M., Branney, M. J., Bonnicksen, B., and McCurry, M. (2008). Rhyolitic ignimbrites in the Rogerson Graben, southern Snake River Plain volcanic province: volcanic stratigraphy, eruption

- history and basin evolution. *Bull. Volcanol.*, 70, 269–291.
- Arzilli, F., Stabile, P., Fabbrizio, A., Landi, P., Scaillet, B., Paris, E., and Carroll, M. R. (2020). Crystallization kinetics of alkali feldspar in peralkaline rhyolitic melts: implications for Pantelleria Volcano. *Front. Earth Sci.* doi:10.3389/feart.2020.00177.
- Avanzinelli, R., Bindi, L., Menchetti, S., and Conticelli, S. (2004). Crystallization and genesis of peralkaline magmas from Pantelleria Volcano, Italy: an integrated petrological and crystal-chemistry study. *Lithos*, 73, 41–69.
- Avanzinelli, R., Braschi, E., Marchionni, S., and Bindi, L. (2014). Mantle melting in within-plate continental settings: Sr-Nd-Pb and U-series isotope constraints in alkali basalts from the Sicily Channel (Pantelleria and Linosa Islands, Southern Italy). *Lithos*, 188, 113–129.
- Baag, C., Helsley, C. E., Xu, S. Z., and Lienert, B. R. (1995). Deflection of paleomagnetic directions due to magnetization of the underlying terrain. *J. Geophys. Res.*, 100, 10013–10027.
- Baginski, B., MacDonald, R., White, J. C., and Jezak, L. (2018). Tuhualite in a peralkaline ignimbrite from Pantelleria, Italy. *Eur. J. Mineral.*, 30, 367–373.
- Baker, D. H. and Vaillancourt, J. (1994). The viscosity of F + H₂O-bearing peralkaline and peraluminous rhyolitic melts. *Miner. Mag.*, 58A, 40–41.
- Barberi, F., Borsi, S., Ferrara, G., and Innocenti, F. (1969). Strontium isotopic composition of some ignimbrites of some recent basic volcanites of the southern Tyrrhenian Sea and Sicily Channel. *Contrib. Mineral. Petrol.*, 23, 157–172.
- Barclay, J., Carroll, M. R., Houghton, B. F., and Wilson, C. J. N. (1996). Pre-eruptive volatile content and degassing history of an evolving peralkaline volcano. *J. Volcanol. Geoth. Res.*, 74, 75–87.
- Behncke, B., Berrino, G., Corrado, G., and Velardita, R. (2006). Ground deformation and gravity changes on the island of Pantelleria in the geodynamic framework of the Sicily Channel. *J. Volcanol. Geoth. Res.*, 150, 146–162.
- Bergeat, A. (1907). Staukuppen. *Nues Jahrb. Mineral. Geol. Paleontol. Festband*, pages 310–329.
- Bigazzi, G., Bonadonna, F. P., Belluomini, G., and Malpieri, L. (1971). Studi sulle ossidiane italiane IV. Datazione con il metodo delle tracce di fissione. *Boll. Soc. Geol. It.*, 90, 469–480.
- Bogue, S. W. and Coe, R. S. (1981). Paleomagnetic correlation of Columbia River basalt flows using secular variation. *J. Geophys. Res.*, 86, 11883–11897.
- Bonaccorso, A. and Mattia, M. (2000). Deflation acting on island of Pantelleria inferred through geodetic data. *Earth Planet. Sci. Lett.*, 180, 91–101.
- Borsi, S., Marinelli, G., Mazzoncini, F., Mittempergher, M., and Tedesco, C. (1963). Reconnaissance of some ignimbrites at Pantelleria and Eolian islands. *Bull. Volcanol.*, 25, 359–363.
- Branney, M. J., Barry, T. L., and Godchaux, M. (2004). Sheathfolds in rheomorphic ignimbrites. *Bull. Volcanol.*, 66, 485–491.
- Branney, M. J. and Kokelaar, P. (2002). *Pyroclastic Density Currents and the Sedimentation of Ignimbrites*, volume 27 VIII of *Geological Society London Memoirs*. Geological Society of London, London.
- Butler, R. F. (1992). *Paleomagnetism: Magnetic Domains to Geologic Terranes*. Blackwell Scientific Publications, Boston.
- Càceres, F., Wadsworth, F. B., Scheu, B., Colombier, M., Madonna, C., Cimarelli, C., Hess, K. U., Kalwoda, M., Ruthensteiner, B., and Dingwell, D. B. (2020). Can nanolites enhance eruption explosivity? *Geology*, 48(10), 997–1001.
- Campagnola, S., Romano, C., Mastin, L., and Vona, A. (2016). Confort-15 model of conduit dynamics: applications to Pantelleria Green Tuff and Etna 122 BC eruptions. *Contrib. Mineral. Petrol.*, 171, 1–25.
- Carmichael, I. S. E. (1967). The iron-titanium oxides of salic volcanic rocks and their associated ferromagnesian silicates. *Contrib. Mineral. Petrol.*, 14, 36–64.
- Carroll, M. R. (2005). Chlorine solubility in evolved alkaline magmas. *Ann. Geophys.-Italy*, 48, 619–631.
- Catalano, S., De Guidi, G., Lanzafame, G., Monaco, C., and Tortorici, L. (2009). Late Quaternary deformation on the island of Pantelleria: new constraints for the recent tectonic evolution of the Sicily Channel Rift (southern Italy). *J. Geodynam.*, 48, 75–82.
- Catalano, S., Grasso, G., Lanzafame, G., and Tortorici, L. (2007). Fenomeni di reomorfismo nell' Ignimbrite Verde di Pantelleria: strutture di flusso primario o secondario? *Rend. Soc. Geol. It.*, 4, 174–176.
- Catalano, S., Tortorici, L., and Viccaro, M. (2014). Regional tectonic control on large size explosive eruptions: insights into the Green Tuff ignimbrite unit of Pantelleria. *J. Geodyn.*, 73, 23–33.

- Civetta, L., Cornette, Y., Crisci, G., Gillot, P. Y., Orsi, G., and Requejo, C. S. (1984). Geology, geochronology and chemical evolution of the island of Pantelleria. *Geol. Mag.*, 121, 541–562.
- Civetta, L., Cornette, Y., Gillot, P. Y., and Orsi, G. (1988). The eruptive history of Pantelleria (Sicily Channel) in the last 50 ka. *Bull. Volcanol.*, 50, 47–57.
- Civetta, L., D'Antonio, M., Orsi, G., and Tilton, G. R. (1998). The geochemistry of volcanic rocks from Pantelleria island, Sicily channel: petrogenesis and characteristics of the mantle source region. *J. Petrol.*, 39, 1453–1491.
- Coe, R. S., Stock, G. M., Lyons, J. J., Beitler, B., and Bowen, G. J. (2005). Yellowstone hotspot volcanism in California? A paleomagnetic test of the Lovejoy flood basalt hypothesis. *Geology*, 33, 697–700.
- Conte, A. M., Martorelli, E., Calarco, M., Sposato, A., Perinelli, C., Coltelli, M., and Chiocci, F. L. (2014). The 1891 submarine eruption offshore Pantelleria Island (Sicily Channel, Italy): Identification of the vent and characterization of products and eruptive style. *Geochem. Geophys. Geosyst.*, 15, 2555–2574.
- Cornette, Y., Crisci, G. M., Gillot, P. Y., and Orsi, G. (1983). The recent volcanic history of Pantelleria: a new interpretation. In: Sheridan M. F. and Barberi F. (eds) Explosive volcanism. *J. Volcanol. Geoth. Res.*, 17, 361–373.
- De Guidi, G. and Monaco, C. (2009). Late Holocene vertical deformation along the coast of Pantelleria Island (Sicily Channel, Italy). *Quat. Int.*, 206, 158–165.
- Di Carlo, I., Rotolo, S. G., Scaillet, B., Buccheri, V., and Pichavant, M. (2010). Phase equilibrium constraints on pre-eruptive conditions of recent felsic explosive volcanism at Pantelleria Island, Italy. *J. Petrol.*, 51, 2245–2276.
- Di Genova, D., Brooker, A. R., Mader, H. R., Drewitt, J. W. E., Longo, A., Deubener, J., Neuville, D. R., Fanara, S., Shebanova, O., Anzellini, S., Arzilli, E., Bamber, E. C., Hennet, L., La Spina, G., and Nobuyoshi, M. (2020). In situ observation of nanolite growth in volcanic melt: a driving force for explosive eruptions. *Sci. Adv.*, 6(39). doi:10.1126/sciadv.abb0413.
- Di Genova, D., Romano, C., Hess, K. U., Vona, A., Giodano, D., Dingwell, D. B., and Behrens, H. (2013). The rheology of peralkaline rhyolites from Pantelleria island. *J. Volcanol. Geoth. Res.*, 249, 201–216.
- Dingwell, D. B., Hess, K. U., and Romano, C. (1998). Extremely fluid behavior of hydrous peralkaline rhyolites. *Earth Planet. Sci. Lett.*, 158, 31–38.
- Druitt, T. and Bacon, C. R. (1986). Lithic breccia and ignimbrite erupted during the collapse of Crater Lake caldera. *Oregon. J. Volcanol. Geoth. Res.*, 29, 1–32.
- Esperança, S. and Crisci, G. M. (1995). The island of Pantelleria: a case of DMM-HIMU isotopic compositions in a long-lived extensional setting. *Earth Planet. Sci. Lett.*, 136, 167–182.
- Esser, R. P., McIntosh, W. C., Heizler, M. T., and Kyle, P. R. (1997). Excess argon in melt inclusions in zero-age anorthoclase feldspar from Mt. Erebus, Antarctica, as revealed by the $^{40}\text{Ar}/^{39}\text{Ar}$ method. *Geochim. Cosmochim. Acta*, 61, 3789–3801.
- Ferla, P. and Meli, C. (2006). Evidence of magma mixing in the “Daly Gap” of alkali suites: a case study from the enclaves of Pantelleria (Italy). *J. Petrol.*, 47, 1467–1507.
- Finn, D. R., Coe, R. S., Brown, E., Brannney, M., Reichow, T., Knott, T., Storey, M., and Bonnicksen, B. (2016). Distinguishing and correlating deposits from large ignimbrite eruptions using paleomagnetism: The Cougar Point Tuffs (mid-Miocene), southern Snake River Plain, Idaho, USA. *J. Geophys. Res.*, 121, 6293–6314.
- Förstner, H. (1881). Nota preliminare sulla geologia dell' Isola di Pantelleria secondo gli studi fatti negli anni 1874 e 1881. *Boll. R. Comit. Geol. It.*, 12, 523–556.
- Fouré, E., Allard, P., Jean-Baptiste, P., Cellura, D., and Parello, F. (2012). $^3\text{He}/^4\text{He}$ ratio in olivines from Linosa, Ustica, and Pantelleria Islands (Southern Italy). *J. Geol. Res.* doi:10.1155/2012/723839.
- Fulignati, P., Malfitano, G., and Sbrana, A. (1997). The Pantelleria caldera geothermal system: data from the hydrothermal minerals. *J. Volcanol. Geoth. Res.*, 75, 251–270.
- Gemmellaro, C. (1829). Sopra l' isola vulcanica di Pantelleria e sopra le osservazioni ivi fatte dal socio corrispondente Conte F. Beffa Negrini. *Atti Accademia Gioenia*, 5, 209–223.
- Gibson, I. L. (1970). A pantelleritic welded ash-flow Tuff from Ethiopian Rift Valley. *Contrib. Mineral. Petrol.*, 28, 89–111.
- Gioncada, A. and Landi, P. (2010). The pre-eruptive volatile contents of recent basaltic and pantelleritic

- magmas at Pantelleria (Italy). *J. Volcanol. Geoth. Res.*, 189, 191–201.
- Giuffrida, M., Nicotra, E., and Viccaro, M. (2020). Changing modes and rates of mafic magma supply at Pantelleria (Sicily Channel, southern Italy): new perspective on the volcano factory drawn upon olivine records. *J. Petrol.*, 61(5), 1–22.
- Grommé, C. S., McKee, E. H., and Blake Jr., M. C. (1972). Paleomagnetic correlations and potassium argon dating of middle Tertiary ashflow sheets in the eastern Great Basin, Nevada and Utah. *Geol. Soc. Am. Bull.*, 83, 1619–1638.
- Hagstrum, J. T. and Champion, D. E. (1994). Paleomagnetic correlation of Late Quaternary lava flows in the lower east rift zone of Kilauea Volcano, Hawaii. *J. Geophys. Res.*, 99, 21679–21690.
- Hughes, E. C., Neave, D. A., Dobson, K. J., Withers, P. J., and Edmonds, M. (2017). How to fragment peralkaline rhyolites: observations on pumice using combined multi-scale 2-D and 3-D imaging. *J. Volcanol. Geoth. Res.*, 226, 179–191.
- Jordan, N. J. (2014). *Pre-Green Tuff Explosive Eruptive History, Petrogenesis and proximal-distal tephra correlations of a peralkaline caldera volcano: Pantelleria, Italy*. PhD thesis, University of Leicester, UK.
- Jordan, N. J., Rotolo, S. G., Williams, R., Speranza, E., McIntosh, W. C., Branney, M. J., and Scaillet, S. (2018). Explosive eruptive history of Pantelleria, Italy: repeated caldera collapse and ignimbrite formation at a peralkaline volcano. *J. Volcanol. Geoth. Res.*, 349, 67–73.
- Jordan, N. J., White, J. C., MacDonald, R., and Rotolo, S. G. (2021). Evolution of the magma system of Pantelleria (Italy) from 190 ka to present. *C. R. Geosci.* this volume, <https://doi.org/10.5802/crgeos.50>.
- Keller, J., Ryan, W. B. F., Ninkovich, D., and Altherr, R. (1978). Explosive volcanic activity in mediterranean over past 200 000 yr as recorded in deep-sea sediments. *Geol. Soc. Amer. Bull.*, 89, 591–604.
- Kelly, T. J., Carey, S., Pistolesi, M., Rosi, M., Croff-Bell, K. L. C., Roman, C., and Marani, M. (2014). Exploration of the 1891 Foerstner submarine vent site (Pantelleria, Italy): insights into the formation of basaltic balloons. *Bull. Volcanol.*, 76(844), 1–18.
- Kirscher, U., Gevorgyan, H., Meliksetian, K., Navasardyan, G., Dallanave, E., Breikreuz, C., and Bachtadse, V. (2020). Pleistocene ignimbrites of western Armenia–Paleomagnetic and magnetic anisotropy constraints on flow direction and stratigraphy. *J. Volcanol. Geoth. Res.*, 402, article no. 106982.
- Korrinda, M. K. (1971). Steeply-dipping welded tuffs mantling the Pantelleria caldera (abstract). In *Conference on Peralkaline Acid Volcanism, Catania*.
- Kovalenko, V. I., Naumov, V. B., Solovova, I. P., Girnis, A. V., Khervig, R. L., and Boriani, A. (1994). Volatile components, composition, and crystallization conditions of the Pantelleria basalt–pantellerite association inferred from the melt and fluid inclusion data. *Petrology*, 2, 19–34.
- Lanza, R., Meloni, A., and Tema, E. (2005). Historical measurements of the Earth's magnetic field compared with remanence directions from lava flows in Italy over the last four centuries. *Phys. Earth Planet. Inter.*, 148, 97–107.
- Lanzo, G., Landi, P., and Rotolo, S. G. (2013). Volatiles in pantellerite magmas: a case study of the Green Tuff Plinian eruption. *J. Volcanol. Geoth. Res.*, 262, 153–163.
- Leat, P. T. (1991). Volcanological development of the Nakuru area of the Kenya rift valley. *J. African Earth Sci.*, 13, 483–498.
- Liszewska, K. M., White, J. C., MacDonald, R., and Bagiński, B. (2018). Compositional and thermodynamic variability in a stratified magma chamber: Evidence from the Green Tuff Ignimbrite (Pantelleria, Italy). *J. Petrol.*, 59, 2245–2272.
- Lowenstern, J. B. (1994). Chlorine, fluid immiscibility, and degassing in peralkaline magmas from Pantelleria, Italy. *Am. Mineral.*, 79, 353–369.
- Lowenstern, J. B. and Mahood, G. A. (1991). New data on magmatic H₂O contents with implications for petrogenesis and eruptive dynamics at Pantelleria. *Bull. Volcanol.*, 54, 78–83.
- Mahood, G. A. (1984). Pyroclastic rocks and calderas associated with strongly peralkaline magmatism. *J. Geophys. Res.*, 89, 8540–8552.
- Mahood, G. A. and Hildreth, W. (1983). Nested calderas and trapdoor uplift at Pantelleria, Strait of Sicily. *Geology*, 11, 722–726.
- Mahood, G. A. and Hildreth, W. (1986). Geology of the peralkaline volcano at Pantelleria, Strait of Sicily. *Bull. Volcanol.*, 48, 143–172.
- Margari, V., Pyle, D. M., Bryant, C., and Gibbard, P. L. (2007). Mediterranean tephra stratigraphy revisited results from a long terrestrial sequence on Lesvos Island, Greece. *J. Volcanol. Geoth. Res.*, 163,

- 34–54.
- Mattia, M., Bonaccorso, A., and Guglielmino, F. (2007). Ground deformations in the island of Pantelleria (Italy): insights into the dynamic of the current intereruptive period. *J. Geophys. Res.*, 112, article no. B11406.
- Neave, D. A. (2020). Chemical variability in peralkaline magmas and magma reservoirs: insight from the Khaggiar lava flow, Pantelleria, Italy. *Contrib. Mineral. Petrol.*, 175, article no. 39.
- Neave, D. A., Fabbro, G., Herd, R. A., Petrone, M. C., and Edmonds, M. (2012). Melting, differentiation and degassing at the Pantelleria volcano, Italy. *J. Petrol.*, 53, 637–663.
- Orsi, G., Ruvo, L., and Scarpati, C. (1991). The recent explosive volcanism at Pantelleria. *Geol. Rundschau*, 80, 187–200.
- Orsi, G. and Sheridan, M. F. (1984). The Green Tuff of Pantelleria: rheoignimbrite or rheomorphic fall? *Bull. Volcanol.*, 47, 611–626.
- Ort, M., Rosi, M., and Anderson, C. D. (1999). Correlation of deposits and vent locations of the proximal Campanian Ignimbrite deposits, Campi Flegrei, Italy, based on natural remanent magnetization and anisotropy of magnetic susceptibility characteristics. *J. Volcanol. Geoth. Res.*, 91, 167–178.
- Ort, M. H., de Silva, S. L., Jiménez, N. C., Jicha, B. R., and Singer, B. S. (2013). Correlation of ignimbrites using characteristic remanent magnetization and anisotropy of magnetic susceptibility, central Andes, Bolivia. *Geochem. Geophys. Geosyst.*, 14, 141–157.
- Perugini, D., Poli, G., and Prosperini, N. (2002). Morphometric analysis of magmatic enclaves: a tool for understanding magma vesiculation and ascent. *Lithos*, 61, 225–235.
- Prosperini, N., Perugini, D., Poli, G., and Manetti, P. (2000). Magmatic enclaves distribution within the Khaggiar lava dome (Pantelleria, Italy): implication for magma chamber dynamics and eruption. *Acta Vulcanol.*, 12, 34–47.
- Quane, S. L. and Russell, J. K. (2005). Ranking welding intensity in pyroclastic deposits. *Bull. Volcanol.*, 67, 129–143.
- Renne, P. R., Sharp, W. D., Deino, A. L., Orsi, G., and Civetta, L. (1997). $^{40}\text{Ar}/^{39}\text{Ar}$ dating into the historic realm: calibration against Pliny the Younger. *Science*, 277, 1279–1280.
- Riccò, A. (1892). Terremoti, sollevamenti e eruzione sottomarina a Pantelleria nella seconda metà di ottobre 1891. *Boll. Soc. Geograf. Ital.*, 29, 1–31.
- Richard, D. (2015). *Crossing the glass transition during volcanic eruptions: a matter of time scale and magma rheology*. MSc. dissertation, retrieved from <https://edoc.ub.uni-muenchen.de/19387/>.
- Rittmann, A. (1967). Studio geovulcanologico e magmatologico dell' Isola di Pantelleria. *Riv. Min. Sic.*, 106, 147–182.
- Romano, P., Andujar, J., Scaillet, B., Romengo, N., Di Carlo, I., and Rotolo, S. G. (2018). Phase equilibria of Pantelleria trachytes (Italy): constraints on pre-eruptive conditions and on the metaluminous to peralkaline transition in silicic magmas. *J. Petrol.*, 59, 559–588.
- Romano, P., Scaillet, B., White, J. C., Andujar, J., Di Carlo, I., and Rotolo, S. G. (2020). Experimental and thermodynamic constraints on mineral equilibrium in pantelleritic magmas. *Lithos*, 376–377, 1–22.
- Romano, P., White, J. C., Ciulla, A., Di Carlo, I., D' Oriano, C., Landi, P., and Rotolo, S. G. (2019). Volatiles and trace elements content in melt inclusions from the zoned Green Tuff ignimbrite (Pantelleria, Sicily): petrological inferences. *Ann. Geophys.*, 62, 1.
- Romengo, N., Landi, P., and Rotolo, S. G. (2012). Evidence of basaltic magma intrusions in a trachytic magma chamber at Pantelleria (Italy). *Per. Mineral.*, 81, 163–178.
- Rotolo, S. G., Agnesi, V., Conoscenti, C., and Lanzo, G. (2017). Pantelleria Island (Strait of Sicily): volcanic history and geomorphological landscape. In Soldati, M. and Marchetti, M., editors, *Landscapes and Landforms of Italy*, pages 479–487. World Geomorphological Landscapes, Springer.
- Rotolo, S. G., La Felice, S., Mangalaviti, A., and Landi, P. (2007). Geology and petrochemistry of the recent (<25 ka) silicic volcanism at Pantelleria Island. *Boll. Soc. Geol. It.*, 126, 191–208.
- Rotolo, S. G., Scaillet, S., La Felice, S., and Vita-Scaillet, G. (2013). A revision of the structure and stratigraphy of pre-Green Tuff ignimbrites at Pantelleria (Strait of Sicily). *J. Volcanol. Geoth. Res.*, 250, 61–74.
- Rotolo, S. G. and Villa, I. M. (2001). $^{39}\text{Ar}/^{40}\text{Ar}$ dating of an alkali-granite enclave from Pantelleria island. *Per. Mineral.*, 70, 269–275.

- Scailliet, S. (2000). Numerical error analysis in $^{40}\text{Ar}/^{39}\text{Ar}$ dating. *Chem. Geol. (Iso. Geosci. Sec.)*, 162, 269–298.
- Scailliet, S., Rotolo, S. G., La Felice, S., and Vita, G. (2011). High resolution $^{40}\text{Ar}/^{39}\text{Ar}$ chronostratigraphy of the post-caldera (<20 ka) volcanic activity at Pantelleria, Sicily Strait. *Earth Planet. Sci. Lett.*, 309, 280–290.
- Scailliet, S., Vita-Scailliet, G., and Rotolo, S. G. (2013). Millennial-scale phase relationships between ice-core and Mediterranean marine records: insights from high-precision $^{40}\text{Ar}/^{39}\text{Ar}$ dating of the Green Tuff of Pantelleria, Sicily Strait. *Quat. Sci. Rev.*, 78, 141–154.
- Schmincke, H. U. (1974). Volcanological aspects of peralkaline silicic ash-flow welded tuffs. *Bull. Volcanol.*, 38, 594–636.
- Schmincke, H. U. and Sumita, M. (1998). Volcanic evolution of Gran Canaria reconstructed from apron sediments: Synthesis of VICAP Project drilling. In Weaver, P. P. E., Schmincke, H.-U., Firth, J. V., and Duffield, W., editors, *Proceedings of the Ocean Drilling Program, Scientific Results*, volume 157, pages 443–469.
- Schmincke, H. U. and Swanson, D. A. (1967). Laminar viscous flowage structures in ash-flow tuffs from Gran Canaria, Canary Islands. *J. Geol.*, 75, 641–664.
- Self, S. (1976). The recent volcanology of Terceira. *Azores. J. Geol. Soc. London*, 132, 645–666.
- Speranza, F., Branca, S., Coltelli, M., D'Ajello Caracciolo, F., and Vigliotti, L. (2006). How accurate is “paleomagnetic dating”? New evidence from historical lavas from Mount Etna. *J. Geophys. Res.*, 111, article no. B12S33.
- Speranza, F., Di Chiara, A., and Rotolo, S. G. (2012). Correlation of welded ignimbrites on Pantelleria, using paleomagnetism. *Bull. Volcanol.*, 74, 341–357.
- Speranza, F., Landi, P., D'Ajello Caracciolo, F., and Pignatelli, A. (2010). Paleomagnetic dating of the most recent silicic eruptive activity at Pantelleria (Strait of Sicily). *Bull. Volcanol.*, 72, 847–858.
- Speranza, F., Pompilio, M., D'Ajello Caracciolo, F., and Sagnotti, L. (2008). Holocene eruptive history of the Stromboli volcano: Constraints from paleomagnetic dating. *J. Geophys. Res.*, 113, article no. B09101.
- Stevenson, R. J. and Wilson, L. (1997). Physical volcanology and eruption dynamics of peralkaline agglutinates from Pantelleria. *J. Volcanol. Geoth. Res.*, 79, 97–122.
- Sumner, J. M. and Branney, M. J. (2002). The emplacement history of a remarkable heterogeneous, chemically zoned, rheomorphic and locally lava-like ignimbrite: “TL” on Gran Canaria. *J. Volcanol. Geoth. Res.*, 115, 109–138.
- Villari, L. (1969). On particular ignimbrites of the island of Pantelleria (Channel of Sicily). *Bull. Volcanol.*, 3, 828–839.
- Villari, L. (1970). The caldera of Pantelleria. *Bull. Volcanol.*, 34, 758–766.
- Villari, L. (1974). The Island of Pantelleria. *Bull. Volcanol.*, 38, 680–724.
- Walker, G. P. L. (1984). Downsag calderas, ring faults, and caldera sizes. *J. Geophys. Res.*, 89(B10), 8407–8416.
- Walker, G. P. L. (1985). Origin of coarse lithic breccias near ignimbrite source vents. *J. Volcanol. Geoth. Res.*, 25, 157–171.
- Wallmann, P. C., Mahood, G. A., and Pollard, D. P. (1988). Mechanical models for correlation of ring-fracture eruptions at Pantelleria, Strait of Sicily, with glacial sea-level drawdown. *Bull. Volcanol.*, 50, 327–339.
- Washington, H. S. (1913a). The volcanoes and rocks of Pantelleria. Part I. *J. Geol.*, 21, 653–670.
- Washington, H. S. (1913b). The volcanoes and rocks of Pantelleria. Part II. *J. Geol.*, 21, 683–713.
- Washington, H. S. (1914). The volcanoes and rocks of Pantelleria. Part III. *J. Geol.*, 22, 16–27.
- White, J. C., Neave, D. A., Rotolo, S. G., and Parker, D. F. (2020). Geochemical constraints on basalt petrogenesis in the Strait of Sicily Rift Zone (Italy): Insights into the importance of short lengthscale mantle heterogeneity. *Chem. Geol.*, 545, 1–18.
- White, J. C., Parker, D. F., and Ren, M. (2009). The origin of trachyte and pantellerite from Pantelleria, Italy: insights from major elements, trace elements, and thermodynamic modelling. *J. Volcanol. Geoth. Res.*, 179, 33–55.
- White, J. C., Ren, M., and Parker, D. F. (2005). Variation in mineralogy, temperature and oxygen fugacity in a suite of strongly peralkaline lavas and tuffs, Pantelleria, Italy. *Can. Mineral.*, 43, 1331–1347.
- Williams, R. (2010). *Emplacement of radial pyroclastic density currents over irregular topography: the chemically-zoned, low aspect-ratio Green Tuff ignimbrite*. PhD thesis, University of Leicester, Pantel-

- leria, Italy, <http://dx.doi.org/10.6084/m9.figshare.789054.v1>.
- Williams, R., Branney, M. J., and Barry, T. L. (2014). Temporal and spatial evolution of a waxing then waning catastrophic density current revealed by chemical mapping. *Geology*, 42, 107–110.
- Wolff, J. A. and Wright, J. V. (1981a). Rheomorphism of welded tuffs. *J. Volcanol. Geoth. Res.*, 10, 13–34.
- Wolff, J. A. and Wright, J. V. (1981b). Formation of the Green Tuff, Pantelleria. *Bull. Volcanol.*, 44, 681–690.
- Wright, J. V. (1980). Stratigraphy and geology of the welded air-fall tuffs of Pantelleria, Italy. *Geol. Rundsch*, 69, 263–291.
- Zanella, E., De Astis, G., and Lanza, R. (2001). Palaeomagnetism of welded, pyroclastic-fall scoriae at Vulcano, Aeolian Archipelago. *J. Volcanol. Geoth. Res.*, 107, 71–86.



Perspectives on alkaline magmas / *Perspectives sur les magmas alcalins*

Evolution of the magma system of Pantelleria (Italy) from 190 ka to present

Nina J. Jordan^{® a}, John C. White^{® *, b}, Ray Macdonald^{c, d} and Silvio G. Rotolo^{® e, f}

^a School of Geography, Geology and the Environment, University of Leicester, University Road, Leicester LE1 7RH, UK

^b Department of Geosciences, Eastern Kentucky University, 521 Lancaster Avenue, Richmond KY 40475, USA

^c IGMiP, Faculty of Geology, University of Warsaw, al. Zwirki i Wigury 93, 02-089 Warszawa, Poland

^d Environment Centre, Lancaster University, Lancaster LA1 4YQ, UK

^e Dipartimento di Scienze della Terra e del Mare, Università di Palermo, Via Archirafi 36, 90123 Palermo, Italy

^f INGV - Istituto Nazionale di Geofisica e Vulcanologia, Sezione di Palermo, Italy
E-mails: njj5@leicester.ac.uk (N. J. Jordan), john.white@eku.edu (J. C. White), raymacdonald186@gmail.com (R. Macdonald), silvio.rotolo@unipa.it (S. G. Rotolo)

Abstract. The eruptive history of Pantelleria has been marked by the eruption of nine peralkaline ignimbrites, with inter-ignimbrite episodes from small, local volcanic centres. New whole-rock geochemical data are presented for seven ignimbrites and used with published data for younger units to track compositional changes with time. From ~190 ka, silicic magmatism was dominated by comenditic trachyte to comendite compositions, evolving along generally similar liquid lines of descent (LLOD). The final ignimbrite, the Green Tuff (~46 ka), was tapped from a compositionally zoned pantelleritic upper reservoir to a trachytic mush zone. Younger (20–7 ka) silicic magmatism has been relatively small scale, with compositions similar to the earliest pre-Green Tuff pantelleritic ignimbrite (Zinedi). These data suggest that the comenditic reservoirs may have been emplaced at deeper levels than the pantelleritic reservoirs. While both types of series evolved along similar LLOD dominated by fractionation of alkali feldspar, it is the fractionation of iron that determines whether comendite or pantellerite is produced. The deeper reservoirs were more oxidizing and wetter, thus leading to the crystallization of magnetite and therefore the fractionation of iron.

Keywords. Pantelleria, Ignimbrite, Magma reservoirs, Compositional changes with time, Comendite, Pantellerite.

Available online 31st March 2021

* Corresponding author.

1. Introduction

The volcanic island of Pantelleria (adj. Pantescan) has, for the past 40 years or so, been an important focus of petrological and volcanological studies of peralkaline silicic magmatism. It is a small island (83 km²; Figure 1), for the most part very accessible and with excellent coastal exposures. It consists of a wide range of rock types (basalt, trachyte, comendite, pantellerite), erupted by a variety of mechanisms (lava flows and dome building, pyroclastic falls and flows), and in the pyroclastic units showing very complex lateral and vertical facies changes. Researchers from many institutions internationally have contributed to studies of Pantescan geology. Foremost among the reasons for this interest are the unusual geochemistry (Pantelleria is the type locality for *pantellerite*, a strongly peralkaline, iron-rich rhyolite) and the extremely complex evolutionary history, despite the volcano's youthfulness (~400 ka of subaerial activity). Attempts to evaluate the nature of, and processes within, the plumbing system have been made *via* geophysics [Gianelli and Grassi, 2001, Mattia *et al.*, 2007], geochemical, and thermodynamic modelling [Avanzinelli *et al.*, 2004, Bagiński *et al.*, 2018, Civetta *et al.*, 1984, 1988, 1998, Giuffrida *et al.*, 2020, Liszewska *et al.*, 2018, Neave *et al.*, 2012, Neave, 2020, Romano *et al.*, 2019, White *et al.*, 2005, 2009, 2020], and high P-T experiments [Di Carlo *et al.*, 2010, Romano *et al.*, 2018, 2020]. There is a broad consensus for the presence of an active geothermal system and shallow magma reservoir (at ~4 km depth) which is currently deflating and cooling [Mattia *et al.*, 2007, Civile *et al.*, 2008]. The majority of studies have been made on the Green Tuff ignimbrite (a major marker unit dated at 45.7 ± 1.0 ka; Scaillet *et al.*, 2013), and younger rocks, such that much less is known of earlier units. In this report, we use the Jordan *et al.* [2018] revision of the pre-Green Tuff stratigraphy and new whole-rock compositional data to examine how the Pantescan magma system may have changed over the period ~190 ka to the present. Detailed petrological studies of the earlier units will be presented elsewhere. A review of the volcanological evolution of Pantelleria is discussed in Rotolo *et al.* [2021]. We fully appreciate that a critical part of any magmatic system is the input from mafic magmas. Basaltic magmas have always been an important part of Pantescan magmatism and are almost

certainly the heat engine that has kept the system active. Here, however, we have concentrated on the silicic magmatism; White *et al.* [2020] provide an account of the distribution, compositions, and mantle sources of the basalts.

2. Geological setting

The island of Pantelleria lies in the Strait of Sicily, a submerged continental rift between Sicily and Tunisia (Figure 1). Most exposed rocks are felsic, ranging from metaluminous trachyte to peralkaline rhyolite, but mafic magmatism has occurred at several stages in the island's history including the most recent, offshore, eruption in 1891. The oldest documented radiometric date for felsic magmatism is 517 ± 19 ka ($^{40}\text{Ar}/^{39}\text{Ar}$), from a pantelleritic microgranite inclusion in an ignimbrite [Rotolo and Villa, 2001]. Rotolo *et al.* [2013] divided the geologic history of the island into three phases. The first phase (~324–190 ka; Mahood and Hildreth, 1986) consists of effusive and explosive activity extensively buried by younger deposits and exposed exclusively along the remote south coast; there are extremely few geochronological or geochemical data available for rocks from this phase. The second phase (~190–46 ka) includes the eruption of eight ignimbrites, ranging in composition from trachyte to comendite/pantellerite, with >20 effusive to strombolian eruptions of pantelleritic magma from small, local centres occurring between the ignimbrite events [Jordan *et al.*, 2018]. The older “La Vecchia” caldera structure on the island formed during this second phase, has been variously dated at 114 ka [Mahood and Hildreth, 1986], between 175 and 133 ka [Speranza *et al.*, 2012], and between 140 and 146 ka [Rotolo *et al.*, 2013]. The third phase began with the 45.7 ± 1.0 ka eruption of the Green Tuff [Scaillet *et al.*, 2013], the caldera-forming ignimbrite of the Cinque Denti caldera, and was followed by a prolonged period of effusive and mildly explosive activity (to ~7 ka; Scaillet *et al.*, 2011).

Jordan *et al.* [2018] applied formal stratigraphic guidelines, along with detailed field studies, palaeomagnetic data, and $^{40}\text{Ar}/^{39}\text{Ar}$ ages, to compile a new eruptive history back to the first major ignimbrite eruption, at ~190 ka, the first of eight pre-Green Tuff peralkaline ignimbrites. Ages and descriptions of the eruption units, designated as Formations,

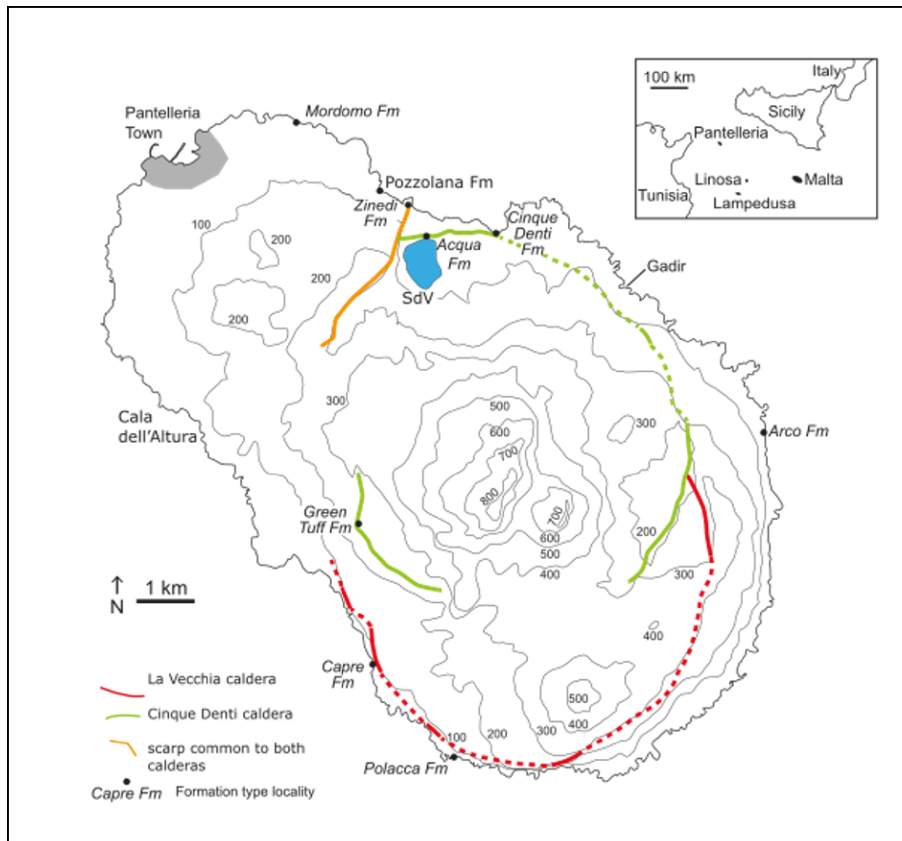


Figure 1. Map of Pantelleria showing topography (CI = 100 m), proposed calderas (after Mahood and Hildreth, 1986), post-caldera faults, type localities of the ignimbrite formations (after Jordan *et al.*, 2018), and selected locations (SdV: Lago Specchio di Venere).

are presented in Table 1 and Figure 2. An important conclusion of their study was that there were at least two and as many as five caldera collapse events associated with the ignimbrite eruptions. The ignimbrites are typically welded and variably rheomorphic and are commonly associated with pumice deposits and lithic breccias, which are interpreted as markers of caldera collapse possibly from reactivated structures [Jordan *et al.*, 2018, Rotolo *et al.*, 2013, 2021]. The onset of eruptions was normally marked by pumiceous air-fall tephra followed by ignimbrite emplacement, which in many cases blanketed the whole island; in one case, the Cinque Denti Formation, pumice fallout followed the ignimbrite emplacement [Jordan *et al.*, 2018]. Jordan *et al.* [2018] estimated the total onshore volume of all nine ignimbrites, including the Green Tuff, to be 2.32 km³ DRE, with individual volumes ranging from 0.003

to 0.64 km³ DRE. They stressed that these are on-shore values only because little is known about the amounts deposited at sea. A noteworthy observation is that eruption sizes decreased from 187 to 85 ka, with an increase in the 45.7 ka Green Tuff (Table 1; Figure 3). Inter-ignimbrite periods were characterized by effusive and explosive eruptions from small pumice cones. They are not considered here but it is acknowledged that they could add some complicating details to the evolutionary history of the magma reservoir.

As noted above, Jordan *et al.* [2018] recognized lithic breccias in several formations as markers of caldera collapse, indicating that they are located close to the inferred source caldera. They also suggested that some collapse events reshaped existing caldera scarps. If calderas can be taken to lie more or less directly above their plumbing systems,

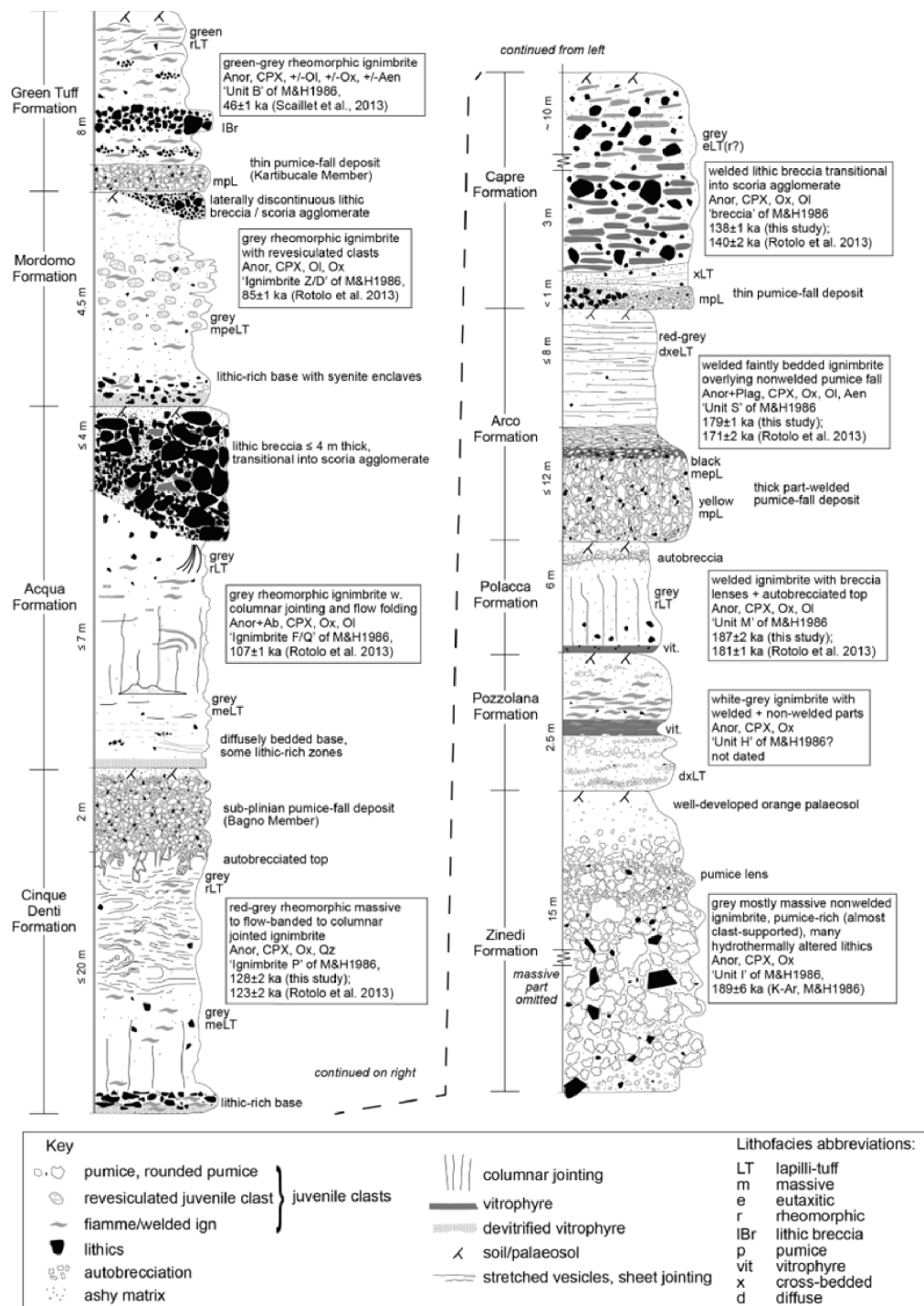


Figure 2. General vertical stratigraphy of ignimbrite-producing eruptions on Pantelleria (not to scale) from Jordan *et al.* [2018]. Logs are from the type localities of each unit. Abbreviations: M&H86, Mahood and Hildreth [1986]; Anor, anorthoclase; Cpx, clinopyroxene; Ol, olivine; Ox, Fe–Ti oxides; Aen, aenigmatite; Ab, albite; Qz, quartz; Plag, plagioclase.

Table 1. Summary of ignimbrite formations, ages, and geochemistry

Formation	Lat (N)	Long (E)	Age (ka)	Source	<i>n</i>	wt% SiO ₂	wt% TA	PI.	wt% FeO ^T	wt% Q*	ppm Zr	Zr/Nb	Ce/Y
Green Tuff	36.7750	11.9745	45.7	(1)	36	63.9–71.3	9.8–11.9	1.0–1.8	4.9–8.3	1.3–39.0	291–2061	5.1 ± 0.5	2.6 ± 0.5
Mordomo	36.8375	11.9631	85	(2)	29	65.5–70.3	10.2–11.6	1.0–1.3	4.6–5.8	5.0–22.2	658–1415	5.0 ± 0.5	2.9 ± 0.9
Acqua	36.8191	11.9872	107	(2)	25	64.5–70.8	10.3–12.1	1.1–1.4	4.3–5.7	1.5–24.9	450–1668	5.0 ± 0.3	2.4 ± 0.4
Cinque Denti	36.8200	12.0005	128	(3)	22	65.1–69.4	10.0–13.2	0.9–1.5	3.8–5.7	6.1–19.3	533–1172	5.0 ± 0.1	2.4 ± 0.3
Carpe	36.7533	11.9790	138	(3)	n.d.	n.d.	n.d.	n.d.	n.d.	n.d.	n.d.	n.d.	n.d.
Arco	36.7890	12.0530	179	(3)	8	64.1–72.8	9.8–12.5	1.0–1.4	4.6–6.3	0.4–36.5	481–2173	5.0 ± 0.5	2.6 ± 0.3
Polacca	36.7382	11.9932	187	(3)	8	65.0–66.7	11.5–12.2	1.1–1.2	5.0–5.6	4.1–10.3	397–835	4.9 ± 0.4	2.6 ± 0.2
Pozzolana	36.8265	11.9790	n.a.	n.a.	5	69.7–70.0	10.5–11.8	1.2–1.4	4.8–5.1	22.3–24.9	1616–1783	5.4 ± 0.1	2.5 ± 0.1
Zinedi	36.8242	11.9844	189	(4)	5	66.8–68.0	10.6–11.7	1.1–1.3	6.8–7.9	16.1–21.6	869–1188	4.9 ± 0.1	2.3 ± 0.2

Formation names from Jordan *et al.* [2018]. Green Tuff data are from Williams *et al.* [2014] and Liszewska *et al.* [2018]. Geographic coordinates are for type sections (see Figure 1), datum WGS84. *n* = Number of samples analysed and used in this report. Sources for ages are: (1) Scaillet *et al.* [2013] ⁴⁰Ar/³⁹Ar; (2) Rotolo *et al.* [2013] ⁴⁰Ar/³⁹Ar; (3) Jordan *et al.* [2018] ⁴⁰Ar/³⁹Ar; (4) Mahood and Hildreth [1986] K–Ar. wt% TA = Na₂O + K₂O; PI. = peralkalinity index (mol Na + K/Al); FeO^T, total iron as FeO; wt% Q* = normative Q renormalized to Q + Or + Ab = 100, calculated following Kelsey [1965] with iron oxides calculated following Le Maitre [1976]. n.a., not analysed/not applicable; n.d., no data.

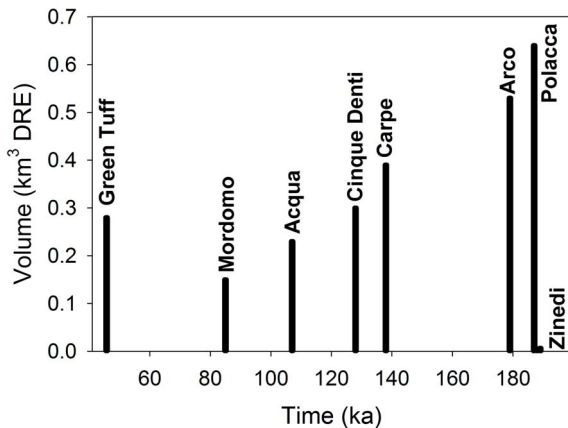


Figure 3. Onshore volumes plotted against eruption ages for the ignimbrite formation (see Table 2; adapted from Jordan *et al.*, 2018).

it seems that the reservoir has been located close to the present reservoir, which geophysical models place at ~4 km below sea level [Mattia *et al.*, 2007]. We assume, therefore, that the magmatic evolution of the island since ~190 ka has been related to one plumbing system, where that system may have varied in its structure and degree of complexity with time.

3. Analytical methods

One hundred and two samples of pre-Green Tuff ignimbrite were collected from Pantelleria during

fieldwork from 2009–2012. Representative whole-rock compositional data are presented in Table 2; the full data set is in Supplementary Table 1. Samples were dried at 100 °C overnight, crushed on a flypress to ~2 mm and then milled on an agate planetary mill to a fine powder. For whole-rock samples of ignimbrite, lithic fragments were removed as much as possible during the crushing. Loss on ignition (LOI) was determined in two steps to avoid sample fusion, which renders the powders unusable for bead making. Fusion beads (for major elements) were made from 0.6 g of powder dried following the first step mixed with a flux consisting of 0.6 g lithium tetraborate and 2.4 g lithium metaborate and melted at 1200 °C for 5–10 min. Powder pellets (for trace elements) were made from 6 g of dried powder and 1.5 g of a paraffin wax binding agent at approximately 138 MPa for 30 s. Fused beads and powder pellets were analysed on a Philips PW4400 Axios WD-XRF with a 4 kW rhodium tube at the University of Leicester. The detection limit for major elements is <0.02 wt% and in most cases ~0.003 wt%. For trace elements, detection limits range between 0.1 and 8.2 ppm. Precision, expressed as relative standard deviation across multiple analyses of any given reference material, is typically ~1–3% for major elements (except P₂O₅ and SO₃) and <10% for trace elements (Supplementary Table 2). In terms of accuracy, data obtained at Leicester tend to be slightly higher than the values accepted on the GeoREM database [Jochum *et al.*, 2007].

Table 2. Representative whole-rock analyses

Formation:	Green Tuff	Green Tuff	Mordomo	Mordomo	Acqua	Acqua	Cignue Denti	Cinque Denti	Arco	Arco	Polacca	Polacca	Pozzolana	Pozzolana	Zinedi	Zinedi
Sample ID:	150522	160542	300512-4	090612-1	100612-3d	191010-1	BDA1b	250511-2	060612-1	140612-1	310511-1	250912-1a	ukn100d	190610-1	051109-2a	061109-2a
Class:	CT	P	CT	CT	CT	C	MT	CT	CT	P	CT	CT	C	C	PT	PT
SiO ₂ , wt%	64.68	69.33	65.38	67.74	63.24	69.56	62.62	66.99	61.59	67.66	64.20	66.04	68.52	68.63	63.97	66.03
TiO ₂	0.69	0.50	0.66	0.52	0.68	0.44	0.79	0.60	0.74	0.35	0.73	0.63	0.44	0.43	0.64	0.58
Al ₂ O ₃	15.21	9.05	15.30	12.80	15.49	12.33	15.21	13.08	15.47	9.04	15.26	14.40	12.11	11.71	12.33	11.43
Fe ₂ O ₃ ^T	5.88	8.59	5.31	5.71	5.34	5.32	5.60	6.04	4.96	6.55	5.42	5.55	5.27	5.49	7.16	8.50
MnO	0.21	0.29	0.20	0.24	0.22	0.21	0.19	0.24	0.20	0.24	0.21	0.23	0.22	0.24	0.27	0.32
MgO	0.47	0.11	0.43	0.27	0.44	0.31	0.52	0.55	1.01	0.34	0.37	0.38	0.17	0.22	0.53	0.25
CaO	1.23	0.39	0.85	0.52	1.17	0.47	1.77	0.96	1.43	0.29	0.96	0.83	0.41	0.34	0.71	0.67
Na ₂ O	6.31	6.51	6.92	6.41	6.97	5.43	6.17	5.91	7.05	4.60	6.77	6.87	7.11	5.67	5.47	5.93
K ₂ O	4.57	4.62	4.58	4.54	4.54	4.72	3.83	4.40	4.00	4.50	4.99	4.55	4.53	5.01	4.57	4.44
P ₂ O ₅	0.15	0.03	0.05	0.05	0.12	0.02	0.08	0.08	0.18	0.02	0.14	0.09	0.04	0.03	0.05	0.04
SO ₃	n.a.	n.a.	0.03	0.05	0.31	bdl	0.02	0.01	0.13	0.09	0.03	0.06	0.13	0.04	0.03	0.03
Cl	n.a.	n.a.	0.57	0.59	0.72	0.41	bdl	0.66	1.14	1.23	0.14	bdl	bdl	bdl	0.22	bdl
LOI	0.20	0.10	0.57	1.27	1.73	0.92	1.38	0.82	2.97	5.94	0.33	0.74	1.93	2.90	4.57	1.75
Sum	99.60	99.52	100.86	100.71	100.95	100.14	98.17	100.33	100.88	100.87	99.55	100.37	100.89	100.71	100.53	99.98
O=Cl	n.a.	n.a.	0.13	0.13	0.16	0.09	0.00	0.15	0.26	0.28	0.03	0.00	0.00	0.00	0.05	0.00
Total	99.60	99.52	100.73	100.58	100.79	100.04	98.17	100.18	100.62	100.59	99.51	100.37	100.89	100.71	100.47	99.98
PI.	1.01	1.74	1.07	1.21	1.06	1.14	0.94	1.11	1.03	1.38	1.08	1.13	1.37	1.26	1.13	1.27
Q*	5.82	34.54	6.25	18.88	2.80	23.40	7.28	16.54	0.40	36.50	5.01	10.25	22.34	24.87	16.09	21.08
Sc, ppm	10.0	3.0	6.5	4.9	9.2	3.4	7.5	4.7	5.5	4.8	7.1	2.6	2.4	4.0	3.7	4.6
V	10.0	13.0	2.3	bdl	bdl	1.6	9.1	7.2	3.4	bdl	2.4	3.0	1.9	1.1	2.0	bdl
Co	1.7	0.2	3.6	3.1	2.4	4.2	5.8	3.0	bdl	2.7	3.2	3.5	2.9	2.9	3.8	3.4
Ni	bdl	bdl	bdl	bdl	bdl	bdl	bdl	4.1	bdl	1.6	bdl	bdl	2.6	2.2	0.7	bdl
Cu	n.a.	n.a.	56.7	58.8	57.7	bdl	0.3	bdl	57.0	61.6	bdl	bdl	3.9	3.6	2.4	bdl
Zn	n.a.	n.a.	146.6	227.4	140.2	222.8	127.9	163.0	131.3	353.7	115.4	171.9	263.7	284.1	208.0	286.1
Ga	31.3	34.7	32.4	34.3	30.8	34.7	28.2	34.2	28.6	33.9	30.9	34.6	35.4	34.9	37.7	40.6
As	n.a.	n.a.	2.5	11.3	1.4	5.4	bdl	2.8	bdl	10.3	bdl	2.4	bdl	bdl	4.8	bdl
Rb	66.0	170.7	77.5	135.4	59.8	144.5	60.8	109.7	57.0	212.3	53.6	83.5	133.5	144.5	96.2	107.6
Sr	65.4	2.8	21.3	13.2	64.3	11.9	240.1	50.0	158.1	11.1	20.1	35.1	12.6	6.8	10.8	19.7
Y	50.5	146.9	44.3	106.6	59.2	95.6	52.5	95.0	51.7	178.7	43.8	77.7	132.8	141.2	92.0	141.3
Zr	552.5	1725.2	658.4	1412.9	449.9	1668.0	533.2	1172.4	523.9	2173.0	396.9	835.1	1616.3	1783.0	868.7	1188.4
Nb	112.1	315.1	146.2	273.0	100.1	325.3	108.6	230.0	110.4	400.1	90.4	172.2	300.8	329.5	180.7	242.1
Mo	n.a.	n.a.	5.6	13.2	6.0	10.7	5.8	5.3	5.6	17.0	5.1	8.9	12.4	19.4	9.4	9.7
Sn	n.a.	n.a.	3.7	9.1	2.5	10.6	bdl	4.3	3.6	16.3	bdl	4.7	bdl	bdl	6.0	bdl
Sb	n.a.	n.a.	bdl	bdl	bdl	bdl	bdl	bdl	bdl	bdl	bdl	1.2	bdl	bdl	bdl	bdl
Cs	0.2	1.8	bdl	7.8	bdl	6.7	bdl	4.3	bdl	16.3	bdl	3.6	10.2	12.5	7.1	8.7
Ba	1893.0	52.0	668.0	142.4	812.8	50.7	1584.2	410.9	1545.6	25.6	903.0	736.6	161.6	119.1	49.0	25.0
La	84.0	212.2	49.8	137.4	68.3	141.8	66.2	134.1	68.0	229.3	53.3	103.3	164.7	181.4	117.9	142.8
Ce	152.4	394.8	96.6	281.4	134.6	301.5	135.7	257.3	135.7	455.8	113.2	210.2	320.3	369.3	223.3	275.5
Nd	67.3	153.7	44.6	108.3	62.4	107.6	53.8	115.4	58.1	175.6	48.8	86.3	125.4	138.1	99.8	119.2
W	n.a.	n.a.	2.4	3.5	1.5	bdl	bdl	2.3	bdl	9.4	1.4	1.6	bdl	bdl	bdl	bdl
Pb	n.a.	n.a.	6.6	10.3	4.9	10.0	6.2	5.7	5.6	15.0	4.1	7.6	10.6	12.9	7.4	8.5
Th	10.8	32.3	9.6	24.1	6.5	28.6	8.1	19.8	9.0	37.5	6.3	13.7	28.2	31.6	14.7	19.7
U	1.3	10.2	2.4	6.2	2.2	6.2	2.8	2.5	2.6	10.8	2.6	3.8	8.4	8.6	4.5	5.1

Full results for pre-Green Tuff Formations are in Supplementary Table 1. Representative Green Tuff samples are from Liszewska *et al.* [2018]. Class (following Le Maitre 2002; Macdonald 1974): MT, Metaluminous Trachyte; CT, Comenditic Trachyte; P, Pantelleritic Trachyte; PT, Pantelleritic Trachyte; Fe₂O₃^T, total iron as Fe₂O₃. LOI, Loss on Ignition. PI., peralkalinity index (= mol [Na + K]/Al). Q* = normative quartz renormalized to Q + Or + Ab = 100, calculated following Kelsey [1965] with iron oxides adjusted following Le Maitre [1976]. n.a., not analysed; bdl, below detection limit. Sample BDA1b collected by Rebecca Williams.

4. Significance of the Green Tuff

The Green Tuff is a very remarkable deposit; along with the post-caldera trachytes, it has provided our

most complete insight into processes in the Pantescan plumbing system. The eruption had the largest drawdown, penetrating a feldspar-rich crystal mush, subsequently erupted as the post-caldera trachytes

[White *et al.*, 2009]. It contains a complete spectrum of compositions from metaluminous trachytes to the most-evolved (pantellerite) melts yet recorded on the island (~ 10 wt% FeO^{T} , 5–3 wt% Al_2O_3 , P.I. [peralkalinity index; $\text{mol}(\text{Na} + \text{K})/\text{Al}] = 2.61$; Liszewska *et al.*, 2018). The trachytes show strong textural disequilibrium, perhaps related to thermal and compositional inputs from more mafic magmas [Ferla and Meli, 2006, Liszewska *et al.*, 2018]. Direct evidence of magma mixing processes occurs in a small lava flow of benmoreite capping the post-caldera trachytes on Montagna Grande [Romengo *et al.*, 2012]. Using olivine compositions, Romengo *et al.* [2012] raised the possibility that the trachytes may have evolved along with more than one liquid line of descent (LLOD). A suite of syenodioritic xenoliths in the trachytes also point to the presence in the system of melts of intermediate composition [Ferla and Meli, 2006]. In an innovative approach to eruptive dynamics, Williams *et al.* [2014] used Zr contents as stratigraphic markers to show that the pyroclastic flow member was deposited from a complex diachronic distribution of density currents. High-resolution analysis of the architecture of the deposit provided new insights into how the flow dynamics evolved. During eruption, mingling between layers, especially in the pantellerites, was ubiquitous, at scales down to the micrometer level, a process revealed only by detailed analysis of within-sample glasses, the first record of such intimate mixing in a peralkaline system [Liszewska *et al.*, 2018].

Thermodynamic modelling and experimental studies have provided precise estimates of conditions within the reservoir. From the bottom to the top of the magma reservoir, temperatures decreased from 900 to 700 °C, oxygen fugacity ($f\text{O}_2$) increased from $\Delta\text{FMQ}-1.5$ to $\Delta\text{FMQ}-0.5$, and silica activity relative to quartz saturation ($a\text{SiO}_2[\text{Qtz}]$) increased from 0.74 to 1.00 [Di Carlo *et al.*, 2010, Liszewska *et al.*, 2018, Romano *et al.*, 2018, 2020, White *et al.*, 2005, 2009]. The change in oxygen fugacity has been interpreted by these authors as reflecting a roofward increase in water content in the magma. However, evidence from melt inclusions revealed nearly identical concentrations of ~ 4 wt% H_2O from the middle and base of the Green Tuff section, but with much lower concentrations (~ 1.2 wt% H_2O) in the comenditic trachyte top of the section [Lanzo *et al.*, 2013, Romano *et al.*, 2019] and may also reflect an increase

of $\text{Fe}^{3+}/\Sigma\text{Fe}$ due to increasing peralkalinity [Stabile *et al.*, 2017]. Finally, using data from olivine zoning in basalts, Giuffrida *et al.* [2020] suggested that eruption of the Green Tuff and collapse of the Cinque Denti caldera had a profound influence on the internal structure of Pantelleria. For example, the supply of magma from deep crustal storage zones decreased after the eruption, while the dynamics of magma transfer in the upper parts of the plumbing system were enhanced.

5. Geochemistry of the pre-Green Tuff Formations

The rocks of the pre-Green Tuff Formations range from metaluminous (P.I. = 0.94–0.99) to peralkaline (P.I. > 1.0). All units plot together on the total-alkalis silica (TAS) diagram (Figure 4a; Le Maitre, 2002), with trachyte being the dominant rock type. In contrast with the Green Tuff, most of the pre-Green Tuff peralkaline types lie in a cluster straddling the comenditic trachyte–comendite boundary on the $\text{FeO}^{\text{T}}-\text{Al}_2\text{O}_3$ classification diagram (Figure 4b; Macdonald, 1974). Some analyses from the Zinedi and Arco Formations plot just within the pantellerite field. Harker diagrams (Figure 5) show that comenditic trachytes (~ 64 wt% SiO_2) from each suite are broadly similar with respect to major element compositions (~ 0.7 wt% TiO_2 , ~ 15.3 wt% Al_2O_3 , ~ 5.4 wt% FeO^{T} , ~ 6.7 wt% Na_2O). With increasing SiO_2 contents, there are decreases in TiO_2 , Al_2O_3 , CaO , and Na_2O for all suites, with Al_2O_3 decreasing more rapidly in the Green Tuff and Zinedi formations. K_2O shows approximately unchanging behaviour in all formations. For nearly all of the pre-Green Tuff Formations, FeO^{T} also demonstrates little variability, decreasing slightly at higher SiO_2 in contrast to the Green Tuff and Zinedi Formations, which show iron-enrichment trends.

SiO_2 is plotted against three other compositional parameters in Figure 6. In all formations, peralkalinity increases with increasing SiO_2 , with the more rapid decrease of Al_2O_3 in the Green Tuff resulting in overall higher peralkalinity. Figure 6b plots SiO_2 versus $1.33 \cdot \text{FeO}^{\text{T}}/(\text{Al}_2\text{O}_3-4.4)$ [hereafter labelled $\text{Fe}^{\text{T}}/\text{Al}$], which has a value of 1.0 along the pantelleritic–comenditic boundary seen in Figure 4b; the trachyte–rhyolite boundary occurs at 69 wt% SiO_2 (Figure 4a). This figure more clearly shows the variation in FeO^{T} relative to Al_2O_3 with increasing SiO_2

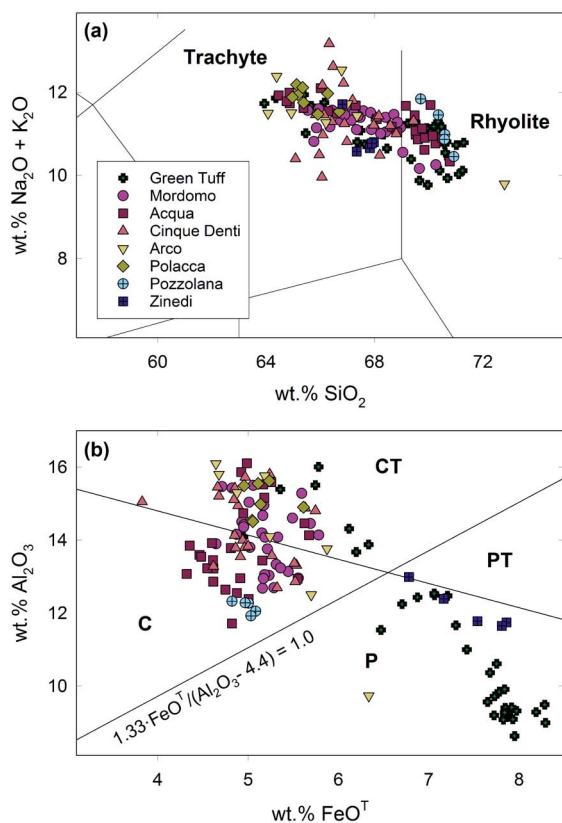


Figure 4. Geochemical classification of the ignimbrites on the (a) total-alkali silica (TAS; Le Maitre, 2002) diagram and on the (b) Macdonald [1974] classification scheme for peralkaline silicic rocks. Green Tuff whole-rock data are from Liszewska *et al.* [2018] and Williams *et al.* [2014]. Pre-Green Tuff data are presented in Supplementary Table 1.

and provides a comprehensive classification scheme consistent with Le Maitre [2002] which we adopt for use in Table 2 and Supplementary Table 1. This plot also shows that, unlike the Green Tuff and Zinedi Formations that have relatively rare comenditic trachyte compositions, comenditic trachyte is the dominant rock type in the pre-Green Tuff Formations, and it evolves towards comendite with only a slight increase in Fe^T/Al . In all formations, there is a generally strong positive correlation and range of values between SiO_2 and Zr (Figure 6c). Normative quartz (Q^*) renormalized to quartz (Q) + orthoclase (Or) + albite (Ab) = 100 is presented in Figure 6d. This parameter is used to quantify silica-oversaturation as the LLOD moves

from the feldspar join ($Q^* = 0$) in the system Q–Or–Ab to a minimum composition on the feldspar–quartz cotectic. To determine these values, iron oxides were adjusted following Le Maitre [1976] and CIPW norms for whole-rock analyses were calculated using the method of Kelsey [1965]. This plot clearly shows that although least-evolved (~ 64 wt% SiO_2) comenditic trachyte in all formations is close to quartz saturation, Q^* in the pre-Green Tuff formations (except Zinedi and Arco) is significantly lower with increasing SiO_2 . Because there is an inverse relationship between silica activity and pressure [Nicholls *et al.*, 1971], this may reflect deeper-seated magma chambers for the comenditic trachyte–comendite formations and shallower magma chambers for the comenditic trachyte–pantellerite formations. This is supported by the experimental work of Tuttle and Bowen [1958], Johannes and Holtz [1996], Wilke *et al.* [2017], and others who document a strong negative correlation between the maximum value of Q^* on the feldspar–quartz cotectic and pressure.

Incompatible trace element ratios are remarkably similar for all units (Figure 7 and Table 1), which suggests that throughout the 190 ka history discussed here the felsic magmas evolved from a similar type of basalt. A common basaltic origin for these rocks is also supported by similar patterns observed in multi-element variation diagrams (Figure 8, normalized to depleted MORB mantle [DMM]; Salters and Stracke, 2004), which are nearly identical in shape to each other and to a representative sample of the low Ti–P, pre-Green Tuff basalt shown in Figure 8a (sample 130911; White *et al.*, 2020) with the exception of the compatible trace elements Ba, Sr, P, and Ti, which may reflect fractionation of feldspar, apatite, and Fe–Ti oxides [cf. Civetta *et al.*, 1998, Neave *et al.*, 2012, White *et al.*, 2009]. For a given concentration of Zr, Sr and Ba are higher in the Mordomo, Cinque Denti, and Arco Formations than the others although they all converge to similar levels at >1500 ppm Zr. The elevated Sr and Ba concentrations in these rocks may suggest a significant role for accumulation of alkali feldspar in these rocks. From basalt to comenditic trachyte, all trace elements in Figure 8 show a similar magnitude of increase, with the exception of P, Sr, and Ti, suggesting these trachytes were derived from basalt via fractionation of plagioclase, Fe–Ti oxides, and apatite. From comenditic trachyte to pantellerite, most elements continue to increase

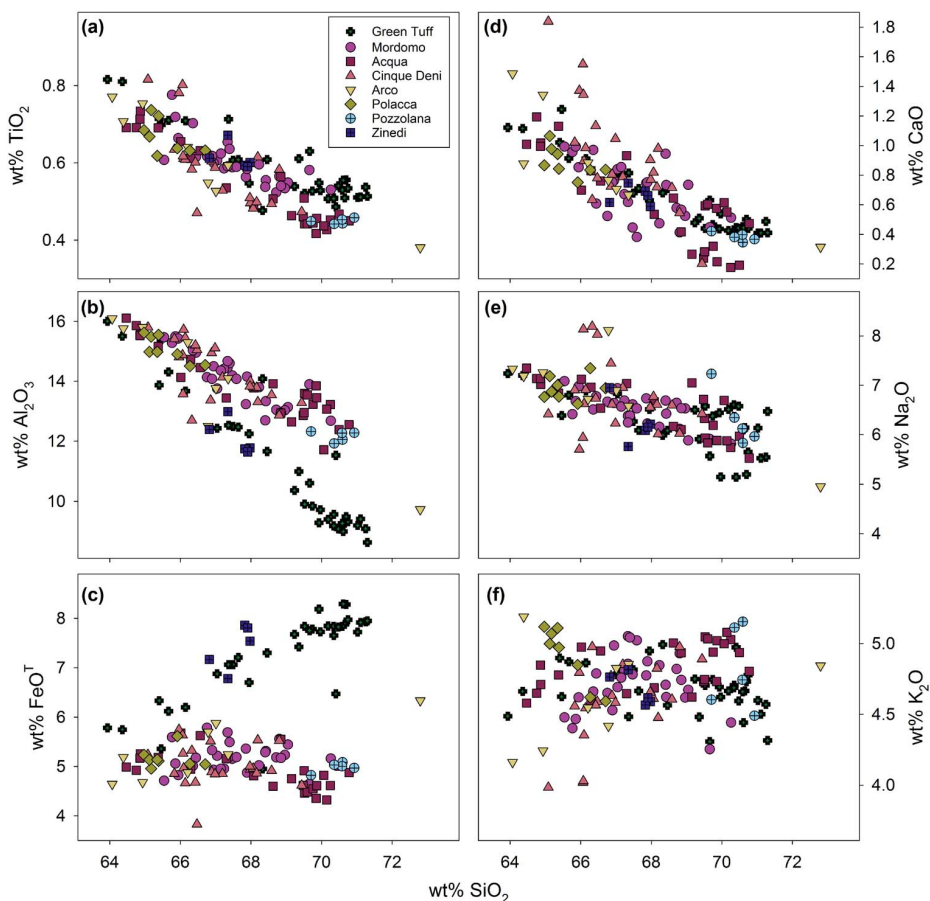


Figure 5. Major element variation diagrams for whole-rock data from the ignimbrites (see Supplementary Table 1). Green Tuff whole-rock data are from Liszewska *et al.* [2018] and Williams *et al.* [2014].

with the exception of K, which shows nearly constant behaviour (cf. Figure 5f), Ti (which decreases slightly), P (apatite fractionation) and Sr and Ba, reflecting a dominant role of alkali feldspar fractionation in the formation of both comendite and pantellerite from comenditic trachyte. The trends are similar to those reported in previous studies of Pantescan suites [Civetta *et al.*, 1998, Liszewska *et al.*, 2018, Neave *et al.*, 2012, White *et al.*, 2009]. The petrology of individual ignimbrite formations is the subject of ongoing investigations.

Coexisting basalt–comendite and basalt–pantellerite series have been documented in other intraplate settings, such as the Boseti volcanic complex, Ethiopia [Ronga *et al.*, 2009], Changbaishan, China–North Korean [Andreeva *et al.*, 2019], and Terceira, Azores [Mungall and Martin, 1995]. At Ter-

ceira, Mungall and Martin [1995] observed that magnetite is the dominant Fe–Ti oxide (>2.5 vol%) in the basalt–comendite series, whereas ilmenite (s.s. with low haematite component) is the dominant oxide (0.4 to 0.6 vol%) in the basalt–pantellerite series. The same seems to be true at Pantelleria: although ilmenite is the dominant or sole oxide phase in the pantellerites [White *et al.*, 2005, 2009], magnetite (s.s. with high ulvöspinel component) is the dominant or sole oxide phase in the comendites [Jordan, 2014]. Experimental studies have shown that fO_2 exerts a strong control on oxide crystallization, with more reducing conditions favouring ilmenite and more oxidizing conditions favouring magnetite [Ishihara, 1977, Toplis and Carroll, 1995], and also favouring fayalitic olivine over clinopyroxene [Romano *et al.*, 2018]. At Terceira, Mungall and Mar-

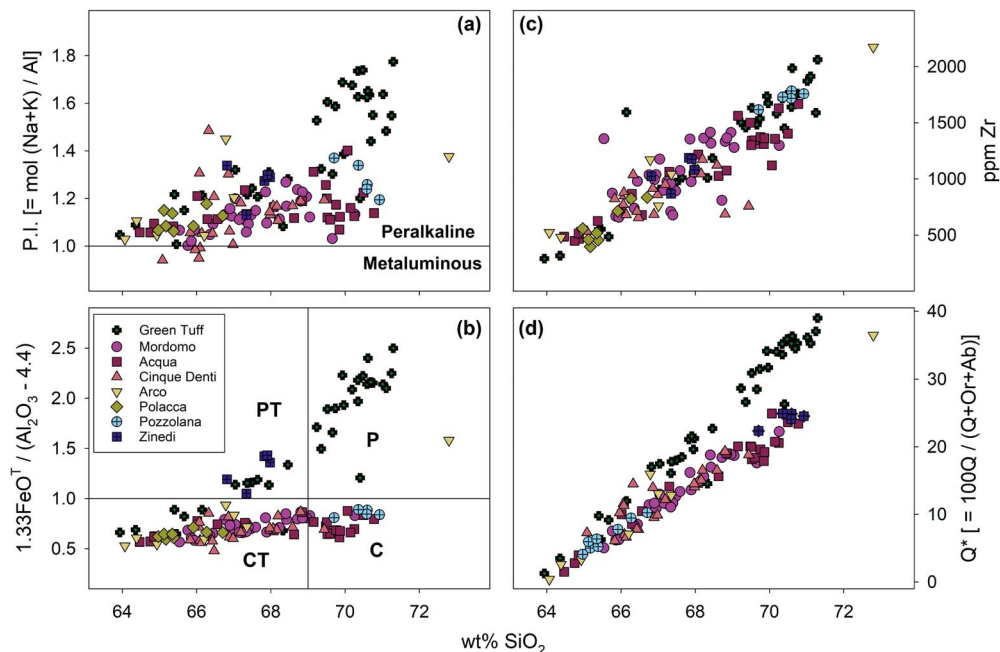


Figure 6. Variation of SiO_2 with (a) the peralkalinity index [P.I.]; (b) relative variability of FeO^T and Al_2O_3 (adapted from Macdonald, 1974); (c) concentration of Zr; and (d) silica-oversaturation, as $Q^* = 100 \cdot Q / (Q + \text{Or} + \text{Ab})$ for the ignimbrites. Green Tuff whole-rock data are from Liszewska *et al.* [2018] and Williams *et al.* [2014].

tin [1995] proposed that the differences between the two series were therefore primarily the result of higher $f\text{O}_2$ in the basalt–comendite series most likely due to higher water content, and a similar process was proposed at Changbaishan [Andreeva *et al.*, 2019]. We propose that the same may also be true at Pantelleria.

6. Post-Green Tuff trachyte and pantellerite

Eruption of caldera-filling metaluminous trachyte lavas that comprise the Monte Gibebe–Montagna Grande shield volcano followed the eruption of the Green Tuff ignimbrite and collapse of the Cinque Denti caldera (K/Ar 44 ± 8 to 28 ± 16 ka; Cornette *et al.*, 1983, Mahood and Hildreth, 1986). The creation of this intracaldera shield volcano was followed by eruption of pantelleritic trachyte to pantellerite lavas and tuffs, which formed a series of at least 24 coalescing domes, cones, and shields mostly along the rim of, or within, the moat of the caldera from 30–7 ka [Cornette *et al.*, 1983, Mahood and Hildreth,

1986, Scaillet *et al.*, 2011]. The pantellerites are generally similar to those formed during the late stages of formation of the post-caldera trachytes. Some, at least, were compositionally zoned, for example, the Khaggiar lava flow and Randazzo pumices, which can be used to typify this phase of magmatism [Landi and Rotolo, 2015, Neave, 2020, Perugini *et al.*, 2002]. The flow and pumices were erupted at ~8 ka from cones north of Montagna Grande. The compositions range from comenditic trachyte to pantellerite, with overall similarities to the Zinedi Formation (Figure 4b). Neave [2020] has found that there were at least three magma types: trachytes, less evolved pantellerites, and more evolved pantellerites. Compositional variability was generated by accumulation of feldspar into evolved pantellerites, the injection of trachyte magma into less evolved pantellerites and the accumulation of relatively primitive feldspars in trachytic magmas.

Importantly, Neave [2020] proposed that the plumbing system experienced several recharge events prior to eruption and raised the possibility that the three magma types were stored in a com-

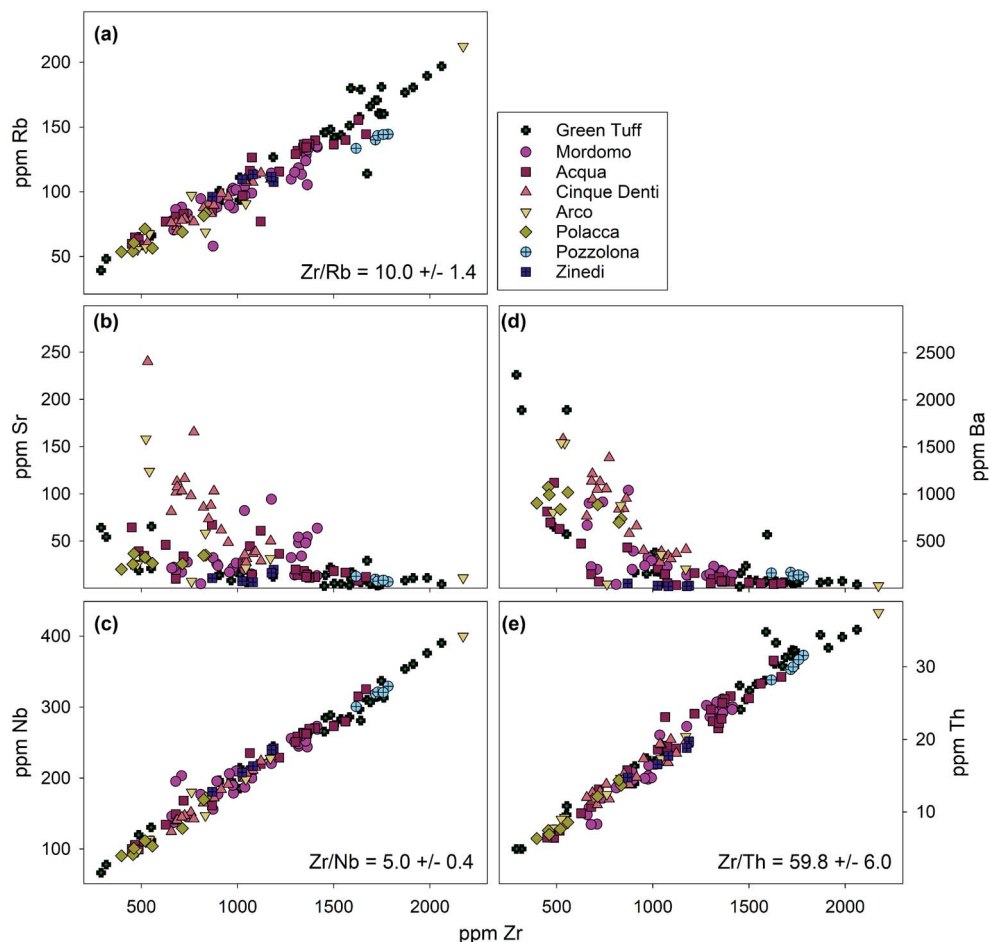


Figure 7. Trace element variation diagrams plotted versus Zr. Incompatible trace element ratios calculated from the entire dataset. Green Tuff whole-rock data are from Liszewska *et al.* [2018] and Williams *et al.* [2014].

partmentalized system and followed different LLOD. His cartoon model of the plumbing system comprises an initial stack of three lens-shaped reservoirs connected by dykes. As time progressed, crystal mush erosion connected the upper two reservoirs and the Randazzo and Khaggiar rocks were erupted from this mixed reservoir. The model is in contrast to models of the Green Tuff reservoir, which show a more standard representation of a trachytic mush zone overlain by a stably stratified reservoir zoned from comenditic trachyte to pantellerite [Landi and Rotolo, 2015, Liszewska *et al.*, 2018, Neave *et al.*, 2012]. If the Green Tuff reservoir structure was indeed replaced by another, the change took place in ~13 ka or less. Nonetheless, Neave [2020] stressed that the

complexity shown by this small event (<0.1 km³ DRE) is analogous to that in much bigger peralkaline eruptions, such as the Green Tuff, and in their calc-alkaline counterparts.

Compositional trends for the post-Green Tuff pantellerites are presented in Figure 9. Trachyte lavas are metaluminous to slightly peralkaline (P.I. = 0.90–1.06, with one sample with 1.17 from the “youngest flow” of pantelleritic trachyte on the northeastern flank of Monte Gibeale) and silica-saturated to slightly oversaturated ($Q^* = 0.0$ –8.75 and 17.8), with Q^* values and Zr concentrations consistent with the compositional trends of the Green Tuff. Post-caldera pantellerite lavas generally follow the trend of the Green Tuff Formation, but are characterized by higher P.I., Zr,

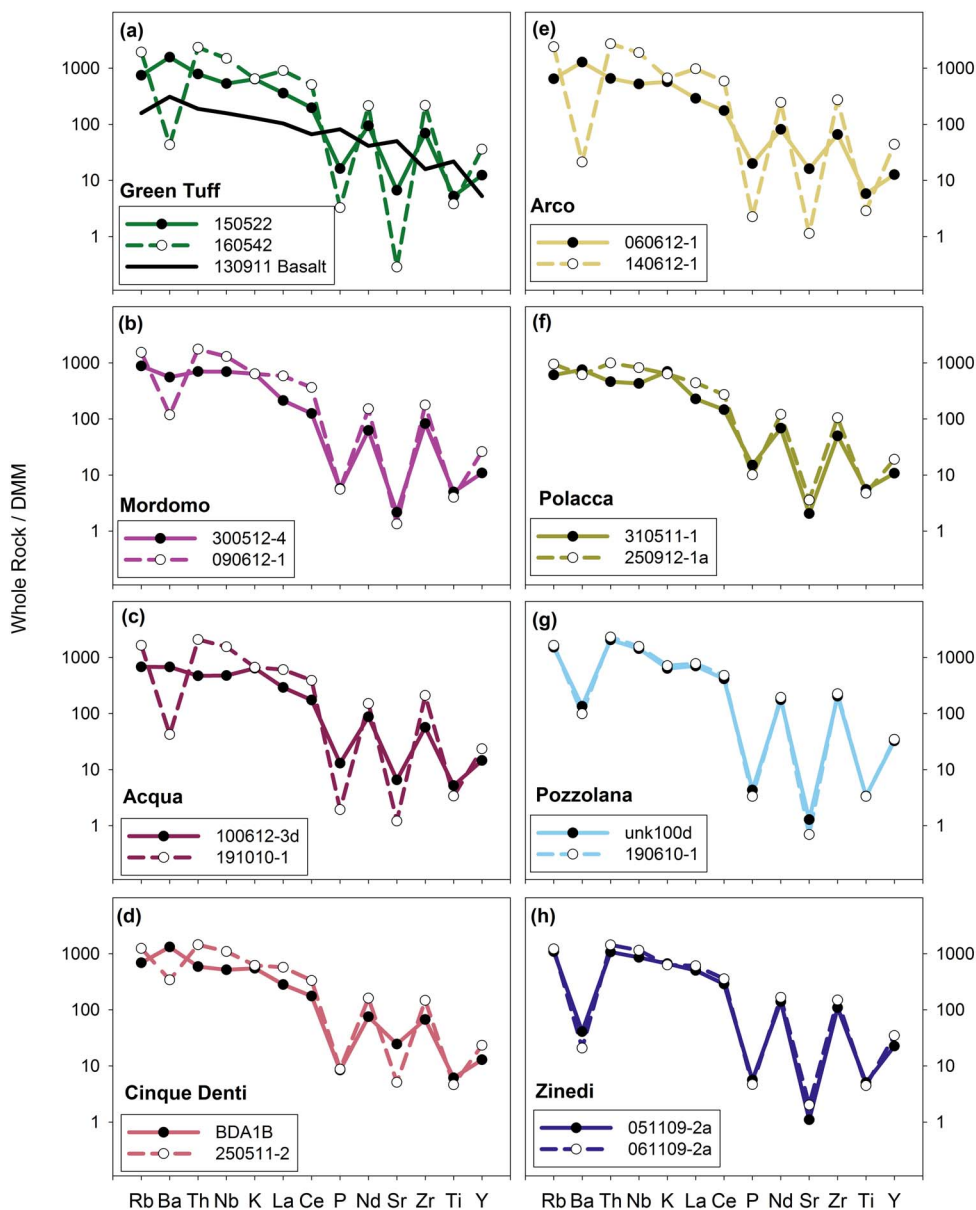


Figure 8. Multi-element variation diagrams normalized to depleted MORB mantle [DMM; Salters and Stracke, 2004] for representative least- and most-evolved samples of each formation (see Table 2). Included with the Green Tuff (a) is a sample of pre-Green Tuff basalt (130911; White *et al.*, 2020) for comparison. Green Tuff data are adapted from Liszewska *et al.* [2018].

and Q^* at a given concentration of SiO_2 . Both trends terminate at approximately the same value of Q^* , which may imply that these magma reservoirs were stored at similar depths.

As to the future, based on high-precision $^{40}\text{Ar}/^{39}\text{Ar}$ ages for activity of the past 20 ka, Scaillet *et al.* [2011]

recognized a long-term (>15 ka) decline in eruptive frequency, from 3.5 ka^{-1} to 0.8 ka^{-1} . Combined with geodetic evidence that the caldera floor is deflating and subsiding [De Guidi and Monaco, 2009, Mattia *et al.*, 2007], Scaillet *et al.* [2011] proposed that the intracaldera system is on the wane, with no evi-

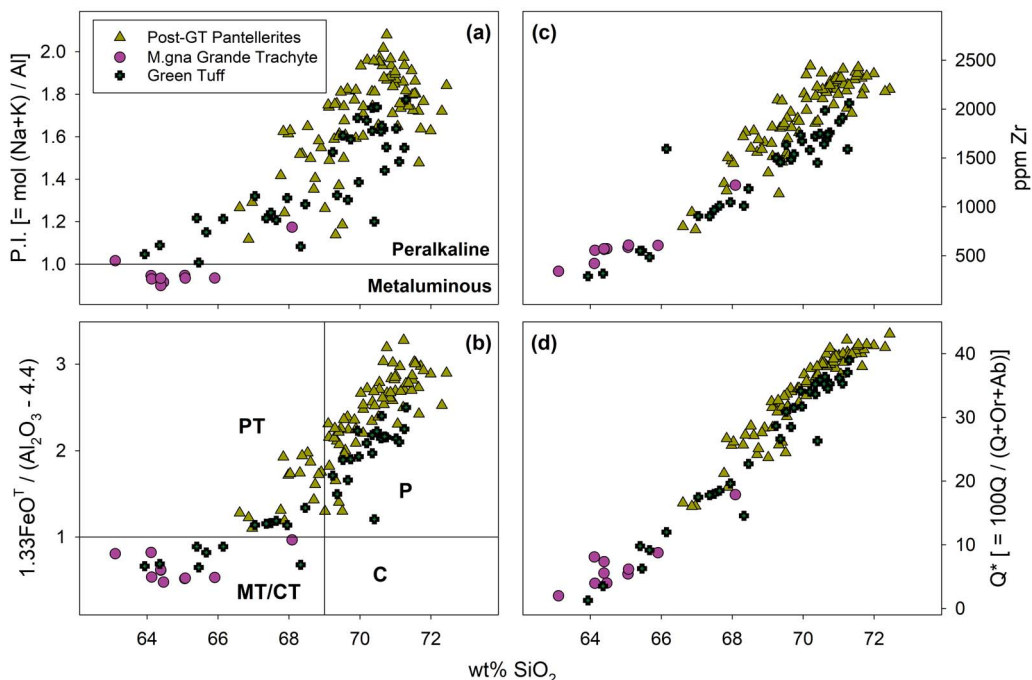


Figure 9. Variation of SiO₂ with (a) the peralkalinity index [P.I.]; (b) relative variability of FeO^T and Al₂O₃ (adapted from Macdonald, 1974); (c) concentration of Zr; and (d) silica-oversaturation, as $Q^* = 100 \cdot Q / (Q + Or + Ab)$ for the post-Green Tuff trachytes and pantellerites. Green Tuff whole-rock data are from Liszewska *et al.* [2018] and Williams *et al.* [2014]. Other data from Civetta *et al.* [1984, 1998], Perugini *et al.* [2002], Avanzinelli *et al.* [2004], Parker and White [2008], White *et al.* [2005, 2009], Ferla and Meli [2006], Rotolo *et al.* [2007].

dence for a forthcoming eruption. However, in noting the similarities between the current period and pre-Green Tuff inter-ignimbrite periods, Jordan *et al.* [2018] cautioned against assuming that no large, catastrophic eruption will occur in the future, although perhaps not imminently.

The Pantelleria trough, in which the volcano is situated, has high average heat flow (94 ± 21 mW·m⁻²; Verzhbitsky and Kononov, 2003) and a strong positive Bouguer anomaly (65–103 mGal; Behncke *et al.*, 2006, Civile *et al.*, 2008), features which have been taken to indicate the presence of abundant basaltic magmas at depth [Della Vedova *et al.*, 1995]. Some workers have suggested that there has been asthenospheric upwelling to ~60 km [Argnani and Torelli, 2001, Civile *et al.*, 2008, Della Vedova *et al.*, 1995, White *et al.*, 2020]. Ascent of basaltic magma into the Pantescan reservoir, perhaps promoted by increased tensional regional stresses, could result in renewed silicic magmatism.

7. Conclusions

- (1) From ~190 to 46 ka, the Pantescan plumbing system erupted eight ignimbritic formations from what is inferred to have been a stably stratified reservoir.
- (2) The earliest ignimbrite (Zinedi Fm.) was pantelleritic whereas later ignimbrites had comenditic affinities.
- (3) The Green Tuff eruption at 45.7 ± 1.0 ka, which produced the ninth and last ignimbrite, was apparently considerably more complex than earlier activity, ranging from metaluminous trachytes to pantellerites. It was immediately followed by a suite of trachytes taken to represent a mush zone in the reservoir.
- (4) Magmatism from 25–7 ka was dominated by pantellerites broadly similar in composition to those of the oldest ignimbrite. The upper

part of the plumbing system has shown signs of increasingly open system behaviour.

- (5) All felsic series evolved from a similar basaltic parent along similar LLOD leading to trachyte, with differences in both pressure (depth of the reservoir) and oxygen fugacity (possibly linked to water content) contributing to whether the trachyte evolved to comendite (under higher pressures and more oxidizing conditions) or to pantellerite (under lower pressures and more reducing conditions). Detailed petrogenetic studies of these older comendite units are necessary and ongoing.

Acknowledgements

NJJ gratefully acknowledges funding from the German Academic Exchange Service, Geological Society of London, Mineralogical Society of Great Britain and Ireland, Geologists' Association, Quaternary Research Association, Volcanic and Magmatic Studies Group, and the Department of Geology at the University of Leicester. We wish to thank Raffaello Cioni and an anonymous reviewer for their helpful comments.

Supplementary data

Supporting information for this article is available on the journal's website under <https://doi.org/10.5802/crgeos.50> or from the author.

References

- Andreeva, O. A., Andreeva, I. A., and Yarmolyuk, V. V. (2019). Effect of redox conditions of the evolution of magmas of Changbaishan Tianchi volcano, China–North Korea. *Chem. Geol.*, 508, 225–233.
- Argnani, A. and Torelli, L. (2001). The Pelagian Shelf and its graben system (Italy/Tunisia). In Ziegler, P. A., Cavassa, W., Robertson, A. H. F., and Crasquin-Soleau, S., editors, *Peri-Tethys Memoir 6: Peri-Tethyan Rift/Wrench Basins and Passive Margins*, volume 186 of *Mem. Mus. Natl. Hist. Nat.*, pages 529–544. Editions du Muséum, Paris.
- Avanzinelli, R., Bindi, L., Menchetti, S., and Conticelli, S. (2004). Crystallization and genesis of peralkaline magmas from Pantelleria Volcano, Italy: an integrated petrological and crystal-chemical study. *Lithos*, 73, 41–69.
- Bagiński, B., Macdonald, R., White, J. C., and Ježak, L. (2018). Tuhualite in a peralkaline rhyolitic ignimbrite from Pantelleria, Italy. *Eur. J. Mineral.*, 30, 367–373.
- Behncke, B., Berrino, G., Corrado, G., and Velardita, R. (2006). Ground deformation and gravity changes on the island of Pantelleria in the geodynamic framework of the Sicily Channel. *J. Volcanol. Geotherm. Res.*, 150, 146–162.
- Civetta, L., Cornette, Y., Crisci, G. M., Gillot, P. Y., Orsi, G., and Requejo, C. S. (1984). Geology, geochronology and chemical evolution of the island of Pantelleria. *Geol. Mag.*, 121, 541–668.
- Civetta, L., Cornette, Y., Gillot, P. Y., and Orsi, G. (1988). The eruptive history of Pantelleria (Sicily Channel) in the last 50 ka. *Bull. Volcanol.*, 50, 47–57.
- Civetta, L., D'Antonio, M., Orsi, G., and Tilton, G. R. (1998). The geochemistry of volcanic rocks from Pantelleria island, Sicily Channel: petrogenesis and characteristics of the mantle source region. *J. Petrol.*, 39, 1453–1491.
- Civile, D., Lodolo, E., Tortorici, L., Lanzafame, G., and Brancolini, G. (2008). Relationships between magmatism and tectonics in a continental rift: the Pantelleria Island region (Sicily Channel, Italy). *Marine Geol.*, 251, 32–46.
- Cornette, Y., Crisci, G. M., Gillot, P. Y., and Orsi, G. (1983). Recent volcanic history of Pantelleria: a new interpretation. *J. Volcanol. Geotherm. Res.*, 17, 361–373.
- De Guidi, G. and Monaco, C. (2009). Late Holocene vertical deformation along the coast of Pantelleria Island (Sicily Channel, Italy). *Quat. Internat.*, 206, 158–165.
- Della Vedova, B., Lucazeau, F., Pasquale, V., Pellis, G., and Verdoya, M. (1995). Heat flow in the tectonic provinces crossed by the southern segment of the European Geotraverse. *Tectonophysics*, 244, 57–74.
- Di Carlo, I., Rotolo, S., Scaillet, B., Buccheri, V., and Pichavant, M. (2010). Phase equilibrium constraints on pre-eruptive conditions of recent explosive volcanism of Pantelleria Island, Italy. *J. Petrol.*, 51, 2245–2276.
- Ferla, P. and Meli, C. (2006). Evidence of magma mix-

- ing in the 'Daly Gap' of alkaline suites: a case study from the enclaves of Pantelleria (Italy). *J. Petrol.*, 47, 1467–1502.
- Gianelli, G. and Grassi, S. (2001). Water-rock interaction in the active geothermal system of Pantelleria, Italy. *Chem. Geol.*, 181, 113–130.
- Giuffrida, M., Nicotra, E., and Viccaro, M. (2020). Changing modes and rates of mafic magma supply at Pantelleria (Sicily Channel, Southern Italy): new perspectives on the volcano factory drawn upon olivine records. *J. Petrol.*, 61, 1–22.
- Ishihara, S. (1977). The magnetite-series and ilmenite-series granitic rocks. *Mining Geol.*, 27, 293–305.
- Jochum, K. P., Nohl, U., Herwig, K., Lammel, E., Stoll, B., and Hofmann, A. W. (2007). GeoReM: A new geochemical database for reference materials and isotopic standards. *Geostand. Geoanal. Res.*, 29, 333–338.
- Johannes, W. and Holtz, F. (1996). The haplogranite system Qz–Ab–Or. In Johannes, W. and Holtz, F., editors, *Petrogenesis and Experimental Petrology of Granitic Rocks*, pages 18–57. Springer, London.
- Jordan, N. J. (2014). *Pre-Green Tuff explosive eruptive history, petrogenesis and proximal-distal tephra correlations of a peralkaline caldera volcano: Pantelleria, Italy*. PhD thesis, University of Leicester, UK.
- Jordan, N. J., Rotolo, S. G., Williams, R., Speranza, E., McIntosh, W. C., Branney, M. J., and Scaillet, S. (2018). Explosive eruptive history of Pantelleria, Italy: Repeated caldera collapse and ignimbrite emplacement at a peralkaline volcano. *J. Volcanol. Geotherm. Res.*, 349, 47–73.
- Kelsey, C. H. (1965). Calculation of the C.I.P.W. norm. *Mineral. Mag.*, 34, 276–282.
- Landi, P. and Rotolo, S. G. (2015). Cooling and crystallization recorded in trachytic enclaves hosted in pantelleritic magmas (Pantelleria, Italy): Implications for pantellerite genesis. *J. Volcanol. Geotherm. Res.*, 301, 169–179.
- Lanzo, G., Landi, P., and Rotolo, S. G. (2013). Volatiles in pantellerite magmas: A case study of the Green Tuff Plinian eruption (Island of Pantelleria, Italy). *J. Volcanol. Geotherm. Res.*, 262, 153–163.
- Le Maitre, R. W. (1976). Some problems of the projection of chemical data into mineralogical classifications. *Contrib. Mineral. Petrol.*, 56, 181–189.
- Le Maitre, R. W., editor (2002). *Igneous Rocks, a Classification and Glossary of Terms: Recommendations of the International Union of Geological Sciences Subcommission on the Systematics of Igneous Rocks*. Cambridge University Press, Cambridge, UK, 2nd edition. 236 p.
- Liszewska, K. M., White, J. C., Macdonald, R., and Bagiński, B. (2018). Compositional and thermodynamic variability in a stratified magma chamber: Evidence from the Green Tuff Ignimbrite (Pantelleria, Italy). *J. Petrol.*, 59, 2245–2272.
- Macdonald, R. (1974). Nomenclature and petrochemistry of the peralkaline oversaturated extrusive rocks. *Bull. Volcanol.*, 38, 498–516.
- Mahood, G. A. and Hildreth, W. (1986). Geology of the peralkaline volcano at Pantelleria, Strait of Sicily. *Bull. Volcanol.*, 48, 143–172.
- Mattia, M., Bonaccorso, A., and Guglielmino, F. (2007). Ground deformations in the Island of Pantelleria (Italy): Insights into the dynamics of the current intereruptive period. *J. Geophys. Res.*, 112, article no. B11406.
- Mungall, J. E. and Martin, R. F. (1995). Petrogenesis of basalt-comendite and basalt-pantellerite series, Terceira, Azores, and some implications for the origin of ocean-island rhyolites. *Contrib. Mineral. Petrol.*, 119, 43–55.
- Neave, D. A. (2020). Chemical variability in peralkaline magmas and magma reservoirs: insights from the Khaggiar lava flow, Pantelleria, Italy. *Contrib. Mineral. Petrol.*, 175, article no. 39.
- Neave, D. A., Fabbro, G., Herd, R. A., Petrone, C. M., and Edmonds, M. (2012). Melting, differentiation and degassing at the Pantelleria volcano, Italy. *J. Petrol.*, 53, 637–663.
- Nicholls, J., Carmichael, I. S. E., and Stormer Jr., J. C. (1971). Silica activity and P_{total} in igneous rocks. *Contrib. Mineral. Petrol.*, 33, 1–20.
- Parker, D. F. and White, J. C. (2008). Large-scale alkalic magmatism associated with the Buckhorn caldera, Trans-Pecos Texas, USA: Comparison with Pantelleria, Italy. *Bull. Volcanol.*, 70, 403–415.
- Perugini, D., Poli, G., and Prosperini, N. (2002). Morphometric analysis of magmatic enclaves: a tool for understanding magma vesiculation and ascent. *Lithos*, 61, 225–235.

- Romano, P., Andújar, J., Scaillet, B., Romengo, N., Di Carlo, I., and Rotolo, S. G. (2018). Phase equilibria of Pantelleria trachytes (Italy): constraints on pre-eruptive conditions and on the metaluminous to peralkaline transition in silicic magmas. *J. Petrol.*, 59, 559–588.
- Romano, P., Scaillet, B., White, J. C., Andújar, J., Di Carlo, I., and Rotolo, S. G. (2020). Experimental and thermodynamic constraints on mineral equilibrium in pantelleritic magmas. *Lithos*, 376–377, article no. 105793.
- Romano, P., White, J. C., Ciulla, A., Di Carlo, I., D'Oriano, C., Landi, P., and Rotolo, S. G. (2019). Volatiles and trace elements content in melt inclusions from the zoned Green Tuff ignimbrite (Pantelleria, Sicily): petrological inferences. *Ann. Geophys.*, 62, article no. VO09.
- Romengo, N., Landi, P., and Rotolo, S. G. (2012). Evidence of basaltic magma intrusions in a trachytic magma chamber at Pantelleria (Italy). *Period. Mineral.*, 81, 163–178.
- Ronga, E., Lustrino, M., Marzoli, A., and Melluso, L. (2009). Petrogenesis of a basalt-comendite-pantellerite rock suite: the Boseti volcanic complex (main Ethiopian rift). *Mineral. Petrol.*, 98, 227–243.
- Rotolo, S. G., La Felice, S., Mangalaviti, A., and Landi, P. (2007). Petrology and geochemistry of the recent (<25 ka) silicic volcanism at Pantelleria island. *Boll. Soc. Geol. Ital.*, 126, 191–208.
- Rotolo, S. G., Scaillet, S., La Felice, S. L., and Vita-Scaillet, G. (2013). A revision of the structure and stratigraphy of pre-Green Tuff ignimbrites at Pantelleria (Strait of Sicily). *J. Volcanol. Geotherm. Res.*, 250, 61–74.
- Rotolo, S. G., Scaillet, S., Speranza, F., White, J. C., Williams, R., and Jordan, N. J. (2021). Volcanological evolution of Pantelleria Island (Strait of Sicily) peralkaline volcano: a review. *C. R. Geosci.*, 353(S2), 111–132.
- Rotolo, S. G. and Villa, L. M. (2001). ^{39}Ar – ^{40}Ar dating of an alkali-granite enclave from Pantelleria. *Period. Mineral.*, 70, 269–275.
- Salters, V. J. M. and Stracke, A. (2004). Composition of depleted mantle. *Geochem. Geophys. Geosyst.*, 5, article no. Q05004.
- Scaillet, S., Rotolo, S. G., La Felice, S., and Vita-Scaillet, G. (2011). High-resolution $^{40}\text{Ar}/^{39}\text{Ar}$ chronostratigraphy of the post-caldera (<20 ka) volcanic activity at Pantelleria, Sicily Strait. *Earth Planet. Sci. Lett.*, 309, 280–290.
- Scaillet, S., Vita-Scaillet, G., and Rotolo, S. G. (2013). Millennial-scale phase relationships between ice-core and Mediterranean marine records: insights from high-precision $^{40}\text{Ar}/^{39}\text{Ar}$ dating of the Green Tuff of Pantelleria, Sicily Strait. *Quat. Sci. Rev.*, 78, 141–154.
- Speranza, F., Di Chiara, A., and Rotolo, S. G. (2012). Correlation of welded ignimbrites on Pantelleria (Strait of Sicily) using paleomagnetism. *Bull. Volcanol.*, 74, 341–357.
- Stabile, P., Giuli, G., Cicconi, M. R., Paris, E., Trapananti, A., and Behrens, H. (2017). The effect of oxygen fugacity and Na/(Na+K) ratio on iron speciation in pantelleritic glasses. *J. Non-Cryst. Solids*, 478, 65–74.
- Toplis, M. J. and Carroll, M. R. (1995). An experimental study of the influence of oxygen fugacity on Fe-Ti oxide stability, phase relations, and mineral-melt equilibria in ferro-basaltic systems. *J. Petrol.*, 36, 1137–1170.
- Tuttle, O. F. and Bowen, N. L. (1958). *Origin of granite in light of experimental studies in the system NaAlSi₃O₈–KAlSi₃O₈–SiO₂–H₂O*, volume 74 of *GSA Memoirs*. Geological Society of America.
- Verzhbitsky, E. V. and Kononov, M. V. (2003). Heat flow and origin of the lithosphere in the central Mediterranean region. *Geotectonics*, 37, 328–336.
- White, J. C., Neave, D. A., Rotolo, S. G., and Parker, D. F. (2020). Geochemical constraints on basalt petrogenesis in the Strait of Sicily Rift Zone (Italy): Insights into the importance of short lengthscale mantle heterogeneity. *Chem. Geol.*, 545, article no. 119650.
- White, J. C., Parker, D. F., and Ren, M. (2009). The origin of trachyte and pantellerite from Pantelleria, Italy: Insights from major element, trace element, and thermodynamic modelling. *J. Volcanol. Geotherm. Res.*, 179, 33–55.
- White, J. C., Ren, M., and Parker, D. F. (2005). Variation in mineralogy, temperature, and oxygen fugacity in a suite of strongly peralkaline lavas and tuffs, Pantelleria, Italy. *Can. Mineral.*, 43, 1331–1347.
- Wilke, S., Holtz, F., Neave, D. A., and Almeev, R. (2017). The effect of anorthite content and wa-

ter on quartz-feldspar cotectic compositions in the rhyolitic system and implications for geobarometry. *J. Petrol.*, 58, 789–818.

Williams, R., Branney, M. J., and Barry, T. L. (2014). Temporal and spatial evolution of a waxing then waning catastrophic density current revealed by chemical mapping. *Geology*, 42, 107–110.



Perspectives on alkaline magmas / *Perspectives sur les magmas alcalins*

Crystallization of peralkaline rhyolitic magmas: pre- and syn-eruptive conditions of the Pantelleria system

Paola Stabile^{*,a}, Fabio Arzilli^b and Michael Robert Carroll^a

^a School of Science and Technology, Geology Division, University of Camerino, Camerino, Italy

^b Department of Earth and Environmental Sciences, University of Manchester, Manchester, UK

E-mails: paola.stabile@unicam.it (P. Stabile), fabio.arzilli@manchester.ac.uk (F. Arzilli), michael.carroll@unicam.it (M. R. Carroll)

Abstract. Pantelleritic magmas are low-viscosity peralkaline rhyolites which exhibit large differences in eruptive style (explosive to effusive). The processes that promote fragmentation and explosive eruptions of pantelleritic magma remain subject to debate, but undoubtedly variations of magma viscosity during magma ascent and degassing contribute to differences in eruptive style. Because crystallization can significantly influence magma rheology, we present a review of equilibrium and disequilibrium crystallization experiments of pantellerites, focusing on the crystallization of the main phases, alkali feldspar, and (lesser) clinopyroxene. Our analysis of data for several explosive pantelleritic eruptions on Pantelleria suggests pre-eruptive pressures of 50–100 MPa, temperatures of 700–800 °C for water-saturated conditions. Given these conditions, we show that the low pre-eruptive crystal fractions (0.08 to 0.15), temperatures between 700 and 800 °C, and the decrease of melt H₂O content during magma ascent/decompression can promote a significant change in viscosity (up to 10⁶–10⁷ Pa·s), leading to magma brittle fragmentation and explosive eruptions. Because of their typical range of viscosity, pantelleritic magmas may show greater variations in eruptive style due to differences in ascent (decompression) rate when compared with metaluminous rhyolites.

Keywords. Alkaline magmas, Alkali feldspar, Clinopyroxene, Crystallization kinetics, Eruptive conditions, Eruptive dynamics.

Available online 5th August 2021

1. Introduction

Pantellerites are typically identified as silica-oversaturated rhyolites with an alkali/alumina molar

ratio $[(\text{Na}_2\text{O} + \text{K}_2\text{O})/\text{Al}_2\text{O}_3]$ (Peralkalinity Index, P. I.) higher than the unity, and they are rich in Na with an excess of Fe over Al [see the trend in MacDonald, 1974, Le Maitre, 2002, Jordan et al., 2021]. They are often associated with comendites, with slightly lower SiO₂ and P.I. [e.g., Scaillet and MacDonald, 2003]. Both occur mainly in interplate settings, including

* Corresponding author.

oceanic islands [Ascension Island; e.g., Jeffery and Gertisser, 2018] to continental rift zones, as for example the Sicily channel rift zone [Pantelleria Island; White *et al.*, 2009], the Kenyan [e.g., Ren *et al.*, 2006, MacDonald *et al.*, 2011] and Ethiopian [e.g., Ronga *et al.*, 2009, Iddon *et al.*, 2018] Rift Valleys, and Mayor Island [NZ-Taupo Volcanic Zone; Barclay *et al.*, 1996].

Peralkaline rhyolites have lower viscosity than calcalkaline rhyolites due to the high alkali content that strongly depolymerizes the melt structure [Stevenson *et al.*, 1998, Mysen, 2007, Mysen and Toplis, 2007, Di Genova *et al.*, 2013, 2017, Stabile *et al.*, 2016, 2017, 2021], and they can shift between explosive and effusive eruptive behaviour, thus producing a wide variety of eruptive styles, ranging from lava flows and fountains to Strombolian to sub-Plinian and Plinian eruptions [e.g., Schmincke, 1974, Mahood and Hildreth, 1986, Duffield, 1990, Lowestern and Mahood, 1991, Houghton *et al.*, 1992, Stevenson *et al.*, 1993, Webster *et al.*, 1993, Wilding *et al.*, 1993, Barclay *et al.*, 1996, Stevenson and Wilson, 1997, Horn and Smincke, 2000, Gottsmann and Dingwell, 2002]. Although peralkaline rhyolites were once thought to be relatively H₂O poor [Bailey and MacDonald, 1987], more recent studies indicate magma water contents as high as 5–6 wt% H₂O [e.g., Kovalenko *et al.*, 1988, Webster *et al.*, 1993, Wilding *et al.*, 1993, Barclay *et al.*, 1996, Gioncada and Landi, 2010, Di Carlo *et al.*, 2010, Lanzo *et al.*, 2013, Romano *et al.*, 2019].

Pre-eruptive magmatic volatile contents and pre- and syn-eruptive crystallization and degassing can strongly affect the rheology of magma in the chamber and during magma ascent, and in turn, they can influence the volcanic eruptive styles of magmas. Many variables, including melt composition, crystallinity, temperature (T), pressure (P), undercooling ($\Delta T = T_{\text{liquidus}} - T_{\text{subliquidus}}$), time, melt water content, oxygen fugacity ($f\text{O}_2$), and cooling and decompression rates, can influence magma crystallization at depth and during ascent to surface [e.g., Couch *et al.*, 2003, Martel and Schmidt, 2003, Hammer, 2006, Brugger and Hammer, 2010, Mollard *et al.*, 2012, Martel, 2012, Shea and Hammer, 2013, Arzilli and Carroll, 2013, Arzilli *et al.*, 2016]. Crystallization has commonly been investigated in pantelleritic melts under equilibrium conditions [Scaillet and MacDonald, 2001, 2003, 2006, Di Carlo *et al.*, 2010, Romano *et al.*, 2020], but disequilibrium crystallization kinetics

deserve additional attention because of possible consequences for conduit flow processes and eruptive dynamics of peralkaline magmas [Arzilli *et al.*, 2020].

In this review, we provide a comprehensive evaluation of the pre-eruptive conditions of volcanic activities at Pantelleria, which have implications for rheological and numerical eruption models that investigate magma ascent and fragmentation of peralkaline rhyolitic magmas. The aim of this contribution is to understand the eruptive dynamics of pantelleritic magmas by studying the phase abundances and chemical compositions of the main mineralogical phases (i.e., alkali feldspar (Afs) and clinopyroxene (Cpx)) present in natural products of the Pantelleria volcanic system. Here, we focus our attention on equilibrium and disequilibrium crystallization of alkali feldspar and clinopyroxene in different experimental and natural pantelleritic products, from Strombolian eruptions of Cuddia del Gallo/Randazzo and Fastuca pantellerite and the Green Tuff Plinian eruption, with the aim of constraining the pre- and syn-eruptive conditions of these eruptions. Specifically, we investigate how different parameters, such as pre-eruptive temperature and crystal fraction of the main mineralogical phases and $(\text{H}_2\text{O})_{\text{melt}}$ (= concentration of H₂O dissolved in melt) influence the eruptive style of pantelleritic magma, contributing to reach magma fragmentation and promoting explosive eruptive behaviour.

2. Pantelleria volcanic system

Pantelleria Island is located in the Mediterranean Sea south of Sicily (Italy) within the Sicily Channel Rift Zone [Rotolo *et al.*, 2007, Civile *et al.*, 2008]. The volcanic island of Pantelleria is composed of “La Vecchia” caldera (114 ka) and the “Cinque Denti” [45.7 ± 1.0 ka; Scaillet *et al.*, 2013, Liszewska *et al.*, 2018], which suggest the presence of magma beneath the central area of the island [Civetta *et al.*, 1984, Mahood and Hildreth, 1986, Rotolo *et al.*, 2013, 2017]. Pantelleria has a bimodal magmatism association of transitional to alkali basalts, located mostly in the north-west sector of the island [Civetta *et al.*, 1988, Rotolo *et al.*, 2007], and trachytes-pantellerites which are more wide spread [e.g., Mahood and Hildreth, 1986, Civetta *et al.*, 1998, White *et al.*, 2005, 2009, Liszewska

et al., 2018, Scaillet *et al.*, 2011, 2013, Williams *et al.*, 2014, Jordan *et al.*, 2018, Rotolo *et al.*, 2021]. There is a clear compositional gap (Daly gap) between alkali basalt and peralkaline rhyolite end-members. Two main hypotheses have been proposed on the origin of the rhyolitic magmas: (i) low-degree partial melting of mafic cumulates in the lower crust to form trachyte, followed by crystal fractionation in shallow reservoirs to generate the most evolved pantellerites [Lowestern and Mahood, 1991, Bohrsen and Reid, 1997, Avanzinelli, 2004, MacDonald *et al.*, 2008, 2011, Marshall *et al.*, 2009]; (ii) fractional crystallization from an alkali basaltic parental magma [Civetta *et al.*, 1998, White *et al.*, 2005, 2009, Neave *et al.*, 2012, Romano *et al.*, 2019, 2020]. Rocks of intermediate compositions (such as mugearite and benmoreite) are rare and, in many cases, are thought to be the result of magma mixing based on textural observations [Romengo *et al.*, 2012, Liszewska *et al.*, 2018]; their rare eruption may represent a physical (density, viscosity) discrimination in the magma reservoirs [Civetta *et al.*, 1988, White *et al.*, 2009, Neave *et al.*, 2012, Liszewska *et al.*, 2018]. For instance, according to this last hypothesis, the Daly gap in Pantelleria compositions can be explained by the fact that the intermediate melts are not erupted because felsic magmas (trachytic to pantelleritic) within the magma chamber behave as a density filter for high-viscosity and crystal-rich intermediate magmas [Mungall and Martin, 1995, Peccerillo *et al.*, 2003]. Moreover, Prosperini *et al.* [2000] proposed a process of mixing plus fractional crystallization between the less evolved comenditic trachyte and the more evolved pantelleritic sample. This magmatic interaction process has been specifically considered the force triggering the magmatic events that produced the Khaggiar lava dome [6–8 ka; Speranza *et al.*, 2010, Scaillet *et al.*, 2011], which was followed by intense volcanic activity, characterized by explosive eruptions and lava flows emissions from different effusive centres [Civetta *et al.*, 1998, Orsi *et al.*, 1991, Scaillet *et al.*, 2011, Neave, 2020].

There exist many debates on pantelleritic magma genesis and their evolution and eruptive behaviour [e.g., see Romano *et al.*, 2018, 2020, and references therein]. Outcrops in Pantelleria show fall units (pumice fall, welded fall (splat-ter), etc.) and deposits of pantelleritic magmas,

which were originated from lava fountains, with a continuous transition from explosive to more effusive style [e.g., Jordan *et al.*, 2018]. An important question remains as to the mechanisms and processes triggering this shift in eruptive style for magmas with almost identical compositions [Schmincke, 1974, Duffield, 1990, Houghton *et al.*, 1992, Stevenson *et al.*, 1993, Webster *et al.*, 1993, Wilding *et al.*, 1993, Barclay *et al.*, 1996, Stevenson and Wilson, 1997, Horn and Smincke, 2000, Gottsmann and Dingwell, 2002, Hughes *et al.*, 2017].

For instance, it is well-known [e.g., Sparks, 1978, Papale and Polacci, 1999] that the increase in magma viscosity due to volatile loss can produce the conditions necessary for magma fragmentation and explosive eruptions [Di Genova *et al.*, 2013]. However, given the low viscosity of pantelleritic liquids [Neave *et al.*, 2012], there should be other mechanisms, which trigger the most explosive style. Previous studies have demonstrated that these peralkaline rhyolites, at low temperatures, have lower viscosity than metaluminous rhyolites due to the effect of alkalis that strongly depolymerize the melt, decreasing their configurational entropy and the viscosity [Di Genova *et al.*, 2013, 2017, Stabile *et al.*, 2016, 2017, 2021].

Viscosity effects on the eruption of pantelleritic magmas are further modelled and discussed by Campagnola *et al.* [2016], who presented numerical simulations on the conduit dynamics of the highly explosive Green Tuff eruption, the most recent catastrophic eruption on Pantelleria Island [Mahood and Hildreth, 1986, Williams, 2010, Williams *et al.*, 2014, Jordan *et al.*, 2018, 2021, Rotolo *et al.*, 2021]. The petrological data and the thermodynamic and numerical modelling indicate that pre-eruptive temperatures of the Pantelleria volcanic system for several explosive eruptions could range between 950 °C (high end-member associated with trachytic magmas) and 720–680 °C (associated with pantelleritic magmas) [White *et al.*, 2005, Di Carlo *et al.*, 2010, Campagnola *et al.*, 2016, Liszewska *et al.*, 2018, Romano *et al.*, 2020].

In the following discussion, we attempt to provide a more refined picture of the most probable pre-eruptive conditions for the Pantelleria eruptions, with a particular focus on the resulting rheological implications and eruptive behaviour.

3. Review of equilibrium and disequilibrium experiments on peralkaline rhyolitic melts

3.1. H_2O solubility in peralkaline rhyolite melts

Phase equilibrium studies can constrain the storage conditions of the specific magma system investigated, providing information on the magma evolution and magma chamber state prior to eruption [Rutherford *et al.*, 1985, Geschwind and Rutherford, 1992, Gardner *et al.*, 1995, Rutherford and Devine, 1996, Barclay *et al.*, 1998, Cottrell *et al.*, 1999, Di Carlo *et al.*, 2010, Romano *et al.*, 2018].

In this work, we consider studies on the phase relations as function of pressure, temperature, and water content in pantelleritic compositions (Table 1). In particular, water abundance in rhyolitic magmas can influence magma physical properties and crystallization behaviour [e.g., Hammer, 2004, Gualda *et al.*, 2012] and in turn, rheological properties and eruptive styles [e.g., Roggensack *et al.*, 1997, Huppert and Woods, 2002, Sparks, 2003, Cashman, 2004, Aiuppa *et al.*, 2007, Edmonds *et al.*, 2008, Stock *et al.*, 2018, Stabile and Carroll, 2020]. Much effort has been devoted to study water solubility in different silicate melt compositions, but only a few studies document water abundance in strongly peralkaline rhyolites and Fe-rich pantelleritic compositions [e.g., Scaillet and MacDonald, 2001, Schmidt and Behrens, 2008, Di Carlo *et al.*, 2010, Stabile *et al.*, 2018, 2020, Romano *et al.*, 2021].

Figure 1a shows the general state of knowledge concerning water solubility in pantelleritic magmas under water-saturated conditions. In the figure, we show solubility calculations as a function of pressure—at 750 °C—for two similar pantellerite compositions [Di Carlo *et al.*, 2010, Arzilli *et al.*, 2020] with all plotted results obtained from the thermodynamic models of Papale *et al.* [2006], Moore *et al.* [1998], and Ghiorso and Gualda [2015]. Generally, the data reflect the well-known strong pressure dependence of water solubility, although we are aware that the Papale *et al.* [2006] model tends to slightly overestimate water solubility in such melt compositions, while Moore *et al.* [1998] better reproduces the solubility data [see Romano *et al.*, 2021]. Overall, the solubility data demonstrate that water loss from pantelleritic melts during ascent can alter the fluid-phase mass fraction produced, depending on initial magma

water content and dynamics of degassing (bubble nucleation, growth, coalescence), and possible eventual fragmentation (for explosive eruptions).

3.2. Liquidus curves of alkali feldspar and clinopyroxene

Previous petrological studies have worked to better define the T – P range and the redox conditions of comenditic to pantelleritic magmas [Scaillet and MacDonald, 2001, 2003, 2006, White *et al.*, 2005, 2009, Di Carlo *et al.*, 2010, Romano *et al.*, 2020], as well as their pre-eruptive water contents [e.g., Giocada and Landi, 2010, Neave *et al.*, 2012, Lanzo *et al.*, 2013, Romano *et al.*, 2019]. The best-estimate alkali feldspar and clinopyroxene liquidus curves for two pantelleritic melts are shown in Figure 1b at temperatures of 700–850 °C and $P(H_2O)$ of 25–150 MPa. The two melts differ slightly in composition, with slightly higher wt% concentrations of FeO and Na₂O for the melt composition used by Arzilli *et al.* [2020], as well as a small difference in the P.I. of 1.46 vs. 1.40 for the Di Carlo *et al.* [2010] study (see Table 1).

Di Carlo *et al.* [2010] studied the role of different intensive parameters (P , T , H_2O in the melt and fO_2 on crystal–liquid equilibria) in a Pantelleria rhyolite belonging to the Fastuca pumice fall eruptive unit. Phase equilibria show that clinopyroxene is the first liquidus phase, followed by alkali feldspar and then quartz (which is here not reported) over the entire range of T – H_2O_{melt} investigated by Di Carlo *et al.* [2010], with aenigmatite being stable at temperature ≤ 700 °C, at pressures ≤ 100 MPa. Slightly different results on the same composition have been found by Romano *et al.* [2020], where the mineralogical assemblage is dominated by alkali feldspar, with minor aenigmatite and clinopyroxene, but also fayalite, amphibole, and quartz occurring in minor amounts at lower temperatures. In particular, the crystallization of fayalite in peralkaline magmas depends on a combination of temperature, fO_2 , and melt peralkalinity (and SiO₂ activity) and for Fastuca it is limited to T between 690–750 °C, for suitable peralkalinity of melt and fO_2 [Romano *et al.*, 2020]. These small differences between Romano *et al.* [2020] and Di Carlo *et al.* [2010] results, despite the use of nominally identical starting materials, are most likely due to the high sensitivity of the phase stabilities to small variation of intensive parameters, as for instance, the slightly

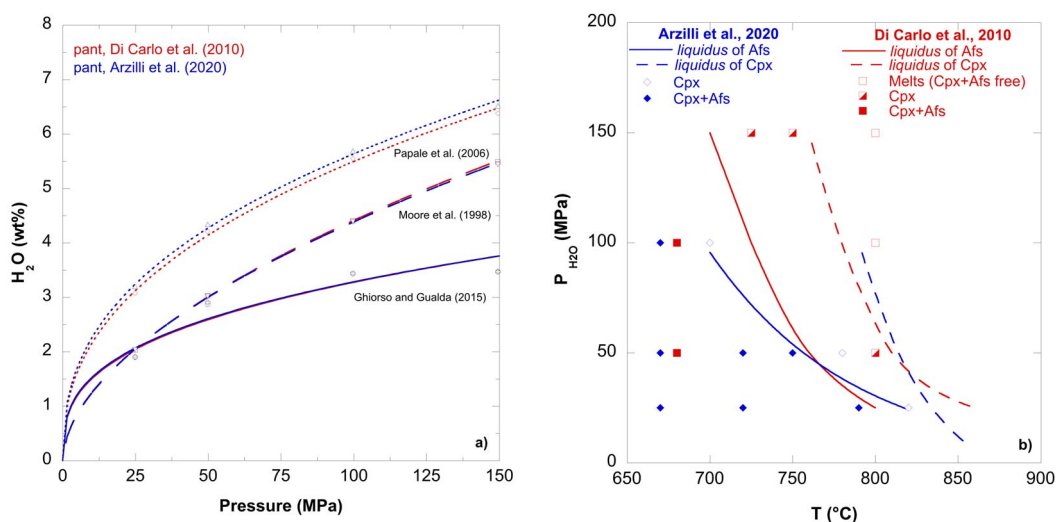


Figure 1. (a) Water content solubility calculations (at 750 °C) as function of pressure for pantelleritic compositions [Di Carlo et al., 2010, Arzilli et al., 2020] obtained by using Papale et al. [2006], Moore et al. [1998], and Ghiorso and Gualda [2015] solubility models. The purpose of the figure is to illustrate the H₂O-saturated conditions for the selected magma compositions for a given P – T range. See Romano et al. [2021] for more detailed discussion on water solubility in pantelleritic melts. (b) Phase diagram for alkali feldspar (Afs) and clinopyroxene (Cpx) under water-saturated conditions at NNO + 0.8 and NNO – 1,2 in pantelleritic compositions from Arzilli et al. [2020] and Di Carlo et al. [2010], respectively.

Table 1. Summary of pantelleritic data used in this study

(wt%)	Experimental data				Natural samples		
	Arzilli et al. [2020] Cuddia del Gallo	Di Carlo et al. [2010] Fastuca	Romano et al. [2020] Fastuca	Romano et al. [2020] Green Tuff	Rotolo et al. [2007] Fastuca (PAN0113)	Campagnola et al. [2016] Green Tuff	Gioncada and Landi [2010] Cuddia del Gallo (PANT15)
SiO ₂	69.13	70.40	69.45	72.60	69.98	69.4	66.3
TiO ₂	0.54	0.48	0.48	0.52	0.47	0.50	0.39
Al ₂ O ₃	10.46	10.30	10.15	9.00	9.75	8.40	10.28
Fe ₂ O ₃	n.a.	—	—	—	8.52	8.60	—
FeO*	8.06	7.52	7.87	6.24	—	8.41	—
MnO	0.30	0.26	0.21	0.24	0.27	0.30	0.29
MgO	0.09	0.06	0.10	0.51	0.00	0.10	0.05
CaO	0.56	0.52	0.53	0.46	0.55	0.40	0.43
Na ₂ O	6.30	5.67	6.71	7.29	7.02	6.30	6.10
K ₂ O	4.54	4.74	4.46	2.87	4.43	4.20	4.29
P ₂ O ₅	0.01	—	0.04	0.06	—	—	0.03
SO ₂	n.a.	—	—	—	—	—	—
F	n.a.	—	—	0.20	—	—	—
Cl	n.a.	—	—	—	—	—	—
Total	99.75	100.00	100.00	100.00	100.00	98.2	99.42
PI ¹	1.46	1.40	1.56	1.68	1.68	1.77	1.43

Notes: PI¹ (Peralkalinity Index) = molar (Na₂O + K₂O)/Al₂O₃. n.a. = not analysed.

lower redox conditions investigated in Romano *et al.* [2020] compared to Di Carlo *et al.* [2010]. However, in these evolved pantelleritic magmas, ferromagnesian phases are always limited to relatively small abundances and Afs, followed by Qz are the main phases to crystallize—these are all near-eutectic-type melts in which incompatible elements can vary widely in abundance, while major elements show only small variations.

In Figure 1b, we also report the liquidus temperatures of alkali feldspar obtained by Arzilli *et al.* [2020] and of clinopyroxene, using the composition of a peralkaline rhyolitic pumice (PANT15) from the eruptive fall unit of Cuddia del Gallo. These liquidii are consistent with those obtained from Di Carlo *et al.* [2010] at similar pressures, near water saturation. Although the oxygen fugacity of NNO +0.8 considered in Arzilli *et al.* [2020] is higher than those investigated (NNO – 1 to NNO – 2) by Di Carlo *et al.* [2010], the liquidii of the alkali feldspar are similar at pressures lower than 50 MPa (Figure 1b), which suggest that alkali feldspar is not strongly sensitive to fO_2 (which mainly influences melt FeO contents, and indirectly, SiO_2 activity). However, at pressures higher than 50 MPa, the alkali feldspar at NNO + 0.8 is stable at slightly lower temperatures compared with experiments at NNO – 1. This temperature difference at pressures higher than 50 MPa may be related to compositional difference between the two peralkaline rhyolitic melts (see Table 1). Moreover, reducing the redox conditions from NNO + 0.8 to NNO – 1.2 shifts the clinopyroxene liquidus at pressures higher than 50 MPa to lower temperatures (temperature difference of ~30 °C). On the other hand, the clinopyroxene liquidus from Di Carlo *et al.* [2010] shows broadly the same pattern than the alkali feldspar liquidus curve, but appearing at higher T (>750 °C). Overall, the relative order of crystallization of the main mineralogical phases is the same and persists over the P – T range for both melt compositions used by Di Carlo *et al.* [2010] and Arzilli *et al.* [2020].

3.3. Composition of alkali feldspar

The compositions of experimental alkali feldspars fall in the range of Or_{28–67} (Figure 2a). A broad negative correlation between Or (mol%) and T (°C) is evident when all the available data are plotted together (Figure 2a). For instance, for the pantellerites

in Arzilli *et al.* [2020], the Or content of alkali feldspar crystals formed at 670 °C ranges from 47 to 67 mol% (different melt H_2O), while the ones crystallized at temperatures ≥ 720 °C are characterized by a lower Or content between 31 and 37 mol% (near the binary Alb–Or minimum). Hence, the alkali feldspar is more sodic at temperatures between 720 and 790 °C, independent of P and H_2O dissolved in the melt [Arzilli *et al.*, 2020]. The grey shaded band in Figure 2a indicates the range of Or contents (between 34 and 38 mol%) in natural alkali feldspar crystals obtained from Cuddia del Gallo (PANT15), Fastuca and Green Tuff eruption products [Di Carlo *et al.*, 2010, Lanzo *et al.*, 2013, Liszewska *et al.*, 2018, Romano *et al.*, 2020]. The variation in Or content with temperature is appreciable only at ≤ 700 °C for experiments from Di Carlo *et al.* [2010] and Romano *et al.* [2020].

When we examine variations of Or content with H_2O_{melt} (Figure 2b), the majority of data displays limited variation with H_2O_{melt} except for the highest H_2O charges which appear to show a general positive correlation between Or and H_2O in the melt. However, when considering each subset of data relative to the melt compositions, which are reported from Di Carlo *et al.* [2010], Or defines a slight positive correlation with H_2O only for $H_2O > 2.5$ wt% at 100–150 MPa. Whereas an almost horizontal trend is obtained at lower H_2O contents for compositions falling in the range Or_{28–39}. Overall, the composition of natural alkali feldspar in pantellerites is well reproduced at 720–750 °C and $(H_2O)_{\text{melt}}$ in the range 2.5–4 wt%. Higher or lower temperatures cannot reproduce the natural alkali feldspar composition (grey band in the figure).

3.4. Composition of clinopyroxene

Experimental clinopyroxenes have compositions in the range of X_{Fe} (=molar Fe/(Fe + Mg), with all Fe as Fe^{2+}) between 0.54 and 0.97 for data reported on GTP (Green Tuff Pantellerite) and FP (Fastuca Pantellerite) from Romano *et al.* [2020], while it varies between 0.84 and 0.99 for data on FP of Di Carlo *et al.* [2010] (Figure 3a).

X_{Fe} shows a negative correlation with temperature in the different pantelleritic products. In particular, at constant H_2O_{melt} , in GTP clinopyroxenes, a decrease in temperature of 50 °C (from 800 to 750 °C) increases X_{Fe} from 0.60 to 0.80, in FP, clinopyroxene

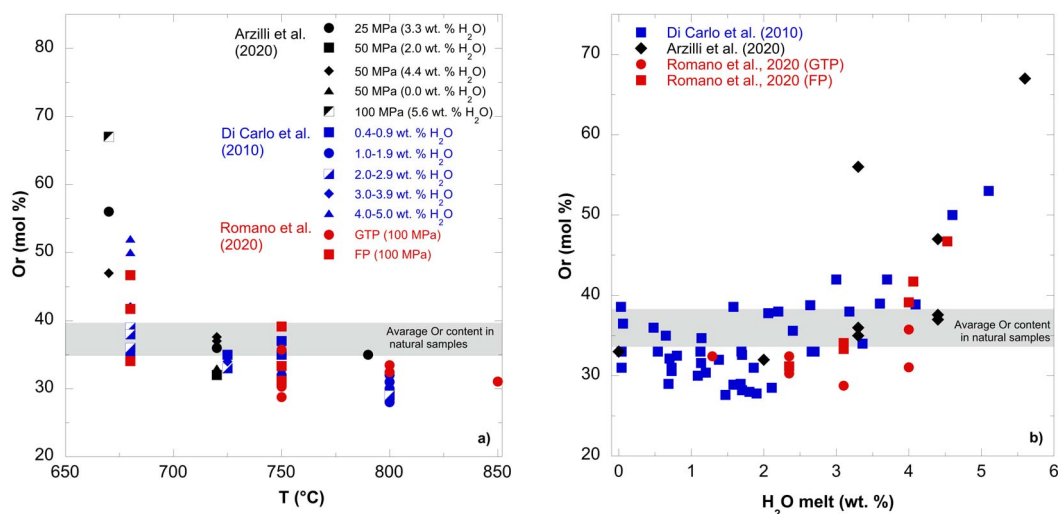


Figure 2. (a) Orthoclase (Or) mol% content of alkali feldspars as a function of experimental temperature (T °C) and (b) H_2O dissolved in the melt in pantelleritic compositions [Di Carlo *et al.*, 2010, Arzilli *et al.*, 2020, Romano *et al.*, 2020]; the total P range considered is between 50 and 150 MPa. GTP in the legend indicates Green Tuff pantellerite, while FP is Fastuca pantellerite [Romano *et al.*, 2020]. The grey shaded band indicates the range of Or contents (34–38 mol%) in natural alkali feldspar phenocrysts [Lanzo *et al.*, 2013].

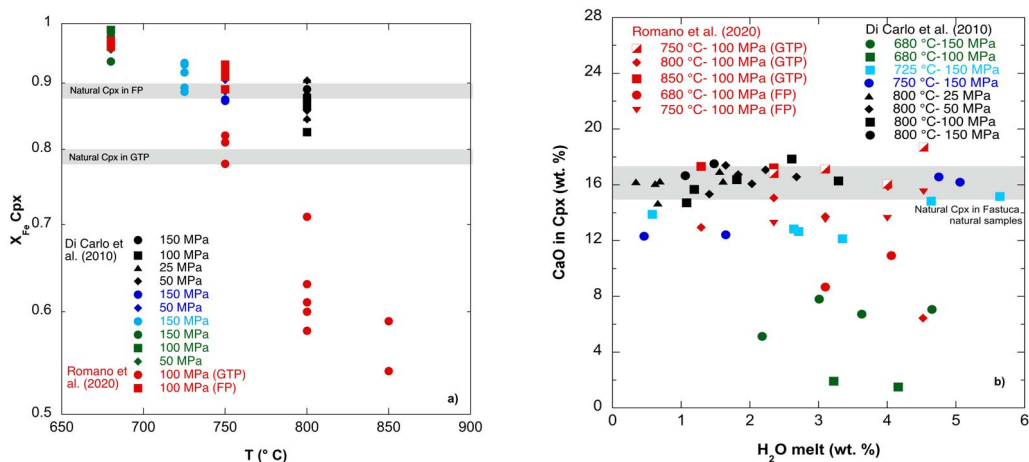


Figure 3. (a) Variation of X_{Fe} ($=FeO^*/(FeO^* + MgO)$ molar), where FeO^* is total iron expressed as FeO of experimental Cpx, with Temperature (°C) at a range of pressures [Di Carlo *et al.*, 2010, Romano *et al.*, 2020]. The grey bands correspond to the natural compositions of Cpx (GTP = Green Tuff Pantellerite; FP = Fastuca Pantellerite). (b) Variation of CaO content (wt%) of experimental Cpx with melt water content (H_2O_{melt} wt%) at a range of temperatures and pressures [Di Carlo *et al.*, 2010, Romano *et al.*, 2020]. The grey band corresponds to the average CaO content of Cpx phenocrysts in the starting rocks (Fastuca and Green Tuff Pantellerite).

only crystallizes at lower temperature ($<800\text{ }^{\circ}\text{C}$), and the X_{Fe} ranges from 0.89 to 0.97. The most Fe-rich clinopyroxene crystals are produced at $680\text{ }^{\circ}\text{C}$ in FP compositions [Romano *et al.*, 2020]. Similarly, experimental data from Di Carlo *et al.* [2010] display the highest X_{Fe} values (between 0.92 and 0.99) at the lowest temperature investigated of $680\text{ }^{\circ}\text{C}$. Clinopyroxene compositions synthesized at $750\text{ }^{\circ}\text{C}$ reproduce the small range of natural clinopyroxene compositions [Romano *et al.*, 2020], while clinopyroxenes obtained by Di Carlo *et al.* [2010] at temperatures between 720 and $800\text{ }^{\circ}\text{C}$ better reproduce the natural clinopyroxene compositions of Fastuca products (upper grey band in Figure 3a).

3.5. Crystallization of alkali feldspar and clinopyroxene

Although the crystallization behaviour of peralkaline rhyolites is relatively well-understood at equilibrium, the prediction of the crystallization kinetics under non-equilibrium, time-dependent conditions is still difficult, even though kinetic data can potentially provide new insights about the timescales of the magmatic processes. Here, we summarize the current understanding of the crystallization kinetics of alkali feldspar and clinopyroxene under both equilibrium and disequilibrium conditions in pantelleritic magma compositions. Alkali feldspars are highly sensitive to variations of intensive variables in volcanic systems, which are recorded by variable textures and compositional zoning patterns, depending on the rate of change of intensive parameters promoting crystallization. Recently, several studies have investigated clinopyroxene crystallization in different alkaline magma because clinopyroxene crystallization can also rapidly change the magma rheology, and chemical zoning of clinopyroxene can provide information on the magma history [e.g., Ni *et al.*, 2014, Polacci *et al.*, 2018, Masotta *et al.*, 2020, Pontesilli *et al.*, 2019, Arzilli *et al.*, 2019]. Here, we report the total crystal fraction (ϕ_{total}), which represents the sum of both alkali feldspar and clinopyroxene crystal fraction, in experimental runs on pantellerites from Cuddia del Gallo, Fastuca, and Green Tuff [Di Carlo *et al.*, 2010, Arzilli *et al.*, 2020, Romano *et al.*, 2020] as function of ΔT_{Cpx} (temperature below the clinopyroxene liquidus).

Results show ϕ_{total} between 0.08 and 0.29 for ΔT_{Cpx} between 10 and $140\text{ }^{\circ}\text{C}$ and $(\text{H}_2\text{O})_{\text{melt}}$ in the range of 3.3–5.6 wt% for Arzilli *et al.* [2020] [consistent with melt inclusion water content estimations in phenocrysts; Gioncada and Landi, 2010]. Considering both experimental data from Di Carlo *et al.* [2010] and Romano *et al.* [2020], ϕ_{total} (clinopyroxene + alkali feldspar phenocrysts) ranges between 0.01 and 0.49 for ΔT_{Cpx} up to $\sim 170\text{ }^{\circ}\text{C}$. The phase abundances along with the total crystal fraction (ϕ) for the investigated experimental conditions in Arzilli *et al.* [2020] are also reported in Table 2. The experimental durations vary between 24 and 288 h [Arzilli *et al.*, 2020] and demonstrate long nucleation delay of alkali feldspar in pantelleritic melts (from several hours to several days). The nucleation delay of alkali feldspar under water-undersaturated conditions can be ~ 230 h, and the nucleation delay time decreases with increasing melt H_2O content at fixed P and/or ΔT . Particularly, under water-saturated conditions, the nucleation delay of alkali feldspar is <50 h, while the nucleation delay of clinopyroxene ranges from minutes to a few hours [Arzilli *et al.*, 2020]. This indicates that clinopyroxene formation timescales can be significantly shorter than timescales for alkali feldspar formation upon changes of magmatic P – T conditions in pantelleritic magmas. Slow feldspar crystallization/recrystallization time scales are also observed in plagioclase-bearing basaltic magmas [Polacci *et al.*, 2018, Masotta *et al.*, 2020, Pontesilli *et al.*, 2019]. Importantly, we observe that despite a wide range of ΔT , the variation of clinopyroxene crystal fraction is relatively small from 0.02 to 0.10 [Di Carlo *et al.*, 2010, Romano *et al.*, 2020]. This implies that peralkaline rhyolites may spend days in sub-liquidus conditions without experiencing significant changes in crystal fraction due to long nucleation delay times for alkali feldspar [discussed in more detail in Arzilli *et al.* [2020]].

4. Discussion

4.1. Pre-eruptive conditions of the Pantelleria volcanic system

4.1.1. Strombolian eruptions

The strombolian pantelleritic products of Fastuca, Cuddia Randazzo, and Cuddia del Gallo have a

Table 2. Experimental run conditions and phase abundances for the data reported in Arzilli *et al.* [2020]

Sample	Pressure (MPa)	Temperature (°C)	H ₂ O (wt%)	<i>t</i> (h)	Phase abundances (wt%)	Total Φ
C136	100	670	5.6	192	Gl(83), Afs(7), Cpx(10), Ox(<1)	0.17
C144	50	750	4.4	288	Gl(92), Afs(6), Cpx(2)	0.08
C155	50	720	4.4	96	Gl(89), Afs(7), Cpx(3), Ox(1)	0.11
C148	50	720	4.4	175	Gl(85), Afs(8), Cpx(6), Ox(1)	0.15
C149	50	720	4.4	195	Gl(83), Afs(10), Cpx(6), Ox(1)	0.17
C141	50	670	4.4	72	Gl(71), Afs(20), Cpx(9)	0.29
C146	25	790	3.3	288	Gl(83), Afs(12), Cpx(3), Ox(2)	0.17
C151	25	720	3.3	130	Gl(75), Afs(19), Cpx(5), Ox(1)	0.25
C138	25	670	3.3	24	Gl(90), Afs(2), Cpx(8), Ox(<1)	0.10

Gl = glass; Afs = Alkali feldspar; Cpx = Clinopyroxene; Ox = oxides (Magnetite–Ülvöspinel solid solution, Fe–Ti oxides). Phase abundances calculated by multiple linear regression using known starting composition and crystal compositions analysed by microprobe; total Φ means total crystal fraction (% crystals/100).

mineral assemblage that consists of alkali feldspar, clinopyroxene, and minor amounts of fayalite, aenigmatite, amphibole, and quartz [Di Carlo *et al.*, 2010, Gioncada and Landi, 2010, Lanzo *et al.*, 2013, Landi and Rotolo, 2015, Romano *et al.*, 2020]. Alkali feldspar is the dominant crystal phase, and together with clinopyroxenes, occurs as both phenocrysts (between 500 μm to mm sizes) and microlites (from a few microns to 100–200 μm) [Di Carlo *et al.*, 2010, Gioncada and Landi, 2010, Romano *et al.*, 2020]. The abundance of phenocrysts is similar among the strombolian products of Fastuca, Cuddia del Gallo, and Cuddia Randazzo. The phenocrysts crystal fraction is ~ 0.15 (alkali feldspar + clinopyroxene). Fastuca samples also contain alkali feldspar phenocrysts, and alkali feldspar and clinopyroxene microlites [Romano *et al.*, 2020]. Similarly, alkali feldspar microlites are present within the ground-mass of the Cuddia Randazzo products. For most of the samples, the abundance of alkali feldspar microlites ranges between 0.56 and 0.66 of total crystals, while mafic mineral crystal fractions are ~ 0.05 – 0.11 [Landi and Rotolo, 2015]. Experimental temperatures between 720 and 800 °C and pressures of 25–100 MPa produce crystal fractions (~ 0.15 ; considering alkali feldspar + clinopyroxene) similar to the phenocryst abundances observed in the strombolian products of Fastuca, Cuddia Randazzo, and Cuddia del Gallo. Experiments also indicate that a crystal fraction of ~ 0.50 can be produced at

temperatures between 680 and 750 °C (Figure 4). Therefore, abundant microlites may be produced within this range of temperature in the strombolian eruptions.

Regarding the Fastuca strombolian eruption, equilibrium experiments indicate that the composition of natural clinopyroxene phenocrysts ($X_{\text{Fe}} = 0.88$ – 0.90) can be reproduced at temperatures between 725 and 800 °C and pressures between 25 and 150 MPa (Figure 3a). Instead, the compositions of natural alkali feldspar phenocrysts are reproduced at temperature between 680 and 750 °C, pressures between 50 and 100 MPa (Figure 2a), and water contents between 2 and 3.5 wt%. These results indicate that there is a narrow temperature window, between 725 and 750 °C, in which clinopyroxene and alkali feldspar can crystallize at the same conditions. This implies that either pre-eruptive temperatures of Fastuca eruption were between 725 and 750 °C or that magma was cooled down in a magma reservoir or during magma ascent from 800 °C to temperatures at which alkali feldspar can crystallize (680–750 °C). Furthermore, the rare occurrence of amphibole in Pantelleria rhyolites [Jordan *et al.*, 2018, Rotolo *et al.*, 2007, White *et al.*, 2009] suggests that this mineral crystallizes from a wetter and cooler magma storage region [Di Carlo *et al.*, 2010]. In this way, amphibole and alkali feldspar would coexist at $T > 680$ °C for crystal contents comparable with those observed in natural pantellerite [Romano *et al.*, 2020].

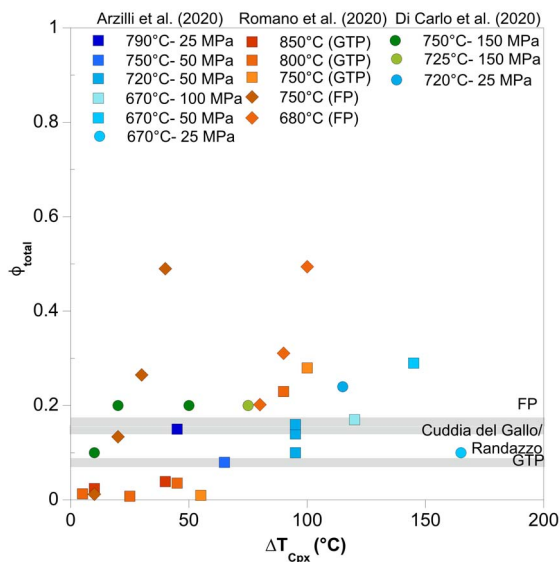


Figure 4. Total crystal fraction (Φ) of Afs + Cpx as function of ΔT_{Cpx} ($^{\circ}\text{C}$ below estimated Cpx liquidus temperature). The diagram shows data for peralkaline rhyolites from Di Carlo *et al.* [2010], Arzilli *et al.* [2020], and Romano *et al.* [2020] and data of total Φ of main eruptive pantellerite products [i.e., Fastuca, Cuddia del Gallo, Green Tuff; Gioncada and Landi, 2010, Lanzo *et al.*, 2013, Landi and Rotolo, 2015]. See text for discussion of ΔT_{Cpx} .

Eruptive temperatures ≥ 800 $^{\circ}\text{C}$, as we have demonstrated in Figures 2, 3 and 4 are not consistent with observations on crystal compositions and abundances of alkali feldspar and clinopyroxene for the different strombolian products considered here (Fastuca, Cuddia Randazzo and Cuddia del Gallo). This is also supported by the presence of aenigmatite, which is only stable at temperature of 750 $^{\circ}\text{C}$ and 50 MPa for dry conditions and 750 $^{\circ}\text{C}$, 100 MPa, and wet conditions, as reported from Di Carlo *et al.* [2010] and Romano *et al.* [2020], respectively.

Considering the total crystal abundance of alkali feldspar and clinopyroxene (phenocrysts and microlites) in the strombolian products and the compositions of alkali feldspar and clinopyroxene phenocrysts observed in Fastuca eruptive products, we propose that the more likely pre-eruption conditions are 680–750 $^{\circ}\text{C}$, 25–100 MPa under water-saturated (or near-saturated) conditions.

4.1.2. Plinian eruption

The Green Tuff Plinian eruption produced an ignimbritic deposit that is compositionally zoned, from pantelleritic at the base to comenditic trachyte at the top of the deposit. This suggests that the magma reservoir of the Green Tuff was also compositionally zoned before the eruption: pantelleritic magma at the top and comenditic trachyte at the bottom of the reservoir [Liszewska *et al.*, 2018].

The mineral assemblage of the pantelleritic magma consists mainly of alkali feldspar, with minor clinopyroxene and aenigmatite, and traces of fayalite and quartz. Alkali feldspar represents the main crystal phase (>85 vol.%) of the phenocryst assemblage in every sample [White *et al.*, 2009]. Microlites are not present within the Green Tuff pantelleritic products [Campagnola *et al.*, 2016]. The textures of pantelleritic pumices erupted from Green Tuff Plinian eruption are mainly vitrophyric and crystal fraction of phenocrysts ranges between 0.05 and 0.25 [White *et al.*, 2009, Lanzo *et al.*, 2013, Campagnola *et al.*, 2016, Liszewska *et al.*, 2018, Romano *et al.*, 2019]. Although the observed crystal fraction covers a broad range, observations on numerous natural samples, suggest an average crystal fraction of 0.08 is representative for the pantelleritic member, with the later trachytic part of the eruption being more crystal-rich compared with the earlier pantelleritic part [Campagnola *et al.*, 2016]. The mineral assemblage of the trachytic member of the Green Tuff eruption consists of alkali feldspar and clinopyroxene, with minor olivine, ilmenite, and apatite [Campagnola *et al.*, 2016, Liszewska *et al.*, 2018, Romano *et al.*, 2020]. Both phenocrysts and microlites are present in the trachytic magmas. Alkali feldspar is the main phase (phenocrysts = 0.18 (%vol); microlites = 0.05), whilst, clinopyroxene is the second main phase in terms of crystal abundance (phenocrysts = 0.04; microlites = 0.06, according to Campagnola *et al.* [2016]).

Previous studies indicate that a thermal gradient was present within the magma reservoir at pre-eruptive conditions: the pantelleritic magma at the top was colder (700–750 $^{\circ}\text{C}$) than the trachytic member (900–950 $^{\circ}\text{C}$) in the lower part of the reservoir [Campagnola *et al.*, 2016, Liszewska *et al.*, 2018]. Water contents range from 1 wt% in the trachytes to 4 wt% in the pantellerites [Liszewska *et al.*, 2018]. Previous studies also estimated ~ 100 MPa as pre-

eruptive pressure, which correspond to depths of 3–4 km [Campagnola *et al.*, 2016, Liszewska *et al.*, 2018]. This depth is consistent with geophysical studies [e.g., Mattia *et al.*, 2007], which place the top of the magma reservoir at 4 km beneath the caldera. This implies that at ~100 MPa, and with 4 wt% of H₂O the pantelleritic magma was likely near water-saturated conditions (see Figure 1a) prior to eruption, particularly if we consider that the Papale *et al.* [2006] model may slightly overestimate H₂O solubility in pantelleritic magmas (as suggested by Romano *et al.* [2021]).

The composition of natural clinopyroxene phenocrysts ($X_{\text{Fe}} = 0.78\text{--}0.80$) of Green Tuff pantelleritic products can be reproduced experimentally at temperatures between 750 and 850 °C at ~100 MPa (Figure 4a,b), whereas the compositions of natural alkali feldspar are reproduced at temperature of 750 °C, 100 MPa, and 3–4 wt% of H₂O. Therefore, crystallization of the pantelleritic magma may occur near water-saturated condition before the Plinian eruption.

As we observed for the Fastuca products, clinopyroxene can crystallize at higher temperatures (750–850 °C) than alkali feldspar. However, the pre-eruptive temperatures of the Green Tuff pantelleritic products under water-saturated conditions cannot be higher than 750 °C, as the alkali feldspar is the main phase in terms of abundance. This is also confirmed by the experimental results of Romano *et al.* [2020], which show alkali feldspar is present only at temperatures ≤ 750 °C at 100 MPa and 4 wt% of H₂O, whereas at temperatures ≥ 800 °C alkali feldspar is not able to crystallize. This implies that either pre-eruptive temperature of the pantelleritic magma was at ~750 °C or that the magma cooled down in a magma reservoir from 850 °C to ~750 °C forming clinopyroxene first at higher temperatures and then alkali feldspar at lower temperatures, before the Plinian eruption was triggered; these scenarios should be further investigated, as they have implications on the triggering of the eruption and the eruption styles.

Experimental results suggest that at ΔT_{Cpx} between 3 and 170 °C and experimental duration between 24 and ~500 h, pantelleritic melts can produce crystal fractions (considering alkali feldspar and clinopyroxene) between 0.02 and ~0.50. Figure 5

shows calculated magma viscosities and crystal fractions for different melt water contents, at temperatures ranging from 700–850 °C (see figure legend for details). In general, low ΔT_{Cpx} (<75 °C) can promote a total crystal fraction similar to the natural pantelleritic products of Green Tuff Plinian eruption which are shown with green arrow in Figure 5 [Lanzo *et al.*, 2013, Campagnola *et al.*, 2016, Romano *et al.*, 2020]. For ΔT_{Cpx} higher than 75 °C, experimental crystal fractions are higher than those observed in the Green Tuff pantelleritic products. One condition in Figure 5 corresponding to $\Delta T_{\text{Cpx}} = 170$ °C (25 MPa, 670 °C) shows a ϕ_{total} of 0.10, which is similar to that of the Green Tuff pantelleritic products, but the ratio of clinopyroxene to alkali feldspar is too high and not representative of the natural samples. This is due to the combination of low temperatures (670 °C) the high ΔT_{Cpx} , which are not likely pre-eruptive conditions of Green Tuff Plinian eruption. Based on the chemical compositions of clinopyroxene and alkali feldspar, the likely pre-eruptive temperatures of the pantelleritic magma is ~750 °C (Figure 5b), which implies relatively small ΔT_{Cpx} (<75 °C). Small ΔT_{Cpx} may promote a nucleation delay of alkali feldspar crystals. Magma stagnation at small ΔT_{Cpx} for a few days prior to the triggering of the eruption may only produce a limited amount of crystallization. This indicates that although the pantelleritic member spends days rather than hours at sub-liquidus conditions, it may not produce drastic changes in (alkali feldspar) crystal fraction [Arzilli *et al.*, 2020]. Instead, the trachytic magma at the bottom of the reservoir is more crystallized than the pantelleritic member, as trachytic magmas can reach faster the equilibrium crystal fraction [Arzilli *et al.*, 2018, 2020]. The injection of hotter mafic-intermediate magma into the cooler reservoir destabilized the system, heating the trachytic magma (whose phenocrysts are partially resorbed but with no evidence of physical and chemical mixing) and triggering the Green Tuff eruption [Landi and Rotolo, 2015, Romano *et al.*, 2018, Liszewska *et al.*, 2018, Neave, 2020]. Thus, we propose that the Green Tuff pantelleritic magma was stored for days at pre-eruptive temperature of ~750 °C, pressure 100 MPa, and under near water-saturation conditions and was erupted suddenly after the injection of hotter magma into the reservoir without having time for significant changes in crystal volume fraction.

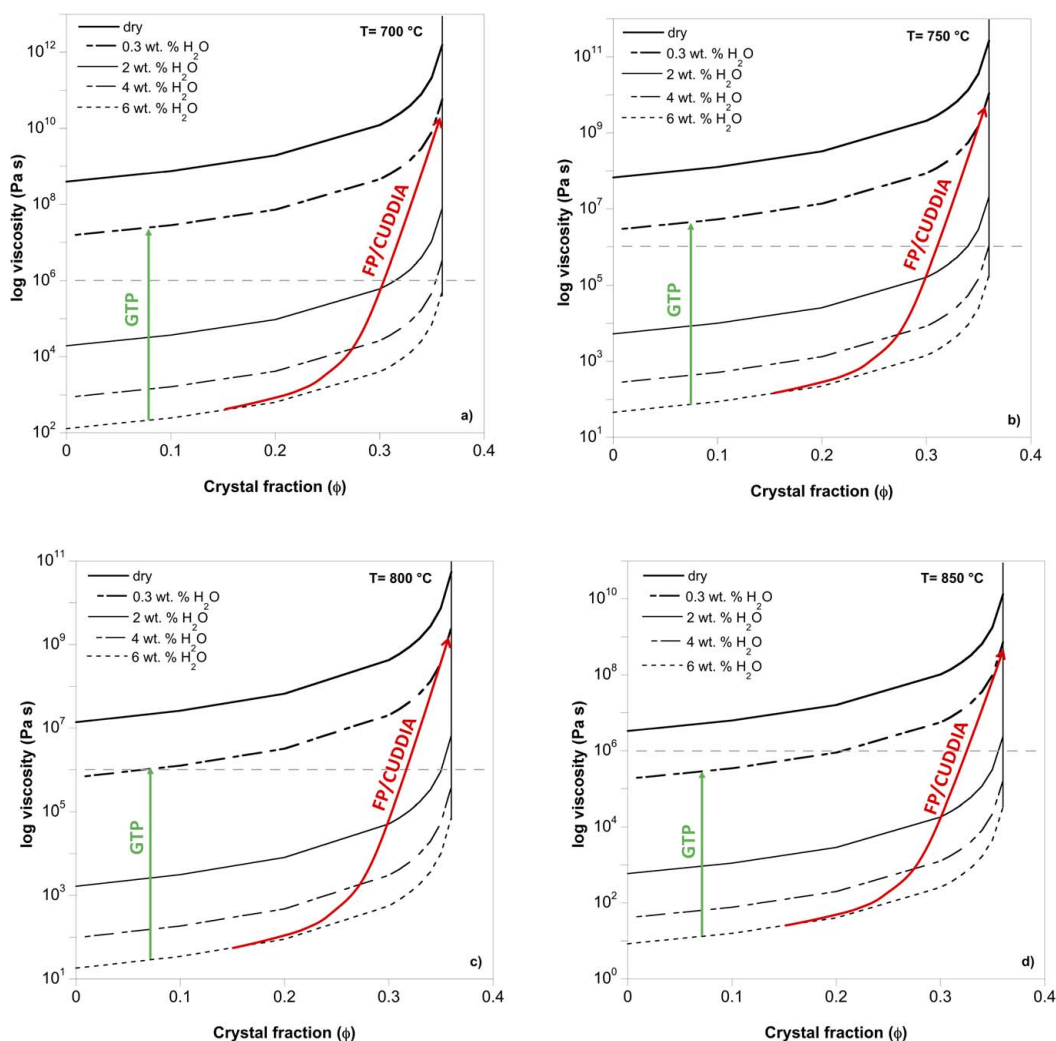


Figure 5. Effect of crystal content on liquid (magma) viscosity as function of water content (from dry conditions to 6 wt% H₂O) at different magmatic temperatures of (a) 700 °C, (b) 750 °C, (c) 800 °C, and (d) 850 °C. The arrows in the figures, starting from the natural phenocryst content (average) of the main eruptive products (Green Tuff or GTP, Cuddia del Gallo/Randazzo, Fastuca eruptions or FP/CUDDIA), indicate the different paths of rising magmas. The grey dashed line indicates the fragmentation level corresponding to a viscosity value of 10⁶ Pa·s. The viscosities of crystal-bearing and vesicle-free suspensions have been estimated by using the Mader et al. [2013] equations as function of crystal fraction, of a strain rate of $\dot{\gamma} = 1 \text{ s}^{-1}$, and a mean crystal aspect ratio of $r_p = 8$. See text for discussion.

In the following, we present and discuss the different effects of the initial temperature, H₂O_{melt}, crystal fraction, and crystal aspect ratio of alkali feldspar and clinopyroxene on the rheology and dynamics of the pantelleritic magma of the Pantelleria volcanic system.

4.2. Syn-eruptive conditions and rheological implications

Viscosity (η) calculations on dry and hydrous pantelleritic magma compositions (Cuddia del Gallo, Fastuca, and Green Tuff) can help understand better the

interactions between magma rheology and eruptive styles. Brittle magma fragmentation occurs when a critical viscosity-dependent strain rate is exceeded [Papale, 1999]. Melt composition, crystal fraction, and vesicularity all influence the bulk magma viscosity [e.g. Giordano *et al.*, 2008, Vona *et al.*, 2011, Mader *et al.*, 2013]. The bulk magma viscosity increases as the magma crystallinity increases and during degassing as magma water content decreases [e.g., Giordano *et al.*, 2008, Vona *et al.*, 2011]. This favours approaching brittle magma fragmentation conditions. Regarding peralkaline rhyolitic explosive eruptions, magma fragmentation still remains an unclear process [Di Genova *et al.*, 2013, Campagnola *et al.*, 2016, Hughes *et al.*, 2017].

For viscosity calculations, we consider the pre-eruptive temperatures of the Pantelleria volcanic system, the melt water content, the crystal fractions (ϕ), and the crystal aspect ratio (r_p). We use the model of Di Genova *et al.* [2013] for the prediction of the initial viscosity of peralkaline silicate melts as a function of temperature and water content. Assuming a pre- to syn-eruptive temperature of 700–850 °C, H_2O_{melt} between 0 and 6 wt%, and pressure of 25–100 MPa, we calculate the viscosities of pantelleritic liquids at this range conditions (Figure 5).

To investigate how the presence of crystals can influence the rheology of peralkaline rhyolitic magmas, the viscosities of crystal-bearing and vesicle-free suspensions have been estimated by using the Mader *et al.* [2013] equations using a strain rate of $\gamma = 1 \text{ s}^{-1}$ and a mean crystal aspect ratio of $r_p = 8$. For simplicity here, a strain rate of 1 s^{-1} has been considered assuming that the crystallization occurs at near-equilibrium conditions, while the crystal aspect ratio represents the average value between alkali feldspar and clinopyroxene obtained from crystallization experiments performed by Arzilli *et al.* [2020] under a wide range of ΔT_{Cpx} (3–170 °C). Viscosities are reported in Figure 5(a–d) as a function of the crystal fraction (alkali feldspar and clinopyroxene phenocrysts) for a given eruptive temperature (700–750–800–850 °C, Figure 5a–d) and H_2O_{melt} varying from 0 (dry conditions) up to 6 wt%. We consider 0.3 wt% of H_2O the residual water content at the exit of the vent, following the modelling of Green Tuff eruption [Campagnola *et al.*, 2016].

Overall, the viscosity increase is not linear with crystal fraction and it becomes steep for ϕ values

>0.35, approaching infinite values for further ϕ increases [a consequence of the form of viscosity-crystal fraction relationship used by Mader *et al.* [2013]]. At a given temperature, the decrease of H_2O_{melt} during magma ascent can change the viscosity by up to 6 log units (Figure 5). At viscosities higher than $10^6 \text{ Pa}\cdot\text{s}$ (grey dashed line corresponding to the fragmentation level in Figure 5), brittle fragmentation may be invoked in agreement with modelling results obtained by Campagnola *et al.* [2016] and the rheological calculations reported by Hughes *et al.* [2017].

The pre-eruptive conditions of the strombolian cases (Fastuca, Cuddia Randazzo, and Cuddia del Gallo—red paths in Figure 5) can promote crystallization of phenocrysts and microlites of alkali feldspar and clinopyroxene at temperatures of 680–750 °C. The high total crystal fraction (phenocrysts and microlites) observed in the strombolian products may be produced during magma stagnation and slow ascent prior to the triggering of the eruption. As shown in Figure 5 large undercoolings and several days at pre-eruptive conditions are needed to produce high crystal fractions of alkali feldspar [Arzilli *et al.*, 2020]. The pre-eruptive conditions proposed for the strombolian eruptions and crystal abundance observed in the natural samples can increase viscosity during magma ascent (Figure 5a,b) at $\eta > 10^6 \text{ Pa}\cdot\text{s}$, which is sufficient to lead to brittle fragmentation.

Regarding the Green Tuff Plinian eruption (green paths in Figure 5), the pre-eruptive conditions of the crystal-poor pantelleritic member are likely a temperature of $\leq 750 \text{ °C}$, a pressure $\sim 100 \text{ MPa}$, and water-saturated conditions (in agreement with Campagnola *et al.* [2016] and Liszewska *et al.* [2018]). Despite the crystal content of the pantelleritic products being relatively low (on average 0.08), magma viscosity can reach values higher than $10^6 \text{ Pa}\cdot\text{s}$ close to the surface (0.3 wt% of H_2O) at temperatures $\leq 750 \text{ °C}$ (Figure 5a,b), which implies that brittle fragmentation may be promoted. At a temperature of 800 °C, magma viscosity can reach a value of $10^6 \text{ Pa}\cdot\text{s}$ only at the surface with a crystallinity of 0.08 (Figure 5c). At temperature of 850 °C this viscosity threshold is not reached (Figure 5d); therefore, it is unlikely that brittle fragmentation and explosive eruptions are promoted at temperatures $\geq 800 \text{ °C}$. This result is in agreement with previous studies [Campagnola *et al.*, 2016, Hughes *et al.*, 2017], however, our simple

model considers only the effect of crystals, temperature, and magma water content at the equilibrium conditions, whilst, the effect of decompression rate, adiabatic cooling ascent rate, strain rate, vesicularity, and outgassing during magma ascent should be considered [La Spina *et al.*, 2021]. For example, Hughes *et al.* [2017] suggest that bubble overpressure driven by rapid decompression and strain localization around crystals may also promote brittle magma fragmentation.

In conclusion, we note that crystal abundance does not play a fundamental role in changing the viscosity of the pantelleritic magma for the Green Tuff Plinian eruption, in agreement with Campagnola *et al.* [2016] and Hughes *et al.* [2017]. This contrasts with basaltic compositions, where fast syn-eruptive crystallization has been proposed as a driving mechanism triggering fragmentation and highly explosive eruptions [e.g., Sable *et al.*, 2006, 2009, Arzilli *et al.*, 2019, Bamber *et al.*, 2020]. The pantelleritic magmas may favour highly explosive eruptions reaching viscosity of 10^6 Pa·s even with a low crystallinity at ≤ 750 °C (Figure 5). Therefore, the tendency of such magmas to fragment brittle or to flow effusively may be strongly controlled by temperature (Figure 5) and/or rapid decompression and strain localization, as suggested by Hughes *et al.* [2017]. Another process that should be considered is the crystallization of nanolites during fast perturbation of undercooling [Mujin and Nakamura, 2014, Di Genova *et al.*, 2020]. Nanolites may form during fast magma ascent in iron-rich peralkaline rhyolitic magmas, and their formation could change the magma viscosity by several orders of magnitude [Di Genova *et al.*, 2020]. All these hypotheses indicate that the complexity of pantellerite eruptive phenomena should be further investigated with more experimental and modelling studies to better understand the fragmentation process and the highly explosive eruptions in peralkaline rhyolitic systems.

Acknowledgements

This research has been supported by PRIN2017 (2017J277S9-MC). We thank John C. White and the other anonymous reviewer for their contribution to the review of this work and useful comments that helped us to improve this manuscript.

References

- Aiuppa, A., Franco, A., Von Glasow, R., Allen, A. G., D'Alessandro, W., Mather, T. A., Pyle, D. M., and Valenza, M. (2007). The tropospheric processing of acidic gases and hydrogen sulphide in volcanic gas plumes as inferred from field and model investigations. *Atmos. Chem. Phys.*, 7, 1441–1450.
- Arzilli, F. and Carroll, M. R. (2013). Crystallisation kinetics of alkali feldspars in cooling and decompression-induced crystallisation experiments in trachytic melt. *Contrib. Mineral. Petrol.*, 166, 1011–1027.
- Arzilli, F. *et al.* (2019). Magma fragmentation in highly explosive basaltic eruptions induced by rapid crystallization. *Nat. Geosci.*, 12, 1023–1028.
- Arzilli, F., Fabbriozio, A., Schmidt, M. W., Petrelli, M., Maimaiti, M., Dingwell, D. B., Paris, E., Burton, M., and Carroll, M. R. (2018). The effect of diffusive re-equilibration time on trace element partitioning between alkali feldspar and trachytic melts. *Chem. Geol.*, 495, 50–66.
- Arzilli, F., Piochi, M., Mormone, A., Agostini, C., and Carroll, M. R. (2016). Constraining pre-eruptive magma conditions and unrest timescales during the Monte Nuovo eruption (1538 AD; Campi Flegrei, Southern Italy): integrating textural and CSD results from experimental and natural trachyphonolites. *Bull. Volcanol.*, 78, 1–20.
- Arzilli, F., Stabile, P., Fabbriozio, A., Landi, P., Scaillet, B., Paris, E., and Carroll, M. R. (2020). Crystallization kinetics of alkali feldspar in peralkaline rhyolitic melts: implications for pantelleria volcano. *Front. Earth Sci.*, 8, article no. 177.
- Avanzinelli, R. (2004). Crystallisation and genesis of peralkaline magmas from Pantelleria Volcano, Italy: an integrated petrological and crystal-chemical study. *Lithos*, 73, 41–69.
- Bailey, D. K. and MacDonald, R. (1987). Dry peralkaline felsic liquids and carbon dioxide flux through the Kenya rift zone. In Mysen, B., editor, *Magmatic Processes: Physicochemical Principles*, volume 1, pages 91–105. Geochemical Society, University Park, PA.
- Bamber, E. C., Arzilli, F., Polacci, M., Hartley, M. E., Fellowes, J., Di Genova, D., Chavarría, D., Saballos, J. A., and Burton, M. R. (2020). Pre- and syn-eruptive conditions of a basaltic Plinian eruption at Masaya Volcano, Nicaragua: the Masaya Triple

- Layer (2.1 ka). *J. Volcanol. Geotherm. Res.*, 392, article no. 106761.
- Barclay, J., Carroll, M. R., Houghton, B. F., and Wilson, C. J. N. (1996). Pre-eruptive volatile content and degassing history of an evolving peralkaline volcano. *J. Volcanol. Geotherm. Res.*, 74, 75–87.
- Barclay, J., Rutherford, M. J., Carroll, M. R., Murphy, M. D., Devine, J. D., Gardner, J., and Sparks, R. S. J. (1998). Experimental phase equilibria constraints on pre-eruptive storage conditions of the Soufriere Hills magma. *Geophys. Res. Lett.*, 25, 3437–3440.
- Bohrson, W. A. and Reid, M. R. (1997). Genesis of silicic peralkaline volcanic rocks in an ocean island setting by crustal melting and open-system processes: Socorro Island, Mexico. *J. Petrol.*, 38, 1137–1166.
- Brugger, C. R. and Hammer, J. E. (2010). Crystallisation kinetics in continuous decompression experiments: implications for interpreting natural magma ascent processes. *J. Petrol.*, 51, 1941–1965.
- Campagnola, S., Romano, C., Mastin, L., and Vona, A. (2016). Confort 15 model of conduit dynamics: applications to Pantelleria Green Tuff and Etna 122 BC eruptions. *Contrib. Mineral. Petrol.*, 171, 1–25.
- Cashman, K. V. (2004). Volatile controls on magma ascent and eruption. In Sparks, R. S. J. and Hawkesworth, C. J., editors, *The State of the Planet: Frontiers and Challenge in Geophysics*, pages 109–124. American Geophysical Union.
- Civetta, L., Cornette, Y., Crisci, G., Gillot, P. Y., Orsi, G., and Requejo, C. S. (1984). Geology, geochronology and chemical evolution of the island of Pantelleria. *Geol. Mag.*, 121, 541–562.
- Civetta, L., Cornette, Y., Gillot, P.-Y., and Orsi, G. (1988). The eruptive history of Pantelleria (Sicily Channel) in the last 50 ka. *Bull. Volcanol.*, 50, 47–57.
- Civetta, L., D'Antonio, M., Orsi, G., and Tilton, G. R. (1998). The geochemistry of volcanic rocks from Pantelleria island, Sicily channel: petrogenesis and characteristics of the mantle source region. *J. Petrol.*, 39, 1453–1491.
- Civile, D., Lodolo, E., Torterici, L., Lanzafame, G., and Brancolini, G. (2008). Relationships between magmatism and tectonics in a continental rift: the Pantelleria Island region (Sicily Channel, Italy). *Mar. Geol.*, 251, 32–46.
- Cottrell, E., Gardner, J. E., and Rutherford, M. J. (1999). Petrologic and experimental evidence for the movement and heating of the pre-eruptive Minoan rhyodacite (Santorini, Greece). *Contrib. Mineral. Petrol.*, 135, 315–331.
- Couch, S., Sparks, R. S. J., and Carroll, M. R. (2003). The kinetics of degassing - induced crystallisation at Soufriere Hills volcano, Montserrat. *J. Petrol.*, 44, 1477–1502.
- Di Carlo, I., Rotolo, S. G., Scaillet, B., Buccheri, V., and Pichavant, M. (2010). Phase equilibrium constraints on pre-eruptive conditions of recent felsic explosive volcanism at Pantelleria Island, Italy. *J. Petrol.*, 5, 2245–2276.
- Di Genova, D., Brooker, R. A., Mader, H. M., Drewitt, J. W., Longo, A., Deubener, J., Neuville, D. R., Fanara, S., Shebanova, O., Anzellini, S., and Arzilli, F. (2020). In situ observation of nanolite growth in volcanic melt: a driving force for explosive eruptions. *Sci. Adv.*, 6(39), article no. eabb0413.
- Di Genova, D., Romano, C., Hess, K.-U., Vona, A., Poe, B. T., Giordano, D., Dingwell, D., and Behrens, H. (2013). The rheology of peralkaline rhyolites from Pantelleria Island. *J. Volcanol. Geotherm. Res.*, 249, 201–216.
- Di Genova, D., Vasseur, J., Hess, K. U., Neuville, D. R., and Dingwell, D. B. (2017). Effect of oxygen fugacity on the glass transition, viscosity and structure of silica- and iron-rich magmatic melts. *J. Non. Cryst. Solids*, 470, 78–85.
- Duffield, W. A. (1990). Eruptive fountains of silicic magma and their possible effects on tin content of fountain-fed lavas. *Geol. Soc. Am. Spec. Pap.*, 246, 251–261.
- Edmonds, M., McGee, K. A., and Doukas, M. P. (2008). Chlorine degassing during the lava dome-building eruption of Mount St. Helens 2004–2005. In Sherrod, D. R., Scott, W. E., and Stauffer, P. H., editors, *A Volcano Rekindled: The Renewed Eruption of Mount St. Helens 2004–2006*, volume 1750, pages 573–589. U.S. Geological Survey Professional Paper. Chap. 27.
- Gardner, J. E., Carey, S., Rutherford, M., and Sigurdson, H. (1995). Petrologic diversity of Mount St. Helens dacites during the last 4000 years: implications for magma mixing. *Contrib. Mineral. Petrol.*, 119, 224–238.
- Geschwind, C.-H. and Rutherford, M. J. (1992). Cumingtonite and the evolution of the Mount St. Helens (Washington) magma system: an experimental study. *Geology*, 20, 1011–1014.

- Ghiorso, M. S. and Gualda, G. A. R. (2015). An H₂O–CO₂ mixed fluid saturation model compatible with rhyolite-MELTS. *Contrib. Mineral. Petrol.*, 169, article no. 53.
- Gioncada, A. and Landi, P. (2010). The pre-eruptive volatile contents of recent basaltic and pantelleritic magmas at Pantelleria (Italy). *J. Volcanol. Geotherm. Res.*, 189, 191–201.
- Giordano, D., Russell, J. K., and Dingwell, D. B. (2008). Viscosity of magmatic liquids: a Model. *Earth Planet. Sci. Lett.*, 271, 123–134.
- Gottsmann, J. and Dingwell, D. B. (2002). The thermal history of a spatter-fed lava flow: the 8-ka pantellerite flow on Mayor Island, New Zealand. *Bull. Volcanol.*, 64, 410–422.
- Gualda, G. A. R., Ghiorso, M. S., Lemons, R. V., and Carley, T. L. (2012). Rhyolite- MELTS: a modified calibration of MELTS optimized for silica-rich, fluid-bearing magmatic systems. *J. Petrol.*, 53, 875–890.
- Hammer, J. E. (2004). Crystal nucleation in hydrous rhyolite: Experimental data applied to classical theory. *Am. Mineral.*, 89, 1673–1679.
- Hammer, J. E. (2006). Influence of *f*O₂ and cooling rate on the kinetics and energetics of Fe-rich basalt crystallization. *Earth Planet. Sci. Lett.*, 248, 618–637.
- Horn, S. and Smincke, H. U. (2000). Volatile emission during the eruption of Baitoushan volcano (China/North Korea) ca. 969 AD. *Bull. Volcanol.*, 61, 537–555.
- Houghton, B. F., Weaver, S. D., Wilson, C. J. N., and Lanphere, M. A. (1992). Evolution of a quaternary peralkaline volcano: Major Island, New Zealand. *J. Volcanol. Geotherm. Res.*, 51, 217–236.
- Hughes, E. C., Neave, D. A., Dobson, K. J., Withers, P. J., and Edmonds, M. (2017). How to fragment peralkaline rhyolites: Observations on pumice using combined multi-scale 2D and 3D imaging. *J. Volcanol. Geotherm. Res.*, 336, 179–191.
- Huppert, H. E. and Woods, A. W. (2002). The role of volatiles in magma chamber dynamics. *Nature*, 420, 493–495.
- Iddon, F., Jackson, C., Hutchison, W., Fontijn, K., Pyle, D. M., Mather, T. A., Yirgu, G., and Edmonds, M. (2018). Mixing and crystal scavenging in the Main Ethiopian Rift revealed by trace element systematics in feldspars and glasses. *Geochem. Geophys. Geosyst.*, 20, 1–30.
- Jeffery, A., J. and Gertisser, R. (2018). Peralkaline felsic magmatism of the Atlantic Islands. *Front. Earth Sci.*, 6, article no. 145.
- Jordan, N. J., John, C., White, R. M., and Rotolo, S. G. (2021). Evolution of the magma system of Pantelleria (Italy) from 190 ka to present. *C. R. Géosci.*, pages 1–17. Online first (2021), <https://doi.org/10.5802/crgeos.50>.
- Jordan, N. J., Rotolo, S. G., Williams, R., Speranza, F., McIntosh, W. C., Branney, M. J., and Scaillet, S. (2018). Explosive eruptive history of Pantelleria, Italy: Repeated caldera collapse and ignimbrite emplacement at a peralkaline volcano. *J. Volcanol. Geotherm. Res.*, 349, 47–73.
- Kovalenko, V. I., Herving, R. L., and Sheridan, M. F. (1988). Ion-microprobe analyses of trace elements in anorthoclase, hedembergite, aenigmatite, quartz, apatite and glass in Pantellerite: evidence for high water content in pantellerite melt. *Am. Miner.*, 73, 1038–1045.
- La Spina, G., Arzilli, F., Llewellyn, E. W., Burton, M. R., Clarke, A. B., Vitturi, M. D. M., Polacci, M., Hartley, M. E., Di Genova, D., and Mader, H. M. (2021). Explosivity of basaltic lava fountains is controlled by magma rheology, ascent rate and outgassing. *Earth Planet. Sci. Lett.*, 553, article no. 116658.
- Landi, P. and Rotolo, S. G. (2015). Cooling and crystallization recorded in trachytic enclaves hosted in pantelleritic magmas (Pantelleria, Italy): implications for pantellerite petrogenesis. *J. Volcanol. Geotherm. Res.*, 301, 169–179.
- Lanzo, G., Landi, P., and Rotolo, S. G. (2013). Volatiles in pantellerite magmas: a case study of the Green Tu Plinian eruption (Island of Pantelleria, Italy). *J. Volcanol. Geotherm. Res.*, 262, 153–163.
- Le Maitre, R. W., editor (2002). *Igneous Rocks, a Classification and Glossary of Terms: Recommendations of the International Union of Geological Sciences Subcommission on the Systematics of Igneous Rocks*. Cambridge University Press, Cambridge, UK, 2nd edition. 236 p.
- Liszewska, K., White, J., MacDonald, R., and Bagiński, B. (2018). Compositional and thermodynamic variability in a stratified magma chamber: evidence from the Green Tuff ignimbrite (Pantelleria, Italy). *J. Petrol.*, 59, 2245–2272.
- Lowestern, J. B. and Mahood, G. A. (1991). New data on magmatic H₂O contents with implications for petrogenesis and eruptive dynamics at Pantelleria.

- Bull. Volcanol.*, 54, 78–83.
- MacDonald, R. (1974). Nomenclature and petrochemistry of the peralkaline oversaturated extrusive rocks. *Bull. Volcanol.*, 38, 498–516.
- MacDonald, R., Bagiński, B., Belkin, H. E., Dzierzanowski, P., and Jeżak, L. (2008). Compositional variations in apatites from a benmoreite-peralkaline rhyolite volcanic suite, Kenya Rift Valley. *Mineral. Mag.*, 72, 1147–1161.
- MacDonald, R., Bagiński, B., Leat, P. T., White, J. C., and Dzierzanowski, P. (2011). Mineral stability in peralkaline silicic rocks: information from trachytes of the Menengai volcano, Kenya. *Lithos*, 125, 553–568.
- Mader, H. M., Llewellyn, E. W., and Müller, S. P. (2013). The rheology of two-phase magmas: a review and analysis. *J. Volcanol. Geotherm. Res.*, 257, 135–158.
- Mahood, G. A. and Hildreth, W. (1986). Geology of the peralkaline volcano at Pantelleria, Strait of Sicily. *Bull. Volcanol.*, 48, 143–172.
- Marshall, A. S., MacDonald, R., Rogers, N. W., Fitton, J. G., Tindle, A. G., Nejbert, K., and Hinton, R. W. (2009). Fractionation of peralkaline silicic magmas: the greater Olkaria volcanic complex, Kenya Rift Valley. *J. Petrol.*, 50, 323–359.
- Martel, C. (2012). Eruption dynamics inferred from microlite crystallization experiments: application to Plinian and dome-forming eruptions of Mt Pelée (Martinique, Lesser Antilles). *J. Petrol.*, 53, 699–725.
- Martel, C. and Schmidt, B. C. (2003). Decompression experiments as an insight into ascent rates of silicic magmas. *Contrib. Mineral. Petrol.*, 144, 397–415.
- Masotta, M., Pontesilli, A., Mollo, S., Armienti, P., Ubide, T., Nazzari, M., and Scarlato, P. (2020). The role of undercooling during clinopyroxene growth in trachybasaltic magmas: insights on landmagma decompression and cooling at Mt. Etna volcano. *Geochim. Cosmochim. Acta*, 268, 258–276.
- Mattia, M., Bonaccorso, A., and Guglielmino, F. (2007). Ground deformations in the Island of Pantelleria (Italy): insights into the dynamic of the current intereruptive period. *J. Geophys. Res.*, 112, article no. B11406.
- Mollard, E., Martel, C., and Bourdier, J. L. (2012). Decompression-induced Crystallisation in Hydrated Silica-rich Melts: empirical models of experimental plagioclase nucleation and growth kinetics. *J. Petrol.*, 53, 1743–1766.
- Moore, G., Vennemann, T., and Carmichael, I. S. E. (1998). An empirical model for the solubility of H₂O in magmas to 3 kilobars. *Am. Mineral.*, 83, 36–42.
- Mujin, M. and Nakamura, M. (2014). A nanolite record of eruption style transition. *Geology*, 42(7), 611–614.
- Mungall, J. E. and Martin, R. F. (1995). Petrogenesis of basalt–columbite and basalt–pantellerite suites, Terceira, Azores, and some implications for the origin of ocean-island rhyolites. *Contrib. Mineral. Petrol.*, 119, 43–55.
- Mysen, B. O. (2007). The solution behaviour of H₂O in peralkaline aluminosilicate melts at high pressure with implication for properties of hydrous melts. *Geochim. Cosmochim. Acta*, 71, 1820–1834.
- Mysen, B. O. and Toplis, M. J. (2007). Structural behaviour of Al³⁺ in peralkaline, metaluminous, and peraluminous silicate melts and glasses at ambient pressure. *Am. Mineral.*, 92, 933–946.
- Neave, D. A. (2020). Chemical variability in peralkaline magmas and magma reservoirs: insights from the Khaggiar lava flow, Pantelleria, Italy. *Contrib. Mineral. Petrol.*, 175, article no. 39.
- Neave, D. A., Fabbro, G., and Herd, R. (2012). Melting, differentiation and Degassing at the Pantelleria Volcano, Italy. *J. Petrol.*, 53, 637–663.
- Ni, H., Keppler, H., Walte, N., Schiavi, F., Chen, Y., Masotta, M., and Li, Z. (2014). *In situ* observation of crystal growth in a basalt melt and the development of crystal size distribution in igneous rocks. *Contrib. Mineral. Petrol.*, 167, article no. 1003.
- Orsi, G., Ruvo, L., and Scarpati, C. (1991). The recent explosive volcanism at Pantelleria. *Geol. Rundsch.*, 80, 187–200.
- Papale, P. (1999). Modelling of the solubility of H₂O + CO₂ fluid in silicate liquids. *Am. Mineral.*, 84, 477–792.
- Papale, P., Moretti, R., and Barbato, D. (2006). The compositional dependence of the saturation surface of H₂O + CO₂ fluids in silicate melts. *Chem. Geol.*, 229, 78–95.
- Papale, P. and Polacci, M. (1999). Role of carbon dioxide in the dynamics of magma ascent in explosive eruptions. *Bull. Volcanol.*, 60, article no. 583e594.
- Peccerillo, A., Barberio, M. R., Yirgu, G., Ayalew, D., Barbieri, M., and Wu, T. W. (2003). Relationships between Mafic and Peralkaline Silicic Magmatism in Continental Rift Settings: a Petrological, Geo-

- chemical and Isotopic Study of the Gedemsa Volcano, Central Ethiopian Rift. *J. Petrol.*, 44, 2003–2032.
- Polacci, M. et al. (2018). Crystallisation in basaltic magmas revealed via *in situ* 4D synchrotron X-ray microtomography. *Sci. Rep.*, 8, article no. 8377.
- Pontesilli, A., Masotta, M., Nazzari, M., Mollo, S., Armienti, P., Scarlato, P., and Brenna, M. (2019). Crystallization kinetics of clinopyroxene and titanomagnetite growing from a trachybasaltic melt: New insights from isothermal time-series experiments. *Chem. Geol.*, 510, 113–129.
- Prosperini, N., Perugini, D., Poli, G., and Manetti, P. (2000). Magmatic enclaves distribution within the Khaggiar lava dome (Pantelleria, Italy): implication for magma chamber dynamics and eruption. *Acta Vulcanol.*, 12, 37–47.
- Ren, M., Omenda, P. A., Anthony, E. Y., White, J. C., MacDonald, R., and Bailey, D. K. (2006). Application of the QUILF thermobarometer to the peralkaline trachytes and pantellerites of the Eburre volcanic complex, East African Rift, Kenya. *Lithos*, 91, 109–124.
- Roggensack, K., Hervig, R. L., McKnight, S. B., and Williams, S. N. (1997). Explosive basaltic volcanism from Cerro Negro volcano: Influence of volatiles on eruptive style. *Science*, 277, 1639–1642.
- Romano, P., Andújar, J., Scaillet, B., Romengo, N., Di Carlo, I., and Rotolo, S. G. (2018). Phase equilibria of Pantelleria trachytes (Italy): constraints on pre-eruptive conditions and on the metaluminous to peralkaline transition in silicic magmas. *J. Petrol.*, 59, 559–588.
- Romano, P., Di Carlo, I., Andújar, J., and Rotolo, S. G. (2021). Water solubility in trachytic and pantelleritic melts: an experimental study. *C. R. Geosci.*, 353(S2), 315–331.
- Romano, P., Scaillet, B., White, J. C., Andújar, J., Di Carlo, I., and Rotolo, S. G. (2020). Experimental and thermodynamic constraints on mineral equilibrium in pantelleritic magmas. *Lithos*, 376–377, article no. 105793. 22 p.
- Romano, P., White, J. C., Ciulla, A., Di Carlo, I., D’Orlando, C., Landi, P., and Rotolo, S. G. (2019). Volatiles and trace elements content in melt inclusions from the zoned Green Tuff ignimbrite (Pantelleria, Sicily): petrological inferences. *Ann. Geophys.*, 62(1), article no. VO09.
- Romengo, N., Landi, P., and Rotolo, S. G. (2012). Evidence of basaltic magma intrusions in a trachytic magma chamber at Pantelleria (Italy). *Period. Mineral.*, 81, 163–178.
- Ronga, F., Lustrino, M., Marzoli, A., and Melluso, L. (2009). Petrogenesis of a basalt-comendite-pantellerite rock suite: the Boseti volcanic complex (main Ethiopian rift). *Mineral. Petrol.*, 98, 227–243.
- Rotolo, S. G., Agnesi, V., Conoscenti, C., and Lanzo, G. (2017). Pantelleria Island (Strait of Sicily): Volcanic history and geomorphological landscape. In Soldati, M. and Marchetti, M., editors, *Landscapes and Landforms of Italy*, World Geomorphological Landscapes. Springer, Cham.
- Rotolo, S. G., La Felice, S., Mangalaviti, A., and Landi, P. (2007). Geology and petrochemistry of the recent (<25 ka) silicic volcanism at Pantelleria Island. *Boll. Soc. Geol. It.*, 126, 191–208.
- Rotolo, S. G., Scaillet, S., La Felice, S., and Vita-Scaillet, G. (2013). A revision of the structure and stratigraphy of pre-Green Tuff ignimbrites at Pantelleria (Strait of Sicily). *J. Volcanol. Geotherm. Res.*, 250, 61–74.
- Rotolo, S. G., Scaillet, S., Speranza, F., White, J. C., Williams, R., and Jordan, N. J. (2021). Volcanological evolution of Pantelleria Island (Strait of Sicily) peralkaline volcano: a review. *C. R. Géosci.*, pages 1–22. Online first (2021), <https://doi.org/10.5802/crgeos.51>.
- Rutherford, M. J. and Devine, J. D. (1996). Pre-eruption pressure-temperature conditions and volatiles in the 1991 dacitic magma of Mount Pinatubo. In Newhall, C. G. and Punongbayan, R. S., editors, *Fire and Mud: Eruptions and Lahars of Mount Pinatubo, Philippines*, pages 751–766. PHIVOLCS and University of Washington Press, Seattle.
- Rutherford, M. J., Sigurdsson, H., Carey, S., and Davis, A. (1985). The May 18, 1980, eruption of Mount St. Helens 1. Melts composition and experimental phase equilibria. *J. Geophys. Res.*, 90, 2929–2947.
- Sable, J. E., Houghton, B., Wilson, C. J. N., and Carey, R. J. (2009). Eruption mechanisms during the climax of the Tarawera 1886 basaltic Plinian eruption inferred from microtextural. In *Studies in Volcanology: The Legacy of George Walker*, volume 2, page 129.
- Sable, J. E., Houghton, B. F., Del Carlo, P., and Coltelli, M. (2006). Changing conditions of magma ascent and fragmentation during the Etna 122 BC

- basaltic Plinian eruption: Evidence from clast microtextures. *J. Volcanol. Geotherm. Res.*, 158(3-4), 333–354.
- Scaillet, B. and MacDonald, R. (2001). Phase Relations of peralkaline silicic magmas and petrogenetic implications. *J. Petrol.*, 42, 825–845.
- Scaillet, B. and MacDonald, R. (2003). Experimental constraints on the relationships between Peralkaline Rhyolites of the Kenya Rift Valley. *J. Petrol.*, 44, 1867–1894.
- Scaillet, B. and MacDonald, R. (2006). Experimental constraints on pre-eruption conditions of pantelleritic magmas: evidence from the Eburru complex, Kenya Rift. *Lithos*, 91, 95–108.
- Scaillet, S., Rotolo, S. G., La Felice, S., and Vita-Scaillet, G. (2011). High-resolution $^{40}\text{Ar}/^{39}\text{Ar}$ chronostratigraphy of the post-caldera (<20 ka) volcanic activity at Pantelleria, Sicily Strait. *Earth Planet. Sci. Lett.*, 309, 280–290.
- Scaillet, S., Vita-Scaillet, G., and Rotolo, S. G. (2013). Millennial-scale phase relationships between ice-core and Mediterranean marine records: insights from high-precision $^{40}\text{Ar}/^{39}\text{Ar}$ dating of the Green Tuff of Pantelleria, Sicily Strait. *Quat. Sci. Rev.*, 78, 141–154.
- Schmidt, B. and Behrens, H. (2008). Water solubility in phonolite melts: Influence of melt composition and temperature. *Chem. Geol.*, 256, 259–268.
- Schmincke, H.-U. (1974). Volcanological aspects of peralkaline silicic welded ash-flow tuffs. *Bull. Volcanol.*, 38, 594–636.
- Shea, T. and Hammer, J. E. (2013). Kinetics of cooling- and decompression-induced crystallization in hydrous mafic-intermediate magmas. *J. Volcanol. Geotherm. Res.*, 260, 127–145.
- Sparks, R. S. J. (1978). The dynamics of bubble formation and growth in magmas: a review and analysis. *J. Volcanol. Geotherm. Res.*, 3, 1–37.
- Sparks, S. R. J. (2003). Dynamics of magma degassing. *Geol. Soc. Lond., Spec. Pub.*, 213, 5–22.
- Speranza, F., Landi, P., Caracciolo, F. D. A., and Pignatelli, A. (2010). Paleomagnetic dating of the most recent silicic eruptive activity at Pantelleria (Strait of Sicily). *Bull. Volcanol.*, 72, 847–858.
- Stabile, P., Appiah, E., Bello, M., Giuli, G., Paris, E., and Carroll, M. R. (2020). New IR spectroscopic data for determination of water abundances in hydrous pantelleritic glasses. *Am. Mineral.*, 105(7), 1060–1068.
- Stabile, P. and Carroll, M. R. (2020). Petrologic experimental data on Vesuvius and Campi Flegrei magmatism: a review. In De Vivo, B., Belkin, H. E., and Rolandi, G., editors, *Vesuvius, Campi Flegrei, and Campanian Volcanism*, pages 323–369. Elsevier. ISBN 9780128164549.
- Stabile, P., Giuli, G., Cicconi, M. R., Paris, E., Trapananti, A., and Behrens, H. (2017). The effect of oxygen fugacity and Na/(Na+K) ratio on iron speciation in pantelleritic glasses. *J. Non-Cryst. Solids*, 478, 65–74.
- Stabile, P., Radica, E., Bello, M., Behrens, H., Carroll, M. R., Paris, E., and Giuli, G. (2018). H₂O solubility in pantelleritic melts: pressure and alkali effects. *N. Jb. Miner. Abh.*, 195, 1–9.
- Stabile, P., Sicola, S., Giuli, G., Paris, E., Carroll, M. R., Deubener, J., and Di Genova, D. (2021). The effect of iron and alkali on the nanocrystal-free viscosity of volcanic melts: A combined Raman spectroscopy and DSC study. *Chem. Geol.*, 559, article no. 119991.
- Stabile, P., Webb, S., Knipping, J. K., Behrens, H., Paris, E., and Giuli, G. (2016). Viscosity of pantelleritic and alkali-silicate melts: effect of Fe redox state and Na/(Na + K) ratio. *Chem. Geol.*, 422, 73–82.
- Stevenson, R. J., Bagdassarov, N. S., Dingwell, D. B., and Romano, C. (1998). The influence of trace amounts of water on the viscosity of rhyolites. *Bull. Volcanol.*, 60, 89–97.
- Stevenson, R. J., Briggs, R. M., and Hodder, A. P. W. (1993). Emplacement history of a low-viscosity, fountain-fed pantelleritic lava flow. *J. Volcanol. Geotherm. Res.*, 57, 39–56.
- Stevenson, R. J. and Wilson, L. (1997). Physical volcanology and eruption dynamics of peralkaline agglutinates from Pantelleria. *J. Volcanol. Geotherm. Res.*, 79, 97–122.
- Stock, M. J., Humphreys, M. C. S., Smith, V. C., Isaia, R., Brooker, R. A., and Pyle, D. M. (2018). Tracking volatile behaviour in sub-volcanic plumbing systems using apatite and glass: Insights into pre-eruptive processes at Campi Flegrei, Italy. *J. Petrol.*, 59(12), 2463–2492.
- Vona, A., Romano, C., Dingwell, D. B., and Giordano, D. (2011). The rheology of crystal-bearing basaltic magmas from Stromboli and Etna. *Geochim. Cosmochim. Acta*, 75, 3214–3236.
- Webster, J. D., Taylor, R. P., and Bean, C. (1993). Pre-eruptive melt composition and constraints on de-

- gassing of a water-rich pantellerite magma, Fantale volcano, Ethiopia. *Contrib. Mineral. Petrol.*, 114, 53–62.
- White, J. C., Parker, D. F., and Ren, M. (2009). The origin of trachyte and pantellerite from Pantelleria, Italy: insights from major elements, trace elements, and thermodynamic modelling. *J. Volcanol. Geotherm. Res.*, 179, 33–55.
- White, J. C., Ren, M., and Parker, D. F. (2005). Variation in mineralogy, temperature, and oxygen fugacity in a suite of strongly peralkaline lavas and tuffs, Pantelleria, Italy. *Canad. Mineral.*, 43, 1331–1347.
- Wilding, M. C., MacDonald, R., Davies, J. E., and Fallick, A. E. (1993). Volatile characteristics of peralkaline rhyolites from Kenya: an ion microprobe, infrared spectroscopic and hydrogen isotope study. *Contrib. Mineral. Petrol.*, 114, 264–275.
- Williams, R. (2010). *Emplacement of Radial Pyroclastic Density Currents Over Irregular Topography: The chemically-zoned, low aspect-ratio Green Tuff ignimbrite, Pantelleria, Italy*. PhD thesis, University of Leicester, Leicester, UK. 224 p., <https://doi.org/10.6084/m9.figshare.789054>.
- Williams, R., Branney, M. J., and Barry, T. L. (2014). Temporal and spatial evolution of a waxing then waning catastrophic density current revealed by chemical mapping. *Geology*, 42, 107–110.



Perspectives on alkaline magmas / *Perspectives sur les magmas alcalins*

Magma mixing and exsolution phenomena in peralkaline rhyolites: insights from the Gold Flat Tuff, Nevada

Ray Macdonald^{a, b}, Bogusław Bagiński^{*, a}, Marcin Stachowicz^a, Harvey E. Belkin^c, Jan Pawłowski^d and Jakub Kotowski^a

^a Department of Geochemistry, Mineralogy and Petrology, University of Warsaw, al. Żwirki i Wigury 93, 02-089 Warszawa, Poland

^b Environment Centre, Lancaster University, Lancaster LA14YQ, UK

^c U.S. Geological Survey retired, 11142 Forest Edge Drive, Reston, VA 20190-4026, USA

^d Biological and Chemical Research Centre, Faculty of Chemistry, University of Warsaw, 02-089 Warszawa, Poland

E-mails: raymacdonald186@gmail.com (R. Macdonald), b.baginski1@uw.edu.pl (B. Bagiński), marcin.stachowicz@uw.edu.pl (M. Stachowicz), harveybelkin@gmail.com (H. E. Belkin), jan.kazimierz.pawlowski@gmail.com (J. Pawłowski), jb.kotowski@gmail.com (J. Kotowski)

Abstract. The distribution and compositions of chevkinite-group minerals (CGMs) in the pantelleritic Gold Flat Tuff, Nevada, USA, are used to examine three aspects of the evolution of the tuff, which we feel are of general significance in peralkaline magmatism. First, both chevkinite-(Ce) and perrierite-(Ce) occur in certain facies, although normally these phases almost invariably occur in different igneous lithologies. Their co-occurrence in the tuff is due to the mixing of pantelleritic and intermediate magmas. Second, the tuff is the first recorded occurrence of a CGM in a pantellerite eruptive, with possible implications for the crystallization conditions. In particular, low values of $a\text{SiO}_2$ may have stabilized ilmenite + chevkinite rather than aenigmatite, although the unusually high LREE contents ($\Sigma\text{La-Sm} \leq 1517$ ppm) in the pantellerite may have played a role. Third, an unusual lamellar texture in the CGM is revealed by Atomic Force Microscopy to be formed by a rutile-like phase. The lamellae may have formed by exsolution from a rutile-like layer in the crystal structure. An electron back-scattered diffraction study of a single crystal showed a structural dislocation not apparent optically or by electron back-scattered imaging. This may have wider implications in mineralogical studies.

Keywords. Gold Flat Tuff, Nevada, Chevkinite-group minerals, Electron back-scattered diffraction, Atomic force microscopy, Magma mixing.

Available online 31st March 2021

* Corresponding author.

1. Introduction

The chevkinite group of REE, Ti-silicates are increasingly being recognized as widespread accessory minerals in a wide range of igneous and metamorphic rocks. Hundreds of localities are known globally, and hundreds more undoubtedly wait to be discovered [Macdonald *et al.*, 2019a]. The two most common members of the group, chevkinite and perrierite, have the general formula $A_4BC_2D_2(Si_2O_7)_2$, where the dominant cations in each site are: A, REE, Ca, Sr; B, Fe^{2+} ; C, Fe^{2+} , Fe^{3+} , Mn, Mg, Ti; D, Ti. In igneous systems, chevkinite and perrierite occupy different paragenesis; chevkinite occurs mainly in evolved, salic rocks, such as syenites and alkali granites (and their extrusive equivalents), and perrierite is known only from rocks of intermediate composition, such as syenodiorites, diorites, latites and trachyandesites [Macdonald and Belkin, 2002, Macdonald *et al.*, 2019a]. Here we report on the unusual case of the occurrence of the two phases in a strongly peralkaline (pantelleritic) rhyolite, which, in addition, is the only record of a chevkinite-group mineral (CGM) crystallizing in a pantelleritic magma.

The CGM under study also displays an unusual textural feature, which has not been reported from the group before. It occurs as lamellae which may be related to some form of exsolution. The lamellae are sufficiently thin ($\leq 2 \mu m$), so that they could not be studied by techniques such as TEM or IR. We chose, therefore, to employ Atomic Force Microscopy (AFM) and electron back-scattered diffraction (EBSD) to examine the nature of the lamellae. The host pantellerite is the Gold Flat Tuff, an ash-flow tuff from the Black Mountain Volcanic Centre in Nevada, USA.

2. Gold Flat Tuff

The multicaldera silicic SW Nevada volcanic field (SWNVF) erupted, over the period 16–7 Ma, more than 20 major ash-flow sheets with the formation of at least eight collapse calderas [Byers Jr *et al.*, 1989, Sawyer *et al.*, 1994]. Associated with the ash-flow tuffs are lava flows and minor pyroclastic rocks which erupted from a large number of smaller vents. The youngest major centre in the field is the Black Mountain Volcanic Centre (BMVC; Figure 1). The centre is

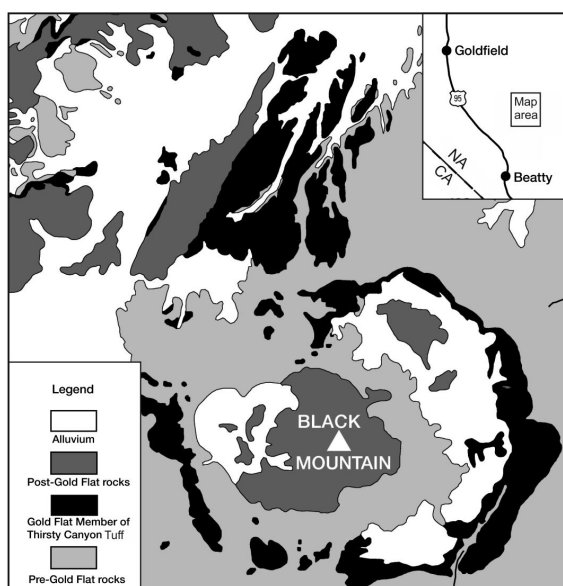


Figure 1. Generalized geological map showing the distribution of the Gold Flat Member of the Thirsty Canyon Group, modified from Noble [1965].

a set of nested collapse structures and constructional volcanoes some 14 km across. Eruptive units of the centre, which are termed the Thirsty Canyon Tuff, comprise ash-flow sheets, lavas and nonwelded tuffs erupted from the Black Mountain caldera between 9.43 and 9.15 Ma [Fleck *et al.*, 1991].

The Gold Flat Tuff is the youngest of the ash-flow sheets (9.15 Ma) in the BMVC, and the only pantelleritic rhyolite in the SW Nevada field, although several earlier BMVC units are comenditic. Noble [1965] reported that the tuff is a compound cooling unit, made up of at least a dozen individual ash-flows in a total thickness of only 30 m and an estimated volume of 20 km^3 [Vogel *et al.*, 1983]. The tuff shows complex vertical and lateral variations in composition and texture, related to a very complex evolutionary history which is still poorly understood. For example, Macdonald *et al.* [2019b] presented mineral chemical evidence, such as a range in feldspar compositions from An_{79-0} and in olivine compositions from $Fo_{54.5-1.9}$, indicating that melts ranging from basaltic through trachyandesitic to comenditic mixed with the pantellerite prior to, or during, eruption.

The pantelleritic component of the tuff has Peralkalinity Indices (P.I.: mol. ($\text{Na}_2\text{O} + \text{K}_2\text{O}/\text{Al}_2\text{O}_3$)) in the range 1.41–1.83 [Macdonald *et al.*, 2019b]. SiO_2 ranges from 70.7 to 73.5 wt% and FeO^* from 5 to 7 wt%. Abundances of MgO and CaO are very low, ≤ 0.03 wt% and ≤ 0.24 wt%, respectively. Notable features are the unusually high contents of F (≤ 2.2 wt%), F + Cl (≤ 2.9 wt%), LREE (La–Sm: ≤ 1517 ppm) and ZrO_2 (≤ 1.04 wt%). We know of no other peralkaline rhyolite with such elevated contents of these elements.

Macdonald *et al.* [2019b] used trachybasalts (belonging to the Basalt of Thirsty Mountain, geographically associated with the Gold Flat Tuff but ~ 4.5 Ma older than it) as proxies for the intermediate component of the tuff. They are $\text{hy} \pm \text{ol} \pm \text{q}$ -normative, with SiO_2 50–51 wt% and Mg-number 0.35–0.46 ($\text{Mg}/(\text{Mg} + \text{Fe})$, with all Fe calculated as Fe^{2+}).

3. Samples and analytical methods

CGMs were studied in two samples of the tuff. Sample GF1 comes from a partially welded tuff, probably of fall origin, at the base of the sheet in Oasis Valley [N37° 05.583' W116° 39.919']. Sample Ttg-hg#1 is from a glassy, welded layer immediately above the basal fall at N37° 20.333' W116° 39.666' and is from the earliest erupted ash flow of the Gold Flat Tuff [Noble, 1965].

Mineral compositions were determined by electron microprobe analysis (EPMA) using a Cameca SX-100 microprobe equipped with four wavelength dispersive spectrometers. The analytical conditions were: accelerating voltage 15 kV and probe current 20–40 nA, with counting times of 20 s on peak and 10 s on each of the two background positions. The standards, crystals and X-ray lines used and generalized detection limits are given in the Appendix. The 'PAP' $\phi(\rho Z)$ program [Pouchou and Pichoir, 1991] was used for corrections. Estimates of analytical precision (1 σ ; wt%) are: Si 0.07, Ti 0.03, Al 0.02, Cr 0.02, Ni 0.03, Fe 0.09, Mn 0.03, Mg 0.04, Ca 0.08, Na 0.01, K 0.01. Representative analyses are given in Table 1; the full data set is given in Supplementary Table 1a.

Analyses were also made of glass in sample GF1 (Supplementary Table 1b). Analyses were conducted with a 10 nA defocused (20 μm) beam. Certain problems can arise with the analysis of glass, related especially to Na volatility. The glass analytical protocol

was optimized by first measuring Na, F and Cl simultaneously, with the interception method to the initial time.

The nature of the lamellar stripes in the CGM was examined using two techniques. Atomic Force Microscopy (AFM) measurements were carried out with a 5500 AFM (Agilent Technologies, Santa Clara, CA, USA). The images were collected in contact mode using PPP-CONT probes (Nanosensors, Neuchâtel, Switzerland) with nominal force constants in the range 0.02–0.77 N/m. Force spectroscopy experiments were performed using AFM PPP-CONT probes. Force versus distance curves were used to obtain the adhesion force with regard to material morphology. Before each experiment, thermal tune methods were employed to determine the spring constants of cantilevers. For each sample, three different 500 nm \times 500 nm squares were probed by force–distance measurements. All experiments were conducted at 23 ± 1 °C.

A diffraction pattern from polished thin sections of chevkinite crystals in sample GF1 exhibiting the lamellar striping feature was captured for Electron Back-Scatter Diffraction (EBSD) analysis. The sample was covered with a 4 nm carbon layer for better surface discharge and measured in a Zeiss Auriga equipped with a Bruker e⁺FlashHR+ detector with integrated ARGUS imaging device. The sample was tilted to 70° using the dedicated stage (tilt about sample *X* axis) for an optimal EBSD signal. Image tilt correction was used on the Zeiss SmartSEM software and no image rotation was applied. The system was calibrated in Bruker ESPRIT 1.9. The crystal was composed of two differently orientated domains, that were measured as Euler angles: $\phi_1 = 169(1)^\circ$, $\Phi = 120(1)^\circ$, $\phi_2 = 141(1)^\circ$ and $\phi_1 = 349(1)^\circ$, $\Phi = 61(3)^\circ$, $\phi_2 = 39(2)^\circ$. The pattern centre (PC), in Bruker fractional coordinates, was measured as $\text{PC}_x = 0.48$, $\text{PC}_y = 0.15$ with a pattern aspect ratio of 1.39 (width/height), detector distance 17.31 mm. Another chevkinite crystal with striping analysed with EBSD had an orientation measured as Euler angles: $\phi_1 = 124.7(9)^\circ$, $\Phi = 42.0(9)^\circ$, $\phi_2 = 197(2)^\circ$; $\text{PC}_x = 0.47$, $\text{PC}_y = 0.47$, detector distance 16.8 mm. The EBSD system uses nonstandard settings of monoclinic unit cells for Euler angle determination. For the chevkinite-type crystal structure it is $a = 11.1$ Å, $b = 13.4$ Å, $c = 5.7$ Å, $\gamma = 79^\circ$. Further analysis and interpretation were conducted with

Table 1. Representative compositions of chevkinite-group minerals

	Chevkinite-(Ce)					Perrierite-(Ce)		
	1	2	3	4	5	6	7	8
wt%								
P ₂ O ₅	bd	0.07	-	-	0.13	0.06	0.05	0.11
Nb ₂ O ₅	1.76	1.13	0.99	1.26	0.15	bd	bd	bd
Ta ₂ O ₅	0.10	0.11	0.11	bd	0.06	0.09	0.13	0.11
SiO ₂	18.70	18.37	19.23	19.85	19.89	20.37	20.62	20.00
TiO ₂	16.70	16.92	17.31	18.87	18.18	19.07	18.92	18.29
ZrO ₂	1.50	0.20	0.37	1.47	0.57	2.03	1.67	0.85
ThO ₂	0.55	0.47	1.15	0.78	2.47	0.71	0.43	0.48
Al ₂ O ₃	bd	bd	0.05	0.27	2.46	2.66	2.69	2.29
Sc ₂ O ₃	bd	bd	-	-	0.24	0.16	0.12	0.19
Y ₂ O ₃	0.48	0.22	0.32	0.38	0.40	0.25	0.22	0.30
La ₂ O ₃	14.41	13.85	12.40	11.94	11.14	11.02	11.53	12.01
Ce ₂ O ₃	21.29	23.32	23.22	21.13	19.25	18.64	19.42	20.57
Pr ₂ O ₃	1.73	1.87	3.00	1.94	1.87	1.35	1.70	1.99
Nd ₂ O ₃	4.38	5.88	6.57	5.47	5.67	4.95	5.08	5.87
Sm ₂ O ₃	0.36	0.41	0.52	0.54	0.77	0.48	0.33	0.52
Gd ₂ O ₃	bd	0.43	0.30	0.32	0.25	bd	0.28	0.44
MgO	0.03	0.04	0.05	0.19	0.88	0.92	0.92	1.14
CaO	3.15	1.52	1.85	4.12	5.01	6.68	6.54	4.85
MnO	0.31	0.27	bd	0.17	0.37	0.24	0.29	0.41
FeO*	10.64	11.38	12.24	11.31	7.80	6.63	6.76	7.32
BaO	bd	bd	-	-	0.14	bd	bd	bd
Total	96.09	96.46	99.68	100.01	97.70	96.31	97.70	97.74
<i>Formulae on the basis of 22 oxygens</i>								
Ca	0.725	0.356	0.418	0.891	1.082	1.415	1.375	1.045
Ba	0.000	0.000	0.000	0.000	0.011	0.000	0.000	0.000
Y	0.055	0.026	0.036	0.041	0.043	0.026	0.023	0.032
La	1.142	1.115	0.964	0.889	0.828	0.804	0.835	0.891
Ce	1.675	1.864	1.792	1.561	1.421	1.349	1.396	1.514
Pr	0.135	0.149	0.230	0.143	0.137	0.097	0.122	0.146
Nd	0.336	0.458	0.494	0.394	0.408	0.350	0.356	0.421
Sm	0.027	0.031	0.038	0.038	0.053	0.033	0.022	0.036
Gd	0.000	0.031	0.021	0.021	0.017	0.000	0.018	0.029
Th	0.027	0.023	0.055	0.036	0.113	0.032	0.019	0.022
Sum A	4.122	4.053	4.048	4.014	4.113	4.106	4.166	4.136

(continued on next page)

Table 1. (continued)

	Chevkinite-(Ce)					Perrierite-(Ce)		
	1	2	3	4	5	6	7	8
Fe ²⁺ (=B)	1.000	1.000	1.000	1.000	1.000	1.000	1.000	1.000
Fe ²⁺	0.912	1.078	1.157	0.909	0.315	0.096	0.110	0.231
Mn	0.056	0.050	0.000	0.029	0.063	0.040	0.048	0.070
Mg	0.010	0.013	0.016	0.057	0.264	0.271	0.269	0.342
Al	0.000	0.000	0.012	0.064	0.584	0.620	0.622	0.543
Sc	0.000	0.000	0.000	0.000	0.042	0.028	0.021	0.033
Zr	0.157	0.021	0.038	0.145	0.056	0.196	0.160	0.083
Nb	0.171	0.112	0.094	0.115	0.014	0.000	0.000	0.000
Ti	0.698	0.778	0.743	0.864	0.755	0.835	0.793	0.765
Sum B	2.004	2.051	2.061	2.183	2.094	2.086	2.022	2.067
Ti (=D)	2.000	2.000	2.000	2.000	2.000	2.000	2.000	2.000
Si	4.018	4.010	4.052	4.006	4.008	4.027	4.047	4.021
P	0.000	0.013	0.000	0.000	0.022	0.010	0.008	0.019
Sum T	4.018	4.023	4.052	4.006	4.031	4.037	4.055	4.040
Σ cations	13.14	13.13	13.16	13.20	13.24	13.23	13.24	13.24

Analyses 3 and 4 from sample Ttg-hg#1, others from GF1. FeO*, all Fe as Fe²⁺; bd, below detection; Dash, not determined. Descriptions of crystals are in Supplementary Table 1.

respect to standard settings of the unit cell axes for chevkinite.

4. Petrography

The pantellerite (Ttg-hg#1) contains 35% modally of megacrysts of feldspar (An₃₉Ab₅₉Or₂–An₀Ab₅₄Or₄₆), quartz, fayalite (Fo_{2–8}), ferrichterite (Mg/(Mg + Fe²⁺) 0.02–0.20), hedenbergite (Ca_{43.6}Mg_{18.6}Fe_{37.9}–Ca_{41.3}Mg_{8.7}Fe_{47.3}), ilmenite (*X*_{ilm} 94.4–98.1), fluorapatite, CGM and fluorite. With the exception of CGM and fluorite, this is a standard phenocryst assemblage for pantellerites [White *et al.*, 2005, 2009]. The matrix consists of, in addition to the ash matrix, three types of glass (Figure 2a): two (G1 and G2) are pantelleritic and the third (G3) is scarce, poorly phyric or aphyric and comenditic. Sample GF1 contains the same phenocrysts as Ttg-hg#1 except fluorite, and, in addition, phenocrysts of andesine–oligoclase, diopside/augite, forsteritic

olivine, calcic amphibole and zircon. The matrix is almost completely devitrified, such that it is difficult to identify the original glassy components (Figure 2b). However, some phenocrysts have thin glassy rims and there are some small glassy fragments, which we were able to analyse.

White *et al.* [2005] showed that the assemblage of mafic phenocrysts in pantellerites varies with whole-rock peralkalinity; in rocks with P.I. ~1.5–1.8, as in the Gold Flat pantellerite, the phenocryst assemblage is hedenbergite–fayalite–ilmenite–aenigmatite. Amphibole is present when the P.I. is ~1.9. Gold Flat differs, therefore, in that amphibole crystallized at slightly lower P.I. and aenigmatite is absent. The large number of “phenocrysts” in GF1 cannot represent an equilibrium assemblage; Macdonald *et al.* [2019b] argued that the assemblages record magma mixing, the more mafic member in the mixing being of intermediate composition. For example, mixing a magma with SiO₂ content of 60 wt% with a magma of

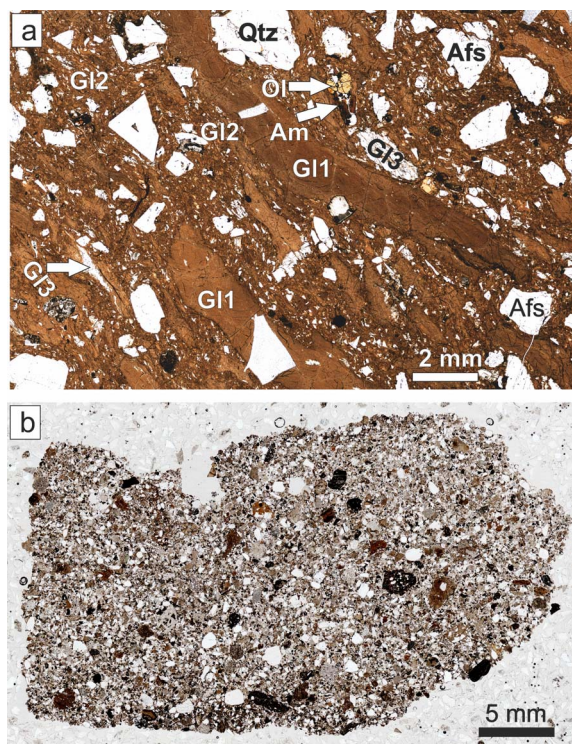


Figure 2. Transmitted-light scans of thin sections of (a) Ttg-hg#1 and (b) GF1. The various types of glass in (a) are described in the text.

Ttg-hg#1 composition (SiO_2 69.6 wt%; Macdonald *et al.*, 2019b) in the proportion 27:73, would produce a magma of GF1 composition (65.5 wt%).

5. Occurrence of CGM

CGMs occur as phenocrysts in both Ttg-hg#1 and GF1, generally forming 10–20 crystals per thin section. They are mainly platy in form, the largest being $114 \times 81 \mu\text{m}$, varying from subhedral to anhedral. They are commonly associated with other phenocrysts (Figures 3a, b). Although some grains are homogeneous on BSE images, the majority show variably complex magmatic zoning (Figure 4). Two types of zoning are most common: oscillatory and sector. The crystal shown in Figure 4a is oscillatory-zoned, with zones showing three main BSE intensities. That shown in Figure 4b also shows magmatic zoning; a compositional profile was made along

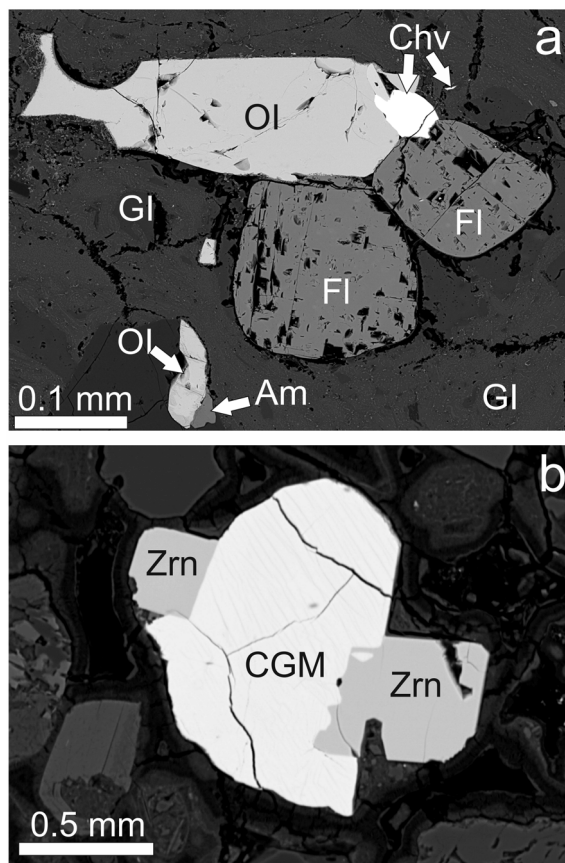


Figure 3. (a) BSE image of chevkinite-(Ce) phenocryst (Chv) associated with olivine and fluorite phenocrysts. Sample Ttg-hg#1. (b) Perrierite-(Ce) associated with phenocrysts of zircon (Zrn). Sample GF1. The CGM shows faint striping, muted by the contrast used.

the marked line (see below). An earlier core with oscillatory zoning has been mantled by a later oscillatory zonation in Figure 4c. A considerably more complex zonation (Figure 4d) shows an unusual “flower-shaped” sector-zoned, dark central zone and a mantling oscillatory-zoned area (upper left).

Most crystals in sample GF1 show, in addition to magmatic zonation, a slight patchiness on BSE images. This is most visible in dark, low-intensity regions, e.g., the upper part of the crystal in Figure 4d and the black patches in the lower-right part of Figure 5d. The patchiness is ascribed below to minor secondary hydration of the crystals (see below).

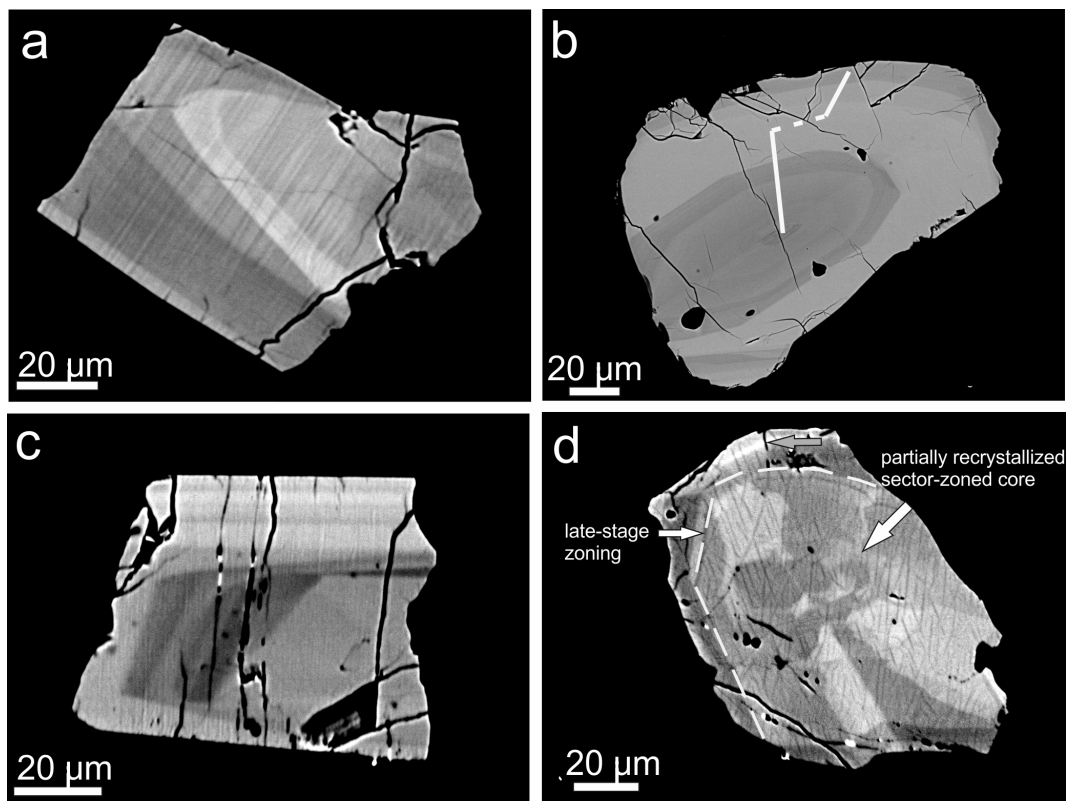


Figure 4. BSE images showing zonation patterns in CGM, all from sample GF1. (a) Oscillatory zonation in chevkinite-(Ce) showing three zones of differing BSE intensity; Supplementary Table 1a, analyses 6–15. (b) Magmatic zonation in chevkinite-(Ce); the compositional range along the marked profile is shown on Figure 6, with the analyses in Supplementary Table 1a, numbers 94–104. (c) Oscillatory zonation formed during two stages of crystallization in chevkinite-(Ce). (d) A partially recrystallized sector-zoned core in perrierite-(Ce) overgrown by an oscillatory-zoned region; analyses 39–50 in Supplementary Table 1a.

An unusual texture is the lamellar striping found in the majority of chevkinite and perrierite crystals, a feature that we have not observed before in CGM. Where present, the feature is restricted to the CGM and is not seen in adjacent crystals (Figures 3a, b). Its apparent absence from some crystals may be a function of the orientation of the texture relative to the thin section cut: the latter may have been parallel to the texture. In Figures 3a and 4b, the contrast used in the BSE images has rather muted the striping, but it is much more clearly visible in Figure 5a. The stripes are 1–2 µm thick, more or less linear, and cut across the compositional zoning. There are variations in the nature of the striping. In Figure 4a, it appears to be perpendicular to the crystal edge. The arrow in

Figure 5a points to a stripe offset. The stripes may (Figure 3a) or may not (Figure 5b) reach the crystal rims. While some stripes are regular and parallel, they may also show dislocations, such as the crystal in Figure 5d.

6. Compositions of CGM

Representative compositions of CGM are presented in Table 1; the full data set is given in Supplementary Table 1a. The minerals are classified using the empirical discriminant of Macdonald *et al.* [2009] (Figure 6). Both chevkinite-(Ce) and perrierite-(Ce) are found in sample GF1, in the approximate ratio 2:1; only chevkinite-(Ce) is present in Ttg-hg#1.

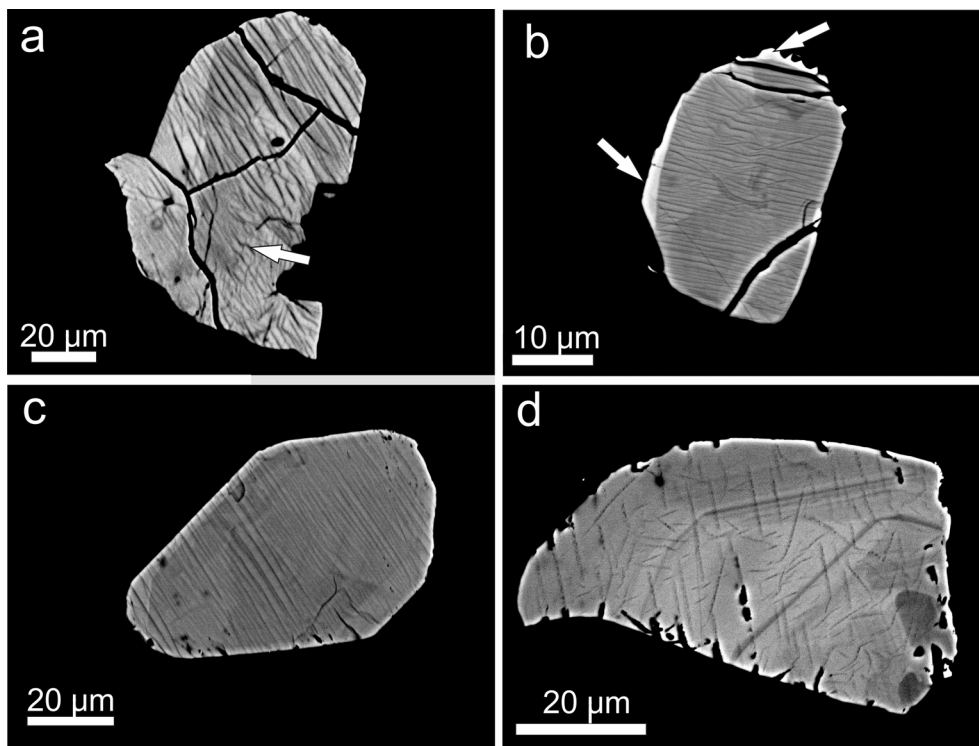


Figure 5. (a) Lamellae strongly developed in partly resorbed chevkinite-(Ce) in sample GF1; Supplementary Table 1a, analyses 65–75. (b) More delicate striping in chevkinite-(Ce), sample Ttg-hg#1. Note that the striping does not reach the bright rim (arrowed). (c) Regular, linear lamellae in perrierite-(Ce), sample GF1. The lamellae reach the rim. (d) Short segments of lamellae cut across oscillatory zoning in chevkinite-(Ce), sample GF1. The darker patches at lower right are slightly more calcic.

Before discussing the compositional features, a comment is required on the analytical totals. In their compilation of 253 analyses of chevkinite and perrierite from the literature, Macdonald *et al.* [2019a] found that the range of analytical totals was 95.5–102.3 wt% (average 98.8 wt%). The low values are due to three effects: (i) some Fe is present in the minerals as Fe^{3+} but is normally reported as Fe^{2+} in EPMA analyses; (ii) the nondetermination of minor elements which can be present at significant levels, e.g., M- and H-REE, Nb, Ta and Hf; and (iii) the incorporation into the structure of H_2O during hydrothermal alteration. In the Gold Flat case, the analytical totals for all determinations range from 93.8 to 101.4 wt% (average 97.3 wt%). The $\text{Fe}^{3+}/\text{Fe}^{2+}$ ratios in the analyses were determined, using stoichiometric criteria, by the method of Droop [1987]; the recalculated FeO and Fe_2O_3 (wt%) and analytical totals are shown in Supplementary Table 1a. The analytical totals now

range from 94.16 to 101.86 wt% (average 97.66 wt%). However, there is an important difference between the minerals in Ttg-hg#1 (chevkinite-(Ce) only) and GF1 (chevkinite-(Ce) and perrierite-(Ce)); the range in Ttg-hg#1 is 99.4–100.5, that in GF1 is 94.2–99.5 wt%. The low values in GF1 are related to the low-BSE-intensity regions in the crystals, as discussed in the Petrography section. This textural feature, and the resulting low totals, are signals of secondary hydration of the minerals [Bagiński *et al.*, 2015]. In Ttg-hg#1, the CGMs are found in nonhydrated pantelleritic glass and have not been secondarily hydrated. GF1 is devitrified and shows signs of late alteration, including an LOI value of 5.41 wt% and the crystals show some signs of the hydration, as noted above.

The chevkinite-(Ce) contains generally higher levels of $\text{La}_2\text{O}_3\text{--Sm}_2\text{O}_3$ (41.02–46.28 wt%) than the perrierite-(Ce) (36.44–40.96 wt%) and also of Nb_2O_5 (0.75–1.76 wt%, b.d. –0.17 wt%, respectively). It also

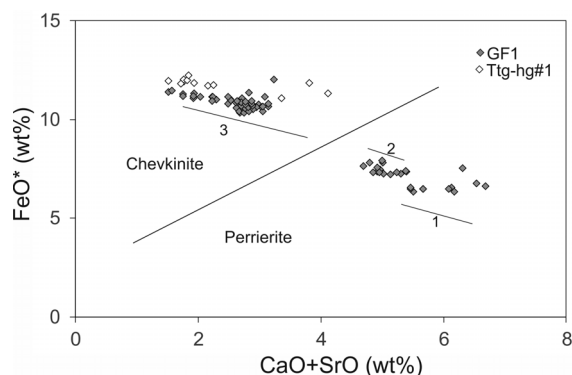


Figure 6. CGM plotted in the empirical discrimination diagram of Macdonald *et al.* [2009]. Data from Supplementary Table 1a. The thin solid lines mark the compositional ranges in three crystals: Supplementary Table 1a, anal. 39–50 (=1), 51–61 (=2) and 94–104 (=3; see Figure 4b).

has lower levels of MgO (b.d. -0.40 wt%, 1.35 – 2.11 wt%), Al_2O_3 (b.d. -0.34 wt%, 2.12 – 2.75 wt%) and Sc_2O_3 (b.d. -0.11 wt%, 0.12 – 0.24 wt%). There is a large overlap of ZrO_2 abundances (0.20 – 1.50 wt%, 0.56 – 2.03 wt%). The compositions of both the chevkinite-(Ce) and perrierite-(Ce) are within the ranges compiled from the literature by Macdonald *et al.* [2019a]. In chevkinite-(Ce), $\text{Fe} > \text{Ti}$ in the C site, while $\text{Ti} > \text{Fe}$ in the perrierite-(Ce). Mineral formulae for the least and most calcic analyses can be written:

$(\text{Ce}_{1.86}\text{La}_{1.12}\text{Nd}_{0.46}\text{Ca}_{0.36}\text{Pr}_{0.15})_{3.95}\text{Fe}^{2+}(\text{Fe}^{2+}_{1.08}\text{Ti}_{0.78}\text{Nb}_{0.11})_{1.97}(\text{Si}_2\text{O}_{11})_2$ and $(\text{Ca}_{1.42}\text{Ce}_{1.35}\text{La}_{0.80}\text{Nd}_{0.35}\text{Pr}_{0.10})_{4.02}\text{Fe}^{2+}(\text{Ti}_{0.84}\text{Al}_{0.62}\text{Zr}_{0.20}\text{Mg}_{0.27}\text{Fe}^{2+}_{0.10})_{2.03}(\text{Si}_2\text{O}_{11})_2$ (Table 1, anal. 2 and 6, respectively). Individual crystals show significant parts of the compositional range (Figure 6), including the profile shown in Figure 4b.

7. Nature and formation of lamellae

The fine scale of the lamellar stripes (1 – $2\ \mu\text{m}$) means that their microprobe analyses are invariably composites of lamella and adjacent crystal. An attempt, therefore, was made to determine their nature using element maps (Figure 7). On the maps, the lamellae are higher in Ti, and to a lesser extent Fe (not shown), and lower in Si, than the host CGM. Those features suggested the possible presence of a TiO_2 phase. An

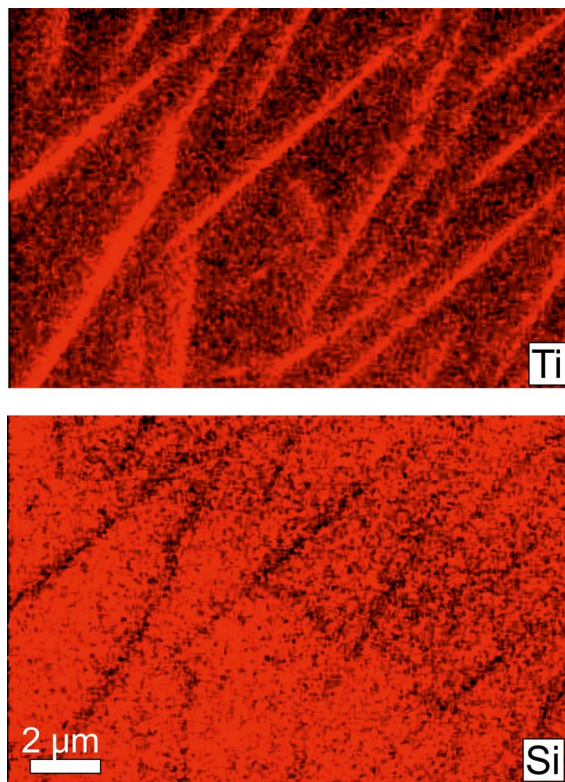


Figure 7. False-colour element maps (Ti and Si) of striping in part of crystal shown in Figure 4a.

attempt was made, therefore, to characterize the Ti-rich zones using Atomic Force Microscopy (AFM).

AFM images of reference rutile and chevkinite-(Ce) free of stripes present similar, even surface topography. In contrast, an image of GF1 chevkinite-(Ce) revealed a stripe-like organization with two distinct domains; the surface topography is displayed as a pseudocolour plot in Figure 8, where the chevkinite domain with grain-like features is separated by lamellar Ti-rich structures. We cautiously suggest that the lamellar structures have an increased degree of disorder and are not fully crystalline. The histograms of counts against adhesion force were determined for a reference chevkinite and showed that its adhesion force range is 3 – 4 nN, and for a reference rutile to be 4 – 8 nN. The range across the lamellae is 3 – 6 and is taken to be a superposition of chevkinite and rutile histograms. The Ti-rich lamellae would appear, therefore, to consist at least partly of a rutile-like phase.

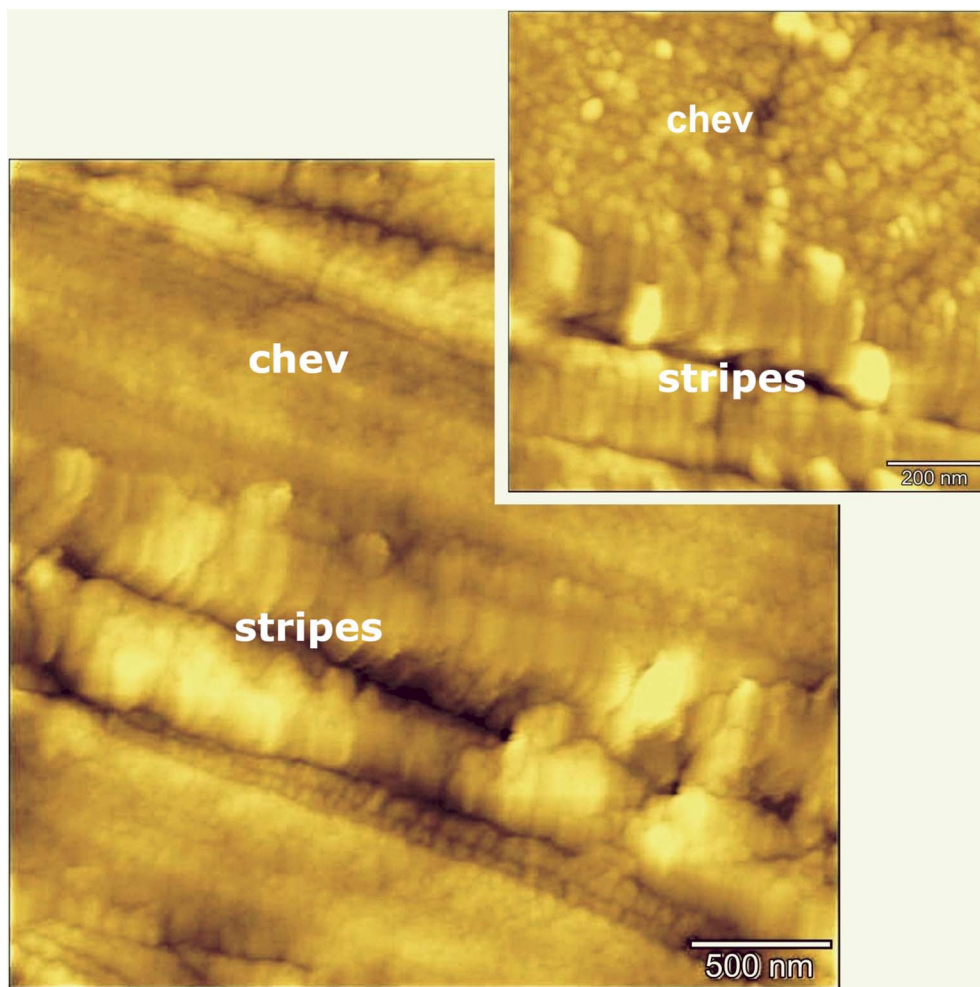


Figure 8. Surface topography of lamellae in chevkinite-(Ce) determined by AFM. Domains related to the host mineral and the stripes are shown. The crystal is that shown in Figure 5b.

The fact that the lamellae are oriented argues for subsolidus precipitation, perhaps by exsolution. Rutile has been recorded as exsolution inclusions in several phases, including biotite [Shau *et al.*, 1991], garnet [Hwang *et al.*, 2007, Keller and Ague, 2019], titanite [Černý *et al.*, 2007], quartz [Adachi *et al.*, 2010] and gem corundum [Palke and Breeding, 2017]. It most commonly occurs as oriented needles, indicating a crystallographic control on the exsolution [Keller and Ague, 2019]. Several workers have drawn attention to the presence of a rutile-like layer in CGM, e.g., Calvo and Faggiani [1974], Gueho *et al.* [1995], Li *et al.* [2005] and Holtstam *et al.* [2017]. In Figure 9, the top panel shows the crystal structure of

rutile and the bottom panel shows chevkinite with a rutile-like layer in the centre. The layer is formed by CO_6 and DO_6 distorted coordination octahedra, the distortion making the oxygen atoms (red) misaligned compared to the rutile arrangement. We speculate that the rutile lamellae in the Gold Flat CGM formed along this rutile-like layer, which might have been energetically/kinetically favourable sites for rutile nucleation.

There are, however, some problems with this proposal. Concentration of Ti in the lamellae should have left neighbouring areas depleted in Ti, but this is not obvious on the chemical maps (Figure 7). A cautious conclusion, therefore, is that during cooling of

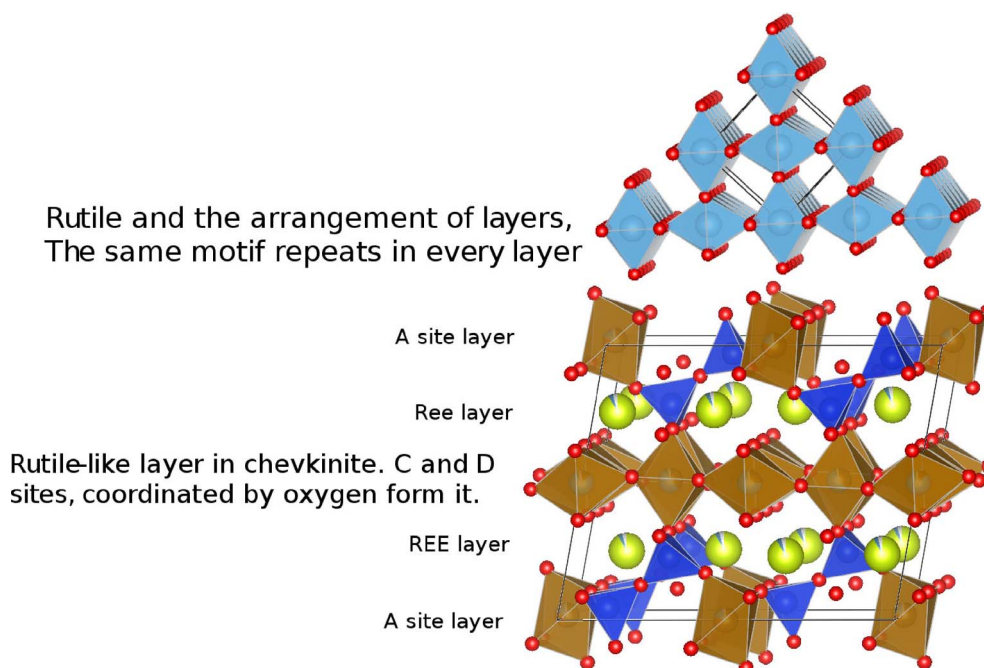


Figure 9. Arrangement of layers in rutile (upper) and a visualization of the rutile-like layer in chevkinite.

the magmas, the CGM structure in both chevkinite-(Ce) and perrierite-(Ce) became unstable and exsolved a rutile-like phase along the rutile-like layer. That does not, however, explain why the lamellar striping is, in our experience, restricted to the Gold Flat Tuff; neither is it clear what promoted the exsolution.

An EBSD study revealed an unexpected aspect of the chevkinite-(Ce) structure. The crystal shown in Figure 10a shows a distinct, if minor, change in direction of the stripes along a line orientated NW–SE. The crystal consists of two structural domains, with one domain rotated relative to the other, as shown by the orientation of the *a*, *b* and *c* axes. The stripes are perpendicular to the crystallographic unit cell direction $b = 5.7 \text{ \AA}$. The grey MO_6 octahedra are parallel to the *ab* crystallographic plane from rutile-like layers in the chevkinite-(Ce) structure. In contrast, the crystal in Figure 10b showing regular, linear stripes does not have the two-domain structure. It is unknown what caused the rotation of the structure in Figure 10a, but it is important to note that its existence was not visible in standard optical and BSE imaging, being revealed only by EBSD. The result raises the possibil-

ity that such structural dislocations occur more frequently than presently understood.

8. Discussion

8.1. Paragenesis of the CGM

Using a $(\text{CaO} + \text{SrO} + \text{MgO} + \text{Al}_2\text{O}_3) - \Sigma(\text{La}_2\text{O}_3 - \text{Sm}_2\text{O}_3) - \text{FeO}^*$ plot, Macdonald and Belkin [2002] showed that in igneous rocks chevkinite generally occurs in evolved rock types, such as rhyolites, granites and nepheline syenites, whereas perrierite is normally found in intermediate rocks. In such a plot (Figure 11), the Gold Flat CGM form two clusters, consistent with formation in different magmas, as already shown by the different phenocryst assemblages. Also shown are perrierites from rocks of intermediate (broadly trachyandesitic) composition, suggesting that more perrieritic minerals at Gold Flat are also formed from intermediate magmas. This is confirmed by the analyses of glassy fragments and crystal rims in GF1 (Supplementary Table 1b). Important features of the analyses are: (i) Some of the analytical totals are low (92.2–100.5 wt%), which can be ascribed to secondary hydration of the glass; (ii) There

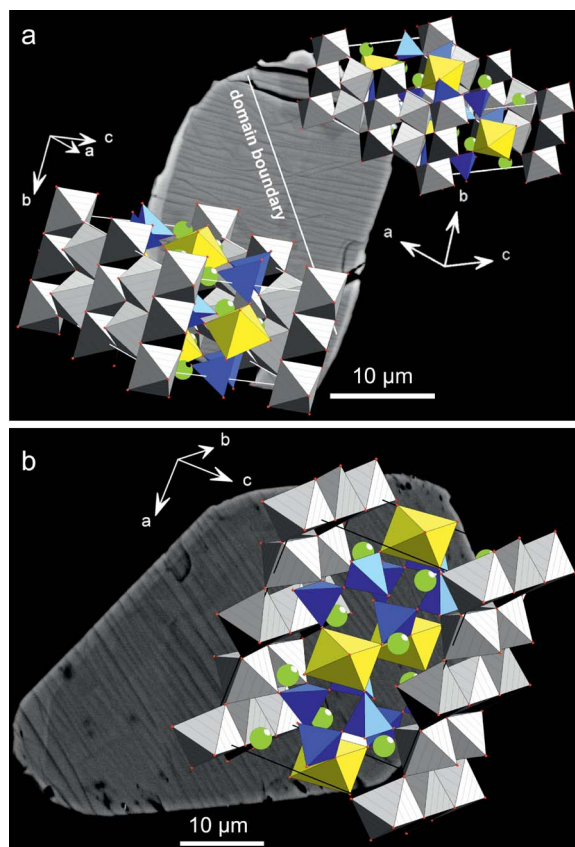


Figure 10. (a) Rotation of the structure in a chevkinite-(Ce) crystal revealed by EBSD, the boundary between the two domains coinciding with minor displacements of the lamellae. The crystal is that shown in Figure 5b. (b) In the crystal (Figure 5c), the lamellae are regular and the structure is not rotated.

has clearly been some mobilization of the alkalis and Ca; (iii) Aluminium, Ti (Figure 12) and Fe show negative trends, and Na a positive trend, plotted against SiO_2 ; (iv) The spread of data encloses for all elements the composition of a trachytic melt inclusion found in a clinopyroxene in a feldspar cluster [Macdonald *et al.*, 2019b]. In the SiO_2 -alkalis classification, the analyses (with SiO_2 in the range 64.8–66.8 wt%, calculated anhydrous to 100%) plot in the trachyte field, close to the border with trachyandesite.

With the caveat that the vertical and lateral variations in lithology in the Gold Flat tuff are not well constrained, the following crystallization history of

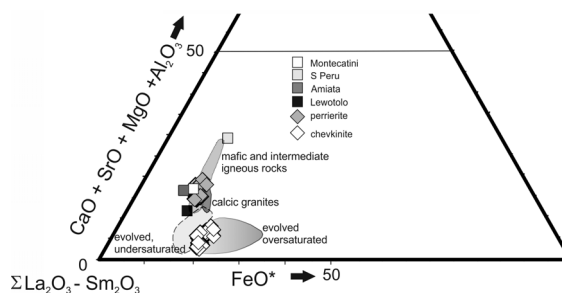


Figure 11. Triangular plot to show the different paragenesis of chevkinite and perrierite (slightly simplified from Macdonald and Belkin, 2002). Data from Supplementary Table 1a. Perrierites from various “trachyandesitic” hosts overlap the Gold Flat field: Mt Amiata, Italy [Van Bergen, 1984]; Montecatini, Italy [Cellai *et al.*, 1993]; Lewotolo, Indonesia [De Hoog and van Bergen, 2000]; southern Peru [Carlier and Lorand, 2008].

CGM in the tuff can be proposed. As shown by glass analyses in sample Ttg-hg#1, the tuff comprises pantelleritic and comenditic magmas. Using various SiO_2 plots, Macdonald *et al.* [2019b] showed that the two magmas had evolved along different trends and were derived from two evolving magma reservoirs. As discussed above, there is also petrographic, and mineral and glass compositional, evidence that intermediate magmas were components in the tuff.

Some information on the crystallization history comes from crystal zoning. Most common in the CGM is oscillatory zoning (Figures 4a, b), generally ascribed to repetitive kinetic effects during crystallization [Paterson and Stephens, 1992, Tepper and Kuehner, 1999]. The other type, particularly well shown in Figure 4d, is sector zoning and we suggest that the texture in that image represents a sector-zoned core which was partially recrystallized during a later stage of crystallization. Sector zoning has been ascribed to slow growth and low diffusivity during crystallization [Schaltegger *et al.*, 1999, Watson and Liang, 1995]. A possible model for the Gold Flat case is, therefore, of a relatively prolonged stage of perrierite-(Ce) growth in an intermediate magma and chevkinite-(Ce) in a pantelleritic magma, followed by more rapid changes promoting oscillatory zoning around the core and recrystallization of the core before magma mixing. The intermediate magma

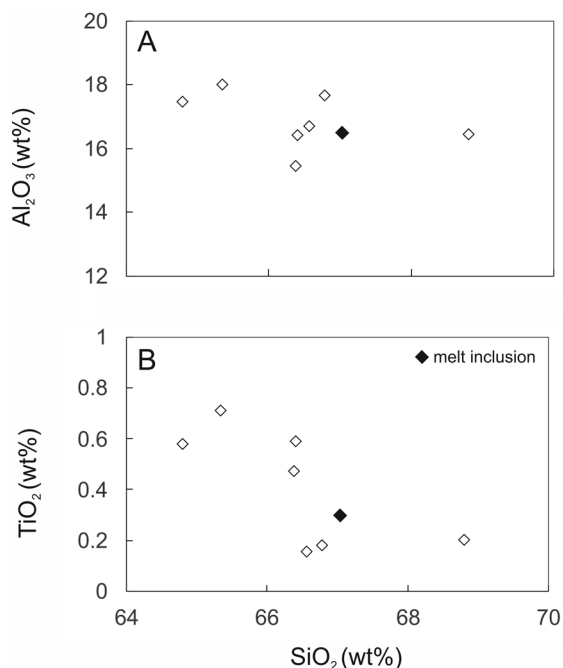


Figure 12. SiO₂ plotted against (a) Al₂O₃ and (b) TiO₂ in matrix glass from GF1. Data from Supplementary Table 1b, recalculated to 100% anhydrous. Also shown is the composition of a trachytic melt inclusion from the Gold Flat Tuff [Macdonald *et al.*, 2019b].

was then mingled with the chevkinite-(Ce)-bearing pantellerite magma but with insufficient time before eruption for new mantles to form on existing crystals.

8.2. Formation of chevkinite-(Ce) in a pantellerite

It was noted earlier that the Gold Flat Tuff is the only pantelleritic extrusive known to carry CGM phenocrysts. Possible explanations for this unusual paragenesis are that it was related to a compositional effect or unusual P–T–*f*O₂–*a*SiO₂ conditions of crystallization. For example, the high LREE contents (La–Sm ≤1517 ppm; Macdonald *et al.*, 2019b), the highest levels in a pantellerite of which we are aware, may have been a critical factor in forming the chevkinite-(Ce). However, chevkinite is a common phase in the comendites in the BMVC which have lower LREE contents (≤600 ppm) than the pantellerite (e.g., Vogel *et al.*, 1983, 1989). Unfortunately, no compositional

or structural information is available on these phases and it is possible that they are antecrystic perrierite, able to crystallize from magmas poorer in REE.

Alternatively, the appearance of CGM may have been related to the crystallization conditions. Little is known about the P–T conditions under which the various Gold Flat magmas evolved, but Macdonald *et al.* [2019b] cautiously suggested, on the basis of comparisons with high P–T experiments on compositionally similar pantellerites from Eburru, Kenya [Scaillet and Macdonald, 2006] and Pantelleria [Di Carlo *et al.*, 2010], that the pantelleritic magma started crystallizing at a temperature of ~740 °C, close to or at water saturation, at *f*O₂ below FMQ. However, the Kenyan and Pantescan rocks and the experiments did not form chevkinite under any conditions. In contrast, Scaillet and Macdonald [2001] synthesized chevkinite-(Ce) in two comendites from the Olkaria complex, Kenya, although its stability field was poorly constrained.

However, the explanation for the formation of chevkinite-(Ce) may lie in the absence of aenigmatite from the Gold Flat pantellerite. On the basis of thermodynamic modelling, Macdonald *et al.* [2011] found the antipathetic relationship between fayalite and aenigmatite to be a function of *T*, *P* and *a*SiO₂, with aenigmatite crystallizing at the expense of fayalite at *T* < 750 °C at *a*SiO₂ close to quartz saturation at 150 MPa. Macdonald *et al.* [2011] showed that the aenigmatite–phyric pantellerites of Pantelleria crystallized at *a*SiO₂ = 1. Using the QUILF programme from olivine–magnetite–ilmenite equilibrium, Andersen *et al.* [1993], Macdonald *et al.* [2019b] calculated the *a*SiO₂ relative to quartz saturation for the Gold Flat pantellerite to be 0.633 at *P* = 1000 bar, potentially favouring the absence of aenigmatite in favour of fayalite + ilmenite. Titanium was not, therefore, partitioned into aenigmatite but instead partitioned between ilmenite and chevkinite-(Ce). In addition to its unusual compositional features and complex evolutionary history, the Gold Flat Tuff pantellerite may have crystallized in an unusual corner of P–T–*f*O₂–*a*SiO₂ space.

9. Conclusions

The study has revealed unusual features of the occurrence and textures of CGM which may be of more general significance in studies of accessory minerals.

More generally, we suggest that the use of AFM will offer to geologists another technique to apply to the study of such phases.

- (1) The coexistence of chevkinite-(Ce) and perrierite-(Ce) in the Gold Flat Tuff was a result of the mixing of pantelleritic and intermediate magmas.
- (2) The unique occurrence of a CGM in a pantelleritic extrusive may have been due to the host magmas crystallizing at a relatively low $a\text{SiO}_2$, favouring the formation of ilmenite and chevkinite rather than aenigmatite. The unusually high contents of LREE may also have played a role in its formation.
- (3) An unusual lamellar texture in the CGM, not previously recorded in the group, may have formed by exsolution of a Ti-rich phase from a rutile-like layer in the crystal structure. We provide no explanation of why the texture has been described only from the Gold Flat Tuff.
- (4) An EBSD study unexpectedly revealed a structural rotation in the crystal, which was not visible optically or by electron back-scattered imaging. The phenomenon may be of wider occurrence than currently recognized.
- (5) Zonation patterns in the CGM have established a complex pre-eruptive evolutionary history in the magma reservoir.

Acknowledgements

We thank Bruno Scaillet for the invitation to contribute this paper to the Special Issue and Donald C. Noble for supplying the sample of Ttg-hg#1. We also thank Lidia Jeřak and Petras Jokubauskas (EPMA) and Marcin Syczewski (SEM) for analytical support. Two anonymous reviewers provided very helpful comments and suggestions, which are much appreciated. The research was funded by National Science Centre, Poland, grant number 2017/26/M/ST10/00407. The work was also supported through the Innovative Economy Operational Program POIG.02.02.00-00-409 025/09 (NanoFun; Cryo-SEM microscopy lab).

Supplementary data

Supporting information for this article is available on the journal's website under <https://doi.org/10.5802/crgeos.45> or from the author.

Appendix

Table 2. Analytical conditions for chevkinite-(Ce)

Element	Line	Crystal	Standard	Approx. detection limit (wt%)
Al	K α	TAP	Orthoclase	0.01
Ba	L α	LiF	Barite	0.12
Ca	L α	PET	CaSiO ₃	0.01
Ce	K α	PET	CeP ₅ O ₁₄	0.04
Fe	K α	LiF	Haematite	0.04
Gd	L β	LiF	GdP ₅ O ₁₄	0.19
La	L α	PET	LaB ₆	0.04
Mg	K α	TAP	Diopside	0.01
Mn	K α	LiF	Rhodonite	0.04
Nb	L α	PET	Nb metal	0.05
Nd	L β	LiF	NdP ₅ O ₁₄	0.18
P	K α	PET	Apatite Jap2	0.02
Pr	L β	LiF	PrP ₅ O ₁₄	0.12
Sc	K α	PET	Sc metal	0.01
Si	K α	TAP	Wollastonite	0.01
Sm	L β	LiF	SmP ₅ O ₁₄	0.19
Ta	M α	TAP	Ta metal	0.04
Th	M α	PET	ThO ₂ Synthetic	0.09
Ti	K α	PET	Rutile	0.02
Y	L α	TAP	Y ₃ Al ₅ O ₁₂	0.04
Zr	L α	PET	Zircon ED2	0.05

Data for accel. voltage 15 kV, probe current 50 nA.

References

- Adachi, T., Hokada, T., Osanai, Y., Toyoshima, T., Baba, S., and Nakano, N. (2010). Titanium behaviour in quartz during retrograde hydration: Occurrence of rutile exsolution and implications for

- metamorphic processes in the Sør Rondane Mountains, East Antarctica. *Polar Sci.*, 3, 222–234.
- Andersen, D. J., Lindsley, D. H., and Davidson, P. M. (1993). A Pascal program to assess equilibria among Fe-Mg-Mn-Ti oxides, pyroxene, olivine, and quartz. *Comp. Geosci.*, 19, 1333–1350.
- Bagiński, B., Macdonald, R., Dzierżanowski, P., Zozulya, D., and Kartashov, P. M. (2015). Hydrothermal alteration of chevkinite-group minerals: products and mechanisms. Part 1. Hydration of chevkinite-(Ce). *Mineral. Mag.*, 79, 1019–1037.
- Byers Jr, F. M., Carr, W. J., and Orkild, P. P. (1989). Volcanic centers of southwestern Nevada: Evolution of understanding, 1960–1988. *J. Geophys. Res.*, 94, 5908–5924.
- Calvo, C. and Faggiani, R. (1974). A re-investigation of the crystal structures of chevkinite and perrierite. *Am. Mineral.*, 59, 1277–1285.
- Carrier, G. and Lorand, J.-P. (2008). Zr-rich accessory minerals (titanite, perrierite, zirconolite, baddeleyite) record strong oxidation associated with magma mixing in the south Peruvian potassic province. *Lithos*, 104, 54–70.
- Cellai, D., Conticelli, S., and Diella, V. (1993). Perrierite-chevkinite in igneous ultrapotassic rocks from Central Italy: chemical data and their petrological significance. *Per. Mineral.*, 62, 57–66.
- Černý, P., Novák, M., Chapman, R., and Ferreira, K. J. (2007). Subsolidus behavior of niobian rutile from the Písek region, Czech Republic: a model for exsolution in W- and Fe²⁺ >> Fe³⁺-rich phases. *J. Geosci.*, 52, 143–159.
- De Hoog, J. C. M. and van Bergen, M. J. (2000). Volatile-induced transport of HFSE, REE, Th and U in arc magmas: evidence from zirconolite-bearing vesicles in potassic lavas of Lewotolo volcano (Indonesia). *Contrib. Mineral. Petrol.*, 139, 485–502.
- Di Carlo, I., Rotolo, S. G., Scaillet, B., Bucchini, V., and Pichavant, M. (2010). Phase equilibrium constraints on pre-eruptive conditions of recent felsic explosive volcanism at Pantelleria Island, Italy. *J. Petrol.*, 51, 2245–2276.
- Droop, G. T. R. (1987). A general equation for estimating Fe³⁺ concentrations in ferromagnesian silicates and oxides from microprobe analyses, using stoichiometric criteria. *Mineral. Mag.*, 51, 431–435.
- Fleck, R. J., Lanphere, M. A., Turrin, B., and Sawyer, D. A. (1991). Chronology of late Miocene to Quaternary volcanism and tectonism in the southwest Nevada volcanic field (abs.). *Geol. Soc. Am. Abstracts with Programs*, 23(2), 25.
- Gueho, C., Giaquinta, D., Mansot, J. L., Ebel, T., and Palvadeau, P. (1995). Structure and magnetism of La₄Mn₅Si₄O₂₂ and La₄V₅Si₄O₂₂: two new rare-earth transition metal sorosilicates. *Chem. Mater.*, 7, 486–492.
- Holtstam, D., Bindi, L., Hålenius, U., and Andersson, U. B. (2017). Delhuyarite-(Ce) – Ce₄Mg(Fe³⁺₂W)□(Si₂O₇)₂O₆(OH)₂ – a new mineral of the chevkinite group, from the Nya Bastnäs Fe-Cu-REE deposit, Sweden. *Eur. J. Mineral.*, 29, 897–905.
- Hwang, S. L., Yui, T. F., Chu, H. T., Shen, P., Schertl, H. P., Zhang, R. Y., and Liou, J. G. (2007). On the origin of oriented rutile needles in garnet from UHP eclogites. *J. Met. Geol.*, 25, 349–362.
- Keller, D. S. and Ague, J. J. (2019). Crystallographic and textural evidence for precipitation of rutile, ilmenite, corundum, and apatite lamellae from garnet. *Am. Mineral.*, 104, 980–995.
- Li, G., Yang, G., Ma, Z., Shi, N., Xiong, M., Fan, H., and Sheng, G. (2005). Crystal structure of natural non-metamict Ti- and Fe²⁺-rich chevkinite-(Ce). *Acta Geol. Sinica*, 79, 325–331.
- Macdonald, R., Bagiński, B., Belkin, H. E., and Stachowicz, M. (2019a). Composition, paragenesis and alteration of the chevkinite group of minerals. *Am. Mineral.*, 104, 349–367.
- Macdonald, R., Bagiński, B., Belkin, H. E., White, J. C., and Noble, D. C. (2019b). The Gold Flat Tuff, Nevada: insights into the evolution of peralkaline silicic magmas. *Lithos*, 328–329, 1–13.
- Macdonald, R., Bagiński, B., Leat, P. T., White, J. C., and Dzierżanowski, P. (2011). Mineral stability in peralkaline silicic rocks: Information from trachytes of the Menengai volcano, Kenya. *Lithos*, 125, 553–568.
- Macdonald, R. and Belkin, H. E. (2002). Compositional variation in minerals of the chevkinite group. *Mineral. Mag.*, 66, 1075–1098.
- Macdonald, R., Belkin, H. E., Wall, F., and Bagiński, B. (2009). Compositional variation in the chevkinite group: new data from igneous and metamorphic rocks. *Mineral. Mag.*, 73, 777–796.
- Noble, D. C. (1965). Gold Flat Member of the Thirsty Canyon Tuff – a pantellerite ash-flow sheet in

- southern Nevada. *US Geol. Surv. Prof. Paper*, 525-B, B85–B90.
- Palke, A. C. and Breeding, C. M. (2017). The origin of needle-like rutile inclusions in natural gem corundum: A combined EPMA, LA-ICP-MS, and nanoSIMS investigation. *Am. Mineral.*, 102, 1451–1461.
- Paterson, B. A. and Stephens, W. E. (1992). Kinematically-induced compositional zoning in titanite: Implications for accessory-phase/melt partitioning of trace elements. *Contrib. Mineral. Petrol.*, 109, 373–395.
- Pouchou, J. L. and Pichoir, J. F. (1991). Quantitative analysis of homogeneous or stratified microvolumes applying the model 'PAP'. In Heinrich, K. F. J. and Newbury, D. E., editors, *Electron Probe Quantification*, pages 31–75. Plenum Press, New York.
- Sawyer, D. A., Fleck, R. J., Lanphere, M. A., Warren, R. G., Broxton, D. E., and Hudson, M. R. (1994). Episodic caldera volcanism in the Miocene southwestern Nevada volcanic field: Revised stratigraphic framework, $^{40}\text{Ar}/^{39}\text{Ar}$ geochronology, and implications for magmatism and extension. *Geol. Soc. Am. Bull.*, 106, 1304–1318.
- Scaillet, B. and Macdonald, R. (2001). Phase relations of peralkaline silicic magmas and petrogenetic implications. *J. Petrol.*, 42, 825–845.
- Scaillet, B. and Macdonald, R. (2006). Experimental constraints on pre-eruption conditions of pantelleritic magmas: evidence from the Eburru complex, Kenya Rift. *Lithos*, 91, 95–108.
- Schaltegger, U., Fanning, C. M., Günther, D., Maurin, J. C., Schulmann, K., and Gebauer, D. (1999). Growth, annealing and recrystallization of zircon and preservation of monazite in high-grade metamorphism: conventional and in-situ U-Pb isotope, cathodoluminescence and microchemical evidence. *Contrib. Mineral. Petrol.*, 134, 186–201.
- Shau, Y. H., Yang, H. Y., and Peacor, D. R. (1991). On oriented titanite and rutile inclusions in sagenitic biotite. *Am. Mineral.*, 76, 1205–1217.
- Tepper, J. H. and Kuehner, S. C. (1999). Complex zonation in apatite from the Idaho batholith: A record of magma mixing and intra-crystalline trace element diffusion. *Am. Mineral.*, 84, 581–595.
- Van Bergen, M. J. (1984). Perrierite in siliceous lavas from Mt Amiata, central Italy. *Mineral. Mag.*, 48, 553–556.
- Vogel, T. A., Noble, D. C., and Younker, L. W. (1983). *Chemical evolution of a high-level magma system: the Black Mountain volcanic center, southern Nevada*. Report No. UCRL-53444. Lawrence Livermore National Laboratory, Livermore, California.
- Vogel, T. A., Noble, D. C., and Younker, L. W. (1989). Evolution of a chemically zoned magma body: Black Mountain volcanic center, southwestern Nevada. *J. Geophys. Res.*, 94, 6041–6058.
- Watson, E. B. and Liang, Y. (1995). A simple model for sector zoning in slowly grown crystals: implications for growth rate and lattice diffusion, with emphasis on secondary minerals in crustal rocks. *Am. Mineral.*, 80, 1179–1187.
- White, J. C., Parker, D. F., and Ren, M. (2009). The origin of trachyte and pantellerite from Pantelleria, Italy: Insights from major element, trace element, and thermodynamic modelling. *J. Volcanol. Geotherm. Res.*, 179, 33–55.
- White, J. C., Ren, M., and Parker, D. F. (2005). Variation in mineralogy, temperature, and oxygen fugacity in a suite of strongly peralkaline lavas and tuffs, Pantelleria, Italy. *Can. Mineral.*, 43, 1331–1347.



Perspectives on alkaline magmas / *Perspectives sur les magmas alcalins*

Whole rock and mineral chemistry of hornblenditic xenoliths in volcanic alkaline rocks from the northern part of Uromieh Dokhtar magmatic belt (NW Iran)

Ali Akbar Khezerlou^{*,a}, Michel Grégoire^b, Nasir Amel^a, Mohsen Moayyed^a, Ahmad Jahangiri^a and Mohammad Kilzi^b

^a Department of Geology, University of Tabriz, Tabriz 51664, Iran

^b Laboratory Geosciences Environnement Toulouse, Toulouse University, CNES-CNRS-IRD-UPS Midi-Pyrenees Observatory, 14 Av. E. Belin, 31400 Toulouse, France

E-mails: ali.khezerlou2@gmail.com (A. A. Khezerlou), michel.gregoire@get.omp.eu (M. Grégoire), n.Amel@Tabrizu.ac.ir (N. Amel), Moayyed@Tabrizu.ac.ir (M. Moayyed), a_jahangiri@Tabrizu.ac.ir (A. Jahangiri), vtc_oxytania_vip@yahoo.com (M. Kilzi)

Abstract. An alkaline volcanic activity with a relative Plio-Quaternary age (based on the succession of layers on the field) occurred in the northern part of Uromieh Dokhtar magmatic belt, Iran. Hornblendite xenoliths mostly displaying cumulitic texture occur in the trachyandesites from this magmatic episode. The thermobarometric results indicate that these xenoliths formed within the crust. Based on mineralogical and chemical characteristics, these xenoliths are divided into two groups. In Group 1, plagioclase (andesine) modal content is less than 10% while amphibole (magnesianhastingsite) and biotite are the main minerals. In Group 2, plagioclase (labradorite) modal content is higher than 20% while amphibole (pargasite) and biotite are the main minerals. Positive anomalies of U, Ba, Ti, and K in hornblendite xenoliths are probably related to the accumulation process of amphibole and biotite. The study of the chemical composition of amphiboles indicates crystallization of amphibole from Group 1 and Group 2 hornblendite xenoliths and host volcanic rock under high oxidation conditions. Hornblendite xenoliths display high LREE/HREE and LREE/MREE ratios. The $^{86}\text{Sr}/^{87}\text{Sr}$ ratios in xenoliths of Groups 1 and 2 and host volcanic rocks are 0.706291, 0.704685, and 0.709545, respectively, while $^{143}\text{Nd}/^{144}\text{Nd}$ ratios are 0.512580, 0.512736, and 0.512561, respectively. Group 1 xenoliths are characterized by a negative Eu anomaly while this anomaly is positive for Group 2. Considering the REE concentrations and distribution patterns, the major element compositions of amphibole, biotite, and plagioclase as well as the Sr and Nd isotopic ratios, it appears that the parental melts of Group 1 and Group 2 xenoliths differ in composition. Those two theoretical parental melts also have different compositions when compared to that of the host volcanic rock. The studied alkaline rocks are commonly located along the main faults. Therefore it seems that the movement of the main faults (especially North Tabriz Fault, North Misho and Tasuj faults) has provided a path for the lavas carrying

* Corresponding author.

the investigated xenoliths to penetrate the continental crust. Taken together the geochemical characteristics of the studied rocks indicate a mantle source variably metasomatized by a subduction event prior to the collision between Eurasian and Arabian continents.

Keywords. Hornblendite, Xenolith, Uromieh, Dokhtar, Iran.

Available online 23rd November 2021

1. Introduction

The Anatolian–Iranian plateau is one of the regions where active continent–continent collision is currently taking place. Previous studies to date [Sengor and Kidd, 1979, Dewey *et al.*, 1986] have shown that collision occurred between Eurasian and Arabian continents, resulting in the formation of an extensive (150,000 km²) high plateau with an average elevation of 2 km above sea level [Ahmadzadeh *et al.*, 2010]. The presence of potassium-rich volcanic rocks in this area is important, because these rocks occur in a variety of tectonic settings including continental convergent margins [Gill *et al.*, 2004], and syn- to post-collisional tectonic settings as in Anatolia and Tibet [Deng *et al.*, 2012, Conticelli *et al.*, 2013].

Alkaline rocks from this area contain various types of xenoliths, such as pyroxenite, gabbro, diorite and hornblendite xenoliths. Amphibole is frequently observed in xenoliths since it may occur in a wide range of pressure and temperature and is among the main constituents of mafic and ultramafic igneous and metamorphic rocks. Amphibole is moreover one of the most suitable minerals for thermobarometry estimates [Putirka, 2016].

Hornblende-rich xenoliths have been reported from several locations worldwide; e.g., northeast of Iran [Yousefzadeh and Sabzehei, 2012], central Mexico [Blatter and Carmichael, 1998], Iberian Peninsula [Capedri *et al.*, 1989], western and central Europe [Downes *et al.*, 2001, 2002, Carraro and Visonà, 2003], and central Spain [Orejana *et al.*, 2006]. The majority of the hornblendite xenoliths are related to the host volcanic rocks [Witt-Eickschen and Kramm, 1998] while some others are witnesses of a metasomatized mantle or cumulates from older magmatic events [e.g., Frey and Prinz, 1978, Irving, 1980, Capedri *et al.*, 1989, Saadat and Stern, 2012, Rajabi *et al.*, 2014, Su *et al.*, 2014, Kheirkhah *et al.*, 2015].

In the study area, volcanic rocks have been previously investigated in terms of their geochemistry and petrology by Khezerlou *et al.* [2008] and Ahmadzadeh *et al.* [2010]. Moreover, pyroxenite

[Khezerlou *et al.*, 2017], gabbro and diorite xenoliths [Khezerlou *et al.*, 2020] have been studied in terms of their geochemistry, isotope, and mineralogy. Studies of volcanic rocks and xenoliths in the study area have shown that their constituent magmas originate from a metasomatized mantle. However, no such information is available about the hornblendite xenoliths. Studying hornblende-rich rocks occurring in volcanic rocks can provide valuable information about their origin and the magmatic history of the investigated area. Hence, the present research was conducted to investigate the petrographic and geochemical characteristics of the hornblendite xenoliths and their host volcanic rocks from the northern part of Uromieh Dokhtar magmatic belt. Moreover, major and trace element data, and ¹⁴³Nd/¹⁴⁴Nd and ⁸⁶Sr/⁸⁷Sr isotopic ratios were evaluated to determine the petrogenesis, and establish the relationship between the magmatic source of these xenoliths and their host volcanic rocks.

2. Geological setting

The Neotethys subduction process that occurred beneath Central Iran during the upper Cretaceous and Paleogene and the collision process between the Iran and Arabia Platforms created four structural zones in Iran. These zones are; the High Zagros belt, the Sanandaj–Sirjan zone, the Uromieh Dokhtar magmatic belt, and the Zagros folded zone [Alavi, 2004]. The study area is located in the northernmost of the Uromieh Dokhtar magmatic belt, characterized by a magmatic activity which started during the late Cretaceous and was active from Eocene to Quaternary. The peak magmatism of this zone occurred during Eocene [Farhoudi, 1978, Emami, 1981, Alavi, 2004]. However, it ceased for a short time and started again during the upper Miocene to Plio-Quaternary [Omranian *et al.*, 2008]. The volcanic rocks from the northwest of Marand overlie the Upper Miocene clastic and evaporitic rocks, being possibly Plio-Quaternary in age.

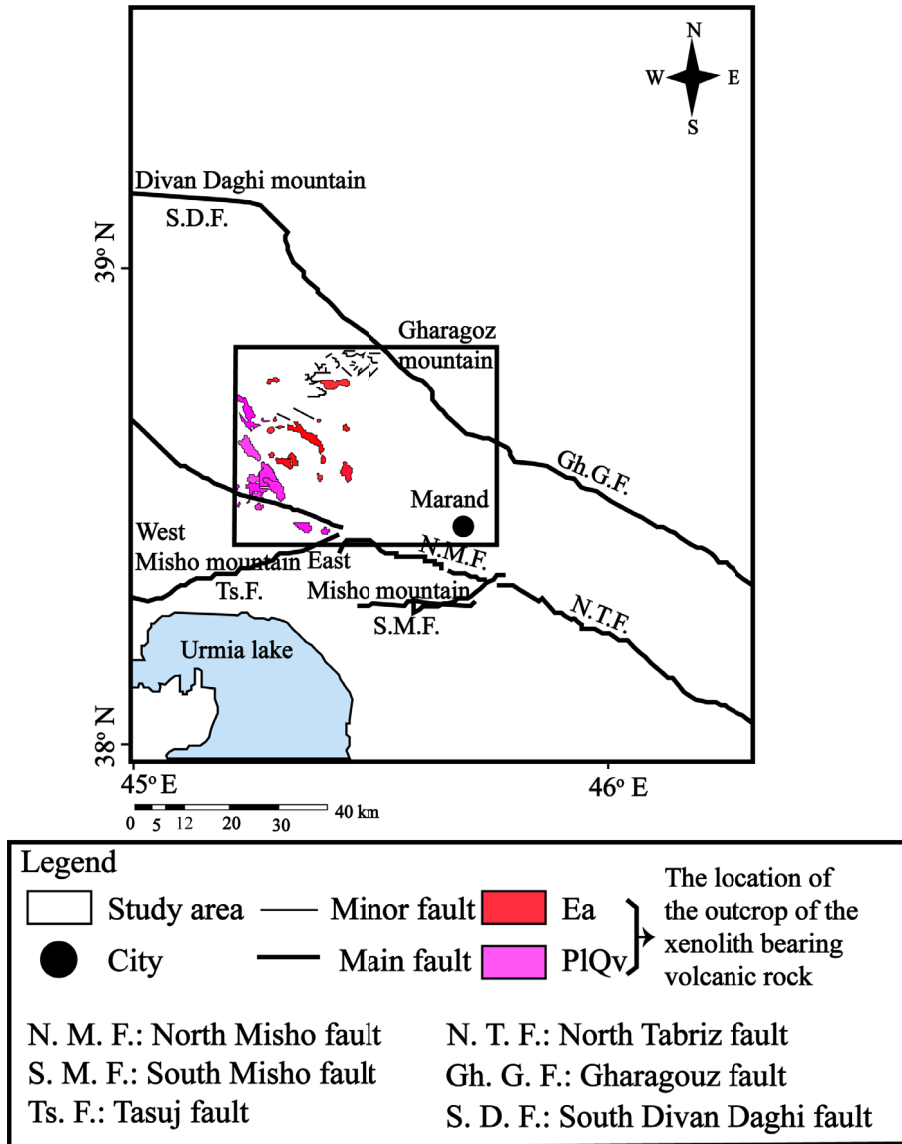


Figure 1. Tectonic map of the investigated area, showing the location of the outcrop of the xenoliths-bearing volcanic rocks [modified after Khezerlou *et al.*, 2020]. Ea (Eocene, pyroxene andesite)–PLQv (Plio-Quaternary, volcanic).

The study area is located between the main faults of the region including North Tabriz (N. T. F), Misho (N. M. F and S. M. F), and Tasuj (Ts. F) faults to the south and Garagouz (Gh. G. F) and South Divan Daghi (S. D. F) faults to the north (Figure 1).

Field surveys revealed a wide range of volcanic and volcanoclastic rocks outcropping in this area (Figure 2). The volcanoclastic rocks from the study area include agglomerate, breccia, and tuff litholo-

gies. The volcanic rocks of the study area are identified in Figure 2 by PLQv (trachyandesite) and Ea (pyroxene andesite) acronyms. In detail, in the area of PLQv, the volcanic rocks also include basanite, tephrite, and basalt trachyandesites, in addition to trachyandesite which is the dominant rock type. There are also tuffs in this area which are in contact with trachyandesite volcanic rocks. In some locations, 2–3 m thick layers of volcanic ashes with a

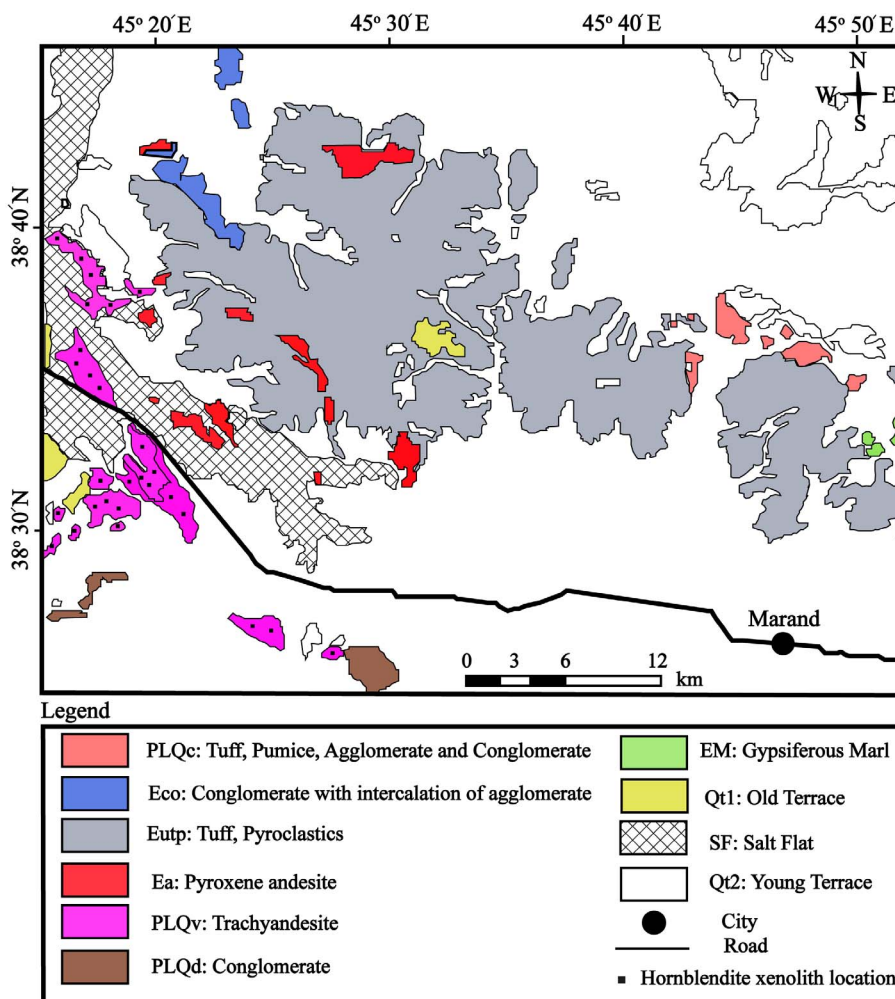


Figure 2. Geological map of the investigated area. (Simplified from the 1:100,000 geological maps of Marand, Jolfa, Gharezyaadin and Tasuj) [modified after Khezerlou *et al.*, 2017]. Location of sampling includes Ea and PLQv.

trachyandesite composition are observed in contact with tuffs [Khezerlou *et al.*, 2008]. Xenoliths occurring in this area (PLQv) are gabbros, diorites, hornblendites, lamprophyres, and pyroxenites hosted by trachyandesites and basalt trachyandesites. In the area of Ea (pyroxene andesite), the volcanic rocks include leucite, leucite-basanite, leucite-tephrite, basanite, tephrite, basalt trachyandesites, trachydacite, and dacite. Xenoliths occurring in this area (Ea) are gabbros, diorites, and pyroxenites hosted by basalt trachyandesites.

Several dykes outcrop in the study area. They are mostly ultrapotassic in composition. Also, some lamprophyric dykes between 9 and 11 Ma (Late Miocene)

in age occur in the study area in Sorkheh, Iran [Ag-hazadeh *et al.*, 2015].

In the southern part of the study area, in the Misho Mountain (Southwest of Marand), some outcrops of mafic rocks including gabbro, diorite, anorthosite and olivine gabbro occur, sometimes associated to ultrabasic rocks ranging from peridotite to highly serpentinized pyroxenite. These rocks are located above the Kahar Formation, and are covered by a weathering shell. Thus, their relative age is estimated to be younger than that of the Kahar Formation and older than the Permian [Azimzadeh, 2013]. In this regard, Saccani *et al.* [2013] ascribe these rocks to the Paleotethys. There

is also a granitoid mass in the Misho Mountain (southwest of Marand), along with intermediate and acidic rocks including diorite, tonalite, monzogranite, granodiorite, and granite, which are S-type granitoids with a potassic calc-alkaline affinity, and which crop out near the Misho gabbros [Shahzeidi, 2013].

3. Analytical methods

The major element compositions of minerals were acquired at the “Centre de Micro Caractérisation Raimond Castaing” (CNRS, University Toulouse III, INPT, INSA, Toulouse, France), using a Cameca SX-Five electron microprobe. The operating conditions were as follows: accelerating voltage 15 kV; beam current 20 nA; analysed surface around $2 \times 2 \mu\text{m}^2$. The following standards were used: albite (Na), periclase (Mg), corundum (Al), sanidine (K), wollastonite (Ca, Si), pyrophanite (Mn), hematite (Fe), Cr_2O_3 (Cr), NiO (Ni) and sphalerite (Zn).

The bulk rock major and minor elements were analyzed using an Inductively Coupled Plasma Atomic Emission Spectrometer (ICP-AES) Horiba Jobin Yvon Ultima 2 at the “Pôle de Spectrométrie Océan” (PSO/IUEM, Plouzané, France), following the protocol adapted from Cotten *et al.* [1995]. Each powdered sample was digested in Teflon vials with HF 32N and HNO_3 14.4N and the dry residue was dissolved in a H_3BO_3 solution. WSE and ACE international standards were used as internal and external control. The precision of measurements performed on that instrument is usually better than 1% for both SiO_2 and TiO_2 , 2% for Al_2O_3 and Fe_2O_3 , and better than 4% for the other major oxides.

Trace element concentrations were determined using a High Resolution Inductively Coupled Plasma Mass Spectrometer (HR ICP-MS) Thermo Finnigan Element II (“Pôle de Spectrométrie Océan” PSO/IUEM, Plouzané, France), following a method adapted from Barrat *et al.* [2007]. About 100 mg of sample were digested in Teflon vials within distilled HF 32N and HNO_3 14.4N. The dry residue was dissolved in HNO_3 14.4N and then in HCl 3N. An aliquot of the solution was diluted in HNO_3 0.3N and spiked with Tm spike. BCR2 and BEN were used as external control and BHVO-2 was used for internal control. The precision of measurements was better than 5% for all elements.

Samples were also analyzed for Sr and Nd radiogenic isotopes. About 200 mg of sample material was weighed and dissolved in Savillex beakers in a mixture of ultrapure distilled HF (24N), and HNO_3 (14N) for four days at 120 °C on a hot plate. Sr and Nd fractions were chemically separated using the Eichrom specific resins TRU-spec, Sr-spec and Ln-spec following conventional column chemistry procedure [Pin and Santos Zalduegui, 1997]. The Sr and Nd isotope compositions were measured in static mode on a Thermo TRITON spectrometer at the PSO (IUEM, Plouzané, France). All measured Sr and Nd ratios were normalized to $^{86}\text{Sr}/^{88}\text{Sr} = 0.1194$ and $^{146}\text{Nd}/^{144}\text{Nd} = 0.7219$, respectively and $^{87}\text{Sr}/^{86}\text{Sr}$ values were normalized to the recommended value of NBS987 (0.710250). During the course of analysis, Nd standard solution La Jolla gave 0.511859 ± 2 ($n = 2$, recommended value 0.511850) and JNdi gave 0.512117 ± 3 ($n = 1$, recommended value 0.512100).

4. Petrography

4.1. Host volcanic rocks

The volcanic series of the study area consists of SiO_2 -undersaturated rocks (e.g., leucitite, leucite-basanite, leucite-tephrite, basanite, and tephrite) to SiO_2 -saturated rocks such as trachyandesite, andesite, trachydacite, and dacite. The hornblende xenoliths occur within the trachyandesite rocks. These rocks show microlitic porphyritic (Figure 3a) or porphyritic (Figure 3d) textures.

Andesine plagioclase is the most abundant mineral phase in these volcanic rocks, making 45–50% of total modal content. The size of this mineral varies from very fine microliths (less than 0.1 mm) occurring within the matrix, to phenocrysts up to 1.2 mm in size. In some cases, the variation in size is transitional, resulting in a seriate texture (Figure 3a). Most of the plagioclases display Carlsbad and polysynthetic twins and some of them display a sieve texture (Figure 3a) or even zoning (Figures 3a, d). Clinopyroxene constitutes 8–10% of the samples. This mineral is observed as phenocryst in the investigated rocks but not as microlite in the matrix. It is euhedral to subhedral and ranges in size from 0.2 to 1.5 mm. The minor mineral phases of these rocks include amphibole, biotite, K-feldspar, apatite, and opaque minerals associated to glass in some samples. Euhedral and subhedral brown hornblende ranging in size from 0.2 to

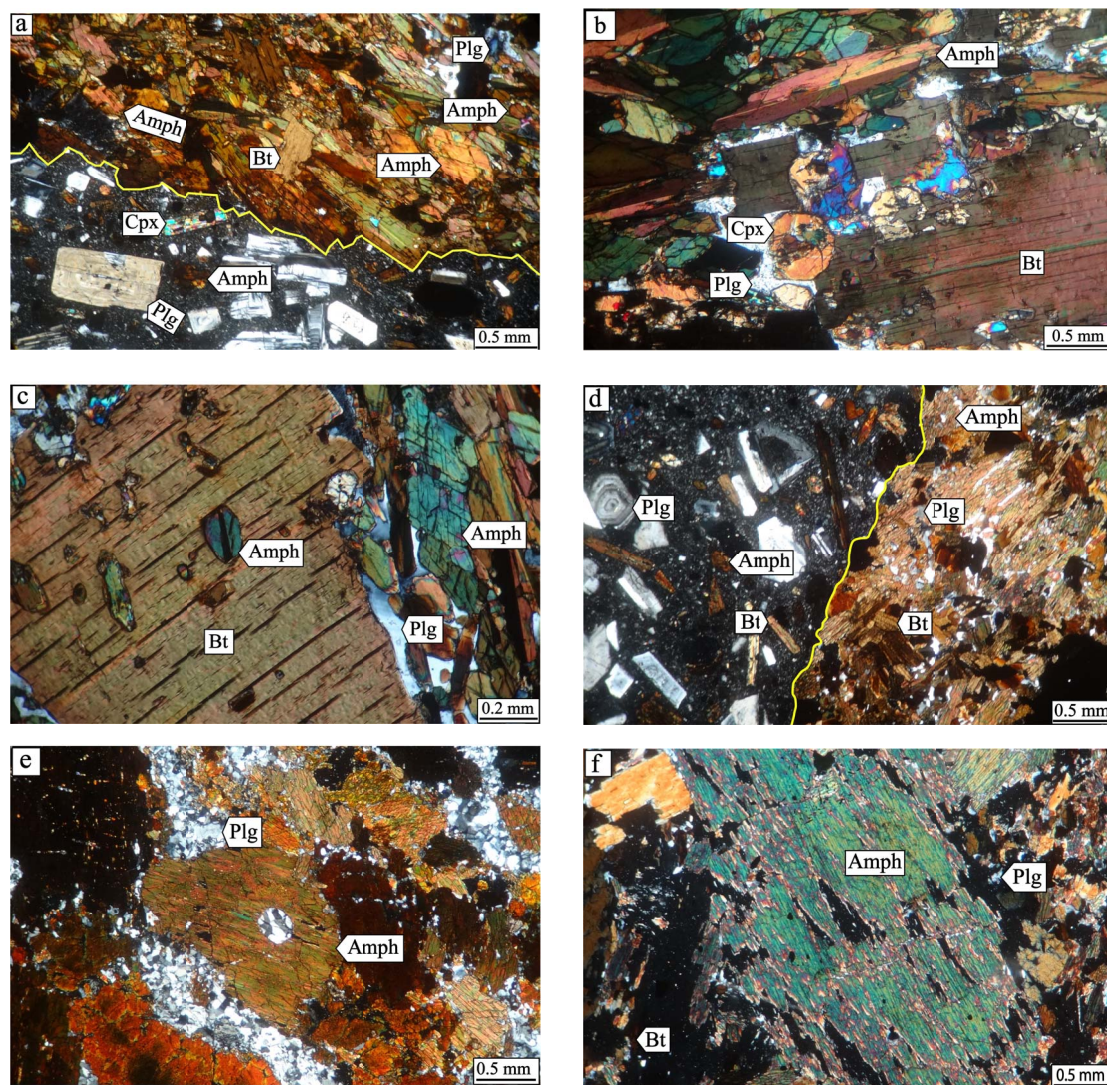


Figure 3. Photomicrographs of host volcanic rocks and hornblende xenoliths from the study area: (a) plagioclase (Plg), clinopyroxene (Cpx), amphibole (Amph) and biotite (Bt) phenocrysts in trachyandesite and hornblende with amphibole and biotite as cumulus phases and plagioclase as intercumulus phase (crossed polars: XPl). (b) Hornblende with amphibole, clinopyroxene and biotite as cumulus phases and plagioclase as intercumulus phase, XPl. (c) Hornblende with amphibole and biotite as cumulus phases and plagioclase as intercumulus phase, XPl. (d) Plagioclase, amphibole and biotite phenocrysts in trachyandesite and hornblende with amphibole and biotite as cumulus phases and plagioclase as intercumulus phase, XPl. (e) Hornblende with amphibole (as cumulus phase) and plagioclase as intercumulus phase, XPl. (f) Hornblende with amphibole and biotite as cumulus phases and plagioclase as intercumulus phase, XPl. Group 1 xenolith: a–c. Group 2 xenolith: d–f.

1 mm is also observed, amounting up to 4–5% of the modal content of samples, some crystals displaying opacitization (Figure 3a). Another minor mineral is

biotite, which makes up to 4–6% of the mode. The size of this mineral ranges from 0.3 to 0.8 mm, and some biotites also display opacitization (Figure 3d).

Apatite and opaque minerals smaller than 0.5 mm (1–2% of the mode) commonly occur.

4.2. *Hornblendite xenoliths*

Hornblendite xenoliths are elliptic black lustrous rock pieces with dimensions of 3×10 cm. Based on the occurrence or absence of clinopyroxene and the plagioclase modal content, these xenoliths are divided into two groups: Group 1 with clinopyroxene and always less than 10% of plagioclase and Group 2 lacking clinopyroxene and with commonly more than 10% of plagioclase.

4.2.1. *Group 1*

Amphibole constitutes 65–80% of the modal content of hornblendites from this group. Biotite and plagioclase are the two other main mineral phases with modal content ranging from 5 to 25% and from 5 to 10%, respectively (Table 7). These rocks are characterized by adcumulus texture with 0.2–0.35 mm subhedral to euhedral brown amphibole as the main cumulus phase (Figures 3a–c). In some amphiboles of this group, a slight color change is seen from the mantle to the rim, so that the color of the rim looks darker than the mantle (Figure 3a). Euhedral and subhedral biotites ranging from 0.5 to 3 mm in size also occur as cumulus phases in these samples. Biotite in this group is more abundant than in Group 2 hornblendite xenoliths and host volcanic rocks. Some samples locally show a poikilitic texture, characterized by tiny opaques and amphiboles included within biotite crystals (Figure 3c). Small anhedral plagioclases constitute the intercumulus phase. Clinopyroxene, opaque, and apatite are minor minerals in Group 1 samples. Clinopyroxene mostly occurs as subhedral crystals less than 1 mm in size (Figure 3b).

4.2.2. *Group 2*

Group 2 hornblendites display orthocumulus texture (Figures 3d–f) with amphibole (55–95%), plagioclase (3–25%), and biotite (3–12%) as the main mineral phases (Table 7). Similar to the Group 1 xenoliths, amphibole and biotite are the cumulus phases while plagioclase is the intercumulus phase. Amphiboles in this group are euhedral and subhedral and range from 0.2 to 5.5 mm. Amphiboles are more abundant in this group compared to the

Group 1 xenoliths and host volcanic rocks, and show no distinct orientation (Figures 3d–f). Biotites are mainly subhedral and 0.5–3 mm in size and are less abundant compared to Group 1. Moreover, 0.2–1 mm large anhedral plagioclases occur in the interstices of these mafic minerals. Unlike the Group 1 xenoliths and host volcanic rocks, this group does not contain clinopyroxene. Opaque minerals and apatite less than 1 mm in size are observed as minor minerals in this group. They are less abundant than in Group 1 hornblendites.

5. Results and discussion

5.1. *Mineral chemistry*

Four samples were analyzed using the electron microprobe technique (two samples from Group 1, one from Group 2 and one from host volcanic). For samples k (v-k), k-6 (v-k-6) and k-8 (v-k-8), the constituent minerals of the host volcanic rock (v-k, v-k-6 and v-k-8) and xenoliths (k, k-6 and k-8) were analyzed, while for sample v-k-20 only the constituent minerals of the host volcanic rock were analyzed.

5.1.1. *Clinopyroxene*

As mentioned above, Group 2 hornblendite xenoliths lack clinopyroxene and thus for comparison, some clinopyroxene of the host volcanic rocks and Group 1 hornblendite xenoliths are presented, in order to determine differences or similarities of composition, magmatic series and conditions of formation of this mineral in the studied samples.

The composition of clinopyroxenes in Group 1 hornblendite xenoliths and host volcanic rocks plot in the field of Quad (Ca-pyroxene) in the Q–J diagram of Morimoto and Kitamura [1983] (Figure 4a). All the investigated clinopyroxenes are diopsides (Figure 4b).

The composition of clinopyroxenes can provide valuable information about the magmas from which they crystallized [Zhang *et al.*, 2018]. The Ti versus Ca+Na diagram [Leterrier *et al.*, 1982] indeed shows that clinopyroxenes from host volcanic rocks lie in the alkaline field and clinopyroxenes from Group 1 hornblendite xenoliths lie in the alkaline field and close to the dividing line (Figure 4c). The position of all investigated clinopyroxenes of host volcanic rocks in the $\text{Na}+\text{Al}^{\text{IV}}$ versus $\text{Cr}+2\text{Ti}+\text{Al}^{\text{VI}}$ diagram

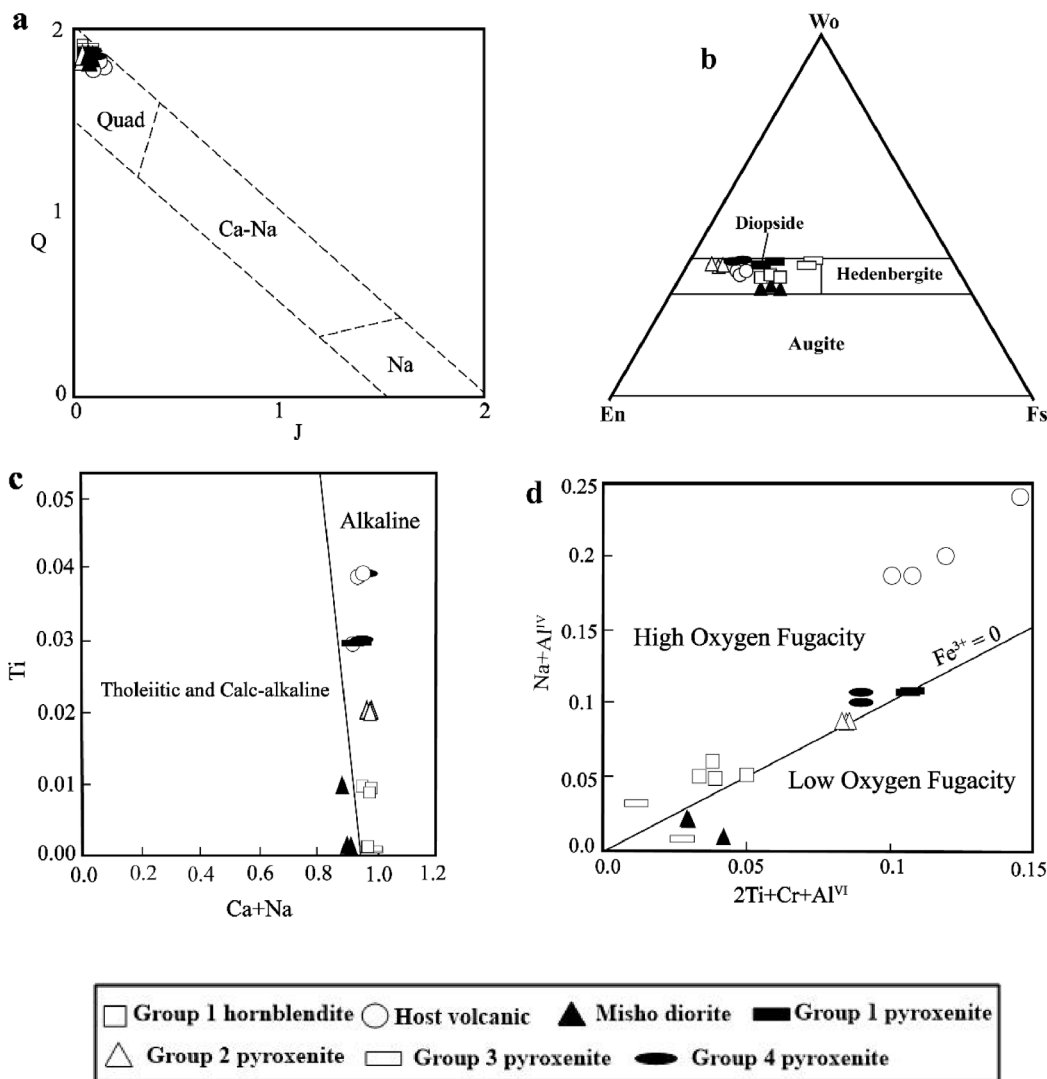


Figure 4. (a) Composition of clinopyroxenes in the Q–J diagram ($J = 2\text{Na}$, $Q = \text{Ca} + \text{Mg} + \text{Fe}^{2+}$) [Morimoto and Kitamura, 1983]. (b) Classification of clinopyroxenes [Morimoto et al., 1988]. (c) Plot of Ti versus Na+Ca for clinopyroxenes from the volcanic rocks and Group 1 hornblende xenoliths [Leterrier et al., 1982]. (d) Plot of $\text{Na} + \text{Al}^{\text{IV}}$ versus $2\text{Ti} + \text{Cr} + \text{Al}^{\text{VI}}$ for clinopyroxenes from the samples [Schweitzer et al., 1979].

[Schweitzer et al., 1979] indicates that they crystallized at high oxygen fugacity conditions (Figure 4d). The clinopyroxenes of Group 1 hornblende xenoliths in this diagram plot also in the high oxygen fugacity field, close to the dividing line, with a sample plotting on the dividing line. The $\text{Mg}/\text{Mg} + \text{Fe}^{2+}$ of clinopyroxenes from Group 1 hornblende xenoliths and host volcanic rocks varies from 0.73 to 0.74 and 0.82 to 0.84, respectively (Table 1).

Figure 4b illustrates the compositional difference between clinopyroxenes from Group 1 hornblende xenoliths and those from volcanic rocks. Clinopyroxenes from Group 1 hornblende xenoliths indeed display higher SiO_2 and MnO contents and lower Al_2O_3 , TiO_2 , and Na_2O contents than those of clinopyroxene from their host volcanic rocks. In order to compare the composition of clinopyroxenes from Group 1 hornblende xenoliths with groups 1,

Table 1. Mineral chemical composition of clinopyroxenes in hornblendite xenoliths, host volcanic rocks and Misho diorites

Mineral	Clinopyroxene										
Rock	Group 1 xenolith				Host volcanic				Misho diorite		
Sample	k	k	k	k	v-k	v-k	v-k	v-k	A2-43	A2-43	A2-43
Location	Core	Core	Core	Core	Core	Core	Core	Core	Core	Core	Core
SiO ₂	52.57	52.93	52.83	52.75	49.44	49.21	46.85	48.54	54.02	53.86	54.34
TiO ₂	0.20	0.18	0.21	0.19	1.21	1.23	1.28	1.27	0.17	0.19	0.13
Al ₂ O ₃	0.92	0.97	1.10	1.11	3.83	3.84	6.21	3.99	0.58	0.63	0.72
Cr ₂ O ₃	0.01	0.00	0.00	0.02	0.01	0.01	0.02	0.01	0.00	0.05	0.04
FeO(t)	8.59	8.77	9.40	8.92	7.94	8.75	9.13	8.33	10.74	10.65	10.18
MnO	0.70	0.72	0.73	0.71	0.45	0.39	0.37	0.41	0.19	0.21	0.26
MgO	13.07	12.88	12.67	12.95	13.18	12.71	11.75	12.72	13.61	13.65	13.05
CaO	22.80	22.75	23.28	22.94	22.39	22.42	22.65	22.23	21.58	21.75	22.42
Na ₂ O	0.39	0.48	0.46	0.42	0.63	0.65	0.61	0.71	0.21	0.20	0.14
K ₂ O	0.00	0.00	0.00	0.00	0.00	0.00	0.02	0.02	0.00	0.00	0.02
Total	99.25	99.66	100.69	100.01	99.08	99.21	98.89	98.23	101.10	101.19	101.30
Cations calculated on the basis of 6 oxygens											
Si	1.98	1.99	1.97	1.98	1.87	1.87	1.79	1.86	2.00	1.99	2.01
Al ^{IV}	0.02	0.01	0.03	0.02	0.13	0.13	0.21	0.14	0.00	0.01	0.00
Al ^{VI}	0.02	0.03	0.02	0.03	0.04	0.04	0.07	0.04	0.03	0.02	0.04
Fe ³⁺	0.02	0.01	0.04	0.03	0.10	0.11	0.16	0.13	0.00	0.00	0.00
Cr	0.00	0.00	0.00	0.00	0.00	0.00	0.00	0.00	0.00	0.00	0.00
Ti	0.01	0.00	0.01	0.01	0.03	0.04	0.04	0.04	0.00	0.01	0.00
Fe ²⁺	0.25	0.26	0.25	0.25	0.15	0.16	0.12	0.13	0.33	0.33	0.32
Mn	0.02	0.02	0.02	0.02	0.01	0.01	0.01	0.01	0.01	0.01	0.01
Mg	0.73	0.72	0.71	0.72	0.74	0.72	0.67	0.73	0.75	0.75	0.72
Ca	0.92	0.91	0.93	0.92	0.91	0.91	0.93	0.91	0.86	0.86	0.89
Na	0.03	0.03	0.03	0.03	0.05	0.05	0.05	0.05	0.02	0.01	0.01
K	0.00	0.00	0.00	0.00	0.00	0.00	0.00	0.00	0.00	0.00	0.00
Total	4.01	4.00	4.01	4.01	4.03	4.04	4.05	4.04	3.99	3.99	3.98
mg#	0.74	0.73	0.74	0.74	0.84	0.82	0.84	0.84	0.69	0.70	0.69
Wo	47.26	47.32	47.70	47.33	47.41	47.52	48.90	47.62	43.98	44.17	45.97
En	37.71	37.28	36.12	37.18	38.83	37.49	35.30	37.91	38.59	38.58	37.23
Fs	15.02	15.40	16.18	15.49	13.76	14.99	15.81	14.47	17.43	17.25	16.80

Misho data are from Shahzeidi [2013].

2, 3 and 4 of pyroxenite xenoliths from study area [Khezerlou *et al.*, 2017], representative analyses of the latter are given in Figures 4a–d. As can be seen in these figures, the compositions of the clinopyroxenes from Group 1 hornblendite xenoliths differ from those of clinopyroxenes from pyroxenite xenoliths of

the study area. They are different in most of the major elements such as SiO₂, Na₂O, MgO, FeO(t), MnO, and Al₂O₃ (Table 1). We also compared the clinopyroxenes from the xenoliths with those from the Misho diorites, located near the study area [Shahzeidi, 2013]. In both cases the clinopyroxenes are diopsides

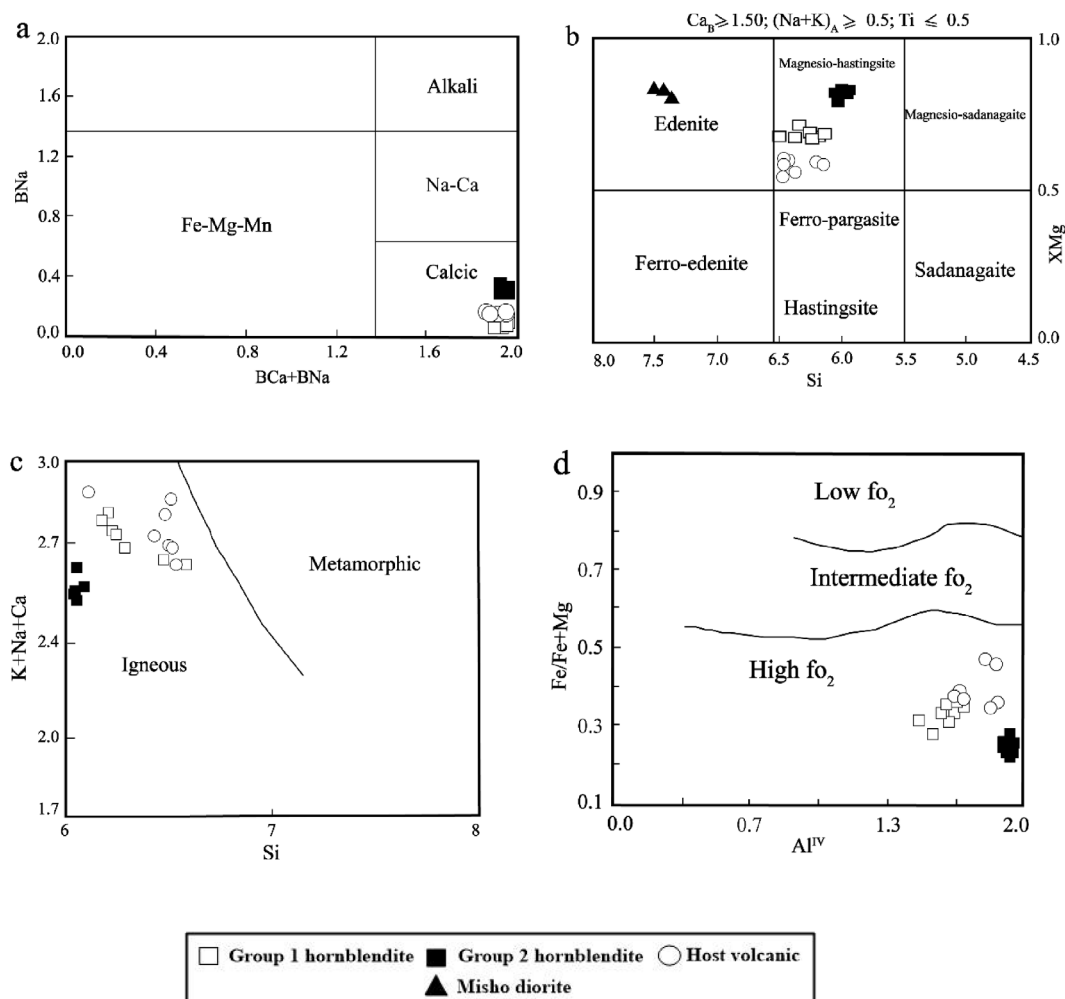


Figure 5. (a) Composition of amphiboles in the BCa+BNa versus BNa diagram [Leake *et al.*, 1997]. (b) Classification of amphiboles [Leake *et al.*, 1997]. (c) Plot of Si versus K+Na+Ca for amphiboles from the investigated samples [Sial *et al.*, 1998]. (d) Plot of Al^{IV} versus $Fe/(Fe+Mg)$ for amphiboles from the host volcanic rocks and hornblende xenoliths [Anderson and Smith, 1995].

(Figure 4b) but those from Group 1 hornblende xenoliths contain more Al_2O_3 , CaO, MnO, and Na_2O and less SiO_2 and FeO compared to those from the Misho diorites (Table 1). As can be seen in Figures 4c and d, the composition of the clinopyroxenes from Group 1 hornblende xenoliths differs from those of clinopyroxenes from the Misho diorites.

5.1.2. Amphibole

As shown in Figure 5a, the amphiboles from all the investigated xenoliths (Group 1 and Group 2) as well as amphiboles from host volcanic rocks are

calcic amphiboles as illustrated by the BNa versus BNa+BCa diagram of Leake *et al.* [1997]. More precisely, according to $Mg/(Mg+Fe^{2+})$ versus Si diagram [Leake *et al.*, 1997], amphiboles from Group 1 xenoliths and host volcanic rocks are magnesiohastingsites while those from Group 2 hornblende xenoliths are pargasites (Figure 5b). In the K+Na+Ca versus Si diagram [Sial *et al.*, 1998], amphiboles from the two groups of hornblende xenoliths plot within the magmatic (igneous) amphiboles field (Figure 5c).

The $Mg/(Mg+Fe^{2+})$ ratio of amphibole from Group 1 and Group 2 xenoliths and host volcanic

rocks vary from 0.67 to 0.72, 0.79 to 0.85, and 0.54 to 0.67, respectively (Table 2). In the Al^{IV} versus $Fe^{2+}/Fe^{2+}+Mg$ diagram [Anderson and Smith, 1995], amphiboles from the xenoliths and host volcanic rocks fall within the high-oxygen fugacity field (Figure 5d). The core, mantle and rim of amphiboles from Group 2 hornblende xenoliths do not show considerable and systematic change in composition. Yet, in some of amphiboles of Group 1, $FeO(t)$, CaO and MnO increase from the mantle to the rim (Table 2).

As shown in Figure 5b, the amphiboles of the host volcanic rock and those of the two groups of hornblende xenoliths display some compositional differences; for instance, amphiboles from Group 1 and Group 2 xenoliths show higher MgO and $Mg/Mg+Fe^{2+}$ values and lower $FeO(t)$, K_2O , and MnO (and also Al_2O_3 for Group 2) contents than those of their equivalent in host volcanic rocks. Furthermore, some differences also occur between amphiboles from the two groups of hornblende xenoliths; for instance, amphiboles from Group 1 have slightly higher TiO_2 , Na_2O , MgO , and CaO contents and a lower Al_2O_3 content than amphibole from Group 2 (Table 2). The composition of amphiboles between different samples (k, k-6) in Group 1 hornblende xenoliths is not homogeneous and there is a slight difference in the content of some of the major elements (for example, SiO_2 , Al_2O_3 , K_2O) (Table 2).

We also compared the amphiboles of the two investigated groups of hornblende xenoliths with those of the Misho diorites [Shahzeidi, 2013]. Amphiboles in the Misho diorites are edenites (Figure 5b), and are different from those from the investigated hornblende xenoliths in terms of major elements such as SiO_2 , TiO_2 , Na_2O , MgO , K_2O , $FeO(t)$, MnO , and Al_2O_3 (Table 2).

5.1.3. Feldspar

According to the classification of Deer *et al.* [1966], the composition of plagioclases in Group 1 and Group 2 hornblende xenoliths is andesine and labradorite, respectively. On the other hand, the composition of feldspars of their host volcanic rocks are oligoclase, andesine and sanidine (Figure 6). Zoning occurs in some volcanic plagioclase phenocrysts, with SiO_2 , Na_2O , and K_2O contents increasing from rim to core while CaO and Al_2O_3 contents decrease (normal zoning) (Table 3).

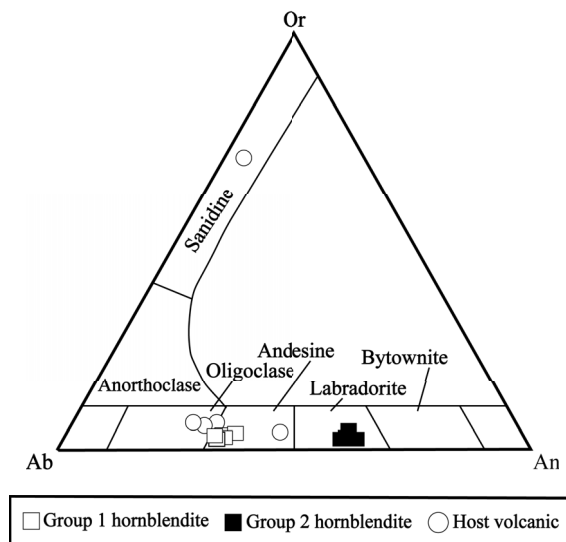


Figure 6. Classification of plagioclases from the host volcanic rocks and hornblende xenoliths [Deer *et al.*, 1966].

5.1.4. Biotite

According to the Al^{IV} versus $Fe^{2+}/Fe^{2+}+Mg$ diagram, micas from Group 1 and Group 2 hornblende xenoliths and host volcanic rocks are biotites (Figure 7a) with $Mg/Mg+Fe^{2+}$ values ranging from 0.62 to 0.66, 0.64 to 0.65 and 0.60 to 0.61, respectively (Table 4).

The ternary diagram $MgO-Fe+MnO-10TiO_2$ can be used to assess the origin of micas [Nachit *et al.*, 2005] which suggests that biotites from Group 1 hornblende xenoliths and host volcanic rocks are primary magmatic micas while those from Group 2 hornblende xenoliths are recrystallized type (Figure 7b).

The biotites from Group 2 hornblende xenoliths do not display compositional variation from core to rim (Table 4), similarly to amphiboles and plagioclases. Biotites in Group 1 hornblende xenoliths display cores respectively higher in Al_2O_3 , SiO_2 , and CaO and lower in MgO , FeO , and K_2O than their rims (Table 4). The compositions of biotites from Group 1 and Group 2 hornblende xenoliths are different (Figure 7a). Biotites from Group 1 hornblende xenoliths have higher SiO_2 and TiO_2 contents and lower MgO , MnO , and Na_2O compared to micas of Group 2 (Table 4). The results show that biotites of Group 1 hornblende xenoliths are also

Table 2. Mineral chemical composition and P – T estimate of amphiboles in hornblendite xenoliths, host volcanic rocks and Misho diorites

Mineral	Amphibole										
Rock	Group 1 xenolith								Misho diorite		
Sample	k	k	k	k-6	k-6	k-6	k-6	k-6	A2-43	A2-43	A2-43
Location	Core	Core	Core	Rim 1	Mantle 1	Core	Mantle 2	Rim 2	Core	Core	Core
SiO ₂	43.52	43.21	43.31	42.74	42.63	42.11	42.00	42.08	52.57	53.61	52.89
TiO ₂	1.82	2.15	2.07	2.13	2.16	2.24	2.26	2.18	0.15	0.14	0.23
Al ₂ O ₃	10.68	11.75	11.78	12.26	12.26	12.56	12.57	12.39	3.54	3.51	3.78
Cr ₂ O ₃	0.01	0.02	0.00	0.02	0.00	0.00	0.01	0.02	0.03	0.01	0.03
FeO(t)	12.27	12.72	11.82	12.98	12.71	12.74	12.82	13.36	15.30	14.48	15.80
MnO	0.13	0.23	0.13	0.20	0.10	0.15	0.10	0.20	0.28	0.02	0.32
MgO	12.68	12.48	13.40	12.81	12.71	12.53	12.63	12.40	14.57	15.49	14.57
CaO	11.47	11.67	11.76	12.08	11.78	11.81	11.98	11.99	10.92	10.75	10.27
Na ₂ O	1.99	2.20	2.23	2.32	2.17	2.24	2.23	2.22	0.33	0.28	0.42
K ₂ O	1.08	1.05	0.95	1.10	1.13	1.16	1.24	1.16	0.25	0.19	0.22
Total	95.64	97.46	97.47	98.63	97.65	97.53	97.84	98.00	97.94	98.48	98.53
Cations calculated on the basis of 23 oxygens											
Si	6.52	6.37	6.35	6.25	6.27	6.22	6.19	6.21	7.46	7.49	7.41
Al ^{IV}	1.48	1.63	1.65	1.75	1.73	1.78	1.81	1.79	0.54	0.51	0.59
Sum T	8.00	8.00	8.00	8.00	8.00	8.00	8.00	8.00	8.00	8.00	8.00
Al ^{VI}	0.41	0.42	0.38	0.36	0.40	0.40	0.38	0.36	0.05	0.07	0.04
Ti	0.21	0.24	0.23	0.23	0.24	0.25	0.25	0.24	0.02	0.01	0.02
Cr	0.00	0.00	0.00	0.00	0.00	0.00	0.00	0.00	0.00	0.00	0.00
Fe ³⁺	0.19	0.22	0.32	0.28	0.31	0.29	0.27	0.31	1.00	1.09	1.26
Fe ²⁺	1.34	1.35	1.13	1.31	1.26	1.29	1.31	1.34	0.81	0.60	0.59
Mn	0.02	0.03	0.02	0.02	0.01	0.02	0.01	0.02	0.03	0.00	0.04
Mg	2.83	2.74	2.93	2.79	2.79	2.76	2.78	2.73	3.08	3.23	3.04
Sum C	5.00	5.00	5.00	5.00	5.00	5.00	5.00	5.00	5.00	5.00	5.00
Ca	1.84	1.84	1.85	1.89	1.86	1.87	1.89	1.89	1.66	1.61	1.54
Na	0.16	0.16	0.15	0.11	0.14	0.13	0.11	0.11	0.09	0.08	0.11
Sum B	2.00	2.00	2.00	2.00	2.00	2.00	2.00	2.00	1.75	1.68	1.66
Na	0.42	0.47	0.48	0.55	0.48	0.51	0.53	0.53	0.00	0.00	0.00
K	0.21	0.20	0.18	0.20	0.21	0.22	0.23	0.22	0.05	0.03	0.04
Sum A	0.63	0.67	0.66	0.75	0.69	0.73	0.76	0.75	0.05	0.03	0.04
mg#	0.68	0.67	0.72	0.68	0.69	0.68	0.68	0.67	0.79	0.84	0.84
K _D	0.93	0.98	0.85	0.97	0.96	0.97	0.97	0.98			
P (Kb)	5.6	6.4	6.3	6.4	6.8	7.1	7.1	6.9			
T (°C)	888	913	923	930	925	936	938	930			

Misho data are from Shahzeidi [2013].

Table 2. (continued)

Mineral	Amphibole											
Rock	Group 2 xenolith						Host volcanic					
Sample	k-8					v-k-20		v-k-8			v-k	
Location	Rim 1	Mantle 1	Core	Mantle 2	Rim 2	Core	Core	Core	Core	Core	Core	Core
SiO ₂	41.43	41.47	41.21	41.68	41.25	43/22	43/43	43/31	41.07	41.84	41.64	41.47
TiO ₂	0.83	0.84	0.91	0.88	0.92	1/81	1/88	1/91	2.66	2.23	2.23	2.34
Al ₂ O ₃	15.85	16.03	16.61	15.56	15.82	9/12	9/08	9/02	12.02	11.31	10.48	10.91
Cr ₂ O ₃	0.05	0.05	0.04	0.08	0.08	0.03	0.02	0.02	0.00	0.10	0.03	0.00
FeO(t)	11.54	11.41	11.57	11.72	11.71	16/98	16/92	16/78	13.70	12.81	18.26	18.01
MnO	0.22	0.17	0.15	0.13	0.12	0/46	0/51	0/52	0.25	0.22	0.51	0.55
MgO	12.64	12.64	12.32	12.64	12.42	11/4	11/23	11/42	12.09	12.57	9.64	9.92
CaO	10.51	10.56	10.71	10.62	10.75	11/12	11/21	11/02	11.57	11.78	11.05	11.36
Na ₂ O	2.97	3.02	2.90	2.98	2.92	2/14	2/06	2/01	2.58	2.12	1.99	2.09
K ₂ O	0.20	0.24	0.31	0.32	0.57	1/43	1/35	1/32	1.19	1.53	1.70	1.69
Total	96.24	96.43	96.73	96.61	96.56	97.70	97.70	97.34	97.12	96.50	97.51	98.34
Cations calculated on the basis of 23 oxygens												
Si	6.02	6.02	5.97	6.05	6.02	6/46	6/50	6/48	6.14	6.28	6.31	6.24
Al ^{IV}	1.98	1.98	2.03	1.95	1.98	1/54	1/50	1/52	1.86	1.72	1.69	1.76
Sum T	8.00	8.00	8.00	8.00	8.00	8	8	8	8.00	8.00	8.00	8.00
Al ^{VI}	0.74	0.76	0.81	0.72	0.74	0/07	0/10	0/07	0.26	0.29	0.18	0.17
Ti	0.09	0.09	0.10	0.10	0.10	0/20	0/21	0/21	0.30	0.25	0.25	0.27
Cr	0.01	0.01	0.00	0.01	0.01	0/01	0/01	0/01	0.00	0.01	0.00	0.00
Fe ³⁺	0.91	0.85	0.81	0.82	0.73	0/60	0/53	0/65	0.32	0.21	0.49	0.46
Fe ²⁺	0.49	0.53	0.59	0.60	0.70	1/52	1/59	1/45	1.40	1.40	1.82	1.80
Mn	0.03	0.02	0.02	0.02	0.01	0/06	0/06	0/07	0.03	0.03	0.07	0.07
Mg	2.74	2.74	2.66	2.74	2.70	2/54	2/50	2/55	2.69	2.81	2.18	2.23
Sum C	5.00	5.00	5.00	5.00	5.00	5	5	5	5.00	5.00	5.00	5.00
Ca	1.64	1.64	1.66	1.65	1.68	1/78	1/80	1/77	1.85	1.90	1.79	1.83
Na	0.36	0.36	0.34	0.35	0.32	0/22	0/20	0/23	0.15	0.10	0.21	0.17
Sum B	2.00	2.00	2.00	2.00	2.00	2	2	2	2.00	2.00	2.00	2.00
Na	0.47	0.49	0.48	0.49	0.51	0/40	0/39	0/35	0.60	0.51	0.38	0.44
K	0.04	0.04	0.06	0.06	0.11	0/27	0/26	0/25	0.23	0.29	0.33	0.32
Sum A	0.51	0.54	0.54	0.55	0.61	0/67	0/65	0/60	0.83	0.81	0.71	0.76
mg#	0.85	0.84	0.82	0.82	0.79	0/63	0/61	0/64	0.66	0.67	0.54	0.55
K _D	0.94	0.93	0.97	0.96	0.97	0/28	0/28	0/27				
P (Kb)	9.8	9.9	10.4	9.5	9.8	6.7	6.1	5.9				
T (°C)	964	968	971	960	965	850	846	846				

different from micas of their host volcanic rocks. The biotites from Group 1 hornblende xenoliths indeed have higher SiO₂, MgO, CaO, and Al₂O₃ contents and lower FeO(t), K₂O, TiO₂, and Na₂O contents than micas from their host volcanic rocks (Table 4).

The composition of the biotites in these xenoliths is finally also different from those of Misho diorites [Shahzeidi, 2013]. They indeed display higher TiO₂, MgO, and Na₂O and lower Al₂O₃, FeO(t), and K₂O compared to those biotites from Misho diorites.

Table 3. Mineral chemical composition of feldspars in hornblende xenoliths and host volcanic rocks

Mineral Rock Sample Location	Feldspar												
	Group 1 xenolith				Group 2 xenolith				Host volcanic				
	k	k	k-6	k-6	k-8	k-8	k-8	v-k	v-k	v-k	v-k	v-k	v-k-6
	Core	Core	Core	Core	Core	Core	Core	Rim 1	Mantle 1	Core 1	Mantle 2	Rim 2	Core
SiO ₂	60.58	60.37	59.00	59.37	51.51	51.12	51.38	60.83	60.44	58.53	60.21	62.35	71.41
TiO ₂	0.00	0.00	0.01	0.03	0.02	0.03	0.04	0.00	0.04	0.04	0.02	0.02	0.15
Al ₂ O ₃	24.56	24.42	25.77	24.68	30.94	30.20	30.88	24.06	25.05	26.39	25.17	23.73	15.13
Cr ₂ O ₃	0.02	0.00	0.00	0.01	0.01	0.02	0.02	0.00	0.00	0.00	0.01	0.00	0.01
FeO(t)	0.16	0.18	0.43	0.21	0.31	0.30	0.32	0.19	0.20	0.18	0.42	0.24	1.18
MnO	0.00	0.00	0.02	0.05	0.02	0.03	0.06	0.04	0.04	0.01	0.00	0.03	0.02
MgO	0.00	0.02	0.00	0.01	0.02	0.02	0.01	0.03	0.01	0.00	0.02	0.02	0.21
CaO	6.92	6.88	8.30	7.36	13.87	13.92	13.94	6.04	6.86	8.63	7.15	5.48	1.36
Na ₂ O	7.07	7.17	6.25	6.92	3.44	3.35	3.28	7.32	7.18	6.39	6.85	7.61	2.19
K ₂ O	0.76	0.73	0.67	0.69	0.12	0.15	0.14	0.89	0.76	0.59	0.81	1.04	5.87
Total	100.07	99.75	100.44	99.32	100.24	99.14	100.07	99.38	100.58	100.76	100.64	100.52	97.53
Cations calculated on the basis of 8 oxygens													
Si	2.42	2.42	2.35	2.39	2.06	2.06	2.05	2.45	2.40	2.32	2.39	2.48	2.93
Al	1.31	1.31	1.37	1.33	1.65	1.62	1.65	1.29	1.33	1.40	1.33	1.26	0.83
Ti	0.00	0.00	0.00	0.00	0.00	0.00	0.00	0.00	0.00	0.00	0.00	0.00	0.01
Fe	0.01	0.01	0.03	0.02	0.02	0.02	0.03	0.02	0.02	0.02	0.03	0.02	0.10
Mn	0.00	0.00	0.00	0.00	0.00	0.00	0.00	0.00	0.00	0.00	0.00	0.00	0.00
Mg	0.00	0.00	0.00	0.00	0.00	0.00	0.00	0.00	0.00	0.00	0.00	0.00	0.02
Zn	0.00	0.00	0.00	0.00	0.00	0.00	0.00	0.00	0.00	0.00	0.00	0.00	0.00
Ca	0.55	0.55	0.66	0.59	1.11	1.12	1.11	0.49	0.55	0.69	0.57	0.44	0.11
Na	1.13	1.15	1.00	1.12	0.55	0.54	0.52	1.15	1.14	1.01	1.09	1.21	0.36
K	0.12	0.12	0.11	0.11	0.02	0.02	0.02	0.14	0.12	0.09	0.13	0.17	0.96
Total	5.55	5.56	5.52	5.56	5.40	5.41	5.39	5.55	5.56	5.53	5.55	5.58	5.32
Or	6.71	6.41	6.01	6.10	1.14	1.43	1.35	8.04	6.70	5.26	7.17	9.11	67.19
Ab	62.61	63.25	56.48	61.30	32.74	32.03	31.57	64.67	63.13	56.54	61.01	66.82	25.04
An	30.68	30.34	37.51	32.61	66.11	66.54	67.08	27.29	30.17	38.21	31.82	24.08	7.77

5.2. Whole-rock major and trace element compositions

Major and trace element analyses of hornblende xenoliths (four samples from Group 1 and three samples from Group 2) are presented in Table 5. In Figure 8a, the samples of the host volcanic rocks plot within the alkaline field (a sample plot within the subalkaline/tholeiitic field) [Cox et al., 1979] while in Figure 8b the host volcanic rocks [Khezerlou et al., 2017], fall within the shoshonite field except for a

sample plotting on the line dividing the shoshonite and calc-alkaline fields. Host volcanic rocks include trachyandesites (samples v-kh-65, v-kh-52 and v-k-20) and basalt trachyandesites (samples v-kh-87, v-kh-93 and k-26), and as mentioned, Group 1 and Group 2 hornblende xenoliths are located within the trachyandesite field.

Host volcanic rocks (trachyandesites) [Khezerlou et al., 2017] contain lower FeO(t), MgO, TiO₂ and CaO contents and higher SiO₂, P₂O₅, K₂O, and Na₂O contents compared to those of Group 1 and Group 2

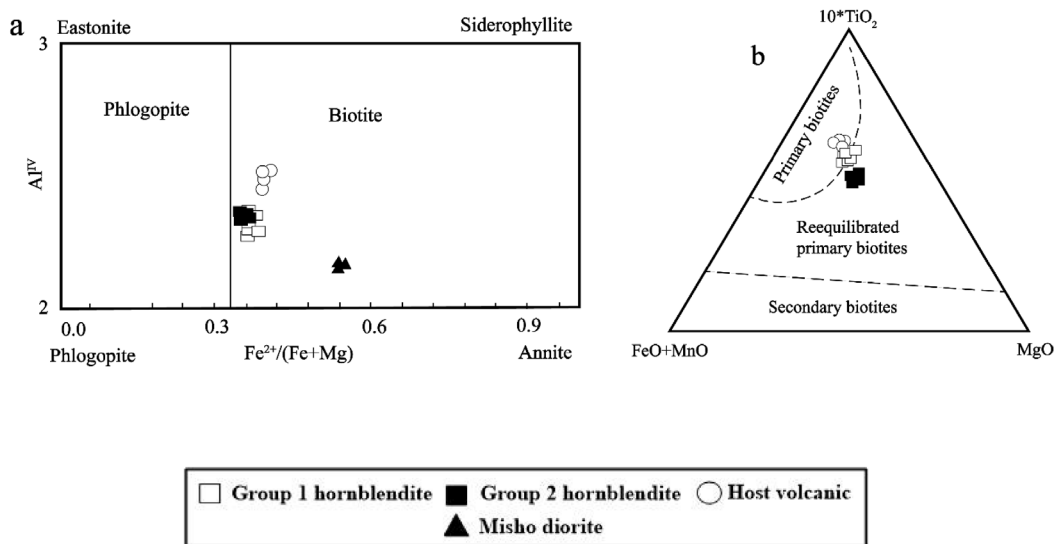


Figure 7. (a) Classification of micas [Speer, 1984]. (b) Composition of biotites in the $10*TiO_2$ -FeO-MgO diagram [Nachit et al., 2005].

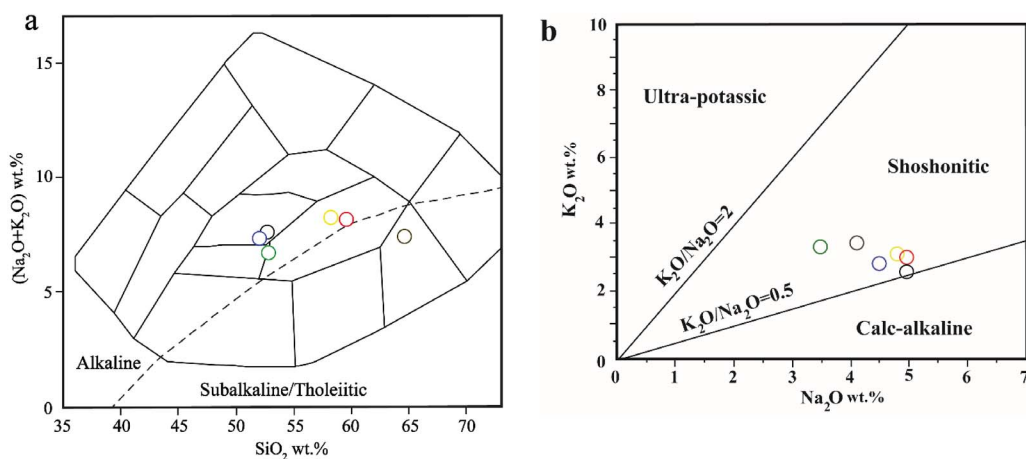


Figure 8. Host volcanic rocks. (a) Plotted in the TAS diagram [Cox et al., 1979]. Dashed line separates subalkaline from alkaline rocks. Most of the data plot in the alkaline field. (b) Plotted in the Na_2O versus K_2O diagram [after Turner et al., 1996]. The trachyandesites (host volcanics) are from Khezerlou et al. [2017]. (The blue, black, and green circles are basalt trachyandesite. The red, yellow, and brown circles are trachyandesite.)

hornblende xenoliths (Table 5). The $Mg/Mg+Fe^{2+}$ values of Group 1 and Group 2 hornblende xenoliths range from 0.42 to 0.63, and 0.49 to 0.64, respectively.

Group 1 and Group 2 hornblende xenoliths are characterized by enrichment in U, Ba, Pb, Sm, Nd,

Cs, Ti, and K and depletion in Th, Nb, and Zr (Figures 9a, c). The Ti, Ba, K, U, and Th contents in Group 1 hornblende xenoliths are higher than those of Group 2 hornblende xenoliths and host volcanic rocks [Khezerlou et al., 2017] (Figures 9a, c, e). The Pb and Sr contents of host volcanic rocks

Table 4. Mineral chemical composition of biotites in hornblendite xenoliths, host volcanic rocks and Misho diorites

Mineral	Biotite										
Rock	Group 1 xenolith					Group 2 xenolith					
Sample	k	k-6	k-6	k-6	k-6	k-6	k-8	k-8	k-8	k-8	k-8
Location	Core	Rim 1	Mantle 1	Core	Mantle 2	Rim 2	Rim 1	Mantle 1	Core	Mantle 2	Rim 2
SiO ₂	37.22	37.47	37.53	38.84	38.69	38.42	37.12	37.05	37.02	37.11	37.06
TiO ₂	3.76	3.50	4.17	3.88	4.07	4.00	3.11	3.02	3.22	3.14	3.04
Al ₂ O ₃	14.46	14.29	14.17	14.96	14.27	13.90	14.52	14.61	14.65	14.55	14.64
Cr ₂ O ₃	0.01	0.00	0.01	0.02	0.01	0.04	0.07	0.05	0.01	0.02	0.03
FeO(t)	13.71	14.53	14.68	12.97	13.91	14.80	14.13	14.01	14.06	14.21	14.08
MnO	0.13	0.16	0.17	0.10	0.15	0.14	0.66	0.74	0.54	0.62	0.54
MgO	14.87	14.64	14.50	13.80	14.23	13.77	14.63	14.74	14.68	14.55	14.76
CaO	0.06	0.06	0.17	0.27	0.16	0.19	0.12	0.11	0.09	0.14	0.10
Na ₂ O	0.36	0.35	0.30	0.18	0.30	0.30	0.49	0.51	0.47	0.45	0.52
K ₂ O	8.30	8.87	8.25	7.72	8.27	8.58	8.21	8.15	8.24	8.26	8.22
Total	92.87	93.89	93.95	92.73	94.05	94.12	93.06	92.99	92.98	93.05	92.99
Cations calculated on the basis of 22 oxygens											
Si	5.64	5.66	5.65	5.82	5.77	5.77	5.65	5.64	5.63	5.65	5.64
Al ^{IV}	2.36	2.34	2.35	2.18	2.23	2.23	2.35	2.36	2.37	2.35	2.36
Al ^{VI}	0.22	0.20	0.16	0.46	0.28	0.23	0.25	0.26	0.25	0.25	0.26
Ti	0.43	0.40	0.47	0.44	0.46	0.45	0.36	0.35	0.37	0.36	0.35
Fe ²⁺	1.74	1.83	1.85	1.62	1.73	1.86	1.80	1.78	1.79	1.80	1.79
Mn	0.02	0.02	0.02	0.01	0.02	0.02	0.09	0.10	0.07	0.08	0.07
Mg	3.36	3.30	3.25	3.08	3.16	3.08	3.32	3.34	3.33	3.30	3.35
Ca	0.01	0.01	0.03	0.04	0.02	0.03	0.02	0.02	0.01	0.02	0.02
Na	0.11	0.10	0.09	0.05	0.09	0.09	0.14	0.15	0.14	0.13	0.15
K	1.60	1.71	1.58	1.47	1.57	1.64	1.59	1.58	1.60	1.60	1.59
Total	15.48	15.57	15.45	15.18	15.34	15.40	15.57	15.58	15.56	15.54	15.58
#Mg	0.66	0.64	0.64	0.65	0.65	0.62	0.64	0.65	0.65	0.64	0.65

[Khezerlou *et al.*, 2017], on the other hand, are higher than those of hornblendite xenoliths. Although these xenoliths have a cumulate nature and may have lost some of their interstitial residual melt, similarly to their host volcanic rocks [Khezerlou *et al.*, 2017], they show an enrichment in LREE compared to HREE (Figures 9b, d, f). HREE and MREE contents in Group 1 hornblendite xenoliths are higher than that in Group 2 hornblendite xenoliths. Also, LREE content in Group 1 hornblendite xenoliths is higher than that in Group 2 hornblendite xenoliths and lower than that of host volcanic rocks [Khezerlou *et al.*, 2017]. Group 1 hornblendite xenoliths,

similarly to their host volcanic rocks, are characterized by a negative Eu anomaly while Group 2 hornblendite xenoliths display a positive Eu anomaly.

5.3. Whole-rock Sr–Nd isotopes

The ⁸⁶Sr/⁸⁷Sr and ¹⁴³Nd/¹⁴⁴Nd isotopic ratios were used to investigate and determine the origin of the investigated hornblendite xenoliths. The analyses and the sampling locations are presented in Table 6 and Figure 10, respectively. The results show that the ⁸⁶Sr/⁸⁷Sr ratio in Group 1 and Group 2 xenoliths are 0.706291 and 0.704685, respectively,

Table 4. (continued)

Mineral	Biotite						
Rock	Host volcanic				Misho diorite		
Sample	v-k-6		v-k-20		A2-39-3-2		
Location	Core	Core	Core	Core	Core	Core	Core
SiO ₂	36.44	36.39	36.28	36.22	37.40	37.30	37.00
TiO ₂	5.04	5.22	5.02	5.13	2.90	2.06	2.25
Al ₂ O ₃	13.62	13.78	13.85	13.92	16.10	17.30	17.20
Cr ₂ O ₃	0.00	0.00	0.00	0.00	0.02	0.00	0.00
FeO	15.62	16.17	16.14	16.08	21.20	21.90	21.40
MnO	0.25	0.25	0.22	0.24	0.24	0.21	0.19
MgO	13.89	13.48	13.54	13.65	8.80	8.91	8.80
CaO	0.07	0.04	0.12	0.14	0.26	0.13	0.13
Na ₂ O	0.62	0.59	0.64	0.69	0.06	0.05	0.08
K ₂ O	9.31	9.27	9.16	9.11	8.49	9.11	9.02
Total	94.86	95.20	94.97	95.18	95.47	96.97	96.07
Cations calculated on the basis of 22 oxygens							
Si	5.52	5.51	5.50	5.48	5.96	5.87	5.87
Al ^{IV}	2.43	2.46	2.48	2.48	2.04	2.13	2.13
Al ^{VI}	0.00	0.00	0.00	0.00	0.97	1.08	1.09
Ti	0.57	0.59	0.57	0.58	0.35	0.24	0.27
Fe ²⁺	1.98	2.05	2.05	2.03	2.82	2.88	2.83
Mn	0.03	0.03	0.03	0.03	0.03	0.03	0.03
Mg	3.14	3.04	3.06	3.08	2.09	2.09	2.08
Ca	0.01	0.01	0.02	0.02	0.04	0.02	0.02
Na	0.18	0.17	0.19	0.20	0.02	0.01	0.03
K	1.80	1.79	1.77	1.76	1.72	1.83	1.83
Total	15.67	15.64	15.67	15.67	16.04	16.18	16.18
#Mg	0.61	0.60	0.60	0.60	0.43	0.42	0.42

Misho data are from Shahzeidi [2013].

while the $^{143}\text{Nd}/^{144}\text{Nd}$ ratio is 0.512580 and 0.512736, respectively. Samples from Group 1 xenoliths plot within EMI and EMII endmembers while those from Group 2 fall within EMII and HIMU fields. To validate the results, some host volcanic rocks and pyroxenite xenoliths [Khezerlou *et al.*, 2017] from the study area and some Misho diorites [Shahzeidi, 2013] were used (Table 6). As illustrated in Figure 10, the host volcanic rocks fall between EMII and upper crust fields (closer to the upper crust). On the other hand, Group 2 pyroxenite xenolith samples fall within EMI and EMII fields while samples from Misho diorite plot far from

xenoliths and host volcanic rocks and closer to EMI endmember.

5.4. Thermobarometry

Since plagioclase in the hornblende xenoliths occurs as the intercumulus phase and therefore formed after cumulus amphibole, the plagioclase–amphibole pairs in these samples cannot be used for thermobarometry. Therefore, only amphibole was used for this purpose. According to Putirka [2016], if $K_D(\text{Fe–Mg})^{\text{amph–liq}}$ is within 0.28 ± 0.11 , then we may

Table 5. Whole-rock major and trace element data for xenoliths and volcanic rocks

Rock Sample	Group 1 xenolith				Group 2 xenolith		
	K	K-6	Kh-52	K-11	K-8	Kh-12	K-21
SiO ₂	43.86	44.20	47.86	48.32	42.52	45.77	44.33
TiO ₂	1.85	1.83	2.21	1.68	1.38	1.49	2.00
Al ₂ O ₃	12.39	12.34	15.10	16.26	15.33	15.50	18.29
Fe ₂ O ₃ (t)	12.62	12.26	14.31	11.67	12.61	12.00	12.24
FeO	7.13	6.93	7.54	6.16	7.32	6.54	6.93
Fe ₂ O ₃	4.56	4.44	5.69	4.65	4.30	4.55	4.43
MnO	0.16	0.16	0.20	0.21	0.16	0.16	0.16
MgO	12.11	11.71	5.42	7.29	13.03	7.69	6.66
CaO	10.40	10.33	8.44	10.28	10.42	9.97	10.19
Na ₂ O	2.25	2.28	3.24	3.73	2.49	2.87	2.72
K ₂ O	1.76	1.85	1.57	1.16	0.80	1.40	1.22
P ₂ O ₅	0.30	0.29	0.30	0.25	0.31	0.16	0.18
LOI	1.12	1.21	2.15	0.78	1.17	2.06	1.07
Total	98.82	98.48	100.80	101.61	100.22	99.08	99.07
Sr	282	300	434	568	303	312	494
Ba	356	361	541	592	127	137	261
V	383	380	308	299	242	263	267
Cr	95	84	275	331	342	310	123
Co	63	62	55	42	78	53	50
Ni	138	136	186	62	349	93	78
Y	27	26	32	40	11	21	14
Zr	57	57	81	58	28	47	54
Nb	5.9	6.0	24.5	9.7	7.9	7.2	11.1
Mo	0.5	0.3	0.9	0.5	0.3	0.7	1.0
La	12.5	10.4	15.4	17.6	7.8	6.4	6.4
Ce	34.8	27.4	39.1	38.5	19.0	16.5	16.3
Pr	5.0	4.1	4.1	4.6	2.5	2.1	1.7
Nd	24.5	19.9	16.7	19.7	10.8	10.2	7.5
Sm	6.4	5.1	3.7	4.6	2.2	2.7	1.6
Eu	1.8	1.4	1.2	1.4	0.8	1.0	0.7
Gd	6.7	5.1	4.0	4.8	2.0	3.0	1.6
Tb	0.9	0.7	0.6	0.7	0.3	0.5	0.2
Dy	4.9	3.8	3.8	4.5	1.5	2.9	1.3
Ho	0.9	0.7	0.8	1.0	0.3	0.6	0.3
Er	2.3	1.8	2.1	2.6	0.7	1.6	0.7
Yb	1.7	1.3	1.7	2.2	0.5	1.3	0.5
Lu	0.2	0.2	0.2	0.3	0.1	0.2	0.1

(continued on next page)

Table 5. (continued)

Rock	Group 1 xenolith				Group 2 xenolith		
Sample	K	K-6	Kh-52	K-11	K-8	Kh-12	K-21
Hf	2.1	2.2	2.1	1.7	0.7	1.5	1.3
W	19.3	15.9	31.3	38.3	19.9	32.3	28.1
Th	0.6	0.7	1.3	0.7	0.1	0.5	0.3
U	0.5	0.6	0.9	0.4	0.2	0.4	0.4
Cu	22.0	19.6	189.9	12.0	3.6	46.3	85.2
Zn	95.8	82.1	137.5	87.8	55.6	90.9	76.8
Ga	15.1	12.6	16.7	16.4	8.7	15.6	16.1
Rb	46.2	28.1	31.3	6.5	3.8	17.2	8.9
Cs	10.5	15.7	1.6	0.7	0.4	4.2	1.5
Ta	0.3	0.3	1.2	0.4	0.3	0.5	0.6
Pb	5.3	5.1	8.2	9.7	2.2	5.6	4.1
Ba/Nb	60	60	22	61	16	19	23
Ba/Ta	1090	1409	446	1367	417	296	432
Nb/La	0.5	0.6	1.6	0.6	1.0	1.1	1.7
(Ce/Yb)N	5.4	5.5	5.9	4.5	9.2	3.2	8.3
(Dy/Yb)N	1.9	1.9	1.4	1.3	1.9	1.5	1.7
Ce/Pb	6.6	5.3	4.7	4.0	8.7	2.9	4.0
#Mg	0.63	0.63	0.42	0.54	0.64	0.54	0.49

Major elements in wt%, trace elements and REE in ppm.

Table 6. Sr and Nd isotopic (whole rock) composition of xenoliths, a volcanic rock from NW Marand area and Misho diorites

Rock	Group 1 xenolith	Group 2 xenolith	Host volcanic	Pyroxenitic xenoliths			Misho diorites	
Sample	k-11	kh-12	v-kh-52	kh-62	kh-64	kh14	A2-43-1	A2-11-1
$^{87}\text{Sr}/^{86}\text{Sr}$	0.706291	0.704685	0.709545	0.707026	0.706825	0.70642	0.704861	0.705815
2σ	0.000003	0.000002	0.000002	0.000003	0.000003	0.000002	0.000013	0.000011
$^{143}\text{Nd}/^{144}\text{Nd}$	0.512580	0.512736	0.512561	0.512525	0.512482	0.512501	0.512155	0.512010
2σ	0.000003	0.000002	0.000002	0.000003	0.000002	0.000002	0.000012	0.000011
ϵNd	-1.06	1.96	-1.27	-1.98	-2.81	-2.45	-0.61	1.2

Host volcanic rock and pyroxenitic xenolith data are from Khezerlou *et al.* [2017] and Misho data are from Shahzeidi [2013].

assume that the amphibole is in equilibrium with the melt. The K_D from the investigated hornblende xenoliths is not equal to 0.28 ± 0.11 (Table 2). As a result, estimate may be obtained from Hammarstrom and Zen [1968] method ($P = -3.92 + 5.03 \text{ Al}_{\text{total}}$). This method independent of the temperature is solely based on the Al_{total} content of the amphibole. The

pressure of formation of amphibole minerals from Group 1 and Group 2 hornblende xenoliths using that equation ranges from 5.5 to 7 kbar and 9.5 to 10.5 kbar, respectively (Table 2). Also, according to the diagram of Al_{total} versus $\text{Fe}/\text{Fe}+\text{Mg}$, the formation pressure of amphiboles of Group 1 and Group 2 hornblende xenoliths has been estimated to be

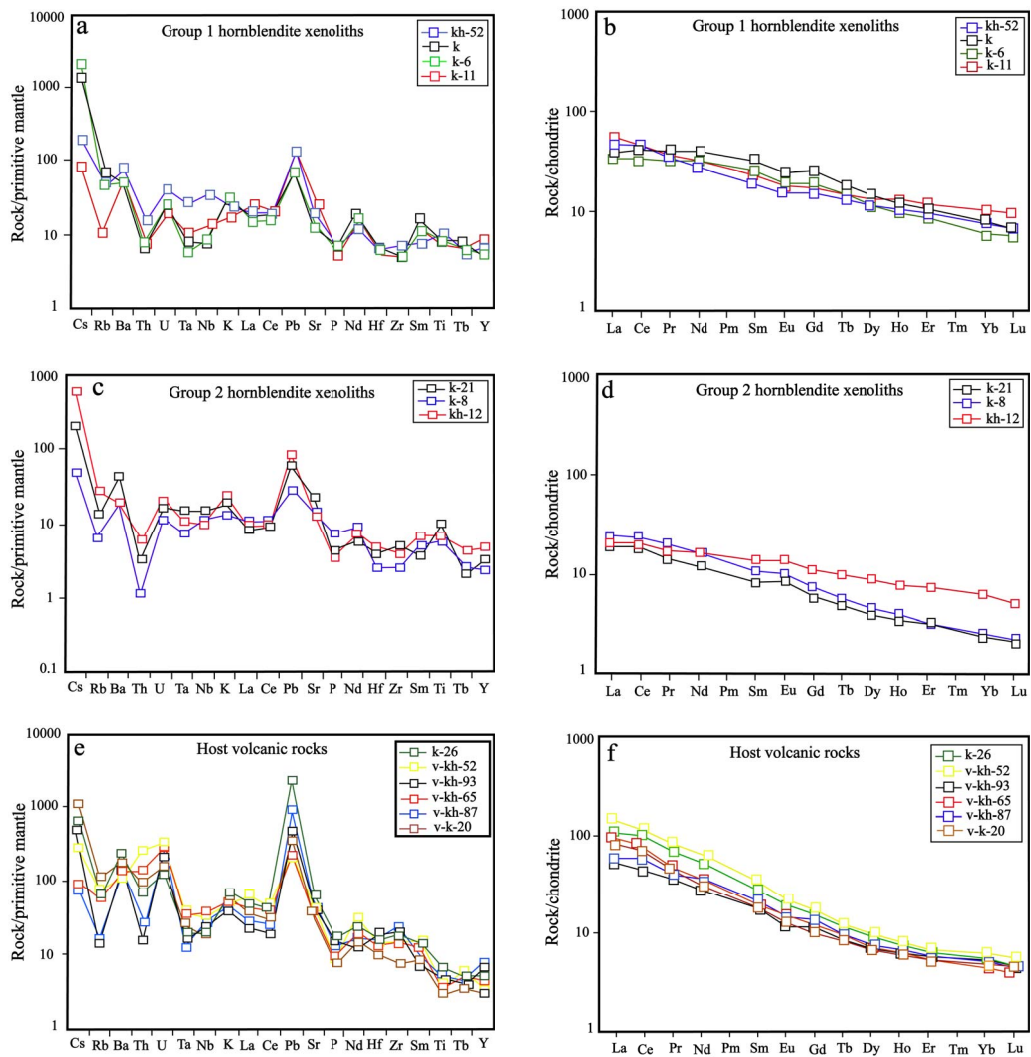


Figure 9. (a, c, e) Primitive mantle normalized spidergrams and (b, d, f) chondrite normalized REE patterns of hornblende xenoliths. Chondrite and primitive mantle values are from Boynton [1984] and Sun and McDonough [1989], respectively. Host volcanics data are from Khezerlou *et al.* [2017].

Table 7. Modal compositions of xenoliths estimated by using the whole rock and constituent minerals' major element compositions and a mixing model based on least squares method

Rock	Sample	Clinopyroxene	Amphibole	Plagioclase	Biotite	Total
Group 1 xenolith	k	1	81	8	10	100
	k-6		84	6.5	9.5	100
Group 2 xenolith	k-8		94	3	3	100

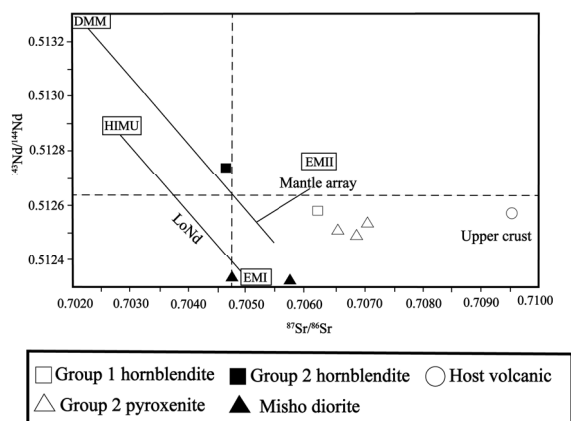


Figure 10. $^{143}\text{Nd}/^{144}\text{Nd}$ versus $^{87}\text{Sr}/^{86}\text{Sr}$ diagram for the whole rock of investigated samples. The fields for DMM, HIMU, EMI, EMII and upper crust are from Zindler and Hart [1986]. LoNd array is from Hart et al. [1986]. Misho data are from Shahzeidi [2013] and pyroxenite xenoliths and host volcanic data are from Khezerlou et al. [2017].

more than 5.5 kbar (Figure 11). Unlike xenoliths, the K_D of the investigated host volcanic rock (0.27–0.28) fall within the range 0.28 ± 0.11 , the chemical composition of their amphibole and whole rock is therefore suitable to be used for barometry, as stressed above. The estimated formation pressures for amphiboles of host volcanic rock (v-k-20 sample) according to the Equation (7c) $\{P(\text{kbar}) = -45.5 - 46.3[\ln(D_{\text{Al}}^{\text{anhyd}})] - 41.1[\ln(X_{\text{Al}_2\text{O}_3}^{\text{anhyd}})] + 439[X_{\text{P}_2\text{O}_5}^{\text{anhyd}}] + 26.6[\text{Al}^{\text{amph}}] + 22.5[\text{K}^{\text{amph}}] + 5.23[\ln(D_{\text{Na}}^{\text{anhyd}})]\}$ proposed by Putirka [2016] are 6–6.7 kbars.

The formation temperatures of amphibole minerals from Group 1 and Group 2 hornblende xenoliths and host volcanic rock (v-k-20 sample) estimated according to the Equation (5) $\{T\text{ }^\circ\text{C} = 1781 - 132.74[\text{Si}^{\text{amph}}] + 116.6[\text{Ti}^{\text{amph}}] - 69.41[\text{Fe}_t^{\text{amph}}] + 101.62[\text{Na}^{\text{amph}}]\}$ proposed by Putirka [2016] range from 890 to 940 $^\circ\text{C}$, 960 to 970 $^\circ\text{C}$, and 846 to 850 $^\circ\text{C}$, respectively (Table 2).

The crystallization depth of amphibole from Group 1 and Group 2 hornblende xenoliths and host volcanic rock was therefore estimated to be 17–20 km, 30–35 km, and 18–20 km, respectively. Since the crustal thickness from the study area has been estimated to range from 40 to 45 km [Dehghani and Makris, 1984], amphiboles from Group 1

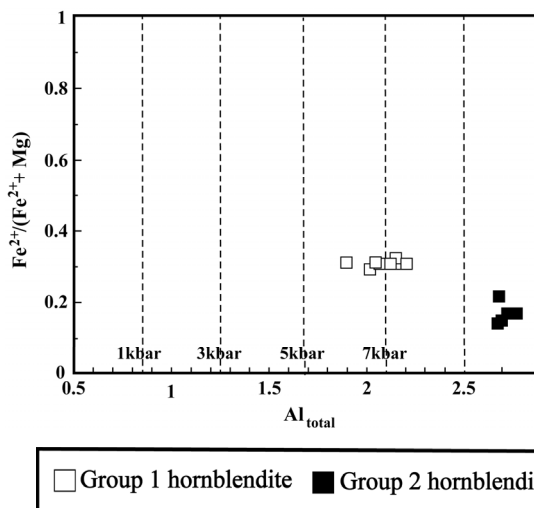


Figure 11. Plot of Al_{total} versus $\text{Fe}/\text{Fe}+\text{Mg}$ for amphiboles from the hornblende xenoliths [Hammarstrom and Zen, 1968].

hornblende xenoliths and host volcanic rocks (trachyandesite) might have been formed within this crust while those of Group 2 hornblende xenoliths have been also formed within the crust but closer to the crust–mantle boundary.

5.5. Oxygen fugacity

The differences observed in the Fe^{3+} content of clinopyroxene from the investigated samples could be ascribed to different oxidation and oxygen fugacity states of the magma they crystallized from [Canil and Fedortchouck, 2000, Aydin, 2008]. The Na, Al(IV), and Fe^{3+} contents of the clinopyroxenes from host volcanic rocks are higher than those of the clinopyroxene from Group 1 hornblende xenoliths, suggesting that they formed at higher oxidation conditions [Schweitzer et al., 1979]. The location of samples in Figure 4d supports such an inference. It can also be seen in this figure (Figure 4d) that clinopyroxenes from the host volcanic rock are formed in conditions of high oxidation compared to the pyroxenite xenoliths of the study area [Khezerlou et al., 2017] and Misho diorites [Shahzeidi, 2013]. Also, the location of samples in Figure 5d indicates crystallization of amphibole from Group 1 and Group 2 hornblende xenoliths and host volcanic rock under high oxidation conditions.

As can be seen in Figure 5d, the amount of Fe^{2+} in amphiboles from Group 2 hornblendite xenoliths is lower than those of amphiboles from Group 1 hornblendite xenoliths and host volcanic rocks, indicating that they formed at higher oxidation conditions. Assuming that the formation pressure of amphiboles is directly related to oxygen fugacity [Stein and Dietl, 2001], it is likely that amphiboles from Group 2 were formed at higher pressures than those from Group 1 and host volcanic rocks, a result consistent with the barometric estimates.

5.6. Characteristics of magma sources

The changes in composition from core to rim of amphibole from Group 1 are normally associated with a temperature increase. These compositional changes in amphibole probably suggest the injection of pulses of magma.

The amphiboles and biotites from Group 2 hornblendite xenoliths do not show clear zoning (Tables 2 and 4, respectively), suggesting their gradual crystallization and equilibration with the melt during the crystallization process. On the other hand the biotites from Group 1 hornblendite xenoliths are zoned with a decrease of Al_2O_3 , SiO_2 , and CaO associated to an increase of MgO , FeO , and K_2O from core to rim (Table 4). It seems that during the crystallization of biotites, plagioclases also crystallized and as Si, Ca, and Al are preferably incorporated within the structure of plagioclase, that process could explain the lower concentrations of those elements in the rim of biotite crystals. As mentioned in the petrography section, plagioclases from Group 1 hornblendite xenoliths are mainly intercumulus and it seems therefore that plagioclases and biotites were not accumulated simultaneously. The normal zoning observed in the plagioclase phenocrysts from the host volcanic rocks (Table 3) indicates a temperature decrease of the residual melt as crystallization proceeded.

The petrographic study (for example the presence of some coarse-grained amphiboles and biotites and euhedral amphiboles) confirms the cumulus texture of the xenoliths. Positive anomalies of U, Ba, Ti, and K in hornblendite xenoliths are probably related to the accumulation process of amphibole and biotite (Figures 9a, c).

Biotites from hornblendite xenoliths and host volcanic rocks display very low Al(VI) content, which

is sometimes totally absent (Table 4), suggesting a magmatic origin [Nachit *et al.*, 2005]. The position of xenoliths and host volcanic rocks in the ternary diagram MgO , $\text{FeO}+\text{MnO}$, and 10TiO_2 also indicates a magmatic origin. Since the amphiboles and biotites in the hornblendite xenoliths and host volcanic rocks are of igneous type, due to the fact that amphibole and biotite are hydrous minerals and they are formed in hydrous conditions, it may be inferred that their parental magmas contained relatively high amounts of water [Otten, 1984].

The anorthite content of plagioclases typically gives constraint on the water content of their parental magma [e.g. Sisson and Grove, 1993]. According to Sisson and Grove [1993], the distribution coefficient of calcium–sodium between plagioclase and melt is sensitive to $P_{\text{H}_2\text{O}}$, and varies from 1 to 5.5 under water-free and water-saturated conditions, respectively. As a result, the high content of anorthite is related to the high water pressure in the melt. Thus, the plagioclases from the Group 2 hornblendite xenoliths might have crystallized from a magma with a higher H_2O content than that of the magma from which the Group 1 hornblendite xenoliths and host volcanic rocks crystallized (Figure 6). However, the anorthite content of plagioclase may also change with the degree of crystal fractionation. The difference in isotope ratios suggests that the xenolith groups and the host volcanic rock were formed from different parental melts.

According to Anderson and Smith [1995] the Mg\# of amphibole is strongly dependent on the degree of crystallization. Therefore, the difference in the Mg\# of amphiboles in Group 1 (0.67–0.72) and Group 2 (0.79–0.85) xenoliths and host magma samples (0.54–0.67) could suggest different degrees of crystallization of their respective parental melts. Yet, the high Mg\# of amphibole is also related to high oxygen fugacity. Therefore, the high Mg\# of amphiboles in Group 2 could also point to a higher oxygen fugacity compared to Group 1 and host volcanic rocks, as suggested by the position of the samples in Figure 5d.

The Ti content in clinopyroxene may give indication on the degree of depletion of the magma mantle source [Pearce and Norry, 1979]. In this regard, the difference in Ti concentration of clinopyroxene from Group 1 hornblendite xenoliths (0.19–0.21) and host volcanic rocks (1.21–1.28) may be attributed to variable depletion and degree of partial melting of their

respective mantle sources. It indicates a higher enriched source for the parental magma of host volcanic rocks compared to that of the Group 1 hornblende xenoliths. This is also confirmed by the $^{86}\text{Sr}/^{87}\text{Sr}$ isotopic ratios (Figure 10).

The lower LREE, Pb, Th, Ba and U contents and low $^{86}\text{Sr}/^{87}\text{Sr}$ ratio in Group 2 xenoliths compared to those of Group 1 indicate a more depleted mantle source for this group (Table 6). Besides, the difference in $^{86}\text{Sr}/^{87}\text{Sr}$ and $^{143}\text{Nd}/^{144}\text{Nd}$ values of Group 1 and Group 2 xenoliths and host volcanic rocks suggests also a difference in composition of their respective mantle sources [Zhang *et al.*, 2006].

Positive Pb anomaly in xenoliths and host volcanic rocks indicates either the influence of mantle wedge metasomatism through fluids from subducting oceanic plate for the sources of magmas or contamination of magmas by the crustal lithosphere [Atherton and Ghni, 2002]. Positive Ba, La, Cs, K, and U anomalies associated with negative Nb and Ta anomalies may be explained by magma contamination by crustal materials [Hofmann, 1997].

In all the investigated xenoliths, a negative Th anomaly is observed (Figures 9a, c). This element has a low mobility in arc settings [Pearce and Peate, 1995] due to its very low solubility in subduction zone fluids. The observed negative Th anomaly is therefore probably due to the effect of fluids released from a subducted oceanic plate. Similarly to host volcanic rocks [Khezerlou *et al.*, 2017], negative Nb and Ta anomalies are also observed in hornblende xenoliths and probably also reflect a subduction-related magmatism (Figures 9a, c, e) [Saunders *et al.*, 1980, Kuster and Harms, 1998]. According to Ionov and Hofmann [1995], amphibole is a very suitable mineral for storing Nb and Ta in the upper mantle and can impart negative anomalies of Nb and Ta on subduction zone magmas. Due to the high thickness of the continental crust in the study area (40–45 km), contamination of magma by crustal materials can also be effective.

As shown in Table 5, the $(\text{Ce}/\text{Pb})_{\text{N}}$ ratio in the investigated xenoliths, similarly to that of host volcanic rocks [Khezerlou *et al.*, 2017], is lower than 18 while for MORB and oceanic arc environments it is 47 and 27, respectively [Hofmann *et al.*, 1986]. This low ratio in xenoliths and host volcanic rocks probably implies the presence of crustal materials in their parental magma sources [Yang *et al.*, 2005]. High

abundance of LREE and LILE in hornblende xenoliths agrees with the involvement of a metasomatized upper mantle in their genesis. Previous studies on volcanic rocks [Ahmadzadeh *et al.*, 2010] and pyroxenite xenoliths [Khezerlou *et al.*, 2017] from the study area also evidenced a metasomatized mantle source leading to the enriched characteristics of the parental magmas.

The higher abundances of U, Ba, and K in Group 1 xenoliths compared to those of Group 2 could be explained by the higher biotite modal content of the former as these three elements are preferentially incorporated by biotite than by amphibole. In addition, the higher MREE content characterizing most of the Group 1 hornblende xenoliths compared to those of Group 2 and host volcanic rocks could be related to their higher amphibole modal content, which is also in agreement with the higher Ti content of Group 1 hornblende xenoliths.

The negative Eu anomaly in Group 1 hornblende xenoliths, similar to that in host volcanic rocks [Khezerlou *et al.*, 2017], evidence early fractionation of Ca-plagioclase from the parental magma during its journey in the crust [Willson, 1989, Martin, 1999, Wu *et al.*, 2003]. On the other hand, the positive Eu anomaly in Group 2 hornblende xenoliths is associated with high plagioclase (labradorite) modal content.

As shown in Figure 8, the amount of SiO_2 , K_2O , and Na_2O in the xenoliths is lower than that of the host volcanic rocks, and this is associated with a higher abundance of LREE (including: La, Ce, Pr and Nd) in the host lava relative to xenoliths. The higher contents of all these elements in the host lava could be related to the contamination of its parental melt by crustal material. The $^{86}\text{Sr}/^{87}\text{Sr}$ ratio of the host volcanic rock (0.709545) is higher than those of the xenoliths (Group 1 = 0.706291 and Group 2 = 0.704685), but its $^{143}\text{Nd}/^{144}\text{Nd}$ ratio does not differ much from that of the xenoliths. As magma contamination by crustal materials increases the $^{86}\text{Sr}/^{87}\text{Sr}$ ratio and decreases the $^{143}\text{Nd}/^{144}\text{Nd}$ ratio, it therefore seems that magma contamination by crustal material cannot explain the high $^{86}\text{Sr}/^{87}\text{Sr}$ ratio of host volcanic rocks. It is likely that the main cause of the differences observed between xenoliths and host volcanic rocks is related to a more enriched mantle source for the parental magma of host volcanic rocks. This explanation could also apply to the difference in the content of LREE of Group 1 and Group 2

xenoliths. The higher LREE content and $^{86}\text{Sr}/^{87}\text{Sr}$ ratio of Group 1 xenoliths compared to those of Group 2 xenoliths could be indeed related to a more enriched mantle source for the parental magma of the Group 1 xenoliths.

The high HREE content of Group 1 xenoliths compared to that of Group 2 xenoliths is probably due to the presence of clinopyroxene in Group 1 samples, because these elements are preferentially incorporated in clinopyroxene. On the other hand the low amounts of MREE of Group 2 could be explained by a lower modal content of amphibole in Group 2 compared to Group 1 xenoliths [Gertisser and Keller, 2000].

The Yb content in the investigated xenoliths is lower than 4 ppm (on average 1.16). Thus, it could be considered that these xenoliths did not crystallize from primary magma [Irving and Frey, 1978]: which suggests in turn that the parental magmas of xenoliths probably underwent fractional crystallization processes of garnet and clinopyroxene prior to xenolith crystallization. The lack of garnet (Group 1 and 2) and paucity (Group 1) or lack of clinopyroxene (Group 2) in the investigated xenoliths seem to confirm this.

5.7. *Generation of the xenoliths*

Many studies have related intra-continental alkaline rocks to the presence of mantle plumes [Hofmann and White, 1982, Willson, 1989]. Magmatism associated with mantle plumes is characterized by a very high production of melts [Willson, 1989], which contrasts with the limited outcrops of alkaline rocks in the investigated area. Usually the shape of mantle plumes are symmetric [Willson, 1989], but Khezerlou *et al.* [2017] have shown that the volcanic shape of the investigated area and of the Uromieh Dokhtar belt is not symmetrical being oriented northwest–southeast and almost parallel to the Zagros orogenic belt. Altogether, geochemical features of host volcanic rocks and the two groups of xenoliths such as Nb and Ta depletion are inconsistent with magmas originated from the activity of a mantle plume.

The two groups of investigated hornblendite xenoliths and host volcanic rocks display distinct LILE and LREE enrichment, Ta and Nb depletion and high Ba/Ta and Ba/Nb ratios, which are among the characteristics of subduction-derived magmatic

rocks. Previous studies attributed the magmatism of Uromieh-Dokhtar zone to the subduction of the Neotethys underneath the Iranian continental crust [e.g. Nicolas, 1989, Hassanzadeh, 1993, Ghasemi and Talbot, 2006] probably during Middle Cretaceous [Ghasemi and Talbot, 2006]. This Neotethys ocean closed during the Upper Cretaceous [Nicolas, 1989]. The subduction of the Neotethys led to the metasomatism of the mantle wedge located above the subducting plate.

The geochemical features of the investigated xenoliths as well as their $^{86}\text{Sr}/^{87}\text{Sr}$ and $^{143}\text{Nd}/^{144}\text{Nd}$ ratios, are in agreement with the occurrence of such type of metasomatism in the northern part of Uromieh Dokhtar magmatic belt. As the subduction continued, the subducted oceanic plate was broken (slab break-off). The uplift of hot asthenosphere through the resulting slab window led to the melting of the metasomatized lithospheric mantle [Keskin, 2003, Jahangiri, 2007, Kheirkhah *et al.*, 2009]. Considering the relative age of the host volcanic rocks (Plio-Quaternary), it appears that the magmatism of the study area occurred at later stages following the collision. Post-collision tension processes activated faults in the study area. As mentioned in the geological setting section, the studied alkaline rocks are commonly located along the main faults. Therefore it seems that the movement of the main faults (especially North Tabriz Fault, North Misho and Tasuj faults) has provided a path for the lavas carrying the investigated xenoliths to penetrate the continental crust. As a result, magmas were trapped during their ascent to the surface at different levels of the crust. Subsequent to their crystallization, amphiboles and micas accumulated on the floor of some temporary deep seated magma chambers. Xenoliths eventually reached the ground surface through the later magmatic activity.

6. Conclusions

Field surveys performed in the present work show that alkaline volcanic rocks from the study area are Plio-Quaternary in age. The results of petrographic studies evidence cumulus processes in these magmatic xenoliths. There are differences in REE content and $^{86}\text{Sr}/^{87}\text{Sr}$ and $^{143}\text{Nd}/^{144}\text{Nd}$ ratios as well as in the chemical composition of their constituent minerals between Group 1 and Group 2

hornblendite xenoliths. This indicates that their respective parental magmas likely were derived from different mantle sources.

The high LREE and LILE contents of both groups of hornblendite xenoliths imply the presence of metasomatized enriched mantle sources beneath the study area. It is likely that as the parental magma ascends upwards some minerals, including olivine and clinopyroxene, separated from the magma after crystallization. The resulting magmas were emplaced at different depths within the crust. An explanation for this observation is that micas and amphiboles from the xenoliths accumulated on the floor of magmatic reservoirs after crystallization in the crust and reached the ground surface through a later magmatic activity. Thermometry results using amphiboles show that crystallization depth of Group 1 and Group 2 xenoliths range from 17 to 20 km and from 30 to 35 km within the crust, respectively.

The difference in isotope ratios and the composition of the clinopyroxenes suggest that the hornblendite xenoliths and the pyroxenite xenoliths from the study area were formed from different parental melts.

Finally by comparing $^{86}\text{Sr}/^{87}\text{Sr}$ and $^{143}\text{Nd}/^{144}\text{Nd}$ ratios and chemical composition of minerals from the investigated xenoliths and Misho diorites, we may conclude that hornblendite xenoliths are not linked to the Misho diorites.

Acknowledgments

This research is a part of the Ph.D. dissertation of the first author which he accomplished with the support of the Vice Chancellor for Research and High Education of Tabriz University (Iran). Hereby, we thank authorities of Tabriz University for their help and cooperation. The authors also thank the Laboratoires Géosciences Environnement Toulouse and Géosciences Marines (Brest) of France that allowed us to perform the various mineralogical and geochemical analyses.

References

- Aghazadeh, M., Prelević, D., Badrzadeh, Z., Braschi, E., Bogaard, P., and Conticelli, S. (2015). Geochemistry Sr–Nd–Pb isotopes and geochronology of amphibole and mica-bearing lamprophyres in north-western Iran: implications for mantle wedge heterogeneity in a paleo-subduction zone. *Lithos*, 216–217, 352–369.
- Ahmazadeh, G., Jahangiri, A., Lentz, D., and Mojtahe, M. (2010). Petrogenesis of Plio-Quaternary post-collisional ultrapotassic volcanism in NW of Marand, NW Iran. *J. Asian Earth Sci.*, 39, 37–50.
- Alavi, M. (2004). Regional stratigraphy of the Zagros folded-thrust belt of Iran and its proforeland evolution. *Am. J. Sci.*, 304, 1–20.
- Anderson, J. L. and Smith, D. R. (1995). The effects of temperature and $f\text{O}_2$ on the Al-in-hornblende barometer. *Am. Mineral.*, 80, 549–559.
- Atherton, M. P. and Ghni, A. A. (2002). Slab break-off: a model for Caledonian, late granite syn-collisional magmatism in the orthotectonic (metamorphic) zone of Scotland and Donegal, Ireland. *Lithos*, 62, 65–85.
- Aydin, F. (2008). Contrasting complexities in the evolution of calc-alkaline and alkaline melts of the Niğde volcanic rocks, Turkey: textural, mineral chemical and geochemical evidence. *Eur. J. Mineral.*, 20, 101–118.
- Azimzadeh, Z. (2013). *Geochemistry and petrogenesis of Misho Mafic Complex (NW Iran)*. PhD thesis, Tabriz University. pp. 160 (in Persian with English abstract).
- Barrat, J. A., Yamaguchi, A., Greenwood, R. C., Bohn, M., Cotton, J., Benoit, M., and Franchi, I. A. (2007). The Stannern trend eucrites: contamination of main group eucritic magmas by crustal partial melts. *Geochim. Cosmochim. Acta*, 71, 4108–4124.
- Blatter, D. L. and Carmichael, I. S. E. (1998). Hornblende peridotite xenoliths from central Mexico reveal the highly oxidized nature of subarc upper mantle. *Geology*, 26, 1035–1038.
- Boynton, W. V. (1984). Geochemistry of the rare earth elements: meteorite studies. In Henderson, P., editor, *Rare Earth Element Geochemistry*, pages 63–114. Elsevier, Amsterdam.
- Canil, D. and Fedortchouk, Y. (2000). Clinopyroxene-liquid partitioning for vanadium and the oxygen fugacity during formation of cratonic and oceanic mantle lithosphere. *J. Geophys. Res.*, 105, 26003–26016.
- Capedri, S., Venturelli, G., Salvioli, M. E., Crawford, A. J., and Barbieri, M. (1989). Upper-mantle xenoliths and megacrysts in an alkali basalt from Tal-

- lante, south-eastern Spain. *Eur. J. Mineral.*, 1, 685–699.
- Carraro, A. and Visonà, D. (2003). Mantle xenoliths in Triassic camptonite dykes of the Predazzo Area (Dolomites, Northern Italy): petrography, mineral chemistry and geothermobarometry. *Eur. J. Mineral.*, 15, 103–115.
- Conticelli, S., Avanzinelli, R., Poli, G., Braschi, E., and Giordano, G. (2013). Shift from lamproitellike to leucititic rocks: Sr–Nd–Pb isotope data from the Monte Cimino volcanic complex vs. the Vico stratovolcano, Central Italy. *Chem. Geol.*, 353, 246–266.
- Cotten, J. L., Dez, A., Bau, M., Mauray, R., Dulsky, P., Fourcade, S., Bohn, M. R., and Brousse, R. (1995). Origin and anomalous rare-earth element and yttrium enrichments in subaerially exposed basalts: evidence from French Polynesia. *Chem. Geol.*, 119, 115–138.
- Cox, K. G., Bell, J. D., and Pankhurst, R. J. (1979). *The Interpretation of Igneous Rocks*. Allen and Unwin, London. page 450.
- Deer, W. A., Howie, R. A., and Zussman, J. (1966). *An Introduction to the Rock Forming Minerals*. Longmans, London. page 528.
- Dehghani, G. A. and Makris, T. (1984). The gravity field and crustal structure of Iran. *Neues Jahrb. Geol. Paläontol. Abh.*, 168, 215–229.
- Deng, J. H., Yang, X. Y., Sun, W. D., Huang, Y., Chi, Y. Y., Yu, L. F., and Zhang, Q. M. (2012). Petrology, geochemistry, and tectonic significance of Mesozoic shoshonitic volcanic rocks, Luzong volcanic basin, eastern China. *Int. Geol. Rev.*, 54, 714–736.
- Dewey, J. F., Hempton, M. R., Kidd, W. S. F., Saroglu, F., and Sengor, A. M. C. (1986). Shortening of continental lithosphere: the neotectonics of Eastern Anatolia—a young collision zone, in collision tectonics. *Geol. Soc. Spec. Publ.*, 19, 3–36.
- Downes, H., Kostoula, T., Iones, P., Beard, D., Thirlwall, F., and Bodinier, L. L. (2002). Geochemistry and Sr–Nd isotopic compositions of mantle xenoliths from the Monte Vulture carbonatite melilitite volcano, central southern Italy. *Contrib. Mineral. Petrol.*, 144, 78–93.
- Downes, H., Upton, B. G. I., Handisyde, E., and Thirlwall, M. F. (2001). Geochemistry of mafic and ultramafic xenoliths from Fidra (Southern Uplands, Scotland): implications for lithospheric processes in Permo-Carboniferous times. *Lithos*, 58, 105–124.
- Emami, H. (1981). *Geologie de la region de Qom-Aran (Iran) contribution a l'etude denamique et geochemique du volcanisme Teriaire del' Iran centaral*. PhD thesis, University of Grenoble. pp. 513.
- Farhoudi, G. (1978). A comparison of Zagros geology to island arcs. *Geology*, 86, 323–334.
- Frey, F. A. and Prinz, M. (1978). Ultramafic inclusions from San Carlos, Arizona; petrologic and geochemical data bearing on their petrogenesis. *Earth Planet. Sci. Lett.*, 38, 129–176.
- Gertisser, R. and Keller, J. (2000). From basalt to dacite: origin and evolution of the calc alkaline series of Salina, Aeolian Arc, Italy. *Contrib. Mineral. Petrol.*, 139, 607–626.
- Ghasemi, A. and Talbot, C. J. (2006). A new tectonic scenario for the Sanandaj-Sirjan Zone (Iran). *J. Asian Earth Sci.*, 26, 683–693.
- Gill, R. C. O., Aparicio, A., El Azzouzi, M., Hernandez, J., Thirlwall, M. F., Bourgeois, J., and Marriner, G. F. (2004). Depleted arc volcanism in the Alboran Sea and shoshonitic volcanism in Morocco: geochemical and isotopic constraints on Neogene tectonic processes. *Lithos*, 78, 363–388.
- Hammarstrom, J. M. and Zen, E.-a. (1968). Aluminum in hornblende: an empirical igneous geobarometer. *Am. Mineral.*, 719, 1297–1313.
- Hart, S. R., Gerlach, D. C., and White, W. M. (1986). A possible new Sr–Nd–Pb mantle array and consequences for mantle mixing. *Geochim. Cosmochim. Acta*, 50, 1551–1557.
- Hassanzadeh, J. (1993). *Metallogenic and tectonomagmatic events in the SE sector of the Cenozoic active continental margin of Iran (Shahre-Babak area, Kerman Province)*. PhD thesis, University of California, Los Angeles. pp. 204.
- Hofmann, A., Jochum, K., Seufert, M., and White, M. (1986). Nb and Pb in oceanic basalts: new constraints on mantle evolution. *Earth Planet. Sci. Lett.*, 33, 33–45.
- Hofmann, A. W. (1997). Mantle geochemistry: the message from oceanic volcanism. *Nature*, 385, 219–229.
- Hofmann, A. W. and White, W. M. (1982). Mantle plumes from ancient oceanic crust. *Earth Planet. Sci. Lett.*, 57, 421–436.
- Ionov, D. A. and Hofmann, A. W. (1995). Nb–Ta rich mantle amphiboles and mica: implication for subduction-related metasomatic trace element fractionations. *Earth Planet. Sci. Lett.*, 131, 341–

- 356.
- Irving, A. J. and Frey, F. A. (1978). Distribution of trace elements between garnet megacrysts and host volcanic liquids of kimberlitic to rhyolitic composition. *Geochim. Cosmochim. Acta*, 42, 771–787.
- Irving, A. I. (1980). Petrology and geochemistry of composite ultramafic xenoliths in alkalic basalts and implications for magmatic processes within the mantle. *Am. J. Sci.*, 280, 389–426.
- Jahangiri, A. (2007). Post-collisional Miocene adakitic volcanism in NW Iran: geochemical and geodynamic implications. *J. Asian Earth Sci.*, 30, 433–447.
- Keskin, M. (2003). Magma generation by slab steepening and breakoff beneath a subduction-accretion complex: an alternative model for collision-related volcanism in Eastern Anatolia, Turkey. *Geophys. Res. Lett.*, 30, 8046–8050.
- Kheirkhah, M., Allen, M. B., and Emami, M. (2009). Quaternary syn-collision magmatism from the Iran/Turkey borderlands. *J. Volcanol. Geotherm. Res.*, 182, 1–12.
- Kheirkhah, M., Neill, I., and Allen, M. B. (2015). Petrogenesis of OIB-like basaltic volcanic rocks in a continental collision zone: late Cenozoic magmatism of Eastern Iran. *J. Asian Earth Sci.*, 106, 19–33.
- Khezerlou, A., Amini, S., and Moayyed, M. (2008). Petrology, geochemistry and mineral chemistry of potassic and ultrapotassic rocks of North West Marand, NW Iran. *Kharazmi Sci.*, 3, 183–204. (in Persian with English abstract).
- Khezerlou, A., Grégoire, M., Nasir, A., Mohsen, M., Ahmad, J., and Kilzi, M. (2020). Origin and formation process of Gabbro and Diorite Xenoliths in the northern part of Uromieh-Dokhtar Magmatic Belt, NW Iran: constraints from mineral and whole-rock chemistries. *J. Geol.*, 128, 227–246.
- Khezerlou, A., Nasir, A., Grégoire, M., Mohsen, M., and Ahmad, J. (2017). Geochemistry and mineral chemistry of pyroxenite xenoliths and host volcanic alkaline rocks from northwest of Marand (NW Iran). *Mineral. Petrol.*, 111(6), 865–885.
- Kuster, D. and Harms, U. (1998). Post-collisional potassic granitoids from the southern and northern parts of the late neoproterozoic East Africa Orogen: a review. *Lithos*, 45, 177–195.
- Leake, B. E., Woolley, A. R., Arps, C. E. S., Birch, W. D., Gilbert, M. C., Grice, J. D., Hawthorne, F. C., Kato, A., Kisch, H. J., Krivovichev, V. G., Linthout, K., Laird, J., Mandarino, J. A., Maresch, W. V., Nichel, E. H., Rock, N. M. S., Schumacher, J. C., Smith, D. C., Stephenson, N. C. N., Ungaretti, L., Whittaker, E. J. W., and Youzhi, G. (1997). Nomenclature of amphiboles: report of the subcommittee on amphiboles of the International Mineralogical Association, Commission on New Minerals and Mineral Names. *Can. Mineral.*, 35, 219–246.
- Leterrier, J., Maury, R. C., Thonon, P., Girard, D., and Marchal, M. (1982). Clinopyroxene composition as a method of identification of the magmatic affinities of paleo-volcanic series. *Earth Planet. Sci. Lett.*, 59, 139–154.
- Martin, H. (1999). Adakitic magmas: modern analogues of Archaean granitoids. *Lithos*, 46, 411–429.
- Morimoto, N., Fabrice, J., Ferguson, A., Ginzburg, I. V., Ross, M., Seifert, F. A., Zussman, J., Akoi, K., and Gottardi, G. (1988). Nomenclature of pyroxenes. *Mineral. Mag.*, 52, 535–555.
- Morimoto, N. and Kitamura, M. (1983). Q-J diagram for classification of pyroxenes. *J. Jpn. Assoc. Mineral. Petrol. Econ. Geol.*, 78, 132–152. (in Japanese).
- Nachit, H., Ibhi, A., Abia, E. H., and Ohoud, M. B. (2005). Discrimination between primary magmatic biotites, reequilibrated biotites and neoformed biotites. *C. R. Geosci.*, 337, 1415–1420.
- Nicolas, A. (1989). *Structures in Ophiolites and Dynamics of Oceanic Lithosphere*. Kluwer, Dordrecht. page 367.
- Omran, J., Agard, P., Whitechurch, H., Bennoit, M., Prouteau, G., and Jolivet, L. (2008). Arc-magmatism and subduction history beneath the Zagros Mountains, Iran: a new report of adakites and geodynamic consequences. *Lithos*, 106, 380–398.
- Orejana, D., Villaseca, C., and Paterson, B. A. (2006). Geochemistry of pyroxenitic and hornblenditic xenoliths in alkaline lamprophyres from the Spanish central system. *Lithos*, 86, 167–196.
- Otten, M. T. (1984). The origin of brown hornblende in the Artfjället gabbro and dolerites. *Contrib. Mineral. Petrol.*, 86, 189–199.
- Pearce, J. A. and Norry, M. J. (1979). Petrogenetic implications of Ti, Zr, Y, and Nb variations in volcanic rocks. *Contrib. Mineral. Petrol.*, 69, 33–47.
- Pearce, J. A. and Peate, D. W. (1995). Tectonic implications of the composition of volcanic arc magmas. *Annu. Rev. Earth Planet. Sci.*, 23, 251–285.
- Pin, C. and Santos Zalduegui, J. F. (1997). Sequential separation of light rare-earth elements, thorium and uranium by miniaturized extraction

- chromatography: application to isotopic analyses of silicate rocks. *Anal. Chem. Acta*, 339, 79–89.
- Putirka, K. (2016). Amphibole thermometers and barometers for igneous systems, and some implications for eruption mechanisms of felsic magmas at arc volcanoes. *Am. Mineral.*, 101, 841–858.
- Rajabi, S., Torabi, G., and Arai, S. (2014). Oligocene crustal xenolith-bearing alkaline basalt from Jandaq area (Central Iran): implications for magma genesis and crustal nature. *Isl. Arc.*, 23, 125–141.
- Saadat, S. and Stern, C. R. (2012). Petrochemistry of a xenolith bearing neogene alkali olivine basalt from northeastern Iran. *J. Volcanol. Geotherm. Res.*, 225–226, 13–29.
- Saccani, E., Azimzadeh, Z., Dilek, Y., and Jahangiri, A. (2013). Geochronology and petrology of the early carboniferous Misho Mafic complex (NW Iran), and implications for the melt evolution of Paleotethyan rifting in Western Cimmeria. *Lithos*, 162, 264–278.
- Saunders, A. D., Tarney, J., and Weaver, S. D. (1980). Transverse geochemical variations across the Antarctic Peninsula: implications for the genesis of calc-alkaline magmas. *Earth Planet. Sci. Lett.*, 46, 344–360.
- Schweitzer, E. L., Papike, J. J., and Bence, A. E. (1979). Statistical analysis of clinopyroxenes from deep-sea basalts. *Am. Mineral.*, 64, 501–513.
- Sengor, A. M. C. and Kidd, W. S. F. (1979). Post-collisional tectonics of the Turkish–Iranian plateau and a comparison with Tibet. *Tectonophysics*, 55, 361–376.
- Shahzeidi, M. (2013). *Geochemistry and petrology of Misho granitoid from south west marand (NW Iran)*. PhD thesis, Tabriz University. pp. 161 (in Persian with English abstract).
- Sial, A. N., Ferreira, V. P., Fallick, A. E., Jeronimo, M., and Cruz, M. (1998). Amphibole-rich clots in calcalkalic granitoids in the Borborema province northeastern Brazil. *J. South Am. Earth Sci.*, 11, 457–471.
- Sisson, T. W. and Grove, T. L. (1993). Experimental investigation of the role of H₂O in calc-alkaline differentiation and subduction zone magmatism. *Contrib. Mineral. Petrol.*, 113, 143–166.
- Speer, J. A. (1984). Mica in igneous rocks. In Bailey, S. W., editor, *Micas Rev. Mineral. Geochem.*, volume 13, pages 299–356.
- Stein, E. and Dietl, E. (2001). Hornblende thermometry of granitoids from the central Odenwald (Germany) and their implication for the Geotectonics Development of the Odenwald. *Mineral. Petrol.*, 72(1–3), 185–207.
- Su, B. X., Chung, S. L., Zarrinkoub, M. H., Pang, K. N., Chen, L., Ji, W. Q., Brewer, A., Ying, J. F., and Khatib, M. M. (2014). Composition and structure of the lithospheric mantle beneath NE Iran: constraints from mantle xenoliths. *Lithos*, 202–203, 267–282.
- Sun, S. S. and McDonough, W. F. (1989). Chemical and isotopic systematics of oceanic basalts: implications for mantle composition and processes. In Saunders, A. D. and Norry, M. J., editors, *Magma-tism in the Ocean Basins*, volume 42 of *Geol. Soc. Lond. Spec. Publ.*, pages 313–345. Geological Society, London.
- Turner, S., Arnaud, N., Liu, J., Rogers, N., Hawkesworth, C., Harris, N., Kelley, S., Calsteren, P. V., and Deng, W. (1996). Post-collision, Shoshonitic volcanism on the Tibetan plateau: implications for convective thinning of the lithosphere and the source of ocean island basalts. *J. Petrol.*, 37(1), 45–71.
- Willson, M. (1989). *Igneous Petrogenesis; A Global Tectonic Approach*. Unwin Hyman, London. page 466.
- Witt-Eickschen, G. and Kramm, U. (1998). Evidence for the multiple stage evolution of the subcontinental lithospheric mantle beneath the Eifel (Germany) from pyroxenite and composite pyroxenite peridotite xenoliths. *Contrib. Mineral. Petrol.*, 131, 258–272.
- Wu, L., Guo, X., and Banuelos, G. S. (2003). Selenium and sulfur accumulation and soil selenium dissipation in planting of four herbaceous plant species in soil contaminated with drainage sediment rich in both selenium and sulfur. *Int. J. Phytomed.*, 5, 25–40.
- Yang, J. H., Chung, S. L., Wilde, S. A., Wu, F., Chu, M. F., Lo, C. H., and Fan, H. (2005). Petrogenesis of post-orogenic syenites in the Sulu orogenic belt, East China: geochronological, geochemical and Nd–Sr isotopic evidence. *Chem. Geol.*, 214, 99–125.
- Yousefzadeh, M. and Sabzehei, M. (2012). Thermobarometry of dacites from Markoh (northeast of Birjand) and its amphibolite xenoliths. *Iran. J. Crystallography Mineralogy*, 1, 43–52. (in Persian with English abstract).
- Zhang, H., Zhang, L., Harris, N., Jin, L., and Honglin,

- Y. (2006). U–Pb zircon ages, geochemical and isotopic compositions of granitoids in Songpan-Garze fold belt, eastern Tibetan plateau: constraints on petrogenesis and tectonic evolution of the basement. *Contrib. Mineral. Petrol.*, 152, 75–88.
- Zhang, Y., Yu, K., and Qian, H. (2018). LA-ICP-MS analysis of Clinopyroxenes in Basaltic Pyroclastic Rocks from the Xisha Islands, Northwestern South China Sea. *Minerals*, 8, article no. 575.
- Zindler, A. and Hart, S. R. (1986). Chemical geodynamics. *Annu. Rev. Earth Planet. Sci.*, 14, 493–571.



Perspectives on alkaline magmas / *Perspectives sur les magmas alcalins*

Crystallisation sequence of a REE-rich carbonate melt: an experimental approach

Valentin Mollé^{*, a}, Fabrice Gaillard^{*, a}, Zineb Naby^a, Johann Tuduri^{*, a, b},
Ida Di Carlo^{*, a} and Saskia Erdmann^{*, a}

^a ISTO, UMR 7327, Université d'Orléans, CNRS, BRGM, F-45071 Orléans, France

^b BRGM, F-45060 Orléans, France

E-mails: valentin.molle@etu.univ-orleans.fr (V. Mollé),

fabrice.gaillard@cnrs-orleans.fr (F. Gaillard), zineb.naby@univ-orleans.fr (Z. Naby),

j.tuduri@brgm.fr (J. Tuduri), ida.di-carlo@cnrs-orleans.fr (I. Di Carlo),

saskia.erdmann@cnrs-orleans.fr (S. Erdmann)

Abstract. Carbonatites host Earth's main REE deposits, with bastnaesite (LREE)CO₃F being the main economic REE-bearing mineral. However, bastnaesite mineralisation processes are debated between hydrothermal or magmatic origin. This study aims to assess if bastnaesite can be magmatic, and to characterise the REE behaviour during carbonatite crystallisation. Crystallisation experiments have been performed from 900 to 600 °C at 1 kbar, on a REE-rich calciocarbonatitic composition. REE-bearing calcite is the dominant crystallising mineral, driving the residual melt towards natrocarbonatitic compositions. Both halogens (i.e., Cl and F) and water decrease the temperature of calcite saturation. REE are slightly incompatible with calcite: for all REE, partition coefficients between carbonate melt and calcite are comprised between 1 and 11, and increase with temperature decrease. Britholite (REE, Ca)₅((Si,P)O₄)₃(F,OH) crystallises at high temperatures (700–900 °C), while pyrochlore (Ca,Na,REE)₂Nb₂O₆(OH,F) crystallises at low temperatures (600–700 °C), as well as REE-rich apatite (600–650 °C). No bastnaesite is found in crystallisation experiments. We thus performed a bastnaesite saturation experiment at 600 °C. The bastnaesite-saturated melt contains 20 wt% of REE: such magmatic saturation is unlikely to happen in nature. Textural evidences imply a Na, Cl, REE-rich fluid at high temperatures and hydrous conditions. We propose that fluids are the main mineralising agent for bastnaesite at hydrothermal stage (<600 °C).

Keywords. Carbonatite, Rare earth elements, Experimentation, Crystallisation, Calcite, Bastnaesite, Natrocarbonatite.

1. Introduction

Carbonatites are magmatic rocks with more than 50% of carbonates [Le Maitre, 2002] and constitute the main rare earth element (REE) deposits on Earth [Verplanck et al., 2016]. With only 527 described

occurrences [Woolley and Kjarsgaard, 2008], carbonatites are rare on the terrestrial surface. Only one occurrence of active carbonatitic magmatism is known: the Ol Doinyo Lengai volcano, in Tanzania [Keller and Zaitsev, 2012]. Although this volcano mainly produces highly peralkaline silicate lavas such as phonolites and nephelinites, it is also the only one to produce alkaline carbonate lavas called natrocarbonatites [Klaudios and Keller, 2006].

* Corresponding author.

The CaCO_3 – Na_2CO_3 – K_2CO_3 system has been experimentally studied to understand natrocarbonatite genesis. Cooper *et al.* [1975] established a phase diagram in the system Na_2CO_3 – CaCO_3 , showing the saturation of nyerereite $\text{Na}_2\text{Ca}(\text{CO}_3)_2$ to divide the system into two subsystems, an alkali- and a calcium-dominated one, with their own eutectics. However, Jago and Gittins [1991] showed that F drastically decreases the temperature of calcite saturation, potentially unifying the two subsystems by suppressing the calcite–nyerereite eutectic.

As natural natrocarbonatites are halogen-rich [Keller and Zaitsev, 2012], Weidendorfer *et al.* [2017] tested this hypothesis by saturating a natural natrocarbonatite with calcite, and proposed a phase diagram in which the calcite–nyerereite eutectic is shifted into a peritectic point at a lower temperature, effectively making a genetic link possible between calcio- and natrocarbonatites.

Extrusive carbonatite occurrences are often described as coexisting with alkaline silicate rocks in the field [Bell *et al.*, 1999, Mitchell, 2005, Woolley and Kjarsgaard, 2008]. The production of carbonatites by immiscibility with an alkaline silicate melt is a well-studied and recognised process [Freestone and Hamilton, 1980, Brooker, 1998, Martin *et al.*, 2013, Naby *et al.*, 2020]. Among the experimental studies on the immiscibility processes between carbonate and silicate melts, some have tackled the REE behaviour between both melts [Veksler *et al.*, 1998, 2012, Martin *et al.*, 2013, Naby *et al.*, 2020]. REE enrichments in the carbonate melt at immiscibility are highly variable. However, the results from Naby *et al.* [2020] demonstrate that carbonate melts can be extremely Ca- and REE-rich if the immiscible silicate melt is strongly differentiated. Such REE-rich carbonate melts could be related to carbonatitic REE deposits.

In natural carbonatites related to REE deposits, REE are mostly contained in different REE minerals, with bastnaesite-(Ce) $(\text{LREE})\text{CO}_3\text{F}$ being the main mineral of interest [Verplanck *et al.*, 2016]. Field literature still debates the magmatic or hydrothermal origin of this mineral [Giebel *et al.*, 2017, Cheng *et al.*, 2018, Guo and Liu, 2019, Anenburg *et al.*, 2020]. Experimental literature on the subject is scarce and inconclusive, with Jones and Wyllie [1986] failing to crystallise magmatic bastnaesite in a CaCO_3 – $\text{Ca}(\text{OH})_2$ – $\text{La}(\text{OH})_3$ system. As such, we currently have

little knowledge on the whereabouts of magmatic REE minerals in carbonatites.

To better understand REE mineral crystallisation in carbonatites, magmatic crystallisation processes need to be assessed. As Ca- and REE-rich carbonate melts can be produced by immiscibility [Naby *et al.*, 2020], the crystallisation sequence of such melts inside the CaCO_3 – Na_2CO_3 – K_2CO_3 system needs to be defined, as well as the REE behaviour along this sequence. Here, we present new crystallisation experiments on a REE-rich calciocarbonatitic composition, in order to define the phase assemblage and characterise the REE behaviour between REE minerals and carbonate melt at the magmatic stage. These crystallisation experiments have been completed with a bastnaesite saturation experiment to determine the magmatic saturation of bastnaesite.

2. Experimental approach

2.1. Starting mixture

Because of extensive alteration, natural carbonatite compositions are not representative of primary carbonatitic melts [Bell *et al.*, 1999, Verplanck *et al.*, 2016]. To determine a theoretical, REE-rich primary carbonatitic composition, we used a natural rock composition database [GEOROC database (<http://georoc.mpch-mainz.gwdg.de/georoc/>, accessed: 2019/01/25) and De Moor *et al.*, 2013, Mattsson *et al.*, 2013, Mana *et al.*, 2015] to first determine a silicate melt composition likely to be in equilibrium with an immiscible REE-rich carbonate melt, based on the work of Naby *et al.* [2020]. This silicate melt, alkaline and differentiated, corresponds to a phonolitic composition. We then used an experimental immiscibility database [Freestone and Hamilton, 1980, Hamilton *et al.*, 1989, Jones *et al.*, 1995, Kjarsgaard *et al.*, 1995, Brooker, 1998, Kjarsgaard, 1998, Veksler *et al.*, 2012, Martin *et al.*, 2013, Massuyeau *et al.*, 2015, Naby *et al.*, 2020] and the model of Naby *et al.* [2020] to determine partition coefficients for major and trace elements.

The carbonatite composition has been calculated using these partition coefficients. This composition was then synthesised using carbonates and oxide powders (Table 1). Details on the calculation to infer a primary carbonatite composition and on the preparation of the starting mixture are given in the Supplementary material.

2.2. Experimental strategy

At each P–T condition, up to three samples have been prepared: (1) with the starting composition (“EXP-P” set, Table 2); (2) with the starting composition and additional water, at a ratio of 95:5 (“EXP-W5” set, Table 2); and (3) with the starting composition and additional pure graphite, at a ratio of 97:3 (“EXP-G3” set, Table 2). Because of powder hygroscopy, the starting mixture holds around 2 wt% H₂O (CHNX analysis, Flash 2000 Thermo). The addition of 5 wt% of water makes EXP-W5 hold around 7 wt% H₂O. The addition of graphite in EXP-G3 reduces the system and consumes water, making them near-anhydrous. Twenty crystallisation experiments have been conducted at a pressure of 1 kbar, and at temperatures between 900 and 600 °C with 50 °C steps (Table 2). Experiments lasted from three days to two weeks.

Bastnaesite is stable below 760 °C at 1 kbar [Hsu, 1992]. To test magmatic bastnaesite saturation, one saturation experiment has been conducted at 600 °C using the starting mixture and additional crushed bastnaesite from the Mianing-Dechang REE belt, at a ratio of 80:20 (“EXP-600B” experiment, Table 2).

Experiments were performed in a vertical internally heated pressure vessel (IHPV) at the Institut des Sciences de la Terre d’Orléans (ISTO). 20 to 30 mg of material were loaded into Au capsules with a diameter of 2.5–2.9 mm and a length of 10 to 15 mm. Sensor capsules were added to the experiments to measure the oxygen fugacity inside the IHPV. These sensor capsules were water-saturated and contained two Ni–Pd–NiO pellets separated by zirconium oxide powder. Ni and Pd molar proportions in the pellets were 0.5–0.5 and 0.15–0.85. We used a double-winding Kanthal furnace allowing near-isothermal conditions (gradient < 2–3 °C/cm) along a 3 cm long hot spot [Andújar *et al.*, 2013]. The capsules were loaded in an alumina tube fixed at the top of the furnace (hot spot) by a Pt wire. Two K-type thermocouples were placed on top and bottom of the alumina tube to monitor temperature, with an accuracy up to ± 5 °C [Andújar *et al.*, 2013]. The capsules were pressurised with 998 bars of Ar and 2 bars of H₂. Pressure monitoring was performed through a transducer calibrated against a Heise Bourdon gauge, accurate up to ±2 MPa [Andú-

Table 1. Starting mixture composition, a REE-rich calciocarbonatite

Components	Starting mixture
SiO ₂	0.36
TiO ₂	0.13
Al ₂ O ₃	0.05
FeO	5.20
MnO	0.50
MgO	1.58
CaO	32.75
Na ₂ O	12.91
K ₂ O	1.61
P ₂ O ₅	0.59
SrO	0.11
BaO	0.24
Cl	1.44
F	4.43
CO ₂	34.56
La	10,610
Ce	12,760
Pr	1,765
Nd	5,753
Sm	751
Eu	108
Gd	543
Tb	65
Dy	368
Y	2,108
Ho	81
Er	152
Yb	127
Lu	16
Nb	248
Total	100.00

Upper part: major elements (wt%). Lower part: trace elements (ppm). Total counts the abundance of trace elements and is in wt%.

jar *et al.*, 2013]. At the end of the experiments, a fast isobaric quench (100 °C/s) was ensured using a drop technique, by electrically fusing the Pt wire [Di Carlo, 2006].

Table 2. Experimental conditions and run products. Partial pressure of H₂ is always 2 bars. Gold capsules were used

Experiment	Set	H ₂ O (wt%)	C (wt%)	Bast (wt%)	P (bar)	T (°C)	ΔNNO	Duration	Phases
EXP-900P	EXP-P	0	0	0	1000	900	-0.29 ± 0.73	38 h and 45 min	Liq, Fl, Brt, OxFe, Dpt
EXP-900W5	EXP-W5	5	0	0	1000	900	-0.29 ± 0.73	38 h and 45 min	Liq, Fl, Brt, OxFe, Dpt
EXP-850P	EXP-P	0	0	0	1000	850	n.a.	73 h and 50 min	Liq, Fl, Brt, OxFe, Dpt
EXP-850W5	EXP-W5	5	0	0	1000	850	n.a.	73 h and 50 min	Liq, Fl, Brt, OxFe, Dpt
EXP-850G3	EXP-G3	0	3	0	1000	850	n.a.	73 h and 50 min	Liq, Fl, Brt, OxFe, Cal, Dpt
EXP-800P	EXP-P	0	0	0	1000	800	0.71 ± 0.41	89 h and 30 min	Liq, Fl, Brt, OxFe, Cal, Dpt
EXP-800W5	EXP-W5	5	0	0	1000	800	0.71 ± 0.41	89 h and 30 min	Liq, Fl, Brt, OxFe, Cal, Dpt, Hl
EXP-800G3	EXP-G3	0	3	0	1000	800	0.71 ± 0.41	89 h and 30 min	Liq, Fl, Brt, OxFe, Cal, Dpt
EXP-750P	EXP-P	0	0	0	1000	750	1.11 ± 0.51	135 h and 45 min	Liq, Fl, Brt, OxFe, Cal, Dpt
EXP-750W5	EXP-W5	5	0	0	1000	750	1.11 ± 0.51	135 h and 45 min	Liq, Fl, Brt, OxFe, Cal, Dpt
EXP-750G3	EXP-G3	0	3	0	1000	750	1.11 ± 0.51	135 h and 45 min	Liq, Fl, Brt, OxFe, Cal, Hl
EXP-700P	EXP-P	0	0	0	1000	700	0.55 ± 0.33	163 h and 00 min	Liq, Fl, Brt, OxFe, Cal, Pyr
EXP-700W5	EXP-W5	5	0	0	1000	700	0.55 ± 0.33	163 h and 00 min	Liq, Fl, Brt, OxFe, Cal, Hl
EXP-700G3	EXP-G3	0	3	0	1000	700	0.55 ± 0.33	163 h and 00 min	Liq, Fl, Brt, OxFe, Cal, Pyr
EXP-650P	EXP-P	0	0	0	1000	650	0.54 ± 0.27	396 h and 20 min	Liq, Fl, OxFe, Cal, Pyr, Phg, Ap
EXP-650W5	EXP-W5	5	0	0	1000	650	0.54 ± 0.27	396 h and 20 min	Liq, Fl, Brt, OxFe, Cal, Pyr, Phg, Ap
EXP-650G3	EXP-G3	0	3	0	1000	650	0.54 ± 0.27	396 h and 20 min	Liq, Fl, OxFe, Cal, Pyr, Phg, Ap
EXP-600P	EXP-P	0	0	0	1000	600	n.a.	311 h and 20 min	Liq, Fl, OxFe, Cal, Pyr, Ap
EXP-600W5	EXP-W5	5	0	0	1000	600	n.a.	311 h and 20 min	Liq, Fl, OxFe, Cal, Pyr, Ap
EXP-600G3	EXP-G3	0	3	0	1000	600	n.a.	311 h and 20 min	Liq, Fl, OxFe, Cal, Pyr, Phg, Ap
EXP-600B	EXP-B	0	0	20	1000	600	n.a.	311 h and 20 min	Liq, Fl, Brt, OxFe, Cal, Dpt, Frg, Bast

H₂O, C and Bast are respectively pure water, pure graphite and natural bastnaesite added to the starting mixture. ΔNNO values are representative of the oxygen fugacity inside the IHPV. The global ΔNNO of the experiments is equal to 0.53 ± 0.21 (n.a. = not analysed). Liq: carbonate melt; Cal: calcite; OxFe: iron oxide; Fl: vesicle (fluid indicator); Dpt: deposit-like vesicle filling; Hl: halite; Brt: britholite; Phg: phlogopite; Ap: fluorapatite; Pyr: pyrochlore; Bast: bastnaesite; Frg: fergusonite.

2.3. Analysis methods

Electronic images (back-scattered electrons: BSE) of the samples have been taken with a Merlin Compact ZEISS scanning electron microscope (SEM), equipped with a GEMINI I column (ISTO, Orléans). Energy dispersive spectroscopy (EDS) has been done with a Bruker QUANTAX XFlash® 6|30 to identify the composition of the different phases. Acquisition parameters were: working distance 10 mm; voltage 15 kV. A TESCAN SEM (FEG-Schottky cathode) has also been used (Bureau de Recherches Géologiques et Minières – BRGM, Orléans), with a working distance of 15 mm and a 15 kV voltage.

Major elements have been analysed with a CAMECA SXFive electron probe micro analyzer (EPMA) (ISTO, Orléans), using wavelength dispersive spectrometry (WDS), with acquisition parameters equal to 15 kV and 6 nA. Standards and counting times were: albite (Na: 10 s, Si: 10 s) – Al_2O_3 (Al: 10 s) – orthoclase (K: 10 s) – andradite (Ca: 10 s) – MnTiO_3 (Mn: 10 s, Ti: 10 s) – Fe_2O_3 (Fe: 10 s) – vanadinite (Cl: 30 s) – topaz (F: 30 s) – dolomite (Mg: 10 s) – NdPO_4 (P: 10 s). The carbonate melt does not quench into a homogeneous glass, so the melt quench products have been analysed with a 5 to 50 μm diameter defocused beam to account for this heterogeneity and to avoid element loss. Routine EPMA analyses were conducted on the sensor pellets to analyse the NiPd alloys. The ΔNNO was then calculated using Taylor *et al.* [1992] and Frost [1991] equations. ΔNNO values are available in Table 2. We specify here that these values are a measurement of the oxygen fugacity inside the IHPV, and may be different than the oxygen fugacity inside the capsules.

LA-ICP-MS (Laser Ablation Inductively Coupled Mass Spectrometry) has been used to quantify the trace elements composition of the experimental run products. Two devices have been used: an Agilent 7500 CS with a 193 nm laser (Laboratoire Magmas et Volcans – LMV, Clermont-Ferrand), and an Agilent 8900-QQQ with a RESOLUTION-SE 193 nm Ar-F laser (ISTO, Orléans). Analysed isotopes were ^{43}Ca , ^{44}Ca , ^{88}Sr , ^{89}Y , ^{93}Nb , ^{137}Ba , ^{139}La , ^{140}Ce , ^{141}Pr , ^{146}Nd , ^{147}Sm , ^{153}Eu , ^{157}Gd , ^{159}Tb , ^{163}Dy , ^{165}Ho , ^{166}Er , ^{172}Yb and ^{175}Lu . The fluence was set to 2 $\text{J}\cdot\text{cm}^{-2}$; and the frequency was set to 2 Hz for the analysis of melts, and to 1 Hz for the analysis of crystals. Phases were analysed with a 5 to 50 μm diameter beam. The anal-

ysis sequence consisted of 20 to 30 s of background followed by 60 to 80 s of ablation, with dwell times of 50 ms per isotope. Raw data was processed using Glitter 4.4 [Van Achterberg *et al.*, 2001]. NIST610 glass [Pearce *et al.*, 1997] was used as an external standard. NIST612 glass [Pearce *et al.*, 1997] and BCR-2G glass [Rocholl, 1998] were used as quality controls. The CaO wt% content of phases, determined at EPMA, was used as the internal standard, for ^{43}Ca contents. Repeat analyses on selected phases and standard analyses ensured that data collected with both devices were within uncertainty.

3. Results

3.1. Carbonatite crystallisation

Table 2 summarises the experiments performed during this study. Figure 1 shows the different phases observed in all the samples.

The carbonate melt quenched into dendritic calcites intergrown with quenched Ca,Na,K-carbonates (Figure 1A). As the temperature decreases, quenched Ca,Na,K-carbonates become dominant and coarser. Calcite is the dominant crystallising phase in the system. Calcite crystals are round to sub-euhedral (Figure 1A), and more abundant with decreasing temperature.

Several minor phases are also observed. Ti-rich iron oxides form sub-euhedral crystals which are often grouped (Figure 1B). Britholite ($\text{REE}, \text{Ca})_5(\text{Si}, \text{P})\text{O}_4)_3(\text{F}, \text{OH})$, a REE-phosphosilicate isomorphic with apatite, occurs only at high temperatures (700–900 °C). Britholite crystals are often grouped, forming small euhedral, hexagonal, columnar prisms (Figure 1B), around 5 to 15 μm in size. Phlogopite is observed at low temperatures, crystallising as euhedral hexagonal prisms, or anhedral elongated crystals. Small, euhedral fluorapatites are found as clusters at low temperatures. Pyrochlore ($\text{Ca}, \text{Na}, \text{REE})_2\text{Nb}_2\text{O}_6(\text{OH}, \text{F})$ [Verplanck *et al.*, 2016] crystallises below 700 °C in small anhedral clusters.

A fluid phase is present as hinted by spherical vesicles in all experiments (Figure 1A,C). The vesicular texture is significantly more abundant in EXP-G3. A Na-rich carbonate lining may be observed on the vesicle walls, which will be referred to as vesicle filling (Figure 1C). This vesicle filling is significantly more present in EXP-W5 and is only observed at

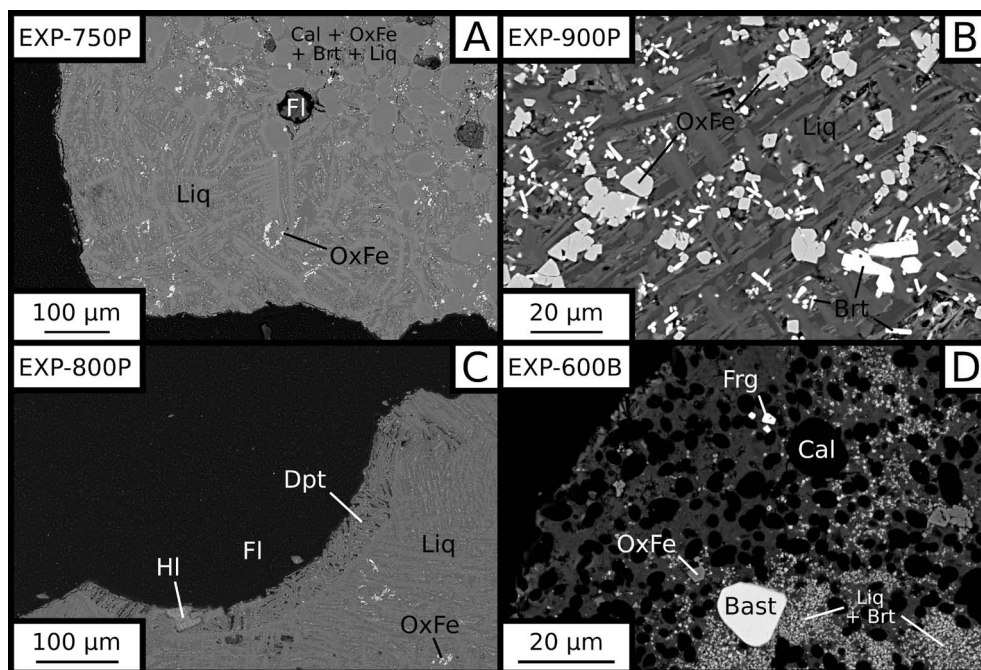


Figure 1. BSE images of samples. (A) melt and segregated calcite, iron oxides and britholite. (B) Euhedral britholites and iron oxides. (C) Vesicle filling hosting anhedral halite inside a vesicle. (D) Bastnaesite and fergusonite in the saturation experiment. Liq: carbonate melt. Cal: calcite. OxFe: iron oxide. Fl: vesicle (fluid indicator). Dpt: deposit-like vesicle filling. Hl: halite. Brt: britholite. Bast: bastnaesite. Frg: fergusonite.

temperatures higher than 700 °C. Halite is occasionally seen both inside vesicles and fractures. Mostly anhedral (Figure 1C), it can also be found as euhedral cubes.

The bastnaesite saturation experiment features a different mineralogy than all of the crystallisation experiments set (Table 2). Large anhedral crystals of bastnaesite are common in the saturation experiment (Figure 1D), whereas bastnaesite is never found in crystallisation experiments. Fergusonite (REE)NbO₄ is also found in the saturation experiment as euhedral crystals (Figure 1D). Britholite is found as large clusters of small anhedral crystals even at this low temperature (600 °C).

At high temperatures (≥ 750 °C), we observe crystal-free zones in carbonate melts and cumulates of crystals (Figure 1A). Some small cumulates are observed along the melt–fluid vesicles interface.

Figure 2 presents a phase diagram in a T–H₂O space for our crystallisation experiments, with H₂O being the wt% H₂O content of the system, for all type of samples as described in Section 2.2). We specify

here that the hydration degree of the system (wt% H₂O in the capsule) is not the same as the hydration degree of the carbonate melt (wt% H₂O dissolved in the melt). The water content of the melt could not be quantified in this study, therefore the water effect discussed here is only qualitative.

Our results suggest that britholite is stable at high temperatures, concentrating REE, Ca, Si, P and F, whereas phlogopite and REE-rich fluorapatite are stable at low temperatures, the former concentrating Si and the latter concentrating REE, Ca, P and F. Pyrochlore crystallises at low temperatures, concentrating Nb and REE. By using the Na-rich vesicle filling and the halite in fluid vesicles as markers for a Na,Cl-rich fluid, we may define a stability domain for this fluid at high temperatures and for hydrous conditions (Figure 2).

3.2. Carbonate melt and calcite composition

The composition of carbonate melts and calcite across all experiments is detailed in the Supplementary material. Carbonate melt from samples

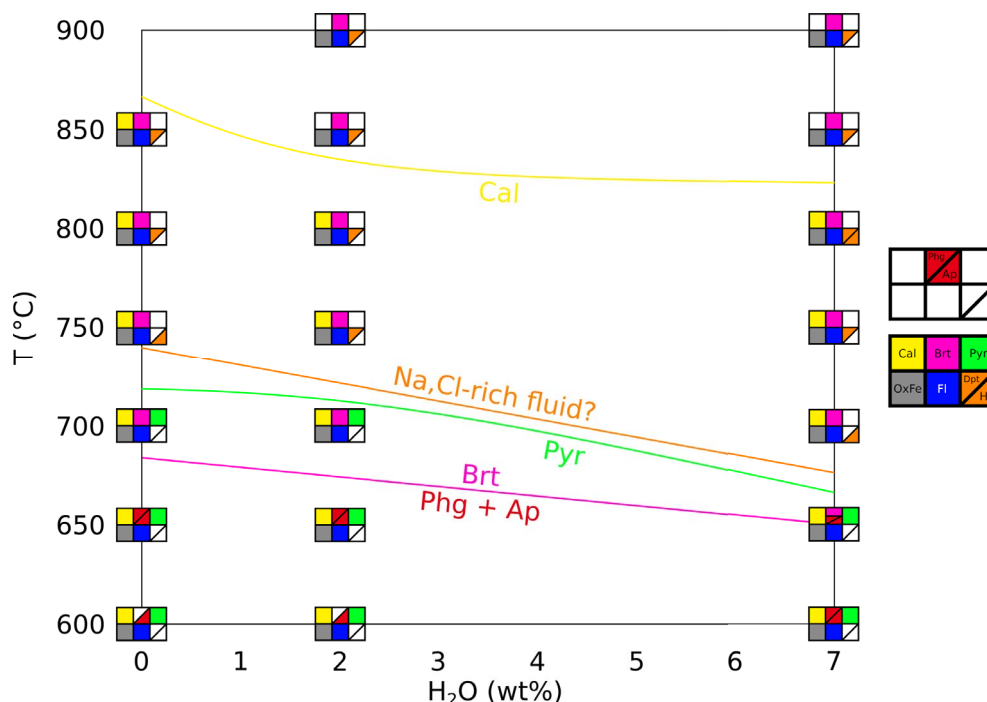


Figure 2. Phase diagram of the REE-rich carbonatite, showing temperature and water effects. Calcite (yellow) starts crystallising at lower temperatures in presence of water. Fluid phase (blue) and iron oxides (grey) are always observed. Britholite (pink) crystallises at high temperature and is replaced by phlogopite (rare, presumed in EXP-600G3 and EXP-600P) and fluorapatite at lower temperature (red). Pyrochlore (green) is a rare phase at low temperature. We may draw a stability domain for a Na,Cl-rich fluid (orange) at high temperature and high water content. Cal: calcite. OxFe: iron oxide. Fl: vesicle (fluid indicator). Dpt: deposit-like vesicle filling. Hl: halite. Brt: britholite. Phg: phlogopite. Ap: fluorapatite. Pyr: pyrochlore.

synthesised at 600 °C in crystallisation experiments have not been analysed, as melt areas were too small.

Below 850 °C, the CaO content of the carbonate melt decreases with temperature as calcite crystallises, from 36.60 ± 1.12 wt% at 900 °C to 20.92 ± 1.43 at 650 °C for EXP-P. The CaO content is ~5 wt% lower in EXP-G3 than in EXP-W5 (Figure 3A). Calcite crystallisation is the main cause for CaO depletion and chemical evolution in the melt. Therefore, we can use the CaO content of the melt as a simple “differentiation index”: with CaO depletion in the melt, the differentiation increases. This qualitative index allows to compare all types of samples into one trend.

Along this index, with a CaO decrease from ~37.5 to ~17.5 wt% in the melt, alkali ($\text{Na}_2\text{O} + \text{K}_2\text{O}$) increases from ~13.5 to ~27.9 wt% and halogens (Cl + F) from ~6.1 to ~9.1 wt%. The REE total also increases

slightly in the melt, from ~26,400 to ~45,000 ppm (Figure 3B). REE enrichment trends are almost parallel in this semi-log space: all REE show a similar behaviour, and REE proportions stay globally the same. Water does not seem to influence the REE content of the melt.

REE content in calcite does not change with temperature, but evolves with the presence of water in the system. Ce content is similar in EXP-P and EXP-G3 (~3,000 ppm), and is lower in EXP-W5 (~2,000 ppm). Only EXP-850G3 yields higher Ce content (~4,000 ppm).

3.3. Partition coefficients

Partition coefficients for carbonate melt and calcite ($D^{\text{Liq/Cal}}$) are detailed in the Supplementary material. REE are slightly incompatible with calcite compared

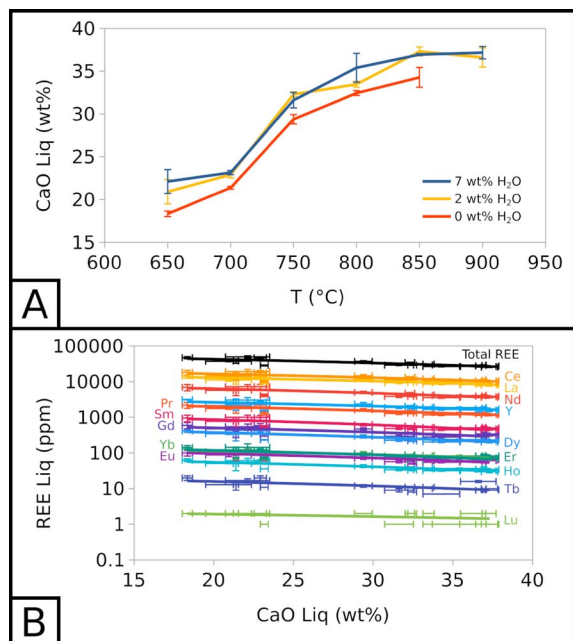


Figure 3. Compositional evolution of carbonate melt. (A) CaO in the carbonate melt as a function of temperature and water content. (B) REE in the carbonate melt as a function of CaO in the carbonate melt. 7 wt% H₂O corresponds to EXP-W5, 2 wt% H₂O to EXP-P, and 0 wt% H₂O to EXP-G3.

to the carbonate melt: for all REE, the partition coefficients are comprised between 1 and 11. Light REE (from La to Sm) have slightly higher partition coefficients than the other REE. From Eu to Yb, partition coefficients display nearly flat patterns, with the exception of a small positive anomaly for Y (Figure 4). Lu concentrations are too low in carbonate melt (1 to 2 ppm, Figure 3B) and calcite (below detection limit to 1 ppm) to determine reliable partition coefficients.

All REE partition coefficients increase as the temperature decreases (Figure 4A), showing that REE are less favourably incorporated in calcite as the temperature decreases: $D_{\text{REE}}^{\text{Liq/Cal}}$ values increase by 3 to 5 with a 200 °C decrease. REE partition coefficients also seem to increase with the water content of the system (Figure 4B). At 800 °C, EXP-800G3 and EXP-800P show almost identical partition coefficients, whereas EXP-800W5 shows slightly higher values.

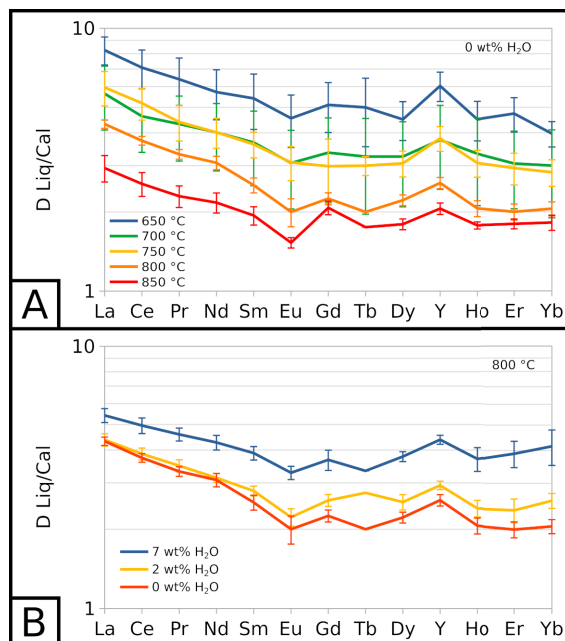


Figure 4. Partition coefficients for REE between carbonate melt and calcite ($D_{\text{REE}}^{\text{Liq/Cal}}$). (A) $D_{\text{REE}}^{\text{Liq/Cal}}$ at near-anhydrous conditions, depending on temperature. (B) $D_{\text{REE}}^{\text{Liq/Cal}}$ at 800 °C, depending on water in the system. 7 wt% H₂O corresponds to EXP-W5, 2 wt% H₂O to EXP-P, and 0 wt% H₂O to EXP-G3. Lu partition coefficients are not plotted as Lu concentrations in both phases are too low to determine reliable partition coefficients.

3.4. Composition of the vesicle filling

As suggested by textural evidences, the vesicle filling is likely to originate from the fluid phase, thus providing an indirect evidence of the fluid composition (Figure 1C). Vesicle filling composition is detailed in the Supplementary material.

The mean alkali content of the vesicle filling is constant with temperature, but increases with the water content in the sample, evolving from 21.30 ± 1.56 wt% (EXP-W5) to 23.51 ± 1.70 wt% (EXP-P) to 27.18 ± 0.21 wt% (EXP-G3). However, EXP-850W5 (Table 2) is significantly different from other experiments, which may be due to off-target analysis.

Cl content in the vesicle filling seems unaffected by the water content in the system but is highly

affected by temperature. Across all experiments, at 900 °C, Cl represents ~2 wt% of the vesicle filling. This value decreases to ~0.5–1 wt% at 850 and 800 °C, and increases to ~3–3.5 wt% at 750 °C (Figure 5A). The vesicle filling is also F-rich, with concentrations between ~8 to ~14 wt% across all experiments, without a clear influence of temperature or water content in the system. As Cl and F, respectively, barely exceed 1 wt% and 8 wt% in crystallisation experiments, the vesicle filling is especially halogen-rich in comparison with the melt.

In all crystallisation experiments, we detected ~10,000 to ~20,000 ppm of Ce in the vesicle filling, without a clear influence of temperature and water content in the system (Figure 5B). This range of values is similar to the range of Ce concentrations in the carbonate melt.

Therefore, the vesicle filling hints at the existence of an alkali-, halogen-, REE-rich fluid phase. The effects of water and temperature on the composition of such a vesicle filling may reflect their influence on the fluid composition.

3.5. Bastnaesite saturation experiment

As no bastnaesite has been found in our crystallisation experiments, bastnaesite saturation has been forced in a dedicated saturation experiment at 600 °C with 20 wt% of bastnaesite added to the starting mixture (Figure 1D, Table 2). This EXP-600B experiment is also saturated with numerous small and clustered britholite crystals, fergusonite, calcite, fluid vesicles, vesicle fillings and iron oxides. Carbonate melt zones are larger in comparison with crystallisation experiments at the same temperature. The carbonate melt is extremely REE-rich, with the REE total representing 20.21 ± 1.87 wt% of the melt.

4. Discussion

4.1. The genetic link between calciocarbonatites and natrocarbonatites

Residual melt compositions have been compared to the literature in the CaCO_3 – Na_2CO_3 – K_2CO_3 system. In all experiments, the $(\text{Na}_2\text{CO}_3)/(\text{Na}_2\text{CO}_3 + \text{K}_2\text{CO}_3)$ ratio in the melt is constant with a ~0.9 value. Therefore, the pseudobinary system CaCO_3 –(0.9 Na_2CO_3 + 0.1 K_2CO_3) is used in this study for data

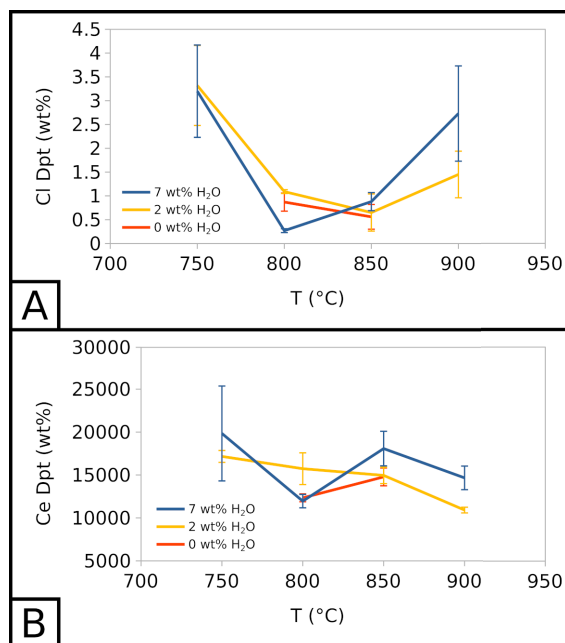


Figure 5. Compositional evolution of vesicle fillings. (A) Cl in the vesicle filling as a function of temperature and water content. (B) Ce in the vesicle filling as a function of temperature and water content. 7 wt% H₂O corresponds to EXP-W5, 2 wt% H₂O to EXP-P, and 0 wt% H₂O to EXP-G3.

projection. As the vesicle filling also yield a ~0.9 (Na_2CO_3)/(Na_2CO_3 + K_2CO_3) ratio, its composition can also be projected on this pseudobinary.

By projecting melt compositions into this pseudobinary, we can define the calcite saturation curves for each experimental set. Along these curves, calcite crystallisation effectively drives the carbonate composition from the calcic pole towards the alkaline pole (Figure 6), as observed by Cooper *et al.* [1975]. The natrocarbonatite composition [sky blue line, Keller and Zaitsev, 2012], however, is never reached in our experiments. As there is still residual melt at 600 °C, the solidus was not reached in our experiments.

Compared to the Cooper *et al.* [1975] data (grey lines, Figure 6), the calcite saturation curve is lowered by ~125 °C for near-anhydrous EXP-G3 (red line) and ~200 °C for 7 wt% H₂O EXP-W5 (blue line). Therefore, according to Wyllie and Tuttle [1960], water lowers the curve, but another process is needed

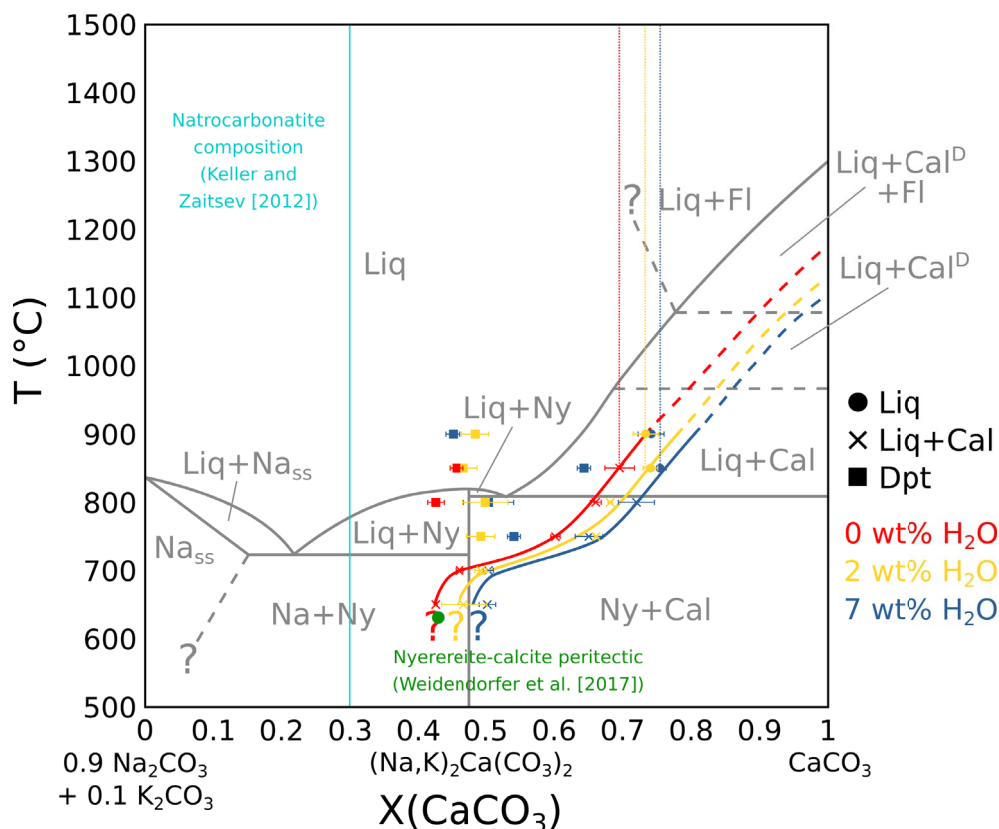


Figure 6. Pseudobinary phase diagram in the $(0.9 \text{ Na}_2\text{CO}_3 + 0.1 \text{ K}_2\text{CO}_3)$ – CaCO_3 system. In grey: Cooper et al. [1975] phase diagram, in a simple system. In red: carbonate melt and carbonate vesicle fillings composition in near-anhydrous EXP-G3. In yellow: carbonate melt and carbonate vesicle filling composition in 2 wt% H_2O EXP-P. In blue: carbonate melt and carbonate vesicle fillings composition in 7 wt% H_2O EXP-W5. Vertical dotted lines show the carbonate melt composition before calcite saturation. Plain lines show the carbonate melt evolution with temperature at calcite saturation. The curves are extended at high temperatures (dotted). The green dot indicates the calcite–nyerereite peritectic from Weidendorfer et al. [2017]. The sky blue line show the Ol Doinyo Lengai natrocarbonatite composition from Keller and Zaitsev [2012]. Liq: carbonate melt. Cal: calcite. Cal^D: disordered calcite. Fl: fluid. Dpt: deposit-like vesicle filling. Ny: nyerereite. Na: alkaline carbonate. Na_{ss}: alkaline carbonate solid solution. Na and Na_{ss} are equivalent to gregoryite in nature.

to explain the lowering in near-anhydrous EXP-G3. In their study, by adding 3.75 wt% F to the system, Jago and Gittins [1991] observed a $\sim 100^\circ\text{C}$ lowering of this curve compared to Cooper et al. [1975]. Because our starting mixture is halogen-rich (4.43 wt% F + 1.44 wt% Cl) (Table 1), halogens could have also strongly impacted the calcite saturation curve in our experiments.

The nyerereite saturation thermal maximum described by Cooper et al. [1975] in a simple CaCO_3 –

Na_2CO_3 – K_2CO_3 system is not observed in our system. Jago and Gittins [1991] suggest that in a halogen-rich complex system, this thermal maximum does not exist due to the lowering of the calcite saturation curve. Indeed, Weidendorfer et al. [2019] also show the absence of this thermal maximum when saturating a halogen-rich natrocarbonatitic composition with calcite. They also show the transformation of the nyerereite–calcite eutectic into a peritectic (green dot, Figure 6), allowing a genetic link between

calciocarbonatitic and natrocarbonatitic melts. However, in our study, even though we reach the position of this peritectic around 650 °C (Figure 6), the peritectic itself seems not to be crossed, as nyerereite is still not observed at 600 °C (Table 2).

Furthermore, according to Keller and Zaitsev [2012], natrocarbonatitic melts are Fe-, Mg- and REE-poor (respectively 0.45 ± 0.19 , 0.44 ± 0.07 and 0.14 ± 0.02 wt%). Our results show that calciocarbonatitic melts are likely to be enriched in these elements during differentiation towards alkali-rich compositions: with a CaO decrease from ~ 37.5 to ~ 17.5 wt% in the melt, the Fe, Mg and REE contents respectively increase from ~ 0.7 to ~ 2.4 wt%, ~ 1.7 to ~ 7.5 wt%, and $\sim 26,400$ to $\sim 45,000$ ppm (Figure 3B). Therefore, given the issues highlighted in this section, we argue that calciocarbonatitic melt differentiation cannot be responsible, at least alone, for natrocarbonatitic genesis.

The vesicle filling is significantly more alkaline than the carbonate melt. Its composition is constant with temperature and water content in the system between a ~ 0.45 to ~ 0.55 (CaCO_3)/($\text{CaCO}_3 + \text{Na}_2\text{CO}_3 + \text{K}_2\text{CO}_3$) ratio, with the exception of the vesicle filling from EXP-850W5 at a ~ 0.64 ratio. This may be due to off-target analysis. At temperatures below the point where the calcite saturation curve crosses the range of vesicle filling compositions, the vesicle filling disappears (Figure 6). Guzmics *et al.* [2019] showed the existence of alkali-rich, carbonate condensates inside fluid vesicles at equilibrium with a calciocarbonatitic melt and a silicic melt. They suggested the remixing of a calciocarbonatitic melt with an alkali-rich fluid as a process to explain natrocarbonatitic melt formation. The vesicle filling in our experiments could be similar to such products. Given its position in the Cooper *et al.* [1975] and Weidenborfer *et al.* [2019] phase diagrams (Figure 6), it could be parental to natrocarbonatitic melts.

4.2. REE incompatibility and melt enrichment

REE (especially LREE) are shown to be increasingly incompatible in calcite with decreasing temperature ($D_{\text{REE}}^{\text{Liq/Cal}}$ increase with decreasing temperature). In addition, the bastnaesite saturation experiment shows carbonatitic melts to be possible hosts for REE, with around 20 wt% REE in the melt at 600 °C. However, as $D_{\text{REE}}^{\text{Liq/Cal}}$ does not exceed ~ 10 regardless

of temperature or water content, REE enrichment by calcite crystallisation seems to be limited, evolving slowly during differentiation (Figures 3B and 4). In addition, britholite crystallisation at high temperature and fluorapatite crystallisation at low temperature may prevent a stronger enrichment of the melt, as they are REE-rich minerals [Verplanck *et al.*, 2016] susceptible to concentrate REE from the melt. The presence of the REE-rich vesicle filling in fluid vesicles suggests that the fluid phase can also act as a REE reservoir. Thus, even though carbonatitic melts may host significant REE contents, melt enrichment by differentiation alone seems insufficient to allow the formation of carbonatitic REE ore deposits. Indeed, bastnaesite cannot crystallise from the melt except for an extremely high REE enrichment, which probably cannot be achieved by simple differentiation.

4.3. Exsolution of a Na- and Cl-rich, REE-bearing fluid

There are several hints in favour of the exsolution of a Na-, Cl-rich fluid phase in our experiments. Given the composition of the vesicle filling, such fluids are also probably CO_3^{2-} -, Ca-, F- and REE-rich.

The presence of halite plus alkali- and halogen-rich vesicle fillings in fluid vesicles is qualitative evidence for the presence of Na and Cl in the fluid phase. The (CaCO_3)/($\text{CaCO}_3 + \text{Na}_2\text{CO}_3 + \text{K}_2\text{CO}_3$) ratio in the carbonate melt is slightly shifted from ~ 0.7 (EXP-G3) to ~ 0.73 (EXP-P) to ~ 0.75 (EXP-W5) (dotted red, yellow and blue vertical lines, Figure 6), i.e., from near-anhydrous to highly hydrated experiments. As no high-temperature minerals allow alkali in their structure, this $X(\text{CaCO}_3)$ shift in hydrated experiments suggests that the formation of a water-dominated fluid withdrew some Na from the melt. When compared with the starting mixture, the carbonate melt is depleted in Cl, especially at high temperature. Since no mineral phase allows Cl in its structure, it is likely that Cl has been partially withdrawn from the melt by the fluid phase.

Williams-Jones *et al.* [2012] studied the solubility of REE in a halogen-bearing aqueous fluid. They showed that REE mainly exist in such fluids as REE-Cl complexes, making a Na-, Cl-rich fluid a good candidate for mobilising REE. According to them, if a high-temperature (~ 400 °C), acidic fluid cools

down (~200 °C) and is being neutralised in pH, the REE solubility drops by several log units. Therefore, we may argue that the fluid phase can play a major role in the formation of carbonatitic REE ore deposits. Indeed, halogen-rich fluids will probably also be REE-rich, as the carbonate melt is increasingly REE-rich with calcite crystallisation. During fluid transport, cooling and neutralisation at the contact with surrounding rocks can then hamper REE mobilisation and trigger REE-bearing mineral crystallisation.

4.4. *Bastnaesite: magmatic or hydrothermal crystallisation?*

Magmatic crystallisation of bastnaesite in nature probably does not occur. Indeed, according to our results, for magmatic bastnaesite saturation, extremely high values of REE concentrations (~20 wt% total REE) are needed at 600 °C. Such a value is unrealistic in nature: one of the most REE-rich carbonatitic ore deposits in the world, Mountain Pass, locally shows only up to 14 wt% REO (rare earth oxides) concentrations [Castor, 2008]. Moreover, no bastnaesite has been found in crystallisation experiments, despite the melt being REE-rich (up to ~5 wt% total REE). Fluid-related processes are probably needed to achieve bastnaesite crystallisation.

The following sequence can be proposed:

- (1) REE are mainly concentrated in a calcicarbonatitic melt during immiscibility with an alkaline silicate melt;
- (2) Differentiation slightly concentrates REE in the residual melt by calcite crystallisation;
- (3) REE are also concentrated in a hydrous, Na-, Cl-bearing fluid phase along the differentiation;
- (4) During the post-magmatic stage, the hydrothermal fluid cools down and is neutralised in pH, whereby the REE solubility drops [Williams-Jones *et al.*, 2012];
- (5) REE minerals like bastnaesite can then crystallise from the fluid phase.

Halogens and water enhance this process by lowering the calcite crystallisation curve, allowing REE enrichment in the melt and the fluid at lower temperature, and increased REE mobilisation by the fluid.

4.5. *REE-bearing minerals at magmatic conditions*

We stress the existence of accessory REE-bearing magmatic minerals in our experiments. In particular, magmatic britholite (a REE, P-bearing silicate isomorphous with apatite) crystallises at high temperature (700–900 °C), even in Si-poor carbonate melts. Britholite crystals concentrate into calcite-britholite-iron oxides cumulates in melt-rich, high-temperature experiments (≥750 °C). To date, britholite has only been described as a low-temperature, hydrothermal mineral in the literature [Verplanck *et al.*, 2016, Giebel *et al.*, 2017]. At low temperature (600–650 °C), REE-bearing apatite is stable instead of britholite. Pyrochlore, a Nb,REE-bearing oxide, crystallises in small amounts at low temperature (600–700 °C).

5. Conclusion

This study provides new insights about carbonatite genesis and REE behaviour inside a complex, natural-like $\text{CaCO}_3\text{--Na}_2\text{CO}_3\text{--K}_2\text{CO}_3$ system. Experiments on Ca, REE-rich carbonatite differentiation show that REE-bearing calcite is the main crystallising phase, forming at low temperature in the presence of halogens and water. Its crystallisation controls the residual melt composition, which will evolve towards a more alkaline composition with decreasing temperature. However, neither the natrocarbonatitic composition [Keller and Zaitsev, 2012] nor the nyerereite–calcite peritectic described by Weidendorfer *et al.* [2017] were reached in our experiments. Thus, a process other than carbonatite differentiation alone is needed to explain natrocarbonatite genesis. The answer may reside in the co-differentiation of a carbonate melt in presence of an immiscible silicate melt, or in fluid–melt interactions resulting in the formation of alkali-rich carbonate products, that could be parental or contribute to natrocarbonatites, as described in Guzmics *et al.* [2019].

REE are slightly incompatible in calcite with respect to the carbonate melt, especially at low temperature and with water in the system. This results in a minor REE enrichment in the carbonate melt with calcite crystallisation. However, such enrichment, even in a REE-rich system, does not permit the crystallisation of magmatic bastnaesite, as bastnaesite

is never observed in our crystallisation experiments. Indeed, REE are highly soluble in carbonate melts, with around 20 wt% REE in the melt at bastnaesite saturation in our saturation experiment at 600 °C. Such concentrations are unlikely to be reached in nature.

Several hints for a Na-, Cl- and REE-rich fluid phase are found in our experiments. As bastnaesite crystallisation is unlikely to be magmatic, it is likely to be due to hydrothermal fluids at a post-magmatic stage, as Cl-rich fluids are reasonable candidates for REE mobilisation [Williams-Jones *et al.*, 2012]. Thus, this experimental study highlights that hydrothermal fluids are probably the main actor for REE mineral crystallisation in carbonatitic REE ore deposits. Further investigations should focus on fluid composition and REE partitioning between carbonatites and fluids.

Conflicts of interest

The authors declare no competing financial interest.

Dedication

The manuscript was written through contributions of all authors. All authors have given approval to the final version of the manuscript.

Acknowledgements

This work was supported by the LabEx VOLTAIRE project (ANR-10-LABX-100-01) and the EquipEx PLANEX (ANR-11-EQPX-0036). We thank colleagues for their advice and remarks throughout this work. We thank technicians and engineers at the ISTO, BRGM and LMV for their work and their help during the preparation and the analyses of the samples.

Supplementary data

Supporting information for this article is available on the journal's website under <https://doi.org/10.5802/crgeos.108> or from the author.

References

Andújar, J., Costa, F., and Scaillet, B. (2013). Storage conditions and eruptive dynamics of central versus flank eruptions in volcanic islands: The case of Tenerife (Canary Islands, Spain). *J. Volcanol. Geotherm. Res.*, 260, 62–79.

Anenburg, M., Mavrogenes, J. A., Frigo, C., and Wall, F. (2020). Rare earth element mobility in and around carbonatites controlled by sodium, potassium, and silica. *Sci. Adv.*, 6(41), article no. eabb6570.

Bell, K., Kjarsgaard, B. A., and Simonetti, A. (1999). Carbonatites—into the twenty-first century. *J. Petrol.*, 39(11, 12), 1839–1845.

Brooker, R. A. (1998). The effect of CO₂ saturation on immiscibility between silicate and carbonate liquids: An experimental study. *J. Petrol.*, 39(11, 12), 1905–1915.

Castor, S. B. (2008). The mountain pass rare-earth carbonatite and associated ultrapotassic rocks, California. *Can. Mineral.*, 46(4), 779–806.

Cheng, Z., Zhang, Z., Aibai, A., Kong, W., and Holtz, F. (2018). The role of magmatic and post-magmatic hydrothermal processes on rare-earth element mineralization: A study of the Bachu carbonatites from the Tarim Large Igneous Province, NW China. *Lithos*, 314–315, 71–87.

Cooper, A. F., Gittins, J., and Tuttle, O. F. (1975). The system Na₂CO₃–K₂CO₃–CaCO₃ at 1 kilobar and its significance in carbonatite petrogenesis. *Am. J. Sci.*, 275, 534–560.

De Moor, J. M., Fischer, T. P., King, P. L., Botcharnikov, R. E., Hervig, R. L., Hilton, D. R., Barry, P. H., Mangasini, F., and Ramirez, C. (2013). Volatile-rich silicate melts from Oldoinyo Lengai volcano (Tanzania): Implications for carbonatite genesis and eruptive behavior. *Earth Planet. Sci. Lett.*, 361, 379–390.

Di Carlo, I. (2006). Experimental crystallization of a high-K Arc basalt: The Golden Pumice, Stromboli Volcano (Italy). *J. Petrol.*, 47(7), 1317–1343.

Freestone, I. C. and Hamilton, D. L. (1980). The role of liquid immiscibility in the genesis of carbonatites? An experimental study. *Contrib. Mineral. Petrol.*, 73(2), 105–117.

Frost, B. R. (1991). Chapter 1. Introduction to oxygen fugacity and its petrologic importance. In Lindsley, D. H., editor, *Oxide Minerals: Petrologic and Magnetic Significance*, pages 1–10. De Gruyter, Berlin, Boston.

Giebel, R. J., Gauert, C. D., Marks, M. A., Costin, G., and Markl, G. (2017). Multi-stage formation of REE minerals in the palabora carbonatite complex, South Africa. *Am. Mineral.*, 102(6), 1218–1233.

Guo, D. and Liu, Y. (2019). Occurrence and geochemistry of bastnaesite in carbonatite-related REE

- deposits, Mianning–Dechang REE belt, Sichuan Province, SW China. *Ore Geol. Rev.*, 107, 266–282.
- Guzmics, T., Berkesi, M., Bodnar, R. J., Fall, A., Bali, E., Milke, R., Vetlén, E., and Szabó, C. (2019). Natro-carbonatites: A hidden product of three-phase immiscibility. *Geology*, 47(6), 527–530.
- Hamilton, D. L., Bedson, P., and Esson, J. (1989). The behaviour of trace elements in the evolution of carbonatites. In Bell, K., editor, *Carbonatites: Genesis and Evolution*, pages 405–427. Unwin Hyman, London, UK.
- Hsu, L. C. (1992). Synthesis and stability of bastnaesites in a part of the system (Ce,La)–F–H–C–O. *Mineral. Petrol.*, 47(1), 87–101.
- Jago, B. C. and Gittins, J. (1991). The role of fluorine in carbonatite magma evolution. *Nature*, 349, 56–58.
- Jones, A. and Wyllie, P. (1986). Solubility of rare earth elements in carbonatite magmas, indicated by the liquidus surface in $\text{CaCO}_3\text{Ca}(\text{OH})_2\text{La}(\text{OH})_3$ at 1 kbar pressure. *Appl. Geochem.*, 1(1), 95–102.
- Jones, J. H., Walker, D., Pickett, D. A., Murrell, M. T., and Beattie, P. (1995). Experimental investigations of the partitioning of Nb, Mo, Ba, Ce, Pb, Ra, Th, Pa, and U between immiscible carbonate and silicate liquids. *Geochim. Cosmochim. Acta*, 59(7), 1307–1320.
- Keller, J. and Zaitsev, A. (2012). Geochemistry and petrogenetic significance of natrocarbonatites at Oldoinyo Lengai, Tanzania: Composition of lavas from 1988 to 2007. *Lithos*, 148, 45–53.
- Kjarsgaard, B. A. (1998). Phase relations of a Carbonated High-CaO Nephelinite at 0.2 and 0.5 GPa. *J. Petrol.*, 39(11, 12), 2061–2075.
- Kjarsgaard, B. A., Hamilton, D. L., and Peterson, T. D. (1995). Peralkaline nephelinite/carbonatite liquid immiscibility: Comparison of phase compositions in experiments and natural lavas from Oldoinyo Lengai. In Johnson, R. W., Mahood, G. A., Scarpa, R., Bell, K., and Keller, J., editors, *Carbonatite Volcanism*, volume 4, pages 163–190. Springer, Berlin, Heidelberg.
- Klaudius, J. and Keller, J. (2006). Peralkaline silicate lavas at Oldoinyo Lengai, Tanzania. *Lithos*, 91(1–4), 173–190.
- Le Maitre, R. W. (2002). Igneous rocks a classification and glossary of terms: Recommendations of the international union of geological sciences. In *Subcommission on the Systematics of Igneous Rocks*. Cambridge University, Cambridge, UK.
- Mana, S., Furman, T., Turrin, B. D., Feigenson, M. D., and Swisher, C. C. (2015). Magmatic activity across the East African North Tanzanian Divergence zone. *J. Geol. Soc.*, 172(3), 368–389.
- Martin, L. H. J., Schmidt, M. W., Mattsson, H. B., and Guenther, D. (2013). Element partitioning between immiscible carbonatite and silicate melts for dry and H_2O -bearing systems at 1–3 GPa. *J. Petrol.*, 54(11), 2301–2338.
- Massuyeau, M., Gardés, E., Morizet, Y., and Gaillard, F. (2015). A model for the activity of silica along the carbonatite–kimberlite–mellilitite–basanite melt compositional joint. *Chem. Geol.*, 418, 206–216.
- Mattsson, H. B., Nandedkar, R. H., and Ulmer, P. (2013). Petrogenesis of the melilititic and nephelinitic rock suites in the Lake Natron–Engaruka monogenetic volcanic field, northern Tanzania. *Lithos*, 179, 175–192.
- Mitchell, R. H. (2005). Carbonatites and carbonatites and carbonatites. *Can. Mineral.*, 43(6), 2049–2068.
- Nabyl, Z., Massuyeau, M., Gaillard, F., Tuduri, J., Iacono-Marziano, G., Rogerie, G., Le Trong, E., Di Carlo, I., Melleton, J., and Bailly, L. (2020). A window in the course of alkaline magma differentiation conducive to immiscible REE-rich carbonatites. *Geochim. Cosmochim. Acta*, 282, 297–323.
- Pearce, N. J., Perkins, W. T., Westgate, J. A., Gorton, M. P., Jackson, S. E., Neal, C. R., and Chenery, S. P. (1997). A compilation of new and published major and trace element data for NIST SRM 610 and NIST SRM 612 glass reference materials. *Geostand. Geoanal. Res.*, 21(1), 115–144.
- Rocholl, A. (1998). Major and trace element composition and homogeneity of microbeam reference material: Basalt glass USGS BCR-2G. *Geostand. Geoanal. Res.*, 22(1), 33–45.
- Taylor, J. R., Wall, V. J., and Pownceby, M. I. (1992). The calibration and application of accurate redox sensors. *Am. Mineral.*, 77, 284–295.
- Van Achterberg, E., Ryan, C. G., Jackson, S. E., and Griffin, W. L. (2001). Data reduction software for LA-ICPMS. In Sylvester, P., editor, *Laser-Ablation-ICPMS in the Earth Sciences: Principles and Applications*, volume 29 of *Short Course Series*, pages 239–243. Mineralogical Association of Canada, Ottawa, Canada.
- Veksler, I. V., Dorfman, A. M., Dulski, P., Kamenetsky, V. S., Danyushevsky, L. V., Jeffries, T., and Dingwell, D. (2002). The evolution of the carbonatite–kimberlite–mellilitite–basanite melt compositional joint. *Chem. Geol.*, 189, 1–16.

- D. B. (2012). Partitioning of elements between silicate melt and immiscible fluoride, chloride, carbonate, phosphate and sulfate melts, with implications to the origin of natrocarbonatite. *Geochim. Cosmochim. Acta*, 79, 20–40.
- Veksler, I. V., Petibon, C., Jenner, G. A., Dorfman, A. M., and Dingwell, D. B. (1998). Trace element partitioning in immiscible Silicate–Carbonate liquid systems: An initial experimental study using a centrifuge autoclave. *J. Petrol.*, 39(11, 12), 2095–2104.
- Verplanck, P. L., Mariano, A. N., and Mariano, A. (2016). *Rare Earth Element Ore Geology of Carbonatites*. Society of Economic Geologists, Littleton, CO, USA.
- Weidendorfer, D., Schmidt, M. W., and Mattsson, H. B. (2017). A common origin of carbonatite magmas. *Geology*, 45(6), 507–510.
- Weidendorfer, D., Schmidt, M. W., and Mattsson, H. B. (2019). Mineral resorption triggers explosive mixed silicate–carbonatite eruptions. *Earth Planet. Sci. Lett.*, 510, 219–230.
- Williams-Jones, A. E., Migdisov, A. A., and Samson, I. M. (2012). Hydrothermal mobilisation of the rare earth elements—a tale of “Ceria” and “Yttria”. *Elements*, 8(5), 355–360.
- Woolley, A. R. and Kjarsgaard, B. A. (2008). Paragenetic types of carbonatite as indicated by the diversity and relative abundances of associated silicate rocks: Evidence from a global database. *Can. Mineral.*, 46(4), 741–752.
- Wyllie, P. J. and Tuttle, O. F. (1960). The system CaO–CO₂–H₂O and the origin of carbonatites. *J. Petrol.*, 1(1), 1–46.



Perspectives on alkaline magmas / *Perspectives sur les magmas alcalins*

No direct effect of F, Cl and P on REE partitioning between carbonate and alkaline silicate melts

Zineb Nabyl^{a,*}, Fabrice Gaillard^a, Johann Tuduri^{a,b} and Ida Di Carlo^a

^a ISTO, UMR 7327, Université d'Orléans, CNRS, BRGM, F-45071 Orléans, France

^b BRGM, F-45060 Orléans, France

E-mails: zineb.nabyl@gmail.com (Z. Nabyl), fabrice.gaillard@cnrs-orleans.fr (F. Gaillard), j.tuduri@brgm.fr (J. Tuduri), ida.di-carlo@cnrs-orleans.fr (I. D. Carlo)

Abstract. This study presents new insights into the effects of halogens (F and Cl) and phosphorous (P) on rare earth element (REE) partitioning between carbonatite and alkaline silicate melts. F, Cl and P are elements that are abundant in carbonatites and alkaline magmatic systems and they are considered to play an important role on the REE behaviour. Nonetheless, their effect on REE partitioning between carbonate and alkaline silicate melts has not yet been constrained.

Here we present new experimental data on REE partitioning between carbonate and alkaline silicate melts doped in F, Cl and P, in order to (1) test the Nabyl et al. [2020] REE partitioning model in F-, Cl- and P-rich systems, and (2) identify the possible role of F, Cl and P in carbonate melt REE enrichments during alkaline-carbonatite magma differentiation. The experiments were performed at 850–1050 °C and 0.8 GPa using piston-cylinder devices. Starting materials consisted of carbonatite and phonolite compositions \pm doped in F, Cl and P. The experimental results show that REE partitioning is similar in F-Cl-P-rich and -poor systems. The silicate melt composition and its molecular structure (i.e. SiO₂ contents, the alumina saturation index and the alkali/alkaline-earth element ratio), which have already been identified as controlling REE partitioning in F-, Cl- and P-poor systems, still operate in doped systems. No direct effect of the F, Cl or P melt concentrations on REE partitioning has been identified. We also propose an application to natural systems.

Keywords. Carbonatites, Alkaline magma, Halogens, Phosphorous, Rare earth elements, Immiscibility processes.

1. Introduction

Carbonatites and alkaline magmatic rocks are known to be the most REE enriched igneous rocks [Nelson et al., 1988, Woolley and Kempe, 1989] and are associated with the most important REE deposits [Chakhmouradian and Zaitsev, 2012, Smith et al., 2016, Verplanck et al., 2016]. These rocks are also enriched in volatile species such as halogens—fluorine

and chlorine (F and Cl)—[Aiuppa et al., 2009, Jago and Gittins, 1991, Jones et al., 2013, Kynicky et al., 2019, Metrich and Rutherford, 1992, Webster et al., 2018], and also phosphorous [Ablay et al., 1998, Jones et al., 2013, Mattsson et al., 2013, Woolley and Kempe, 1989]. These elements can reach more than 1 weight % (wt%) in alkaline silicate magmatic rocks [Ablay et al., 1998, Aiuppa et al., 2009, Baudouin et al., 2016, Mangler et al., 2014, Mattsson et al., 2013, Webster et al., 2018]. F, Cl and P concentrations are also high in carbonatites [Jones et al., 2013, Woolley and Kempe, 1989], especially in the

* Corresponding author.

natrocarbonatites—the alkali-rich carbonatite lavas from the Ol Doinyo Lengai volcano in Tanzania—in which concentrations can reach more than 4, 3 and 1 wt% respectively [Dawson, 1962, Keller and Zaitsev, 2012]. These elements are also found in minerals present in carbonatites and alkaline magmatic rocks and constitute major components of important REE mineral phases [Verplanck *et al.*, 2016]. In fact, the REE are mostly contained in fluoro-carbonates such as bastnaesite and synchisite, or in phosphates such as monazite and apatite [Smith *et al.*, 2016, Verplanck *et al.*, 2016]. The REE mineralisation is frequently described as resulting from late- to post-magmatic processes involving fluid circulation, which are often characterised as F-, Cl- and P-rich [Gysi and Williams-Jones, 2015, Smith *et al.*, 2016, Verplanck *et al.*, 2016, Williams-Jones *et al.*, 2012]. These elements play an important role in the concentration, redistribution and deposition processes of REE [Jia and Liu, 2020, Louvel *et al.*, 2015, Migdisov *et al.*, 2016, Williams-Jones *et al.*, 2012]. Nonetheless, primary monazite or bastnaesite crystals have also been recognised and defined as magmatic phases in carbonatites [Castor, 2008, Feng *et al.*, 2020, Mariano and Mariano, 2012, Néron *et al.*, 2018, Verplanck *et al.*, 2016, Wall and Mariano, 1996]. The REE mineralisation can therefore originate from both magmatic or hydrothermal processes, and the boundary between the two mechanisms remains unclear [Anenburg *et al.*, 2020, Chakhmouradian and Zaitsev, 2012, Verplanck *et al.*, 2016].

Salt-rich melts (including F-, Cl-, P- and S-rich melts) formed at the magmatic stage have been directly demonstrated by the study of natrocarbonatites enriched in F, Cl, P and SO₃ [Dawson, 1962, Keller and Zaitsev, 2012, Mangler *et al.*, 2014, Potter *et al.*, 2017]. Melt inclusion studies have also highlighted the existence of salt melts coexisting with silicate melts [Feng *et al.*, 2020, Frezzotti, 2001, Panina, 2005, Panina and Motorina, 2008], and especially F-, Cl- and P-rich immiscible alkaline silicate and carbonate melts [Berkesi *et al.*, 2020, Guzmics *et al.*, 2019]. Such occurrences, combined with the fact that the most important REE-minerals in carbonatites correspond to fluoro-carbonates and phosphates, raise the question as to whether there is a link between F, Cl and P and the behaviour of REE in conjugate carbonate and silicate melts.

Here we focus on the immiscibility processes be-

tween carbonate and silicate melts. This is motivated by the strong association of carbonatites and alkaline silicate rocks observed in the field [Kjarsgaard and Hamilton, 1988, Mitchell, 2005, Woolley and Kjarsgaard, 2008], by melt inclusion studies of conjugate carbonate and silicate melts, as mentioned above [Baudouin *et al.*, 2018, Berkesi *et al.*, 2020, Guzmics *et al.*, 2012, 2019, Mitchell, 2009], and also by experimental investigations simulating the immiscibility between carbonate and silicate melts [Brooker, 1998, Brooker and Kjarsgaard, 2011, Hamilton *et al.*, 1989, Lee and Wyllie, 1994, Martin *et al.*, 2012, 2013, Massuyeau *et al.*, 2015, Nabyl *et al.*, 2020, Veksler *et al.*, 1998, 2012]. Experimental studies on trace element partitioning between carbonate and silicate melts [Hamilton *et al.*, 1989, Martin *et al.*, 2013, Nabyl *et al.*, 2020, Veksler *et al.*, 1998, 2012] have shown that carbonate melt immiscible with silicate melt can either be strongly depleted or, on the contrary, enriched in REE. This large variation has been linked by Nabyl *et al.* [2020] to the silicate melt composition and structure. Nabyl *et al.* [2020] have proposed a modelling of carbonatite REE enrichment along the alkaline magma differentiation course which is exclusively based on the silicate melt composition. This model allows the REE composition of a carbonate melt immiscible with a silicate melt to be calculated from parameters relative to the silicate melt composition: the silica content (SiO₂), the alumina saturation index (Al₂O₃/(CaO + Na₂O + K₂O)) and the alkali/alkaline-earth cation ratio [(Na₂O + K₂O)/(CaO + MgO); Nabyl *et al.*, 2020]. Using this model, Nabyl *et al.* [2020] have shown that REE-rich carbonate melts can be immiscible with highly differentiated and polymerised alkaline silicate melts of phonolitic/phonotrachytic type, and hence that the degree of silicate melt differentiation plays a key role in the conjugate carbonate melt REE enrichment. The parameterisation of the model has been performed in experimental studies mentioned above [Hamilton *et al.*, 1989, Martin *et al.*, 2013, Nabyl *et al.*, 2020, Veksler *et al.*, 1998, 2012]. However, this model does not take into account the role of F, Cl and P in carbonate melt REE enrichments.

In the pure salt melt (pure fluoride/chloride/phosphate) and silicate melt systems [Chebotarev *et al.*, 2019, Veksler *et al.*, 2005, 2012], experimental studies have broadly shown that REE have a strong affinity for salt melts, with the enrich-

ment varying by two orders of magnitude [Veksler *et al.*, 2012]. Kynicky *et al.* [2019] and Feng *et al.* [2020] have also proposed that carbonate melt salt components (F- and P-rich carbonate melts respectively) can significantly favour REE enrichment. Besides, these elements are critical in the silicate melt structure. Fluorine has been shown to be highly soluble in silicate melts [Dingwell, 1986], creating potential complexes with major elements such as Ca, Na, Si and Al [Baasner *et al.*, 2014, Schaller *et al.*, 1992], or with REE [Ponader and Brown, 1989], and as being involved in the silicate melt polymerisation as well as depolymerisation [Ponader and Brown, 1989], in addition to affecting its viscosity [Baasner *et al.*, 2013a,b]. Baasner *et al.* [2014] have also shown that F can create bonds with network-modifying cations such as Ca and Na in peralkaline silicate melts, whereas it creates complexes with network-building cations such as Si and Al in peraluminous melts. Chlorine has also been described as having an effect on silicate melt viscosity [Baasner *et al.*, 2013b,a]. Several studies have also characterised P as playing a role in the silicate melt structure [Mysen, 1998, Mysen *et al.*, 1981, Toplis and Dingwell, 1996], forming complexes with Ca, Mg, Na and Al [Mysen, 1998, Mysen *et al.*, 1981], and increasing the viscosity of peralkaline silicate melts [Toplis and Dingwell, 1996]. Altogether, this suggests that F, Cl and P can have an effect on the structure of alkaline silicate melt coexisting with carbonate melt, hence influence the REE behaviour between both melts. However, the current experimental database does not allow us to determine the impact of these elements on the REE partitioning between carbonate and silicate melts.

The aim of this study is to test the Nabyl *et al.* [2020] model in F-, Cl- and P-rich environments and to characterise the role of these elements in the REE partitioning between carbonate and alkaline silicate melts. We present high temperature–high pressure experiments simulating the immiscibility between carbonate and alkaline silicate melts of evolved nephelinite–phonolite type, in F-, Cl- and P-rich systems. The experiments were performed at 850–1050 °C and 0.8 GPa. We show that F, Cl and P do not play a direct role in carbonate melt REE enrichment, and that REE partitioning in F-, Cl- and P-rich systems can be predicted using the Nabyl *et al.* [2020] model.

2. Methodology

2.1. Experimental strategy

Four compositions were synthesized (Table 1) with a base composition of a phonolite–carbonatite mixture in a ratio of 50:50 for the major elements (including Si, Ti, Al, Fe, Mn, Mg, Ca, Na, K, P, Ba, Sr, F and Cl). The selected mixture composition corresponds to the immiscible carbonate melt and silicate melt of phonolitic composition from experiment T19_01 of Nabyl *et al.* [2020]. This base composition (composition PhCbn1, see Table 1; named “non-doped” in the following text) contains small amounts of F, Cl and P (F ~ 1 wt%; Cl ~ 0.3 wt%; P₂O₅ ~ 0.7 wt%; Table 1). In order to characterise and isolate a possible volatile effect on the REE partitioning, three compositions were doped with ca. 5 wt% of P₂O₅ (composition PhCbn2, Table 1), F (composition PhCbn3, Table 1) and Cl (composition PhCbn4, Table 1) respectively. All four starting materials also contain 0.1 wt% of Σ REE–Y–Sc and other trace elements (see Table 1).

Most experiments were performed at 850 °C and 0.8 GPa [similar to experiment T19_01 in Nabyl *et al.*, 2020]. Additional experiments were also performed at a higher temperature (1050 °C). Moreover, different amounts of water (0, 3 or 6 wt%) were added to the starting material to test its effect on each chemical system.

2.2. Starting compositions

The four starting compositions (Table 1) were prepared by mixing synthetic powders (SiO₂, TiO₂, Al₂O₃, AlPO₄, AlF₃, AlCl₃, FeO, FeS, MnCO₃, CaCO₃, Na₂CO₃, K₂CO₃, BaCO₃, SrCO₃ and Cr₂O₃) and natural dolomite (CaMg(CO₃)₂). For the three \pm F-, Cl- and P-doped compositions (PhCbn2, PhCbn3 and PhCbn4 respectively, Table 1), additional AlF₃, AlCl₃ and AlPO₄ powders were used to reach the respective F, Cl and P concentrations needed (Table 1). The starting compositions are CO₂-rich, with bulk concentrations of ca. 24 wt%. REE and other trace elements were also added to the four compositions in the form of oxides, fluorides or pure elements (La₂O₃, CeO₂, Pr₆O₁₁, Nd₂O₃, Sm₂O₃, Eu₂O₃, GdF₃, Tb, Dy₂O₃, HoF₃, Er₂O₃, Yb₂O₃, Lu, Y₂O₃, Sc₂O₃, Nb₂O₅, Ta₂O₅, ZrO₂ and HfO₂).

The synthetic powders were maintained in a dry oven at 120 °C, except for the strong hydrophilic

Table 1. Starting material compositions

	PhCbn 1	PhCbn 2	PhCbn 3	PhCbn 4
Major elements in wt%				
SiO ₂	25.47	24.32	24.37	24.01
TiO ₂	0.34	0.32	0.32	0.31
Cr ₂ O ₃	0.01	0.01	0.01	0.01
Al ₂ O ₃	9.47	9.36	8.95	8.88
Fe ₂ O ₃	3.88	3.67	3.7	3.52
MnO	0.31	0.29	0.29	0.28
MgO	1.06	1	0.98	0.97
CaO	14.88	14.16	14.25	13.65
Na ₂ O	12.19	11.51	11.5	11.07
K ₂ O	4.01	3.95	3.7	3.54
P ₂ O ₅	0.76	5.13	0.76	0.71
SrO	0.77	0.7	0.68	0.66
BaO	0.56	0.54	0.54	0.54
F	1.12	1.03	5.83*	1.03
Cl	0.34	0.34	0.28	4.72*
S	0.06	0.06	0.06	0.05
LOI	24.77	23.72	23.78	26.07
Total	100	100	100	100
Trace elements in µg/g (ppm)				
Ba	5340	5080	5370	5410
Sr	7000	6450	6380	6120
Hf	23.4	22.5	17.9	24.4
Zr	407	379	371	377
Nb	197	198	185	163.5
Ta	12.4	9.7	4.4	6
La	52.5	50.9	49.8	48.9
Ce	61	59.6	60.4	56.6
Pr	51	51.4	49.4	47.2
Nd	53.6	53.6	51	50.2
Sm	56.1	55.8	54.3	50.1
Eu	55	55.7	53.9	52.5
Gd	61.5	55.3	56.6	55.4
Tb	52.4	50.7	52.1	50.1
Dy	57.3	56.8	56.5	56.7
Ho	52.6	53.3	54.2	52.5
Er	57.7	57.2	58.8	58.5
Yb	54.9	55.3	56	54.6
Lu	49.9	49.7	49.9	48.3

(continued)

Table 1. (continued)

	PhCbn 1	PhCbn 2	PhCbn 3	PhCbn 4
Y	67.4	67.7	64.9	63.5
Sc	64	58	56	60
Cr	140	120	120	120
Major elements (wt%) and trace elements (µg/g, ppm) were analysed by ICP-MS analysis on powders (ALS Global); *: concentrations calculated on a normalised basis. Experimental conditions and run products. <i>P</i> : total pressure; <i>T</i> : temperature; SL: silicate liquid; CL: carbonate liquid; CPx: clinopyroxene (diopside–hedenbergite–wollastonite solution); Nph: nepheline; Gnt: garnet (andradite); Ap: apatite; Fe-Spl: iron-spinel (magnetite–titanomagnetite solid solution); Spl: spinel; Afs: alkali feldspar; Cal: calcite; Fl: fluorite; Fst: feldspathoid; “CL2”: second carbonate liquid phase; V: vapour phase.				

Na₂CO₃ and K₂CO₃ powders which were preserved in an oven at 200 °C. Moreover, the AlF₃, AlCl₃ and AlPO₄ powders were also strongly hydrophilic at atmospheric conditions and could not be preserved at temperatures higher than 50 °C. Those powders and both the PhCbn3 and PhCbn4 compositions (Table 1) were thus manipulated using a Captair Pyramid 2200 ANM-XLS at controlled atmosphere under Argon gas to avoid any atmospheric water contamination, and maintained in a vacuum bell jar. For each composition, the powders were first mixed by hand in an agate mortar (30 min) and then in an automatic grinder with an agate mortar and ball mill (at least two times for 15 min).

2.3. Piston-cylinder experiments

We synthesized 20 experimental charges at 0.8 GPa, 850 and 1050 °C using an end-loaded piston-cylinder apparatus (Table 2). The starting materials were packed into Au capsules (diameter of 2.5–2.9 mm) for low temperature experiments (850 °C) and Au₈₀Pd₂₀ capsules for higher temperature ones (1050 °C). For experiments performed at 850 °C and 0.8 GPa and for almost all the starting materials, four capsules were

synthesized: one capsule containing only the starting material, two capsules containing 3 and 6 wt% of water respectively (Table 2), and one capsule with additional graphite (+1 wt%, see Table 2). Water and graphite were added in order to test their effect on carbonate and silicate melt compositions.

The capsules were introduced into an alumina tube with a powder composed of 50% AlSiMag (mixture of Al, Si and Mg)–50% haematite, and closed at the top and bottom with MgO-plugs. The fO_2 for the experiments was estimated at between FMQ and FMQ+2, due to the presence of the haematite powder which creates an oxidised environment (i.e. H_2 -poor). Graphite-bearing experiments were more reduced, likely in the range FMQ–2 [Stagno and Frost, 2010]. The whole assemblage was packed into a 3/4-inch piston-cylinder assembly, composed of graphite, pyrex and talc. Two steel-plugs surrounded by pyrophyllite were placed at the top and bottom of the assembly to maintain the assemblage in place; the thermocouple (B-type, Pt₉₄Rh₆–Pt₇₀Rh₃₀) was introduced in the top of the assemblage. For the experiments conducted at 850 °C (Table 2), the samples were first taken up to 975 °C for two hours to ensure bulk composition melting and homogenisation, then the final temperature (850 °C) was reached within a few minutes (cooling rate of 10 °C per minute). Each experiment was quenched by switching off the heat source at isobaric conditions. Uncertainties for the temperature and the pressure are considered to be ± 12 °C and ± 0.1 GPa respectively [Dasgupta *et al.*, 2004, Sifré *et al.*, 2014].

2.4. Analytical methods

Polished sections were prepared from the experimental charges, and observed using a Merlin Compact Zeiss electron microscope (voltage 15 kV), equipped with a micro-analyser system EDS (Bruker-QUANTAX-XFlash6, resolution 129 eV) at the ISTO laboratory, in order to determine the phases and their textures. Carbonate and silicate melt sections were then analysed with a Cameca SXFive electron microprobe equipped with 5 WDS detectors (ISTO, France) at 15 kV and 6 nA. Analyses were performed with a large beam size (from 10 to 70 μ m) to avoid any Na-loss and to average carbonate melt compositions. The standards used for the calibration were

albite, apatite, orthose, andradite, topaz, vanadinite, MgO, Al₂O₃, Fe₂O₃, MnTiO₃, BaSO₄, and SrCO₃. The counting time was 10 s for all the elements, except for Ba (20 s), Sr and Nb (30 s) and S (60 s). Higher counting times were also needed for F, Cl and P to ensure representative analyses (30 s for Cl, 60 s for F, and 60 or 120 s for P).

Trace elements were analysed using two different LA-ICP-MS (Laser Ablation Inductively Coupled Plasma Mass Spectrometry) devices: the Agilent 7500 CS Quadrupole ICP-MS of the LMV laboratory (Clermont-Ferrand, France; He: 550 mL/min; Ar: 850 mL/min; N₂: 2 mL/min) and the Agilent 7900 Quadrupole ICP-MS of the ISTO laboratory (Orléans, France; He: 350 mL/min; Ar: 930 mL/min). Both mass spectrometers are coupled to a 193 nm excimer laser ablation system (Resonetics), with He flushing the ablation cell. Carbonate and silicate melt analyses were performed with a frequency of 2 Hz, an ablation energy of 1.5–3 mJ and a beam size of 14 to 60 μ m in diameter, depending on both melt/crystal-free areas. Carbonate and silicate melts from several samples were analysed with both spectrometers to ensure similar trace element concentrations were obtained and that no bias was induced by using the two different machines. The following isotopes were analysed: ⁴³Ca, ⁴⁴Ca, ²⁹Si, ¹³⁹La, ¹⁴⁰Ce, ¹⁴¹Pr, ¹⁴⁶Nd, ¹⁴⁷Sm, ¹⁵³Eu, ¹⁵⁷Gd, ¹⁵⁹Tb, ¹⁶³Dy, ¹⁶⁵Ho, ¹⁶⁶Er, ¹⁷²Yb, ¹⁷⁵Lu, ⁸⁹Y, ⁴⁵Sc, ⁴⁹Ti, ⁵³Cr, ⁵⁵Mn, ⁸⁸Sr, ¹³⁷Ba, ⁹³Nb, ¹⁸¹Ta, ⁹⁰Zr, ¹⁷⁸Hf, ¹⁹⁷Au and ¹⁰⁵Pd to verify any potential contamination by the capsule during the experiment.

Data reduction and trace element concentrations were carried out using the GLITTER4.4 software [Van Achterbergh *et al.*, 2001] for both the carbonate and silicate melts. The elements were quantified using the NIST 610 standard glass [Pearce *et al.*, 1997] and other standards were used to check the analysis validity [NIST 612 and BCR-2G natural basaltic glass; Pearce *et al.*, 1997, Rocholl, 1998, Jochum *et al.*, 2016]. The standards were analysed at the same beam size, frequency and energy ablation as the samples to verify the efficiency of the analysis. The Ca was used as the internal standard, its concentration having first been determined by electron microprobe analyses in both the carbonate and the silicate phases.

Table 2. Experimental conditions and run products

Experiment	Starting material	Added volatile	P (GPa)	T (°C)	Duration (h)	Capsule material	Added water (wt%)	Added graphite (wt%)	Phases
PCPC1_01	PhCbn1	—	0.8	850	50	Au	—	—	SL + CL + CPx + Nph + Gnt + Spl + Fe-Spl + V (+“CL2”)
PCPC1_02	PhCbn1	—	0.8	850	50	Au	3	—	SL + CL + CPx + Nph + Gnt + Fe-Spl + V (+“CL2”)
PCPC1_03	PhCbn1	—	0.8	850	50	Au	6	—	SL + CL + Fe-Spl + V
PCPC1_04	PhCbn1	—	0.8	850	50	Au	—	1	CL + Cpx + Nph + Gnt + Afs
PCPC2_01	PhCbn1	—	0.8	1050	28	Au ₈₀ Pd ₂₀	—	—	SL + CL + Nph
PCPC3_01	PhCbn2	P	0.8	850	67.5	Au	—	—	SL + CL + Nph + Ap + Spl + Fe-Spl
PCPC3_02	PhCbn2	P	0.8	850	67.5	Au	3	—	SL + CL + Ap + Spl + Fe-Spl
PCPC3_03	PhCbn2	P	0.8	850	67.5	Au	6	—	SL + CL + Ap + Fe-Spl
PCPC3_04	PhCbn2	P	0.8	850	67.5	Au	—	1	CL + Cpx + Nph + Gnt + Ap + Fe-Spl + Afs
PCPC4_01	PhCbn3	F	0.8	850	88.5	Au	—	—	SL + CL + Fl + Cal + Fe-Spl
PCPC4_02	PhCbn3	F	0.8	850	88.5	Au	3	—	SL + CL + Fl + Cal + Fe-Spl
PCPC4_03	PhCbn3	F	0.8	850	88.5	Au	6	—	SL + CL + Fl + Cal + Fe-Spl
PCPC4_04	PhCbn3	F	0.8	850	88.5	Au	—	1	CL + Fl + Cpx + Nph + Gnt + Fl + Spl + Fe-Spl + Afs + Fst
PCPC5_02	PhCbn4	Cl	0.8	850	88.5	Au	3	—	SL + CL + CPx + Gnt + Ap + Cal + V
PCPC5_03	PhCbn4	Cl	0.8	850	88.5	Au	6	—	SL + CL + CPx + Gnt + Ap + V
PCPC5_04	PhCbn4	Cl	0.8	850	88.5	Au	—	1	CL + Cpx + Nph + Gnt + Ap + Cal + Afs + Fst
PCPC6_01	PhCbn3	F	0.8	1050	23.5	Au ₈₀ Pd ₂₀	—	—	SL + CL
PCPC6_02	PhCbn4	Cl	0.8	1050	23.5	Au ₈₀ Pd ₂₀	—	—	SL + CL
PCPC6_03	PhCbn2	P	0.8	1050	23.5	Au ₈₀ Pd ₂₀	—	—	SL + CL + Ap

P: total pressure; T: temperature; SL: silicate liquid; CL: carbonate liquid; CPx: clinopyroxene (diopside–hedenbergite–wollastonite solution); Nph: nepheline; Gnt: garnet (andradite); Ap: apatite; Fe-Spl: iron-spinel (magnetite–titanomagnetite solid solution); Spl: spinel; Afs: alkali feldspar; Cal: calcite; Fl: fluorite; Fst: feldspathoid; “CL2”: second carbonate liquid phase; V: vapour phase.

3. Results

3.1. Carbonate and silicate melt textures

Nineteen samples were synthesized at 0.8 GPa and 850 and 1050 °C. For the sake of clarity, each chemical system is represented with a different colour in all the figures: black for the non-doped system, red for the P-rich system, green for the Cl-rich system and blue for the F-rich system.

For all starting materials (\pm F, Cl and P), all run products have an alkaline silicate liquid conjugated with a carbonate liquid, apart from those produced at 850 °C with graphite (samples noticed "..._04", see Table 2) which have only a carbonate melt coexisting with a few silicate crystals. The silicate liquids quenched into homogeneous glass in all the samples (Figures 1 and 2). The coexisting carbonate melts show typical textures of quenched crystallised dendritic blebs in almost all the systems (non-doped system, P- and Cl-rich system; Figures 1 and 2), the exception being the F-rich system where they have a near-glassy texture (Figures 1c, 2e and f). In the Cl-rich system (Figures 1d and 2g), carbonate blebs display a porous texture. For almost all the samples, the clear contact between both liquids, the homogeneous chemical compositions and the size of the carbonate melts (up to 200 μ m) indicate that equilibrium has been attained between both liquids at given P–T conditions, and this attests to the fact that immiscibility is not related to quench processes [Brooker and Kjarsgaard, 2011]. In two samples from the non-doped system that were synthesized at 850 °C (PCPC1_01 and PCPC1_02, Figures 2a and b; Table 2), a second distinct carbonate liquid phase is observed (noted "CL2", in Figure 2b), characterised by carbonate blebs of <15 to 50 μ m. This phase will be treated separately in the following section of the results.

In some samples (Table 2), bubbles are observed (Figure 1d; Figures 2d and f) and attest to the presence of a fluid phase coexisting with both liquids. Moreover, at 0.8 GPa and 1050 °C carbonate melts contain a large amount of apatite crystals in the P-rich sample (Figure 1b), while no apatite are observed in the F- and Cl-rich systems (Figures 1c and d respectively). At the lower temperature (850 °C), all charges contain crystals (Figure 2 and Table 2). Clinopyroxene is mainly present in non-doped samples (Figures 2a and b) and in Cl-rich samples (in

green, Figure 2g). Apatite is also present in significant proportions in the carbonate melt zones of P-rich samples (Figures 2c and d; Table 2), and a few apatite crystals are also observed in the Cl-rich samples (Figure 2g, Table 2). Other phases are also observed, such as nepheline, garnet, spinel, alkali feldspar, feldspathoid, calcite and fluorite (Table 2, see Figure 2). The chemical composition of all minerals is not discussed here as this study is mainly focused on the effect of F, Cl and P on REE partitioning between the carbonate and alkaline silicate melts.

3.2. Chemical composition of the melts

The major element concentrations of the conjugate silicate and carbonate melts are presented in Table 3.

At 0.8 GPa and 1050 °C for all four chemical systems, the silicate melts present a composition of alkaline nephelinite type, with the SiO₂ content varying slightly from 42.9 ± 0.2 wt% (sample PCPC6_02 in the Cl-rich system, Table 3) to 46.3 ± 0.6 wt% (sample PCPC6_03 in the P-rich system, Table 3), and alkali contents (Na₂O + K₂O) from 15.1 ± 0.8 wt% (sample PCPC6_02 in the Cl-rich system, Table 3) to 17.8 ± 0.6 wt% (sample PCPC6_01 in the non-doped system, Table 3). Figure 3 presents ternary diagrams in the Hamilton projection—i.e. in the (Na₂O + K₂O)–(SiO₂ + TiO₂ + Al₂O₃)–(CaO + MgO + FeO) space—which is widely used to represent the miscibility gap between carbonate and silicate melts [Freestone and Hamilton, 1980, Kjarsgaard and Hamilton, 1988]. The silicate melts in the P- and F-rich systems are slightly richer in silica and alkali elements compared to those in the non-doped and Cl-rich systems (Figure 3a, see Table 3). The conjugate carbonate melt compositions vary in the four chemical systems from 10.1 ± 1.6 to 17.1 ± 0.7 wt% Na₂O (samples PCPC6_02 and PCPC6_03 respectively, Table 3) and from 29.4 ± 0.9 to 34.3 ± 1.2 wt% CaO (samples PCPC6_03 and PCPC2_01, respectively, Table 3). The carbonate melts of the Cl-rich system are poorer in Na₂O content compared to the others, and thus closer to the (CaO + MgO + FeO) pole (Figure 3a).

The F, Cl and P₂O₅ silicate melt concentrations at 1050 °C for all the systems are relatively high, reaching almost 4, 1.3 and 1 wt% in the F-, Cl- and P-rich systems respectively (Table 3). In the carbonate

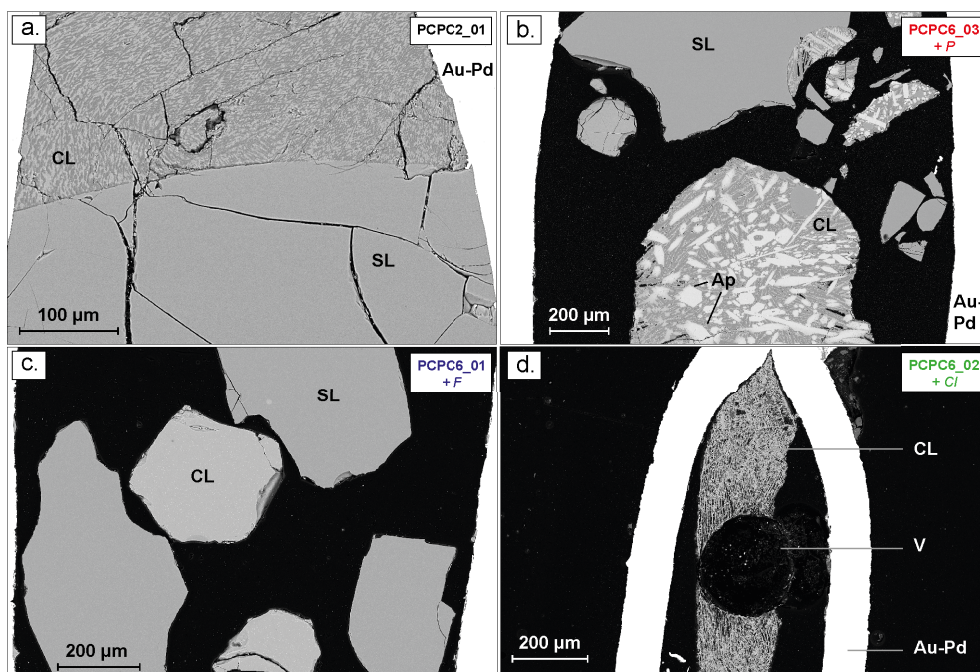


Figure 1. BSE images of typical experimental carbonate and silicate liquid immiscibility at 1050 °C and 0.8 GPa, in the non-doped system in black (a), in the P-rich system in red (b); in the F-rich system in blue (c) and in the Cl-rich system in green (d). SL: silicate liquid; CL: carbonate liquid; Ap: apatite; V: fluid phase; Au-Pd: gold–palladium capsule.

melts, F and P_2O_5 concentrations are much higher in the F- and P-rich systems: F reaches 11.8 ± 0.7 wt% in the F-rich system (sample PCPC6_01, Table 3), and the carbonate melt in the P-rich system contains 9.5 ± 0.9 wt% P_2O_5 (sample PCPC6_03, Table 3). However, in the Cl-rich system for the carbonate melt the Cl concentration remains low (0.9 ± 0.3 wt%, sample PCPC6_02, Table 3).

At the lower temperature (850 °C, Figure 3b and Table 2), partial crystallisation changes the silicate melt composition from evolved nephelinite to phonolite type, i.e. from 45.8 ± 0.9 to 53.7 ± 0.8 wt% SiO_2 (samples PCPC5_03 and PCPC4_01 respectively, Table 3) and 16.2 ± 0.6 to 18.0 ± 0.5 wt% $Na_2O + K_2O$ (samples PCPC5_03 and PCPC3_03 respectively, Table 3). For all four chemical systems, the miscibility gap between the carbonate and silicate melts is enlarged as temperature decreases from 1050 to 850 °C (Figures 3a and b), with silicate melts getting closer to the ($SiO_2 + TiO_2 + Al_2O_3$) pole and carbonate melts getting closer to

the ($CaO + MgO + FeO$) pole. Silicate melts present similar compositions for all the chemical systems (Figure 3b; Table 3) and for samples \pm hydrated (dashed and dotted lines, 3 and 6 wt% of H_2O respectively, Figure 3b). In contrast, the conjugate carbonate melts vary significantly in the four chemical systems. Carbonate melts are broadly richer in CaO with concentrations varying from 31.0 ± 1.4 to 36.8 ± 5.1 wt% (samples PCPC1_03 and PCPC5_03 respectively, see Table 3), except for the P-rich system, which shows lower CaO concentrations, between 24.4 ± 1.8 and 25.4 ± 2.8 wt% (samples PCPC3_01 and PCPC3_02, Table 3). Carbonate melts are also slightly richer in Na_2O in the non-doped system and in the F- and P-rich systems, with concentrations varying from 14.7 ± 0.7 to 20.6 ± 0.7 wt% (samples PCPC1_01 and PCPC3_03 respectively, Table 3). On the contrary, the Na_2O contents are lower in the Cl-rich system (<11 wt%, see Table 3). In fact, carbonate melts become much richer in CaO (35.1 ± 5.6 and 36.8 ± 5.1 wt% of CaO, samples PCPC5_02 and PCPC5_03 in the

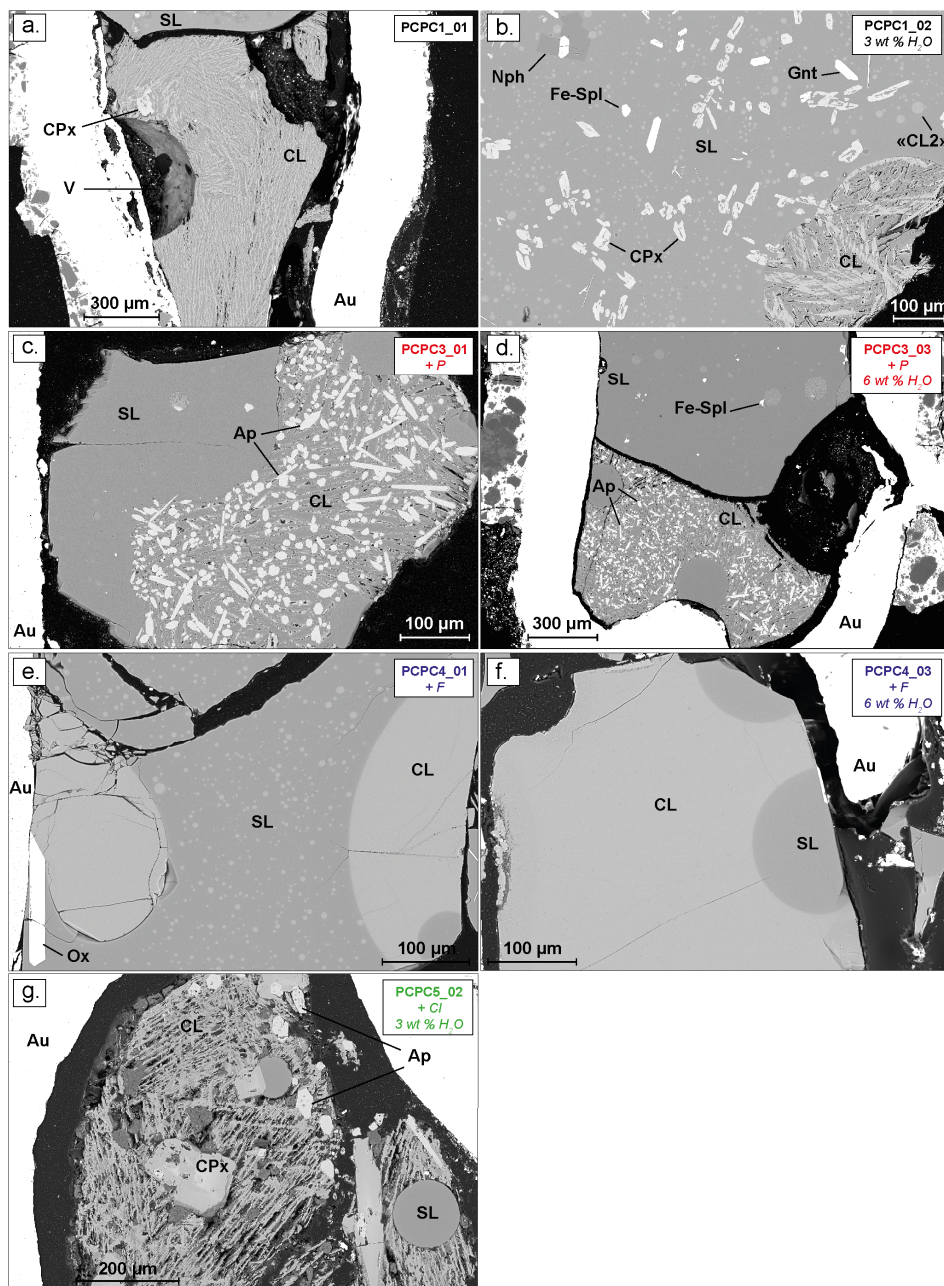


Figure 2. BSE images of typical experimental carbonate and silicate liquid immiscibility at 850 °C and 0.8 GPa, in the non-doped system in black (a and b), in the P-rich system in red (c and d); in the F-rich system in blue (e and f) and in the Cl-rich system in green (g). SL: silicate liquid; CL: carbonate liquid; CPx: clinopyroxene; Nph: nepheline; Gnt: garnet; Ap: apatite; Fe-Spl: ferrosplinel; Ox: Fe-Ti oxide; “CL2”: second carbonate liquid phase; V: fluid phase; Au: gold capsule.

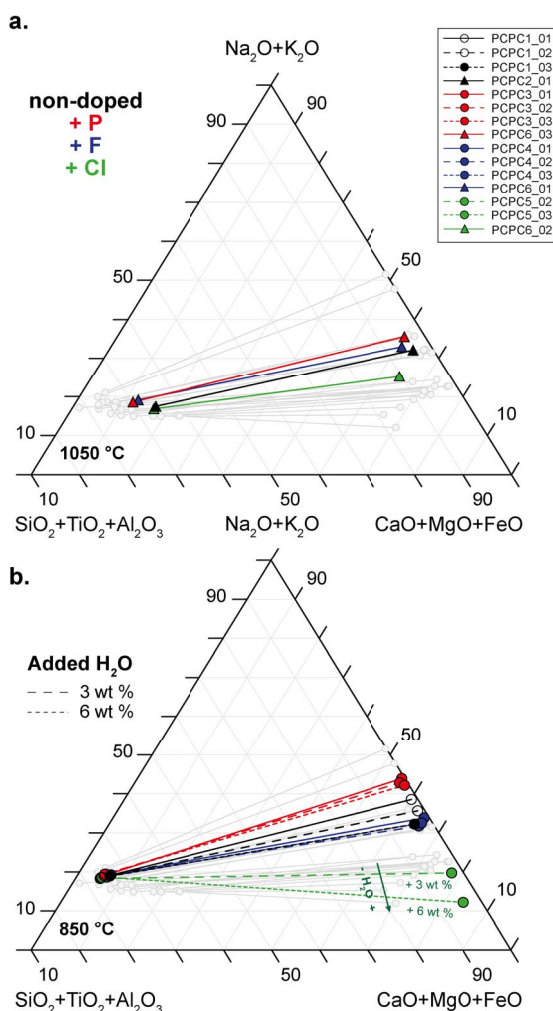


Figure 3. Hamilton projection of experimental immiscible silicate and carbonate liquids in the non-doped system and in P-, F- and Cl-rich systems at 0.8 GPa and 1050 °C (a) and 850 °C (b). Each line relates a pair of immiscible silicate and carbonate liquids in equilibrium at given P–T condition. Samples synthesized at both temperatures in the non-doped system (black), and in the systems doped in P (red), F (blue) and Cl (green) are represented, as well as hydrated samples (dashed line, 3 wt% of H₂O; dotted lines: 6 wt% of H₂O). The green arrow in (b) indicates the increase of sample H₂O contents in the Cl-rich systems (green). Carbonate and silicate melts of nephelinite–phonolite composition from Nabyl *et al.* [2020] are shown in grey. Empty symbols correspond to samples suspected to not be in equilibrium (PCPC1_01 and PCPC1_02).

Table 3) and poorer in Na₂O (8.2 ± 3.5 and 4.8 ± 2.3 wt% of Na₂O, Table 3) and K₂O (1.2 ± 0.7 and 0.8 ± 0.2 , Table 3) with increasing bulk water content (from 3 to 6 wt%; see the green arrow in Figure 3b). The carbonate melts thus slightly deviate from the (Na₂O

+ K₂O) pole and evolve towards the (CaO + MgO + FeO) pole (Figure 3b). This water effect that was predominant in the Cl-rich system is not observed in the non-doped system or the P- and F-rich systems (Figure 3b).

Table 3. Major element compositions of silicate and carbonate liquids (wt%) analysed by EMPA

	<i>PCPC1_01</i>		<i>PCPC1_02</i>		<i>PCPC1_03</i>		<i>PCPC1_04</i>		<i>PCPC2_01</i>		<i>PCPC3_01</i>		<i>PCPC3_02</i>	
	<i>P</i> (Gpa)	0,8	<i>P</i> (Gpa)	0,8	<i>P</i> (Gpa)	0,8	<i>P</i> (Gpa)	0,8	<i>P</i> (Gpa)	0,8	<i>P</i> (Gpa)	0,8	<i>P</i> (Gpa)	0,8
Starting material	<i>T</i> (°C)		<i>T</i> (°C)		<i>T</i> (°C)		<i>T</i> (°C)		<i>T</i> (°C)		<i>T</i> (°C)		<i>T</i> (°C)	
	850	850	850	850	850	850	850	850	1050	1050	850	850	850	850
Silicate liquid	<i>PhCbn1</i>		<i>PhCbn1</i>		<i>PhCbn1</i>		<i>PhCbn1</i>		<i>PhCbn1</i>		<i>PhCbn2</i>		<i>PhCbn2</i>	
	8	<i>s.d.</i>	7	<i>s.d.</i>	5	<i>s.d.</i>	—	<i>s.d.</i>	11	<i>s.d.</i>	8	<i>s.d.</i>	8	<i>s.d.</i>
<i>N</i>	53.08	0.91	52.55	1.40	48.81	0.48	—	—	43.78	0.65	51.18	0.53	49.80	0.36
SiO ₂	0.38	0.10	<i>bdl</i>	—	0.40	0.08	—	—	0.52	0.09	0.44	0.08	0.51	0.05
TiO ₂	19.35	0.59	19.83	0.34	18.46	0.25	—	—	16.74	1.02	19.14	0.50	19.07	0.14
Al ₂ O ₃	4.03	0.34	3.65	0.16	4.09	0.17	—	—	6.02	0.46	4.08	0.19	4.07	0.26
FeO	<i>bdl</i>	—	<i>bdl</i>	—	<i>bdl</i>	—	—	—	0.40	0.07	<i>bdl</i>	—	<i>bdl</i>	—
MnO	0.20	0.03	0.26	0.02	0.48	0.05	—	—	1.15	0.08	0.34	0.03	0.38	0.03
MgO	0.93	0.15	1.06	0.05	1.72	0.03	—	—	8.78	0.60	0.83	0.05	0.83	0.02
CaO	11.16	0.12	11.07	0.48	11.56	0.31	—	—	11.87	0.53	11.68	0.23	11.57	0.22
Na ₂ O	6.60	0.20	6.47	0.39	5.69	0.27	—	—	4.38	0.29	6.15	0.16	6.39	0.15
K ₂ O	<i>bdl</i>	—	<i>bdl</i>	—	<i>bdl</i>	—	—	—	0.30	0.06	0.20	0.03	<i>bdl</i>	—
P ₂ O ₅	<i>bdl</i>	—	0.15	0.01	0.20	0.01	—	—	0.37	0.03	0.14	0.01	0.15	0.02
BaO	<i>bdl</i>	—	<i>bdl</i>	—	<i>bdl</i>	—	—	—	0.44	0.05	<i>bdl</i>	—	<i>bdl</i>	—
SrO	<i>bdl</i>	—	<i>bdl</i>	—	<i>bdl</i>	—	—	—	<i>bdl</i>	—	<i>bdl</i>	—	<i>bdl</i>	—
SO ₂	0.41	0.09	0.39	0.07	0.32	0.06	—	—	0.55	0.11	0.41	0.07	0.37	0.08
F	0.07	0.01	0.07	0.01	0.07	0.01	—	—	0.06	0.01	0.08	0.01	0.08	0.01
Cl	96.21	—	95.51	—	91.80	—	—	—	95.37	—	94.68	—	93.23	—
Total	17.76	0.32	17.54	0.87	17.26	0.58	—	—	16.25	0.82	17.83	0.38	17.96	0.37
Na ₂ O + K ₂ O	0.71	—	0.73	—	0.65	—	—	—	0.42	—	0.70	—	0.69	—
ASI [Al ₂ O ₃ /(CaO + Na ₂ O + K ₂ O)]	0.25	—	0.24	—	0.32	—	—	—	0.75	—	0.27	—	0.28	—
NBO/T	11.54	—	9.79	—	5.80	—	—	—	1.29	—	10.91	—	10.44	—
(Na ₂ O + K ₂ O)/(CaO + MgO)	−0.04	—	−0.04	—	−0.05	—	—	—	−0.05	—	−0.05	—	−0.05	—
Al [Al ₂ O ₃ − (Na ₂ O + K ₂ O)]	(continued on next page)													

Table 3. (continued)

	PCPC1_01		PCPC1_02		PCPC1_03		PCPC1_04		PCPC2_01		PCPC3_01		PCPC3_02	
<i>P</i> (Gpa)	0.8		0.8		0.8		0.8		0.8		0.8		0.8	
<i>T</i> (°C)	850		850		850		850		1050		850		850	
Starting material	<i>PhCbn1</i>		<i>PhCbn1</i>		<i>PhCbn1</i>		<i>PhCbn1</i>		<i>PhCbn1</i>		<i>PhCbn2</i>		<i>PhCbn2</i>	
Carbonate liquid														
<i>N</i>	6	<i>s.d.</i>	8	<i>s.d.</i>	8	<i>s.d.</i>	8	<i>s.d.</i>	9	<i>s.d.</i>	6	<i>s.d.</i>	6	<i>s.d.</i>
SiO ₂	0.51	0.13	0.79	0.21	1.75	0.35	0.22	0.07	2.16	0.46	0.33	0.17	0.87	0.50
TiO ₂	<i>bdl</i>	—	<i>bdl</i>	—	<i>bdl</i>	—	<i>bdl</i>	—	<i>bdl</i>	—	<i>bdl</i>	—	<i>bdl</i>	—
Al ₂ O ₃	<i>bdl</i>	—	<i>bdl</i>	—	0.28	0.12	<i>bdl</i>	—	0.28	0.07	<i>bdl</i>	—	<i>bdl</i>	—
FeO	0.41	0.09	0.37	0.10	0.62	0.09	1.19	0.21	0.98	0.16	2.04	1.06	1.94	0.34
MnO	0.51	0.14	0.40	0.08	0.50	0.15	<i>bdl</i>	—	0.38	0.06	0.66	0.05	0.60	0.14
MgO	1.61	0.22	1.70	0.17	1.96	0.18	1.07	0.07	1.57	0.09	3.00	0.84	2.58	0.71
CaO	30.94	1.59	31.25	2.33	30.99	1.42	31.58	0.51	34.34	1.18	24.43	1.82	24.95	1.37
Na ₂ O	18.52	1.70	16.51	1.65	14.72	0.72	18.62	0.79	15.67	0.52	20.49	1.25	19.51	0.89
K ₂ O	2.55	0.21	2.33	0.22	2.14	0.24	3.22	0.18	2.89	0.22	2.79	0.16	3.13	0.12
P ₂ O ₅	1.92	0.24	1.82	0.16	1.86	0.17	1.94	0.12	2.75	0.26	1.69	0.06	2.17	0.41
BaO	1.16	0.14	1.24	0.07	1.30	0.10	1.01	0.07	0.99	0.07	2.01	0.85	1.46	0.56
SrO	1.66	0.15	1.69	0.20	1.65	0.09	1.76	0.13	1.56	0.14	1.96	0.30	1.68	0.29
SO ₂	0.28	0.05	0.33	0.12	0.28	0.04	0.10	0.01	0.13	0.03	0.36	0.10	0.34	0.07
F	2.91	0.13	2.95	0.32	2.28	0.25	3.15	0.23	2.07	0.22	2.99	1.34	2.38	0.43
Cl	0.15	0.04	0.12	0.02	0.05	0.01	0.56	0.06	0.31	0.01	0.41	0.26	0.20	0.10
Total	63.12	—	61.51	—	60.37	—	64.43	—	66.08	—	63.15	—	61.79	—
Na ₂ O + K ₂ O	21.07	1.91	18.84	1.86	16.86	0.96	21.84	0.97	18.56	0.75	23.28	1.41	22.64	1.00

(continued on next page)

Table 3. (continued)

P (Gpa)	PCPC3_03		PCPC3_04		PCPC4_01		PCPC4_02		PCPC4_03		PCPC4_04	
	0.8	850	0.8	850	0.8	850	0.8	850	0.8	850	0.8	850
T (°C)												
Starting material	PhCbn2		PhCbn2		PhCbn3		PhCbn3		PhCbn3		PhCbn3	
Silicate liquid												
N	8	s.d.	8	s.d.	6	s.d.	11	s.d.	8	s.d.	8	s.d.
SiO ₂	50.15	0.57	—	—	53.67	0.81	47.83	0.68	50.36	0.26	—	—
TiO ₂	0.41	0.09	—	—	0.40	0.05	0.41	0.06	0.37	0.10	—	—
Al ₂ O ₃	19.33	0.35	—	—	19.10	0.46	18.03	0.34	19.16	0.37	—	—
FeO	4.08	0.35	—	—	4.32	0.31	4.36	0.21	4.04	0.27	—	—
MnO	bdl	—	—	—	bdl	—	bdl	—	0.28	0.04	—	—
MgO	0.33	0.03	—	—	0.26	0.05	0.34	0.02	0.26	0.02	—	—
CaO	0.81	0.04	—	—	0.81	0.08	1.56	0.06	1.12	0.05	—	—
Na ₂ O	11.88	0.13	—	—	10.99	0.10	11.63	0.11	11.42	0.21	—	—
K ₂ O	6.15	0.35	—	—	6.08	0.08	5.61	0.21	5.81	0.13	—	—
P ₂ O ₅	0.21	0.04	—	—	bdl	—	bdl	—	bdl	—	—	—
BaO	0.16	0.03	—	—	0.14	0.01	0.17	0.04	0.14	0.01	—	—
SrO	bdl	—	—	—	bdl	—	bdl	—	bdl	—	—	—
SO ₂	bdl	—	—	—	bdl	—	bdl	—	bdl	—	—	—
F	0.37	0.06	—	—	1.38	0.12	1.84	0.11	1.66	0.08	—	—
Cl	0.08	0.02	—	—	0.07	0.01	0.10	0.01	0.09	0.02	—	—
Total	93.96	—	—	—	97.21	—	91.88	—	94.71	—	—	—
Na ₂ O + K ₂ O	18.03	0.49	—	—	17.07	0.18	17.24	0.32	17.23	0.34	—	—
ASI [Al ₂ O ₃ /(CaO + Na ₂ O + K ₂ O)]	0.70	—	—	—	0.73	—	0.64	—	0.71	—	—	—
NBO/T	0.28	—	—	—	0.24	—	0.33	—	0.26	—	—	—
(Na ₂ O + K ₂ O)/(CaO + MgO)	11.45	—	—	—	11.65	—	6.82	—	9.36	—	—	—
Al [Al ₂ O ₃ -(Na ₂ O + K ₂ O)]	-0.05	—	—	—	-0.04	—	-0.05	—	-0.04	—	—	—

(continued on next page)

(continued on next page)

Table 3. (continued)

		PCPC3_03		PCPC3_04		PCPC4_01		PCPC4_02		PCPC4_03		PCPC4_04	
<i>P</i> (Gpa)		0.8		0.8		0.8		0.8		0.8		0.8	
<i>T</i> (°C)		850		850		850		850		850		850	
Starting material		PhCbn2		PhCbn2		PhCbn3		PhCbn3		PhCbn3		PhCbn3	
Carbonate liquid													
<i>N</i>	7	s.d.	4	s.d.	9	s.d.	11	s.d.	10	s.d.	9	s.d.	
SiO ₂	0.51	0.25	0.33	0.05	0.47	0.09	1.54	0.25	0.98	0.38	0.25	0.06	
TiO ₂	bdl	—	0.29	0.08	bdl	—	bdl	—	bdl	—	bdl	—	
Al ₂ O ₃	bdl	—	bdl	—	0.15	0.01	0.31	0.07	0.28	0.08	bdl	—	
FeO	2.57	0.70	3.34	0.17	0.36	0.09	0.40	0.06	0.40	0.09	2.79	0.51	
MnO	0.70	0.15	0.70	0.06	0.58	0.15	0.52	0.10	0.48	0.10	0.44	0.12	
MgO	2.89	0.74	2.18	0.23	2.88	0.29	2.39	0.06	2.53	0.12	2.14	0.19	
CaO	25.43	2.82	25.44	0.83	34.27	0.32	34.65	0.37	33.92	0.83	30.59	1.68	
Na ₂ O	20.62	0.74	20.95	1.04	17.46	0.29	16.03	0.35	16.22	1.16	20.49	0.77	
K ₂ O	2.22	0.75	3.45	0.19	1.95	0.11	2.17	0.10	2.10	0.11	2.44	0.18	
P ₂ O ₅	2.99	0.78	2.76	0.89	1.81	0.14	1.96	0.11	1.92	0.19	1.83	0.28	
BaO	1.54	0.35	1.46	0.19	1.13	0.06	1.01	0.03	0.98	0.06	0.50	0.10	
SrO	1.65	0.22	1.75	0.14	1.93	0.10	1.85	0.12	2.19	0.21	1.21	0.12	
SO ₂	0.31	0.04	0.31	0.09	0.25	0.03	0.30	0.04	0.38	0.16	0.17	0.04	
F	2.54	0.63	3.57	0.40	10.92	0.33	11.46	0.24	10.70	0.24	11.35	0.97	
Cl	0.37	0.14	0.74	0.08	0.53	0.02	0.46	0.03	0.55	0.01	0.35	0.15	
Total	64.34	—	67.26	—	74.67	—	75.03	—	73.63	—	74.54	—	
Na ₂ O + K ₂ O	22.83	1.49	24.40	1.23	19.42	0.40	18.20	0.45	18.32	1.27	22.93	0.95	

(continued on next page)

Table 3. (continued)

Starting material	PCPC5_02		PCPC5_03		PCPC5_04		PCPC6_01		PCPC6_02		PCPC6_03	
	P (Gpa)	T (°C)	0.8	850	0.8	850	0.8	1050	0.8	1050	0.8	850
Starting material	PhCbn5	PhCbn6	PhCbn7	PhCbn3	PhCbn4	PhCbn2	PhCbn2	PhCbn2	PhCbn2	PhCbn2	PhCbn2	PhCbn2
Silicate liquid												
N	7	s.d.	18	s.d.	17	s.d.	3	s.d.	6	s.d.	6	s.d.
SiO ₂	50.07	0.45	45.79	0.86	—	—	42.92	0.47	46.32	0.22	46.32	0.60
TiO ₂	0.30	—	bdl	—	—	—	0.42	0.10	0.48	0.03	0.48	0.10
Al ₂ O ₃	20.54	0.32	19.54	0.28	—	—	16.34	0.28	18.50	0.34	18.50	0.25
FeO	2.40	0.25	2.48	0.19	—	—	5.34	0.34	5.69	0.24	5.69	0.19
MnO	bdl	—	bdl	—	—	—	bdl	0.05	bdl	—	bdl	—
MgO	0.34	0.02	0.45	0.04	—	—	1.02	0.04	0.77	0.03	0.77	0.03
CaO	2.08	0.05	2.64	0.04	—	—	9.00	0.30	4.64	0.19	4.64	0.17
Na ₂ O	11.65	0.20	11.18	0.41	—	—	11.40	0.39	12.78	0.23	12.78	0.26
K ₂ O	5.28	0.14	5.02	0.19	—	—	3.75	0.19	4.62	0.06	4.62	0.23
P ₂ O ₅	bdl	—	bdl	—	—	—	0.37	0.05	0.95	0.05	0.95	0.11
BaO	0.17	0.02	0.25	0.04	—	—	0.34	0.05	0.29	0.05	0.29	0.05
SrO	bdl	—	bdl	—	—	—	0.52	0.06	bdl	0.04	bdl	—
SO ₂	bdl	—	bdl	—	—	—	bdl	—	bdl	—	bdl	—
F	0.43	0.07	1.00	0.07	—	—	0.73	0.83	0.56	0.03	0.56	0.07
Cl	0.77	0.01	0.83	0.02	—	—	1.29	0.01	0.11	0.02	0.11	0.02
Total	94.03	—	89.18	—	—	—	93.44	—	95.69	—	95.69	—
Na ₂ O + K ₂ O	16.94	0.34	16.21	0.59	—	—	15.15	0.58	17.40	0.28	17.40	0.49
ASI [Al ₂ O ₃ /(CaO + Na ₂ O + K ₂ O)]	0.72	—	0.68	—	—	—	0.42	—	0.54	—	0.54	—
NBO/T	0.23	—	0.28	—	—	—	0.73	—	0.52	—	0.52	—
(Na ₂ O + K ₂ O)/(CaO + MgO)	5.37	—	4.01	—	—	—	1.20	—	2.51	—	2.51	—
Al [Al ₂ O ₃ -(Na ₂ O + K ₂ O)]	-0.03	—	-0.03	—	—	—	-0.04	—	-0.05	—	-0.05	—

(continued on next page)

Table 3. (continued)

		PCPC5_02		PCPC5_03		PCPC5_04		PCPC6_01		PCPC6_02		PCPC6_03	
<i>P</i> (Gpa)		0.8		0.8		0.8		0.8		0.8		0.8	
<i>T</i> (°C)		850		850		850		1050		1050		850	
Starting material	PhCbn5	PhCbn6		PhCbn7		PhCbn3		PhCbn4		PhCbn2			
Carbonate liquid													
<i>N</i>	7	s.d.	16	s.d.	11	s.d.	16	s.d.	6	s.d.	7	s.d.	
SiO ₂	1.02	0.36	1.49	0.68	0.18	0.04	2.87	0.68	4.51	0.54	1.97	0.46	
TiO ₂	—	—	bdl	—	bdl	—	0.18	0.01	bdl	—	bdl	—	
Al ₂ O ₃	bdl	—	0.30	0.19	bdl	—	0.60	0.19	0.87	0.22	0.38	0.11	
FeO	0.32	0.07	0.43	0.17	1.89	0.27	1.25	0.23	1.49	0.24	1.78	0.14	
MnO	0.51	0.13	0.58	0.16	0.42	0.09	0.41	0.06	0.50	0.07	0.44	0.07	
MgO	1.70	0.30	1.86	0.48	0.89	0.11	2.10	0.10	1.73	0.26	2.09	0.24	
CaO	35.10	5.62	36.82	5.11	29.35	1.89	33.10	0.73	29.94	1.95	29.37	0.94	
Na ₂ O	8.18	3.53	4.84	2.34	15.94	1.46	16.66	0.33	10.09	1.56	17.14	0.68	
K ₂ O	1.19	0.67	0.82	0.21	3.95	0.33	3.01	0.19	2.92	0.20	2.49	0.12	
P ₂ O ₅	1.53	0.40	1.48	0.44	1.49	0.13	1.75	0.20	1.98	1.03	9.47	0.95	
BaO	1.53	0.25	1.60	0.12	0.82	0.10	1.04	0.03	0.96	0.10	1.23	0.19	
SrO	2.22	0.22	2.17	0.27	1.43	0.14	1.59	0.13	1.54	0.15	1.60	0.19	
SO ₂	0.25	0.08	0.38	0.25	0.27	0.03	0.25	0.02	0.26	0.03	0.37	0.09	
F	3.52	0.80	5.63	0.75	—	—	11.79	0.67	3.62	0.76	2.34	0.27	
Cl	0.73	0.25	0.59	0.30	3.23	2.59	0.51	0.03	0.91	0.33	0.48	0.14	
Total	57.80	—	59.00	—	59.85	—	77.10	—	61.33	—	71.16	—	
Na ₂ O + K ₂ O	9.37	4.20	5.66	2.55	19.89	1.78	19.67	0.52	13.02	1.75	19.63	0.80	

N: number of analysis; bdl: below detection limit; s.d.: standard deviation; ASI: alumina saturation index; Al: alkaline index; NBO/T: non-bridging oxygen per tetrahedrally coordinated cation. The ASI, NBO/T, alkali/alkaline-earth ratio and NBO/T are in molar fractions; Italics: samples in which equilibrium between carbonate and silicate liquids is assumed not to have been attained.

A second carbonate liquid phase is observed in two samples from the non-doped system that were synthesized at 850 °C (PCPC1_01 and PCPC1_02, Table 2; see Figure 3b, empty black circles). In comparison to the main carbonate melts (Table 3), this second carbonate liquid is rare, presents higher CaO concentrations and higher totals during the EMPA analyses (see Supplementary Table 1). The occurrence of this second carbonate phase suggests that the equilibrium was not achieved in these two samples. When plotted in the chemical diagrams (see results and discussion sections, empty black circles in figures), the corresponding data points are outliers. For the sake of clarity, these two samples are included in the diagrams, but are not discussed further here.

The F, Cl and P₂O₅ silicate melt concentrations at 850 °C for all the systems are lower than those at 1050 °C. In the non-doped system (see Table 2), the silicate melts contain relatively small amounts of F (0.3–0.4 wt%), Cl (0.07 wt%), and P₂O₅ is below the detection limit (samples PCPC1, Table 3). The concentrations are slightly higher in F, Cl or P doped systems (Table 2), varying from 1.4 to 1.8 wt% for F in the F-rich system (samples PCPC4, Table 3), 0.6 to 0.8 wt% for the Cl in the Cl-rich system (samples PCPC5, Table 3) and only around 0.2 wt% for the P₂O₅ in the P-rich system (samples PCPC3, Table 3). Carbonate melts are also more enriched in those elements at the higher temperature, although P₂O₅ and Cl carbonate melt concentrations remain low in the P- and Cl-doped systems respectively (see samples PCPC3 and PCPC5_05, Table 3).

Trace element concentrations—including the REE—of both silicate and carbonate melts are presented in Table 4. At 1050 °C, the silicate melts contain 18.2 ± 0.5 to 35.9 ± 0.7 ppm of La as representative of other LREE (light REE), and 32.1 ± 0.9 to 50.3 ± 0.7 ppm of Lu, as representative of other HREE (high REE; Table 4), whereas REE concentrations in the carbonate melts are higher and vary from 87.6 ± 2.8 to 108.1 ± 5.6 for La and 50.0 ± 2.3 to 74.9 ± 2.7 ppm for Lu (Table 4). The silicate melt REE concentrations are lower at 850 °C, varying from 1.8 ± 0.0 to 8.4 ± 0.1 ppm of La, and from 3.9 ± 0.0 to 17.87 ± 3.1 ppm of Lu (Table 4). At this temperature, carbonate melt REE concentrations are generally much higher than at 1050 °C, varying from 77.7 ± 5.4 to 140.5 ± 9.8 ppm and 51.6 ± 3.3 to 116.2 ± 5.2 for La and Lu re-

spectively (Table 4). In the Cl-rich system, the middle REE and high REE (MREE and HREE) concentrations decrease slightly in the carbonate melts with increasing water content (67.0 ± 1.9 to 34.8 ± 5.0 ppm of Gd and 34.0 ± 1.3 to 13.0 ± 1.9 ppm of Lu, samples PCPC5_02 to PCPC5_03, from 3 to 6 wt% of water; Table 4), whereas no significant variation in concentration is observed in the silicate melts (Table 4). This behaviour is not observed in other chemical systems.

3.3. REE partitioning between carbonate and silicate liquids

Trace element partitioning is defined using the Nernst partition coefficient D which corresponds to the mass concentration ratio in ppm of the element x in the carbonate liquid (CL) and the silicate liquid (SL; $D_x^{CL/SL} = x^{CL}/x^{SL}$). Trace element partition coefficients (including REE) are presented in the Table 5.

Figure 4 presents REE partition coefficients for the four chemical systems investigated. For all samples and for all experimental conditions, REE partition coefficients vary greatly, by almost two orders of magnitude. The large $D_{REE}^{CL/SL}$ variation observed in the literature [Hamilton *et al.*, 1989, Martin *et al.*, 2013, Nabyl *et al.*, 2020, Veksler *et al.*, 2012, 1998] also occurs in F-, Cl- and P-rich systems. The $D_{REE}^{CL/SL}$ are higher for LREE (light REE) than for HREE (heavy REE). For most charges in the four chemical systems, carbonate melts are richer in REE than silicate melts ($D_{REE}^{CL/SL} > 1$, Figure 4). At 850 °C, the $D_{REE}^{CL/SL}$ in the non-doped system vary from 10.7 ± 2.2 to 29.6 ± 3.3 for La and from 1.7 ± 0.3 to 5.8 ± 1.1 for Lu (Figure 4). The carbonate melt REE enrichment is greater in the P- and F-rich systems (Figure 4), being almost two times higher than in the non-doped system, with the $D_{La}^{CL/SL}$ varying from 37.1 ± 4.1 to 46.2 ± 6.2 and from 26.5 ± 1.8 to 43.0 ± 5.7 in the P- and the F-rich systems respectively, and the $D_{Lu}^{CL/SL}$ varying from 5.6 ± 0.4 to 6.8 ± 0.5 and from 7.3 ± 1.8 to 8.7 ± 2.0 (Figure 4, Table 5).

No clear effect of water on REE partitioning is identified in the non-doped system and the P- and F-rich systems (Figure 4 and Table 5). In the Cl-rich system, the REE partition coefficients decrease with the addition of water (3 and 6 wt% of water, samples PCPC5_02 and PCPC5_03, Table 2), from 21.3 ± 1.6 to 14.8 ± 2.0 for $D_{La}^{CL/SL}$ and 4.6 ± 0.5 to 3.3 ± 0.5

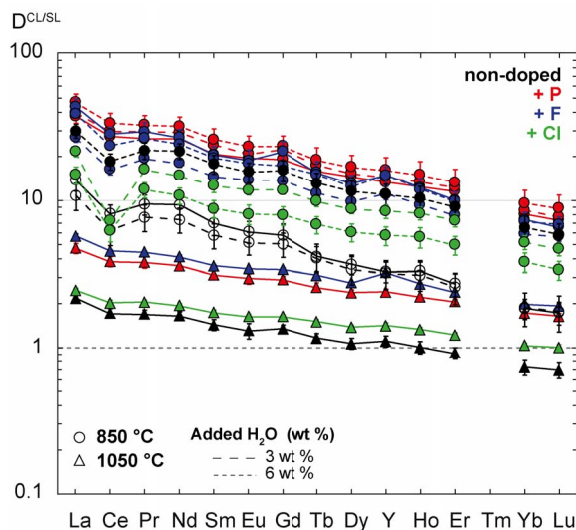


Figure 4. REE partition coefficients ($D^{\text{CL/SL}}$) between carbonate and silicate liquids (CL and SL), in the non-doped system in black, the P-rich system in red, the F-rich system in blue and the Cl-rich system in green. Samples synthesized at 850 °C (circles) and at 1050 °C (triangles) are shown in all chemical systems, as well as hydrated samples (dashed line, 3 wt% of H_2O ; dotted lines: 6 wt% of H_2O). Empty symbols correspond to samples suspected to not be in equilibrium (PCPC1_01 and PCPC1_02).

for $D_{\text{Lu}}^{\text{CL/SL}}$ (samples PCPC5_02 and PCPC5_03, green dashed and dotted lines in Figure 4).

For some samples, the Ce partition coefficients show a negative anomaly. The $D_{\text{Ce}}^{\text{CL/SL}}$ is lower compared to that of other LREE. This is particularly marked in Cl-rich samples (PCPC5_02 and PCPC5_03, green circles in Figure 4; Table 5), in the non-doped system (samples PCPC1_01 to PCPC1_03, black circles in Figure 4; Table 5) and in the F-rich system (PCPC4_02, blue circles in Figure 4; Table 5). This $D_{\text{Ce}}^{\text{CL/SL}}$ decrease reflects the higher Ce concentrations in the silicate liquids for all these samples compared to other LREE, whereas the carbonate melt Ce concentrations do not present any particular variation (see Tables 4 and 5).

At the higher temperature (1050 °C, triangles in Figure 4), the carbonate melt enrichments in REE are lower in all four chemical systems, especially in the non-doped system with a $D_{\text{La}}^{\text{CL/SL}}$ and a $D_{\text{Lu}}^{\text{CL/SL}}$ of 2.2 ± 0.1 and 0.7 ± 0.1 respectively (Table 5). As for the experiments at 850 °C, REE partitioning is more in favour of carbonate liquids for samples doped in P and F (red and blue triangles, Figure 4), with a $D_{\text{La}}^{\text{CL/SL}}$ of 4.7 ± 0.4 and 5.7 ± 0.2 respectively in the P- and

F-rich systems, and a $D_{\text{Lu}}^{\text{CL/SL}}$ of 1.6 ± 0.1 and 1.9 ± 0.1 (Table 5).

To summarise the REE partitioning, the experimental $D_{\text{REE}}^{\text{CL/SL}}$ vary by two orders of magnitude; their values increase as temperature decreases and in addition are higher in the F- and P-rich systems. Nabyl *et al.* [2020] proposed an equation relating the REE partitioning between carbonate and silicate melts to the degree of alkaline silicate melt differentiation (i.e. composition, alkalinity and polymerisation of the silicate melt). The question arises as to whether this silicate melt composition effect still applies in systems rich in F, Cl or P, or whether these elements play a key role in REE concentrations in F-, Cl- or P-rich systems. This is tested below.

4. Discussion

4.1. REE partitioning: silicate melt composition effect in F-, Cl- and P-rich environments?

In order to investigate the effect of F, Cl and P on $D_{\text{REE}}^{\text{CL/SL}}$, we compared the data in this study with the model presented in Nabyl *et al.* [2020]. The latter, which does not consider F, Cl and P, uses parameters

Table 4. Trace element concentrations of silicate and carbonate liquids (ppm) measured by LA-ICP-MS

<i>P</i> (Gpa)	<i>PCPC1_01</i> *		<i>PCPC1_02</i> *		<i>PCPC1_03</i> *		<i>PCPC1_04</i> *		<i>PCPC2_01</i> *		<i>PCPC3_01</i> *	
<i>T</i> (°C)	0.8	850	0.8	850	0.8	850	0.8	1050	0.8	850	0.8	850
Starting material	<i>PhCbn1</i>		<i>PhCbn1</i>		<i>PhCbn1</i>		<i>PhCbn1</i>		<i>PhCbn1</i>		<i>PhCbn2</i>	
Silicate liquid												
<i>N</i>	7	<i>s.d.</i>	7	<i>s.d.</i>	6	<i>s.d.</i>	9	<i>s.d.</i>	7	<i>s.d.</i>	7	<i>s.d.</i>
Sc	15.17	3.54	34.96	9.76	21.84	2.90	—	—	82.89	4.24	39.25	1.95
Ti	1722.11	126.26	2282.59	426.48	862.60	52.74	—	—	2239.38	98.18	1867.08	114.38
Cr	<i>bdl</i>	—	6.07	1.61	1.66	0.32	—	—	105.21	5.28	3.56	1.88
Mn	903.56	56.98	1249.54	445.68	472.90	29.53	—	—	2159.03	70.74	537.31	17.23
Sr	450.72	16.06	730.14	95.67	397.74	2.44	—	—	2572.65	43.23	378.68	4.86
Zr	580.26	43.20	755.17	128.74	279.51	16.76	—	—	523.19	31.47	464.28	12.99
Nb	208.32	14.51	295.54	58.84	86.68	5.53	—	—	176.48	6.98	180.16	10.04
Ba	777.66	22.57	1171.89	201.80	622.28	8.40	—	—	2544.81	100.89	709.05	15.87
La	6.68	1.08	10.92	2.21	2.97	0.31	—	—	33.60	1.38	2.10	0.10
Ce	11.66	1.69	19.87	4.01	4.90	0.60	—	—	41.67	2.20	2.85	0.15
Pr	8.18	1.28	13.96	2.75	3.54	0.44	—	—	34.81	1.66	2.37	0.15
Nd	8.50	1.30	14.35	2.69	3.60	0.44	—	—	36.38	1.61	2.38	0.15
Sm	10.90	1.90	18.12	3.35	4.10	0.56	—	—	42.00	2.30	2.87	0.16
Eu	13.11	2.09	22.11	3.77	4.85	0.70	—	—	52.00	4.21	3.57	0.23
Gd	13.41	2.50	19.50	3.55	4.44	0.71	—	—	36.74	1.61	2.99	0.09
Tb	16.47	3.23	23.05	4.18	5.47	0.87	—	—	39.11	1.82	3.92	0.35
Dy	19.24	2.62	30.66	5.85	6.04	1.08	—	—	47.94	2.80	5.26	0.49
Y	23.46	3.38	35.93	7.17	6.88	1.16	—	—	52.38	2.92	6.78	0.64
Ho	21.41	3.29	33.41	6.63	6.65	1.27	—	—	51.99	3.21	6.16	0.61
Er	22.16	3.61	35.07	6.85	6.59	1.27	—	—	47.54	2.70	6.78	0.71
Yb	32.06	3.89	48.50	9.54	9.11	1.72	—	—	58.23	4.26	10.90	1.08
Lu	29.42	4.06	45.02	9.25	8.90	1.61	—	—	52.45	4.03	11.02	1.12

(continued on next page)

Table 4. (continued)

<i>P</i> (Gpa)	<i>PCPC1_01*</i>		<i>PCPC1_02*</i>		<i>PCPC1_03*</i>		<i>PCPC1_04*</i>		<i>PCPC2_01*</i>		<i>PCPC3_01*</i>	
	0.8	850	0.8	850	0.8	850	—	—	0.8	1050	0.8	850
Starting material	<i>PhCbn1</i>	<i>PhCbn1</i>	<i>PhCbn1</i>	<i>PhCbn1</i>	<i>PhCbn1</i>	<i>PhCbn1</i>	<i>PhCbn1</i>	<i>PhCbn1</i>	<i>PhCbn1</i>	<i>PhCbn1</i>	<i>PhCbn2</i>	<i>PhCbn2</i>
Hf	42.35	18.44	42.85	14.25	15.37	1.18	—	—	23.17	2.78	15.84	1.02
Ta	15.29	1.89	15.59	4.41	5.16	0.72	—	—	13.42	1.17	8.95	2.80
Carbonate liquid												
<i>N</i>	7	<i>s.d.</i>	8	<i>s.d.</i>	8	<i>s.d.</i>	8	<i>s.d.</i>	9	<i>s.d.</i>	6	<i>s.d.</i>
Sc	16.55	5.58	25.72	8.22	36.68	3.68	5.91	0.22	22.82	1.82	67.67	9.06
Ti	417.75	71.91	435.16	69.26	635.91	66.01	409.73	19.12	512.03	37.31	524.79	162.22
Cr	—	0.60	4.82	0.85	9.57	1.03	3.46	0.34	36.49	1.65	4.00	2.08
Mn	2856.29	336.42	3187.73	618.01	3047.76	286.54	1976.40	64.70	2164.52	82.90	4819.84	598.04
Sr	10765.74	186.60	11208.43	521.58	10494.11	272.33	10980.47	308.52	10543.97	151.78	9573.38	166.70
Zr	12.66	3.19	13.89	2.12	29.88	4.17	29.38	1.71	22.59	5.48	17.15	12.49
Nb	123.19	8.08	115.54	9.70	119.03	10.82	145.17	8.26	96.08	5.11	87.58	24.27
Ba	8306.41	374.70	8108.73	627.56	8532.66	584.38	6905.15	377.24	7382.78	327.68	8069.63	581.14
La	91.07	1.98	116.82	6.49	87.67	3.65	90.47	4.53	72.46	2.86	78.08	7.79
Ce	93.48	2.08	122.93	8.30	89.68	3.12	96.01	4.06	70.92	3.68	77.12	7.43
Pr	76.58	2.16	106.25	5.08	76.86	2.96	74.04	2.62	58.55	2.79	62.00	6.58
Nd	78.65	2.30	105.17	5.24	77.34	2.47	75.45	2.26	59.56	2.77	62.59	5.46
Sm	75.31	2.60	104.14	5.49	71.88	2.43	75.98	2.65	59.58	4.04	58.47	10.20
Eu	79.58	3.70	113.03	5.70	75.24	2.78	76.19	1.88	67.33	6.10	68.66	11.71
Gd	76.86	3.68	97.65	3.41	70.44	2.80	69.95	1.78	49.04	2.51	56.22	10.39
Tb	67.96	4.73	92.25	7.70	71.14	3.45	61.83	1.41	45.09	2.29	61.10	11.06
Dy	70.10	4.78	103.01	10.52	68.82	2.97	63.68	1.63	50.73	3.25	75.93	16.02
Y	76.37	4.96	113.69	10.32	74.80	4.51	72.33	2.32	57.64	3.96	88.99	18.30
Ho	70.32	5.51	102.89	10.96	68.12	3.74	62.39	1.70	51.94	3.89	75.80	14.71
Er	59.78	4.72	89.49	11.25	59.12	3.44	53.15	1.53	43.34	3.14	77.41	13.70

(continued on next page)

Table 4. (continued)

	<i>PCPC1_01*</i>		<i>PCPC1_02*</i>		<i>PCPC1_03*</i>		<i>PCPC1_04*</i>		<i>PCPC2_01*</i>		<i>PCPC3_01*</i>	
<i>P</i> (Gpa)	0.8		0.8		0.8		0.8		0.8		0.8	
<i>T</i> (°C)	850		850		850		850		1050		850	
Starting material	<i>PhCbn1</i>		<i>PhCbn1</i>		<i>PhCbn1</i>		<i>PhCbn1</i>		<i>PhCbn1</i>		<i>PhCbn2</i>	
Yb	59.02	5.90	90.03	14.80	58.81	3.93	46.64	1.18	42.16	3.92	86.84	19.02
Lu	50.68	5.59	78.83	13.92	51.55	3.33	37.47	1.06	36.27	3.45	80.26	17.71
Hf	0.52	0.20	0.48	0.09	1.08	0.14	0.61	0.06	0.64	0.11	0.48	0.39
Ta	1.29	0.13	1.08	0.26	1.73	0.23	2.57	0.42	2.77	0.44	0.68	0.29
<i>P</i> (Gpa)	0.8		0.8		0.8		0.8		0.8		0.8	
<i>T</i> (°C)	850		850		850		850		850		850	
Starting material	<i>PhCbn2</i>		<i>PhCbn2</i>		<i>PhCbn3</i>		<i>PhCbn3</i>		<i>PhCbn3</i>		<i>PhCbn3</i>	
Silicate liquid												
<i>N</i>	7	s.d.	6	s.d.	10	s.d.	7	s.d.	7	s.d.	7	s.d.
Sc	39.91	1.22	34.95	0.65	50.18	5.94	41.81	1.33	35.83	1.34	—	—
Ti	1760.76	70.24	1757.33	62.49	1748.28	167.15	1833.56	25.31	1797.32	24.89	—	—
Cr	3.40	0.51	2.24	0.51	5.87	4.27	2.91	0.21	2.66	0.60	—	—
Mn	558.63	15.79	513.90	7.26	808.71	98.81	957.86	21.90	770.69	14.67	—	—
Sr	374.99	4.69	362.90	2.65	402.67	23.67	659.56	22.10	514.72	17.37	—	—
Zr	453.15	13.88	452.70	21.67	540.17	42.31	486.15	11.39	483.61	5.61	—	—
Nb	167.10	6.54	208.97	3.42	162.48	111.38	185.76	36.18	119.17	7.10	—	—
Ba	714.74	14.37	681.30	4.34	591.25	42.20	867.69	25.01	638.31	9.81	—	—
La	1.98	0.02	1.80	0.05	2.99	0.38	4.16	0.11	2.84	0.10	—	—
Ce	2.69	0.05	2.41	0.09	5.12	0.56	7.38	0.21	4.89	0.29	—	—
Pr	2.16	0.02	1.97	0.07	4.43	0.63	5.22	0.18	3.73	0.19	—	—
Nd	2.18	0.03	1.99	0.05	4.86	0.60	5.76	0.16	3.99	0.22	—	—
Sm	2.61	0.08	2.43	0.06	6.50	0.84	7.42	0.28	5.10	0.35	—	—
Eu	3.13	0.08	3.01	0.14	7.51	1.34	6.97	0.15	5.43	0.28	—	—
Gd	2.96	0.09	2.79	0.14	7.36	0.99	8.64	0.54	5.88	0.47	—	—

(continued on next page)

Table 4. (continued)

<i>P</i> (Gpa) <i>T</i> (°C)	PCPC3_02*		PCPC3_03*		PCPC4_01*		PCPC4_02*		PCPC4_03*		PCPC4_04*	
	0.8	850	0.8	850	0.8	850	0.8	850	0.8	850	0.8	850
Starting material	PhCbn2	PhCbn2	PhCbn2	PhCbn2	PhCbn3	PhCbn3	PhCbn3	PhCbn3	PhCbn3	PhCbn3	PhCbn3	PhCbn3
Tb	3.43	0.11	3.33	0.19	8.65	1.36	8.16	0.44	5.58	0.39	—	—
Dy	4.86	0.18	4.46	0.22	11.54	1.53	10.55	0.35	7.89	0.50	—	—
Y	6.12	0.24	5.63	0.34	11.18	1.50	10.71	0.37	7.83	0.42	—	—
Ho	5.63	0.25	5.17	0.35	12.28	1.77	10.79	0.48	8.35	0.55	—	—
Er	6.32	0.27	5.68	0.42	13.57	1.79	11.61	0.51	9.01	0.59	—	—
Yb	10.16	0.52	9.25	0.76	19.66	2.54	16.43	0.66	13.11	0.92	—	—
Lu	10.11	0.48	9.15	0.69	17.87	3.07	13.94	0.54	11.07	0.71	—	—
Hf	20.77	3.60	18.89	0.66	14.49	1.50	27.54	4.84	28.19	1.77	—	—
Ta	10.89	2.03	11.80	0.62	4.89	3.69	22.92	6.98	9.06	4.48	—	—
Carbonate liquid												
<i>N</i>	6	s.d.	7	s.d.	5	s.d.	11	s.d.	6	s.d.	5	s.d.
Sc	73.11	11.04	79.57	10.03	88.83	3.83	75.85	3.24	72.39	2.74	82.41	2.03
Ti	520.20	164.35	947.61	137.79	475.87	30.90	729.92	60.19	674.37	16.28	1002.95	40.94
Cr	8.65	2.55	5.82	0.06	2.44	0.69	7.12	1.29	5.99	1.37	5.83	1.13
Mn	5113.86	470.08	4822.68	496.32	4107.32	273.08	3301.18	196.25	3389.16	80.25	3615.10	25.16
Sr	9528.76	617.79	10292.20	513.75	13647.83	164.16	12793.00	533.91	13799.87	463.88	9027.72	125.16
Zr	7.69	1.33	28.71	8.40	9.08	1.73	26.99	7.01	18.93	3.35	173.69	33.16
Nb	92.84	22.37	180.84	31.09	44.97	4.73	153.34	23.82	84.49	8.25	228.43	9.65
Ba	7819.33	1186.38	9474.97	646.82	8228.87	120.45	7843.84	342.81	7263.80	123.90	4263.01	81.33
La	77.67	5.41	83.11	10.93	128.67	4.97	110.32	7.00	109.17	3.15	103.41	2.06
Ce	78.80	4.66	80.27	13.66	143.52	5.61	118.43	8.38	114.60	3.09	111.10	2.37
Pr	62.89	4.31	63.51	10.11	129.00	6.05	99.80	5.61	97.82	2.30	91.90	1.30
Nd	62.80	2.42	63.22	9.21	129.24	4.66	102.55	5.95	95.36	3.17	94.32	1.63
Sm	61.74	2.41	62.71	11.02	131.42	5.42	106.40	7.04	98.00	5.48	91.60	1.68

(continued on next page)

Table 4. (continued)

<i>P</i> (Gpa)	PCPC3_02*		PCPC3_03*		PCPC4_01*		PCPC4_02*		PCPC4_03*		PCPC4_04*	
	0.8	850	0.8	850	0.8	850	0.8	850	0.8	850	0.8	850
Starting material	PhCbn2	PhCbn2	PhCbn2	PhCbn2	PhCbn3	PhCbn3	PhCbn3	PhCbn3	PhCbn3	PhCbn3	PhCbn3	PhCbn3
Eu	64.14	3.02	69.32	12.07	139.11	7.44	95.41	4.07	95.56	2.75	106.80	1.87
Gd	65.22	8.07	64.83	10.61	156.76	16.55	116.71	11.75	100.35	5.81	105.18	1.88
Tb	58.92	3.79	62.08	13.19	132.83	11.91	90.71	5.50	82.88	3.88	84.93	1.79
Dy	73.55	4.50	74.34	15.22	148.93	6.75	102.40	5.93	97.33	4.23	96.41	2.05
Y	86.94	6.30	89.67	18.97	164.07	8.28	117.38	8.64	115.00	4.72	106.62	3.30
Ho	74.60	4.72	76.56	17.44	148.44	7.26	99.67	6.93	98.73	3.94	93.68	1.71
Er	76.80	5.96	74.88	15.38	134.91	5.56	91.03	4.64	88.10	3.78	86.27	1.54
Yb	85.98	7.47	87.28	19.17	143.49	5.25	96.00	6.00	92.84	3.86	92.06	1.71
Lu	77.40	6.02	79.99	17.27	116.18	5.21	78.27	4.53	75.25	2.97	74.34	1.52
Hf	0.27	0.07	0.70	0.26	0.21	0.04	0.90	0.23	0.76	0.24	4.56	1.00
Ta	0.55	0.25	1.72	0.34	0.29	0.34	3.44	1.12	1.35	0.56	1.69	0.16
PCPC5_02**#												
<i>P</i> (Gpa)	PCPC5_02**#		PCPC5_03*		PCPC5_04*		PCPC6_01*		PCPC6_02*		PCPC6_03#	
	0.8	850	0.8	850	0.8	850	0.8	850	0.8	850	0.8	850
Starting material	PhCbn4	PhCbn4	PhCbn4	PhCbn4	PhCbn3	PhCbn3	PhCbn3	PhCbn3	PhCbn3	PhCbn3	PhCbn2	PhCbn2
Silicate liquid												
<i>N</i>	3	s.d.	6	s.d.	6	s.d.	6	s.d.	6	s.d.	6	s.d.
Sc	6.05	0.20	5.77	0.14	—	—	66.59	3.94	74.22	1.07	88.83	1.42
Ti	612.58	13.30	527.99	5.43	—	—	2402.61	154.04	2361.75	35.60	2868.19	71.36
Cr	bdl	—	1.83	0.26	—	—	98.02	4.99	66.76	1.03	107.96	7.94
Mn	639.17	38.43	910.95	7.22	—	—	1770.07	66.64	1863.55	24.96	2023.31	26.64
Sr	974.34	19.03	1211.86	14.66	—	—	1825.38	37.09	3296.04	48.13	2484.08	19.47
Zr	310.69	8.11	284.47	3.79	—	—	517.10	33.40	468.16	7.35	662.16	26.19
Nb	116.31	1.80	115.81	1.13	—	—	233.27	10.97	239.08	1.87	207.30	6.47

(continued on next page)

Table 4. (continued)

P (Gpa) T (°C)	PCPC5_02*#		PCPC5_03*		PCPC5_04*		PCPC6_01*		PCPC6_02*		PCPC6_03#	
	0.8	850	0.8	850	0.8	850	0.8	1050	0.8	1050	0.8	1050
Starting material	PhCbn4	PhCbn4	PhCbn4	PhCbn4	PhCbn3	PhCbn3	PhCbn3	PhCbn3	PhCbn3	PhCbn3	PhCbn2	PhCbn2
Ba	1095.46	8.07	1696.68	25.25	—	—	2033.84	61.31	2442.04	42.44	2623.17	31.88
La	6.60	0.14	8.37	0.11	—	—	18.21	0.48	35.92	0.66	23.13	1.32
Ce	15.09	0.31	15.99	0.21	—	—	23.70	0.37	46.62	0.77	28.81	1.44
Pr	6.33	0.02	7.77	0.08	—	—	20.08	0.35	36.54	0.72	23.44	1.30
Nd	6.41	0.03	7.08	0.08	—	—	20.94	0.42	37.34	0.55	23.94	1.14
Sm	5.98	0.26	6.32	0.18	—	—	22.86	0.37	40.86	0.87	28.88	0.98
Eu	5.80	0.19	5.10	0.05	—	—	25.18	0.40	42.14	0.93	31.18	1.32
Gd	5.01	0.05	4.42	0.09	—	—	31.75	0.74	45.63	0.95	31.76	1.77
Tb	3.99	0.12	4.01	0.04	—	—	25.62	0.36	43.41	0.67	29.91	1.28
Dy	4.74	0.06	4.01	0.05	—	—	29.94	0.61	46.50	0.89	37.06	1.02
Y	5.49	0.18	5.02	0.07	—	—	31.02	0.71	51.43	0.76	42.40	1.36
Ho	4.37	0.22	3.80	0.03	—	—	31.57	0.71	49.84	0.76	39.05	1.39
Er	4.07	0.22	3.49	0.03	—	—	29.83	0.75	43.62	0.66	39.36	1.25
Yb	5.16	0.12	4.21	0.05	—	—	36.48	0.94	52.56	1.12	50.36	0.94
Lu	4.79	0.16	3.90	0.05	—	—	32.12	0.87	50.31	0.68	45.94	1.04
Hf	12.26	0.65	10.04	0.12	—	—	36.48	1.49	15.90	0.27	31.21	1.12
Ta	7.64	0.25	8.86	0.18	—	—	1.73	0.09	14.07	0.23	6.37	1.10
Carbonate liquid												
N	7	s.d.	8	s.d.	8	s.d.	7	s.d.	11	s.d.	6	s.d.
Sc	6.54	1.00	4.86	1.03	9.98	0.42	53.15	0.62	36.92	1.98	64.64	7.37
Ti	328.34	63.91	265.10	52.93	448.59	26.27	841.60	21.28	1033.07	100.60	1193.03	124.36
Cr	—	2.80	14.53	3.77	7.88	0.54	69.66	2.12	94.58	12.42	100.91	15.54

(continued on next page)

Table 4. (continued)

Starting material	PCPC5_02**		PCPC5_03*		PCPC5_04*		PCPC6_01*		PCPC6_02*		PCPC6_03#	
	P (Gpa)	T (°C)	0.8	850	0.8	850	0.8	1050	0.8	1050	0.8	1050
	PhCbn4	PhCbn4	PhCbn4	PhCbn4	PhCbn4	PhCbn4	PhCbn3	PhCbn3	PhCbn3	PhCbn3	PhCbn2	PhCbn2
Mn	3690.77	532.50	4723.97	458.62	2943.49	77.26	2743.15	10.07	2853.87	140.87	4062.84	308.27
Sr	16991.89	1297.96	15848.10	915.96	10373.42	135.30	11368.69	66.30	11250.34	278.61	13607.86	562.29
Zr	10.28	2.59	8.24	2.64	29.31	1.62	46.92	2.45	51.76	7.86	57.89	6.78
Nb	132.66	28.73	129.93	28.67	188.87	6.85	175.58	2.36	201.28	17.62	180.34	10.51
Ba	10845.25	1728.56	11756.56	1482.52	6453.81	136.46	7706.21	52.41	6960.76	441.99	10612.55	1058.95
La	140.48	9.79	123.54	16.44	86.77	1.75	103.32	1.14	87.61	2.83	108.09	5.60
Ce	109.18	5.91	98.47	15.28	87.22	1.52	106.09	1.30	93.18	3.99	109.41	6.24
Pr	102.18	5.17	90.71	10.68	68.96	0.89	88.55	0.92	74.01	1.74	87.87	6.57
Nd	93.26	4.04	75.43	9.52	68.67	1.16	85.81	1.25	71.65	1.60	85.18	5.29
Sm	74.46	7.05	54.76	7.35	63.84	0.94	81.48	0.96	70.41	2.21	89.29	4.43
Eu	67.40	4.29	40.70	5.99	66.39	0.85	85.87	1.03	68.30	1.83	91.13	6.05
Gd	58.29	3.35	34.76	5.02	61.28	0.77	106.95	1.29	73.71	1.66	90.98	2.21
Tb	38.98	2.92	27.20	3.59	52.04	0.66	78.63	1.08	64.90	2.08	76.11	4.48
Dy	40.86	2.84	24.11	3.43	61.00	0.61	81.70	0.86	63.89	1.67	86.96	2.73
Y	45.83	4.36	28.71	4.21	70.66	1.35	99.27	0.63	72.43	2.56	101.05	2.86
Ho	35.37	2.84	21.24	3.39	59.44	0.72	84.56	1.24	66.00	2.24	85.78	1.70
Er	29.38	2.47	17.15	2.54	52.29	0.82	70.44	0.80	52.85	1.48	80.40	1.70
Yb	26.53	2.94	15.95	2.41	50.14	0.91	71.53	0.95	54.14	1.95	86.00	1.71
Lu	22.24	2.27	13.01	1.93	37.57	0.95	61.22	0.90	50.05	2.31	74.90	2.73
Hf	0.20	0.09	0.26	0.06	4.48	0.20	2.19	0.11	1.37	0.22	1.58	0.24
Ta	1.50	0.25	1.82	0.48	0.71	0.03	0.49	0.01	4.56	0.54	1.85	0.33

N: number of analysis; Bdl: below detection limit; s.d.: standard deviation. Italics: samples in which equilibrium between carbonate and silicate liquids is assumed not to have been attained. *: sample analysed by the Agilent 7500 CS Quadrupole ICP-MS; #: sample analysed by the Agilent 7900 Quadrupole ICP-MS.

Table 5. Partition coefficients between silicate and carbonate liquids, for Ca, volatiles and trace elements

<i>P</i> (Gpa) <i>T</i> (°C)	<i>PCPC1_01</i>		<i>PCPC1_02</i>		<i>PCPC1_03</i>		<i>PCPC2_01</i>		<i>PCPC3_01</i>		<i>PCPC3_02</i>		<i>PCPC3_03</i>		<i>PCPC4_01</i>	
	0,8 850	0,8 850	0,8 850	0,8 850	0,8 850	0,8 850	0,8 1050	0,8 1050	0,8 850	0,8 850	0,8 850	0,8 850	0,8 850	0,8 850	0,8 850	0,8 850
Starting material	<i>PhCbn1</i>	<i>s.d.</i>	<i>PhCbn1</i>	<i>s.d.</i>	<i>PhCbn1</i>	<i>s.d.</i>	<i>PhCbn1</i>	<i>s.d.</i>	<i>PhCbn2</i>	<i>s.d.</i>	<i>PhCbn2</i>	<i>s.d.</i>	<i>PhCbn2</i>	<i>s.d.</i>	<i>PhCbn3</i>	<i>s.d.</i>
Ca	33.10	5.69	29.47	2.65	18.00	0.89	3.91	0.30	29.43	2.87	29.99	1.84	31.55	3.85	42.46	4.43
F	7.140	1.549	7.469	1.587	7.200	1.591	3.786	0.855	7.322	3.496	6.378	1.762	6.806	2.060	7.913	0.731
Cl	2.160	0.620	1.866	0.405	0.626	0.194	5.126	0.492	5.039	3.316	2.497	1.290	4.442	1.880	7.725	1.576
P ₂ O ₅	—	—	—	—	—	—	9.018	1.961	8.601	1.339	—	—	14.365	4.824	—	—
Sc	1.091	0.447	0.736	0.312	1.679	0.279	0.275	0.026	1.724	0.246	1.832	0.282	2.277	0.290	1.770	0.223
Ti	0.243	0.045	0.191	0.047	0.737	0.089	0.229	0.019	0.281	0.089	0.295	0.094	0.539	0.081	0.272	0.031
Cr	—	—	0.794	0.253	5.765	1.275	0.347	0.023	1.125	0.834	2.541	0.839	2.602	0.591	0.416	0.324
Mn	3.161	0.422	2.551	1.036	6.445	0.727	1.003	0.051	8.970	1.150	9.154	0.880	9.384	0.975	5.079	0.706
Sr	23.886	0.946	15.351	2.135	26.384	0.704	4.098	0.091	25.281	0.547	25.411	1.678	28.361	1.431	33.893	2.034
Zr	0.022	0.006	0.018	0.004	0.107	0.016	0.043	0.011	0.037	0.027	0.017	0.003	0.063	0.019	0.017	0.003
Nb	0.591	0.057	0.391	0.084	1.373	0.153	0.544	0.036	0.486	0.137	0.556	0.136	0.865	0.149	0.277	0.192
Ba	10.681	0.573	6.919	1.306	13.712	0.957	2.901	0.173	11.381	0.858	10.940	1.674	13.907	0.954	13.918	1.014
La	13.628	2.220	10.695	2.245	29.565	3.317	2.157	0.123	37.141	4.098	39.217	2.758	46.195	6.208	43.034	5.710
Ce	8.018	1.177	6.187	1.316	18.315	2.333	1.702	0.126	27.094	2.979	29.346	1.819	33.307	5.803	28.026	3.260
Pr	9.361	1.489	7.613	1.546	21.738	2.822	1.682	0.113	26.168	3.236	29.077	2.013	32.250	5.257	29.153	4.360
Nd	9.254	1.445	7.329	1.422	21.513	2.695	1.637	0.105	26.306	2.833	28.744	1.196	31.753	4.703	26.577	3.440
Sm	6.908	1.229	5.746	1.104	17.553	2.470	1.419	0.124	20.382	3.731	23.672	1.192	25.788	4.574	20.209	2.744
Eu	6.070	1.010	5.113	0.909	15.512	2.317	1.295	0.157	19.210	3.509	20.506	1.107	23.052	4.146	18.531	3.453
Gd	5.731	1.103	5.008	0.927	15.882	2.606	1.335	0.090	18.818	3.520	22.038	2.800	23.198	3.966	21.308	3.644
Tb	4.126	0.859	4.002	0.798	13.002	2.172	1.153	0.079	15.582	3.150	17.171	1.227	18.660	4.103	15.360	2.780

(continued on next page)

Table 5. (continued)

<i>P</i> (Gpa) <i>T</i> (°C)	<i>PCPC1_01</i>		<i>PCPC1_02</i>		<i>PCPC1_03</i>		<i>PCPC2_01</i>		<i>PCPC3_01</i>		<i>PCPC3_02</i>		<i>PCPC3_03</i>		<i>PCPC4_01</i>	
	0,8	850	0,8	850	0,8	850	0,8	1050	0,8	850	0,8	850	0,8	850	0,8	850
Starting material	<i>PhCbn1</i>	<i>s.d.</i>	<i>PhCbn1</i>	<i>s.d.</i>	<i>PhCbn1</i>	<i>s.d.</i>	<i>PhCbn1</i>	<i>s.d.</i>	<i>PhCbn2</i>	<i>s.d.</i>	<i>PhCbn2</i>	<i>s.d.</i>	<i>PhCbn2</i>	<i>s.d.</i>	<i>PhCbn3</i>	<i>s.d.</i>
Dy	3.644	0.554	3.359	0.727	11.400	2.099	1.058	0.092	14.427	3.328	15.148	1.080	16.656	3.508	12.903	1.803
Y	3.255	0.515	3.164	0.694	10.880	1.956	1.100	0.097	13.125	2.966	14.208	1.173	15.918	3.504	14.671	2.109
Ho	3.285	0.567	3.080	0.694	10.251	2.039	0.999	0.097	12.297	2.678	13.240	1.025	14.809	3.517	12.092	1.844
Er	2.698	0.488	2.552	0.593	8.966	1.798	0.912	0.084	11.413	2.347	12.161	1.080	13.194	2.877	9.939	1.373
Yb	1.841	0.290	1.856	0.476	6.456	1.291	0.724	0.086	7.969	1.916	8.459	0.851	9.439	2.214	7.298	0.980
Lu	1.723	0.305	1.751	0.475	5.790	1.112	0.692	0.084	7.281	1.769	7.657	0.698	8.739	1.999	6.501	1.155
Hf	0.012	0.007	0.011	0.004	0.070	0.010	0.027	0.006	0.030	0.025	0.013	0.004	0.037	0.014	0.015	0.003
Ta	0.084	0.013	0.069	0.026	0.336	0.064	0.206	0.037	0.076	0.040	0.050	0.025	0.146	0.030	0.059	0.082
<i>P</i> (Gpa)		<i>PCPC4_02</i>		<i>PCPC4_03</i>		<i>PCPC5_02</i>		<i>PCPC5_03</i>		<i>PCPC6_01</i>		<i>PCPC6_02</i>		<i>PCPC6_03</i>		
<i>T</i> (°C)		0,8	850	0,8	850	0,8	850	0,8	850	0,8	1050	0,8	1050	0,8	1050	
Starting material	<i>PhCbn3</i>	<i>s.d.</i>	<i>PhCbn3</i>	<i>s.d.</i>	<i>PhCbn4</i>	<i>s.d.</i>	<i>PhCbn4</i>	<i>s.d.</i>	<i>PhCbn4</i>	<i>s.d.</i>	<i>PhCbn3</i>	<i>s.d.</i>	<i>PhCbn4</i>	<i>s.d.</i>	<i>PhCbn2</i>	<i>s.d.</i>
Ca	22.24	0.86	30.40	1.56	16.89	2.74	13.93	1.95	6.64	0.42	3.32	0.23	6.34	0.31		
F	6.225	0.408	6.442	0.333	8.245	2.285	5.630	0.834	3.060	0.684	4.933	1.058	4.204	0.706		
Cl	4.680	0.493	6.288	1.281	0.950	0.329	0.718	0.368	5.883	0.992	0.706	0.257	4.423	1.481		
P ₂ O ₅	—	—	—	—	—	—	—	—	11.747	3.925	5.418	2.925	9.934	1.542		
Sc	1.814	0.097	2.020	0.108	1.082	0.169	0.843	0.179	0.798	0.048	0.497	0.028	0.728	0.084		
Ti	0.398	0.033	0.375	0.010	0.536	0.105	0.502	0.100	0.350	0.024	0.437	0.043	0.416	0.045		
Cr	2.448	0.477	2.254	0.727	—	—	7.956	2.357	0.711	0.042	1.417	0.187	0.935	0.159		
Mn	3.446	0.220	4.398	0.134	5.774	0.903	5.186	0.505	1.550	0.059	1.531	0.078	2.008	0.155		

(continued on next page)

Table 5. (continued)

<i>P</i> (Gpa) <i>T</i> (°C)	PCPC4_02		PCPC4_03		PCPC5_02		PCPC5_03		PCPC6_01		PCPC6_02		PCPC6_03	
	0.8	850	0.8	850	0.8	850	0.8	850	0.8	1050	0.8	1050	0.8	1050
Starting material	PhCbn3	s.d.	PhCbn3	s.d.	PhCbn4	s.d.	PhCbn4	s.d.	PhCbn3	s.d.	PhCbn4	s.d.	PhCbn2	s.d.
Sr	19.396	1.038	26.811	1.277	17.439	1.375	13.077	0.772	6.228	0.132	3.413	0.098	5.478	0.230
Zr	0.056	0.014	0.039	0.007	0.033	0.008	0.029	0.009	0.091	0.008	0.111	0.017	0.087	0.011
Nb	0.825	0.206	0.709	0.081	1.141	0.248	1.122	0.248	0.753	0.037	0.842	0.074	0.870	0.057
Ba	9.040	0.473	11.380	0.261	9.900	1.580	6.929	0.880	3.789	0.117	2.850	0.188	4.046	0.407
La	26.519	1.831	38.475	1.709	21.285	1.549	14.759	1.973	5.675	0.161	2.439	0.091	4.672	0.360
Ce	16.054	1.222	23.416	1.509	7.234	0.419	6.159	0.959	4.477	0.089	1.999	0.092	3.797	0.288
Pr	19.135	1.254	26.194	1.478	16.133	0.818	11.682	1.380	4.411	0.089	2.025	0.062	3.749	0.349
Nd	17.799	1.145	23.924	1.551	14.557	0.634	10.659	1.351	4.099	0.102	1.919	0.051	3.558	0.279
Sm	14.348	1.093	19.231	1.704	12.459	1.296	8.671	1.189	3.565	0.071	1.723	0.065	3.092	0.186
Eu	13.685	0.657	17.603	1.035	11.621	0.832	7.980	1.178	3.410	0.068	1.621	0.056	2.922	0.230
Gd	13.513	1.602	17.062	1.686	11.634	0.678	7.869	1.147	3.369	0.089	1.616	0.050	2.864	0.174
Tb	11.120	0.901	14.841	1.238	9.761	0.789	6.782	0.897	3.069	0.060	1.495	0.053	2.544	0.185
Dy	9.706	0.647	12.329	0.947	8.621	0.610	6.010	0.859	2.729	0.062	1.374	0.044	2.347	0.098
Y	10.960	0.889	14.687	0.987	8.353	0.838	5.715	0.843	3.200	0.076	1.408	0.054	2.383	0.102
Ho	9.234	0.763	11.817	0.907	8.093	0.764	5.597	0.893	2.678	0.072	1.324	0.049	2.197	0.090
Er	7.843	0.527	9.781	0.768	7.225	0.725	4.915	0.729	2.361	0.065	1.212	0.039	2.043	0.078
Yb	5.844	0.435	7.084	0.577	5.145	0.581	3.787	0.574	1.961	0.057	1.030	0.043	1.708	0.047
Lu	5.615	0.390	6.797	0.513	4.639	0.497	3.338	0.496	1.906	0.059	0.995	0.048	1.631	0.070
Hf	0.033	0.010	0.027	0.009	0.016	0.007	0.026	0.006	0.060	0.004	0.086	0.014	0.051	0.008
Ta	0.150	0.067	0.149	0.096	0.197	0.034	0.206	0.055	0.281	0.017	0.324	0.038	0.291	0.072

s.d.: standard deviation, calculated statistical uncertainty. Italics: samples in which equilibrium between carbonate and silicate liquids is assumed not to have been attained.

related to the silicate melt composition and structure to define $D_{La}^{CL/SL}$ (La being used as representative of other REE) for all samples from the four chemical systems. These parameters are:

- the CaO content, which is a good proxy of mineral fractionation during alkaline magma differentiation (Figure 5a, Table 3);
- the alumina saturation index, abbreviated to ASI ($Al_2O_3/(CaO + Na_2O + K_2O)$; Figure 5b, Table 3), which indicates the degree of peralkalinity of the silicate melt; we note here that all the silicate liquids from this study are peralkaline, with an ASI < 1 and a negative alkalinity index (abbreviated to A.I. in Table 3);
- the alkali/alkaline-earth cation ratio ($(Na_2O + K_2O)/(CaO + MgO)$, Figure 5c).

In this discussion, we also systematically use the NBO/T [non-bridging oxygen per tetrahedrally coordinated cation; Mysen *et al.*, 1982], a classic parameter used to indicate the degree of polymerisation of silicate melts (Figure 5d).

For the 19 samples synthesized at 850–1050 °C and 0.8 GPa, in the four chemical systems (non-doped, + F, + Cl or + P) and \pm additional water (Table 2), the $D_{La}^{CL/SL}$ decreases while the silicate melt CaO contents increase (Figure 5a). This effect indicates that REE-rich carbonate melts (high $D_{La}^{CL/SL}$) coexist with fractionated silicate liquids (i.e. with low CaO contents) in all chemical systems, including those doped in F, Cl and P. The $D_{La}^{CL/SL}$ also correlates with the ASI of the silicate melts (Figure 5b): the most peralkaline silicate liquid (ASI < 0.5 in Figure 5b; samples PCPC2_01, PCPC6_01 and PCPC6_02, Table 3) corresponds to the lowest $D_{La}^{CL/SL}$ (Table 5), whereas less peralkaline silicate liquids (ASI > 0.6, Figure 5b) have the highest $D_{La}^{CL/SL}$. Moreover, $D_{La}^{CL/SL}$ increases with the $(Na_2O + K_2O)/(CaO + MgO)$ ratio (Figure 5c): as this ratio increases (representing an increase in alkali in the silicate melts relative to the CaO and the MgO contents; Figure 5c and Table 3), the REE concentrations in the conjugate carbonate melts increase; this is observed in all charges whether or not doped in F, Cl and P. Lastly, Figure 5d shows an inverse correlation between $D_{La}^{CL/SL}$ and NBO/T, with $D_{La}^{CL/SL}$ increasing as NBO/T decreases (indicating a more polymerised silicate liquid). These effects have also all been observed in previous investigations on immiscible carbonate and

alkaline silicate melts [grey symbols in Figure 5; Hamilton *et al.*, 1989, Martin *et al.*, 2013, Nabyl *et al.*, 2020, Veksler *et al.*, 2012, 1998]. In both non-doped and F-, Cl- and P-doped systems, REE-rich carbonate melts can coexist with highly fractionated (low CaO, Figure 5a), weakly peralkaline (low ASI and AI, Figure 5b and Table 3) and highly polymerised (low NBO/T, Figure 5d) alkaline silicate melts. The trends shown in Figure 5 do not allow any sub-systems to be distinguished.

4.2. The role of F, Cl and P in the silicate melt composition

As suggested by Figure 5, the highest REE partition coefficients, which correspond to the F- and P-rich charges (Figures 4 and 5), demonstrate that the conjugate silicate melts are among the most fractionated, the least peralkaline and the most polymerised silicate melts. This could suggest that the addition of F and P has an impact on the composition of the silicate melts in equilibrium with carbonate melts. As described in the Introduction section, the addition of F, Cl and P has important effects on the physical properties of silicate melts. However, the new data in this study show that, only F or Cl could have a significant effect on the silicate melt structure and composition, since P_2O_5 concentrations are generally below the detection limit for all the experimental charges (see Table 3).

It has been shown that the addition of water, the composition of the silicate melt and the F concentration all affect F speciation in synthetic peralkaline silicate melts [Baasner *et al.*, 2014]. Baasner *et al.* [2013a] also highlighted that the effect of Cl on the silicate melt structure depends on the melt composition, and that Cl and F have opposing effects on peralkaline silicate melt viscosity: Cl increases the viscosity, whereas F decreases it. Thus the F and Cl effects could impact the structure and composition of the peralkaline silicate melts of nephelinite-phonolite type used in this study, and consequently the REE partitioning between carbonate and silicate melts.

The F and Cl partition coefficients (see Table 5) are plotted in Figure 6 against NBO/T and ASI which are taken as proxies of the silicate melt composition and structure. $D_F^{CL/SL}$ values are in the range of 5–9 (Table 5) and show weak negative and positive

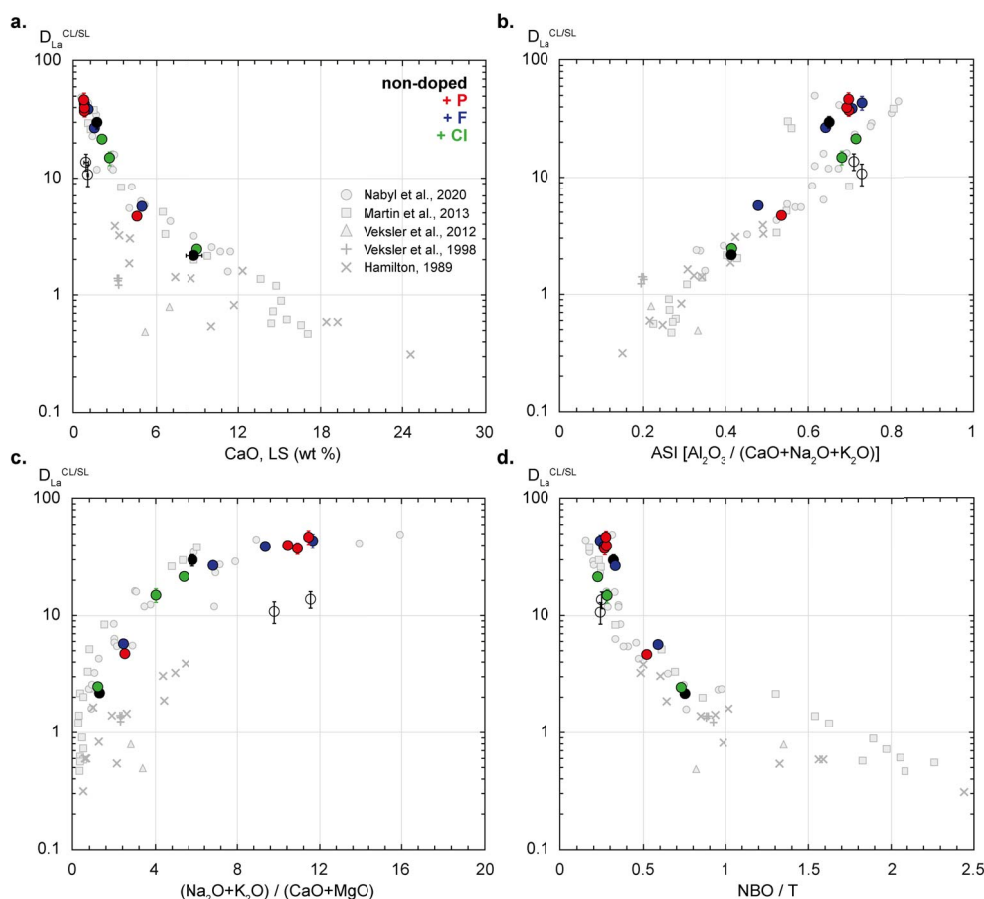


Figure 5. Silicate melt composition and structure effects on the La partition coefficient ($D_{La}^{CL/SL}$) between carbonate and silicate liquids (CL and SL), for all the samples synthesized in the four chemical systems (in black for the system with no additional volatile, red for the P-rich system, blue for the F-rich system and green for the Cl-rich system), at 850 °C–1050 °C–0.8 GPa and \pm additional H_2O . The $D_{La}^{CL/SL}$ are represented against the CaO concentrations in wt% (a), the ASI (alumina saturation index; b), the alkali/alkaline-earth cation ratio (c) and the NBO/T (d) of the silicate liquids. The grey symbols correspond to previous experimental studies on carbonate and silicate melt immiscibility [Hamilton et al., 1989, Martin et al., 2013, Nabyl et al., 2020, Veksler et al., 2012, 1998]. Empty symbols correspond to samples suspected to not be in equilibrium (PCPC1_01 and PCPC1_02).

correlations with NBO/T (Figure 6a) and ASI parameters (Figure 6b) respectively. $D_{Cl}^{CL/SL}$ values range from 0.6 to 8, but show no correlation with either the composition or the structure of the silicate melt (Figures 6c–d). We note, however, that $D_{Cl}^{CL/SL}$ values are much lower for Cl-rich systems.

No clear correlation between $D_{REE}^{CL/SL}$ and the silicate–carbonate melt F and Cl contents has emerged so far (see Supplementary Figure 1), nei-

ther in this study nor in previous investigations (grey symbols, Supplementary Figure 1). REE seem to concentrate in carbonate melts (high $D_{REE}^{CL/SL}$), which can coexist with both F-/Cl-rich silicate melts and F-/Cl-poor silicate melts. Furthermore, no relationship has been observed between La and either F or Cl partitioning (Table 5). This suggests that no significant direct effect of volatile concentrations on carbonate–silicate melt REE partitioning has been detected.

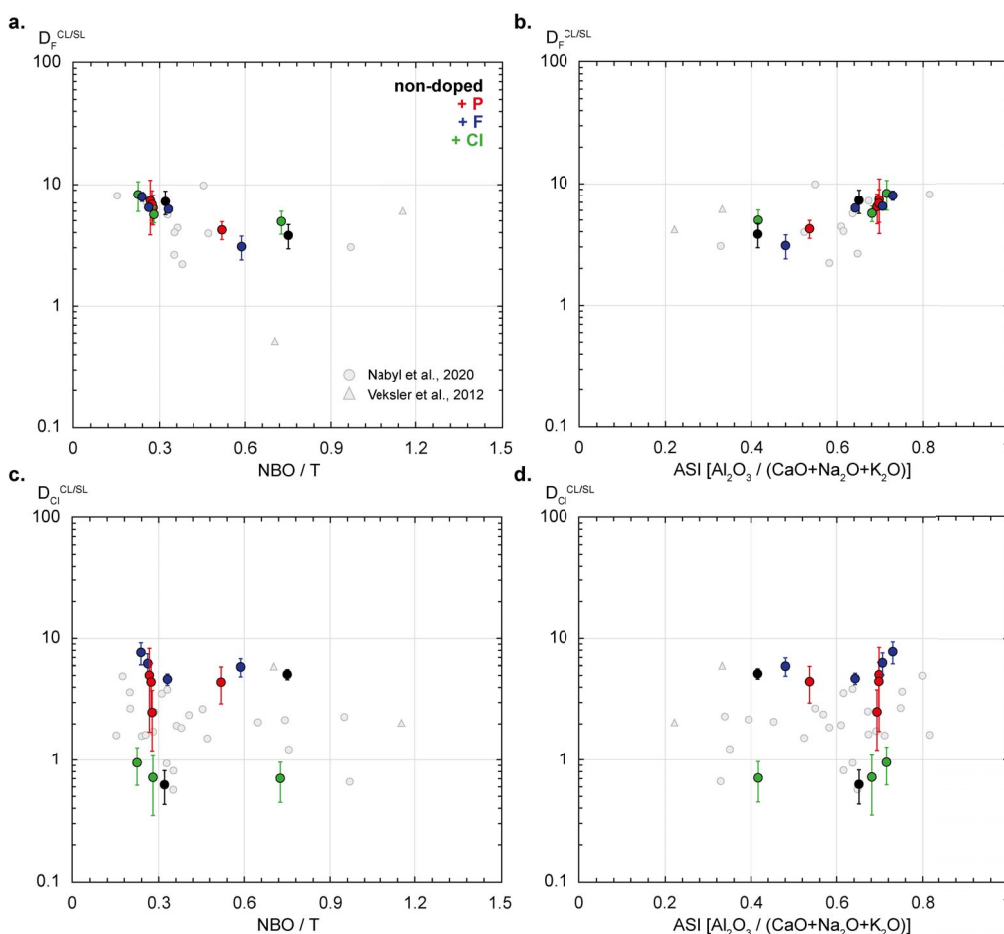


Figure 6. Fluorine and chlorine partition coefficients between carbonate and silicate liquids (CL and SL; $D_F^{CL/SL}$ and $D_{Cl}^{CL/SL}$ respectively) plotted against the silicate melt NBO/T (a and b, molar fraction) and the ASI (c and d; molar fraction). All samples synthesized in the four chemical systems (in black for the system with no additional volatile, red for the P-rich system, blue for the F-rich system and green for the Cl-rich system), at 850 °C–1050 °C–0.8 GPa and \pm additional H₂O are shown. The grey symbols correspond to previous experimental studies on carbonate and silicate melt immiscibility [Nabyl *et al.*, 2020, Veksler *et al.*, 2012].

The lower $D_{Ce}^{CL/SL}$ compared with other LREE (see Section 3.3; Figure 4) appear to be related to slightly higher Ce concentrations in the silicate melts (Table 4). This may be linked to Ce–F complexes which form in the silicate melt structure, as suggested by Ponader and Brown [1989] for La, Gd and Yb. Alternatively, the negative $D_{Ce}^{CL/SL}$ anomaly could reflect a change in oxidation state of Ce in the silicate melt. This element usually occurs in the Ce³⁺ form, but can also occur in the less common oxidised

form Ce⁴⁺ [Adachi and Imanaka, 1998, Burnham and Berry, 2014]. Burnham and Berry [2014] have shown that Ce³⁺ remains the dominant form in the silicate melts, but also that the stability of Ce⁴⁺ can be enhanced in depolymerised silicate melts in synthetic systems (SMFAC-Ce system). The negative $D_{Ce}^{CL/SL}$ anomaly could therefore be explained by the oxidation of Ce³⁺ to Ce⁴⁺. This anomaly is low at 850 °C in the non-doped system and in the F-rich systems (black and blue lines respectively, Figure 4),

but is particularly marked in the Cl-rich systems (green lines, Figure 4). This suggests that Cl-rich samples are more oxidised and that the oxidation state could favour the formation of Ce^{4+} -Cl complexes. However, it is not possible at this stage to reach any definite conclusions on the redox state and its impact on the behaviour of Ce.

4.3. Prediction of carbonate melt REE contents in F-Cl-P-rich systems

4.3.1. Application of the carbonatite REE enrichment model to F-, Cl- and P-rich systems

The REE partitioning model between carbonate and silicate liquids of Nabyl et al. [2020] relates $D_{\text{Ca}}^{\text{CL/SL}}$ and $D_{\text{REE}}^{\text{CL/SL}}$ to the silicate melt composition. This model is based on the correlation between $D_{\text{Ca}}^{\text{CL/SL}}$ and $D_{\text{REE}}^{\text{CL/SL}}$ shown in Figure 7 for La, including both data from the literature [Hamilton et al., 1989, Martin et al., 2013, Nabyl et al., 2020, Veksler et al., 2012] and the new data in this work. The data points illustrating the systems doped in F, Cl and P are indistinguishable from the literature data containing much lower amounts of these elements (Figure 7).

The Nabyl et al. [2020] partitioning equations have been used to calculate $D_{\text{Ca}}^{\text{CL/SL}}$ and $D_{\text{REE}}^{\text{CL/SL}}$ for the F-, Cl- and P-rich samples. In detail, the calculations are carried out as follows (see the online application tools, <http://calcul-isto.cnrs-orleans.fr/apps/REE-carb-melt/>):

The $D_{\text{Ca}}^{\text{CL/SL}}$ were calculated using three parameters relating to the silicate melt composition (the SiO_2 content in wt%, the ASI and the $(\text{Na}_2\text{O} + \text{K}_2\text{O})/(\text{CaO} + \text{MgO})$ ratio in molar fraction) in the following equation:

$$\ln(D_{\text{Ca}}^{\text{CL/SL}}) = a_0 + a_1 * \text{SiO}_2 + a_2 * \frac{\text{Al}_2\text{O}_3}{(\text{CaO} + \text{Na}_2\text{O} + \text{K}_2\text{O})} + a_3 * \frac{(\text{Na}_2\text{O} + \text{K}_2\text{O})}{(\text{CaO} + \text{MgO})}. \quad (1)$$

The $D_{\text{REE}}^{\text{CL/SL}}$ were estimated from the calculated $D_{\text{Ca}}^{\text{CL/SL}}$ based on the correlation shown in Figure 7 for La, and for all the other REE [Nabyl et al., 2020]:

$$D_{\text{REE}}^{\text{CL/SL}} = a * (D_{\text{Ca}}^{\text{CL/SL}})^b. \quad (2)$$

The calculated $D_{\text{Ca}}^{\text{CL/SL}}$ and $D_{\text{La}}^{\text{CL/SL}}$ from this model are plotted against the measured $D_{\text{Ca}}^{\text{CL/SL}}$ and $D_{\text{La}}^{\text{CL/SL}}$ (Figures 8a and b respectively). Both the $D_{\text{Ca}}^{\text{CL/SL}}$ and $D_{\text{La}}^{\text{CL/SL}}$ values for the F-, Cl- and P-rich systems are

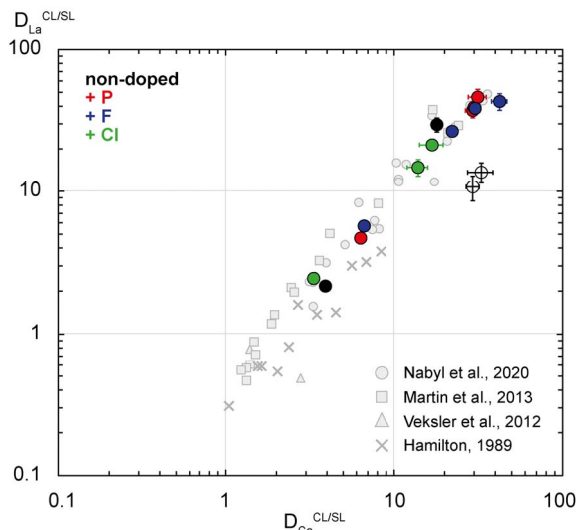


Figure 7. La partition coefficients ($D_{\text{La}}^{\text{CL/SL}}$) versus Ca partition coefficient ($D_{\text{Ca}}^{\text{CL/SL}}$) between carbonate and silicate liquids (CL and SL), for all the samples synthesized in the four chemical systems (in black for the system with no additional volatile, red for the P-rich system, blue for the F-rich system and green for the Cl-rich system), at 850 °C–1050 °C–0.8 GPa and \pm additional H_2O . Previous experimental studies of carbonate and silicate melt immiscibility are also represented [grey symbols; Hamilton et al., 1989, Veksler et al., 2012, Martin et al., 2013, Nabyl et al., 2020]. Empty symbols correspond to samples suspected to not be in equilibrium (PCPC1_01 and PCPC1_02).

well reproduced (close to the 1-1 line; Figure 8) and fall in the compositional field of the experimental studies used to calibrate the model (grey field, Figure 8). The REE partitioning model of Nabyl et al. [2020] predicts, within uncertainty, the measured REE partition coefficients in the F, Cl and P enriched magmatic systems.

Although the two partitioning data points from the secondary carbonate liquid phase (“CL2”, see Section 3.2; Figure 1b) are outliers in Figures 7 and 8b (empty black circles), they are also well-predicted in terms of $D_{\text{Ca}}^{\text{CL/SL}}$ (Figure 8a). This suggests that the Ca partitioning between the carbonate and silicate liquids is in equilibrium, unlike the case of trace elements including REE.

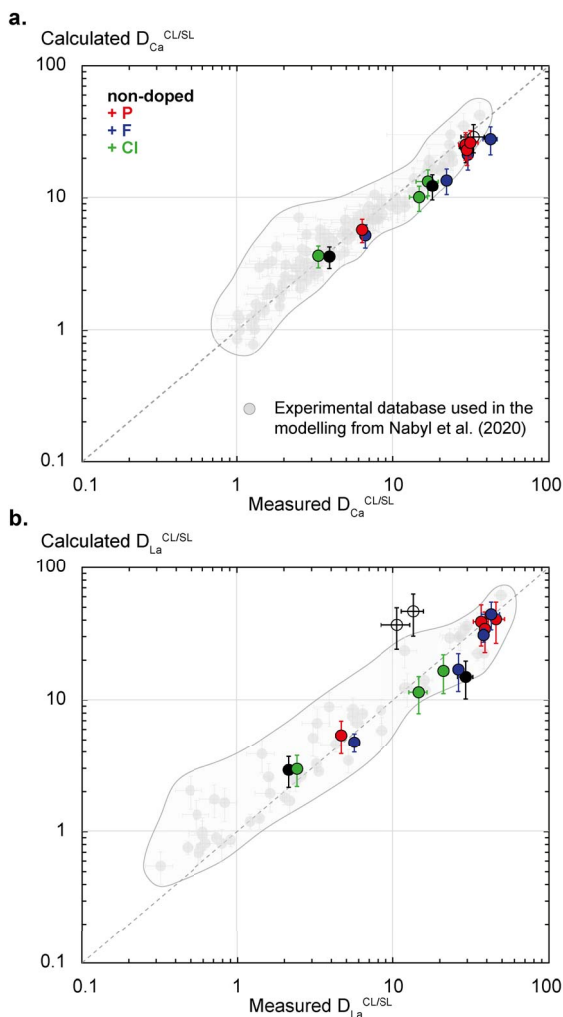


Figure 8. Application of the carbonate melt REE enrichment model from Nabyl *et al.* [2020] in the experimental F-Cl-P-rich carbonate and silicate liquids from this study. (a) Modelled Ca partition coefficients between carbonate and silicate liquids (Calculated $D_{Ca}^{CL/SL}$) versus the experimentally measured Ca partition coefficients (Measured $D_{Ca}^{CL/SL}$) from this study and the experimental database used for the Nabyl *et al.* [2020] model [Brooker, 1998, Freestone and Hamilton, 1980, Hamilton *et al.*, 1989, Jones *et al.*, 1995, Kjarsgaard, 1998, Kjarsgaard *et al.*, 1995, Martin *et al.*, 2013, 2012, Massuyeau *et al.*, 2015, Veksler *et al.*, 2012, 1998] (b) Modelled La partition coefficients between carbonate and silicate liquids (Calculated $D_{La}^{CL/SL}$) versus the experimentally measured La partition coefficients (Measured $D_{La}^{CL/SL}$) from this study and the experimental database [Hamilton *et al.*, 1989, Martin *et al.*, 2013, Veksler *et al.*, 2012]. All the samples synthesized in the four chemical systems (in black for the system with no additional volatile, red for the P-rich system, blue for the F-rich system and green for the Cl-rich system), at 850 °C–1050 °C–0.8 GPa and \pm additional H₂O are represented. The grey field corresponds to the experimental database used to calibrate the model from Nabyl *et al.* [2020]. Empty symbols correspond to samples suspected to not be in equilibrium (PCPC1_01 and PCPC1_02).

Veksler *et al.* [2012] have defined rare metal partitioning between salt melts—such as fluoride ($F > 38$ wt%), phosphate ($P_2O_5 > 45$ wt%) and chloride melts—and silicate melts. Fluoride and phosphate melts can be 100 times more enriched in REE than silicate melts [$D_{\text{REE}}^{\text{Fluoride or Phosphate liquid/SL}} > 100$, Veksler *et al.*, 2012], which indicates a strong affinity for the salt melts. Figure 9 shows the La partition coefficients between fluoride/phosphate and silicate liquids versus the Ca partition coefficients from Veksler *et al.* [2012], compared to the samples from this study (carbonate and silicate liquids enriched \pm in F, Cl and P, see Figure 7). The same correlation between the La and the Ca partitioning is observed: the Ca-rich fluoride (blue empty triangle, Figure 9) and phosphate liquids (red empty triangle, Figure 9) are enriched in La ($D_{\text{La}}^{\text{Fluoride or Phosphate liquid/SL}} > 100$). In other words, fluoride and phosphate liquids coexisting with Ca-poor silicate liquids are highly enriched in REE. This implies that the silicate melt composition and the structural effect governing REE partitioning in the carbonate–silicate liquid system [Figure 5; see Nabyl *et al.*, 2020] must also operate for REE partitioning between fluoride/phosphate and silicate liquids. As expected from the relationships between silicate melt polymerisation and REE partitioning, the silicate melts coexisting with salt melts from Veksler *et al.* [2012] have highly polymerised compositions (SiO_2 : 60 to 80 wt%; CaO : 0.03 to 7 wt%). Although these melts are not alkaline magmas, Figure 9 indicates that there is a seemingly universal trend linking Ca and REE partitioning between silicate and ionic melts.

4.3.2. Application to natural carbonate and silicate melt inclusions

Melt inclusion studies of alkaline magmatic rocks have highlighted the existence of inclusions containing alkaline silica–undersaturated silicate melts (melilitic to phonolitic compositions) coexisting with carbonate melts [Berkesi *et al.*, 2020, Guzmics *et al.*, 2012, 2019, Mitchell, 2009]. Guzmics *et al.* [2019] and Berkesi *et al.* [2020] have shown the existence of carbonate and silicate melt inclusions containing relatively high F, Cl and P concentrations, with up to 14 wt% of F, 5 wt% of P_2O_5 and 4 wt% of Cl in the carbonate melts. Those concentration ranges are similar to the melt concentrations reported in this study (see Table 3). The Nabyl *et al.* [2020] model (1) and (2)

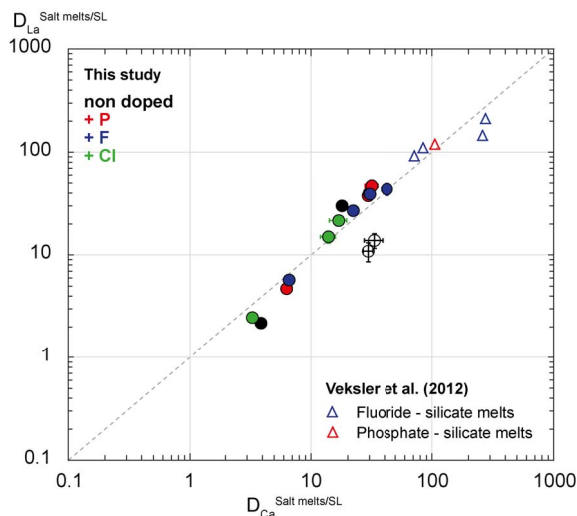


Figure 9. La partition ($D_{\text{La}}^{\text{Salt melts/SL}}$) versus Ca partition coefficient ($D_{\text{Ca}}^{\text{Salt melts/SL}}$) between carbonate melts from this study/salt melts from Veksler *et al.* [2012] and silicate liquids (Salt melts and SL). All samples from this study (samples synthesized in the four chemical systems: in black for the system with no additional volatile, red for the P-rich system, blue for the F-rich system and green for the Cl-rich system; at 850 °C–1050 °C–0.8 GPa; \pm additional H_2O) are compared to a sample in the fluoride–silicate liquid system [blue triangle, Veksler *et al.*, 2012] and one in the phosphate–silicate liquid system [red triangle, Veksler *et al.*, 2012].

has been applied to the conjugate carbonate and silicate melt inclusions, including in F-rich system. Only the $D_{\text{Ca}}^{\text{CL/SL}}$ has been modelled as the REE have not been analysed in the aforementioned melt inclusions studies; the calculated Ca partitioning are plotted against the measured ones in black in Figure 10 [Guzmics *et al.*, 2012, Mitchell, 2009], and in blue for F-rich melt inclusions [Berkesi *et al.*, 2020, Guzmics *et al.*, 2019]. For all melt inclusions, the $D_{\text{Ca}}^{\text{CL/SL}}$ in carbonate and silicate melts \pm rich in F, Cl and P are well reproduced by the modelling (Figure 10). This methodology can therefore be used as a test of equilibrium and a measure of the level of REE enrichment in carbonate melts during magmatic processes. For the cases illustrated in Figure 10, the $D_{\text{Ca}}^{\text{CL/SL}}$ values of around 20 imply $D_{\text{La}}^{\text{CL/SL}}$ values of around 30–40, in

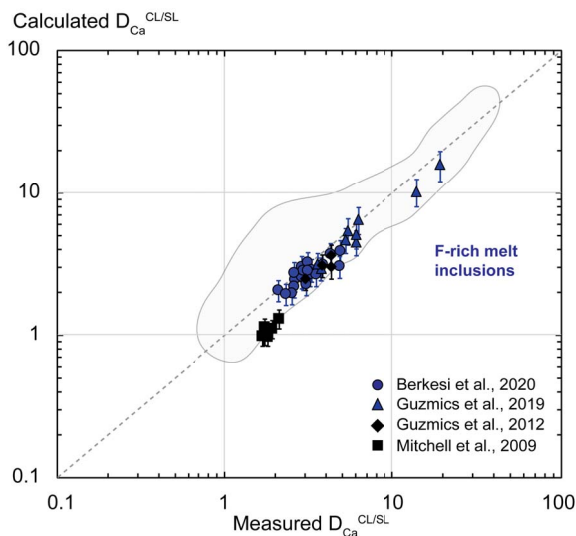


Figure 10. Application of the carbonate melt REE enrichment model from Nabyl *et al.* [2020] on natural carbonate and silicate melt inclusions. Modelled Ca partition coefficients between carbonate and silicate liquids (Calculated $D_{Ca}^{CL/SL}$) are shown together with measured Ca partition coefficients, for carbonate and silicate melt inclusions [in black; data from Mitchell, 2009, Guzmics *et al.*, 2012] and F-rich melt inclusions [in blue; data from Berkési *et al.*, 2020, Guzmics *et al.*, 2019]. The grey field corresponds to the experimental database used to calibrate the model from Nabyl *et al.* [2020].

other words the carbonatite melts must be strongly enriched in REE.

4.4. Role of the fluid phase

This section aims at highlighting a possible role of the fluid phase in REE behaviour between carbonate and alkaline silicate melts. As explained in Section 3.1, some charges present the texture of a fluid phase in contact with the carbonate and the silicate liquids (Figure 1d; Figures 2a, d and f; see Table 2), and the evidences presented above indicate its possible implication in Cl, alkali and REE behaviour.

The carbonate and silicate liquids in the Cl-rich system have low Cl concentrations (Cl < 1 wt%; samples PCPC5_02, PCPC5_03 and PCPC6_02; see Tables 2 and 3), despite the starting material contain-

ing 4.72 wt% of Cl (PhCbn 4, Table 1). The $D_{Cl}^{CL/SL}$ values of these samples are also relatively low (Figures 6c and d; Table 5). Apart from apatite, the other phases (clinopyroxene, garnet, and nepheline; see Table 2) at equilibrium with both liquids cannot concentrate Cl; still, only a few crystals of apatite have been observed in the charge (Figure 2g) and they do not explain such a Cl-loss during the experiment. It can therefore be assumed that Cl has been concentrated into the fluid phase during the experiments, especially in hydrated samples at 850 °C (3 and 6 wt% of H₂O, PCPC5_02 and PCPC5_03; see Table 2).

Moreover, the alkali content of carbonate melts decreases in the Cl-rich system with the addition of water (3 and 6 wt% of H₂O, samples PCPC5_02 and PCPC5_03, see Section 3.2 and Figure 3d). As the carbonate melts show a porous texture (Figures 1d and 2g), we can presume that Cl⁻ forms complexes with Na⁺ or K⁺ that concentrate into the fluid phase at equilibrium with other liquid and crystal phases. The addition of water increases the amount of fluid phase, which accordingly enhances the removal of Na, K and Cl from both melts. The fluid phase plays an important role in the carbonate melt composition in the Cl-rich system, therefore leading to a change in the concentrations of alkali elements in carbonate melts.

Furthermore, the carbonate melt REE concentrations are also slightly lower in the Cl-rich samples with additional water (PCPC5_02 and PCPC5_03, Table 4; see Section 3.3), whereas the silicate melt REE concentrations do not vary significantly (Table 4), apart from the Ce concentration as described above. This results in a decrease in $D_{REE}^{CL/SL}$ with the addition of water (Figure 4d). In fact, the REE have been shown to be mobile in aqueous fluids, especially in Cl- and F-rich fluids [Humphris and Henderson, 1984, Migdisov *et al.*, 2016, Williams-Jones *et al.*, 2012]. Migdisov *et al.* [2016] also characterised Cl as the principal agent of REE transport in aqueous fluids. We thus propose that REE also concentrate into the magmatic fluid phase in Cl-rich system, potentially creating complexes with Cl and alkali elements. In these samples, alkalis, Cl and REE seem to mainly interact in the fluid phase. This may well affect REE behaviour during the differentiation of alkaline/carbonatite systems, as well as REE ore forming processes [Gysi and Williams-Jones, 2015,

Smith *et al.*, 2016, Verplanck *et al.*, 2016, Williams-Jones *et al.*, 2012].

5. Conclusion

This study presents experiments on the REE partitioning between immiscible alkaline silicate melts of nephelinite–phonolite type and carbonate melts, for systems that are doped in F, Cl and P. The partitioning data for these doped systems are indistinguishable from those previously modelled by Nabyl *et al.* [2020] in F-, Cl- and P-poor systems. The Nabyl *et al.* [2020] REE partitioning model can therefore be applied on any system. We use this model on natural melt inclusions revealing carbonate–silicate pairs that can be used as a test of equilibrium and to predict the level of REE enrichment in the carbonatite melt. We suggest that Cl-rich systems tend to form magmatic fluids that are likely enriched in Na and REE. Further studies on the fluid phase are nevertheless necessary to link the magmatic processes and the late magmatic hydrothermal processes thought to be commonly involved in the formation of REE-rich deposits.

Conflicts of interest

Authors have no conflict of interest to declare.

Acknowledgements

This study was a part of Z. Nabyl's PhD, and was supported by the European Research Council (Grant no. 279790), the LABEX VOLTAIRE project (ANR-10-LABX-100-01) and the BRGM. Part of the experiments used was funded by the EquipEx PLANEX project (ANR-11-EQPX-0036). We thank J.-L. Devidal from the LMV laboratory (Laboratoire Magmas et Volcans, Clermont-Ferrand, France) and S. Erdmann from the ISTO laboratory (Orléans, France) for their support with LA-ICP-MS analysis and data treatment. We are grateful to two anonymous reviewers for their constructive comments and thoughtful advices on this manuscript.

Supplementary data

Supporting information for this article is available on the journal's website under <https://doi.org/10.5802/crgeos.104> or from the author.

References

- Ablay, G. J., Carroll, M. R., Palmer, M. R., Martí, J., and Sparks, R. S. J. (1998). Basanite–phonolite lineages of the teide–pico viejo volcanic complex, tenerife, canary islands. *J. Petrol.*, 39, 905–936.
- Adachi, G. and Imanaka, N. (1998). The binary rare earth oxides. *Chem. Rev.*, 98, 1479–1514.
- Aiuppa, A., Baker, D. R., and Webster, J. D. (2009). Halogens in volcanic systems. *Chem. Geol.*, 263, 1–18. Special Issue: Halogens in Volcanic Systems and Their Environmental Impacts.
- Anenburg, M., Mavrogenes, J. A., Frigo, C., and Wall, F. (2020). Rare earth element mobility in and around carbonatites controlled by sodium, potassium, and silica. *Sci. Adv.*, 6, article no. eabb6570.
- Baasner, A., Schmidt, B. C., Dupree, R., and Webb, S. L. (2014). Fluorine speciation as a function of composition in peralkaline and peraluminous Na_2O – CaO – Al_2O_3 – SiO_2 glasses: A multinuclear NMR study. *Geochim. Cosmochim. Acta*, 132, 151–169.
- Baasner, A., Schmidt, B. C., and Webb, S. L. (2013a). The effect of chlorine, fluorine and water on the viscosity of aluminosilicate melts. *Chem. Geol.*, 357, 134–149.
- Baasner, A., Schmidt, B. C., and Webb, S. L. (2013b). Compositional dependence of the rheology of halogen (F, Cl) bearing aluminosilicate melts. *Chem. Geol.*, 346, 172–183. Special Issue: 9th Silicate Melts Workshop.
- Baudouin, C., Parat, F., Denis, C. M. M., and Man-gasini, F. (2016). Nephelinite lavas at early stage of rift initiation (Hanang volcano, North Tanzanian Divergence). *Contrib. Mineral. Petrol.*, 171, article no. 64.
- Baudouin, C., Parat, F., and Michel, T. (2018). CO_2 -rich phonolitic melt and carbonatite immiscibility in early stage of rifting: Melt inclusions from Hanang volcano (Tanzania). *J. Volcanol. Geotherm. Res.*, 358, 261–272.
- Berkesi, M., Bali, E., Bodnar, R. J., Szabó, A., and Guzmics, T. (2020). Carbonatite and highly peralkaline nephelinite melts from Oldoinyo Lengai Volcano, Tanzania: The role of natrite–normative fluid degassing. *Gondwana Res.*, 85, 76–83.
- Brooker, R. A. (1998). The effect of CO_2 saturation on immiscibility between silicate and carbonate

- liquids: an experimental study. *J. Petrol.*, 39, 1905–1915.
- Brooker, R. A. and Kjarsgaard, B. A. (2011). Silicate–carbonate liquid immiscibility and phase relations in the system $\text{SiO}_2\text{--Na}_2\text{O--Al}_2\text{O}_3\text{--CaO--CO}_2$ at 0.1–2.5 GPa with applications to carbonatite genesis. *J. Petrol.*, 52, 1281–1305.
- Burnham, A. D. and Berry, A. J. (2014). The effect of oxygen fugacity, melt composition, temperature and pressure on the oxidation state of cerium in silicate melts. *Chem. Geol.*, 366, 52–60.
- Castor, S. B. (2008). The Mountain Pass rare-earth carbonatite and associated ultrapotassic rocks, California. *Can. Mineral.*, 46, 779–806.
- Chakhmouradian, A. R. and Zaitsev, A. N. (2012). Rare earth mineralization in igneous rocks: sources and processes. *Elements*, 8, 347–353.
- Chebotarev, D. A., Veksler, I. V., Wohlgemuth-Ueberwasser, C., Doroshkevich, A. G., and Koch-Müller, M. (2019). Experimental study of trace element distribution between calcite, fluorite and carbonatitic melt in the system $\text{CaCO}_3 + \text{CaF}_2 + \text{Na}_2\text{CO}_3 \pm \text{Ca}_3(\text{PO}_4)_2$ at 100 MPa. *Contrib. Mineral. Petrol.*, 174, article no. 4.
- Dasgupta, R., Hirschmann, M. M., and Withers, A. C. (2004). Deep global cycling of carbon constrained by the solidus of anhydrous, carbonated eclogite under upper mantle conditions. *Earth Planet. Sci. Lett.*, 227, 73–85.
- Dawson, J. B. (1962). Sodium carbonate lavas from Oldoinyo Lengai, Tanganyika. *Nature*, 195, 1075–1076.
- Dingwell, D. B. (1986). Volatile solubilities in silicate melts. In *Silicate Melts: Their Properties and Structure Applied to Problems in Geochemistry, Petrology, Economic Geology, and Planetary Geology*, pages 93–129. Mineralogical Association of Canada, Québec, Canada.
- Feng, M., Song, W., Kynicky, J., Smith, M., Cox, C., Kotlanova, M., Brtnicky, M., Fu, W., and Wei, C. (2020). Primary rare earth element enrichment in carbonatites: Evidence from melt inclusions in Ulgii Khiid carbonatite, Mongolia. *Ore Geol. Rev.*, 117, article no. 103294.
- Freestone, I. C. and Hamilton, D. L. (1980). The role of liquid immiscibility in the genesis of carbonatites—an experimental study. *Contrib. Mineral. Petrol.*, 73, 105–117.
- Frezzotti, M.-L. (2001). Silicate-melt inclusions in magmatic rocks: applications to petrology. *Lithos*, 55, 273–299. Special Issue: Fluid Inclusions: Phase Relationships - Methods - Applications. A Special Issue in honour of Jacques Touret.
- Guzmics, T., Berkesi, M., Bodnar, R. J., Fall, A., Bali, E., Milke, R., Vetlényi, E., and Szabó, C. (2019). Natro-carbonatites: A hidden product of three-phase immiscibility. *Geology*, 47, 527–530.
- Guzmics, T., Mitchell, R. H., Szabó, C., Berkesi, M., Milke, R., and Ratter, K. (2012). Liquid immiscibility between silicate, carbonate and sulfide melts in melt inclusions hosted in co-precipitated minerals from Kerimasi volcano (Tanzania): evolution of carbonated nephelinitic magma. *Contrib. Mineral. Petrol.*, 164, 101–122.
- Gysi, A. P. and Williams-Jones, A. E. (2015). The thermodynamic properties of bastnäsite-(Ce) and parisite-(Ce). *Chem. Geol.*, 392, 87–101.
- Hamilton, D. L., Bedson, P., and Esson, J. (1989). The behaviour of trace elements in the evolution of carbonatites. In Bell, K., editor, *Carbonatites, Genesis and Evolution*, pages 405–427. Unwin-Hyman, London, UK.
- Humphris, S. E. and Henderson, P. (1984). The mobility of the rare earth elements in the crust. *Rare Earth Element Geochem.*, 2, 317–342.
- Jago, B. C. and Gittins, J. (1991). The role of fluorine in carbonatite magma evolution. *Nature*, 349, 56–58.
- Jia, Y. and Liu, Y. (2020). REE enrichment during magmatic–hydrothermal processes in carbonatite-related REE deposits: A case study of the Weishan REE deposit, China. *Minerals*, 10, article no. 25.
- Jochum, K. P., Weis, U., Schwager, B., Stoll, B., Wilson, S. A., Haug, G. H., Andreae, M. O., and Enzweiler, J. (2016). Reference values following ISO guidelines for frequently requested rock reference materials. *Geostand. Geoanalytical Res.*, 40, 333–350.
- Jones, A. P., Genge, M., and Carmody, L. (2013). Carbonate melts and carbonatites. *Rev. Mineral. Geochem.*, 75, 289–322.
- Jones, J. H., Walker, D., Pickett, D. A., Murrell, M. T., and Beattie, P. (1995). Experimental investigations of the partitioning of Nb, Mo, Ba, Ce, Pb, Ra, Th, Pa, and U between immiscible carbonate and silicate liquids. *Geochim. Cosmochim. Acta*, 59, 1307–1320.
- Keller, J. and Zaitsev, A. N. (2012). Geochemistry and petrogenetic significance of natrocarbonatites at

- Oldoinyo Lengai, Tanzania: Composition of lavas from 1988 to 2007. *Lithos*, 148, 45–53.
- Kjarsgaard, B. A. (1998). Phase relations of a carbonated high-CaO nephelinite at 0.2 and 0.5 GPa. *J. Petrol.*, 39, 2061–2075.
- Kjarsgaard, B. A. and Hamilton, D. L. (1988). Liquid immiscibility and the origin of alkali-poor carbonatites. *Mineral. Mag.*, 52, 43–55.
- Kjarsgaard, B. A., Hamilton, D. L., and Peterson, T. D. (1995). Peralkaline nephelinite/carbonatite liquid immiscibility: comparison of phase compositions in experiments and natural lavas from Oldoinyo Lengai. In *Carbonatite Volcanism Oldoinyo Lengai and the Petrogenesis of Natrocarbonatite*, IAVCEI Proceedings in Volcanology, pages 163–190. Springer, Berlin, Heidelberg.
- Kynicky, J., Smith, M. P., Song, W., Chakhmouradian, A. R., Xu, C., Kopriva, A., Galiova, M. V., and Brtnicky, M. (2019). The role of carbonate-fluoride melt immiscibility in shallow REE deposit evolution. *Geosci. Front. Clim. Change Impacts Environ. Geosci.*, 10, 527–537.
- Lee, W. and Wyllie, P. J. (1994). Experimental data bearing on liquid immiscibility, crystal fractionation, and the origin of calciocarbonatites and natrocarbonatites. *Int. Geol. Rev.*, 36, 797–819.
- Louvel, M., Bordage, A., Testemale, D., Zhou, L., and Mavrogenes, J. (2015). Hydrothermal controls on the genesis of REE deposits: Insights from an in situ XAS study of Yb solubility and speciation in high temperature fluids ($T < 400$ °C). *Chem. Geol.*, 417, 228–237.
- Mangler, M. F., Marks, M. A. W., Zaitzev, A. N., Eby, G. N., and Markl, G. (2014). Halogens (F, Cl and Br) at Oldoinyo Lengai volcano (Tanzania): Effects of magmatic differentiation, silicate–natrocarbonatite melt separation and surface alteration of natrocarbonatite. *Chem. Geol.*, 365, 43–53.
- Mariano, A. N. and Mariano, A. (2012). Rare earth mining and exploration in North America. *Elements*, 8, 369–376.
- Martin, L. H. J., Schmidt, M. W., Mattsson, H. B., and Guenther, D. (2013). Element partitioning between immiscible carbonatite and silicate melts for dry and H₂O-bearing systems at 1–3 GPa. *J. Petrol.*, 54, 2301–2338.
- Martin, L. H. J., Schmidt, M. W., Mattsson, H. B., Ulmer, P., Hametner, K., and Günther, D. (2012). Element partitioning between immiscible carbonatite–kamaufugite melts with application to the Italian ultrapotassic suite. *Chem. Geol.*, 320–321, 96–112.
- Massuyeau, M., Gardés, E., Morizet, Y., and Gaillard, F. (2015). A model for the activity of silica along the carbonatite–kimberlite–mellilitite–basanite melt compositional joint. *Chem. Geol.*, 418, 206–216.
- Mattsson, H. B., Nandedkar, R. H., and Ulmer, P. (2013). Petrogenesis of the melilititic and nephelinitic rock suites in the Lake Natron–Engaruka monogenetic volcanic field, northern Tanzania. *Lithos*, 179, 175–192.
- Metrich, N. and Rutherford, M. J. (1992). Experimental study of chlorine behavior in hydrous silicic melts. *Geochim. Cosmochim. Acta*, 56, 607–616.
- Migdisov, A., Williams-Jones, A. E., Brugger, J., and Caporuscio, F. A. (2016). Hydrothermal transport, deposition, and fractionation of the REE: Experimental data and thermodynamic calculations. *Chem. Geol.*, 439, 13–42.
- Mitchell, R. H. (2005). Carbonatites and carbonatites and carbonatites. *Can. Mineral.*, 43, 2049–2068.
- Mitchell, R. H. (2009). Peralkaline nephelinite–natrocarbonatite immiscibility and carbonatite assimilation at Oldoinyo Lengai, Tanzania. *Contrib. Mineral. Petrol.*, 158, article no. 589.
- Mysen, B. O. (1998). Phosphorus solubility mechanisms in haplogranitic aluminosilicate glass and melt: effect of temperature and aluminum content. *Contrib. Mineral. Petrol.*, 133, 38–50.
- Mysen, B. O., Ryerson, F. J., and Virgo, D. (1981). The structural role of phosphorus in silicate melts. *Am. Mineral.*, 66, 106–117.
- Mysen, B. O., Virgo, D., and Seifert, F. A. (1982). The structure of silicate melts: Implications for chemical and physical properties of natural magma. *Rev. Geophys.*, 20, 353–383.
- Nabyl, Z., Massuyeau, M., Gaillard, F., Tuduri, J., Iacono-Marziano, G., Rogerie, G., Le Trong, E., Di Carlo, I., Melleton, J., and Bailly, L. (2020). A window in the course of alkaline magma differentiation conducive to immiscible REE-rich carbonatites. *Geochim. Cosmochim. Acta*, 282, 297–323.
- Nelson, D. R., Chivas, A. R., Chappell, B. W., and McCulloch, M. T. (1988). Geochemical and isotopic systematics in carbonatites and implications for the evolution of ocean-island sources. *Geochim.*

- Cosmochim. Acta*, 52, 1–17.
- Néron, A., Bédard, L. P., and Gaboury, D. (2018). The saint-honoré carbonatite REE Zone, Québec, Canada: combined magmatic and hydrothermal processes. *Minerals*, 8, article no. 397.
- Panina, L. I. (2005). Multiphase carbonate-salt immiscibility in carbonatite melts: data on melt inclusions from the Krestovskiy massif minerals (Polar Siberia). *Contrib. Mineral. Petrol.*, 150, 19–36.
- Panina, L. I. and Motorina, I. V. (2008). Liquid immiscibility in deep-seated magmas and the generation of carbonatite melts. *Geochem. Int.*, 46, 448–464.
- Pearce, N. J. G., Perkins William, T., Westgate John, A., Gorton Michael, P., Jackson Simon, E., Neal Clive, R., and Chenery Simon, P. (1997). A compilation of new and published major and trace element data for NIST SRM 610 and NIST SRM 612 glass reference materials. *Geostand. Newsl.*, 21, 115–144.
- Ponader, C. W. and Brown, G. E. (1989). Rare earth elements in silicate glassmelt systems: II. Interactions of La, Gd, and Yb with halogens. *Geochim. Cosmochim. Acta*, 53, 2905–2914.
- Potter, N. J., Kamenetsky, V. S., Simonetti, A., and Goemann, K. (2017). Different types of liquid immiscibility in carbonatite magmas: A case study of the Oldoinyo Lengai 1993 lava and melt inclusions. *Chem. Geol.*, 455, 376–384. Special Issue: The Role of Intraplate Magmas and their Inclusions in Earth's Mantle Evolution.
- Rocholl, A. (1998). Major and trace element composition and homogeneity of microbeam reference material: basalt glass USGS BCR-2G. *Geostand. Newsl.*, 22, 33–45.
- Schaller, T., Dingwell, D. B., Keppler, H., Knöller, W., Merwin, L., and Sebal, A. (1992). Fluorine in silicate glasses: A multinuclear nuclear magnetic resonance study. *Geochim. Cosmochim. Acta*, 56, 701–707.
- Sifré, D., Gardés, E., Massuyeau, M., Hashim, L., Hier-Majumder, S., and Gaillard, F. (2014). Electrical conductivity during incipient melting in the oceanic low-velocity zone. *Nature*, 509, 81–85.
- Smith, M. P., Moore, K., Kavecsánszki, D., Finch, A. A., Kynicky, J., and Wall, F. (2016). From mantle to critical zone: a review of large and giant sized deposits of the rare earth elements. *Geosci. Front.*, 7, 315–334. Special Issue: Giant Mineral Deposits.
- Stagno, V. and Frost, D. J. (2010). Carbon speciation in the asthenosphere: Experimental measurements of the redox conditions at which carbonate-bearing melts coexist with graphite or diamond in peridotite assemblages. *Earth Planet. Sci. Lett.*, 300, 72–84.
- Toplis, M. J. and Dingwell, D. B. (1996). The variable influence of P₂O₅ on the viscosity of melts of differing alkali/aluminium ratio: Implications for the structural role of phosphorus in silicate melts. *Geochim. Cosmochim. Acta*, 60, 4107–4121.
- Van Achterbergh, E., Ryan, C., and Griffin, W. (2001). GLITTER user's manual: on-line interactive data reduction for the LA-ICP-MS microprobe. Version 4.
- Veksler, I. V., Dorfman, A. M., Dulski, P., Kamenetsky, V. S., Danyushevsky, L. V., Jeffries, T., and Dingwell, D. B. (2012). Partitioning of elements between silicate melt and immiscible fluoride, chloride, carbonate, phosphate and sulfate melts, with implications to the origin of natrocarbonatite. *Geochim. Cosmochim. Acta*, 79, 20–40.
- Veksler, I. V., Dorfman, A. M., Kamenetsky, M., Dulski, P., and Dingwell, D. B. (2005). Partitioning of lanthanides and Y between immiscible silicate and fluoride melts, fluorite and cryolite and the origin of the lanthanide tetrad effect in igneous rocks. *Geochim. Cosmochim. Acta*, 69, 2847–2860.
- Veksler, I. V., Petibon, C., Jenner, G. A., Dorfman, A. M., and Dingwell, D. B. (1998). Trace element partitioning in immiscible silicate-carbonate liquid systems: an initial experimental study using a centrifuge autoclave. *J. Petrol.*, 39, 2095–2104.
- Verplanck, P. L., Mariano, A. N., and Mariano Jr., A. (2016). Rare earth element ore geology of carbonatites. *Rev. Econ. Geol.*, 18, 5–32.
- Wall, F. and Mariano, A. (1996). Rare earth minerals in carbonatites: a discussion centred on the Kangankunde Carbonatite, Malawi. In Jones, A. P., Wall, F., and Williams, C. T., editors, *Rare Earth Minerals, Chemistry, Origin and Ore Deposits*, Mineralogical Society Series, pages 193–226. Chapman & Hall, London, UK.
- Webster, J. D., Baker, D. R., and Aiuppa, A. (2018). Halogens in mafic and intermediate-silica content magmas. In Harlov, D. E. and Aranovich, L., editors, *The Role of Halogens in Terrestrial and Extraterrestrial Geochemical Processes: Surface, Crust, and Mantle*, Springer Geochemistry, pages 307–430. Springer International Publishing, Cham, Switzerland.

- Williams-Jones, A. E., Migdisov, A. A., and Samson, I. M. (2012). Hydrothermal mobilisation of the rare earth elements—a tale of “Ceria” and “Yttria”. *Elements*, 8, 355–360.
- Woolley, A. R. and Kempe, D. R. C. (1989). Carbonatites: nomenclature, average chemical compositions, and element distribution. In Bell, K., editor, *Carbonatites, Genesis and Evolution*, pages 1–14. Unwin-Hyman, London, UK.
- Woolley, A. R. and Kjarsgaard, B. A. (2008). Paragenetic types of carbonatite as indicated by the diversity and relative abundances of associated silicate rocks: evidence from a global database. *Can. Mineral.*, 46, 741–752.



Perspectives on alkaline magmas / *Perspectives sur les magmas alcalins*

Early carbonatite magmatism at Oldoinyo Lengai volcano (Tanzania): carbonatite–silicate melt immiscibility in Lengai I melt inclusions

Lydéric France^{*, a}, Florian Brouillet^{a, b} and Sarah Lang^{a, c}

^a Université de Lorraine, CNRS, CRPG, F-54000 Nancy, France

^b School of Earth and Environmental Sciences, University of St Andrews, St Andrews KY16 9AL, UK

^c Department of Earth Sciences, Sapienza - University of Rome, P. le Aldo Moro 5, 00185 Roma, Italy

E-mails: lyderic.france@univ-lorraine.fr (L. France), fcgb1@st-andrews.ac.uk (F. Brouillet), sarah.lang@uniroma1.it (S. Lang)

Abstract. Carbonatites are unusual C-rich alkaline magmas that have been reported throughout the geological record. Nevertheless, there is only one currently active carbonatite system on Earth: Oldoinyo Lengai stratovolcano in northern Tanzania (God's mountain in Maasai culture). Present-day Lengai carbonatites are natrocarbonatites, peculiar Na-rich carbonatites that, under atmospheric conditions, alter and leach to compositions similar to the more common Ca-carbonatites within weeks, preventing any long-term geological record of such Na-rich magmas. It follows that the oldest report of natrocarbonatites at Oldoinyo Lengai dates to the 19th century. Here, by using samples from the Lengai I cone (>11 ka), we show that immiscible silicate–carbonatite melts were already present at reservoir conditions at that time. Measurements of three-phase (carbonatite + silicate + gas) melt inclusions from Lengai I highlight that their chemical compositions were similar to those of immiscible melts recently present in the reservoir. Alkaline carbonatites in melt inclusions from both Lengai I and historical explosive eruptions are enriched in Ca relative to those historically effused at the surface and likely record higher equilibrium temperatures (>1100 °C). We also report chemical maps that qualitatively document elemental partitioning between immiscible silicate–carbonatite melts. We show that at the melt inclusions' entrapment conditions Si, Fe, K, Na, and Cl are compatible with the silicate phase when C, Ca, P, Sr, Ba, and F are compatible with the carbonate phase.

Keywords. Carbonatite, Melt inclusion, Tanzania, Oldoinyo Lengai, Phonolite, Immiscibility.

Available online 8th December 2021

1. Introduction

Carbonatites are relatively rare magmas that contain >50% carbonate minerals [Le Bas et al., 1972]

and, along with associated alkaline silicate magmas, constitute the main rare earth element (REE) deposits worldwide [e.g., Ling et al., 2013, Verplanck et al., 2014]. Although carbonatitic magmas are rare compared to silicate magmas, they have been produced throughout Earth's History, from the Archean

* Corresponding author.

to present day [Woolley and Kjarsgaard, 2008]. More than 500 occurrences have been reported globally; 35% in Africa, 30% in Asia, and 22% in North America [Woolley and Kjarsgaard, 2008]. Although reported in various geodynamic contexts, carbonatites are most commonly associated with rift environments; ~90% are intrusive and 80% are associated with alkaline silicate magmas [Woolley and Kjarsgaard, 2008].

Carbonatites are highly reactive at atmospheric conditions and alkali-rich compositions leach within weeks [Dawson *et al.*, 1987, Zaitsev and Keller, 2006], making it highly challenging to identify the original chemical compositions of older deposits [e.g., Kogarko *et al.*, 1991, Chen *et al.*, 2013]. Although directly sampling fresh lava avoids this issue, only one carbonatitic volcano is presently active on Earth, the Oldoinyo Lengai [Tanzania; Dawson, 1962a]. The highly alkaline carbonatites that erupted there, natrocarbonatites, differ from the Ca-carbonatites that represent the overwhelming majority of fossil carbonatite occurrences. Nevertheless, the rare available data directly documenting carbonatite melt compositions (i.e., from melt inclusions that shelter carbonatites from surface weathering) indicate the alkaline character of parental carbonatite magmas in various regions [Kogarko *et al.*, 1991, Mitchell, 2009, Sharygin *et al.*, 2012, Chen *et al.*, 2013, Guzmics *et al.*, 2015, Mollex, 2017, Weidendorfer *et al.*, 2017]. This raises the question of whether Ca-carbonatites effectively represent the magmatic composition or rather represent the leaching products of initially alkaline carbonatites [e.g., Dawson, 1962b, Hay, 1983, Keller and Zaitsev, 2006, Chen *et al.*, 2013].

Traces of alkaline carbonatites have been identified at various sites: Oka carbonatite [Canada; Chen *et al.*, 2013], Guli carbonatite [polar Siberia; Kogarko *et al.*, 1991], and various volcanoes from the Natron Lake magmatic province in northern Tanzania, including Oldoinyo Lengai [Mitchell, 2009, Sharygin *et al.*, 2012, Guzmics *et al.*, 2015]. Although the volcano is famous worldwide for its natrocarbonatite emissions, such carbonatite products have only been reported for the most recent deposits and represent <5% of the Oldoinyo Lengai edifice [e.g., Klaudius and Keller, 2006]. This is likely due to how quickly natrocarbonatite lavas alter under atmospheric conditions. Nonetheless, the oldest report of natrocarbonatites can be attributed to the German missionaries Krapf and Erhardt, who reported snow at the

summit of Oldoinyo Lengai in a map dated 14 March 1855 [Dawson *et al.*, 1995a]; they likely misinterpreted the presence of snow, which is unlikely at such elevations in northern Tanzania, as altered natrocarbonatites, which are bright whitish and may resemble snow cover. The first known direct observation of what would later be called natrocarbonatites was by Uhlig [1905], who described “mudflows [...] covered with efflorescence of a white sodium salt”. There is no direct evidence of any older carbonatite magmatism at Oldoinyo Lengai, and it is our aim to provide such evidence here.

Oldoinyo Lengai stratovolcano [edifice volume ~41 km³; Kervyn *et al.*, 2008] is in the Gregory rift, which forms the eastern branch of the East African rift. The oldest deposits of the volcano itself date to 350 ka [Sherrod *et al.*, 2013] and form a phonolite cone comprising tuffs and lava flows (Lengai I, ~60% of the present-day edifice; Figure 1). After a major sector collapse before 11 ka [Kervyn *et al.*, 2008, Sherrod *et al.*, 2013], an alkaline-nephelinite cone comprising tuffs and lava flows grew [Lengai II, ~35% of the present-day cone; Figure 1; Klaudius and Keller, 2006]. During the last century, eruptive activity has consisted of decades of low-temperature, low-viscosity effusions of natrocarbonatite lava flows punctuated by sub-Plinian eruptions that emit both silicate (alkaline nephelinite and phonolite) and carbonatite magmas [Keller *et al.*, 2010, Kervyn *et al.*, 2010]. Although the genesis of carbonatites may be related to alternative processes in other geodynamic contexts [e.g., the direct formation of Ca-carbonatite from carbonated peridotites; Hammouda *et al.*, 2014], Oldoinyo Lengai carbonatites are clearly related to liquid immiscibility between carbonatite and evolved silicate alkaline magmas [alkaline nephelinite and phonolite; e.g., Peterson, 1989, Fischer *et al.*, 2009, Casola *et al.*, 2020]. Indeed, conjugate carbonatite–silicate immiscible melts in melt inclusions (MIs) within various minerals from the 1917 and 2007–2008 explosive eruptions of Oldoinyo Lengai [e.g., Mitchell, 2009, Sharygin *et al.*, 2012, de Moor *et al.*, 2013, Mollex, 2017, Baudouin *et al.*, 2020] attest to the coexistence of both melts within the Lengai reservoir and to their evolved character. Although carbonatites from MIs are less enriched in Na than erupted natrocarbonatites, they are alkali-rich and in equilibrium with their coexisting evolved silicate magmas, which are similar

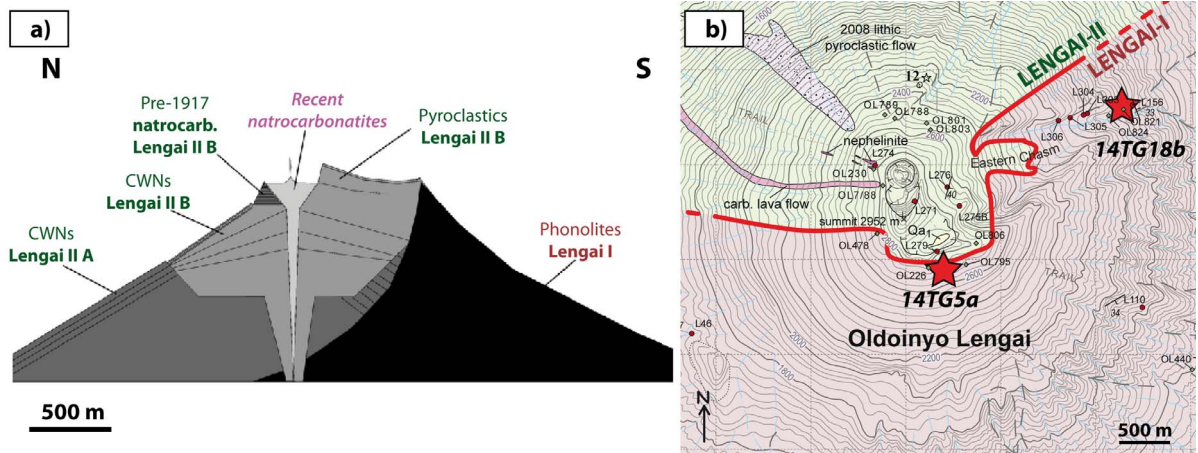


Figure 1. Sample setting and Oldoinyo Lengai architecture. (a) Synthetic N–S cross section highlighting the architecture of Oldoinyo Lengai stratovolcano, comprising >11 ka phonolite deposits of Lengai I to the south and combeite wollastonite nephelinite (CWN) and natrocarbonatite deposits of Lengai II to the north. This section is reproduced from Klaudius and Keller [2006]. (b) Map of the Oldoinyo Lengai summit area, showing the two sampling sites (red stars) from the present study. The limit between Lengai I and Lengai II (red line) proposed by Klaudius and Keller [2006] is also shown along with their sampling sites (used to define the delimitation) and those of Sherrod *et al.* [2013]. This map is modified from Sherrod *et al.* [2013].

to those of the older Lengai I and II deposits. This raises the question of whether immiscible carbonatites were present at the time of Lengai I and II, carbonatites that certainly would have weathered during their >11 ka of surface exposure. Here, we use nepheline-hosted MIs sampled from Lengai I phonolite lava flows (>11 ka) to demonstrate that carbonatite was present within the Lengai I reservoir and to document its composition.

2. Samples and petrography

2.1. Phonolite lavas

Two lava flows from the Lengai I edifice were sampled for the present study in two different areas of Lengai I cone. Sampling sites were selected based on the chemical architecture of Oldoinyo Lengai defined by Klaudius and Keller [2006], and we followed their sampling strategy (Table 1). Sample 14TG18bB was sampled at an elevation of 1678 m on the north-east flank of Oldoinyo Lengai, on the northern rim of the Eastern Chasm (Figure 1). Sample 14TG05a was sampled at ~2780 m elevation on the southern flank of the south crater, ~20 m-S below the

southern rim (Figure 1). Both samples are massive porphyritic lava flows comprising microlite matrix (~50%), vesicles (~25%), and phenocrysts (~25%; Figure 2). Phenocrysts include colorless, euhedral nepheline (up to 5 mm; ~60% and 80% in 14TG18bB and 14TG05a, respectively), green, euhedral clinopyroxene (up to 3 mm; ~30% and 10% in 14TG18bB and 14TG05a, respectively), and subordinate Fe–Ti oxides (~8%), titanite (~1%), and melanite (Ti-garnet; ~1%). This mineral assemblage is characteristic of Oldoinyo Lengai phonolites and related ijolite cumulates [e.g., Dawson *et al.*, 1995b, Klaudius and Keller, 2006, Mollex *et al.*, 2018, Baudouin and France, 2019, Baudouin *et al.*, 2020]. In both samples, clinopyroxene and nepheline host green composite MIs (Figure 3).

2.2. Melt inclusions

In both samples, MIs are oval to roundish, 10–40 μm wide, and commonly comprise three phases: green silicate glass, a carbonatite phase, and a shrinkage gas bubble (Figure 3). When only two phases are present, they are silicate glass and a shrinkage bubble. Because MIs are difficult to identify and describe

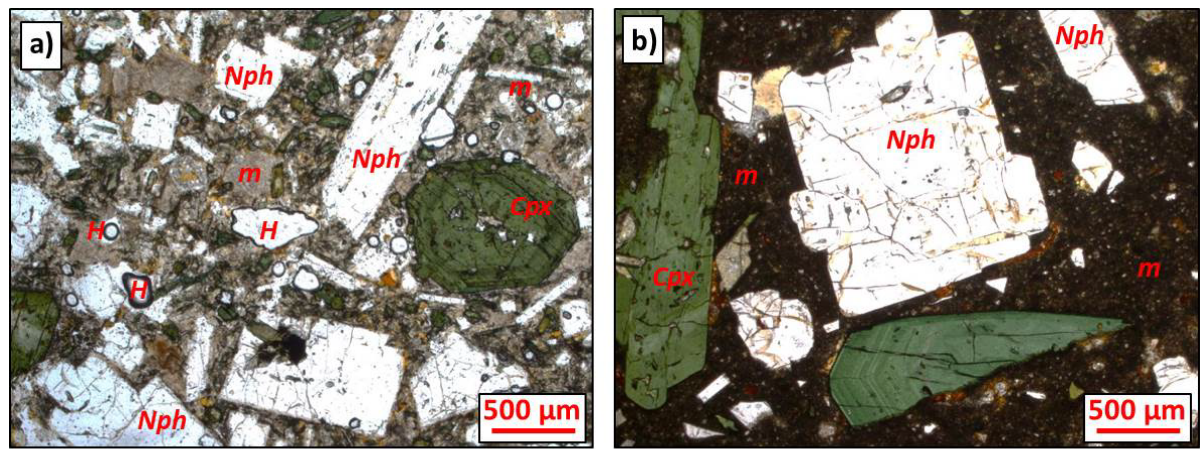


Figure 2. Microphotographs of phonolite lava flows studied herein (plane-polarized light): (a) sample 14TG05a and (b) sample 14TG18b. Cpx, clinopyroxene; Nph, nepheline; H, hole; m, matrix (microlites + crystallites + glass).

Table 1. Sample locations

Sample	Latitude	Longitude	Elevation	Location
14TG18b	2° 45' 14.00" S	35° 56' 2.00" E	1678 m	East flank
14TG05	2° 46' 1.49" S	35° 55' 2.17" E	2845 m	Southern flank of south crater

in similarly colored green clinopyroxenes, we focused on nepheline-hosted MIs. The carbonatite phase is either present as a spherical globule (Figure 3a, b) or a thin film wetting the shrinkage bubble (Figure 3c, d). Some inclusions contain silicate glass, a shrinkage bubble, and several carbonatite globules of various diameters (Figure 3e).

3. Methods

Whole-rock major and trace element concentrations of the two samples were determined by inductively coupled plasma optical emission spectrometry and inductively coupled plasma mass spectrometry, respectively at the Service d'Analyse des Roches et des Minéraux (SARM, CRPG, Nancy, France). Analyses were performed using HNO₃ solutions prepared from fused glass. Details of sample preparation, analytical settings and conditions, and detection limits, are reported in Carignan *et al.* [2001]. Analytical uncertainties are 2% and 5–10% for major and trace element concentrations, respectively.

MIs were studied both in thin sections and on separated grains. Separated grains containing

three-phase MIs (gas, silicate, and carbonate) were picked under a binocular microscope and polished using Al disks to expose the inclusions; polishing was performed without water to prevent carbonate dissolution. Polished grains were then pressed into indium mounts. Thin sections were also prepared without water to prevent carbonate dissolution. Exposed inclusions were first imaged by scanning electron microscopy (SEM) to identify µm-sized carbonate phases in X-ray chemical maps. Because carbonates are commonly wetting gas bubbles, the carbonate layer is often too thin for EPMA (Electron Probe Microanalysis); only the compositions of carbonate layers thicker than 3 µm were tentatively quantified with EPMA.

Mineral major element compositions were determined using a CAMECA SX100 microprobe at the Service Commun de Microscopie Electronique et de Microanalyses X (SCMEM, Université de Lorraine, Nancy, France) equipped with five spectrometers and the “Peak sight” operating system. Analyses were performed using a 10 kV accelerating potential, a static (fixed) beam, K α emissions for all elements, and a matrix correction based on Pouchou and Pichoir

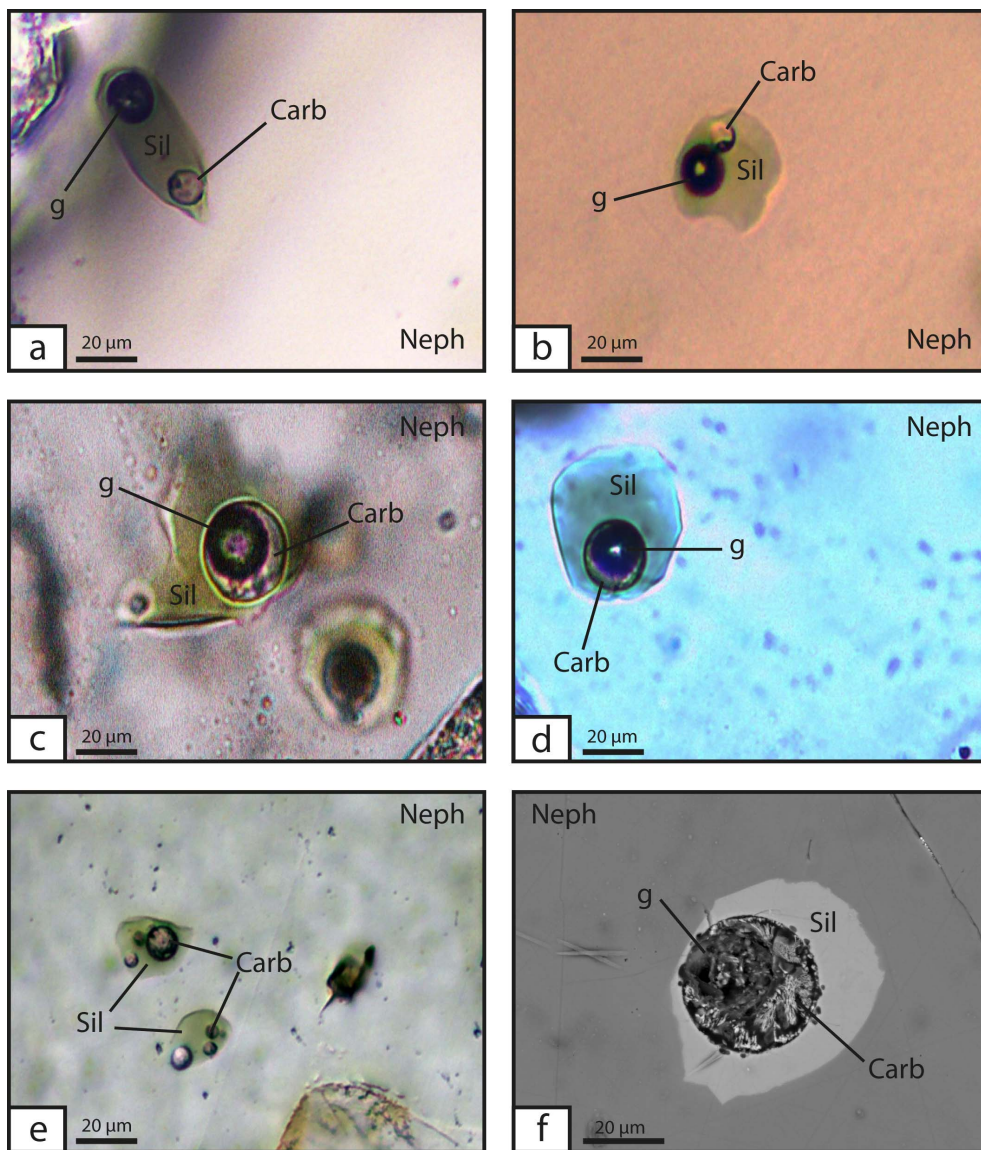


Figure 3. Microphotographs (a–e, sample 14TG18b) and backscattered electron image (f, sample 14TG05a) of nepheline-hosted three-phase melt inclusions containing silicate glass (“Sil”), carbonate “glass” (“Carb”, actually microcrystalline as evident in (f)), and gas bubbles resulting from shrinkage (“g”). (a, b) Single, isolated carbonate globules in melt inclusions. (c, d, f) Carbonate melt rimming the gas bubble. (e) Multiple carbonate globules are present in some melt inclusions.

[1991]. Crystals were analyzed with a beam current of 10 nA using a focused beam and counting times of 20 s on background, and 40 s on peak (15 s for K and Na that were measured first). Both carbonate and silicate glasses were analyzed with a beam current of 5 nA using a defocused beam 3–15 µm in diameter

depending on the size of the inclusion. To minimize elemental migration, background and peak counting times for inclusions were reduced to 10 s and 20 s, respectively (10 s on peak for K and Na, again measured first). In addition to in situ measurements, semi-quantitative chemical maps were obtained for

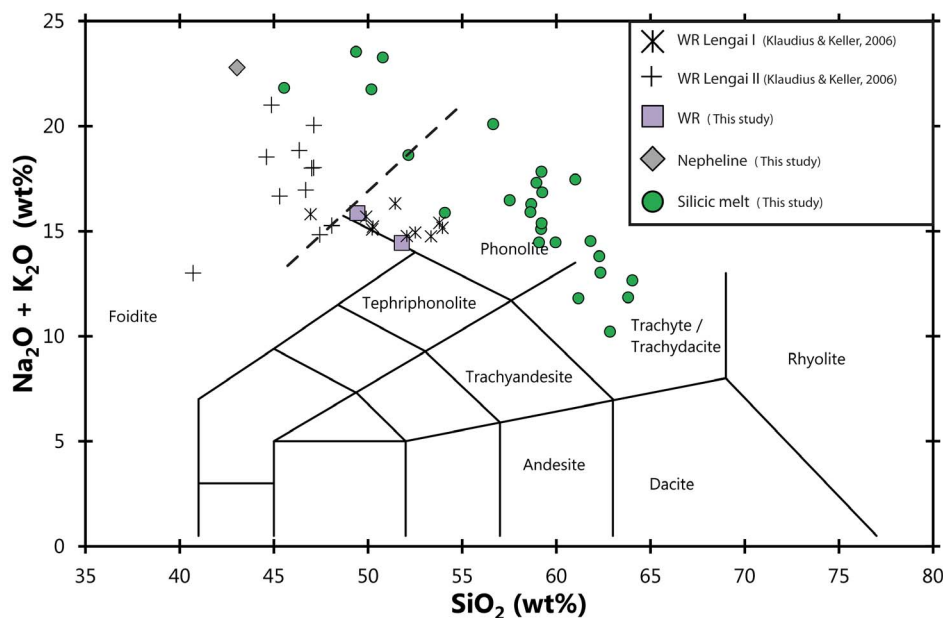


Figure 4. Total alkali versus silica diagram [after Le Maitre *et al.*, 1989] showing the compositions of silicate melts from the Lengai I melt inclusions studied herein and the average composition of their host nephelines. Whole-rock (WR) compositions are also presented and compared to the Lengai I/II data of Klaudius and Keller [2006]. The samples studied herein are phonolites, compositionally similar to Lengai I deposits. The dashed line denotes the proposed division between the Foidite and Phonolite fields.

major elements and some trace elements (Ce, Ba, Sr, Cl, S, Mn) using a JEOL 7600F (Schottky field-emission gun) SEM equipped with an Oxford Instruments SDD-type energy dispersive spectrometer at the SCMEM. Chemical maps were acquired using an accelerating voltage of 15 kV, a beam current of 20 nA, and a dwell time of 24 ms/pixel, and data were deconvoluted pixel by pixel using the Oxford algorithm.

4. Chemical compositions

4.1. Whole-rock compositions

Whole-rock compositions (Table S1 in the supplementary materials) display relatively high loss on ignition (LOI), consistent with the relatively altered character of the rocks forming Oldoinyo Lengai stratovolcano [e.g., Klaudius and Keller, 2006]. Once recalculated on an anhydrous basis, the samples are classified as phonolites (Figure 4) with similar compositions to those defining the Lengai I series according to Klaudius and Keller [2006], confirming that the samples correspond to this oldest series (whereas the Lengai II

series is relatively enriched in alkalis and depleted in silica). On average, the studied samples contain (once recalculated on an anhydrous basis) 50.6 wt% SiO₂, 17.6 wt% Al₂O₃, 7.8 wt% Fe₂O₃ (total iron), 10 wt% Na₂O, 5 wt% K₂O, 5.7 wt% CaO, 1.2 wt% MgO, 1.2 wt% TiO₂, ~0.2 wt% Cl, and ~0.2 wt% F.

4.2. Silicate glass compositions

The studied inclusions are hosted in nepheline crystals with compositions characteristic of nephelines from Oldoinyo Lengai phonolites and related ijolite cumulates [Table 2; e.g., Dawson *et al.*, 1995b, Klaudius and Keller, 2006, Bosshard-Stadlin *et al.*, 2014, Mollex, 2017, Berkesi *et al.*, 2020]. Silicate glasses range in composition from trachyte to phonolite (Figure 4) with alkaline contents varying from ~10 wt% to more than 20 wt%. Some rare MIs are particularly enriched in K₂O (up to 9.5 wt%, Figure 5). On average, silicate glasses contain 54 ± 4.5 wt% SiO₂, 11.1 ± 2.1 wt% Na₂O, 11 ± 1.5 wt% FeO (total iron), 5.3 ± 1.0 wt% CaO, 4.3 ± 1.1 wt% Al₂O₃, 4.3 ± 2.7 wt% K₂O, 1.4 ± 0.3 wt% TiO₂, 0.65 ± 0.2

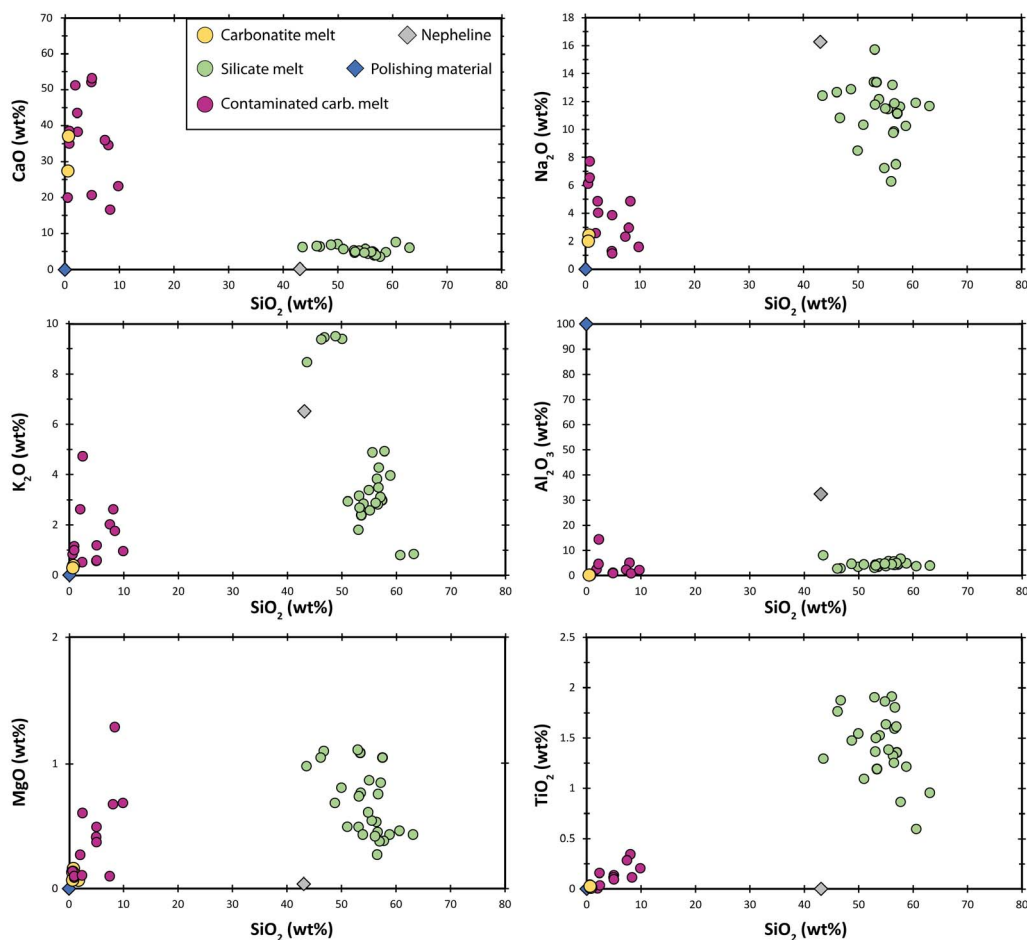


Figure 5. Chemical compositions of three-phase melt inclusions from Lengai I phonolite lava flows. Grains were polished with Al-discs to prevent carbon contamination, and we document the composition of the polishing material as a potential contaminant of the measurements. The two yellow circles (“Carbonatite melt”) are considered to be representative of the carbonatite phase composition because those data were obtained on portions of carbonatite large enough to ensure accurate measurements. Other data (purple circles, “Contaminated carb. melt”) were measured on smaller carbonatite globules and likely represent carbonatite analyses that included some portion(s) of silicate melt, the host nepheline, and/or polishing material.

wt% MgO, 1.3 ± 0.4 wt% F, 0.8 ± 0.4 wt% SO₂, and 0.5 ± 0.2 wt% Cl (Table 2, Figures 4 and 5). Silicate glass from two-phase and three-phase melt inclusions display similar chemical compositions. The chemical trend defined by the silicate glass major element contents does not align with the host nepheline composition (Figure 5); therefore, the corresponding chemical variability is not related to post-entrapment processes. The silicate glasses in nepheline-hosted MIs studied herein are similar to

those reported in MIs from the 1917 Oldoinyo Lengai explosive eruption (Figure 6; 1917 data from Sharygin *et al.* [2012] are represented by a brown square in Figure 6).

4.3. Carbonate “glass” composition

It is very challenging to accurately determine the compositions of carbonatite globules in the composite nepheline-hosted MIs because the carbon-

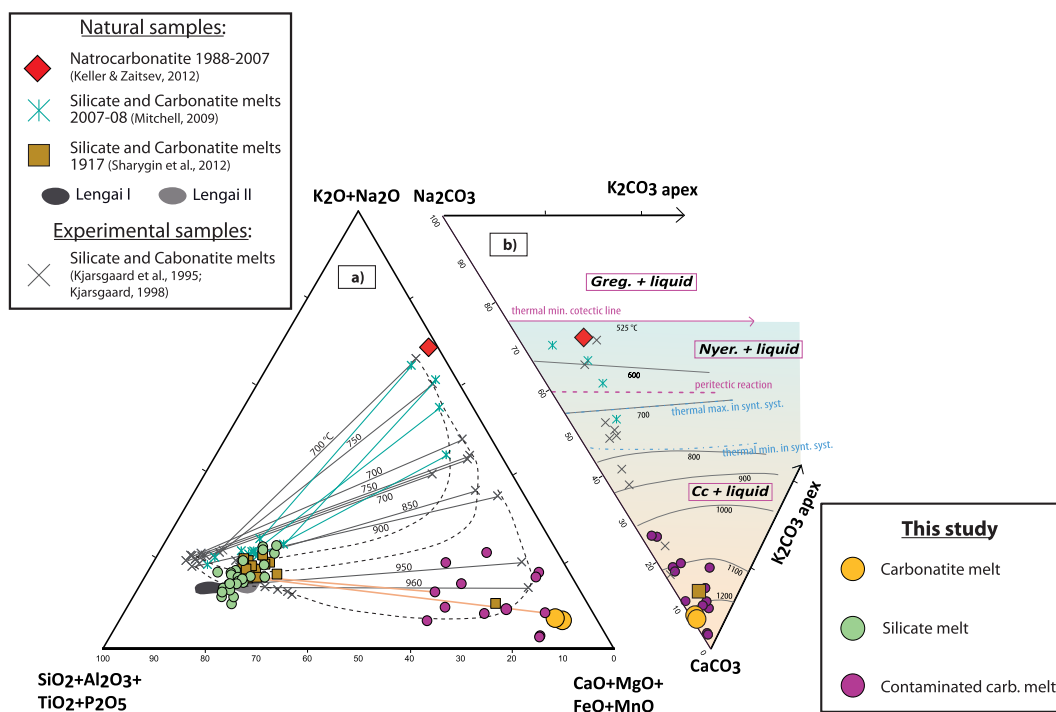


Figure 6. (a) Pseudoternary multicomponent diagram grouping the network forming elements (bottom left), network modifying elements (bottom right), and alkalis [top; after Freestone and Hamilton, 1980]. The silicate and carbonatite melts from the present study are compared to the average natrocarbonatite composition of Keller and Zaitsev [2012], the compositions of immiscible silicate and carbonatite melts in melt inclusions from the 1917 [Sharygin et al., 2012] and 2007–2008 eruptions [Mitchell, 2009], and the compositions of experimental silicate–carbonatite melt pairs [only data for pressures <4 kbar are shown; Kjarsgaard et al., 1995, Kjarsgaard, 1998]. Dashed curves represent the extent of the miscibility gap as a function of increasing peralkalinity. Solid lines are tie lines between conjugate natural and experimental melts; numbers adjacent to experimental tie lines indicate the corresponding equilibrium temperature ($^{\circ}\text{C}$). (b) Carbonatite melts plotted on the Na–K–Ca–carbonate ternary of Cooper et al. [1975]. Liquidus surfaces are derived from Weidendorfer et al. [2017] and are valid for the natural system. The thermal minimum, thermal maximum, and peritectic reactions are from Cooper et al. [1975]; they apply to the synthetic system and are presented for comparison. Cc, calcite; Greg., gregoryite; Nyer., nyerereite.

atites are finely crystallized, are usually present in the form of a thin micron-thick film wetting the shrinkage bubble rims, and because some of the polishing material (Al-rich) regularly fills the bubble cavities. For these reasons, chemical maps are particularly valuable for identifying carbonatite melts (Figure 7). Also, chemical maps are useful because the intensity contrast between the silicate and carbonatite melts highlights the partitioning behavior of various chemical elements between the two melts (Figure 8). Ca-rich, Si-poor globules within the sili-

cate MIs (Figure 7) correspond to the visually identified carbonatite globules (Figure 3). Detailed maps highlight that the carbonatite melts are depleted in Si, K, Fe, Na, and Cl and enriched in C, Ca, P, F, Sr, and Ba compared to the silicate MIs (Figures 7, 8). Although challenging, in situ measurements of very rare large inclusions (e.g., Figure 3f) provide some quantitative compositions that can be used herein as a reference (Figure 5). Other carbonatite globule measurements were contaminated by either the silicate melt, some polishing material trapped in the

bubble cavity, or the host nepheline. The least contaminated measurements are reported for comparison in Figure 5 and allow us to better discuss the accurate measurements (e.g., depletion in Na of the carbonatite relative to the silicate melt).

5. Discussion

5.1. *Carbonatite magma was already present during early Oldoinyo Lengai evolution*

The results presented herein clearly document the presence of carbonatite–silicate melt immiscibility in nepheline-hosted MIs from Lengai I products. The presence of carbonatites within the Lengai I MIs is at odds with the lack of such magmas in the geological record of the Lengai I cone, but is likely explained by the fact that MIs are shielded from the atmosphere, and therefore from leaching. Nevertheless, before we can conclude that those immiscible melts were present within the magma reservoir >11 ka, we must first discuss the potential effect of post-entrapment crystallization on the bulk compositions of the inclusions [e.g., Rose-Koga *et al.*, 2021]. Given the compositions of the host nepheline phenocrysts, post-entrapment crystallization should result in an overall increase in the Si content and decreases in the Na and K contents of the bulk MIs. According to experimental constraints and related applications to natural systems, such compositional variations would shift the bulk compositions of the inclusions out of the miscibility gap [Kjarsgaard and Peterson, 1991, Martin *et al.*, 2013, Weidendorfer *et al.*, 2016, 2017, Schmidt and Weidendorfer, 2018]. Thus, the effects of post-entrapment crystallization would diminish, not enhance, any evidence of carbonate–silicate immiscibility. Our results thus clearly demonstrate that immiscible carbonatite and silicate melts were present at depth within the Lengai I magmatic reservoir >11 ka.

The carbonatite component in the Lengai I MIs is an alkaline Ca-carbonatite (up to 37 wt% CaO, ~2 wt% Na₂O; Figure 6; Table 2). It is less sodic and more calcic than (i) the natrocarbonatites historically erupted at Oldoinyo Lengai [15.6 wt% CaO, ~32 wt% Na₂O; Keller and Zaitsev, 2012] and (ii) the alkaline carbonatites present as immiscible melts within MIs from the most recent sub-Plinian eruption of Oldoinyo Lengai in 2007–2008 [18.3 wt% CaO,

26.3 wt% Na₂O; e.g., Mitchell, 2009, Mollex, 2017]. It is, however, similar to the immiscible alkaline carbonatite melts reported within MIs from the 1917 sub-Plinian eruption of Oldoinyo Lengai [~37 wt% CaO, 3.4 wt% Na₂O; Sharygin *et al.*, 2012]. Experimental results have demonstrated that carbonatites become less calcic and more sodic with decreasing temperature during magma differentiation [Figure 6; Kjarsgaard *et al.*, 1995, Kjarsgaard, 1998, Weidendorfer *et al.*, 2017, Nabyi *et al.*, 2020]. These results strongly suggest that the alkaline carbonatites present within the igneous reservoir during the Lengai I stage (this study) or during the 1917 eruption [Sharygin *et al.*, 2012] were equilibrated at higher temperatures than those present in the reservoir during the 2007–2008 eruption [Mitchell, 2009] or erupted at surface during historical times [Keller and Zaitsev, 2012]. The phase diagram shown in Figure 6 highlights that the equilibrium temperatures of the Lengai I alkaline Ca-carbonatites were likely 1100–1200 °C [Weidendorfer *et al.*, 2017], consistent with the minimum temperature of 1130 °C obtained by Sharygin *et al.* [2012] for the entrapment conditions of the 1917 MIs based on a thermometric approach. Furthermore, Baudouin *et al.* [2020]; using the clinopyroxene–melt thermometer of Masotta *et al.* [2013] obtained lower equilibrium temperatures of 930–1060 °C for 2007–2008 ijolite samples containing MIs similar to those described by Mitchell [2009]. Those equilibrium temperatures are much higher than the eruptive temperatures reported for historical natrocarbonatites, 490–600 °C [Keller and Krafft, 1990, Dawson *et al.*, 1995b], temperatures that are again consistent with phase diagram constraints [Figure 6; Weidendorfer *et al.*, 2017].

These results support that high-temperature (>900 °C), immiscible, alkali-poor alkaline carbonatites are present at reservoir depth, whereas cooler, alkali-rich natrocarbonatites are emitted during present-day surface eruptions. The transition from ~900 °C alkaline carbonatites to <600 °C natrocarbonatites is not directly documented herein, but has been shown to be feasible during the protracted differentiation of magmas compositionally similar to those of the Natron Lake igneous province [Weidendorfer *et al.*, 2017]. Such protracted differentiation likely occurred at reservoir conditions or during magma ascent.

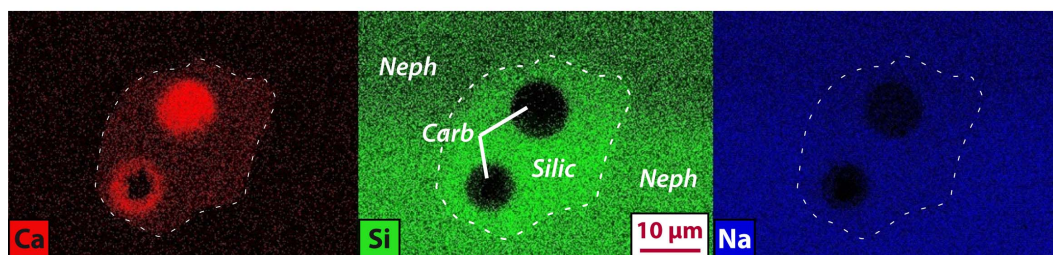


Figure 7. Ca, Si, and Na chemical maps for a three-phase melt inclusion hosted in a nepheline crystal (“Neph”) in sample 14TG18b. Two Ca-rich, Si-poor carbonatite globules (“Carb”) are present within the silicate melt (“Silic”). The white dashed line delimits the melt inclusion.

Our new results eventually highlight the coexistence of alkaline carbonatite and alkaline silicate melts in the igneous reservoir during the Lengai I period (>11 ka), and thus document a similar igneous configuration than during historical eruptions. We can thus propose here that although there is no direct evidence that alkaline carbonatites or natrocarbonatites were erupted during the Lengai I period, carbonatite eruptions similar to the present-day ones most likely occurred at that time.

5.2. Implications for elemental partitioning between immiscible silicate–carbonatite melts

Direct compositional measurements of carbonatite globules are very challenging, and we are unable to provide quantitative data on elemental partitioning between immiscible silicate–carbonatite melts (see Sections 3 and 4.3). Nevertheless, chemical maps of the composite MIs qualitatively characterize the behaviors of various elements, and we here estimate the pressure–temperature conditions for which those partitioning constraints are valid. The chemical compositions of the identified carbonatites and previous experimental results strongly suggest that the equilibrium temperatures of the studied immiscible melts were 1100–1200 °C (e.g., Figure 6, see Section 5.1). The pressure conditions preserved by MIs roughly correspond to the entrapment pressure, which is likely the reservoir depth. At Oldoinyo Lengai, the recent upper crustal reservoir is likely at 10–15 km depth, corresponding to pressures of 3–5 kbar [Baer *et al.*, 2008, Albaric *et al.*, 2010, Mollex, 2017]. Given that magmatic compositions during the Lengai I period were quite similar to those evidenced

by historical eruptions, we expect that the plumbing system architecture was also largely similar. Therefore, the partitioning constraints provided hereafter are valid for such pressure–temperature conditions (3–5 kbar, 1100–1200 °C). Chemical maps presented in Figures 7 and 8 highlight that Si, Fe, and K are preferentially incorporated into the silicate melt whereas C, Ca, P, Sr, and Ba are preferentially incorporated in the carbonate melt, consistent with previous natural and experimental data [Hamilton *et al.*, 1989, Jones *et al.*, 1995, Veksler *et al.*, 1998, 2012, Guzmics *et al.*, 2012, Martin *et al.*, 2013]. Notably, our results show that Na, which has been reported as compatible with the carbonate melt in most experimental studies, is rather slightly enriched in the silicate melt at the studied conditions (Figures 5, 7). Similar preferential incorporation of Na in the silicate melt has nevertheless been reported in some experiments by Kjarsgaard *et al.* [1995], Kjarsgaard [1998], and Nabyal *et al.* [2020], but there is no evident relation between this behavior and specific temperature and pressure conditions, or with composition. Fewer literature data are available for halogens; our results highlight that F strongly partitions into the carbonate phase, consistent with Kjarsgaard *et al.* [1995], Kjarsgaard [1998], Guzmics *et al.* [2012], Nabyal *et al.* [2020], whereas Cl rather partitions into the silicate melt. This latter result is consistent with previous experimental constraints as although Kjarsgaard *et al.* [1995], Kjarsgaard [1998], and Nabyal *et al.* [2020] have shown that Cl is compatible with the carbonate in most cases, partition coefficients as low as 0.6 were reported for some experiments. Again there is no evident relation between this behavior and specific temperature and pressure conditions, or

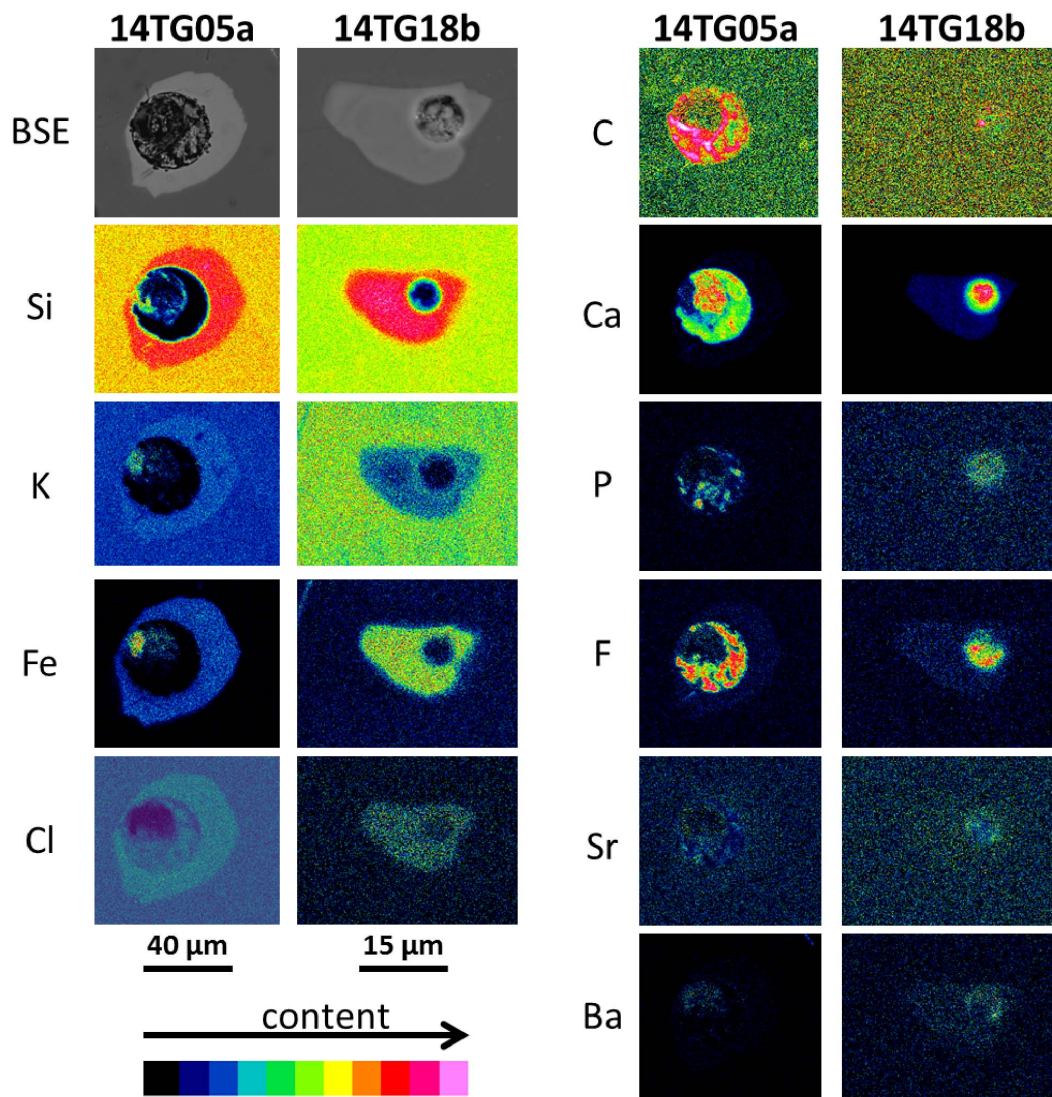


Figure 8. Backscattered electron (BSE) images and chemical maps for various elements in three-phase nepheline-hosted melt inclusions from two Lengai I samples. These maps qualitatively show elemental partitioning behaviors between immiscible silicate and carbonatite melts. Si, K, Fe, and Cl are enriched in the silicate relative to the carbonatite phase, whereas C, Ca, P, F, Sr, and Ba are enriched in the carbonatite relative to the silicate phase.

with composition, and further experimental work dedicated to the study of halogens partitioning between immiscible carbonatite–silicate melts would be required to better understand Cl behavior.

6. Summary

Oldoinyo Lengai is currently the only active carbonatite volcano worldwide, but the oldest previous evi-

dence of carbonatite magmas there dates only to the 19th century. Here, based on nepheline-hosted melt inclusions that preserve immiscible carbonatite and conjugate silicate melts from surface weathering and leaching, we reported evidence of carbonatite magmas predating 11 ka at Oldoinyo Lengai. These newly identified carbonatites are enriched in Ca and depleted in Na compared to the modern natrocarbonatites historically emitted at the summit. In contrast

Table 2. Phase compositions (wt%)

Phase	Measurement no	SiO ₂	TiO ₂	Al ₂ O ₃	FeO _t	MnO	MgO	CaO	Na ₂ O	K ₂ O	P ₂ O ₅	F	SO ₂	Cl	Total
Silicate melt	14TG18b_S03	57.21	1.35	4.27	11.27	0.40	0.85	5.18	11.02	2.99	0.13	1.12	0.58	0.47	96.84
Silicate melt	14TG18b_S04	53.53	1.21	3.04	16.10	0.35	0.77	5.37	13.38	2.34	0.27	1.58	0.60	0.43	98.97
Silicate melt	14TG05A_C020	43.56	1.29	7.88	10.81	0.44	0.98	6.22	12.40	8.47	0.41	2.14	0.86	0.17	95.63
Silicate melt	14TG05A_S05	49.99	1.54	3.38	12.35	0.25	0.81	7.06	8.46	9.40	0.16	1.52	0.63	0.30	95.85
Silicate melt	14TG05A_S06	60.66	0.59	3.64	9.07	0.04	0.47	7.63	11.88	0.80	0.17	1.20	0.25	0.74	97.14
Silicate melt	14TG05A_S07	63.15	0.95	3.81	9.18	0.58	0.44	6.06	11.65	0.84	0.00	0.74	0.33	0.90	98.63
Silicate melt	14TG18b_S08	58.84	1.21	4.73	10.82	0.50	0.44	4.83	10.23	3.97	0.10	1.18	0.58	0.51	97.94
Silicate melt	14TG05A_1-04	46.74	1.87	2.77	12.85	0.72	1.10	6.36	10.80	9.46	0.34	n.a.	1.82	0.25	95.08
Silicate melt	14TG05A_1-05	46.17	1.76	2.67	12.55	0.61	1.05	6.48	12.64	9.38	0.23	n.a.	1.87	0.28	95.69
Silicate melt	14TG05A_1-07	48.78	1.47	4.49	10.72	0.55	0.69	6.86	12.85	9.51	0.15	n.a.	0.79	0.34	97.20
Silicate melt	14TG18b_4-2	53.12	1.36	4.13	10.54	0.57	0.50	4.63	15.69	3.16	0.09	n.a.	0.87	0.48	95.14
Silicate melt	14TG18b_3-2	56.39	1.32	4.17	10.04	0.50	0.54	5.07	13.16	3.83	0.12	n.a.	0.71	0.45	96.30
Silicate melt	14TG18b_5-2	57.77	0.86	6.49	8.53	0.52	0.39	3.51	11.61	4.93	0.10	n.a.	0.23	0.39	95.33
Silicate melt	14TG18b_7-2	52.98	1.90	2.94	11.73	0.75	1.11	5.36	13.37	1.81	0.17	n.a.	1.22	0.57	93.91
Silicate melt	14TG18b_8-1	55.56	1.38	5.52	10.08	0.40	0.55	4.37	11.43	4.89	0.10	n.a.	1.05	0.59	95.92
Silicate melt	14TG18b_10-1	55.08	1.63	3.60	11.07	0.81	0.87	5.73	11.48	2.58	0.21	n.a.	1.02	0.66	94.74
Silicate melt	14TG18b_19-2	56.65	1.59	4.08	10.22	0.37	0.46	4.72	9.83	3.49	0.16	n.a.	0.86	0.45	92.88
Silicate melt	14TG18b_18-2	56.73	1.80	4.95	10.74	0.56	0.76	3.86	11.85	4.28	0.18	n.a.	0.98	0.57	97.26
Silicate melt	14TG18b_43_Si	53.92	1.52	4.57	10.57	0.45	0.44	5.27	12.12	2.85	0.17	0.79	0.22	0.34	93.23
Silicate melt	14TG18b_44_Si	56.54	1.25	5.39	9.70	0.46	0.28	4.60	9.73	2.82	0.07	1.56	0.42	0.34	93.15
Silicate melt	14TG18b_36_Si	51.05	1.09	4.24	9.47	0.49	0.50	5.69	10.31	2.94	0.37	1.42	0.73	0.50	88.81
Silicate melt	14TG18b_37_Si	53.20	1.50	3.88	11.09	0.66	0.74	4.97	11.76	2.68	0.26	1.12	0.53	0.54	92.92
Silicate melt	14TG18b_39_Si3	57.01	1.61	4.75	10.63	0.41	0.39	3.98	7.49	3.10	0.00	1.43	0.95	0.56	92.30
Silicate melt	14TG18b_19_Si	56.15	1.91	4.31	11.87	0.67	0.43	4.92	6.26	2.88	0.00	0.51	0.95	0.43	91.27
Silicate melt	14TG18b_17_Si	54.89	1.86	4.58	11.80	0.48	0.62	4.70	7.21	3.39	0.23	2.05	0.21	0.59	92.60
Carbonatite melt	14TG05A_1-02	0.73	0.01	0.05	0.17	0.06	0.17	37.06	2.41	0.38	2.24	n.a.	0.13	0.18	43.59
Carbonatite melt	14TG05A_1-03	0.61	0.02	0.00	0.11	0.00	0.14	27.38	1.97	0.29	2.03	n.a.	0.14	0.16	32.85
Contam. carb. melt	14TG18b_19-1	1.96	0.00	2.33	0.52	0.00	0.28	51.26	2.56	2.62	1.73	n.a.	0.21	1.05	64.52
Contam. carb. melt	14TG18b_18-1	2.39	0.03	14.24	0.32	0.17	0.61	38.31	4.01	4.73	2.69	n.a.	0.44	0.98	68.92
Contam. carb. melt	14TG18b_9-1	8.01	0.34	4.90	1.28	0.03	0.68	34.61	2.94	2.62	3.51	n.a.	0.41	0.85	60.18
Contam. carb. melt	14TG18b_12-2	7.39	0.28	2.20	1.85	0.19	0.11	35.97	2.30	2.03	1.75	n.a.	0.29	0.42	54.78
Contam. carb. melt	14TG05A_C014	0.85	0.00	0.00	0.00	0.10	0.10	38.57	7.69	1.16	2.25	23.69	0.06	0.10	74.57
Contam. carb. melt	14TG05A_C015	0.55	0.04	0.15	0.00	0.00	0.15	20.00	6.09	0.83	3.69	4.05	0.35	0.13	36.03
Contam. carb. melt	14TG05A_C017	8.32	0.11	0.72	0.00	0.01	1.29	16.66	4.84	1.76	5.03	0.14	0.27	0.08	39.23
Contam. carb. melt	14TG05A_C018	4.97	0.13	1.00	0.00	0.09	0.50	20.66	3.84	1.19	1.56	11.06	0.21	0.07	45.28
Contam. carb. melt	14TG05A_C021	0.85	0.01	0.13	0.00	0.00	0.11	35.04	6.53	1.00	2.33	23.78	0.11	0.11	70.00
Contam. carb. melt	14TG18b_C029	4.91	0.11	0.84	0.00	0.12	0.42	52.14	1.27	0.57	2.37	11.56	0.29	0.11	74.71
Contam. carb. melt	14TG18b_C030	4.98	0.09	0.76	0.14	0.00	0.38	53.18	1.10	0.59	2.74	12.06	0.45	0.11	76.58
Contam. carb. melt	14TG18b_C033	9.83	0.20	2.06	0.00	0.00	0.69	23.22	1.57	0.96	1.23	2.62	0.36	0.28	43.02
Contam. carb. melt	14TG18b_39_c2	2.32	0.15	4.45	0.58	0.06	0.12	43.54	4.84	0.52	3.02	19.36	0.28	0.66	79.88
Average nepheline		42.7	0.01	31.8	1.82	0.02	0.02	0.09	15.9	7.6	0.00	—	—	—	99.90

Contaminated carbonatite melt (“contam. carb. melt”) indicates analyses of carbonatite melt that may have included adjacent silicate melt, host nepheline, and/or polishing material (see Sections 3 and 4.3). FeO_t is for total iron expressed as FeO.

they are similar to carbonatites that were recently present in the upper crustal igneous reservoir and preserved in melt inclusions from recent explosive eruptions. By comparison with previous experimental results, we suggest that this discrepancy highlights the presence of Ca-rich, Na-poor carbonatites at reservoir conditions (>1100 °C), which then differentiate to Na-rich, Ca-poor compositions during their ascent to the surface and related cooling. We also provide new qualitative data on elemental partitioning between immiscible carbonate and silicate melts.

Conflicts of interest

Authors have no conflict of interest to declare.

Acknowledgments

Céline Baudouin is thanked for numerous discussions about the Oldoinyo Lengai system and alkaline magmatism. Marine Boulanger is thanked for discussions and sample preparation advice. Andreï Lecomte and Jean Cauzid are thanked for assistance

with acquiring chemical maps and signal deconvolution. Gaëlle Mollex, Gilles Chazot, Pete Burnard, and Emmanuel Kazimoto are thanked for assistance and discussions during field work. We thank the two anonymous reviewers for their constructive comments, and Bruno Scaillet for his editorial handling and for his invitation to contribute to this special issue “Perspectives on alkaline magmas”. We also thank the Tanzania Commission for Science and Technology (COSTECH) for field permits and all the guides and porters for their help during field work. This work was supported by the French National Research Agency through the national program “Investissements d’avenir” with the reference ANR-10-LABX-21-01/LABEX RESSOURCES21, and through the project GECO-REE (ANR-16-CE01-0003-01; P.I., Lydéric France). This study was also supported by the Région Lorraine, and PNP and CESSUR programs from INSU-CNRS (grants to Lydéric France). This is CRPG contribution number 2810 and GECO-REE contribution number 5.

Supplementary data

Supporting information for this article is available on the journal’s website under <https://doi.org/10.5802/crgeos.99> or from the author.

References

- Albaric, J., Perrot, J., Déverchère, J., Deschamps, A., Le Gall, B., Ferdinand, R. W., Petit, C., Tiberu, C., Sue, C., and Songo, M. (2010). Contrasted seismogenic and rheological behaviours from shallow and deep earthquake sequences in the North Tanzanian Divergence, East Africa. *J. Afr. Earth Sci.*, 58(5), 799–811.
- Baer, G., Hamiel, Y., Shamir, G., and Nof, R. (2008). Evolution of a magma-driven earthquake swarm and triggering of the nearby Oldoinyo Lengai eruption, as resolved by InSAR, ground observations and elastic modeling, East African Rift, 2007. *Earth Planet. Sci. Lett.*, 272(1–2), 339–352.
- Baudouin, C. and France, L. (2019). Trace element partitioning between wollastonite and alkaline silicate magmas. *Chem. Geol.*, 523, 88–94.
- Baudouin, C., France, L., Boulanger, M., Dalou, C., and Devidal, J. L. (2020). Trace element partitioning between clinopyroxene and alkaline magmas. *Contrib. Mineral. Petrol.*, 175, article no. 42.
- Berkési, M., Bali, E., Bodnar, R. J., Szabó, A., and Guzmics, T. (2020). Carbonatite and highly peralkaline nephelinite melts from Oldoinyo Lengai volcano, Tanzania: The role of natrite-normative fluid degassing. *Gondwana Res.*, 85, 76–83.
- Bosshard-Stadlin, S. A., Mattsson, H. B., and Keller, J. (2014). Magma mixing and forced exsolution of CO₂ during the explosive 2007–2008 eruption of Oldoinyo Lengai (Tanzania). *J. Volcanol. Geotherm. Res.*, 285, 229–246.
- Carignan, J., Hild, P., Mevelle, G., Morel, J., and Yeghicheyan, D. (2001). Routine analyses of trace element in geological samples using flow injection and low pressure on-line liquid chromatography coupled to ICP-MS: a study of geochemical reference materials BR, DR-N, UB-N, AN-G and GH. *Geostand. Newsl.*, 25, 187–198.
- Casola, V., France, L., Galy, A., Bouden, N., and Vileneuve, J. (2020). No evidence for carbon enrichment in the mantle source of carbonatites in eastern Africa. *Geology*, 48, 971–975.
- Chen, W., Kamenetsky, V. S., and Simonetti, A. (2013). Evidence for the alkaline nature of parental carbonatite melts at Oka complex in Canada. *Nat. Commun.*, 4, article no. 2687.
- Cooper, A. F., Gittins, J., and Tuttle, O. F. (1975). The system Na₂CO₃–K₂CO₃–CaCO₃ at 1 kilobar and its significance in carbonatite petrogenesis. *Am. J. Sci.*, 275, 534–560.
- Dawson, J. B. (1962a). Sodium carbonate lavas from Oldoinyo Lengai, Tanganyika. *Nature*, 195, 1075–1076.
- Dawson, J. B. (1962b). The geology of Oldoinyo Lengai. *Bull. Volcanol.*, 24, 348–387.
- Dawson, J. B., Garson, M. S., and Roberts, B. (1987). Altered former alkalic carbonatite lava from Oldoinyo Lengai, Tanzania: inferences for calcite carbonatite lavas. *Geology*, 15, 765–768.
- Dawson, J. B., Keller, J., and Nyamweru, C. (1995a). Historic and recent eruptive activity of Oldoinyo Lengai. In Bell, K. and Keller, J., editors, *Carbonatite Volcanism: Oldoinyo Lengai and the Petrogenesis of Natrocarbonatites. IAVCEI Proc Volcanol 4*, pages 4–22. Springer, Berlin, Heidelberg.
- Dawson, J. B., Pinkerton, H., Norton, G. E., Pyle, D. M., Browning, P., Jackson, D., and Fallick, A. E. (1995b). Petrology and geochemistry of Oldoinyo Lengai lavas extruded in november 1988: magma source, ascent and crystallization. In Bell, K. and

- Keller, J., editors, *Carbonatite Volcanism. IAVCEI Proceedings in Volcanology*, volume 4, pages 44–69. Springer, Berlin, Heidelberg.
- de Moor, J. M., Fischer, T. P., King, P. L., Botcharnikov, R. E., Hervig, R. L., Hilton, D. R., Barry, P. H., Mangasini, F., and Ramirez, C. (2013). Volatile-rich silicate melts from Oldoinyo Lengai volcano (Tanzania): Implications for carbonatite genesis and eruptive behavior. *Earth Planet. Sci. Lett.*, 361, 379–390.
- Fischer, T. P., Burnard, P., Marty, B., Hilton, D. R., Füre, E., Palhol, F., Sharp, Z. D., and Mangasini, F. (2009). Upper-mantle volatile chemistry at Oldoinyo Lengai volcano and the origin of carbonatites. *Nature*, 459, 77–80.
- Freestone, I. C. and Hamilton, D. L. (1980). The role of liquid immiscibility in the genesis of carbonatites—An experimental study. *Contrib. Mineral. Petrol.*, 73, 105–117.
- Guzmics, T., Mitchell, R. H., Szabó, C., Berkesi, M., Milke, R., and Ratter, K. (2012). Liquid immiscibility between silicate, carbonate and sulfide melts in melt inclusions hosted in co-precipitated minerals from Kerimasi volcano (Tanzania): evolution of carbonated nephelinitic magma. *Contrib. Mineral. Petrol.*, 164, 101–122.
- Guzmics, T., Zajacz, Z., Mitchell, R. H., Szabó, C. S., and Wälle, M. (2015). The role of liquid–liquid immiscibility and crystal fractionation in the genesis of carbonatite magmas: insights from Kerimasi melt inclusions. *Contrib. Mineral. Petrol.*, 169, article no. 17.
- Hamilton, D. L., Bedson, P., and Esson, J. (1989). The behaviour of trace elements in the evolution of carbonatites. In Bell, K., editor, *Carbonatites: Genesis and Evolution*, pages 405–427. Unwin Hyman, London.
- Hammouda, T., Chantel, J., Manthilake, G., Guignard, J., and Crichton, W. (2014). Hot mantle geotherms stabilize calcic carbonate magmas up to the surface. *Geology*, 42(10), 911–914.
- Hay, R. L. (1983). Natrocarbonatite tephra of Kerimasi volcano, Tanzania. *Geology*, 11, 599–602.
- Jones, J. H., Walker, D., Pickett, D. A., Murrell, M. T., and Beattie, P. (1995). Experimental investigations of the partitioning of Nb, Mo, Ba, Ce, Pb, Ra, Th, Pa, and U between immiscible carbonate and silicate liquids. *Geochim. Cosmochim. Acta*, 59(7), 1307–1320.
- Keller, J., Klaudius, J., Kervyn, M., Ernst, G. G. J., and Mattsson, H. B. (2010). Fundamental changes in the activity of the natrocarbonatite volcano Oldoinyo Lengai, Tanzania. I. New magma composition. *Bull. Volcanol.*, 72, 893–912.
- Keller, J. and Krafft, M. (1990). Effusive natrocarbonatite activity at Oldoinyo Lengai, June 1988. *Bull. Volcanol.*, 52, 629–645.
- Keller, J. and Zaitsev, A. N. (2006). Calciocarbonatitic dykes at Oldoinyo Lengai, Tanzania: the fate of natrocarbonatite. *Can. Mineral.*, 44, 857–876.
- Keller, J. and Zaitsev, A. N. (2012). Reprint of “Geochemistry and petrogenetic significance of natrocarbonatites at Oldoinyo Lengai, Tanzania: Composition of lavas from 1988 to 2007”. *Lithos*, 148, 45–53.
- Kervyn, M., Ernst, G. G. J., Keller, J., Vaughan, G., Klaudius, J., Pradal, E., Belton, F., Mattsson, H., Mbede, E., and Jacobs, P. (2010). Fundamental changes in the activity of the natrocarbonatite volcano Oldoinyo Lengai, Tanzania. II. Eruptive behaviour. *Bull. Volcanol.*, 72, 913–931.
- Kervyn, M., Klaudius, J., Keller, J., Mbede, E., Jacobs, P., and Ernst, G. G. J. (2008). Remote sensing study of sector collapses and debris avalanche deposits at Oldoinyo Lengai and Kerimasi volcanoes, Tanzania. *Int. J. Rem. Sens.*, 29, 6565–6595.
- Kjarsgaard, B. and Peterson, T. (1991). Nephelinite-carbonatite liquid immiscibility at Shombole volcano, East Africa: petrographic and experimental evidence. *Mineral. Petrol.*, 43(4), 293–314.
- Kjarsgaard, B. A. (1998). Phase relations of a carbonated high-CaO nephelinite at 0.2 and 0.5 GPa. *J. Petrol.*, 39(11–12), 2061–2075.
- Kjarsgaard, B. A., Hamilton, D. L., and Peterson, T. D. (1995). Peralkaline nephelinite/carbonatite liquid immiscibility: Comparison of phase compositions in experiments and natural lavas from Oldoinyo Lengai. In Bell, K. and Keller, J., editors, *Carbonatite Volcanism. IAVCEI Proceedings in Volcanology*, volume 4, pages 163–190. Springer, Berlin, Heidelberg.
- Klaudius, J. and Keller, J. (2006). Peralkaline silicate lavas at Oldoinyo Lengai, Tanzania. *Lithos*, 91, 173–190.
- Kogarko, L. N., Plant, D. A., Henderson, C. M. B., and Kjarsgaard, B. A. (1991). Na-rich carbonate inclusions in perovskite and calzirtite from the Guli intrusive Ca-carbonatite, polar Siberia. *Contrib. Mineral. Petrol.*, 109(1), 124–129.

- Le Bas, M. J., Mills, A. A., and Rankin, A. H. (1972). Preliminary evidence on the nature and composition of carbonatite magma. *Nature*, 239, 215.
- Le Maitre, R. W., Bateman, P., Dudek, A., Keller, J., Lameyre, J., Le Bas, M. J., Sabine, P. A., Schmid, R., Sorensen, H., Streckeisen, A., Woolley, A. R., and Zanettin, B. (1989). *A Classification of Igneous Rocks and Glossary of Terms*. Blackwell Scientific Oxford Bibliografia. pages 130–171.
- Ling, M. X., Liu, Y. L., Williams, I. S., Teng, F. Z., Yang, X. Y., Ding, X., Wei, G. J., Xie, L. H., Deng, W. F., and Sun, W. D. (2013). Formation of the world's largest REE deposit through protracted fluxing of carbonatite by subduction-derived fluids. *Sci. Rep.*, 3, article no. 1776.
- Martin, L. H. J., Schmidt, M. W., Mattsson, H. B., and Guenther, D. (2013). Element partitioning between immiscible carbonatite and silicate melts for dry and H₂O-bearing systems at 1–3 GPa. *J. Petrol.*, 54(11), 2301–2338.
- Masotta, M., Mollo, S., Freda, C., Gaeta, M., and Moore, G. (2013). Clinopyroxene–liquid thermometers and barometers specific to alkaline differentiated magmas. *Contrib. Mineral. Petrol.*, 166(6), 1545–1561.
- Mitchell, R. H. (2009). Peralkaline nephelinite–natrocarbonatite immiscibility and carbonatite assimilation at Oldoinyo Lengai, Tanzania. *Contrib. Mineral. Petrol.*, 158, 589–598.
- Mollex, G. (2017). *Architecture de la plomberie du volcan carbonatitique Oldoinyo Lengai: nouvelles contraintes sur la source, les transferts hydrothermaux, et la différenciation magmatique dans la chambre active*. PhD thesis, Université de Lorraine.
- Mollex, G., Füre, E., Burnard, P., Zimmermann, L., Chazot, G., Kazimoto, E. O., Marty, B., and France, L. (2018). Tracing helium isotope compositions from mantle source to fumaroles at Oldoinyo Lengai volcano, Tanzania. *Chem. Geol.*, 480, 66–74.
- Nabyl, Z., Massuyeau, M., Gaillard, F., Tuduri, J., Iacono-Marziano, G., Rogerie, G., Le Trong, E., Di Carlo, I., Melleton, J., and Bailly, L. (2020). A window in the course of alkaline magma differentiation conducive to immiscible REE-rich carbonatites. *Geochim. Cosmochim. Acta*, 282, 297–323.
- Peterson, T. D. (1989). Peralkaline nephelinites II. Low pressure fractionation and the hypersodic lavas of Oldoinyo L'engai. *Contrib. Mineral. Petrol.*, 102, 336–346.
- Pouchou, J. L. and Pichoir, F. (1991). Quantitative analysis of homogeneous or stratified microvolumes applying the model “PAP”. In Heinrich, K. F. J. and Newbury, D. E., editors, *Electron Probe Quantification*, pages 31–75. Plenum, New York.
- Rose-Koga, E., Bouvier, A.-S., Gaetani, G., Wallace, P. J., Allison, C. M., Andrys, J. A., et al. (2021). Silicate melt inclusions in the new millennium: a review of recommended practices for preparation, analysis, and data presentation. *Chem. Geol.*, 570, article no. 120145.
- Schmidt, M. W. and Weidendorfer, D. (2018). Carbonatites in oceanic hotspots. *Geology*, 46, 435–438.
- Sharygin, V. V., Kamenetsky, V. S., Zaitsev, A. N., and Kamenetsky, M. B. (2012). Silicate–natrocarbonatite liquid immiscibility in 1917 eruption combeite–wollastonite nephelinite Oldoinyo Lengai Volcano Tanzania: melt inclusion study. *Lithos*, 152, 23–39.
- Sherrod, D. R., Magigita, M. M., and Kwelwa, S. (2013). Geologic map of Oldoinyo Lengai (Oldoinyo Lengai) and surroundings, Arusha Region, United Republic of Tanzania. U. S. Geological Survey Open-File Report No. 2013-1306.
- Uhlig, C. (1905). Bericht über die Expedition der Otto-Winter-Stiftung nach den Umgebungen des Meru. *Zeitschrift der Gesellschaft für Erdkunde zu Berlin*, 1905, 120–123.
- Veksler, I. V., Dorfman, A. M., Dulski, P., Kamenetsky, V. S., Danyushevsky, L. V., Jeffries, T., and Dingwell, D. B. (2012). Partitioning of elements between silicate melt and immiscible fluoride, chloride, carbonate, phosphate and sulfate melts, with implications to the origin of natrocarbonatite. *Geochim. Cosmochim. Acta*, 79, 20–40.
- Veksler, I. V., Petibon, C., Jenner, G. A., Dorfman, A. M., and Dingwell, D. B. (1998). Trace element partitioning in immiscible silicate–carbonate liquid systems: an initial experimental study using a centrifuge autoclave. *J. Petrol.*, 39(11–12), 2095–2104.
- Verplanck, P. L., Van Gosen, B. S., Seal, R. R., and McCafferty, A. E. (2014). A deposit model for carbonatite and peralkaline intrusion-related rare earth element deposits. In *Mineral Deposit Models for Resource Assessment*, page 58. U.S. Geological Survey.
- Weidendorfer, D., Schmidt, M. W., and Mattsson, H. B. (2016). Fractional crystallization of Si-undersaturated alkaline magmas leading to un-

- mixing of carbonatites on Brava Island (Cape Verde) and a general model of carbonatite genesis in alkaline magma suites. *Contrib. Mineral. Petrol.*, 171, article no. 43.
- Weidendorfer, D., Schmidt, M. W., and Mattsson, H. B. (2017). A common origin of carbonatite magmas. *Geology*, 45(6), 507–510.
- Woolley, A. R. and Kjarsgaard, B. A. (2008). *Carbonatite occurrences of the world: map and database*. Natural Resources Canada. Geological Survey of Canada, Open File 5796, 28 pages (1 sheet).
- Zaitsev, A. N. and Keller, J. (2006). Mineralogical and chemical transformation of Oldoinyo Lengai natrocarbonatites, Tanzania. *Lithos*, 91, 191–207.



Perspectives on alkaline magmas / *Perspectives sur les magmas alcalins*

Experimental determination of H₂O and CO₂ solubilities of mafic alkaline magmas from Canary Islands

María Jiménez-Mejías^{*, a, b, c, d}, Joan Andújar^a, Bruno Scaillet^a
and Ramón Casillas^d

^a Institut des Sciences de la Terre d'Orléans (ISTO), UMR 7327, Université d'Orléans, CNRS, BRGM, 1A rue de la Férollerie, F-45071 Orléans, France

^b Geosciences Barcelona (GEO3BCN-CSIC), C/Lluís Solé i Sabarís s/n, 08028, Barcelona, Spain

^c Instituto Geográfico Nacional, Centro Geofísico de Canarias, C/ La Marina 20, 2°, 38001 Santa Cruz de Tenerife, Spain

^d Departamento de Biología Animal, Edafología y Geología. Facultad de Ciencias. Universidad de La Laguna. C/Astrofísico Francisco Sánchez S/N. 38206. La Laguna, Santa Cruz de Tenerife, Spain

E-mails: maria.jimenez@cnrs-orleans.fr (M. Jiménez-Mejías),
juan.andujar@cnrs-orleans.fr (J. Andújar), bruno.scaillet@cnrs-orleans.fr (B. Scaillet),
rcasilla@ull.es (R. Casillas)

Abstract. We present new H₂O and CO₂ solubility data in mafic to intermediate alkaline magmas from Fasnía and Garachico volcanoes, Tenerife. H₂O- and CO₂-saturated experiments were conducted at ~50–400 MPa, 1200 °C, and *f*O₂ from 2 log units below the NiNiO solid buffer to 3.2 log units above it. Although existing solubility models for alkali-rich mafic magmas broadly describe H₂O and CO₂ behaviour, associated errors are worthy of consideration since they usually exceed 15–20%. For this reason, we have determined the specific solubility laws of basanitic and phonotephritic melts from the Canary Islands. Results show similar H₂O solubilities for both compositions, whereas the basanite can dissolve an average of ~45% more CO₂ than the phonotephrite. By combining these data, we have established a simple empirical model that allows us to calculate melt inclusion entrapment pressures accurately and, therefore, better understand the inner workings of volcanic oceanic islands. Application to El Hierro 2011–2012 and young (<20 ka) basanites from this location shows that previous barometric estimates were, on average, overestimated by 15–28%. Our results suggest that magmas rising from depth experienced a first but short episode of equilibration at 8–10 km, whereas the bulk of the crystallization occurred during the subsequent dyke injection, ascent, and degassing at *P* < 200 MPa (6–1.5 km).

Keywords. H₂O, CO₂, Solubility, Canary Islands, Alkaline magmas, Melt inclusions, El Hierro.
Available online 5th November 2021

* Corresponding author.

1. Introduction

Understanding magmatic volatiles behaviour in terms of the maximum amount that can be dissolved in a silicate melt under a given set of conditions (pressure, temperature, melt composition, and redox state) is crucial for improving the knowledge of magmatic processes and degassing mechanisms involved in volcanic eruptions [Moore, 2008, Moore and Carmichael, 1998, Oppenheimer *et al.*, 2014].

Among other species (CO_2 , S, F, and Cl), water is the most abundant volatile phase in magmas on Earth, exerting an important control on their physical and rheological properties [i.e., density, viscosity; Andújar and Scaillet, 2012a, Giordano *et al.*, 2008, Stolper, 1982a] and phase equilibria [Andújar *et al.*, 2015, 2017, Scaillet and Evans, 1999, Scaillet *et al.*, 2008]. The amount of volatiles along with the level, rate, and efficiency of the exsolution process (especially for H_2O) during magma ascent, largely control the explosive–effusive style of an eruption [Andújar and Scaillet, 2012b, Burnham, 1979, Sparks, 1978]. Therefore, understanding the mechanisms that control the solubility of the different volatile species dissolved in magmas is crucial to decipher surface gas signals, changes in the eruptive dynamic, and correctly interpretate melt inclusion (MI) data.

For this reason, the solubility of H_2O and CO_2 and their speciation in melts have been the focus of numerous experimental studies, which have explored the dissolution behaviour of pure H_2O [e.g., Carroll and Blank, 1997, Lesne *et al.*, 2011a, Moore *et al.*, 1998, Mysen and Cody, 2004, Schmidt and Behrens, 2008, Stolper, 1982a,b], pure CO_2 [e.g., Brooker *et al.*, 2001a,b, Dixon and Pan, 1995, Jendrzewski *et al.*, 1997, Lesne *et al.*, 2011b, Moore *et al.*, 2000, Mysen *et al.*, 1975, Pan *et al.*, 1991], and mixed H_2O – CO_2 fluids [e.g., Allison *et al.*, 2019, Botcharnikov *et al.*, 2005, Dixon *et al.*, 1995, Dixon and Stolper, 1995, Iacono-Marziano *et al.*, 2012, Iacovino *et al.*, 2013, Moussallam *et al.*, 2016, Newman and Lowenstern, 2002, Schanowski *et al.*, 2019, Shishkina *et al.*, 2010, 2014, Tamic *et al.*, 2001, Vetere *et al.*, 2014] over a large range of melt compositions and experimental P – T conditions.

Pioneering works [e.g., Burnham and Jahns, 1962, Goranson, 1931, 1936] already pointed out the strong dependence of water solubility on pressure, melt composition, and to a lesser degree, temperature.

Theoretical considerations and spectroscopic studies show that water dissolves in silicate melts either as hydroxyl (OH^-) groups [e.g., Burnham, 1975, Burnham and Davis, 1971, 1974] or H_2O molecules [e.g., Carroll and Blank, 1997, McMillan and Remele, 1986, Mysen and Virgo, 1986a,b, Newman *et al.*, 1986, Stolper, 1982a,b], and their relative proportion varying significantly with total water content. At low H_2O concentrations (<1 wt%), the hydroxyl species predominates while at high $\text{H}_2\text{O}_{\text{total}}$, molecular water dominates [e.g., Silver *et al.*, 1990, Stolper, 1982a,b]. The CO_2 solubility is also highly dependent on pressure and composition but compared to H_2O , magmas can incorporate relatively low amounts of carbon under the same P – T conditions. The difference in solubility gives rise to the exsolution of a CO_2 -rich fluid at very initial stages of magma ascent, which gets enriched in water as decompression proceeds, in particular during the very last steps of ascent [e.g., Dixon *et al.*, 1995, Dixon and Stolper, 1995, Edmonds and Wallace, 2017]. Consequently, CO_2 plays an important role in generating vapour-saturation conditions at crustal pressures with strong implications on eruption triggers and changes in the eruptive dynamic [e.g., Anderson, 1975, Newman and Lowenstern, 2002, Pichavant *et al.*, 2013].

The dependence of CO_2 solubility with magma composition is commonly described as a function of the NBO/T parameter (average number of nonbridging oxygens per tetrahedrally coordinated cation), which is considered as a proxy for the degree of (de)polymerization of a silicate melt [e.g., Mysen *et al.*, 1982, Mysen, 1990, 1991]. The increase of NBO/T species in the melt enhances CO_2 solubility [e.g., Brooker *et al.*, 2001a,b, Iacono-Marziano *et al.*, 2012]. However, this parameter alone cannot fully capture the details of CO_2 solubility behaviour observed in magmas of broadly similar compositions. In particular, CaO and K_2O contents also play an important role in enhancing CO_2 solubility in magmas [e.g., Behrens *et al.*, 2009, Dixon, 1997, Lesne *et al.*, 2011b, Moore, 2008, Scaillet and Pichavant, 2005, Vetere *et al.*, 2014].

Despite all the existing H_2O and/or CO_2 solubility models, associated errors generally exceed 15–20%, translating into differences of ± 1 –2 wt% H_2O and ± 1000 –2000 CO_2 ppm at ≥ 300 MPa, namely up to ± 6 km in depth. Such uncertainties have a significant impact on the estimates of the saturation and entrap-

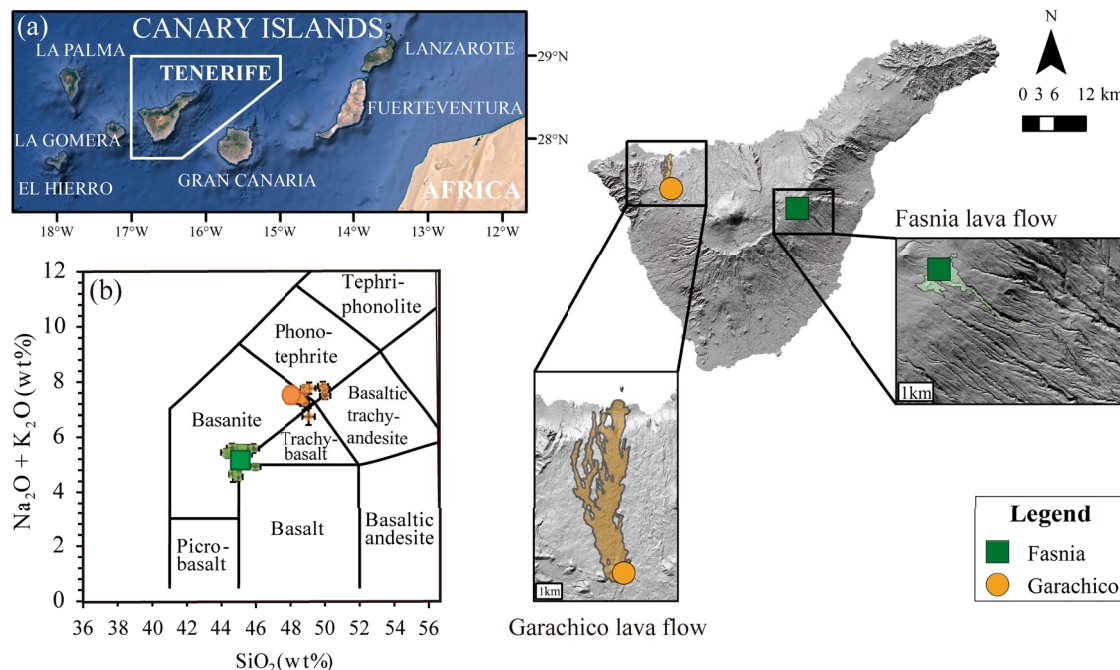


Figure 1. (a) Geographic location of Canary Islands. Digital elevation model of Tenerife, showing the location of the two historical monogenetic eruptions of Fasnía (in green) and Garachico (in orange) and their sampling points (green square and orange circle, respectively). (b) Classification of the starting experimental glasses based on the total alkalis versus silica diagram [TAS, Le Bas *et al.*, 1986]. The large dark green square and orange circle represent the starting compositions of Fasnía (basanite) and Garachico (phonotephrite), respectively. The smaller light green squares (Fasnía) and orange circles (Garachico) correspond to experimental run products. Each symbol represents the average of 10–15 single EPMA analyses.

ment pressures of magmas and melt inclusions, and consequently, on the interpretation of storage conditions and degassing processes. Thus, in order to obtain the most accurate barometric information on magmas and related degassing processes, it is imperative to determine solubility laws for the most abundant species (H_2O – CO_2) adapted to the magma composition emitted by each volcanic system.

Here we report the results of water and carbon dioxide solubility experiments performed on basanitic and phonotephritic magmas from Tenerife (Canary Islands, Figure 1) at 1200 °C and pressures ranging from 50 to 400 MPa. Concentrations of molecular water (H_2O), hydroxyl groups (^-OH), and carbonate ion complexes (CO^{3-}) of quenched glasses were measured by Fourier Transform Infrared Spectroscopy (FTIR) on glasses drop-quenched at high pressures. Two other complementary and independent techniques, Nanoscale Secondary Ion Mass

Spectrometry (NanoSIMS) and Elemental Analyzer (EA) were used, when possible, to complement FTIR results.

These concentrations were subsequently used to establish empirical H_2O and CO_2 solubility models specifically calibrated for the mafic–intermediate alkaline compositions from the Canary Islands, allowing us to calculate, first, the H_2O and CO_2 fugacities and partial pressures and, second, to re-evaluate volatile entrapment conditions recorded by melt inclusions from different eruptions of El Hierro, including the 2011–2012 event [Longpré *et al.*, 2014, 2017, Taracsák *et al.*, 2019].

2. Experimental and analytical techniques

Solubility experiments and the characterization of run products were performed using established procedures which are detailed in Supplementary

Material. In short, experiments were performed in internally heated pressure vessels equipped with a drop quench set-up and allowing redox conditions to be controlled. Run products were characterized by EPMA (Electron Probe Micro-Analysis), SEM (Scanning Electron Microscopy), FTIR, NanoSIMS (Nanoscale Secondary Ion Mass Spectrometry), and EA (Elemental Analyzer) techniques.

3. Results

3.1. Major element compositions and Fe-loss in experimental charges

The major element compositions of our experimental glasses are presented in Table S1 after recalculation to a 100% anhydrous basis. Almost all of our supra-liquidus melts are crystal-free and compositionally homogeneous, as indicated by the low standard deviations obtained (often ≤ 0.4 wt%), closely matching (within analytical errors) the starting material composition (Table 1). It should be noted that some samples (e.g., F3a, F4a and G3a) show slightly higher silica and lower iron contents than the starting composition (Table 1) due to some iron-loss towards the capsule [e.g., Grove, 1982, Hall *et al.*, 2004, Kawamoto and Hirose, 1994] or the crystallization of small Fe-oxides. The apparent loss or gain of FeO (all iron as FeO) was calculated as follows: for crystal-free charges and those containing a low amount of quench crystals (Table 2), the Fe-loss was estimated considering the iron content of experimental glasses (FeO_{gl}) relative to such the starting material (FeO_{st}) following the expression: $100 \cdot \text{FeO}_{\text{gl}} / \text{FeO}_{\text{st}}$; for the three oxide-bearing charges G3a, F3a, and F4a, we performed least-square mass balance calculations to retrieve the phase proportions and iron-loss, considering the corresponding oxide and residual glass compositions. Overall, in CO_2 and H_2O -saturated experiments, approximately 80 to 100% of the iron was kept in the melt, except for FC4b, GC05, GC3b, and GC4b, in which the loss reaches 22–25%. Despite that the SEM inspection of these four charges did not reveal the presence of mineral phases within the glasses, we cannot rule out the possibility of an occasional crystallization of Fe–Ti oxides non-detectable by SEM (< 0.5 μm in size), which could explain such slightly higher iron-loss. Glasses from G3a, F3a, and F4a charges have lower iron contents compared to the starting material, owing to the crystallization of

different proportions of Fe–Ti oxides which depleted the residual melt in FeO (Table 2).

3.2. H_2O concentrations

As stated above, the water contents of our experimental glasses were analysed by FTIR and EA whenever possible. The comparison of the results shows that the retrieved H_2O concentrations agree to less than 0.3 wt% H_2O , even considering the associated analytical errors (Table 2) and are consistent with the measured $^{16}\text{OH}^- / ^{28}\text{Si}^-$ ratio by the NanoSIMS. Given the similarities between the data, in the following we use the H_2O contents obtained with FTIR.

For both compositions, the general trend is to increase the amount of dissolved water with pressure, from ~ 2.3 wt% at 50 MPa up to 7.6 wt% at 400 MPa (Figure 2). In this case, the differences in composition of the studied materials (2–3.5 wt% in major oxides; Table 1) or imposed $f\text{O}_2$ do not have any significant effects on water solubility. Based on the observed relationships, we have mathematically regressed the H_2O content- P dependence according to expressions of the form $\text{H}_2\text{O}_{\text{melt}}$ (wt%) = $a \cdot P^b$ (P in MPa) obtaining the equations shown in Figure 2. These expressions back-calculate analysed water contents to within $\sim 2\%$.

3.2.1. Determination of H_2O fugacities

For any volatile species dissolved in a silicate melt that is fluid-saturated, the condition of equilibrium requires that the fugacity (f) of each species (i) in the melt equals that of the fluid, i.e., for water: $f\text{H}_2\text{O}_{\text{melt}} = f\text{H}_2\text{O}_{\text{fluid}}$. At very low pressures (1 bar) and high temperatures (> 600 °C), the fugacity of a pure gas is well described by the ideal gas law. However, as pressure increases, departure from ideality occurs, which is described by the fugacity coefficient, Φ_i . For a pure fluid (i.e., one species i), the relationship is

$$\Phi_i = f_i / P_{\text{tot}}, \quad (1)$$

where P_{tot} is total pressure (in bars).

In mixed fluids, the total pressure is replaced by the partial pressure (P_i):

$$P_i = f_i / \Phi_i \quad (2)$$

With the constraint that:

$$P_{\text{tot}} = \sum P_i$$

So, assuming that H_2O and CO_2 are the main volatile species present in the melt, we obtain the

Table 1. Starting compositions (wt%)

Composition Sample	Basanite FAS ^a	Phonotephrite GCH ^a	Basanite Fasn ^b	Phonotephrite Garachico ^b
SiO ₂	45.08 <i>0.14</i>	48.06 <i>0.37</i>	44.46	48.56
TiO ₂	3.82 <i>0.13</i>	3.15 <i>0.15</i>	3.71	3.09
Al ₂ O ₃	14.45 <i>0.17</i>	17.77 <i>0.20</i>	15.01	17.47
FeO ^c	12.51 <i>0.27</i>	9.43 <i>0.37</i>	12.12	9.32
MnO	0.28 <i>0.05</i>	0.19 <i>0.07</i>	0.19	0.20
MgO	7.16 <i>0.22</i>	3.98 <i>0.09</i>	7.71	4.05
CaO	10.82 <i>0.17</i>	8.42 <i>0.14</i>	10.68	8.80
Na ₂ O	3.60 <i>0.10</i>	5.34 <i>0.09</i>	3.83	5.40
K ₂ O	1.57 <i>0.07</i>	2.19 <i>0.10</i>	1.54	2.21
P ₂ O ₅	0.71 <i>0.07</i>	1.25 <i>0.16</i>	0.76	1.25
Na ₂ O + K ₂ O	5.17	7.53	5.37	7.61
LOI			−0.55	−0.34
Total	100	100	100	100

Compositions normalized to 100% anhydrous melt.

^aOxide concentrations were measured by EPMA at ISTO-CNRS.

Standard deviations are italicized.

^bOxide concentrations determined by XRF analyses at CRPG-Nancy, France, for comparison.

^cTotal iron expressed as FeO.

following equations:

$$P_{\text{H}_2\text{O}} = f_{\text{H}_2\text{O}} / \Phi_{\text{H}_2\text{O}} \quad (3)$$

$$P_{\text{CO}_2} = f_{\text{CO}_2} / \Phi_{\text{CO}_2} \quad (4)$$

Therefore, since according to our FTIR, NanoSIMS and EA results, all charges devoted to study water solubility in melts are CO₂-free (Table 2), the fugacity coefficient of pure H₂O can be calculated at the corresponding *P* and *T* using the modified Redlich–Kwong equation of state [Holloway, 1977]. Then, the *f*H₂O at given *P*–*T* of each charge is computed using

the expression

$$f_{\text{H}_2\text{O}} = \Phi_{\text{H}_2\text{O}} * X_{\text{H}_2\text{O}} * P_{\text{tot}}, \quad (5)$$

where *X*_{H₂O} is the mole fraction of water in the fluid. Since in H₂O-saturated experiments, the *X*_{H₂O} is equal to one, the previous relationship can be transformed to

$$X_{\text{H}_2\text{O}} = \frac{f_{\text{H}_2\text{O}}}{\Phi_{\text{H}_2\text{O}} * P_{\text{tot}}} \rightarrow X_{\text{H}_2\text{O}} = 1 \rightarrow f_{\text{H}_2\text{O}} = \Phi_{\text{H}_2\text{O}} * P_{\text{tot}} \quad (6)$$

*P*_{tot} (in bars).

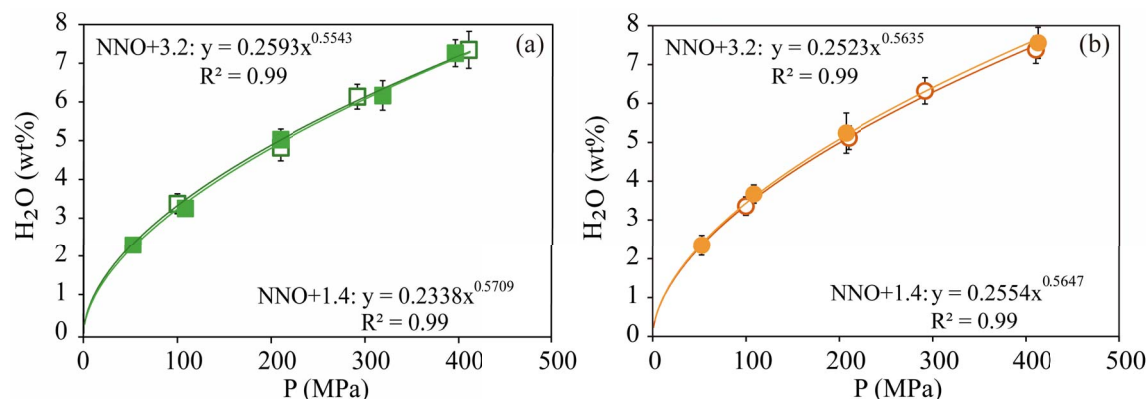


Figure 2. Dissolved water contents in experimental glasses plotted as a function of pressure for (a) Fasnía basanite (green squares) and (b) Garachico phonotephrite (orange circles). The filled and empty symbols represent experiments performed at NNO + 1.4 and NNO + 3.2, respectively.

The calculated fugacities and the determined water contents were then regressed using power-law equations that allowed a close fit between both parameters ($R^2 = 0.99$) (Figure 3), yielding for each case the following equations:

$$f_{\text{H}_2\text{O}}^{1200\text{ }^\circ\text{C}} = 10.6616 * (\text{wt\% H}_2\text{O})^{1.8774}$$

$$R^2 = 0.99 \quad \text{for Fasnía at NNO} + 3.2 \quad (7)$$

$$f_{\text{H}_2\text{O}}^{1200\text{ }^\circ\text{C}} = 11.5813 * (\text{wt\% H}_2\text{O})^{1.8407}$$

$$R^2 = 0.99 \quad \text{for Fasnía at NNO} + 1.4 \quad (8)$$

$$f_{\text{H}_2\text{O}}^{1200\text{ }^\circ\text{C}} = 10.3418 * (\text{wt\% H}_2\text{O})^{1.8693}$$

$$R^2 = 0.99 \quad \text{for Garachico at NNO} + 3.2 \quad (9)$$

$$f_{\text{H}_2\text{O}}^{1200\text{ }^\circ\text{C}} = 9.9808 * (\text{wt\% H}_2\text{O})^{1.8725}$$

$$R^2 = 0.99 \quad \text{for Garachico at NNO} + 1.4 \quad (10)$$

These empirical relationships allow us to calculate the water fugacities of basanitic and phonotephritic melts from Tenerife at different oxidation states considering the dissolved water contents in residual glasses or melt inclusions with an accuracy of 95%.

3.3. CO₂

The dissolved CO₂ contents that we present here correspond to those determined using the absorbances of the carbonate doublet ($\sim 1430\text{ cm}^{-1}$ and $\sim 1520\text{ cm}^{-1}$) in the mid-infrared (MIR) since no molecular CO₂ was detected in our experimental glasses [Blank and Brooker, 1994, Botcharnikov *et al.*, 2005, Dixon *et al.*, 1995].

CO₂ dissolved content gradually increases with pressure from 278–484 ppm at 50 MPa up to 3400–5800 ppm at 400 MPa for the phonotephrite and the basanite, respectively (Figure 4). Contrary to H₂O, our results define a negative relationship between CO₂ solubility and alkalinity since at a given P , the basanite dissolves up to 40–49% more CO₂ than its phonotephritic counterpart (Figure 5).

Even if no water was initially added to the CO₂-bearing charges (Table 3), all the run products contain variable amounts of H₂O, as evidenced in FTIR spectra (Figure S2c). H₂O contents of CO₂-bearing charges range from 0.18 up to 1.84 wt%, indicating that, despite our efforts, the experiments are not strictly CO₂ pure. The presence of water can be related to the following factors [e.g., Behrens *et al.*, 2009, Gaillard *et al.*, 2003, Holloway *et al.*, 1992, Lesne *et al.*, 2011b]:

- (1) The starting glass was synthesized at relatively oxidizing conditions compared to those imposed during experiments. The re-equilibration to the new f_{O_2} conditions generates H₂O following the bulk reaction $\text{Fe}_2\text{O}_3 + \text{H}_2 \leftrightarrow 2\text{FeO} + \text{H}_2\text{O}$. The H₂ source comes from the Ar + H₂ gas used to pressurize the vessel.
- (2) To a lesser extent, during capsule preparation, both the silver oxalate used as a CO₂ source and the starting glass can adsorb small but finite amounts of atmospheric water.

Table 2. Experimental results

Sample	<i>P</i> (MPa)	<i>T</i> ^a (°C)	Density (g/l) ^a	%FeO loss ^b	% Oxides ^c	<i>f</i> H ₂ O (MPa) ^d	<i>f</i> CO ₂ (MPa) ^d	XH ₂ O ^e	XCO ₂ ^e	ΦH ₂ O ^f	ΦCO ₂ ^f	ΔNNO ^g	Calculated log(<i>f</i> O ₂) ^g	wt% H ₂ O E _A ^h	wt% H ₂ O A3500 ⁱ	wt% H ₂ O A4500 ⁱ	wt% H ₂ O A5200 ⁱ	wt% H ₂ O 4500 + 5200 ⁱ	CO ₂ (ppm) Al430 ^j	Comments for run products
F05	52	1200	2748 28	0.93		52		1		0.99	1.13	1.40	-6.32	2.54 0.07	2.29					
F1a	100	1200	2669 83	14.34		99		1		0.99	1.26	3.18	-4.53			1.65	1.72	3.37	3.32	
F1c	108	1200	2750 22	1.24		107		1		0.99	1.29	1.44	-6.28			1.62	1.63	3.25	0.26	
F2a	210	1200	2626 65	14.68		213		1		1.02	1.70	3.25	-4.45	4.84 0.32	4.81	2.25	2.58	4.82	0.17	oxides
F2b	210	1200	2720 27	5.19		213		1		1.02	1.70	1.38	-6.32		5.05	2.06	2.97	5.03	0.35	
F3a	292	1200	2785 87	4.47*	6.6	308		1		1.05	2.27	3.18	-4.51	5.66 0.10	6.10	2.39	3.75	6.14	0.27	oxides
F3c2	319	1200	2727 31	4.88		341		1		1.07	2.51	1.34	-6.35		6.03	1.14	5.03	6.17	0.32	few quench crystals
F4a	411	1200	2690 61	4.53*	7.3	464		1		1.13	3.62	3.22	-4.44	6.90 0.29	7.20	1.28	6.06	7.35	0.38	oxides
F4b	397	1200	2737 36	5.50		444		1		1.12	3.42	1.20	-6.48	7.26 0.35	0.88			0.48		quench crystals
G05	52	1200	2661 30	-0.39		52		1		0.99	1.13	1.40	-6.32		2.35					
G1a	100	1200	2523 78	6.73		99		1		0.99	1.26	3.18	-4.53	3.48 0.60	3.45	1.71	1.65	3.36	0.25	few oxides
G1b	108	1200	2543 16	1.32		107		1		0.99	1.29	1.44	-6.28		3.71	1.98	1.69	3.67	0.40	
G2a	210	1200	2533 81	5.71		213		1		1.02	1.70	3.25	-4.45	5.15 0.05	4.92	2.57	2.55	5.12	0.23	few oxides
G2b	207	1200	2632 16	0.19		210		1		1.01	1.69	1.38	-6.32		5.36	2.09	3.14	5.24	0.30	
G3a	292	1200	2642 89	3.17*	3.9	308		1		1.05	2.27	3.18	-4.51	6.20 0.19	6.21	2.55	3.77	6.32	0.61	oxides
G4a	411	1200	2567 61	6.07		464		1		1.13	3.62	3.22	-4.44	7.45 0.08	7.31	2.75	4.64	7.38	0.34	oxides
G4b	413	1200	2551 27	-1.13		468		1		1.13	3.66	1.20	-6.48		1.05	1.38	6.18	7.56	0.35	few quench crystals
FC05	60	1200	2746 34	12.63		16	51	0.266	0.734	0.99	1.13	0.37	-7.35		1.19				484	
FC1c	113	1200	2787 33	15.93		24	116	0.214	0.786	0.99	1.26	0.14	-7.58		1.49				1205	
															0.12			0.40	35	55

(continued on next page)

Table 2. (continued)

Sample	<i>P</i> (MPa)	<i>T</i> ^a (°C)	Density (g/l) ^a	%FeO loss ^b	% Oxides ^c	<i>f</i> H ₂ O (MPa) ^d	<i>f</i> CO ₂ (MPa) ^d	XH ₂ O ^e	XCO ₂ ^e	ΦH ₂ O ^f	ΦCO ₂ ^f	ΔNNO ^g	Calculated log(<i>f</i> O ₂) ^g	wt% H ₂ O E.A. ^h	wt% H ₂ O A4500 ⁱ	wt% H ₂ O A5200 ⁱ	wt% H ₂ O 4500 + 5200 ⁱ	CO ₂ (ppm) Al430 ^j	Comments for run products
FC2b	210	1200	2748 23	20.33		31	306	0.145	0.855	1.02	1.70	-0.30	-8.00	1.70				2713	
FC3b	294	1200	2771 31	16.02		32	600	0.102	0.898	1.05	2.27	-0.73	-8.42	1.72				4209	
FC4b	397	1200	2779 19	22.55		35	1247	0.080	0.920	1.13	3.62	-1.00	-8.67	1.84				5748	few oxides
GC05	60	1200	2651 30	24.91		13	54	0.224	0.776	0.99	1.15	0.22	-7.50	1.17				278	
GC1a	102	1200	2669 49	-1.06		1	129	0.011	0.989	0.99	1.27	-0.52	-8.24	0.30				620	
GC2a	194	1200	2654 99	2.75		0	314	0.002	0.998	1.01	1.62	-1.89	-9.59	0.19				1291	few oxides
GC2b	207	1200	2638 33	13.51		16	324	0.074	0.926	1.01	1.69	-0.89	-8.59	1.27				1419	
GC3b	294	1200	2548 34	2.06		18	630	0.057	0.943	1.05	2.28	-1.24	-8.92	1.35				2166	
GC4a	399	1200	2586 124	13.20		1	1373	0.002	0.998	1.12	3.45	-2.16	-9.83	0.25				3046	few oxides
GC4b	413	1200	2555 27	24.46		22	1438	0.048	0.952	1.13	3.66	-1.40	-9.07	1.54				3356	
Volatile concentrations used to determine the solubility equations are listed in bold type. Numbers in italic: standard deviations.																			

^aDensity measured using Archimedes' method.

^bFe-loss estimated considering the iron content of experimental glasses (FeO_g) relative to such the starting material (FeO_{st}) following the expression: 100*FeO_g/FeO_{st}.

^cProportion of oxides calculated from least squares mass balance.

^dFugacities of pure water were calculated using a modified Redlich-Kwong equation of state [Holloway, 1977], assuming that $P_{H_2O} = P_{tot}$. Fugacities at given P - T calculated following the expression: $f_{H_2O} = \Phi_{H_2O} * X_{H_2O} * P_{tot}$. In CO₂ experiments, fugacities were calculated using (7)–(10). See Sections 3.2 and 3.3 for explanation.

^eMolar fraction of H₂O and CO₂ in fluid phase. See Section 3.2.1 for details.

^fFugacity coefficients of H₂O and CO₂ used for each experiment.

^gOxygen fugacity calculated from NiO–NiPd metallic sensors.

^hElemental analyzer measurements in H₂O-saturated experiments.

ⁱFTIR measurements.

^jFe-loss estimated after performing least-square mass balance calculations to retrieve the phase proportions and iron-loss considering the corresponding oxide and residual glass composition.

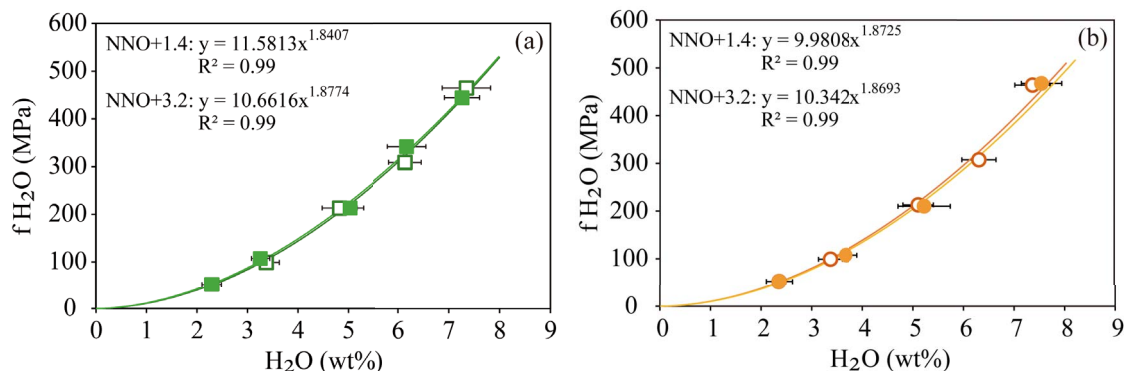


Figure 3. Relationship between water fugacity [calculated with the modified Redlich–Kwong equation of state, Holloway, 1977] and dissolved water in the basanitic (a) and phonotephritic (b) melts (in wt%). Curves represent power regressions of the data ($R^2 = 0.99$). The filled and empty symbols represent experiments performed at NNO + 1.4 and NNO + 3.2, respectively.

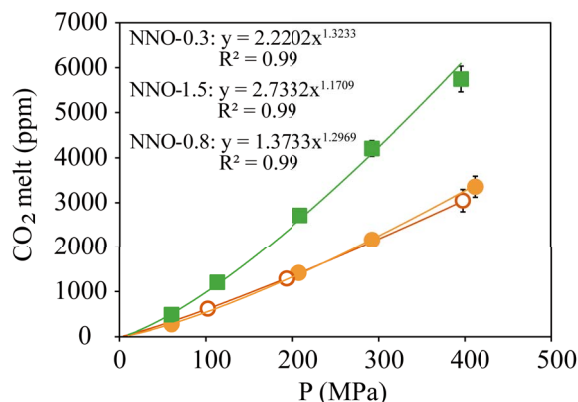


Figure 4. Dissolved CO_2 measured in the experimental glasses of the Fasnía basanite at NNO - 0.3 (green squares) and the Garachico phonotephrite at NNO - 0.8 (filled orange circles), and NNO - 1.5 (empty orange circles); for which obtained power regression laws are $CO_2 = 2.2202 \cdot P^{1.3233}$, $CO_2 = 1.3733 \cdot P^{1.2969}$ and $CO_2 = 2.7332 \cdot P^{1.1709}$, respectively.

The combination of these factors explains the higher water contents analysed in moderately reduced experiments ($f_{O_2} \sim NNO + 1.4$) compared to their oxidized counterparts (e.g., 1.54 wt% H_2O in GC4b and 0.24 wt% H_2O in GC4a, Table 2).

3.3.1. Determination of CO_2 fugacities

The presence of dissolved water in all the CO_2 experiments have allowed us to calculate their water fu-

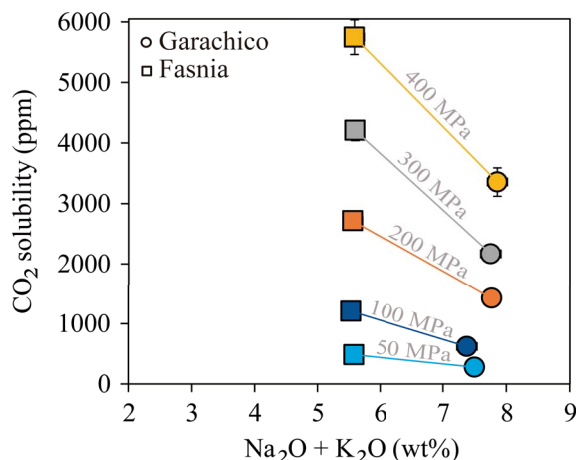


Figure 5. CO_2 solubility plotted as a function of the melt alkalinity showing a negative correlation for our compositions. Squares correspond to the basanitic melt and circles to the phonotephritic melt. Experimental pressures are represented with different colours: light blue (50 MPa), dark blue (100 MPa), orange (200 MPa), grey (300 MPa), and yellow (400 MPa).

gacity using the power-law regressions defined above for both compositions (7)–(10). To achieve this goal, we assume that the low CO_2 concentrations measured in our melts do not affect the thermodynamics of H_2O dissolution [e.g., Lesne *et al.*, 2011b].

Table 3. Details of experimental capsules

Name	<i>P</i> (MPa)	Mass H ₂ O (mg)	Mass Ag ₂ C ₂ O ₄ (mg)	Mass rock (mg)	Final mass of CO ₂ (mg)	<i>X</i> _{H₂O}	wt% H ₂ O ^a added	wt% CO ₂ ^b added
F1a	100	4.20	—	60.10	—	1.00	6.53	—
F2a	210	5.90	—	60.30	—	1.00	8.91	—
F3a	292	5.60	—	60.60	—	1.00	8.46	—
F4a	411	6.00	—	60.10	—	1.00	9.08	—
F05b	52	3.61	—	80.01	—	1.00	4.32	—
F1c	108	7.11	—	79.80	—	1.00	8.18	—
F2b	210	8.00	—	80.00	—	1.00	9.09	—
F3c2	319	5.60	—	79.90	—	1.00	6.55	—
F4b	397	8.20	—	80.10	—	1.00	9.29	—
G1a	100	4.20	—	60.00	—	1.00	6.54	—
G2a	210	6.00	—	60.10	—	1.00	9.08	—
G3a	292	6.00	—	60.00	—	1.00	9.09	—
G4a	411	6.00	—	60.00	—	1.00	9.09	—
G05	52	3.70	—	80.00	—	1.00	4.42	—
G1b	108	7.00	—	80.00	—	1.00	8.05	—
G2b	207	8.00	—	80.00	—	1.00	9.09	—
G4b	413	8.00	—	80.00	—	1.00	9.09	—
FC05	60	—	0.82	80.01	0.87	—	—	1.08
FC1	113	—	6.00	80.00	1.74	—	—	2.13
FC2	210	—	6.10	80.00	1.77	—	—	2.16
FC3	294	—	9.00	80.00	2.61	—	—	3.16
FC4	397	—	9.10	80.00	2.64	—	—	3.19
GC1a	102	—	5.00	60.00	1.45	—	—	2.36
GC2a	194	—	5.00	60.00	1.45	—	—	2.36
GC4a	399	—	8.10	60.00	2.35	—	—	3.76
GC05b	60	—	3.00	80.00	0.87	—	—	1.07
GC2b	207	—	6.00	80.00	1.74	—	—	2.13
GC3b	294	—	9.00	80.00	2.61	—	—	3.16
GC4b	413	—	8.10	60.00	2.35	—	—	3.76

All represent amounts of starting material, liquid H₂O, and silver oxalate (Ag₂C₂O₄) loaded into the capsule before experimental run.

Dashes indicate that no fluid was added to the capsule.

^aH₂O wt.% calculated as 100*(mass H₂O (mg)/mass H₂O (mg) + mass rock (mg) + Final mass CO₂ (mg)).

^bCO₂ wt.% calculated as 100*(final mass CO₂ (mg)/mass H₂O (mg) + mass rock (mg) + final mass CO₂ (mg)).

So, once the $f_{\text{H}_2\text{O}}$ of each charge and the fugacity coefficients derived from the Redlich–Kwong equation of state are obtained [Holloway, 1977], the corresponding water molar fraction ($X_{\text{H}_2\text{O}}$) can be determined by reorganizing (5):

$$X_{\text{H}_2\text{O}} = \frac{f_{\text{H}_2\text{O}}}{\Phi_{\text{H}_2\text{O}} * P_{\text{tot}}} \quad (11)$$

We assume an ideal mixing between real fluids (Lewis and Randall rule) rather than a real mixing since the latter has a minor effect on computed fugacity coefficients at our experimental conditions [≤ 400 MPa and 1200°C ; Holloway, 1977]. To calculate the molar fraction of CO_2 , we further assume that H_2O and CO_2 are the sole species present in the fluid phase [Holloway and Blank, 1994, Pawley *et al.*, 1992], so in this case

$$X_{\text{H}_2\text{O}} + X_{\text{CO}_2} = 1 \rightarrow X_{\text{CO}_2} = 1 - X_{\text{H}_2\text{O}} \quad (12)$$

Therefore, the CO_2 fugacity of each experiment at the given P – T conditions was determined as

$$f_{\text{CO}_2} = \Phi_{\text{CO}_2} * X_{\text{CO}_2} * P_{\text{tot}} \quad (13)$$

The CO_2 -contents- f_{CO_2} data base (up to 400 MPa) was used to derive third-order polynomial equations which provided the closest fit for the entire dataset ($R^2 = 0.99$; Figure 6):

$$\begin{aligned} f_{\text{CO}_2}^{1200^\circ\text{C}} &= 7.2170794265 \times 10^{-9} * \text{CO}_2 \text{ (ppm)}^3 \\ &\quad - 2.5187981515 \times 10^{-5} * \text{CO}_2 \text{ (ppm)}^2 \\ &\quad + 0.122917162244295 * \text{CO}_2 \text{ (ppm)} \\ R^2 &= 0.99 \quad \text{for Fasnía at NNO} - 0.3 \end{aligned} \quad (14)$$

$$\begin{aligned} f_{\text{CO}_2}^{1200^\circ\text{C}} &= 1.8778812876 \times 10^{-8} * \text{CO}_2 \text{ (ppm)}^3 \\ &\quad + 1.2729586197 \times 10^{-5} * \text{CO}_2 \text{ (ppm)}^2 \\ &\quad + 0.1744557037290380 * \text{CO}_2 \text{ (ppm)} \\ R^2 &= 0.99 \quad \text{for Garachico at NNO} - 0.8 \end{aligned} \quad (15)$$

$$\begin{aligned} f_{\text{CO}_2}^{1200^\circ\text{C}} &= 2.7077368969 \times 10^{-8} * \text{CO}_2 \text{ (ppm)}^3 \\ &\quad + 1.0456281240 \times 10^{-6} * \text{CO}_2 \text{ (ppm)}^2 \\ &\quad + 0.1963801023546240 * \text{CO}_2 \text{ (ppm)} \\ R^2 &= 0.99 \quad \text{for Garachico at NNO} - 1.5 \end{aligned} \quad (16)$$

It is important to note that the application of these equations (14)–(16) is restricted to melt compositions, water contents (0.18–2 wt%), and pressures (50–400 MPa) similar to those investigated here.

4. Discussion

Despite the frequent occurrence of alkaline magmas in specific volcanic settings (i.e., oceanic islands, in-

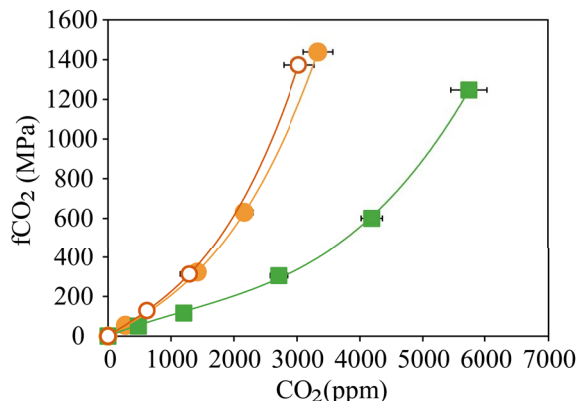


Figure 6. Relationship between the CO_2 fugacity of the Fasnía basanite at NNO – 0.3 (green squares) and the Garachico phonotephrite at NNO – 0.8 (empty orange circles) and NNO – 1.5 (filled orange circles), calculated with an MRK equation of state [Holloway, 1977], and the amount of CO_2 dissolved in the melts (in ppm). Curves represent third-order polynomial regressions of the data ($R^2 = 0.99$). See Section 3.3 for explanation.

traplate settings), H_2O solubility data of basanitic–phonotephritic melts are still scarce. Their calc-alkaline to mid-alkaline counterparts have been the focus of extensive research concerning volatile solubilities, from which various models allowing H_2O – CO_2 melt content to be calculated have been derived [e.g., Dixon, 1997, Iacono-Marziano *et al.*, 2012, Lesne *et al.*, 2011a,b, Papale *et al.*, 2006, Shishkina *et al.*, 2014, among others]. Whereas these works highlighted the relatively minor control exerted by composition on H_2O solubility in mafic melts at given P – T , this is not the case of CO_2 , for which variations in alkalinity, Fe-content, and oxidation state impact to various extents the solubilities of C-bearing species. For this reason, each model incorporates different compositional [i.e., Π , Π^* ; Dixon, 1997, Shishkina *et al.*, 2014 respectively] or structural parameters [i.e., NBO/O, NBO/T; Iacono-Marziano *et al.*, 2012, Vetere *et al.*, 2014 respectively] to take into account the compositional effect on their calculations. However, despite their seemingly universal character, the application of existing models to a given set of H_2O – CO_2 melt inclusion contents results in a non-negligible difference in the calculated

vapour-saturation conditions, differences between model outputs reaching in some cases ± 200 –400 MPa [equivalent to 6–12 km of depth, i.e., Longpré *et al.*, 2017]. Obviously, such an uncertainty strongly impacts our understanding of the architecture of the plumbing system of the volcano, hence the interpretation of related degassing processes. Below, the aforementioned models are applied to our experimental charges and calculated H_2O – CO_2 contents are compared to our measurements. Our aim is not to carry out an exhaustive comparison with all existing experimental works or solubility models since this has been already performed elsewhere [i.e., Iacono-Marziano *et al.*, 2012, Iacovino *et al.*, 2013, Ni and Keppler, 2013, Shishkina *et al.*, 2014] but merely to evaluate the applicability of available models in the Canarian context.

4.1. Comparison with H_2O experimental data

Overall, the water concentrations measured in this work are in good agreement (within errors) with those obtained on similar basanitic, alkali basalts or even mid-ocean ridge basalt (MORB) compositions at equivalent P – T conditions (Figure 7). For example, Shishkina *et al.* [2014] and Holloway and Blank [1994] [this last reporting data from Cocheo, 1993] present H_2O -saturated experiments performed on two basanites at 100 MPa and 1250 °C and 1200 °C, respectively, both containing ~ 3.2 wt% H_2O , an amount that closely matches those measured on our 100 MPa equivalent basanitic charges (3.3–3.4 wt% H_2O at 1200 °C; Table 2). Similarly, the study of Dixon *et al.* [1995] performed on a MORB at 50 MPa and 1200 °C reports water contents (2.2 wt% H_2O , experiment 21H) comparable to those from Fasnía basanite under the same P – T conditions (2.3 wt% H_2O).

Regarding our phonotephritic composition, Figure 7 shows that up to 300 MPa it displays a similar H_2O solubility compared to the K-rich phonotephritic lava from Mt. Mellone (Alban Hills, Italy) studied by Behrens *et al.* [2009] at 1200–1250 °C, and the alkali basalts from Lesne *et al.* [2011a] at 1200 °C. In contrast, our sample dissolves between 0.5 to 1 wt% less water above this pressure (>300 MPa) than the other two compositions. At first sight, the higher solubility displayed by the Behrens *et al.* [2009] phonotephrite above

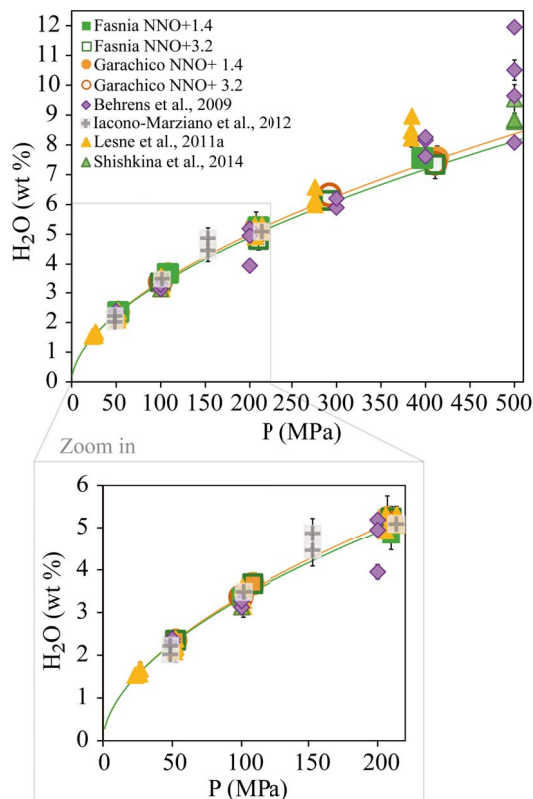


Figure 7. Comparison between the water contents measured in this study versus results of various other mafic to intermediate compositions at pressures from 50 MPa to 400 MPa (see Section 4.1 for explanation). Data at 500 MPa are shown for visualization. The *filled* and *empty orange circles* represent our Garachico experiments performed at NNO + 1.4 and NNO + 3.2, respectively. The *filled* and *empty green squares* correspond to Fasnía experiments performed under different $f\text{O}_2$ conditions (NNO + 1.4 and NNO + 3.2, respectively). The solubility curves of Fasnía (*green line*) and Garachico (*orange line*) at NNO + 3.2 are shown. H_2O -pure experimental results from other studies are represented as *violet diamonds* [Alb-1, Behrens *et al.*, 2009], *grey cross-square* [Etna, Iacono-Marziano *et al.*, 2012], *yellow triangles* [VES-9, ETN-1 and PST-9, Lesne *et al.*, 2011a], *green triangles* [A2549-basanite, OB93-alkali basalt, Etna and MORB, Shishkina *et al.*, 2014]. The wide range of the data comes from the different compositions used, or the $\text{H}_2\text{O}/\text{CO}_2$ ratios added initially in each study.

300 MPa can be explained by its alkali-rich character (9.5 wt% $K_2O + Na_2O$) compared to the Garachico phonotephrite (7.5 wt% $K_2O + Na_2O$), as suggested by Lesne *et al.* [2011a]. However, Lesne *et al.* [2011a] determined approximately the same water content as Behrens *et al.* [2009] (~8.3 wt%) at an almost equivalent pressure (384 MPa) for a tephrite which is compositionally equivalent (in terms of $Na_2O + K_2O$) to Garachico. Thus, in this case, the variations in the total alkali content of a melt cannot alone explain the different solubility trends observed above 300 MPa. In detail, the Tenerife and Vesuvius samples mostly differ by their K/Na ratios (3.1 for Ves-9 and 0.4 for Garachico), which suggests that the K-rich character of the Vesuvius compositions may be responsible for their enhanced water solubility above 300 MPa. We conclude that the total alkali content is not the sole parameter controlling water solubility, the K/Na ratio likely playing an important role on the amount of H_2O that can be incorporated into alkaline mafic melts. In summary, the lack of significant differences (>1 wt% H_2O) between the water contents measured on mafic to intermediate alkaline compositions, in this and equivalent studies, confirms the minor effect of magma composition on their H_2O solubility at crustal P (up to 300 MPa), in particular for a given magma family [i.e., basalts *sensu stricto*; Lesne *et al.*, 2011a, Shishkina *et al.*, 2014]. We cannot rule out the possibility that at higher pressures (≥ 400 –500 MPa), the effect of composition on water solubility is more significant [as in Benne and Behrens, 2003], but exploring volatile solubility at these conditions was beyond the scope of this study.

4.2. Application of available water-solubility models

Predicted H_2O contents by the aforementioned models are listed in Table S2. Overall, for the basanitic composition, there is a good concordance (considering associated errors) between predicted and measured water contents in the pressure range 50–100 MPa. Above these pressures, we observe a slight overestimate of ~10–15% at 200 MPa, rising to 20% as pressure increases from 300 MPa to 400 MPa.

Whereas for the previous composition, the predictions made by the three considered models progressively deviated from the experimental values, this

is not the case of the phonotephrite, where back-calculated H_2O contents and foretold solubility behaviour are strongly model-dependent. As for the basanite, the contents returned by the models of Lesne *et al.* [2011a] and Shishkina *et al.* [2014] at 50–100 MPa are in reasonable agreement with our measurements (Table S2). However, above these pressures, the two empirical equations proposed by these authors overestimate the measured values in our experimental melts; the maximum observed differences (1–2 wt%) were obtained at 300–400 MPa.

Conversely, the Iacono-Marziano *et al.* [2012] empirical equation systematically underestimates measured water contents by 0.5–1.2 wt% for the phonotephritic melt. In general, the three models better predict the solubility of water in basanitic melts (± 1 wt%) compared to phonotephritic compositions at conditions up to 300 MPa.

4.3. Comparison with other CO_2 or H_2O – CO_2 experimental studies

Only a few studies have explored in some detail the CO_2 solubility behaviour of basanites and phonotephrites at crustal P – T conditions [Behrens *et al.*, 2009, Holloway and Blank, 1994, Shishkina *et al.*, 2014, Allison *et al.*, 2019].

As previously mentioned, our results define a negative relationship between CO_2 solubility and alkalinity (Figure 5). This trend is in contrast with the results obtained in similar works, in which a positive relationship between alkalinity and dissolved CO_2 was observed [Lesne *et al.*, 2011b, Shishkina *et al.*, 2014]. A similar (but less apparent) relationship is observed between CO_2 content and the aluminium saturation and agpaite index, or NBO/O but, based on the poor correlation existing between the different parameters ($R^2 = 0.6$ in the first case and $R^2 < 0.5$ in the last two), we do not recommend their use for describing the CO_2 solubility in this type of magmas.

To a first order, the difference between previous works and our results can be related to the compositional variations of the starting materials used in each study, which in some cases exceeds 20% relative [i.e., $Na_2O + K_2O$, FeO; CaO; Behrens *et al.*, 2009, Dixon, 1997, Lesne *et al.*, 2011b, Moore, 2008, Vetere *et al.*, 2014]. These differences highlight again the strong control that magma composition exerts on CO_2 solubility, a factor that should be carefully considered

when applying H₂O–CO₂ solubility laws that were not specifically calibrated for the target composition.

From a more general perspective, we observe a good correspondence between the CO₂ contents measured in our basanite and that of Shishkina *et al.* [2014]; however, at 300 MPa, the basanite of Shishkina *et al.* [2014] incorporates up to 1300 ppm more than our starting material (Figure 8). In contrast, the basanite of Holloway and Blank [1994], systematically dissolves lower contents (~807 ppm CO₂ at 1200 °C and 100 MPa) compared to the two other basanites. The most significant difference between the three compositions is their CaO content: a positive relationship is indeed observed between CaO and the glass CO₂ contents.

The effect of magma composition in controlling CO₂ solubility is also seen for the phonotephrite: Behrens *et al.* [2009] identified K as an element that enhances CO₂ solubility [see also Scaillet and Pichavant, 2005]. At 200 MPa and 1200–1250 °C, their phonotephrite (with 5 wt% more K₂O) dissolves 2870 ppm CO₂ compared to 1291 ppm for Garachico (Table 2). However, the compositional difference between both phonotephrites is also due to CaO which, in the melt of Behrens *et al.* [2009], is ~3 wt% higher than in our sample. Thus, the combined effects of CaO and K₂O likely explain the differences in the CO₂ solubilities as already pointed out by previous studies [e.g., Behrens *et al.*, 2009, Botcharnikov *et al.*, 2006, Lesne *et al.*, 2011b, Liu *et al.*, 2005, Moore, 2008].

4.4. Application of available CO₂ or H₂O–CO₂ solubility models

For CO₂, we have tested three different models to verify their ability to reproduce the CO₂ contents of our experimental runs and hence, their applicability to the Canary Islands magmas (Table S2). The first model we checked is that of Dixon [1997], who, to calculate the CO₂ solubility in alkaline magmas, proposed an empirical equation that incorporates a compositional parameter (Π) to account for both the ability of the different network modifier elements to form carbonate species and the degree of melt depolymerization.

In Figure 9, we plot the factor Π of Dixon [1997] against the CO₂ concentrations analysed in our two compositions at the *P*–*T* conditions considered by

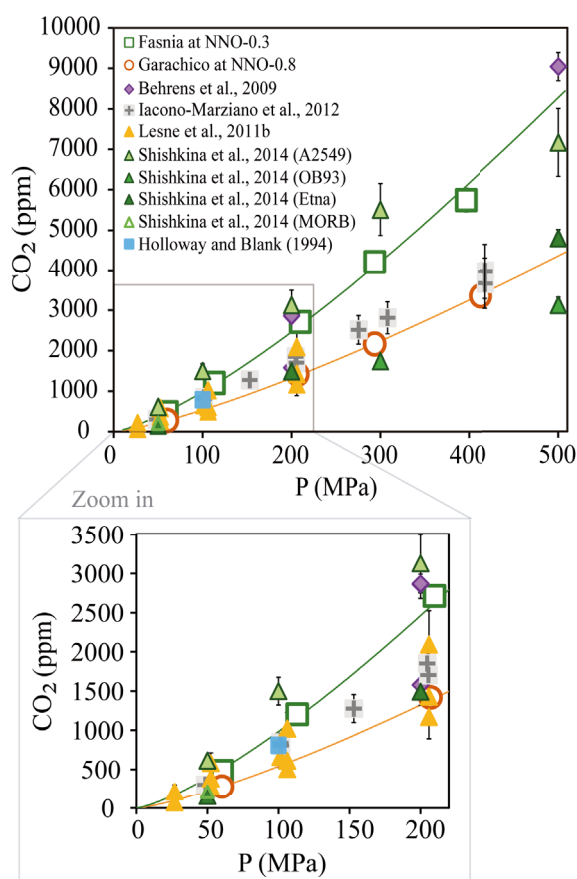


Figure 8. Comparison between the CO₂ contents measured in this study and the experimental results from other mafic to intermediate melts with no water added. The *empty orange circles* represent our phonotephritic composition at NNO – 0.8 and its solubility curve (*orange line*). The *empty green squares* correspond to the basanitic composition at NNO – 1.5 and its solubility curve (*green line*). Results from other studies correspond to *violet diamonds* [Alb-1, Behrens *et al.*, 2009], *grey cross-square* [Etna, Iacono-Marziano *et al.*, 2012], *yellow triangles* [VES-9, ETN-1 and PST-9, Lesne *et al.*, 2011a], *green triangles* [A2549-basanite, OB93-alkali basalt, Etna and MORB, Shishkina *et al.*, 2014] and *blue square* [basanite from Holloway and Blank, 1994]. The wide range of certain data comes from the different compositions used in those studies. See Sections 4.3 and 4.4 for more explanations.

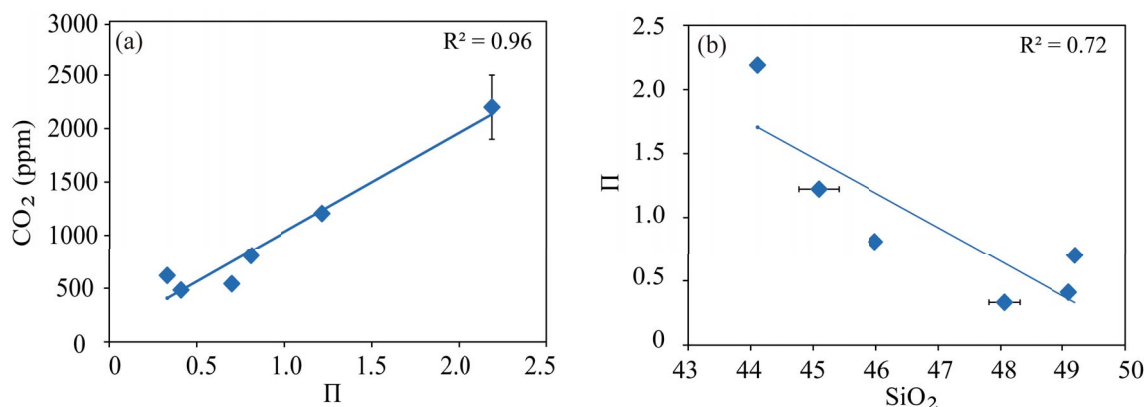


Figure 9. Correlation of the Π parameter [Dixon, 1997] with (a) the dissolved CO_2 contents measured in Fasnía, Garachico, and other mafic melts [MORB, Kilauea, basanite, and leucitite from Dixon, 1997] at 100 MPa and 1200°; and (b) the silica content of each composition.

this author, and we obtained a similar linear relationship between both parameters. However, this trend cannot explain the difference in the CO_2 concentrations calculated by Dixon's model for our basanitic and phonotephritic melts. Whereas for the former, the parameterization yields a content that closely matches the one measured here (1222 and 1205 ppm CO_2 , respectively), for Garachico phonotephrite, Dixon's model predicts a CO_2 content twice less the measured value (332 ppm CO_2 instead of 620 ppm CO_2 measured). To explain such a difference, we hypothesize that in our samples, the order of increasing ability of a cation to enhance CO_2 solubility may be different from that assumed by Dixon [1997] [$\text{Ca}^{2+} > \text{K}^+ > \text{Na}^+ \gg \text{Mg}^{2+} \approx \text{Fe}^{2+}$, according to Spera and Bergman, 1980]. Therefore, the role played by the different cations may vary depending on magma composition and P - T - $f\text{O}_2$ conditions. The other possibility is that the model of Dixon [1997] was calibrated using the data obtained on the basanite of Holloway and Blank [1994], which as stated before, dissolves less CO_2 than Fasnía basanite at the same P - T conditions (see above). However, the detailed study of cation effects on CO_2 solubility is beyond the scope of this work.

The second model considered here is the one of Shishkina *et al.* [2014], who explored the solubility of this gas species over a large range of magmatic compositions (42–51 SiO_2 wt%) and P - T conditions between 50–500 MPa and 1200 to 1250 °C. These authors derived a new equation to calculate the CO_2 content in magmatic melts (see this work for further

details), which incorporates an updated parameterization of the Π factor of Dixon [1997] termed Π^* since the former is derived from a narrower range of magma compositions (40–49 SiO_2 wt%) and requires normalization at 100 MPa. Therefore, Shishkina *et al.* [2014] fitted an exponential equation in terms of $\ln(\text{CO}_2)$ as a function of Π (or Π^*) and $\ln P$ to predict the CO_2 solubility over the explored range of compositions. Overall, this model predicts lower than observed CO_2 contents for the Fasnía basanite and Garachico phonotephrite, with differences achieving >20% above $P \geq$ at 200 MPa (Table S2).

Third, we have tested three variants of the Iacono-Marziano *et al.* [2012] model for our compositions at 1200 °C and pressures from 50 to 400 MPa: (1) CO_2 solubility model as a function of pressure (H_2O -free system), (2) H_2O - CO_2 solubility model that considers the composition of the fluid phase ($X_{\text{H}_2\text{O}}$), and (3) equilibrium pressures at 1200 °C for given H_2O and CO_2 contents in the melt. Model predictions were calculated using the web application of Iacono-Marziano *et al.* [2012] under the mentioned P - T conditions. Input uncertainties were: ± 5 °C, ± 20 bars and the standard deviation associated with the EPMA analysis of each major element oxides.

In the first case, the model underestimates the CO_2 solubility in the basanitic melt by 15–20%, the higher differences arising at 400 MPa. Contrarily, for the phonotephrite, the first variant of the model highly overestimates the CO_2 contents, exceeding 50% in some cases (Table S2). Similar variations are also observed in CO_2 contents calculated for the

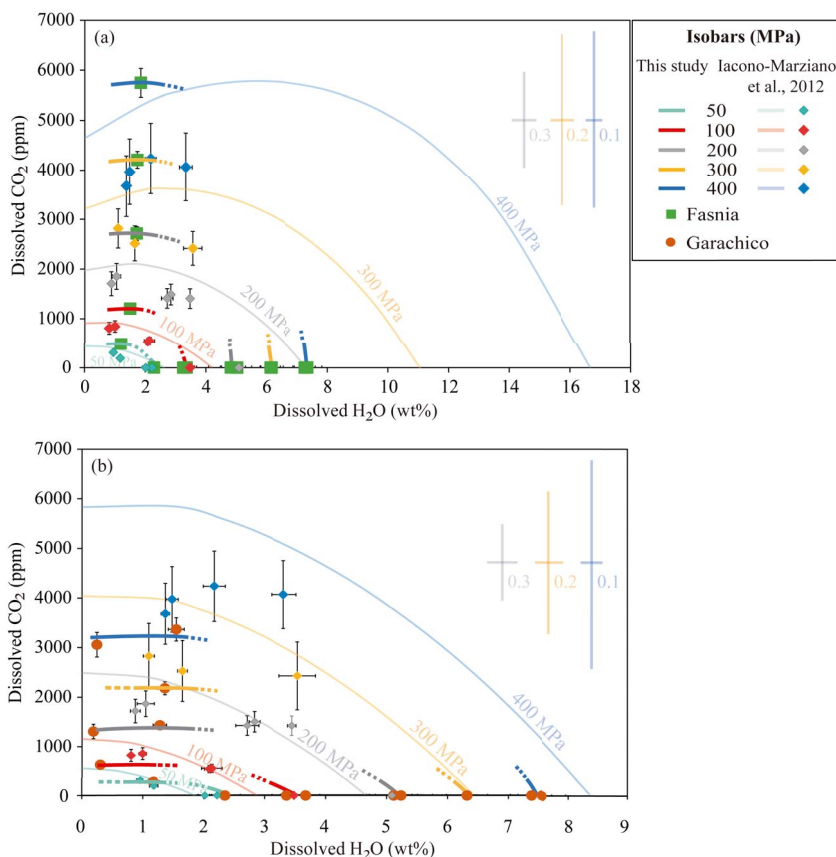


Figure 10. H₂O and CO₂ solubility data from the experiments of (a) the Fasnias basanite (*green squares*) at NNO-0.3 and (b) the Garachico phonotephrite (*orange circles*) at NNO+0.8, compared with the predicted solubility curves (*lighter coloured lines*) calculated with the H₂O-CO₂ model of Iacono-Marziano *et al.* [2012] at 1200 °C, pressures between 50 and 400 MPa, different water molar fractions (from $X_{\text{H}_2\text{O}} = 0$ to $X_{\text{H}_2\text{O}} = 1$) and the starting compositions (in Table 1). *Lighter coloured error bars* represent the uncertainties associated with the Iacono-Marziano's model at 400 MPa (in *blue*), 300 MPa (in *yellow*), and 200 MPa (in *grey*) for water molar fractions of 0.1, 0.2, and 0.3, respectively, and are shown at the right side of the diagram. *Diamonds* represent H₂O-CO₂ contents measured in the Etna experimental glasses by Iacono-Marziano *et al.* [2012] and the different colours correspond to different pressures as described below. *Thick and darker coloured lines* correspond to isobars obtained in this study for different pressures 50 MPa (in *light blue*), 100 MPa (in *orange*), 200 MPa (in *grey*), 300 MPa (in *yellow*), and 400 MPa (in *dark blue*). Symbol error bars indicate the uncertainty of FTIR measurements (propagated errors). There is a significant overestimation of the H₂O solubility at $X_{\text{H}_2\text{O}} = 1$ in the basanitic melt and the CO₂ solubility in the phonotephritic melt (see Section 4.4 for details).

Garachico phonotephrite using the mixed H₂O-CO₂ model. Comparatively, as for the first variant, the mixed model slightly underestimates the CO₂ solubility by 10–20% for our basanitic charges.

The solubility curves were computed with the H₂O-CO₂ model for water molar fractions varying

from $X_{\text{H}_2\text{O}} = 0$ to $X_{\text{H}_2\text{O}} = 1$. As shown in Figure 10 and Table S2, the model yields contrasted results depending on the composition and the volatile species considered in the calculations. Surprisingly, the mixed solubility calculations return H₂O and CO₂ contents for our experiments that differ considerably from

those predicted by the pure-volatile solubility variants, but in better agreement (10–20%) with our results (see above).

For the Fasnía basanite, the H₂O–CO₂ model predicts extremely high solubilities and saturation pressures for pure H₂O and mixed-volatile runs, increasing the differences in the back-calculated contents by up to 30–50% as the pressure rises (i.e., 16 wt% H₂O at 400 MPa; Figure 10a). Comparatively, the differences with the experimental values are relatively lower when the phonotephritic composition is used in the calculations, since saturation pressures and volatile contents differ by 10–40%. However, for these samples, results from the CO₂ solubility model are doubled compared to experiments (Figure 10b). This is not a trivial difference, since the isobars predicted by the Iacono-Marziano's model clearly differ from those determined in our CO₂-saturated experiments.

Another important issue that needs to be considered when using the mixed equation of Iacono-Marziano *et al.* [2012] is the errors associated with the calculated CO₂ contents, which at pressures above 100 MPa, exceed 1000–2000 ppm (Figure 10, Table S2). If these errors are projected on the mixed H₂O–CO₂ solubility isobars (see error bars associated with the solubility curves for a given pressure and water molar fraction in Figure 10a, b), the uncertainty in the location of a given isobar over the H₂O–CO₂ diagram proportionally increases with pressure and H₂O content. This results in an important overlapping of the curves at $P \geq 200$ MPa. Neglecting the associated CO₂ errors will have important consequences, not only when applying the H₂O–CO₂ model to calculate the saturation and entrapment pressures of melt inclusions having basanitic–phonotephritic compositions but also for the interpretation of storage conditions and associated degassing processes: errors of ± 1000 or 2000 ppm translate into depth differences of up to 6 km (see Figure 10). For this reason, we do not recommend the use of this model to calculate H₂O–CO₂ solubilities of mafic to intermediate magmas from Canary Islands, since these compositions are outside the range considered by Iacono-Marziano *et al.* [2012], as also pointed out by Shishkina *et al.* [2014].

Finally, we tested the equilibrium pressure model of Iacono-Marziano *et al.* [2012] to back-calculate the equilibration or entrapment pressure of a given melt (i.e., MI) when H₂O and CO₂ contents are

known. Results obtained for our H₂O-saturated experiments are underestimated by 20–50% for the basanitic melts (at 50–400 MPa) and overestimated by ~10–40% in the phonotephrite at 50–300 MPa, whereas at 400 MPa, the model underestimates it. For the CO₂-saturated experiments, model predictions yield similar pressures for our basanite (within 10–20%) but underestimate by ~30% the phonotephritic melt (Table S2).

4.5. *Application of the empirical power laws to melt inclusions data from El Hierro, Canary Islands*

The Canary Islands are an important alkaline group of oceanic volcanoes which have been the focus of a large number of volcanological studies. Up to recently there was limited knowledge of the magmatic volatile budget associated with this system [e.g., Gurenko and Schmincke, 2000, Hansteen *et al.*, 1991, 1998, Wallace, 1998]. Yet, the recent eruption of El Hierro in 2011–2012 has provided a unique opportunity to fill this gap [e.g., Longpré *et al.*, 2017].

Our experimental results allow us to revisit samples of the 2011–2012 submarine eruption at El Hierro, Canary Islands [Longpré *et al.*, 2017], and those from young (<20 ka) tephra collected at different locations in El Hierro [Taracsák *et al.*, 2019], owing to the compositional similarities between the bulk-rock, MI, and our starting materials. As a first step, we have used the amounts of CO₂ + H₂O dissolved in the MI which give minimum entrapment pressures [e.g., Esposito *et al.*, 2011, 2014, Gennaro *et al.*, 2019, Steele-Macinnis *et al.*, 2011]. However, MIs often have vapour bubbles containing a substantial portion of bulk volatiles [e.g., Moore *et al.*, 2015, Rose-Koga *et al.*, 2021], so, whenever possible, the restored CO₂ concentrations (dissolved + exsolved) were considered in our calculations. We note that even if the investigated MI contained detectable amounts of S, Cl [Longpré *et al.*, 2017, Taracsák *et al.*, 2019], these volatiles are considered to have a minor effect on calculated pressures [e.g., Lesne *et al.*, 2011c], though their consideration would inevitably increase calculated P values [e.g., Lesne *et al.*, 2015].

4.5.1. *The 2011–2012 submarine eruption at El Hierro*

This is the most recent eruption of the Canary archipelago and the first to be fully monitored in

real time [López et al., 2012]. Magma products emitted during this eruption were petrologically characterized by different authors [Martí et al., 2013b, Meletlidis et al., 2015, among others] but only Longpré et al. [2014, 2017] analysed the melt inclusions (MIs) trapped in phenocrysts (mainly olivines). MIs are basanitic–phonotephritic in composition [42–50 wt% SiO₂; Longpré et al., 2014], contain remarkably high concentrations of dissolved volatiles, with up to 3420 ppm CO₂, 3 wt% H₂O, and 5080 ppm S [Longpré et al., 2017]. Saturation pressures were previously calculated in this study using the models of Iacono-Marziano et al. [2012], Newman and Lowenstern [2002], Papale et al. [2006] and Shishkina et al. [2014]. Depending on the model, the retrieved pressures vary from 260 to 630 MPa; however, for consistency with the applied degassing software [D-compress, Burgisser et al., 2015] Longpré et al. [2017] considered only the results given by the Iacono-Marziano et al. [2012] model, since this was already implemented in the above software. This gave a more restricted entrapment pressure range between 7 to 260 MPa for olivine hosted MIs, corresponding to depths ≤10 km beneath El Hierro. Additionally, Longpré et al. [2017] calculated H₂O–CO₂ solubilities as a function of pressure at 1150 °C for the 2011–2012 average matrix glass composition.

In order to compare these data with our results, we assume that the possible variations in the H₂O–CO₂ solubility for a temperature difference of 50 °C are within the associated error [Holloway and Blank, 1994].

The application of our basanitic empirical solubility laws to the 2011–2012 El Hierro melt inclusions yields entrapment pressures between 11 and 280 MPa, with a maximum difference of +33 MPa (~1.5 km) compared to those determined by Longpré et al. [2017]. In both cases, the distribution of H₂O–CO₂ suggests that these magmas experienced a continuous degassing from 260–280 MPa down to 50–100 MPa (Figure 11). Although Longpré et al. [2017] have not analysed the inclusion-hosted bubbles, they have obtained a theoretical estimate of how much CO₂ may be sequestered in the bubble using the method of Shaw et al. [2008]. From 29 theoretically reconstructed MI, we can apply our model to 15 MI with ≤6153 ppm CO₂ (which fall within our calibrated range), resulting in very similar entrapment pressures. Only two of them give $P > 280$ MPa, cor-

responding to 337 and 432 MPa (Figure 11). These new pressures are in full agreement with petrological and seismic data, which indicate a storage/re-equilibration level at 10–15 km [López et al., 2012, Martí et al., 2013b].

The other set of 14 MI yields reconstructed CO₂ contents between 0.8–1.3 wt% to up to 2.3 wt%, which prompted the authors to estimate entrapment pressures ≥1 GPa, equivalent to depths ≥30 km. Whereas those MI containing 0.8–1.1 wt% CO₂ would represent magmas rising from deep levels (600–800 MPa or 20–25 km), in line with information gained from fluid inclusions, cpx–melt geobarometry and volcano-tectonic seismicity [Hansteen et al., 1991, 1998, Klügel et al., 2015, Longpré et al., 2014, 2017, López et al., 2012], those with CO₂ concentrations between 1.3–2.3 wt% are more problematic to interpret since they point to entrapment levels amid 1–2 GPa (≥30–40 km) using the solubility data of Holloway and Blank [1994] for basanitic compositions. Such pressures–depths clearly exceed those recorded by other methods during the unrest episode [Domínguez Cerdeña et al., 2013, López et al., 2012].

4.5.2. Information gained on young (<20 ka) basanites from El Hierro

To test if the previous 2011–2012 volatile contents are representative of the recent (<20 ka) mafic volcanism of El Hierro, Taracsák et al. [2019] analysed the composition and volatile contents of MIs from tephra samples collected at different locations on El Hierro island. Most of the analysed MIs have H₂O and CO₂ contents comparable to those analysed in the recent 2011–2012 eruption (Figures 11–12), varying mainly between 0.1–2 wt% and <2500 ppm, respectively. The relatively high MI volatile contents (i.e., CO₂ up to 3600 ppm and S up to 4290 ppm) along with the occasional presence of large bubbles (>10 vol.%) within MI suggest that the different magmas were volatile-saturated at the time of entrapment. However, independently of their volatile endowment, almost all the considered magmas experienced a similar degassing during their ascent towards the surface (Figure 12). Taracsák et al. [2019] also used D-compress [Burgisser et al., 2015] to calculate both the mixed H₂O–CO₂ solubility isobars and melt inclusion volatile saturation pressures at 1200 °C. In this case, the highest volatile saturation

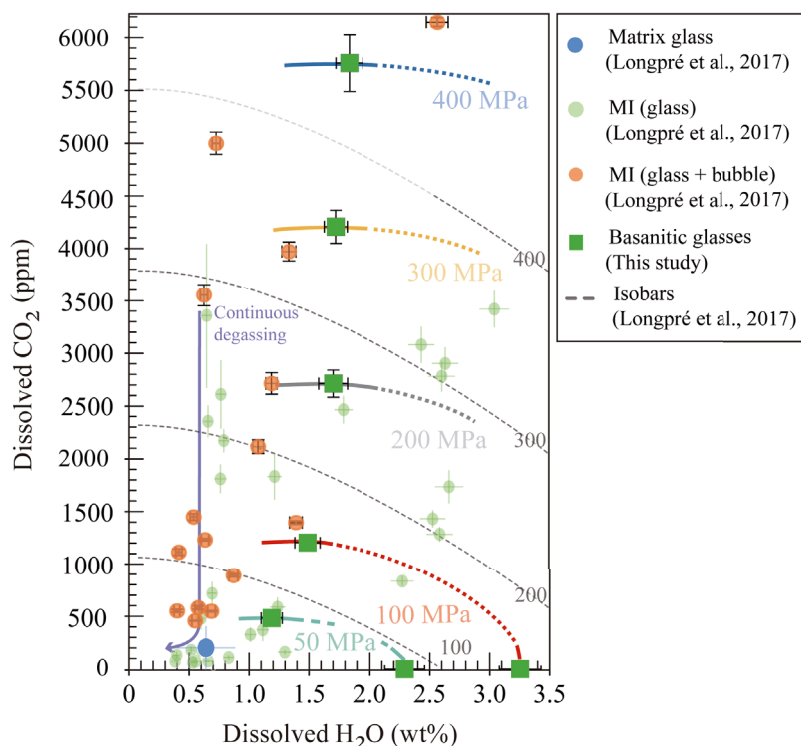


Figure 11. H₂O and CO₂ solubility curves determined in basaltic experimental glasses (*thick lines*) at 50 MPa (in *light blue*), 100 MPa (in *red*), 200 MPa (in *grey*), 300 MPa (in *yellow*), and 400 MPa (in *dark blue*), compared to solubility curves calculated by Longpré et al. [2017] with the model of Iacono-Marziano et al. [2012] (*dashed grey lines*). *Green squares* represent the basaltic glasses from this study. *Green, orange, and blue circles* correspond to olivine-hosted MI glass phases, reconstructed MI (bubble + glass), and averaged matrix glass composition from El Hierro 2011–2012 eruption, respectively (Figure 4a in Longpré et al. [2017]). Solubility curves from Longpré et al. [2017] are moderately overestimated compared to the isobars of this study. Melt inclusions distribution suggests a continuous degassing from pressures of 260–280 MPa down to 50–100 MPa.

pressures calculated for their MI fall between 150–355 MPa (6–13 km) or 350–700 MPa (13–24 km), depending on whether the CO₂ dissolved in the MI glass is only considered or that stored in bubbles is also into account.

Similar to the recent 2011–2012 eruption, we applied our empirical laws to determine MIs entrapment pressures. For the <20 ka eruptions, our calculations (using only dissolved H₂O and CO₂ contents of MI) yield somewhat lower *P*-saturation values, from 16 to 258 MPa (Figure 12), most of the data falling between the 100–200 MPa isobars. This implies a difference in the equilibration conditions for the MI glass of ~100 MPa, or equivalent to 3–4 km depth. Regarding the restored volatile contents

of melt inclusions (i.e., glass + bubble CO₂), Taracsák et al. [2019] have studied 47 inclusion-hosted bubbles, 25 of which contained detectable CO₂. Of these, 8 MI glass phases were also analysed, and the entrapment pressures for the 6 MIs with CO₂ falling within the calibrated range of the empirical equations, vary between 262 and 443 MPa (or 8–13 km depth). Two MIs have CO₂ contents (0.9–1.2 wt%) outside model calibration range. Using the data of Holloway and Blank [1994], these high CO₂ contents suggest deeper entrapment levels at ~1 GPa (~30 km).

In summary, our results suggest that the last, but also recent (<20 ka), magmas erupted at El Hierro record a main episode of crystallization-entrapment at 250–443 MPa followed by a second one at *P* <

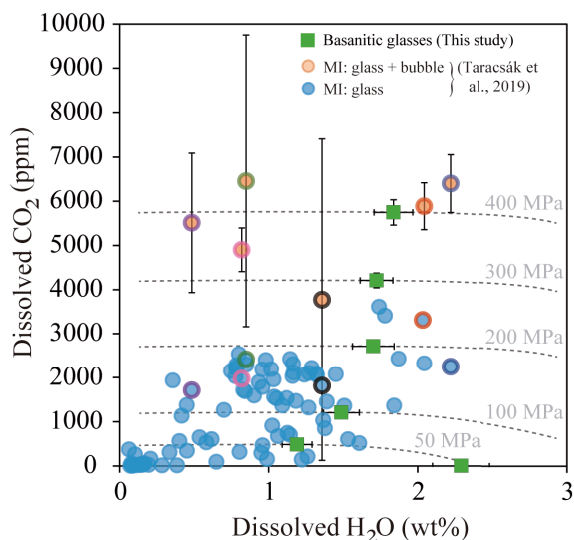


Figure 12. Comparison between H_2O – CO_2 contents from olivine- and clinopyroxene-hosted basanite melt inclusions from El Hierro, Canary Islands [Taracsák *et al.*, 2019] and the H_2O – CO_2 solubility curves (*dashed lines*) determined for our basanitic melt (*green squares*) at pressures from 50 MPa to 400 MPa. *Light blue circles* represent MI glass phases and *orange circles* correspond to reconstructed melt inclusions (bubble + glass). Coloured borders indicate pairs of unreconstructed and reconstructed MI. Most melt inclusions (glass phases) are located between the 100–200 MPa isobars (equivalent to 3–6 km), whereas the restored MI gives higher pressures (280–440 MPa).

200 MPa–50 MPa, corresponding to depths of 8–13 km and 6–1.5 km, respectively (Figures 11 and 12).

Over the range of pressures proposed, our deeper estimates coincide with the location of the crust–mantle discontinuity at El Hierro, which according to previous authors [e.g., González *et al.*, 2013, Klügel *et al.*, 2015, Martí *et al.*, 2013a,b], operated as the main level of crystallization for the magmas erupted in the 2011–2012 event (i.e., at 10–15 km). These observations are consistent with the upper depths of the seismic swarm observed during the unrest period of the 2011–2012 submarine eruption [Domínguez Cerdeña *et al.*, 2013, López *et al.*, 2012], those estimated using length–thickness ratios of feeder dykes at El Hierro [11–13 km; Becerril *et al.*, 2013], and the

low-pressure equilibration recorded by some cpx-hosted fluid inclusions [280–450 MPa, Longpré *et al.*, 2014]. Compared to the above, our crystallization–entrapment depths ≤ 6 km are consistent with the interpretation of geodetic data associated with the 2011–2012 event [González *et al.*, 2013] and the presence of high-density bodies (i.e., possibly representing cumulates) at shallow depths beneath the island, both suggesting the low-pressure equilibration conditions experienced by these magmas prior to their eruption [1–6 km; Montesinos *et al.*, 2006]. This last episode may explain the formation of volatile-poor melt inclusions and, thus, the lower calculated entrapment pressures for these magmas.

Altogether, the distribution of volatile contents from El Hierro MIs, the dominant population composition of the host olivines (Fo 78–80), their crystal shape, and the new range of MI entrapment conditions inferred in our work, allow us to provide a robust scenario for the plumbing system feeding basanitic eruptions at El Hierro. Magmas rising from the deep mantle [>20 –25 km; López *et al.*, 2012, Martí *et al.*, 2013a,b] experience a first but “short” (1–2 months, according to olivine diffusion modelling and the scarce occurrence of Fo > 84 –88 olivines recording these conditions [Longpré *et al.*, 2014, Martí *et al.*, 2013b]; Figure 11–12) crystallization episode at 8–13 km. The subsequent fast injection of dykes from this first level of magma ponding towards the surface [Becerril *et al.*, 2013] produces the isothermal (?) syn-eruptive crystallization (characterized by Fo_{78–80}) accompanied by progressive H_2O – CO_2 degassing of the magma. This dynamic scenario promotes the rapid growth of crystals, as witnessed by disequilibrium textures [e.g., incomplete, resorbed, skeletal; see Martí *et al.*, 2013b, Welsch *et al.*, 2012] along with the entrapment of melt aliquots having different compositions and variable volatile contents, recording their journey towards the surface.

5. Conclusions

We report new H_2O and CO_2 solubility data in basanitic and phonotephritic melts representative of the Canary Islands magmas, from which empirical solubility laws have been derived. Whereas H_2O displays broadly similar behaviour in both compositions, this is not the case of CO_2 , for which the role of cations such as Ca^{2+} , K^+ , Na^+ , Fe^{2+} , and Mg^{2+} signif-

icantly impact CO₂ solubility [e.g., Dixon, 1997], in a manner still not well accounted for by existing models. Our study suggests that for compositions having similar total alkali contents, differences in CaO, MgO, and FeO* may play an important role in enhancing or decreasing the CO₂ solubility.

The application of existing H₂O–CO₂ empirical models yields reasonable water contents for our compositions at low pressures (50–200 MPa), whereas the difference increases up to 1–2 wt% at 300–400 MPa. For CO₂, the amounts calculated by the models differ compared to those measured by at least 10–20% and up to 85%. As stated above, the observed differences reflect the incomplete compositional coverage of available models.

Application of our results at El Hierro suggests a simple scenario in which magmas rising from the deep mantle (>25 km) experience a first transient episode of crystallization at 8–13 km, followed by the crystallization occurred during the subsequent dyke injection, ascent, and degassing at $P \leq 200$ MPa (6–1.5 km).

Acknowledgements

This work was supported by (1) the Institut des Sciences de la Terre d'Orléans (ISTO-CNRS), the LABEX VOLTAIRE (ANR-10-LABX-100-01), and the PLANEX projects (11-EQPX-0036); (2) the European Volcano Early Warning System (EVE) project grant agreement: 826292 through the Group of Volcanology of Geociencias Barcelona (GEO3BCN-CSIC), and (3) the National Geographic Institute of Spain (IGN, Canary Islands). We thank L. Remusat from the MNHN in Paris for his support with NanoSIMS analysis; Ida Di Carlo and Aneta Slodczyk from ISTO-CNRS for their assistance in EPMA and FTIR analysis, respectively; and Ma J. Blanco, Francisco Quirós and Stavros Meletlidis from IGN, and Michel Pichavant, for their help in field tasks, as well as Joan Martí from GEO3BCN-CSIC for discussions and field support. We kindly thank the constructive comments of two anonymous reviewers and the editorial handling of the Editor François Chabaux.

Supplementary data

Supporting information for this article is available on the journal's website under <https://doi.org/10.5802/crgeos.84> or from the author.

References

- Allison, C. M., Roggensack, K., and Clarke, A. B. (2019). H₂O–CO₂ solubility in alkali-rich mafic magmas: new experiments at mid-crustal pressures. *Contrib. Mineral. Petrol.*, 174, article no. 58.
- Anderson, A. T. (1975). Some basaltic and andesitic gases. *Rev. Geophys.*, 13, 37–55.
- Andújar, J., Martel, C., Pichavant, M., Samaniego, P., Scaillet, B., and Molina, I. (2017). Structure of the plumbing system at Tungurahua volcano, Ecuador: Insights from phase equilibrium experiments on July–August 2006 eruption products. *J. Petrol.*, 58, 1249–1278.
- Andújar, J. and Scaillet, B. (2012a). Experimental constraints on parameters controlling the difference in the eruptive dynamics of phonolitic magmas: the case of Tenerife (Canary Islands). *J. Petrol.*, 53, 1777–1806.
- Andújar, J. and Scaillet, B. (2012b). Relationships between pre-eruptive conditions and eruptive styles of phonolite–trachyte magmas. *Lithos*, 152, 122–131.
- Andújar, J., Scaillet, B., Pichavant, M., and Druitt, T. H. (2015). Differentiation conditions of a basaltic magma from Santorini, and its bearing on the production of andesite in arc settings. *J. Petrol.*, 56, 765–794.
- Becerril, L., Galindo, I., Gudmundsson, A., and Morales, J. M. (2013). Depth of origin of magma in eruptions. *Sci. Rep.*, 3, article no. 2762.
- Behrens, H., Misiti, V., Freda, C., Vetere, F., Botcharnikov, R. E., and Scarlato, P. (2009). Solubility of H₂O and CO₂ in ultrapotassic melts at 1200 and 1250 C and pressure from 50 to 500 MPa. *Am. Mineral.*, 94, 105–120.
- Benne, D. and Behrens, H. (2003). Water solubility in haplobasaltic melts. *Eur. J. Mineral.*, 15, 803–814.
- Blank, J. and Brooker, R. (1994). Experimental studies of carbon dioxide in silicate melts: solubility, speciation, and stable carbon isotope behavior. In Carroll, M. and Holloway, J., editors, *Volatiles in Magmas*, pages 157–186. De Gruyter, Berlin, Boston.
- Botcharnikov, R., Freise, M., Holtz, F., and Behrens, H. (2005). Solubility of C–O–H mixtures in natural melts: new experimental data and application range of recent models. *Ann. Geophys.*, 48, 633–646.
- Botcharnikov, R. E., Behrens, H., and Holtz, F. (2006). Solubility and speciation of C–O–H fluids in an-

- desitic melt at $T = 1100\text{--}1300\text{ }^{\circ}\text{C}$ and $P = 200$ and 500 MPa . *Chem. Geol.*, 229, 125–143.
- Brooker, R. A., Kohn, S. C., Holloway, J. R., and McMillan, P. F. (2001a). Structural controls on the solubility of CO_2 in silicate melts: Part I: bulk solubility data. *Chem. Geol.*, 174, 225–239. 6th International Silicate Melt Workshop.
- Brooker, R. A., Kohn, S. C., Holloway, J. R., and McMillan, P. F. (2001b). Structural controls on the solubility of CO_2 in silicate melts: Part II: IR characteristics of carbonate groups in silicate glasses. *Chem. Geol.*, 174, 241–254. 6th International Silicate Melt Workshop.
- Burgisser, A., Alletti, M., and Scaillet, B. (2015). Simulating the behavior of volatiles belonging to the C–O–H–S system in silicate melts under magmatic conditions with the software D-Compress. *Comput. Geosci.*, 79, 1–14.
- Burnham, C. W. (1975). Water and magmas; a mixing model. *Geochim. Cosmochim. Acta*, 39, 1077–1084.
- Burnham, C. W. (1979). The importance of volatile constituents. In Yoder, H. S., editor, *The Evolution of the Igneous Rocks*, pages 439–482. Princeton University Press, Princeton, NJ.
- Burnham, C. W. and Davis, N. F. (1971). The role of H_2O in silicate melts; I, P–V–T relations in the system $\text{NaAlSi}_3\text{O}_8\text{--H}_2\text{O}$ to 10 kilobars and 1000 degrees C. *Am. J. Sci.*, 270, 54–79.
- Burnham, C. W. and Davis, N. F. (1974). The role of H_2O in silicate melts; II, Thermodynamic and phase relations in the system $\text{NaAlSi}_3\text{O}_8\text{--H}_2\text{O}$ to 10 kilobars, 700 degrees to 1100 degrees C. *Am. J. Sci.*, 274, 902–940.
- Burnham, C. W. and Jahns, R. H. (1962). A method for determining the solubility of water in silicate melts. *Am. J. Sci.*, 260, 721–745.
- Carroll, M. R. and Blank, J. G. (1997). The solubility of H_2O in phonolitic melts. *Am. Mineral.*, 82, 549–556.
- Cocheo, P. A. (1993). The solubility of water in basanitic melts at low pressures. Master's thesis. Arizona State University.
- Dixon, J. E. (1997). Degassing of alkalic basalts. *Am. Mineral.*, 82, 368–378.
- Dixon, J. E. and Pan, V. (1995). Determination of the molar absorptivity of dissolved carbonate in basanitic glass. *Am. Mineral.*, 80, 1339–1342.
- Dixon, J. E. and Stolper, E. M. (1995). An experimental study of water and carbon dioxide solubilities in Mid-Ocean Ridge Basaltic liquids. Part II: Applications to degassing. *J. Petrol.*, 36, 1633–1646.
- Dixon, J. E., Stolper, E. M., and Holloway, J. R. (1995). An experimental study of water and carbon dioxide solubilities in Mid-Ocean Ridge Basaltic liquids. Part I: Calibration and solubility models. *J. Petrol.*, 36, 1607–1631.
- Domínguez Cerdeña, I., del Fresno, C., and Gomis Moreno, A. (2013). Seismicity patterns prior to the 2011 El Hierro eruption. *Bull. Seismol. Soc. Am.*, 104(1), 567–575.
- Edmonds, M. and Wallace, P. J. (2017). Volatiles and exsolved vapor in volcanic systems. *Elements*, 13, 29–34.
- Esposito, R., Bodnar, R. J., Danyushevsky, L. V., de Vivo, B., Fedele, L., Hunter, J., Lima, A., and Shimizu, N. (2011). Volatile evolution of magma associated with the Solchiaro eruption in the Phlegrean Volcanic District (Italy). *J. Petrol.*, 52, 2431–2460.
- Esposito, R., Hunter, J., Schiffbauer, J., Shimizu, N., and Bodnar, R. J. (2014). An assessment of the reliability of melt inclusions as recorders of the pre-eruptive volatile content of magmas. *Am. Mineral.*, 99, 976–998.
- Gaillard, F., Schmidt, B., Mackwell, S., and McCammon, C. (2003). Rate of hydrogen–iron redox exchange in silicate melts and glasses. *Geochim. Cosmochim. Acta*, 67, 2427–2441.
- Gennaro, E., Iacono-Marziano, G., Paonita, A., Rottolo, S. G., Martel, C., Rizzo, A. L., Pichavant, M., and Liotta, M. (2019). Melt inclusions track melt evolution and degassing of Etnean magmas in the last 15 ka. *Lithos*, 324–325, 716–732.
- Giordano, D., Russell, J. K., and Dingwell, D. B. (2008). Viscosity of magmatic liquids: A model. *Earth Planet. Sci. Lett.*, 271, 123–134.
- González, P. J., Samsonov, S. V., Pepe, S., Tiampo, K. F., Tizzani, P., Casu, F., Fernández, J., Camacho, A. G., and Sansosti, E. (2013). Magma storage and migration associated with the 2011–2012 El Hierro eruption: Implications for crustal magmatic systems at oceanic island volcanoes. *J. Geophys. Res. Solid Earth*, 118, 4361–4377.
- Goranson, R. W. (1931). Solubility of water in granite magmas. *Eos, Trans. AGU*, 12, 183–183.
- Goranson, R. W. (1936). Silicate-water systems: The solubility of water in albite-melt. *Eos, Trans. AGU*, 17, 257–259.
- Grove, T. L. (1982). Use of FePt alloys to eliminate

- the iron loss problem in 1 atmosphere gas mixing experiments: Theoretical and practical considerations. *Contrib. Mineral. Petrol.*, 78, 298–304.
- Gurenko, A. A. and Schmincke, H. U. (2000). S concentrations and its speciation in Miocene basaltic magmas north and south of Gran Canaria (Canary Islands): constraints from glass inclusions in olivine and clinopyroxene. *Geochim. Cosmochim. Acta*, 64, 2321–2337.
- Hall, L. J., Brodie, J., Wood, B. J., and Carroll, M. R. (2004). Iron and water losses from hydrous basalts contained in Au 80 Pd 20 capsules at high pressure and temperature. *Mineral. Mag.*, 68, 75–81.
- Hansteen, T. H., Andersen, T., Neumann, E.-R., and Jelsma, H. (1991). Fluid and silicate glass inclusions in ultramafic and mafic xenoliths from Hierro, Canary Islands: implications for mantle metasomatism. *Contrib. Mineral. Petrol.*, 107, 242–254.
- Hansteen, T. H., Klügel, A., and Schmincke, H. U. (1998). Multi-stage magma ascent beneath the Canary Islands: evidence from fluid inclusions. *Contrib. Mineral. Petrol.*, 132, 48–64.
- Holloway, J. and Blank, J. (1994). Application of experimental results to C–O–H species in natural melts. *Rev. Mineral.*, 30, 187–230.
- Holloway, J. R. (1977). Fugacity and activity of molecular species in supercritical fluids. In Fraser, D. G., editor, *Thermodynamics in Geology*, NATO Advanced Study Institutes Series (Series C, Mathematical and Physical Sciences), pages 161–181. Springer, Dordrecht.
- Holloway, J. R., Pan, V., and Guðmundsson, G. (1992). High-pressure fluid-absent melting experiments in the presence of graphite: oxygen fugacity, ferric/ferrous ratio and dissolved CO₂. *Eur. J. Mineral.*, 4, 105–114.
- Iacono-Marziano, G., Morizet, Y., Le Trong, E., and Gaillard, F. (2012). New experimental data and semi-empirical parameterization of H₂O–CO₂ solubility in mafic melts. *Geochim. Cosmochim. Acta*, 97, 1–23.
- Iacovino, K., Moore, G., Roggensack, K., Oppenheimer, C., and Kyle, P. (2013). H₂O–CO₂ solubility in mafic alkaline magma: applications to volatile sources and degassing behavior at Erebus volcano, Antarctica. *Contrib. Mineral. Petrol.*, 166, 845–860.
- Jendrzewski, N., Trull, T. W., Pineau, F., and Javoy, M. (1997). Carbon solubility in Mid-Ocean Ridge basaltic melt at low pressures (250–1950 bar). *Chem. Geol.*, 138, 81–92.
- Kawamoto, T. and Hirose, K. (1994). Au–Pd sample containers for melting experiments on iron and water bearing systems. *Eur. J. Mineral.*, 6, 381–385.
- Klügel, A., Longpré, M.-A., García-Cañada, L., and Stix, J. (2015). Deep intrusions, lateral magma transport and related uplift at ocean island volcanoes. *Earth Planet. Sci. Lett.*, 431, 140–149.
- Le Bas, M. J., Maitre, R. W. L., Streckeisen, A., and Zanettin, B. (1986). IUGS Subcommission on the systematics of igneous rocks. A chemical classification of volcanic rocks based on the total alkali-silica diagram. *J. Petrol.*, 27, 745–750.
- Lesne, P., Kohn, S. C., Blundy, J., Witham, F., Botcharnikov, R. E., and Behrens, H. (2011c). Experimental simulation of closed-system degassing in the system basalt–H₂O–CO₂–S–Cl. *J. Petrol.*, 52, 1737–1762.
- Lesne, P., Scaillet, B., and Pichavant, M. (2015). The solubility of sulfur in hydrous basaltic melts. *Chem. Geol.*, 418, 104–116.
- Lesne, P., Scaillet, B., Pichavant, M., and Beny, J.-M. (2011b). The carbon dioxide solubility in alkali basalts: an experimental study. *Contrib. Mineral. Petrol.*, 162, 153–168.
- Lesne, P., Scaillet, B., Pichavant, M., Iacono-Marziano, G., and Beny, J.-M. (2011a). The H₂O solubility of alkali basaltic melts: an experimental study. *Contrib. Mineral. Petrol.*, 162, 133–151.
- Liu, Y., Zhang, Y., and Behrens, H. (2005). Solubility of H₂O in rhyolitic melts at low pressures and a new empirical model for mixed H₂O–CO₂ solubility in rhyolitic melts. *J. Volcanol. Geotherm. Res.*, 143, 219–235.
- Longpré, M.-A., Klügel, A., Diehl, A., and Stix, J. (2014). Mixing in mantle magma reservoirs prior to and during the 2011–2012 eruption at El Hierro, Canary Islands. *Geology*, 42, 315–318.
- Longpré, M.-A., Stix, J., Klügel, A., and Shimizu, N. (2017). Mantle to surface degassing of carbon- and sulphur-rich alkaline magma at El Hierro, Canary Islands. *Earth Planet. Sci. Lett.*, 460, 268–280.
- López, C., Blanco, M. J., Abella, R., Brenes, B., Rodríguez, V. M. C., Casas, B., Cerdeña, I. D., Felpeto, A., Villalta, M. E., de Fresno, C., del García, O., García-Arias, M. J., García-Cañada, L., Moreno, A. G., González-Alonso, E., Pérez, J. G., Iribarren, I., López-Díaz, R., Luengo-Oroz, N., Meletlidis, S., Moreno, M., Moure, D., Pablo, J. P., de Roderio, C.,

- Romero, E., Sainz-Maza, S., Domingo, M. A. S., Torres, P. A., Trigo, P., and Villasante-Marcos, V. (2012). Monitoring the volcanic unrest of El Hierro (Canary Islands) before the onset of the 2011–2012 submarine eruption. *Geophys. Res. Lett.*, 39, article no. L13303.
- Martí, J., Castro, A., Rodríguez, C., Costa, F., Carrasquilla, S., Pedreira, R., and Bolos, X. (2013b). Correlation of magma evolution and geophysical monitoring during the 2011–2012 El Hierro (Canary Islands) submarine eruption. *J. Petrol.*, 54, 1349–1373.
- Martí, J., Pinel, V., López, C., Geyer, A., Abella, R., Tárrega, M., Blanco, M. J., Castro, A., and Rodríguez, C. (2013a). Causes and mechanisms of the 2011–2012 El Hierro (Canary Islands) submarine eruption: El Hierro eruption. *J. Geophys. Res. Solid Earth*, 118, 823–839.
- McMillan, P. F. and Remmele, R. L. (1986). Hydroxyl sites in SiO₂ glass: A note on infrared and Raman spectra. *Am. Mineral.*, 71, 772–778.
- Meletlidis, S., Roberto, A. D., Cerdeña, I. D., Pompilio, M., García-Cañada, L., Bertagnini, A., Benito-Saz, M. A., Carlo, P. D., and Aparicio, S. S. M. (2015). New insight into the 2011–2012 unrest and eruption of El Hierro Island (Canary Islands) based on integrated geophysical, geodetical and petrological data. *Ann. Geophys.*, 58, article no. 0546.
- Montesinos, F. G., Arnoso, J., Benavent, M., and Vieira, R. (2006). The crustal structure of El Hierro (Canary Islands) from 3-D gravity inversion. *J. Volcanol. Geotherm. Res.*, 150, 283–299.
- Moore, G. (2008). Interpreting H₂O and CO₂ contents in melt inclusions: Constraints from solubility experiments and modeling. *Rev. Mineral. Geochem.*, 69, 333–362.
- Moore, G. and Carmichael, I. S. E. (1998). The hydrous phase equilibria (to 3 kbar) of an andesite and basaltic andesite from western Mexico: constraints on water content and conditions of phenocryst growth. *Contrib. Mineral. Petrol.*, 130, 304–319.
- Moore, G., Chizmeshya, A., and McMillan, P. F. (2000). Calibration of a reflectance FTIR method for determination of dissolved CO₂ concentration in rhyolitic glasses. *Geochim. Cosmochim. Acta*, 64, 3571–3579.
- Moore, G., Vennemann, T., and Carmichael, I. S. E. (1998). An empirical model for the solubility of H₂O in magmas to 3 kilobars. *Am. Mineral.*, 83, 36–42.
- Moore, L. R., Gazel, E., Tuohy, R., Lloyd, A. S., Esposito, R., Steele-MacInnis, M., Hauri, E. H., Wallace, P. J., Plank, T., and Bodnar, R. J. (2015). Bubbles matter: An assessment of the contribution of vapor bubbles to melt inclusion volatile budgets. *Am. Mineral.*, 100, 806–823.
- Moussallam, Y., Morizet, Y., and Gaillard, F. (2016). H₂O–CO₂ solubility in low SiO₂-melts and the unique mode of kimberlite degassing and emplacement. *Earth Planet. Sci. Lett.*, 447, 151–160.
- Mysen, B. O. (1990). Relationships between silicate melt structure and petrologic processes. *Earth Sci. Rev.*, 27, 281–365.
- Mysen, B. O. (1991). Relations between structure, redox equilibria of iron, and properties of magmatic liquids. In Perchuk, L. L. and Kushiro, I., editors, *Physical Chemistry of Magmas, Advances in Physical Geochemistry*, pages 41–98. Springer, New York, NY.
- Mysen, B. O., Arculus, R. J., and Eggler, D. H. (1975). Solubility of carbon dioxide in melts of andesite, tholeiite, and olivine nephelinite composition to 30 kbar pressure. *Contrib. Mineral. Petrol.*, 53, 227–239.
- Mysen, B. O. and Cody, G. (2004). Solubility and solution mechanism of H₂O in alkali silicate melts and glasses at high pressure and temperature. *Geochim. Cosmochim. Acta*, 68, 5113–5126.
- Mysen, B. O. and Virgo, D. (1986a). Volatiles in silicate melts at high pressure and temperature. Water in melts along the join NaAlO₂–SiO₂ and a comparison of solubility mechanisms of water and fluorine. *Chem. Geol.*, 57(1986), 333–358.
- Mysen, B. O. and Virgo, D. (1986b). Volatiles in silicate melts at high pressure and temperature. Interaction between OH groups and Si⁴⁺, Al³⁺, Ca²⁺, Na⁺ and H⁺. *Chem. Geol.*, 57(1986), 303–331.
- Mysen, B. O., Virgo, D., and Seifert, F. A. (1982). The structure of silicate melts: Implications for chemical and physical properties of natural magma. *Rev. Geophys.*, 20, 353–383.
- Newman, S. and Lowenstern, J. B. (2002). Volatile-Calc: a silicate melt–H₂O–CO₂ solution model written in Visual Basic for excel. *Comput. Geosci.*, 28, 597–604.
- Newman, S., Stolper, E. M., and Epstein, S. (1986). Measurement of water in rhyolitic glasses; calibra-

- tion of an infrared spectroscopic technique. *Am. Mineral.*, 71, 1527–1541.
- Ni, H. and Keppler, H. (2013). Carbon in silicate melts. *Rev. Mineral. Geochem.*, 75, 251–287.
- Oppenheimer, C., Fischer, T. P., and Scaillet, B. (2014). Volcanic degassing: process and impact. In Holland, H. D. and Turekian, K. K., editors, *Treatise on Geochemistry*, pages 111–179. Elsevier, Oxford, 2nd edition.
- Pan, V., Holloway, J. R., and Hervig, R. L. (1991). The pressure and temperature dependence of carbon dioxide solubility in tholeiitic basalt melts. *Geochim. Cosmochim. Acta*, 55, 1587–1595.
- Papale, P., Moretti, R., and Barbato, D. (2006). The compositional dependence of the saturation surface of H₂O+CO₂ fluids in silicate melts. *Chem. Geol.*, 229, 78–95.
- Pawley, A. R., Holloway, J. R., and McMillan, P. F. (1992). The effect of oxygen fugacity on the solubility of carbon–oxygen fluids in basaltic melt. *Earth Planet. Sci. Lett.*, 110, 213–225.
- Pichavant, M., Di Carlo, I., Rotolo, S. G., Scaillet, B., Burgisser, A., Le Gall, N., and Martel, C. (2013). Generation of CO₂-rich melts during basalt magma ascent and degassing. *Contrib. Mineral. Petrol.*, 166, 545–561.
- Rose-Koga, E. F., Bouvier, A.-S., Gaetani, G. A., Wallace, P. J., Allison, C. M., Andrys, J. A., Angeles de la Torre, C. A., Barth, A., Bodnar, R. J., Bracco Gartner, A. J. J., Butters, D., Castillejo, A., Chilson-Parks, B., Choudhary, B. R., Cluzel, N., Cole, M., Cottrell, E., Daly, A., Danyushevsky, L. V., DeVitre, C. L., Drignon, M. J., France, L., Gaborieau, M., Garcia, M. O., Gatti, E., Genske, F. S., Hartley, M. E., Hughes, E. C., Iveson, A. A., Johnson, E. R., Jones, M., Kagoshima, T., Katzir, Y., Kawaguchi, M., Kawamoto, T., Kelley, K. A., Koornneef, J. M., Kurz, M. D., Laubier, M., Layne, G. D., Lerner, A., Lin, K.-Y., Liu, P.-P., Lorenzo-Merino, A., Luciani, N., Magalhães, N., Marschall, H. R., Michael, P. J., Monteleone, B. D., Moore, L. R., Moussallam, Y., Muth, M., Myers, M. L., Narváez, D. F., Navon, O., Newcombe, M. E., Nichols, A. R. L., Nielsen, R. L., Pamukcu, A., Plank, T., Rasmussen, D. J., Roberge, J., Schiavi, E., Schwartz, D., Shimizu, K., Shimizu, K., Shimizu, N., Thomas, J. B., Thompson, G. T., Tucker, J. M., Ustunisik, G., Waelkens, C., Zhang, Y., and Zhou, T. (2021). Silicate melt inclusions in the new millennium: A review of recommended practices for preparation, analysis, and data presentation. *Chem. Geol.*, 570, article no. 120145.
- Scaillet, B. and Evans, B. W. (1999). The 15 June 1991 eruption of Mount Pinatubo. I. Phase equilibria and pre-eruption P – T – f_{O_2} – $f_{\text{H}_2\text{O}}$ conditions of the dacite magma. *J. Petrol.*, 40, 381–411.
- Scaillet, B. and Pichavant, M. (2005). A model of sulphur solubility for hydrous mafic melts: application to the determination of magmatic fluid compositions of Italian volcanoes. *Ann. Geophys.*, 48(4/5), 671–698.
- Scaillet, B., Pichavant, M., and Cioni, R. (2008). Upward migration of Vesuvius magma chamber over the past 20,000 years. *Nature*, 455, 216–219.
- Schanofski, M., Fanara, S., and Schmidt, B. C. (2019). CO₂–H₂O solubility in K-rich phonolitic and leucitic melts. *Contrib. Mineral. Petrol.*, 174, article no. 52.
- Schmidt, B. C. and Behrens, H. (2008). Water solubility in phonolite melts: Influence of melt composition and temperature. *Chem. Geol.*, 256, 259–268. 8th Silicate Melt Workshop.
- Shaw, A. M., Hauri, E. H., Fischer, T. P., Hilton, D. R., and Kelley, K. A. (2008). Hydrogen isotopes in Mariana arc melt inclusions: Implications for subduction dehydration and the deep-Earth water cycle. *Earth Planet. Sci. Lett.*, 275, 138–145.
- Shishkina, T. A., Botcharnikov, R. E., Holtz, F., Almeev, R. R., Jazwa, A. M., and Jakubiak, A. A. (2014). Compositional and pressure effects on the solubility of H₂O and CO₂ in mafic melts. *Chem. Geol.*, 388, 112–129.
- Shishkina, T. A., Botcharnikov, R. E., Holtz, F., Almeev, R. R., and Portnyagin, M. V. (2010). Solubility of H₂O- and CO₂-bearing fluids in tholeiitic basalts at pressures up to 500 MPa. *Chem. Geol.*, 277, 115–125.
- Silver, L. A., Ihinger, P. D., and Stolper, E. (1990). The influence of bulk composition on the speciation of water in silicate glasses. *Contrib. Mineral. Petrol.*, 104, 142–162.
- Sparks, R. S. J. (1978). The dynamics of bubble formation and growth in magmas: A review and analysis. *J. Volcanol. Geotherm. Res.*, 3, 1–37.
- Spera, F. J. and Bergman, S. C. (1980). Carbon dioxide in igneous petrogenesis. I. *Contrib. Mineral. Petrol.*, 74, 55–66.
- Steele-Macinnis, M., Esposito, R., and Bodnar, R. J. (2011). Thermodynamic model for the effect of

- post-entrapment crystallization on the H₂O–CO₂ systematics of vapor-saturated, silicate melt inclusions. *J. Petrol.*, 52, 2461–2482.
- Stolper, E. (1982a). Water in silicate glasses: An infrared spectroscopic study. *Contrib. Mineral. Petrol.*, 81, 1–17.
- Stolper, E. (1982b). The speciation of water in silicate melts. *Geochim. Cosmochim. Acta*, 46, 2609–2620.
- Tamic, N., Behrens, H., and Holtz, F. (2001). The solubility of H₂O and CO₂ in rhyolitic melts in equilibrium with a mixed CO₂–H₂O fluid phase. *Chem. Geol.*, 174, 333–347.
- Taracsák, Z., Hartley, M. E., Burgess, R., Edmonds, M., Iddon, E., and Longpré, M.-A. (2019). High fluxes of deep volatiles from ocean island volcanoes: Insights from El Hierro, Canary Islands. *Geochim. Cosmochim. Acta*, 258, 19–36.
- Vetere, F., Holtz, F., Behrens, H., Botcharnikov, R. E., and Fanara, S. (2014). The effect of alkalis and polymerization on the solubility of H₂O and CO₂ in alkali-rich silicate melts. *Contrib. Mineral. Petrol.*, 167, article no. 1014.
- Wallace, P. J. (1998). Water and partial melting in mantle plumes: Inferences from the dissolved H₂O concentrations of Hawaiian basaltic magmas. *Geophys. Res. Lett.*, 25, 3639–3642.
- Welsch, B., Faure, E., Famin, V., Baronnet, A., and Bachèlery, P. (2012). Dendritic crystallization: A single process for all the textures of olivine in basalts? *J. Petrol.*, 54, 539–574.



Perspectives on alkaline magmas / *Perspectives sur les magmas alcalins*

Water solubility in trachytic and pantelleritic melts: an experimental study

Pierangelo Romano^{✉, a, b}, Ida Di Carlo^c, Joan Andújar^c and Silvio G. Rotolo^{a, b}

^a Istituto Nazionale di Geofisica e Vulcanologia, sezione di Palermo, Via Ugo la Malfa 153, 90146 Palermo, Italy

^b Dipartimento di Scienze della Terra e del Mare (DiSTeM), Università degli Studi di Palermo, Via Archirafi 22, 90123 Palermo, Italy

^c Institut des Sciences de la Terre d'Orléans (ISTO) UMR 7327, Université d'Orléans – CNRS – BRGM, Campus Géosciences, 1A rue de la Férollerie, 45071 Orléans Cedex 2, France

E-mails: pierangeloromano@gmail.com (P. Romano), ida.di-carlo@cnrs-orleans.fr (I. Di Carlo), joan.andujar@cnrs-orleans.fr (J. Andújar), silvio.rotolo@unipa.it (S. G. Rotolo)

Abstract. Solubility experiments were performed on a trachyte and a pantellerite from Pantelleria. The trachyte has $\text{SiO}_2 = 65.2$ wt%, $\text{Al}_2\text{O}_3 = 15.2$ wt% and a peralkaline index (P.I. = $\text{molar}[(\text{Na}_2\text{O} + \text{K}_2\text{O})/\text{Al}_2\text{O}_3]) \sim 1$ while the pantellerite has $\text{SiO}_2 = 72.2$ wt%, $\text{Al}_2\text{O}_3 = 11$ wt% and a P.I. = 1.3. Solubility experiments were performed in the pressure range of 50–300 MPa at $T = 950$ °C for the trachyte and 50–200 MPa at $T = 850$ °C for the pantellerite. The water content of experimental glasses was determined by Karl Fischer titration, elemental analyser and FT-IR spectroscopy. Water content appears similar in both compositions for analogous pressure conditions, varying from ~2.5 wt% at 50 MPa to ~5.8 at 200 MPa. Comparison of the experimental data with the thermodynamic models shows that the empirical model of Moore et al. [1998] better matches the experimental data for both compositions, while the thermodynamic models of Papale et al. [2006] and Ghiorso and Gualda [2015] tend to overestimate melt water content, probably due to the paucity of peralkaline melt compositions used for calibration. One inference of these new solubility data is on MI-derived depth of felsic reservoirs at Pantelleria which deepens from 2.4 to 3.5 km.

Keywords. Trachyte, Pantellerite, Water solubility, Experiments, Alkaline magmas.

Available online 8th September 2021

1. Introduction

Water solubility in silicate melts has been widely investigated because of the important effects it has on magma properties, such as viscosity and density [e.g. Dingwell et al., 1996, Richet et al.,

1996], liquidus and solidus temperatures, phase compositions [e.g. Sisson and Grove, 1993] and mineral stabilities [Housh and Luhr, 1991, Holtz et al., 1992], and crystallization kinetics [e.g. Watson, 1994, Cashman and Mangan, 1994, Arzilli et al., 2020] and eruptive dynamics [e.g. Cassidy et al., 2018]. Water solubility has been thoroughly investigated in basaltic and rhyolitic compositions [e.g. Hamilton et al., 1964, Silver et al., 1990, Dixon et al., 1995,

* Corresponding author.

Moore *et al.*, 1998, Behrens and Jantos, 2001, Tamic *et al.*, 2001, Liu *et al.*, 2005, Lesne *et al.*, 2010] for which the general effects of composition, particularly that of alkalis and silica contents [e.g. Johannes and Holtz, 1996, Romano *et al.*, 1996, Dingwell *et al.*, 1997, Holtz *et al.*, 2000, Behrens *et al.*, 2001, Schmidt and Behrens, 2008, Stabile *et al.*, 2018, 2020], and pressure–temperature are well established [e.g. Holtz *et al.*, 1992, 1995, Behrens *et al.*, 2001]. More recently, several studies have also focused their attention on intermediate compositions such as andesite–dacite [Mandeville *et al.*, 2002, Botcharnikov *et al.*, 2006, Behrens *et al.*, 2004], phonotephrite [Behrens *et al.*, 2009] and phonolite [Carroll and Blank, 1997, Larsen and Gardner, 2004, Iacono-Marziano *et al.*, 2007, Schmidt and Behrens, 2008] melts. In contrast, less attention has been paid to compositions such as trachytic melts, which usually represents the parental composition to peralkaline rhyolite/phonolite melts: only Di Matteo *et al.* [2004] and Fanara *et al.* [2015] have obtained solubility data on such compositions. Trachyte and pantellerite magmas are involved in explosive eruptions, some of which can be of large magnitude (e.g. Tambora 1815, Campanian Ignimbrite 39 kyr, Green Tuff 45 kyr), and it is therefore vital to accurately constrain water solubility in such melts. Enlarging the spectrum of available solubility data is also crucial to further improve already existing solubility models [e.g. Papale *et al.*, 2006, Ghiorso and Gualda, 2015].

Here, we present new experimental H₂O solubility data obtained on trachytic and pantelleritic melts over the pressure range of 50–300 MPa. The trachyte and pantellerite used in this study are representative of the most abundant magmas on Pantelleria island. The water contents dissolved in experimental glasses have been determined by FT–IR spectroscopy, Karl Fischer titration (KFT) and elemental analyser (EA). The necessity of performing additional experiments arises from the observed dependence of water solubility on the composition of silicate melts, as several studies quoted above have illustrated. In particular, a small variation in melt chemical composition influences not only water solubility but also the extrapolation of molar absorption coefficients. FT–IR spectroscopy is a common tool used to determine the water content of natural volcanic products (melt inclusions and glassy groundmasses) but its accuracy is strongly related to the use of proper absorp-

tion coefficients, calibrated on compositions similar to that of natural glasses investigated. Otherwise, the extrapolation of absorption coefficients outside the calibration range may lead to a significant error in water determination. For this reason, in this work, we also used the results of FT–IR spectroscopy, KFT and EA analyses to determine the IR molar absorption coefficients for 4500 and 5200 cm^{−1} bands by using the peak intensity and a straight line correction procedure [Stabile *et al.*, 2020, and reference therein].

2. Starting material and experimental strategy

2.1. Starting material and charges preparation

We used, as starting materials, natural samples representative of the trachytic and peralkaline rhyolite (pantellerite) of Pantelleria Island (Table 1). Pantelleria, located in the Sicily Channel, is the type locality for pantellerite, an iron-rich rhyolite characterized by alkali/alumina molar ratio [(Na₂O + K₂O)/Al₂O₃] > 1 [Macdonald, 1974]. Pantellerites and trachytes are the most abundant rocks outcropping in the island and also in other localities, usually representing the felsic end member in continental rift zones (Pantelleria, Ethiopian Rift valley, etc.) or in oceanic islands (Mayor Island, Azores, etc.). The trachyte (sample GTT) and pantellerite (sample Pan113) specimen used in this study have been the subject of phase equilibrium experiments by Di Carlo *et al.* [2010] and Romano *et al.* [2018, 2020]. To prepare the starting materials, the selected rocks were finely crushed and the resulting powders were melted twice at 1300 °C for 3 h, then rapidly quenched. The glasses obtained were grinded in an agate mortar obtaining a powder of 10–40 µm mesh size. This technique, used in several previous experimental works [Di Carlo *et al.*, 2010, Romano *et al.*, 2020], allows to produce a crystal-free and homogeneous glass with a composition similar to the starting bulk rock. Experimental charges were prepared by loading 50–100 mg of dry glass powder and 5–10 mg distilled water in gold capsules, ensuring volatile saturation at experimental conditions. At 50 MPa, the amount of water loaded was slightly lower, to avoid the risk of capsule rupture. Once prepared, capsules were weighed and welded, then weighed again to verify any water loss during welding. Gold capsules were preferred to platinum or gold–palladium containers in order to minimize iron loss to the capsule walls, since the duration

Table 1. Chemical composition of experimental glasses

	<i>T</i> (°C)	<i>P</i> (MPa)	SiO ₂	TiO ₂	Al ₂ O ₃	FeO	MnO	MgO	CaO	Na ₂ O	K ₂ O	P ₂ O ₅	Total	Original total	P.I.
Green Tuff Trachyte (GTT)															
Starting material			64.12	0.85	15.04	6.27	0.27	0.62	1.48	6.58	4.6	0.17	100		1.05
GT R11-1	950	50	65.27	0.87	15.07	5.32	0.19	0.63	1.45	6.74	4.7	0.21	100	94.82	1.07
sd			0.62	0.07	0.32	0.31	0.08	0.04	0.06	0.26	0.09	0.09		0.98	
GT R10-1	950	100	65.62	0.77	15.46	4.79	0.24	0.6	1.33	6.33	4.65	0.21	100	95.57	1.00
sd			0.55	0.08	0.17	0.25	0.09	0.03	0.05	0.73	0.16	0.07		0.89	
GT R 9-1	950	150	65.23	0.95	15.24	5.34	0.35	0.65	1.54	6.46	4.55	0.29	100	94.51	1.02
sd			0.36	0.07	0.11	0.23	0.07	0.03	0.04	0.81	0.18	0.09		0.94	
GT R 15-1	985	200	65.60	0.88	14.86	5.58	0.22	0.62	1.50	6.17	4.37	0.20	100	95.59	1.00
sd			0.36	0.10	0.18	0.26	0.12	0.03	0.06	0.62	0.14	0.09		0.67	
GT R 18-2	985	200	65.14	0.86	15.00	5.56	0.20	0.63	1.48	6.51	4.43	0.20	100	95.59	1.03
sd			0.46	0.09	0.22	0.19	0.09	0.03	0.05	0.56	0.14	0.08		0.73	
GT R19-1	985	300	65.06	0.80	15.04	5.25	0.23	0.61	1.42	7.14	4.28	0.18	100	91.76	1.09
sd			0.33	0.11	0.15	0.29	0.11	0.03	0.04	0.35	0.11	0.09		0.57	
GT R16-1	985	300	65.28	0.87	15.55	5.64	0.21	0.60	1.50	5.39	4.57	0.39	100	90.84	0.89
sd			0.74	0.09	0.65	0.26	0.10	0.03	0.05	0.20	0.16	0.12		0.50	
Pantellerite (Pan113)															
Starting Material			69.45	0.48	10.15	7.87	0.21	0.10	0.53	6.71	4.46	0.04	100		1.56
Run C-Run L	850	50	72.64	0.37	10.90	5.28	0.32	0.19	0.35	5.02	4.94		100	93.49	1.25
sd			0.96	0.11	0.33	0.56	0.16	0.21	0.38	0.21	0.17			0.69	
Run A-RunH	850	100	72.56	0.44	11.20	4.85	0.23	0.22	0.37	5.12	5.00		100	91.89	1.24
sd			0.47	0.07	0.14	0.27	0.14	0.03	0.03	0.58	0.19			0.38	
Run B2	850	150	72.83	0.36	11.61	4.40	0.30	0.15	0.23	5.03	5.09		100	90.06	1.19
sd			0.14	0.06	0.13	0.16	0.10	0.04	0.05	0.21	0.17			0.56	
Run F	850	200	70.91	0.42	10.35	7.58	0.29	0.08	0.51	5.16	4.61		100	89.25	1.30
sd			0.31	0.06	0.15	0.23	0.13	0.01	0.09	0.10	0.13			0.76	

sd: standard deviation; P.I.: peralkalinity index.

of the experiments exceeded the 24 h. The applied temperature was higher than 950 °C for trachytes and 850 °C for pantellerites, conditions that in both cases ensured to be above the liquidus in our experimental runs [Di Carlo *et al.*, 2010, Romano *et al.*, 2018, 2020]. Prior to experiments, capsules were left at least for 24 h in an oven at 120 °C to allow the homogenisation of water throughout the capsule.

2.2. Experimental strategy

Experiments were performed in internally heated pressure vessels (at Institut des Sciences de la Terre d'Orléans) equipped with a molybdenum furnace and a fast quench device. As pressurizing medium, a mixture of argon and hydrogen loaded in the vessel at room temperature was used: the Ar/H₂ ratio was fixed to reach redox condition around the FMQ buffer [e.g. Scaillet *et al.*, 1992, 1995, Romano *et al.*, 2020]. The pressure was recorded by a transducer calibrated against an Heise-Bourdon tube gauge (uncertainty ± 20 bar) while the temperature

was continuously controlled through S-type thermocouples (accuracy ± 5 °C). Experiments were performed in a *T* range 950–985 °C for trachytes and at 850 °C for pantellerites. The pressure range explored varied from 50 to 300 MPa (at 50 MPa intervals) and the duration of each experiment was between 96 and 125 h. Experiments were terminated using the drop-quench technique, which ensures a fast quench of the capsules from the top to the bottom of the vessel (quench rate >100 °C·s⁻¹). After the experiments, capsules were weighed to check for leaks and if the post run weight difference was >0.4 mg, capsules were discarded. The excess of H₂O within the capsule was confirmed by the occurrence of small water drops during the opening of the capsules, establishing that saturation conditions were reached during the experiment. For each capsule, around one-third of the run product was embedded in epoxy resin for qualitative analysis by a scanning electron microscope (SEM-EDS) and chemical analysis by an electron microprobe (EMP) while the remaining part was used to determine water contents.

3. Analytical methods

3.1. Scanning electron microscope and electron microprobe analyses

Glass fragments mounted in epoxy resin were first observed with a SEM and then analysed by an EMP to check glass for composition and homogeneity. EMP analyses were performed with a Cameca SX-Five located at CNRS-ISTO laboratory (France). Analytical conditions were an accelerating voltage of 15 kV, a beam current of 6 nA and a defocused beam of $10 \times 10 \mu\text{m}$. Na and K were analysed first to minimize volatile loss during the analyses. Microprobe analyses of alkali-rich hydrous glasses in some cases resulted problematic due to the alkali (mostly sodium) migration out of the excited volume. As suggested by Morgan and London [2005], we have used a current density of $0.006 \text{ nA}/\mu\text{m}^2$ that limits the Na migration under the beam and also provides adequate excitation of all elements.

3.2. Karl Fischer titration and elemental analyser

The total water contents of experimental glasses were determined by KFT and EA (EA Thermo Scientific Flash 2000) both housed at CNRS-ISTO laboratory. In KFT analysis, 10–20 mg of glass fragments are placed within a Pt crucible in an induction furnace and heated up to 1300°C . Water liberated during the heating of glass fragments reacts quantitatively in a titration cell with iodine. The EA allows determining the concentration of H–C–N in experimental samples. In our case, only H_2 was measured to infer water content. The glass in the EA is first heated to 1800°C upon which the substance oxidizes into simple compounds, which are in turn quantified by thermal conductivity detection. Moussallam *et al.* [2015] used this technique to determine water and CO_2 contents in kimberlite melts. The EA was calibrated before each analytical session using pure pyrophyllite, which is known to contain 5 wt% of stoichiometric H_2O in its crystalline structure. The experimental samples for the EA were prepared by grinding 1–10 mg of experimental glass into a fine powder and then loading it in a tin capsule folder. The instrument was tested repeatedly using an international standard with known amounts of carbon, hydrogen and

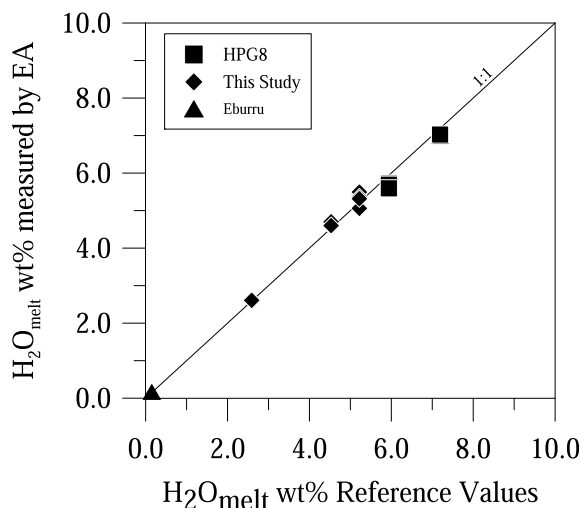


Figure 1. Comparison between water content in silica-rich melts analysed by EA and KFT; analyses on experimental glasses synthesized in this study, haplogranite (HPG8) composition [Dingwell *et al.*, 1997] and Eburru obsidian [Scaillet and Macdonald, 2006].

nitrogen and also using other hydrated glass samples (as internal standards) prepared for this purpose and for which water concentration was already known (haplogranite) or already analysed with KFT. In Figure 1 (Table 2), the water content determined by EA is compared with literature data for haplogranite composition [Dingwell *et al.*, 1997], Eburru obsidian [Scaillet and Macdonald, 2006] and KFT analyses of this study; a good correlation is observed between H_2O contents retrieved by these different techniques.

3.3. Density determination

Densities of anhydrous trachytic and pantelleritic starting glasses were measured by weighing single pieces of glass in air and ethanol. The determination of hydrous glass densities was more difficult because of the limited amount of run products; a minimum weight of 15 mg is indeed required to perform an accurate Archimedean density measure. Only for three hydrous trachytic glasses were reliable density data obtained (Figure 2a, Table 3), which was used to derive an empirical relationship of the form $\rho = -4.4017(\text{H}_2\text{O}_{\text{melt}}) \text{ wt\%} + 2329$. Standard deviation for

Table 2. Comparison of water content measured by Elemental Analyser and reference value

	Experimental pressure (MPa)	Elemental analyser	Reference values*
HPG8 GT R18-5	200	5.72	5.94
HPG8 GT R18-5	200	5.69	5.94
HPG8 GT R18-5	200	5.59	5.94
HPG8 GT R19-4	300	6.99	7.19
HPG8 GT R19-4	300	6.99	7.19
HPG8 GT R19-4	300	7.03	7.19
Pan 113 RUNB-1	150	5.06	5.22
Pan 113 RUNB	150	5.49	5.22
Pan 113 RUNB-2	150	5.36	5.22
Pan 113 RUN B	150	5.32	5.22
Pan 113 RUN C	50	2.61	2.59
Pan 113 RUNH	100	4.70	4.53
Pan 113 RUNH	100	4.57	4.53
Pan 113 RUNH	100	4.60	4.53
Eburru natural sample		0.17	0.15

* Reference value for HPG8 are from Dingwell *et al.* [1997].

Pan 113 and Eburru natural sample were analysed by Karl Fischer titration.

density values was estimated from repeated measures of glass fragments. For comparison, the densities of hydrous experimental glasses were also calculated using the procedure of Ochs and Lange [1999], calculated values being 4 to 11% higher than those measured. A less clear relationship has been found between density and melt water content for pantelleritic experimental glasses (Figure 2b, Table 3) and calculated densities are 1 to 6% higher relative to measured ones. To maintain internal consistency, we preferred to use the density measured or calculated from the above empirical relationship, knowing that density measurements are affected by relative errors in the range 0.1–2.5%.

3.4. FT-IR spectroscopy

Fourier Transform Infrared analyses were performed using a Nicolet 760 Magna spectrometer connected to an IR microscope (fluxed with H₂O-free compressed air) housed at ISTO laboratory. The spectrometer was equipped with an MCT detector, a Globar light source and a KBr beam splitter. Absorption spectra were acquired for each sample in the range 1000–6000 cm⁻¹ with 128 scans and a resolution of 4 cm⁻¹. Experimental glass chip samples were placed on an NaCl crystal plate, which is transparent

to the infrared beam; for each glass chip 3–5 points (50 × 50 μm spot size) were analysed. Experimental glasses were double-polished to obtain 100–300 μm thin wafers, and then carefully washed under acetone and ethanol in order to remove any impurities. The areas of the sample analysed were always checked optically to avoid bubble or impurities. The thickness of each glass chip was measured microscopically during the analysis, with an uncertainty of ±1–3 μm. Absorption spectra were converted in H₂O concentration according to the Beer–Lambert equation:

$$C \text{ (wt\%)} = (MW * A) / t * \rho * \epsilon, \quad (1)$$

where C (wt%) is the water content dissolved in the melt, MW the molecular weight of water, A the height of the absorbance peak, t the thickness (cm) of the glass wafer, ρ the density (g/l) of the glass and ε the molar absorption extinction coefficient (L·mol⁻¹·cm⁻¹). To calculate the water content, we considered the absorption bands at 5200 cm⁻¹ (molecular H₂O) and 4500 cm⁻¹ (OH⁻ concentration) of the IR spectra. Only for a few samples the fundamental OH⁻ stretching vibration at 3530 cm⁻¹ was also measured, which required glass wafers of extremely thin thickness (<30 μm); thickness measures in the range 40–60 ± 2 μm are affected by a relative error of 2–5% while for a higher range of

Table 3. Experimental conditions and results of near-infrared FT-IR spectroscopy, elemental analyser and KFT analyses

	<i>T</i> (°C)	<i>P</i> (MPa)	H ₂ O _t (wt%- EA)	H ₂ O (wt%- KFT)	Density (g/L)*	Density (g/L)**	Thickness (cm)	A (OH ⁻)	sd	A (H ₂ O _{mol})	sd	OH (wt%)	sd	H ₂ O _m (wt%)	sd	H ₂ O wt% (FT-IR)	sd
Trachyte Starting Material					2330	2590											
GTT R11-1	950	50	2.86		2317		0.0273	0.0433	0.0039	0.0768	0.0060	1.35	0.03	1.33	0.10	2.68	0.07
GTT R10-1	950	100	3.84		2310	2460	0.0268	0.0525	0.0037	0.1210	0.0041	1.81	0.14	2.19	0.14	4.00	0.26
GTT R 9-1	950	150	4.95		2308		0.0177	0.0380	0.0016	0.1062	0.0044	1.92	0.04	2.86	0.11	4.78	0.13
GTT R 15-1	985	200	5.98 (±0.08)		2304		0.0193	0.0410	0.0023	0.1514	0.0094	1.89	0.20	3.70	0.24	5.73	0.42
GTT R 18-2	985	200	5.87 (±0.23)		2304		0.0208	0.0424	0.0032	0.1780	0.0102	1.81	0.15	4.03	0.29	5.89	0.28
GTT R16-1	985	300	6.87 (±0.04)		2298	2400	0.0286	0.0644	0.0062	0.3294	0.0083	2.00	0.19	5.42	0.11	7.42	0.25
GTT R19-1	985	300	7.37 (±0.20)		2400		0.0211	0.0415	0.0054	0.1980	0.0143	1.75	0.21	4.42	0.29	6.17	0.45
Pantellerite Starting Material (Pan113)					2471	2547											
Pan113 Run C-Run L	850	50	2.61	2.59	2411	2434	0.0178	0.0327	0.0015	0.0633	0.0015	1.14	0.13	1.41	0.13	2.56	0.26
Pan113 Run A-RunH	850	100	4.62 (±0.06)	4.53	2345	2390	0.0196	0.0460	0.0026	0.1528	0.0155	1.49	0.12	3.17	0.36	4.66	0.35
Pan113 Run B2	850	150	5.30 (±0.22)	5.22	233	2366											
Pan113 Run F-Run I	850	200		5.79	2382	2404	0.0182	0.0415	0.0031	0.1953	0.0033	1.43	0.11	4.29	0.10	5.72	0.20
Pan113 Run I	850	200			2310		0.0172	0.0375	0.0019	0.1813	0.0041	1.40	0.06	4.35	0.08	5.75	

Density (g/L)*: Density calculated from Archimedeian density measure; Density (g/L)**: density from Ochs and Lange [1999] procedure; AOH- and AH₂O: absorbance; sd: standard deviation.

thickness measures (~200 µm) an incertitude in ±10 correspond to a relative error of 5%.

4. Results

4.1. Microscopic observation and major element analyses

The run products consisted of microlite-free glasses. Most of the quenched glasses present also bubbles at the melt/capsule interface indicating fluid saturation during the experiment; however, bubble content never exceeded the 0.1 vol.%. Major element composition of experimental glasses (Table 1) resulting from analyses with a defocused beam (10 × 10 µm) [Morgan and London, 2005] matches in a high extent the composition of starting materials.

4.2. Water solubility in trachyte and pantelleritic melts

The total H₂O content dissolved in experimental glasses is reported in Table 3. Water content ranges from 2.9 wt% at 50 MPa to 7.1 wt% at 300 MPa for trachytic experimental glasses. At 200 and 300 MPa, two additional experiments were performed to check for the reproducibility of H₂O solubility at high pressure (Table 3). In pantelleritic experimental glasses,

the water content ranges from 2.6 at 50 MPa to 5.8 at 200 MPa and also in this case two additional experiments were performed at 2 MPa (Table 3). Figure 3(a,b) shows the variation of water content dissolved in the melt against pressure, confirming the general trend of increasing melt water content with increasing pressure as observed for all silicate melts (from basalt to rhyolite). The water solubility data in trachyte melt as a function of pressure can be described through an equation of the form $C_{H_2O_{melt}} = 0.3557 * P^{0.526}$ ($R^2 = 0.994$), where P is pressure in MPa. For pantellerites, a similar power law describes the variation of melt water content with pressure reading as: $C_{H_2O_{melt}} = 0.2786 * P^{0.5834}$ ($R^2 = 0.957$). All experimental studies on trachyte and pantellerite melts show an increase of melt water concentration with pressure but yield different slopes. Our experimental results will be compared below with available experimental data on Campi Flegrei trachytes [Di Matteo et al., 2004, Fanara et al., 2015] and with the experimental data of Stabile et al. [2018] on Kenyan haplo-pantellerites.

4.3. Analyses of IR spectra and molar absorption coefficients calibration

The bands of IR spectra at 5200 cm⁻¹ and 4500 cm⁻¹ for water species are the most used to determine water content in geological samples (Figure 4). The

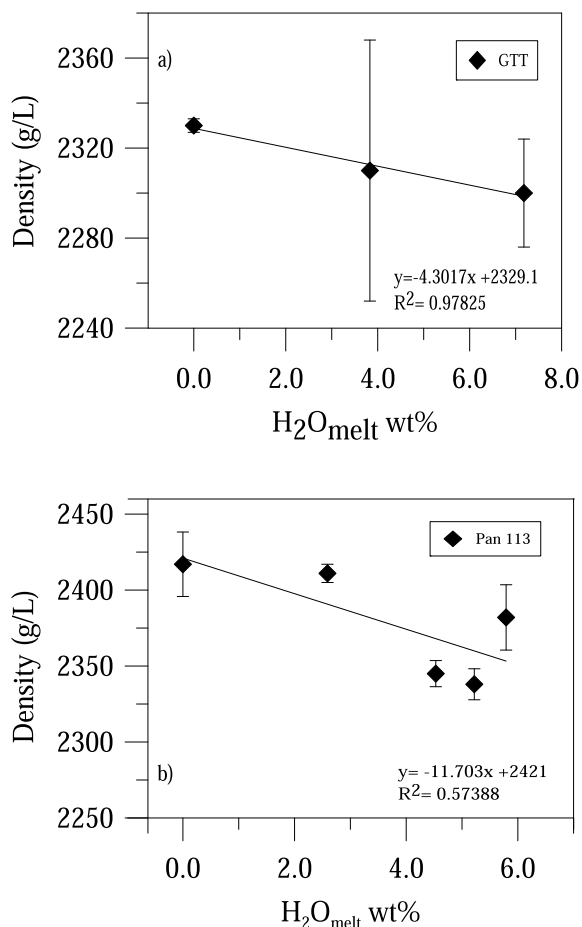


Figure 2. Dissolved H₂O_{melt} versus glass density measured through the Archimedeian method. Error bars indicate the standard deviation of repeated (~10) measures.

former is assigned to the combination of stretching and bending mode of H₂O molecules (H₂O_m) while the second to the combination of stretching and bending of hydroxyls (OH⁻) groups [Stolper, 1982]. To avoid an incorrect estimation of absorption band peak height, a baseline correction is required. Following the previous studies of Withers and Behrens [1999], Ohlhorst *et al.* [2001] and Mandeville *et al.* [2002], we used a simple straight baseline [TT baseline, Ohlhorst *et al.*, 2001] connecting 4500 and 5200 backgrounds. We preferred to use this simple procedure knowing that a possible small underestimation of OH⁻ band cannot be excluded, owing to the presence of the 4000 cm⁻¹ band. As suggested by Stabile *et al.* [2020], depending on sample compo-

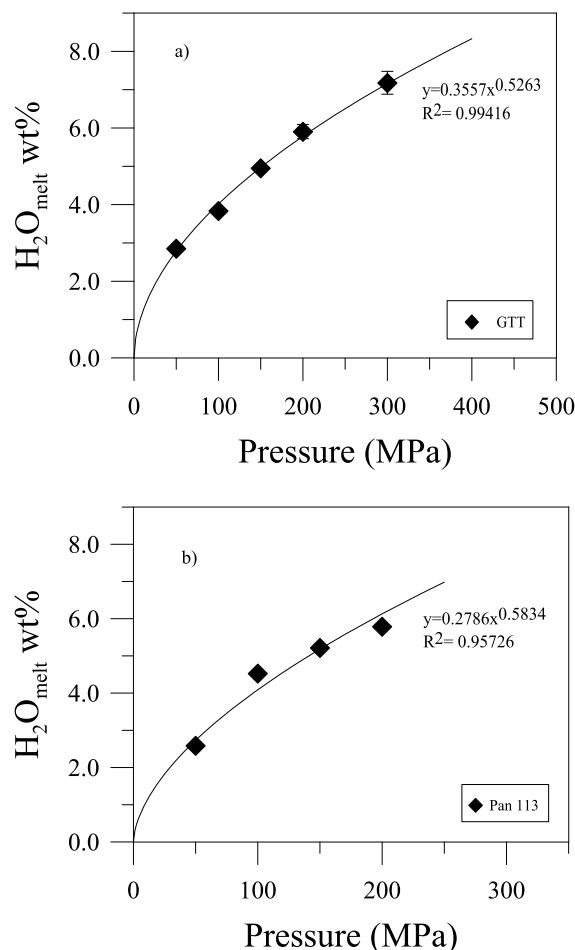


Figure 3. Dissolved H₂O_{melt} as a function of pressure for trachyte (a) and pantellerite (b) melt compositions.

sition and spectral variation, a critical evaluation of the approach used for the baseline correction has to be taken into account. Absorbance (peak intensity), density and thickness of the glass allow us to determine molar absorption coefficients (ϵ), in our case for the bands of molecular H₂O (5200 cm⁻¹) and OH⁻ groups (4500 cm⁻¹). The total water content dissolved in the experimental glasses is the sum of water species (H₂O_m and OH⁻) and the Beer-Lambert equation can be rewritten as:

$$C \text{ (wt\%)} = C_{\text{H}_2\text{O}} + C_{\text{OH}^-} = 18.01 * A_{4500} / \rho * t * \epsilon_{4500} + 18.01 * A_{5200} / \rho * t * \epsilon_{5200}. \quad (2)$$

Knowing C (wt%) from KFT or EA, Equation (2) can be solved to determine the molar absorption

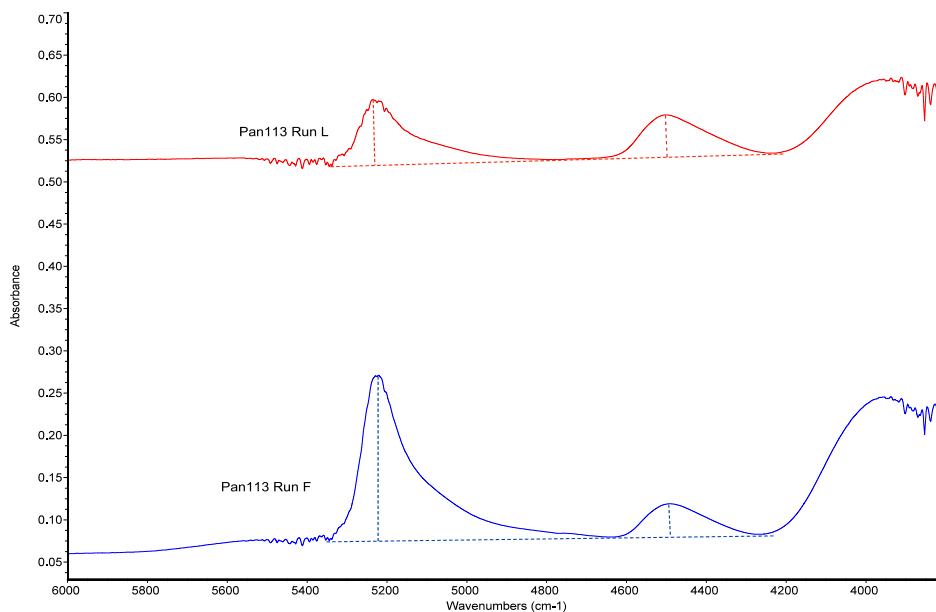


Figure 4. Near-infrared spectrum showing the two peaks related to OH^- group (at 4500 cm^{-1}) and molecular water (5200 cm^{-1}). The dashed lines tangential to the minima connecting the 4500 and the 5200 cm^{-1} peaks are illustrated to indicate the TT baseline correction procedure.

coefficients by plotting the absorbance of 5200 and 4500 bands normalized to density, thickness and water content. Using a linear regression the intercepts on X and Y axes are the ϵ_{4500} and ϵ_{5200} values (Figure 5a,b). Molar absorption coefficients were calculated assuming a linear relationship between the water species concentration and intensities of IR spectra bands. We obtained, for trachytic glasses, absorption coefficients of $0.88\text{ L/mol}\cdot\text{cm}^{-1}$ (ϵ_{4500}) and $1.6\text{ L/mol}\cdot\text{cm}^{-1}$ (ϵ_{5200}) while for pantellerite glasses ϵ_{4500} is $1.21\text{ L/mol}\cdot\text{cm}^{-1}$ and (ϵ_{5200}) $1.89\text{ L/mol}\cdot\text{cm}^{-1}$. Molar absorption coefficients are calibrated for a melt water content ranging between 2.6 and 7.4 in trachytic glasses and between 2.6 and 5.8 for pantelleritic ones. Regarding the uncertainties on the thickness and density measures, we can consider that the epsilon values are affected by relative errors in the range 2 – 7% .

5. Discussion

5.1. Comparison with previous works

(i) Trachyte compositions. Di Matteo *et al.* [2004] and Fanara *et al.* [2015] presented solubility experi-

ments on Campi Flegrei trachytes, obtained between 25 and 50 MPa (Figure 6a,b). Campi Flegrei trachytes are broadly similar in composition to Pantelleria trachytes, having a lower content in calcium, aluminium, potassium together with similar or slightly higher contents in silica, iron and sodium. Our solubility curve differs significantly from that of Di Matteo *et al.* [2004]. For instance, at 100 MPa the GTT melt has $\sim 1.2\text{ wt}\%$ less H_2O compared to the trend obtained by Di Matteo *et al.* [2004], the difference between the two sets of data increasing with pressure. Considering also the more mafic trachyte used by Di Matteo *et al.* [2004] (Pr38P), the difference in water content at 150 and 200 MPa is 0.94 to $1.6\text{ wt}\%$ lower. Compared to the experimental results of Fanara *et al.* [2015], melt water contents in our experiments are $0.4\text{ wt}\%$ to $0.7\text{ wt}\%$ higher in the investigated pressure range (100 – 300 MPa). The relationship between water solubility and pressure can be also compared with the calculated water solubility models of Moore *et al.* [1998], Papale *et al.* [2006] and Ghiorso and Gualda [2015] using GTT and Pan113 as starting compositions. Calculated values with Papale *et al.* model are higher by $0.5\text{ wt}\%$ to $1\text{ wt}\%$, depending on pressure, while Ghiorso and Gualda [2015]’s model calculates

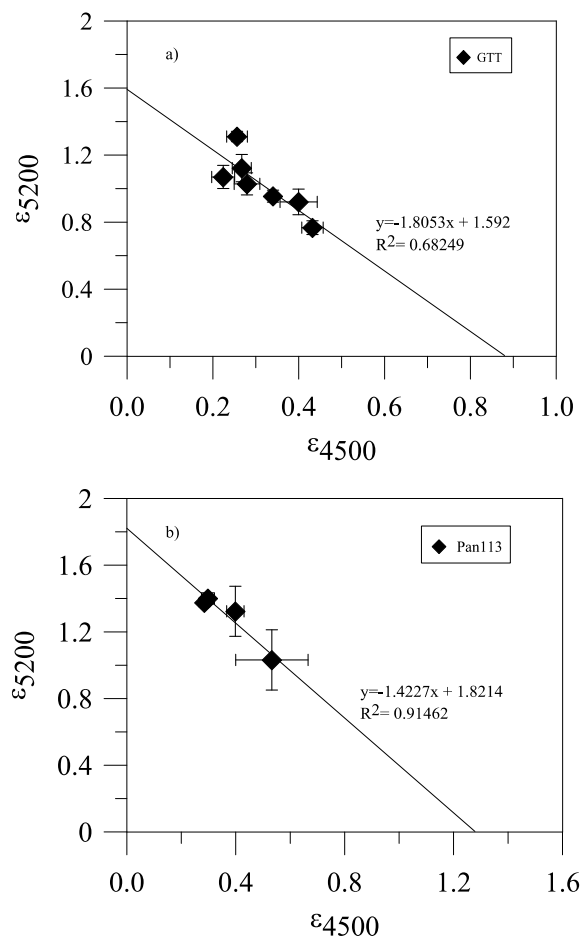


Figure 5. Resolution of Equation (2) in the text to obtain the molar absorptivity coefficient ϵ_{4500} and ϵ_{5200} . Each point is calculated from Equation (2). Normalized absorbance obtained for (a) trachyte and (b) pantellerite.

values that are higher by 0.3–0.7 wt% below 200 MPa, but at pressures >300 MPa the difference exceeds 1 wt%. On the contrary, Moore *et al.* [1998] matches better our experimental data, to within 0.1–0.4 wt% (Figure 6a).

(ii) Pantellerite compositions. Our experimental results on pantelleritic melt can be compared with the recent experimental works of Stabile *et al.* [2018] and Moore *et al.* [1998]. The solubility curves show notable differences, the water content of our pantelleritic melt at 100 MPa being ~1 wt% lower and up to ~2 wt% lower at higher pressure relative to the data of Stabile *et al.* [2018]; our solubility data are very simi-

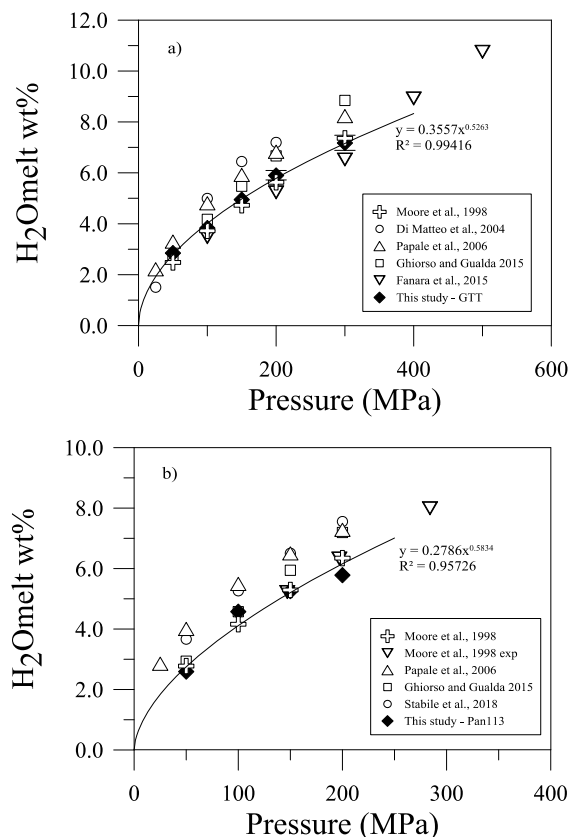


Figure 6. Water contents solubilized in the melt as a function of pressure obtained in this study for trachyte and pantellerite compared with (a) Di Matteo *et al.* [2004], Fanara *et al.* [2015] experimental data and solubility models of Moore *et al.* [1998], Papale *et al.* [2006] and Ghiorso and Gualda [2015]. Experimental results on pantellerite compared with (b) Moore *et al.* [1998], Stabile *et al.* [2018] experimental data and solubility models of Moore *et al.* [1998], Papale *et al.* [2006] and Ghiorso and Gualda [2015].

lar to the experimental results of Moore *et al.* [1998] at 150 and 200 MPa (Figure 6b) remembering that Stabile *et al.* data are based on synthetic pantellerite. The water solubility model of Papale *et al.* [2006] predicts water content higher than 1 wt% to 1.5 wt% than those of our experiments while considering the Ghiorso and Gualda [2015]'s model, the difference between the calculated solubility and the experimental data ranges between 0.2 wt% and 1.2 wt%. Over-

Table 4. Chemical composition of trachyte [Di Matteo *et al.*, 2004] and pantellerite [Moore *et al.*, 1998, Stabile *et al.*, 2018] used in other experimental studies

	Di Matteo <i>et al.</i> [2004]	Fanara <i>et al.</i> [2015]	This study	Moore <i>et al.</i> [1998]	Stabile <i>et al.</i> [2018]	This study
	ZAC		GTT	NZC-4	Ebu-B	Pan 113
SiO ₂	61.71	60.31	64.12	71.8	76.58	69.45
TiO ₂	0.45	0.42	0.85	0.24		0.48
Al ₂ O ₃	18.56	18.32	15.04	9.7	8.48	10.15
FeO*	3.17	5.21	6.27	5.77	5.48	7.87
MnO	0.27		0.27	0.14		0.21
MgO	0.23	1.31	0.62	0.01	0.02	0.1
CaO	1.64	4.11	1.48	0.2	0.23	0.53
Na ₂ O	6.11	2.81	6.58	5.3	4.72	6.71
K ₂ O	7.09	7.47	4.6	4.47	3.68	4.46
P ₂ O ₅	0.02		0.17	0.02		0.04
Total	99.25	100.08	100	97.6	99.2	100
P.I.	0.95	0.69	1.05	1.40	1.39	1.40

all, the model of Moore *et al.* [1998] better reproduces our experimental solubility data, these latter resulting lower by 0.1 to 0.5 wt% of the calculated ones. In contrast, the model of Papale *et al.* [2006] tends to overestimate significantly the melt water contents of our compositions.

(iii) The effect of small variations in bulk composition. To a first approximation, these differences in water solubility can be ascribed to small differences in chemical composition between the starting materials considered (Table 4). As stated previously, the dependence of water solubility in trachyte and pantelleritic melts with respect to small variation in chemical composition has not yet been fully investigated. For instance, the trachyte of this study has aluminium and potassium content almost 3 wt% lower with respect to the trachyte and trachyphonolite of Di Matteo *et al.* [2004] and Fanara *et al.* [2015] which has a higher K/Na ratio (0.71 respect to 0.46 of GTT trachyte); on the contrary, the GTT trachyte has higher silica and iron contents. Considering pantelleritic composition [Moore *et al.*, 1998, Stabile *et al.*, 2018], the differences in water solubility are also related to slight differences in melt composition (Table 4). Our pantellerite and that of Moore *et al.* [1998] indeed present similar oxides concentration with respect to that of Stabile *et al.* [2018], which has lower iron, aluminium, sodium and higher silica content. Water solubility has been also shown to correlate positively with metal ionization potential and negatively with Al₂O₃ content [Behrens and Jantos, 2001, Mysen, 2002]. Di Matteo

et al. [2004] and Stabile *et al.* [2018] explored the effect of alkalis on water solubility evidencing that for both trachyte and pantellerite melts, higher Na content favour H₂O incorporation in the melt, in accord with other studies on silicic compositions [Holtz *et al.*, 1995, Dingwell *et al.*, 1997, Carroll and Blank, 1997]. All these effects may explain the range in water contents obtained at the same P–T between the different sets of experiments. We note, however, that our comparison with previous experimental studies does not take into account the difference in experimental temperature, yet a clear relationship between temperature and water solubility has been evidenced for rhyolite [Yamashita, 1999] and phonolite melts [Schmidt and Behrens, 2008]. Such an effect still needs to be determined for peralkaline felsic compositions.

5.2. Effect of molar absorption coefficients

The molar absorption coefficients determined for our experimental glasses differ from those determined previously for trachytic by Di Matteo *et al.* [2004] and Fanara *et al.* [2015] and pantelleritic glasses by Stabile *et al.* [2020]. As stated above, molar absorption coefficients are determined assuming that they are constant over the range of water contents considered [Silver *et al.*, 1990]. The general agreement between water contents obtained with EA (Figure 7a) and KFT (Figure 7b) versus the total water content obtained by FT-IR spectroscopy, using the calibrated absorption coefficients, supports such an

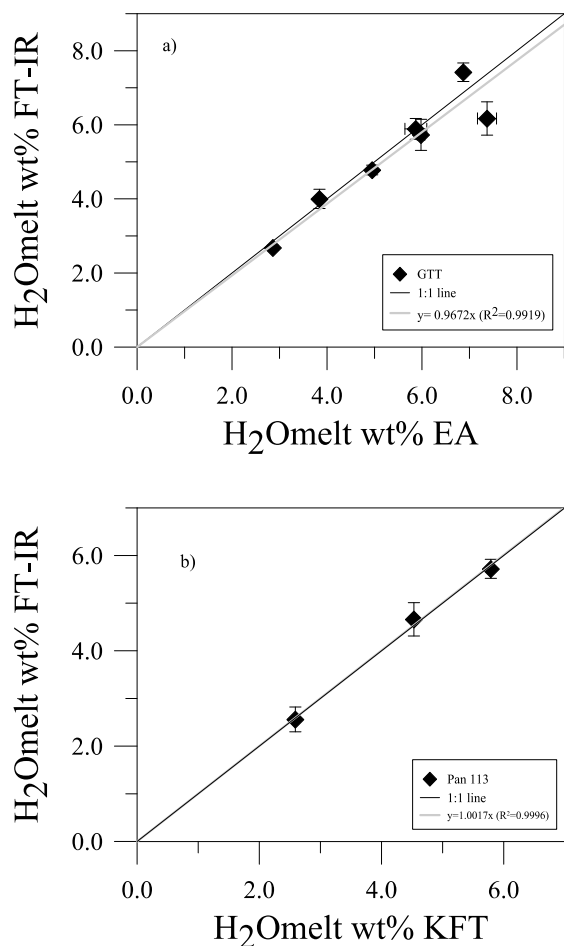


Figure 7. Total water content measured by elemental analyser (EA) and KFT versus water content obtained from FT-IR spectroscopy analysis for (a) trachyte and (b) pantellerite.

assumption (Figure 7a,b). There is a general consensus on the fact that absorption coefficients are composition dependent. Dixon *et al.* [1995] evidenced that absorption coefficients (ϵ_{4500} , ϵ_{5200}) correlate positively with the sum of cations Si and Al, suggesting that such a linear relationship can be used to calculate molar absorptivities of silicate melts. Other studies have shown a relation of ϵ with Na/K ratio, silica content and excess of aluminium [Stolper, 1982, Silver *et al.*, 1990, Behrens *et al.*, 1996] while Ohlhorst *et al.* [2001] reported a systematic increase of absorption coefficients from basalt to rhyolite and proposed a parabolic equation to calculate ϵ as a

function of silica content. The calculated absorption coefficients proposed for glasses having similar SiO_2 content to our trachyte and pantellerite [Ohlhorst *et al.*, 2001] are broadly similar to that determined in our study; yet, several authors [e.g. Dixon *et al.*, 1995, Mandeville *et al.*, 2002] suggest that a direct calibration for a specific composition yield to most accurate results. With respect to the published epsilon values on trachyte, we note that our epsilon values are 14–45% higher for $\epsilon(H_2O)$ and 26–44% lower for $\epsilon(OH)$; for pantelleritic glasses, $\epsilon(H_2O)$ is 2% lower and $\epsilon(OH)$ is 20% higher with respect to the value of Stabile *et al.* [2020]. Anyway, we used the absorption coefficients obtained in the studies on experimental glasses of Di Matteo *et al.* [2004], Fanara *et al.* [2015] for trachyte and Stabile *et al.* [2020] for pantellerite (Table 5). Using the absorption coefficients obtained by Di Matteo *et al.* [2004] to determine the water content from our IR spectra decreases the retrieved values; for instance, at 100 MPa the melt water content decrease from 5 to 4.6, i.e. values are 8% lower. On the other hand, if our absorption coefficients are used on the data of Di Matteo *et al.* [2004], their water contents increase by 0.1–0.6 wt%. Doing the same exercise on pantelleritic glasses, and using the absorption coefficients of Stabile *et al.* [2020], the water content increase by 0.04–0.4 wt%. Using our absorption coefficients for the data of Stabile *et al.* [2020], the water content decrease by 0.2–0.5 wt%. Differences in absorption coefficients influence above all the estimation of water species that could reflect either an incorrect estimation of OH^- relative to molecular species or the opposite. Taking as an example our results on pantellerite glasses, the OH/H_2O_m ratio increases from 0.07 to 0.2 when the absorption coefficients of Stabile *et al.* [2020] are used (i.e. ϵ_{4500} is 0.98 L/(mol·cm⁻¹) instead of 1.21 L/(mol·cm⁻¹) as determined in our study).

5.3. Water speciation

Water species concentration (OH^- and H_2O_m) in the experimental glasses as a function of total water content are shown in Figure 8a,b, for trachyte and pantelleritic glasses. As already shown for other quenched hydrous glasses, the OH^- group concentration is higher at low water content whereas molecular H_2O dominates for water contents above ~3 wt% [e.g. Stolper, 1982, Xue and Kanzaki, 2004, Dixon

Table 5. Molar absorption coefficients for OH⁻ and H₂O_m species for trachyte and pantellerite hydrous glasses

	SiO ₂ (wt%)	Al ₂ O ₃ (wt%)	Na/Na+K	ϵ (OH) L/mol·cm ⁻¹	ϵ (H ₂ O) L/mol·cm ⁻¹
Trachyte					
This Study	64.12	15.04	0.47	0.88	1.6
Di Matteo et al. [2004]	61.71	18.56	0.35	1.58	1.36
Fanara et al. [2015]	60.31	18.32	0.19	1.19	0.98
Pantellerite					
This Study	69.45	10.15	0.49	1.21	1.89
Stabile et al. [2020]	76.6	8.55	0.45	0.98	1.92

et al., 1995, Carroll and Blank, 1997, Withers and Behrens, 1999]. Our experimental glasses have water contents higher than 2.5 wt% so that we cannot appreciate the water speciation at low water concentrations. Anyway, it is evident in Figure 8a that the experimental glass with ~2.5 wt% represents the point at which OH⁻ and H₂O_m are present at equivalent concentrations. This appears less clear in the experimental glasses of pantelleritic composition, in which molecular water is slightly higher than OH⁻ at total water contents around 2.5 wt%. However, the speciation model of Dixon et al. [1995] and the experimental results on water speciation seem to be in good agreement within errors. Molecular water and hydroxyl species proportion in the experimental glasses at room temperature may reflect the structural re-equilibration during quench; this leads to an increase of molecular H₂O over hydroxyls with respect to the proportions at high temperature and pressure conditions [Silver et al., 1990, Zhang et al., 1995, Nowak and Behrens, 1995, Carroll and Blank, 1997]. For instance, Withers and Behrens [1999] investigated the effect of quenching on rhyolitic glasses containing 3 and 5 wt% H₂O. Glasses with initial OH/H₂O ratios of 1 and 0.6, after being reheated at 800 °C and at 300 MPa and rapidly quenched, showed a slight increase of their OH/H₂O ratios (1.17 and 0.72, respectively); they inferred that effect of quenching rate on water speciation was relatively minor at that melt water content. This gives information on the apparent equilibrium temperature (T_{ae}) [Zhang, 1994, 1999] considered the equilibrium temperature corresponding to the final speciation. However, we do not have sufficient data to appreciate if such a conclusion equally applies to other melt water contents.

5.4. Volcanological implications

Trachyte and pantellerite of Pantelleria show a similar capability to solubilize water content in the melt. We note only a subtle difference between the two compositions, water content in pantellerites being slightly higher (but always <1 wt%) with respect to trachytes. As evidenced by several works performed on melt inclusions [Lanzo et al., 2013, and references therein], water contents characteristic of natural pantellerites of Pantelleria are in the range 2–4.9 wt%. To date, the difference in H₂O content has not yet been related with changes in eruptive dynamic of pantelleritic products (lava flow, strombolian and sub-plinian eruptions). However, a part of water, other factors can play an important role in controlling the eruptive styles [Cassidy et al., 2018] as already identified for mafic volcanism in a typical basaltic volcano as Mt. Etna [Moretti et al., 2018, and reference therein]. The study of water solubility in silicate melts has several implications for the study of hydrous natural glasses (melt inclusions and glass matrices). Ideally, melt inclusion studies allow one to assess the pre-eruptive volatile content of a magma, which can be then used to infer the (minimum) entrapment pressure (i.e. storage conditions if entrapment occurs in the reservoir) considering adequate solubility models and absence of diffusion towards the host crystal, post entrapment crystallization, etc. In the case of Pantelleria, several recent studies have determined the volatile content of melt inclusions trapped in phenocrysts of trachytic and pantelleritic rocks [Neave et al., 2012, Lanzo et al., 2013, Romano et al., 2019] of some key explosive eruptions. The maximum water content measured in melt inclusion with pantelleritic composition was

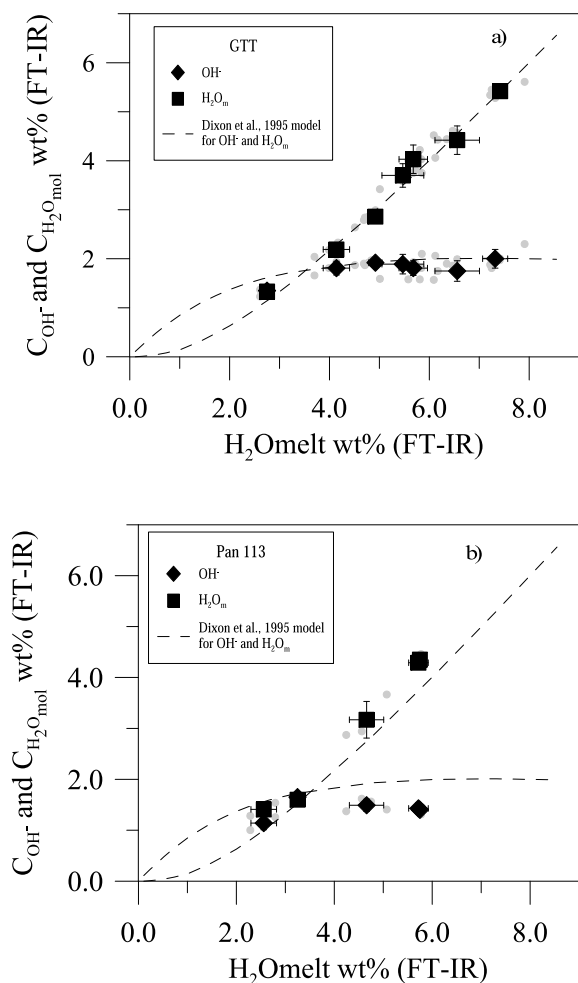


Figure 8. Water speciation in experimental glasses in (a) trachytic and (b) pantelleritic compositions. Grey dots are single point analysis while black ones represent the average values. Experimental data are compared with the model of Dixon et al. [1995].

4.5 wt% [Lanzo et al., 2013] while the water content estimated for trachytic melt through thermodynamical modelling and mass balance by White et al. [2009] ranges between 3.4 and 4 wt%. Romano et al. [2019] report water contents in melt inclusions of trachytic composition (0.15 to 1.05 wt%), suggesting that melt inclusions experienced volatile loss through the crystals. Considering 4 wt% of water dissolved in the trachytic melt, the protracted crystallization to generate a pantellerite liquid derivate [~80% of crystallization;

White et al., 2009, Romano et al., 2018] will lead to an excess of volatiles in the magmatic system and a consequent outgassing of volatiles, which could be the deep source of the diffusive degassing observed at Pantelleria nowadays.

Considering now the results of phase equilibria obtained on representative trachyte and pantellerite magmas, the magmatic felsic system of Pantelleria is inferred to evolve close to water saturation conditions, water and chlorine (during the late stage of evolution) being the dominant volatile species [Lanzo et al., 2013]. Evolution at volatile saturation conditions has been recently proposed for similar peralkaline magmatic systems elsewhere [Iddon and Edmonds, 2020] with reservoirs located at pressures <200 MPa. Using the highest water content measured in trachytic and pantelleritic melt inclusions at Pantelleria (water is the main volatile component, with no detectable CO₂), the model of Papale et al. [2006] gives storage pressures between 55 and 75 MPa for trachyte and pantellerite, respectively. Our experimental data constrain a pressure range between 70 and 110 MPa, or values which are 30% higher. Evolution of peralkaline felsic magmas in shallow reservoirs around 100 MPa is suggested by phase equilibrium and geophysical constraints [e.g. Di Carlo et al., 2010, Mattia et al., 2007]. Although such a difference might appear small, it corresponds to a difference of the top-depth of magma storage region (calculated assuming an average crustal density of 2600 kg·m⁻³) of ~1 km. Underestimating by ~1 km the depth of magma storage region in a shallow volcanic system such as Pantelleria might have important consequences with regard to volcanic hazard issues; for instance, it will affect the estimated travel time needed for the magma to breach the surface. The difference in solubilities may also affect the magma porosity evolution during magma ascent as simulated in numerical models, with an obvious impact on the explosive-effusive transition: the critical porosity of 70% beyond which fragmentation of an ascending magma might occur, will happen at deeper levels in a model using our solubility data instead of that of Di Matteo et al. [2004]. This underscores the importance of using accurate volatile solubility laws, hence the need to carry out specific hydrothermal experiments on representative compositions, if those laws are not available or if models are used too far from the compositional calibrated range.

6. Conclusions

This study was aimed at constraining the water solubility in trachyte and pantellerite melts from Pantelleria island. It is largely accepted that the solubility of water in silicate melt is composition-specific not only at the broad scale (silica-rich, silica-poor magmas) but also for variations in major element abundance within the same magma type (for instance, Pantelleria trachyte and Campi Flegrei trachyte). We thus performed this experimental study in order to add to the existing experimental data set on water solubility in felsic magmas, the missing data for trachytes straddling the chemical divide that separates metaluminous from peralkaline magmas. Our results place tighter constraints on water solubility-related arguments specific to eruptive phenomena (eruption style, pre-eruptive conditions, magmatic outgassing) but also on fundamental petrogenetic processes in which dissolved water plays a role (i.e. liquid line of descent oriented towards pantellerite melts).

Experiments were carried out in a pressure range 50–300 MPa in an IHPV, with only H₂O as the sole volatile component. The FT-IR study of experimental glasses resulted in the definition of the following molar absorptivity coefficients $\epsilon_{4500} = 0.88 \text{ L/mol}\cdot\text{cm}^{-1}$ and $\epsilon_{5200} = 1.6 \text{ L/mol}\cdot\text{cm}^{-1}$ for trachyte and $\epsilon_{4500} = 1.21 \text{ L/mol}\cdot\text{cm}^{-1}$ and $\epsilon_{5200} = 1.89 \text{ L/mol}\cdot\text{cm}^{-1}$ for pantellerite glasses. Absorption coefficients are different from those estimated in other trachyte [Di Matteo *et al.*, 2004, Fanara *et al.*, 2015] or phonolite [Carroll and Blank, 1997] melt compositions, and hence contribute to define an important composition-specific variable needed for FT-IR studies of such melt compositions.

Our experimental data were tested against the models of Moore *et al.* [1998], Papale *et al.* [2006] and Ghiorso and Gualda [2015]. The Papale *et al.* [2006] model overestimates the H₂O_{melt} content for Na-rich magma, such as Pantelleria felsic magmas. This effect has significant implications when applied to the study of melt inclusions, whose volatile abundances are used to derive the depth of magma storage region. In the specific case of Pantelleria, trachyte and pantellerite storage pressure derived from the model of Papale *et al.* [2006] are about 50–70 MPa, for a dissolved H₂O content in the range 3.4–4.5 wt%, which implies a magma storage depth of ~2.4 km. Using our experimental solubility model the calculated depth

increases to ~3.5 km, a 30% difference, not trivial for such shallow magma bodies.

Acknowledgements

PR is deeply grateful for all the support received from the “MagmaTeam” of ISTO during the experimental work. IDC and JA acknowledge support from both LabEx VOLTAIRE (LABX-100-01) and EquipEx PLANEX (ANR-11-EQPX-0036) projects. The authors thank Paola Stabile and Michael R. Carroll for their thorough and helpful comments.

References

- Arzilli, F., Stabile, P., Fabbrizio, A., Landi, P., Scaillet, B., Paris, E., and Carroll, M. R. (2020). Crystallization kinetics of alkali feldspar in peralkaline rhyolitic melts: implications for Pantelleria volcano. *Front. Earth Sci.*, 8, article no. 177.
- Behrens, H. and Jantos, N. (2001). The effect of anhydrous composition on water solubility in granitic melts. *Am. Mineral.*, 86, 14–20.
- Behrens, H., Meyer, M., Holtz, F., Benne, D., and Nowak, M. (2001). The effect of alkali ionic radius, temperature and pressure on the solubility of water in MAISI3O8 melts (M = Li, Na, K, Rb). *Chem. Geol.*, 174, 275–289.
- Behrens, H., Misiti, V., Freda, C., Vetere, E., Botcharnikov, R., and Scarlato, P. (2009). Solubility of H₂O and CO₂ in ultrapotassic melts at 1200 and 1250 °C and pressure from 50 to 500 MPa. *Am. Mineral.*, 94, 105–120.
- Behrens, H., Ohlhorst, S., Holtz, F., and Champenois, M. (2004). CO₂ solubility in dacitic melts equilibrated with H₂O–CO₂ fluids: implications for modeling the solubility of CO₂ in silicic melts. *Geochim. Cosmochim. Acta*, 68, 4687–4703.
- Behrens, H., Romano, C., Nowak, M., Holtz, F., and Dingwell, D. B. (1996). Near-infrared spectroscopic determination of water species in glasses of the system MAISI3O8 (M = Li, Na, K): an interlaboratory study. *Chem. Geol.*, 128, 41–63.
- Botcharnikov, R. E., Behrens, H., and Holtz, F. (2006). Solubility and speciation of C–O–H fluids in andesitic melt at T = 1100–1300 °C and P = 200 and 500 MPa. *Chem. Geol.*, 229, 125–143.

- Carroll, M. R. and Blank, J. G. (1997). The solubility of H₂O in phonolitic melts. *Am. Mineral.*, 82, 1111–1115.
- Cashman, K. V. and Mangan, M. T. (1994). Physical aspects of magmatic degassing II: Constraints on vesiculation processes from textural studies of eruptive products. In Carroll, M., editor, *Volatiles in Magmas*, pages 447–478. Mineralogical Society of America.
- Cassidy, M., Manga, M., Cashman, K., and Bachmann, O. (2018). Controls on explosive-effusive volcanic eruption styles. *Nat. Commun.*, 9, article no. 2839.
- Di Carlo, I., Rotolo, S. G., Scaillet, B., Bucchini, V., and Pichavant, M. (2010). Phase equilibrium constraints on pre-eruptive conditions of recent felsic explosive volcanism at Pantelleria Island, Italy. *J. Petrol.*, 51, 2245–2276.
- Di Matteo, V., Carroll, M. R., Behrens, H., Vetere, F., and Brooker, R. A. (2004). Water solubility in trachytic melts. *Chem. Geol.*, 213, 189–196.
- Dingwell, D. B., Holtz, F., and Behrens, H. (1997). The solubility of H₂O in peralkaline and peraluminous melts. *Am. Mineral.*, 82, 434–437.
- Dingwell, D. B., Romano, C., and Hess, K. U. (1996). The effect of water on the viscosity of haplogranitic melt under P–T–X conditions relevant to silicic volcanism. *Contrib. Mineral. Petrol.*, 124, 19–28.
- Dixon, T. E., Stolper, E., and Holloway, J. R. (1995). An experimental study of water and carbon dioxide solubilities in mid-ocean basalt liquids: Part I. Calibration and solubility models. *J. Petrol.*, 36, 1607–1631.
- Fanara, S., Botcharnikov, R. E., Palladino, D. M., Adams, F., Buddensieck, J., Mulch, A., and Behrens, H. (2015). Volatiles in magmas related to the Campanian Ignimbrite eruption: Experiments vs. natural findings. *Am. Mineral.*, 100, 2284–2297.
- Ghiorso, M. S. and Gualda, G. A. R. (2015). An H₂O–CO₂ mixed fluid saturation model compatible with rhyolite-Melts. *Contrib. Mineral. Petrol.*, 169, article no. 53.
- Hamilton, D. L., Burnham, C. W., and Osborn, E. F. (1964). The solubility of water and effects on fugacity and water content on crystallization in mafic magmas. *J. Petrol.*, 5, 21–39.
- Holtz, F., Behrens, H., Dingwell, D. B., and Johannes, W. (1995). H₂O solubility in haplogranitic melts: compositional, pressure and temperature dependence. *Am. Mineral.*, 80, 94–108.
- Holtz, F., Behrens, H., Dingwell, D. B., and Taylor, R. P. (1992). Water solubility in aluminosilicate melts of haplogranite composition at 2 Kbar. *Chem. Geol.*, 96, 289–302.
- Holtz, F., Roux, J., Behrens, H., and Pichavant, M. (2000). Water solubility in silica and quartzofeldspathic melts. *Am. Mineral.*, 85, 682–686.
- Housh, T. B. and Luhr, J. F. (1991). Plagioclase-melt equilibria in hydrous systems. *Am. Mineral.*, 76, 477–492.
- Iacono-Marziano, G., Schmidt, B. C., and Dolfi, D. (2007). Equilibrium and disequilibrium degassing of a phonolitic melt (Vesuvius A.D. 79 “White Pumice”) simulated by decompression experiments. *J. Volcanol. Geoth. Res.*, 161, 151–164.
- Iddon, F. and Edmonds, M. (2020). Volatile-rich magmas distributed through the upper crust in the main Ethiopian rift. *Geochem. Geophys. Geosyst.*, 21.
- Johannes, W. and Holtz, F. (1996). Petrogenesis and experimental petrology of granitic rocks. In *Minerals and Rocks*, volume 22. Springer Verlag, Berlin. 335 pp.
- Lanzo, G., Landi, P., and Rotolo, S. G. (2013). Volatiles in pantellerite magmas: A case study of the Green Tuff Plinian eruption (Island of Pantelleria, Italy). *J. Volcanol. Geoth. Res.*, 262, 153–163.
- Larsen, J. F. and Gardner, J. E. (2004). Experimental study of water degassing from phonolite melts: implications for volatile oversaturation during magmatic ascent. *J. Volcanol. Geoth. Res.*, 134, 109–124.
- Lesne, P., Scaillet, B., Pichavant, M., Iacono-Marziano, G., and Beny, J. M. (2010). The H₂O solubility of alkali basalts: an experimental study. *Contrib. Mineral. Petrol.*, 162, 133–151.
- Liu, Y., Zhang, Y., and Behrens, H. (2005). Solubility of H₂O in rhyolitic melts at low pressures and a new empirical model for mixed H₂O–CO₂ solubility in rhyolitic melts. *J. Volcanol. Geoth. Res.*, 143, 219–235.
- Macdonald, R. (1974). Nomenclature and petrochemistry of the peralkaline oversaturated extrusive rocks. *Bull. Volcanol.*, 38, 498–505.
- Mandeville, C. W., Webster, J. D., Rutherford, M. J.,

- Taylor, B. E., Timbal, A., and Faure, K. (2002). Determination of molar absorptivities for infrared absorption bands of H₂O in andesitic glasses. *Am. Mineral.*, 87, 813–821.
- Mattia, M., Bonaccorso, A., and Guglielmino, F. (2007). Ground deformations in the island of Pantelleria (Italy): insights into the dynamic of the current intereruptive period. *J. Geophys. Res.*, 112, article no. B11406.
- Moore, G., Vennemann, T., and Carmichael, I. S. E. (1998). An empirical model for the solubility of H₂O in magmas to 3 kilobars. *Am. Mineral.*, 83, 36–42.
- Moretti, R., Metrich, N., Arienzo, I., Di Renzo, V., Aiuppa, A., and Allard, P. (2018). Degassing vs. eruptive styles at Mt Etna volcano (Sicily, Italy). Part I: Volatile stocking, gas fluxing, and the shift from low-energy to highly explosive basaltic eruptions. *Chem. Geol.*, 482, 1–17.
- Morgan, G. B. and London, D. (2005). Effect of current density on the electron microprobe analysis of alkali aluminosilicate glasses. *Am. Mineral.*, 90, 1131–1138.
- Moussallam, Y., Morizet, Y., Massuyeau, M., Lauzonier, M., and Gaillard, F. (2015). CO₂ solubility in kimberlite melts. *Chem. Geol.*, 418, 198–205.
- Mysen, B. O. (2002). Water in peralkaline aluminosilicate melts to 2 GPa and 1400 °C. *Geochim. Cosmochim. Acta*, 66, 2915–2918.
- Neave, D. A., Fabbro, G., Herd, R. A., Petrone, C. M., and Edmonds, M. (2012). Melting, differentiation and degassing at the Pantelleria volcano, Italy. *J. Petrol.*, 53, 637–663.
- Nowak, M. and Behrens, H. (1995). The speciation of water in haplogranitic glasses and melts determined by in situ near-infrared spectroscopy. *Geochim. Cosmochim. Acta*, 59, 504–511.
- Ochs, F. A. and Lange, R. A. (1999). The density of hydrous magmatic liquids. *Science*, 283, 1314–1317.
- Ohlhorst, S., Behrens, H., and Holtz, F. (2001). Compositional dependence of molar absorptivities of near-infrared OH- and H₂O bands in rhyolitic to basaltic glasses. *Chem. Geol.*, 174, 5–20.
- Papale, P., Moretti, R., and Barbato, D. (2006). The compositional dependence of the saturation surface of H₂O + CO₂ fluids in silicate melts. *Chem. Geol.*, 229, 78–95.
- Richet, P., Lejeune, A. M., Holtz, F., and Roux, J. (1996). Water and the viscosity of andesite melts. *Chem. Geol.*, 128, 185–197.
- Romano, C., Dingwell, D. B., Behrens, H., and Dolfi, D. (1996). Compositional dependence of H₂O solubility along the joins NaAlSi₃O₈–KAlSi₃O₈, NaAlSi₃O₈–LiAlSi₃O₈, and KAlSi₃O₈–LiAlSi₃O₈. *Am. Mineral.*, 81, 452–461.
- Romano, P., Andújar, J., Scaillet, B., Romengo, N., Di Carlo, I., and Rotolo, S. G. (2018). Phase equilibria of Pantelleria trachytes (Italy): Constraints on pre-eruptive conditions and on the metaluminous to peralkaline transition in silicic magmas. *J. Petrol.*, 59, 559–588.
- Romano, P., Scaillet, B., White, J. C., Andujar, J., Di Carlo, I., and Rotolo, S. G. (2020). Experimental and thermodynamic constraints on mineral equilibrium in pantelleritic magmas. *Lithos*, 376–377, 1–22.
- Romano, P., White, J. C., Ciulla, A., Di Carlo, I., D’Oriano, C., Landi, P., and Rotolo, S. G. (2019). Volatiles and trace elements content in melt inclusions from the zoned Green Tuff ignimbrite (Pantelleria, Sicily): petrological inferences. *Ann. Geophys.*, 62(1).
- Scaillet, B. and Macdonald, R. (2006). Experimental constraints on pre-eruption conditions of pantelleritic magmas: evidence from the Eburreu complex, Kenya Rift. *Lithos*, 91, 95–108.
- Scaillet, B., Pichavant, M., and Roux, J. (1995). Experimental crystallization of leucogranite magmas. *J. Petrol.*, 36, 635–705.
- Scaillet, B., Pichavant, M., Roux, J., Humbert, G., and Lefèvre, A. (1992). Improvements of the Shaw membrane technique for measurement and control of fH₂ at high temperatures and pressures. *Am. Mineral.*, 77, 647–655.
- Schmidt, B. C. and Behrens, H. (2008). Water solubility in phonolite melts: Influence of melt composition and temperature. *Chem. Geol.*, 256, 258–267.
- Silver, L. A., Ihinger, P. D., and Stolper, E. (1990). The influence of bulk composition on the speciation of water in silicate glasses. *Contrib. Mineral. Petrol.*, 104, 142–162.
- Sisson, T. W. and Grove, T. L. (1993). Experimental investigation of the role of H₂O in calcalkaline differentiation and subduction zone magmatism. *Con-*

- trib. Mineral. Petrol.*, 113, 143–166.
- Stabile, P., Appiah, E., Bello, M., Giuli, G., Paris, E., and Carrol, M. R. (2020). New IR spectroscopic data for determination of water abundances in hydrous pantelleritic glasses. *Am. Mineral.*, 105, 1060–1068.
- Stabile, P., Radica, F., Bello, M., Behrens, H., Carroll, M. R., Paris, E., and Giuli, G. (2018). H₂O solubility in pantelleritic melts: Pressure and alkali effects. *Neues Jahrbuch für Mineralogie—Abhandlungen*, 195, 1–9.
- Stolper, E. (1982). The speciation of water in silicate melts. *Geochim. Cosmochim. Acta*, 46, 2609–2620.
- Tamic, N., Behrens, H., and Holtz, F. (2001). The solubility of H₂O and CO₂ in rhyolitic melts in equilibrium with a mixed CO₂–H₂O fluid phase. *Chem. Geol.*, 174, 333–347.
- Watson, E. B. (1994). Diffusion in volatile-bearing magmas. In Carroll, M. R. and Holloway, J. R., editors, *Volatiles in Magmas*, volume 30 of *Review in Mineralogy*, pages 371–411. Mineralogical Society of America.
- White, J. C., Parker, D. F., and Ren, M. (2009). The origin of trachyte and pantellerite from Pantelleria, Italy: insights from major element, trace element, and thermodynamic modelling. *J. Volcanol. Geoth. Res.*, 179, 33–55.
- Withers, A. C. and Behrens, H. (1999). Temperature induced changes in the NIR spectra of hydrous albitic and rhyolitic glasses between 300 and 100 K. *Phys. Chem. Minerals*, 27, 119–132.
- Xue, Y. and Kanzaki, M. (2004). Dissolution mechanism of water in depolymerised silicate melts: constraints from H and Si NMR spectroscopy and ab initio calculations. *Geochim. Cosmochim. Acta*, 68, 5027–5058.
- Yamashita, S. (1999). Experimental study of the effect of temperature on water solubility in natural rhyolite melt to 100 MPa. *J. Petrol.*, 40, 1497–1507.
- Zhang, Y. (1994). Reaction kinetics, geospeedometry, and relaxation theory. *Earth Planet. Sci. Lett.*, 122, 373–391.
- Zhang, Y. (1999). H₂O in rhyolitic glasses and melts: measurement, speciation, solubility, and diffusion. *Rev. Geophys.*, 37, 493–516.
- Zhang, Y., Stolper, E. M., and Ihinger, P. D. (1995). Kinetics of reaction H₂O + O = 2OH in rhyolitic glasses: Preliminary results. *Am. Mineral.*, 80, 593–612.

Comptes Rendus

Géoscience

Objet de la revue

Les *Comptes Rendus Géoscience* sont une revue électronique évaluée par les pairs de niveau international, qui couvre l'ensemble des domaines des sciences de la Terre et du développement durable. Ils publient des articles originaux de recherche, des articles de revue, des mises en perspective historiques, des textes à visée pédagogique ou encore des actes de colloque, sans limite de longueur, en anglais ou en français. Les *Comptes Rendus Géoscience* sont diffusés selon une politique vertueuse de libre accès diamant, gratuit pour les auteurs (pas de frais de publication) comme pour les lecteurs (libre accès immédiat et pérenne).

Directeur de la publication : Étienne Ghys

Rédacteurs en chef : Éric Calais, Michel Campillo, François Chabaux, Ghislain de Marsily

Comité éditorial : Jean-Claude André, Pierre Auger, Mustapha Besbes, Sylvie Bourquin, Yves Bréchet, Marie-Lise Chanin, Philippe Davy, Henri Décamps, Sylvie Derenne, Michel Faure, François Forget, Claude Jaupart, Jean Jouzel, Eric Karsenti, Amaëlle Landais, Sandra Lavorel, Yvon Le Maho, Mickaele Le Ravalec, Hervé Le Treut, Benoit Noetinger, Carole Petit, Valérie Plagnes, Pierre Ribstein, Didier Roux, Bruno Scaillet, Marie-Hélène Tusseau-Vuillemin, Élisabeth Vergès

Secrétaire éditoriale : Adenise Lopes

À propos de la revue

Toutes les informations concernant la revue, y compris le texte des articles publiés qui est en accès libre intégral, figurent sur le site <https://comptes-rendus.academie-sciences.fr/geoscience/>.

Informations à l'attention des auteurs

Pour toute question relative à la soumission des articles, les auteurs peuvent consulter le site <https://comptes-rendus.academie-sciences.fr/geoscience/>.

Contact

Académie des sciences
23, quai de Conti, 75006 Paris, France
Tél. : (+33) (0)1 44 41 43 72
CR-Geoscience@academie-sciences.fr



Les articles de cette revue sont mis à disposition sous la licence
Creative Commons Attribution 4.0 International (CC-BY 4.0)
<https://creativecommons.org/licenses/by/4.0/deed.fr>

COMPTES RENDUS DE L'ACADÉMIE DES SCIENCES

Géoscience Sciences de la Planète

Volume 353, n° S2, 2021

Special issue / Numéro thématique

Perspectives on alkaline magmas / *Perspectives sur les magmas alcalins*

Guest editor / Rédacteur en chef invité

Bruno Scaillet (Institut des Sciences de la Terre d'Orléans, CNRS, France)

Cover illustration / Illustration de couverture

© Bruno Scaillet, in "Perspectives on alkaline magmas", p. 3

Bruno Scaillet

Perspectives on alkaline magmas 1-5

Ray Macdonald, John C. White, Harvey E. Belkin

Peralkaline silicic extrusive rocks: magma genesis, evolution, plumbing systems and eruption 7-59

Violaine Sautter, Valerie Payre

Alkali magmatism on Mars: an unexpected diversity 61-90

Daniele Maestrelli, Giacomo Corti, Marco Bonini, Domenico Montanari, Federico Sani

Caldera collapse and tectonics along the Main Ethiopian Rift: reviewing possible relationships 91-109

Silvio G. Rotolo, Stéphane Scaillet, Fabio Speranza, John C. White, Rebecca Williams, Nina J. Jordan

Volcanological evolution of Pantelleria Island (Strait of Sicily) peralkaline volcano: a review 111-132

Nina J. Jordan, John C. White, Ray Macdonald, Silvio G. Rotolo

Evolution of the magma system of Pantelleria (Italy) from 190 ka to present 133-149

Paola Stabile, Fabio Arzilli, Michael Robert Carroll

Crystallization of peralkaline rhyolitic magmas: pre- and syn-eruptive conditions of the Pantelleria system 151-170

Ray Macdonald, Boguslaw Bagiński, Marcin Stachowicz, Harvey E. Belkin, Jan Pawłowski, Jakub Kotoski

Magma mixing and exsolution phenomena in peralkaline rhyolites: insights from the Gold Flat Tuff, Nevada 171-186

Ali Akbar Khezerlou, Michel Grégoire, Nasir Amel, Mohsen Moayyed, Ahmad Jahangiri, Mohammad Kilzi

Whole rock and mineral chemistry of hornblenditic xenoliths in volcanic alkaline rocks from the northern part of Uromieh Dokhtar magmatic belt (NW Iran) 187-215

Valentin Mollé, Fabrice Gaillard, Zineb Naby, Johann Tuduri, Ida Di Carlo, Saskia Erdmann

Crystallisation sequence of a REE-rich carbonate melt: an experimental approach 217-231

Zineb Naby, Fabrice Gaillard, Johann Tuduri, Ida Di Carlo

No direct effect of F, Cl and P on REE partitioning between carbonate and alkaline silicate melts 233-272

Lydéric France, Florian Brouillet, Sarah Lang

Early carbonatite magmatism at Oldoinyo Lengai volcano (Tanzania): carbonatite-silicate melt immiscibility in Lengai I melt inclusions 273-288

María Jiménez-Mejías, Joan Andújar, Bruno Scaillet, Ramón Casillas

Experimental determination of H₂O and CO₂ solubilities of mafic alkaline magmas from Canary Islands 289-314

Pierangelo Romano, Ida Di Carlo, Joan Andújar, Silvio G. Rotolo

Water solubility in trachytic and pantelleritic melts: an experimental study 315-331

1778-7025 (electronic)

COMPTES RENDUS
DE L'ACADÉMIE DES SCIENCES

Géoscience Volume 353, n° S2, 2021